APPLIED AND NUMERICAL HARMONIC ANALYSIS

BIRKHÄUSER

Qian Tao
Vai Mang I
Xu Yuesheng
Editors

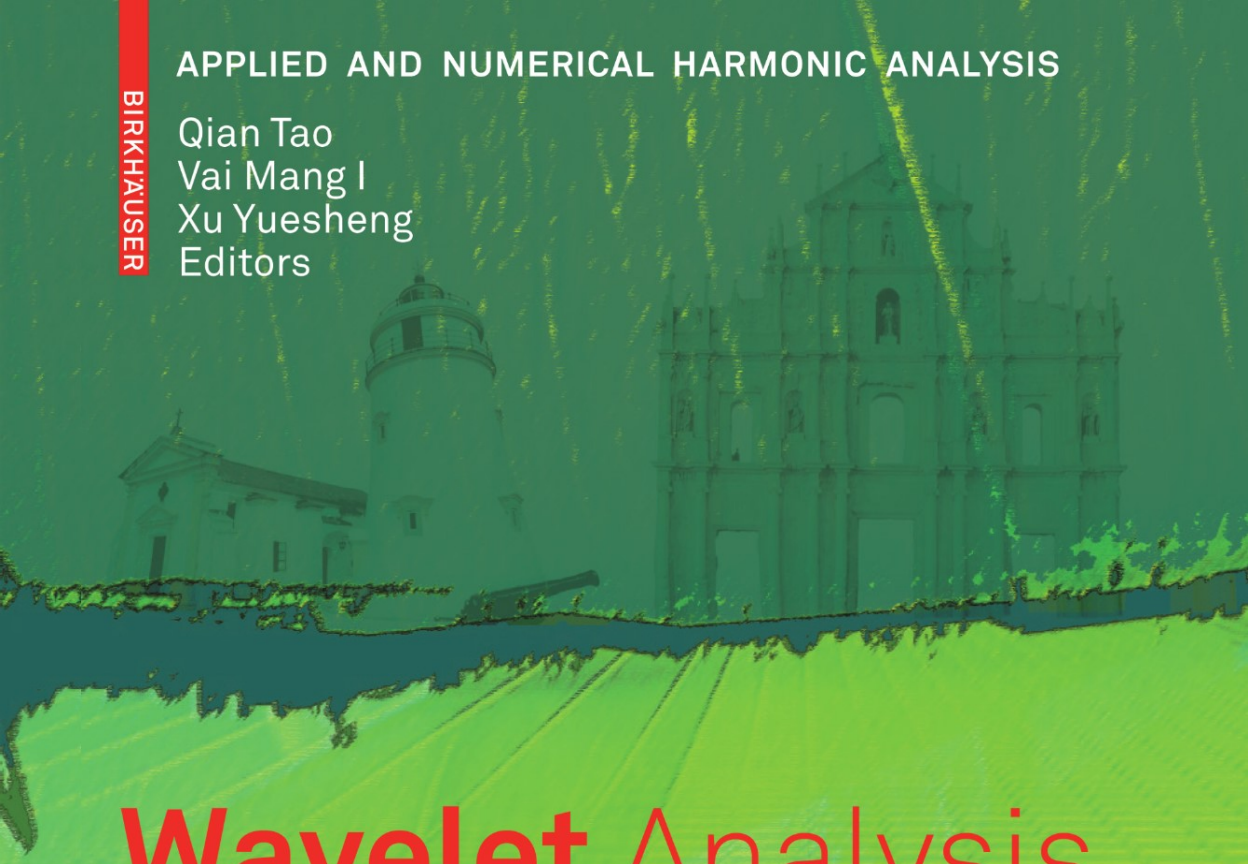

Wavelet Analysis and Applications

BIRKHÄUSER

Applied and Numerical Harmonic Analysis

Wavelet Analysis and Applications

Qian Tao
Vai Mang I
Xu Yuesheng
Editors

Birkhäuser Verlag
Basel · Boston · Berlin

Autoren:

Qian Tao
Vai Mang I
Faculty of Science and Technology
University of Macau
P.O. Box 3001
Macau

Xu Yuesheng
Department of Mathematics
215 Carnegie Hall
Syracuse University
Syracuse, NY 13244-1150
USA

2000 Mathematical Subject Classification 03H05, 26E35, 46S20 (primary); 03C20, 03C62, 03C98, 26A03, 46A99, 46B08, 46M07, 54A99, 54E15 (secondary)

Library of Congress Control Number: 2006936001

Bibliographic information published by Die Deutsche Bibliothek
Die Deutsche Bibliothek lists this publication in the Deutsche Nationalbibliografie; detailed bibliographic data is available in the Internet at <http://dnb.ddb.de>.

ISBN 978-3-7643-7777-9 Birkhäuser Verlag, Basel – Boston – Berlin

ISBN 10: 3-7643-7777-1
ISBN 13: 978-3-7643-7777-9
e-ISBN-10: 3-7643-7778-X
e-ISBN-13: 978-3-7643-7778-6

9 8 7 6 5 4 3 2 1 www.birkhauser.ch

Dedicated to

Professor Rui Paulo da Silva Martins

Preface

The 41 articles collected in this volume are selected from 170 submissions to the conference Wavelet Analysis and Applications 2005 (WAA2005) held during the 29th November to the 2nd December, 2005, at University of Macau. The articles selected are the outgrowth and further development of the talks presented at the conference by international participants from 22 different countries and areas, including Australia, Belgium, Brazil, China, Ethiopia, France, Germany, India, Iran, Hong Kong, Japan, Korea, Macao, Malaysia, Mexico, Portugal, Russia, Taiwan, Thailand, Tunisia, UK, United States, and in both the applied and pure mathematics fields. Most of them are up-to-date new research. We include a number of comprehensive surveys, also containing new results, in several particular areas of research. All the papers are strictly refereed. This volume reflects some of the latest development in the area of wavelet analysis and its applications. It contains two major components: Part I - Wavelet Theory, and Part II - Wavelet Applications. We note that for the reader's convenience the book contains a colored-printed RAM disc although the book itself is in black and white.

There are four chapters in Part I on wavelet theory. In Chapter one, we include seven articles on approximation theory and Fourier analysis. In a paper by S. K. Bloshanskaya and I. L. Bloshanskii some local smoothness conditions are obtained in order to guarantee convergence almost everywhere on some sets of positive measure of the double Walsh-Fourier series summed over rectangles. We also include a paper by the latter in which the problem on convergence of Fourier series of composed function $f \circ m$, where m is a linear transformation, is studied in terms of smoothness of the function f and properties of the transformation m. N. A. Sheikh in his article generalizes the Sidon inequality for the trigonometric system to wavelets and obtains convergence of wavelet series in the L^1 norm. The article of G-B. Ren and H. R. Malonek formulates and proves an extension of the Almansi decomposition for the iterated Dunkl-Helmholtz equation. Included in this chapter the article by M. G. Cowling and M. Sandari, and another by E. S. M. Hitzer and B. Mawardi, study Uncertainty Principles in different contexts. The former proves the Hardy's Uncertainty Principle for operators, and the latter proves an Uncertainty Principle for some Clifford geometric algebras based on Clifford Fourier Transformation.

Chapter two contains ten articles on frame theory and construction of wavelets. In the paper by H-X. Cao and B-M. Yu, wavelet theory for general Hilbert spaces is formulated. In the paper of C-Y. Li and H-X. Cao close relationship between

operator frames for bounded linear operators on a Hilbert space and the usual frames for the Hilbert space is studied. D. R. Larson in his paper presents, as an application of operator algebra, a profound operator-interpolation approach to wavelet theory in separable Hilbert spaces by using the local commutant of a unitary system. In other articles G. Wang and Z-X. Cheng study the stability of multi-wavelet frames; J-W. Yang, Y-Y. Tang, Z-X. Cheng and X-G. You construct bi-orthogonal wavelets from two-dimensional interpolatory functions; X-X. Feng, Z-X. Cheng and Z-P. Yang obtain a complete parametrization for the M-channel FIR orthogonal filter bank with linear phase while the number of the required parameters is reduced to $(N = 2)(\frac{M}{2})$; Y. Li, Z-D. Deng and Y-C. Liang study multivariate orthonormal wavelets with trigonometric vanishing moments and propose a practical construction algorithm; Z. Yao, N. Rajpoot and R. Wilson study multiscale directional cosine transform and multiscale Fourier transform in order to effectively describe oriented features and linear discountinuities in image processing; P. Cerejeiras, M. Ferreira and U. Kähler present a group-theoretical approach for the continuous wavelet transform on the sphere S^{n-1} based on the Lorentz group $\mathrm{Spin}(1, n)$ that provides different representations for the Hilbert space $L^2(S^{n-1})$ and the Hardy space $H^2(S^{n-1})$; finally, F. Brackx, N.D. Schepper and F. Sommen present their study on Clifford-Jacobi polynomials and the associated continuous wavelet transform in Euclidean spaces within the Clifford analysis framework.

Chapter three deals with fractal and multi-fractal theory, wavelet algorithms and wavelets in numerical analysis. In their comprehensive article S. Jaffard, B. Lashermes and P. Abry compare several multifractal formalisms based on wavelet coefficients from mathematical and numerical points of view, and show that the formalism has to be based on wavelet leaders in order to yield the entire and correct spectrum of Hölder singularities. K. Markwardt in his paper studies discrete embedding of system operators in identification models on the base of Fast Wavelet Transform. J. Bai and X-C. Feng in their paper propose a digital curvelet reconstruction algorithm to detect singularities in anisotropic images. H. Diao and Y. Wei study structured condition numbers for Toeplitz under-determined systems with full row rank, compared in the probability sense with unstructured condition numbers. J. Maes and A. Bultheel present their study on Powell-Sabin spline prewavelets on the hexagonal lattice, providing an explicit construction of compactly supported, two-dimensional, piecewise quadratic finite element space of $L^2(\mathbb{R}^2)$.

Chapter four is on time-frequency Analysis and adaptive representation of nonlinear and non-stationary signals. In his paper N. E. Huang introduces his empirical mode decomposition algorithm (EMD) and Hilbert spectral analysis (HHT), and briefly reviews the recent developments. He appeals for a mathematical foundation of the invented method. The article of Q-H. Chen, L-Q. Li and T. Qian shows that the non-linear Fourier atoms $e^{i\theta_a(t)}, |a| < 1$, which are the boundary values of the normalized Möbius transforms parameterized by the zeros of the transforms, form a Riesz basis, and possess a number of good properties including Shannon sampling. In his paper T. Qian reviews recent developments aiming to

establish mathematical foundation of EDM and HHT, and presents his new results on starlike mapping and constructing mono-components of the form $\rho(t)e^{i\theta_a(t)}$ for non-trivial $\rho(t) \geq 0$ without using Bedrosian's theorem.

In Part II on wavelet applications, in the paper by X-L. Tian, X-K. Li, Y-K. Sun and Z-S. Tang a new algorithm based on wavelet transform to transfer colors from images of Chinese Virtual Human Dada (CVHD) to Magnetic Resonance Images (MRI) is proposed and implemented. In their second paper a novel algorithm for the multimodalities medical images fusion based on wavelet transform is proposed and implemented. The paper by Y-Y. Qu, C-H. Li, N-N. Zheng, Z-J. Yuan and C-Y. Ye describes how wavelet transform may be used to detect salient building from a single nature image. In the paper of Y. Wu, X. Wang and G-S. Liao a despeckling method is proposed based on stationary wavelet transform (SWT) for synthetic aperture radar (SAR) images. In a paper by C-S. Tong and K-T. Leung, to reconstruct a high resolution image from a set of shifted and blurred low resolution images, a direct method based on Haar wavelet transform is proposed. In the paper of F-X. Yan, L-Z. Cheng and H-X. Wang, a design scheme for biorthogonal dual tree complex wavelet transform filter is proposed, and its implementation to iris image enhancement is presented. The other subjects include that the paper of S-K. Choy and C-S. Tong studies supervised learning using characteristic generalized Gaussian density and its applications to Chinese materia medica identification; T-Z. Tan and J-W. Huang propose an algorithm of singular points detection for fingerprint images by the Poincaré index method; G-J. Shi and S-L. Peng present a new receiver scheme for doubly-selective channels to combat the annoying Doppler diversity; by using the support vector machine method (SVM) C-F. Wong, J-K. Zhu, M-I. Vai, P-U. Mak and W-K. Ye present a face retrieval scheme based on lifting wavelets features; S-W. Pei, H-Y. Feng and M-H. Du propose a method based on a wavelet lifting scheme to increase the order of vanishing moments for high-resolution image reconstruction; B. Pradhan, K. Sandeep, S. Mansor, A.R. Ramli and A.R.B.M. Sharif in their paper study multiresolution spatial data compression using the lifting scheme; Y-Y. Ren, S. Wang, S-Y. Yang and L-C. Jiao put forward a method making use of ridgelet transform in remote sensing image recognition; Z-C. Cai, H. Ma, W. Sun and D-X. Qi present their analysis on frequency spectrum for geometric modelling of digital geometry; and, in the paper of M-H. Yang, Z-Y. Xiao and S-L. Peng they demonstrate a Hidden Markov Tree (HMT) model with localized parameters and a fast parameter estimation algorithm. Two papers on implementation of EMD and HHT are included of which one is by Z-H. Yang, L-H. Yang and D-X. Qi on detection of spindles in sleep EEGs; and the other by M. J. Brenner, S. L. Kukreja and R. J. Prazenica on the utility of the Hilbert-Huang algorithm for the analysis of aeroelastic flight data.

Since the corner-stone lecture of Yves Meyer presented in ICM1990, Kyoto, in some extent wavelet analysis in the last 15 years may be said to have been an applied and theoretical-applied area. Yet, we gladly noted that among the attendances of the conference a significant percentage were prominent mathematicians

working mainly in pure mathematical areas. This indicates that the concept of wavelets is one that stretches continuously across various disciplines of mathematics.

The idea of organizing the conference at University of Macau was first initialized by Daniel Chi Wai Tse, Chairman of University Council, and Rui Paulo da Silva Martins, Vice Rector of the university, that was endowed through Vai Pan Iu, Rector of the university, whose support made possible the success of the conference. The editors wish to sincerely thank the mentioned university leaders for their kind and generous support. This volume is specially designed to be dedicated to Rui Paulo da Silva Martins, for his unflagging support to mathematics in the university, including the conference. We are grateful to all the university staff members and those in the scientific and organization committees who made this conference possible. Finally, we sincerely thank the referees for their extremely valuable assistance in creating this volume. The publication of this volume is partially supported by Macao Science and Technology development Fund (FDCT) 051/2005/A.

Contents

Part 2. Wavelet Applications

Part 1. Wavelet Theory

Chapter 1: Approximation and Fourier Analysis

Wavelet Analysis and Applications
Tao Qian, Mang I. Vai and Xu Yuesheng, Eds.
Applied and Numerical Harmonic Analysis, 3–11

Local Smoothness Conditions on a Function Which Guarantee Convergence of Double Walsh-Fourier Series of This Function

S.K. Bloshanskaya and I.L. Bloshanskii

Abstract. The local smoothness conditions on a function are obtained, which guarantee convergence almost everywhere on some set of positive measure of the double Walsh-Fourier series of this function summed over rectangles.

Mathematics Subject Classification (2000). Primary 42C10; Secondary 42B05.

Keywords. Double Walsh-Fourier series, summation over rectangles, convergence almost everywhere, localization principle.

1. Discussion and Setting of the Problem

Studies on convergence (including convergence almost everywhere) of series with respect to the classical orthonormal systems (in particular, the trigonometric and the Walsh systems) is one of the central problems in the modern theory of Fourier series.

In the present paper we shall consider Fourier series with respect to the Walsh-Paley system (which have different applications and, in particular, are used in the digital data processing).

As it is known, in 1961 E.Stein [1] proved that the one-dimensional Walsh-Fourier series of a function $f \in L_1(\mathbb{I}^1)$, where $\mathbb{I}^1 = [0, 1)$, can unboundedly diverge almost everywhere (a.e.) on $\mathbb{I}^1$. Moreover, in 2004 S.V.Bochkarev [2] obtained the following result: there exists a function $f \in \Phi(\mathbb{I}^1) = \Phi_L(\mathbb{I}^1)$ (where $\Phi_u = u\varphi(u)$, and $\varphi(u)$ is a non-decreasing on $[0, \infty)$ function, $\varphi(0) = 1$ and $\varphi(u) = o((\log u)^{\frac{1}{2}})$ as $u \to \infty$), whose Walsh-Fourier series unboundedly diverges everywhere on $\mathbb{I}^1$. On the other hand, as it was proved in 2003 by P.Sjolin and F.Soria [3], if a

This work was supported by grant 05-01-00206 of the Russian Foundation for Fundamental Research.

function $f \in \mathcal{F}_1(\mathbb{I}^1) = L(\log^+ L)(\log^+ \log^+ \log^+ L)(\mathbb{I}^1)$ then Walsh-Fourier series of this function already converges a.e. on $\mathbb{I}^1$.

The question arises: if for some measurable set $E \subset \mathbb{I}^1$, $\mu E > 0$ (μ is the Lebesgue measure on line) a function $f \in \mathcal{F}_1(E) \cap \Phi(\mathbb{I}^1)$, or (in the "scale" of Lebesgue classes) a function $f \in L_p(E) \cap L_1(\mathbb{I}^1)$, $p > 1$, then what can be said about convergence a.e. of the one-dimensional Walsh-Fourier series of this function, in particular, about convergence a.e. on the set E (where the function f is "sufficiently smooth") or on some of its subsets $E_1 \subset E$, $\mu E_1 > 0$?

In this case, the following question naturally arises: what must be the structure of the set E – open, closed, G_δ, etc., what must be its boundary.

The analogous question can be posed as well for the N - dimensional ($N > 1$) Walsh-Fourier series, namely: on what measurable subsets $E \subset \mathbb{I}^N$, where $\mathbb{I}^N = [0,1)^N$ is the N-dimensional cube, it is possible to "localize" these or those conditions on a function f, defined on the whole $\mathbb{I}^N$, which "guarantee" convergence a.e. on the whole $\mathbb{I}^N$ of the multiple Walsh-Fourier series summed over rectangles. In the multiple case besides the question concerning the structural characteristics of the set E the question arises concerning the geometric characteristics of this set.

Denote as $\mathcal{F}(\mathbb{I}^N)$ the class of summable (on $\mathbb{I}^N$) functions such that for any f in this class ($f \in \mathcal{F}(\mathbb{I}^N)$) the multiple Walsh-Fourier series (summed over rectangles) of the function f converges a.e. on $\mathbb{I}^N$. So, we are interested in the question concerning correlation between the *structural and geometric characteristics of the set* E and the *smoothness of the function* in the framework of these or those subspaces $\mathcal{F}$ of the space L_1.

In the present paper we shall give some solutions of the posed question for double Walsh-Fourier series summed over rectangles.

As to the one-dimensional case, taking account of the classical principle of localization (see [4] or [5, p. 70])[1], and the mentioned earlier result by P.Sjolin and F.Soria [3], we can give a partial answer to the posed above question: for any open a.e.[2] set E, $E \subset \mathbb{I}^1$, $\mu E > 0$ and for any function $f \in \mathcal{F}_1(E) \cap \Phi(\mathbb{I}^1)$ (for any function $f \in L_p(E) \cap L_1(\mathbb{I}^1)$, $p > 1$) the one-dimensional Walsh-Fourier series of this function converges a.e. on the set E.

Note that in the setting of the problem we posed the question about convergence a.e. of Walsh-Fourier series in the classes $\mathcal{F}(E) \cap L_1(\mathbb{I}^1)$ on the set E (or on some of its subsets $E_1 \subset E$), and this is connected with the fact that outside the set E the Walsh-Fourier series of a function $f \in \mathcal{F}(E) \cap L_1(\mathbb{I}^1)$ can, in general, diverge. For example, it is not difficult to prove (taking account of [2] and [4]), that for any open set E with boundary of measure zero or for any closed set E, $E \subset \mathbb{I}^1$, $\mu E > 0$ there exists a function $f \in L_\infty(E) \cap \Phi(\mathbb{I}^1)$, whose Walsh-Fourier series unboundedly diverges a.e. outside the set E.

[1] Walsh-Fourier series of a function $f \in L_1(\mathbb{I}^1)$, $f(x) = 0$ on an open interval $J \subset \mathbb{I}^1$ converges uniformly to zero on each segment which is entirely contained in J.

[2] The set E is called *open a.e.*, if there exists an open set E_1 such that $\mu(E \triangle E_1) = 0$.

For trigonometric Fourier series investigations of this type were carried in the one-dimensional case by G.Alexits, N.K.Bari, S.B.Stechkin, P.L.Ul'yanov (see [6, p. 350-354]), and in the multi-dimensional case ($N > 1$) by I.L.Bloshanskii [7].

2. Notation

Let us denote as $\{\omega_n\}_{n=0}^{\infty} = \{\omega_n(x)\}_{n=0}^{\infty}$, $x \in [0,1) = \mathbb{I}^1$ the Walsh system in Paley enumeration (see, e.g., [5]), i.e. the system of functions constructed as follows. Let us consider the function

$$r_0(x) = \begin{cases} 1, & \text{for } x \in [0, \frac{1}{2}), \\ -1, & \text{for } x \in [\frac{1}{2}, 1). \end{cases}$$

Continue this function with period 1 to the entire number line and define the Rademacher system $\{r_k\}_{k=0}^{\infty}$ by setting $r_k(x) = r_0(2^k x)$, $k = 0, 1, \dots$.

Next, we represent each positive integer m as the sum $m = \sum_{i=0}^{k} \varepsilon_i 2^i$, with $\varepsilon_i = 0$ or 1 for $i = 0, 1, \dots, k-1$ and $\varepsilon_k = 1$.

The Walsh functions $\omega_m(x)$ are defined as follows: $\omega_0(x) \equiv 1$,

$$\omega_m(x) = \prod_{i=0}^{k} (r_i(x))^{\varepsilon_i}, \quad m = 1, 2, \dots .$$

Note that the system $\{\omega_n\}_{n=0}^{\infty}$ is orthonormal on $\mathbb{I}^1$ and complete in the space $L_p(\mathbb{I}^1)$ for each p, $1 \le p < \infty$.

Let $\mathbb{Z}^N$, $\mathbb{Z}^N \subset \mathbb{R}^N$, $N \ge 1$ be a set of all vectors with integer coordinates, assume $\mathbb{Z}_\alpha^N = \{n = (n_1, \dots, n_N) \in \mathbb{Z}^N : n_j \ge \alpha,\ j = 1, \dots, N\}$, $\alpha \in \mathbb{Z}^1$. Further, for $x = (x_1, \dots, x_N) \in \mathbb{I}^N$, where $\mathbb{I}^N = [0,1)^N$ and $k = (k_1, \dots, k_N) \in \mathbb{Z}_0^N$, denote as $\omega_k(x) = \omega_{k_1}(x_1) \times \dots \times \omega_{k_N}(x_N)$ the multiple Walsh-Paley system. Let a function $f \in L_1(\mathbb{I}^N)$ be expanded into a multiple Walsh-Fourier series with respect to the system $\{\omega_k\}_{k \in \mathbb{Z}_0^N}$:

$$f(x) \sim \sum_{k \in \mathbb{Z}_0^N} c_k \, \omega_k(x),$$

where

$$c_k = c_{k_1, \dots, k_N} = \int_{\mathbb{I}^N} f(x) \, \omega_k(x) \, dx \tag{1}$$

are Walsh-Fourier coefficients of the function f.

We consider the rectangular partial sum of this series

$$S_n(x; f) = \sum_{k_1=0}^{n_1-1} \dots \sum_{k_N=0}^{n_N-1} c_k \, w_k(x), \quad n = (n_1, \dots, n_N) \in \mathbb{Z}_1^N,$$

whose particular case is the square partial sum $S_{n_0}(x; f)$, when $n_1 = \dots = n_N = n_0$.

Let E be an arbitrary measurable set, $E \subset \mathbb{I}^N$, $\mu E > 0$ ($\mu = \mu_N$ is the N-dimensional Lebesque measure), and let $\mathcal{F}(E)$ be a subspace of $L_1(E)$ such

that the multiple Walsh-Fourier series (summed over rectangles) of any function $f \in \mathcal{F}(\mathbb{I}^N)$ converges a.e. on $\mathbb{I}^N$.

We study the behavior of $S_n(x; f)$ as $n \to \infty$, i.e. $\min_{1 \le j \le N} n_j \to \infty$ (or $S_{n_0}(x; f)$ as $n_0 \to \infty$) on $\mathbb{I}^N$ depending on the smoothness of the function f (i.e. on the type of the space $\mathcal{F}(\mathbb{I}^N)$) and on the structural and geometric characteristics of the set E.

3. Some Results on Convergence of Double Walsh-Fourier Series

For square summation the double Walsh-Fourier series (as follows from the result of F. Móricz, [8]) converges a.e. on $\mathbb{I}^2$ for functions in the class $L_2(\mathbb{I}^2)$, whereas for rectangular summation the double Walsh-Fourier series can diverge a.e. on $\mathbb{I}^2$ even for the continuous on $\mathbb{I}^2$ function (see the result of R.D.Getsadze [9]). From the theorem of E.M.Nikishin [10] concerning the Weyl multipliers (for convergence over rectangles of the double Fourier series with respect to the system of the form $\{\psi_{n_1}(x_1) \cdot \psi_{n_2}(x_2)\}_{n_1, n_2=1}^{\infty}$, where $\{\psi_{n_s}(x_s)\}_{n_s=1}^{\infty}$, $s = 1, 2$ is the orthonormal on a segment system of functions) and the result of P.Billard [11] concerning convergence of the one-dimensional Walsh-Fourier series of functions in L_2 it follows: if the following condition on Fourier coefficients (1) of the function $f \in L_2(\mathbb{I}^2)$ is true:

$$\sum_{k_1, k_2=0}^{\infty} |c_{k_1, k_2}|^2 \cdot \log^2[\min(|k_1|, |k_2|) + 2] < \infty, \tag{2}$$

then the double Walsh-Fourier series summed over rectangles of the function f converges a.e. on $\mathbb{I}^2$.

Let us note, that in solution of the problem (considered in the present paper) for one-dimensional Walsh-Fourier series we used (see section 1) the validity (for $N = 1$ in the class L_1) of the principle of the classical localization, which permits to state that for any open (nonempty) set $E \subset \mathbb{I}^1$ and for any function $f \in L_1(\mathbb{I}^1)$ such that $f(x) = 0$ on E

$$\lim_{n \to \infty} S_n(x; f) = 0 \quad \text{uniformly on any compact set} \quad K \subset E. \tag{3}$$

Unfortunately, for multiple (i.e. for $N \ge 2$) Fourier series (both with respect to the trigonometric system and to Walsh system) such localization is not true even for continuous functions (for more details see our papers [12], [13]).

Being in the framework of the classes $L_p(\mathbb{I}^N)$, $p \ge 1$ we "replaced" in (3) the uniform convergence by the convergence a.e., introducing the following concept of *the generalized localization almost everywhere* (see [14], [15][3]).

Let E, $E \subset \mathbb{I}^N$, $N \ge 1$ be an arbitrary set of positive measure. On the set E for multiple Fourier series of functions in the classes $L_p(\mathbb{I}^N)$, $p \ge 1$ *the generalized*

[3] In the paper [14] the concept of *the generalized localization a.e.* was introduced for trigonometric Fourier series.

localization almost everywhere is valid if for any function $f \in L_p(\mathbb{I}^N)$, $f(x) = 0$ on E the multiple Fourier series of the function f converges a.e. to zero on the set E.

In 1995 in [12] for $N = 2$ we proved the validity of the generalized localization a.e. for the double Walsh-Fourier series summed over rectangles on arbitrary open (open a.e.) set in the classes $L_p(\mathbb{I}^2)$, $p > 1$ (see [12, Theorem 1]).

Concerning the cases $N = 2$, $p = 1$ and $N > 2$, $p > 1$, in the same paper [12] (see also [15]) we ascertained the invalidity of the generalized localization a.e. in the indicated cases not only on the open sets, but also on any non-dense in $\mathbb{I}^N$ set.

Later in [16] (see also [17] and [18]) we (extending the notion of generalized localization a.e. on the Lebesgue-Orlicz classes) strengthened the result (of Theorem 1) of the paper [12], proving the following theorem

Theorem A. *Let E, $E \subset \mathbb{I}^2$ be an arbitrary open a.e. set, $\mu E > 0$. For any function $f \in L(\log^+ L)^2(\mathbb{I}^2)$, $f(x) = 0$ on E*

$$\lim_{n\to\infty} S_n(x; f) = 0 \quad \textit{almost everywhere on} \quad E.$$

Thus, for double Walsh-Fourier series summed over rectangles of the function in the classes $L(\log^+ L)^2(\mathbb{I}^2)$ the generalized localization a.e. is true on the open a.e. sets, but, as it was already said, the generalized localization a.e. is not true in the class $L_1(\mathbb{I}^2)$ on the wide class of sets, in particular, it is not true on the open sets.

Being again in the framework of classes $L_p(\mathbb{I}^N)$, $p \geq 1$, it was natural (the same way, as for the trigonometric system, see [15]) to pass to a more refined apparatus for studying the behavior of the Fourier series of a function f on the sets where f equals zero, namely, to the concept of "*the weak generalized localization a.e.*" (on the set E *the weak generalized localization almost everywhere* is true, if for any function $f \in L_p(\mathbb{I}^N)$, $f(x) = 0$ on E the multiple Fourier series of the function f converges a.e. to zero on some subset E_0, $E_0 \subset E$, $\mu E_0 > 0$).

In the paper [13] (see also [15], [18]) we obtained the criteria of the weak generalized localization a.e. in the class $L_1(\mathbb{I}^N)$, $N \geq 1$. For $N = 2$ let us formulate the particular case of this result (see [13, Theorem $2'$]), and for this let us give the following definitions.

Let us consider on the axis Ox_j an arbitrary (nonempty) open set $\Omega_j \subset \mathbb{I}^1$, $j = 1, 2$, and denote as W^0 and W the sets

$$W^0 = \left(\Omega_1 \times \mathbb{I}^1\right) \cap \left(\mathbb{I}^1 \times \Omega_2\right) \tag{4}$$

and

$$W = W(W^0) = \left(\Omega_1 \times \mathbb{I}^1\right) \cup \left(\mathbb{I}^1 \times \Omega_2\right). \tag{5}$$

We shall say that a set E possesses property $\mathbb{B}_1$ if there exists a set W of the form (5) such that $\mu(W \setminus E) = 0$; property $\mathbb{B}_1$ is property $\mathbb{B}_1(W^0)$ if $W = W(W^0)$.

Further, let us denote by $pr_{(x_j)}\{P\}$ the orthogonal projection of the set P, $P \subset I^2$ onto the axis Ox_j, $j = 1, 2$; by $int\,(P)$ the set of interior points of P; by $\overline{P}$ the closure of the set P and by $Fr\,P$ the boundary of P.

Let E be an arbitrary measurable set, $E \subset \mathbb{I}^2$, $\mu E > 0$. Let us denote $G = \mathbb{I}^2 \setminus E$ and consider the following two conditions on $Fr\, E$:

$$\mu\left(G \setminus \overline{int\,(G)}\ \right) = 0, \text{ [4]} \tag{6}$$

$$\mu_1\left(Fr\, pr_{(x_j)}\{int\,(G)\}\right) = 0, \quad j = 1, 2, \tag{7}$$

where $\mu = \mu_2$ is the measure on the plane, μ_1 is the measure on the line.

Theorem B. *Let E be an arbitrary measurable set, $E \subset \mathbb{I}^2$, $\mu E > 0$, and let $G = \mathbb{I}^2 \setminus E$.*

1. *If for some set W^0 of the form (4) the set E possesses property $\mathbb{B}_1(W^0)$, then for any function $f \in L_1(\mathbb{I}^2)$, $f(x) = 0$ on E*

$$\lim_{n\to\infty} S_n(x; f) = 0 \quad \textit{almost everywhere on} \quad W^0.$$

2. *Let in addition the set E satisfy conditions (6) and (7). If the set E does not possess property $\mathbb{B}_1$, then there exists a function $f^{(0)} \in L_1(\mathbb{I}^2)$, $f^{(0)}(x) = 0$ on E such that*

$$\overline{\lim_{n\to\infty}}\, |S_n(x; f^{(0)})| = +\infty \quad \textit{almost everywhere on} \quad \mathbb{I}^2.$$

4. Main Results

In the present paper, basing on Theorem A, we have obtained the result which shows possibility "to localize on an open a.e. subset" $E \subset \mathbb{I}^2$ condition (2) of convergence a.e. on the whole cube $\mathbb{I}^2$ of double Walsh-Fourier series.

Let E, $E \subset \mathbb{I}^2$ be an arbitrary set of positive measure. Assume

$$\mathcal{F}(E) = \left\{ f \in L_2(E) : \sum_{k_1,\, k_2=0}^{\infty} \left| \iint_E f(x_1,\, x_2)\, \omega_{k_1}(x_1)\, \omega_{k_2}(x_2)\, dx_1\, dx_2 \right|^2 \right.$$
$$\left. \times \log^2[\min(|k_1|,\, |k_2|) + 2] < +\infty \right\}.$$

Theorem 4.1. *Let E be an arbitrary open a.e. set, $E \subset \mathbb{I}^2$, $\mu E > 0$. For any function $f \in \mathcal{F}(E) \cap L_p(\mathbb{I}^2)$, $1 < p \le 2$*

$$\lim_{n\to\infty} S_n(x; f) = f(x) \quad \textit{almost everywhere on} \quad E.$$

Further, taking into account geometry of the set $E \subset \mathbb{I}^2$, and basing on Theorem B, we can get the following result, which shows under what conditions it is possible "to localize on some subset" of the set E condition (2) (of convergence a.e. on the whole cube $\mathbb{I}^2$ of the double Walsh-Fourier series) in the case when on the whole $\mathbb{I}^2$ the function is in the class L_1 only.

[4] In particular, the sets G such that $\mu\{int\, G\} = \mu G$ satisfy this condition; in it's turn the, last condition is true, for example, for an arbitrary open set.

Theorem 4.2. *Let E be an arbitrary measurable set, $E \subset \mathbb{I}^2$, $\mu E > 0$, with conditions on the boundary $Fr\, E$ – (6) and (7), and let the set E have an open (nonempty) subset E^0. For any function $f \in \mathcal{F}(E^0) \cap L(\log^+ L)^2(E) \cap L_1(\mathbb{I}^2)$,*

$$\lim_{n\to\infty} S_n(x; f) = f(x) \quad \text{almost everywhere on} \quad E^0 \subset W^0$$

if and only if the set E possesses property $\mathbb{B}_1(W^0)$, where

$$W^0 = \left(pr_{(x_1)}\{E^0\} \times \mathbb{I}^1\right) \cap \left(\mathbb{I}^1 \times pr_{(x_2)}\{E^0\}\right). \tag{8}$$

Remark 4.3. *In the part of sufficiency the result of Theorem 4.2 is true without the restrictions* (6) *and* (7).

Taking into account "more fine" structural and geometric characteristics of the sets E and E^0 (which appear in Theorem 4.2), it is possible to obtain the following result

Theorem 4.4. *Let E be an arbitrary measurable set, $E \subset \mathbb{I}^2$, $\mu E > 0$, with conditions on the boundary $Fr\, E$ – (6) and (7), and let E^0 be an open (nonempty) subset of E. If the set E possesses property $\mathbb{B}_1(W^0)$, where the set W^0 is defined in* (8)*, but for any set $\widetilde{W}^0$ of the form* (4) *such that $\mu(\widetilde{W}^0 \setminus W^0) > 0$ the set E does not possess property $\mathbb{B}_1(\widetilde{W}^0)$, then*

1. *If $\mu(\mathbb{I}^2 \setminus W^0) > 0$, then there exists a function $f \in \mathcal{F}(E^0) \cap L(\log^+ L)^2(E) \cap L_1(\mathbb{I}^2)$ such that*

$$\overline{\lim_{n\to\infty}} |S_n(x; f)| = +\infty \quad \text{almost everywhere on} \quad \mathbb{I}^2 \setminus W^0.$$

2. *If $\mu(W^0 \setminus E^0) > 0$, and $\mu\, Fr\, E^0 = 0$, then there exists a function $f^{(1)} \in \mathcal{F}(E^0) \cap L(\log^+ L)^2(E) \cap L_1(\mathbb{I}^2)$ such that*

$$\overline{\lim_{n\to\infty}} |S_n(x; f^{(1)})| = +\infty \quad \text{almost everywhere on} \quad \mathbb{I}^2 \setminus E^0.$$

And finally, let us once more turn our attention to the questions of convergence a.e. of Walsh-Fourier series in the classes $\mathcal{F}(E) \cap L_p(\mathbb{I}^N)$, $p \geq 1$, $N \geq 1$ outside the set E (see section 1), this time for $N = 2$. Basing on the result concerning general properties of sequences of linear operators obtained by I.L.Bloshanskii in [19] (see [19, Theorem 1]) and using the function constructed by R.D.Getsadze in [9] we can get the following result.

Theorem 4.5. *For any closed set $E \subset \mathbb{I}^2$, $\mu E > 0$ there exists a function $f \in L_\infty(\mathbb{I}^2)$, $f(x) = 0$ on E such that*

1. $\lim_{n\to\infty} S_n(x; f) = 0$ *almost everywhere on* E,
2. $\overline{\lim_{n\to\infty}} |S_n(x; f)| = +\infty$ *almost everywhere on* $\mathbb{I}^2 \setminus E$.

Remark 4.6. *For any (nonempty) open set E, $E \subset \mathbb{I}^2$ with the boundary of measure zero the result similar to the result of Theorem 4.5 directly follows from* [9] *and* [15].

References

[1] E. Stein, *On Limits of Sequences of Operators.* Ann. of Math. **74** (1961), 140–170.

[2] S. V. Bochkarev, *Everywhere Convergent Fourier Series with Respect to Walsh System and Multiplicative Systems.* Uspekhi-Mat.-Nauk **59** (2004) 103–124; English transl. in Russ. Math. Surv. **59** (2004).

[3] P. Sjölin, F. Soria, *Remarks on a Theorem by N. Y. Antonov.* Studia Math. **158** (2003), 79–97.

[4] N. J. Fine, *On the Walsh functions.* Trans. Amer. Math. Soc. **65** (1949), 372–414.

[5] F. Schipp, W. R. Wade, P. Simon, J. Pal, *Walsh Series: An Introduction to Dyadic Harmonic Analysis.* Budapest: Akad. Kiado (1990).

[6] N. K. Bari, *Trigonometric series.* Fizmatgiz, Moscow, 1961; English transl.: N. Bary, *A Treatise on Trigonometric Series.* Vols. I, II, Pergamon Press Oxford, and Macmillan, New York, 1964.

[7] I. L. Bloshanskii, *Structural and Geometric Characteristics of Sets of Convergence and Divergence of Multiple Fourier Series of Functions which Equal Zero on Some Set.* Intern. J. of Wavelets, Multiresolution and Inform. Processing **2** (2004), 187–195.

[8] F. Móricz, *On the Convergence of Double Orthogonal Series.* Anal. Math. **2** (1976), 287–304.

[9] R. D. Getsadze, *A Continuous Function with Multiple Fourier Series with Respect to the Walsh-Paley System which is Divergent Almost Everywhere.* Mat.Sb. **128** (1985), 269–286; English transl. in Math. USSR-Sb. **56** (1987).

[10] E. M. Nikishin, *Weyl Multipliers for Multiple Fourier Series.* Mat.Sb. **89** (1972), 340–348; English transl. in Math. USSR-Sb. **89** (1972).

[11] P. Billard, *Sur la Convergence Presque Partout des Series de Fourier-Walsh des Fonctions de l'Éspace $L_2([0,1])$.* Stud. Math. **28** (1966-1967) 363–388.

[12] S. K. Bloshanskaya, I. L. Bloshanskii, *Generalized Localization for Multiple Walsh-Fourier Series of Functions in L_p, $p \geq 1$.* Mat.Sb. **186** (1995), 21–36; English transl. in Math. USSR-Sb. **186** (1995).

[13] S. K. Bloshanskaya, I. L. Bloshanskii, *Weak Generalized Localization for Multiple Walsh-Fourier Series of Functions from L_p, $p \geq 1$.* Trudy Mat. Inst. im. Steklova **214** (1997), 83–106; English transl. in Proc. Steklov Inst. Math. **214** (1996).

[14] I. L. Bloshanskii, *Generalized Localization Almost Everywhere and Convergence of Double Fourier Series.* Dokl. Akad. Nauk SSSR **242** (1978), 11–13; English transl. in Soviet Math. Dokl. **19** (1978).

[15] S. K. Bloshanskaya, I. L. Bloshanskii, *Generalized and Weak Generalized Localizations for Multiple Walsh-Fourier Series of Functions in L_p , $p \geq 1$.* Dokl. Ross. Akad. Nauk **332** (1993), 549–552; English transl. in Russian Acad. Sci. Dokl. Math. **48** (1994).

[16] S. K. Bloshanskaya, I. L. Bloshanskii, *On the Validity of Generalized Localization for Double Walsh-Fourier Series of Functions in $L(\log^+ L)^2$.* Intern. Conf. on Teory of Approx. Of Functions. Abstracts of papers, vol.1, Kaluga (1996), 34–36; (Russian)

[17] S. K. Bloshanskaya, I. L. Bloshanskii, T. Yu. Roslova, *Generalized Localization for Double Trigonometric Fourier Series and Walsh-Fourier Series of Functions in $L(\log^+ L)(\log^+ \log^+ L)$.* Mat.Sb. **189** (1998), 21–46; English transl. in Math. USSR-Sb. **189**(1998).

[18] S. K. Bloshanskaya, *The Criteria of Weak Generalized Localization for multiple Walsh-Fourier series of Functions in Orlicz Classes.* Intern. J. of Wavelets, Multiresolution and Inform. Processing **2** (2004), 430–435.

[19] I. L. Bloshanskii, *On Sequence of Linear Operators.* Trudy Mat.Inst. im. Steklova **201** (1992), 43–78; English transl. in Proc. Steklov Inst. Math. **2**(1994).

S.K. Bloshanskaya
Moscow Engineering Physics Institute (State University) 31, Kashirskoe sh.
Moscow
115409, Russia
e-mail: i.bloshn@g23.relcom.ru

I.L. Bloshanskii
Moscow State Regional University 10 a, Radio Street
Moscow
105005, Russia
e-mail: i.bloshn@g23.relcom.ru

Wavelet Analysis and Applications
Tao Qian, Mang I. Vai and Xu Yuesheng, Eds.
Applied and Numerical Harmonic Analysis, 13–24

Linear Transformations of $\mathbb{R}^N$ and Problems of Convergence of Fourier Series of Functions Which Equal Zero on Some Set

I.L. Bloshanskii

Abstract. Let $\mathfrak{M}$ be a class of (all) linear transformations of $\mathbb{R}^N$, $N \geq 1$. Let $\mathcal{A} = \mathcal{A}(\mathbb{T}^N)$, $\mathbb{T}^N = [-\pi, \pi)^N$ be some linear subspace of $L_1(\mathbb{T}^N)$, and let $\mathfrak{A}$ be an arbitrary set of positive measure $\mathfrak{A} \subset \mathbb{T}^N$.

We consider the problem: how are the sets of convergence and divergence everywhere or almost everywhere (a.e.) of trigonometric Fourier series (in case $N \geq 2$ summed over rectangles) of function $(f \circ \mathfrak{m})(x) = f(\mathfrak{m}(x))$, $f \in \mathcal{A}$, $f(x) = 0$ on $\mathfrak{A}$, $\mathfrak{m} \in \mathfrak{M}$, changed depending on the smoothness of the function f (i.e. on the space $\mathcal{A}$), as well as on the transformation $\mathfrak{m}$.

In the paper a (wide) class of spaces $\mathcal{A}$ is found such that for each $\mathcal{A}$ the system of classes (of nonsingular linear transformations) Ψ_k, $\Psi_k \subset \mathfrak{M}$ $(k = 0, 1, \ldots, N)$, which "change" the sets of convergence and divergence everywhere or a.e. of the indicated Fourier expansions is defined.

Mathematics Subject Classification (2000). Primary 42B05.

Keywords. Multiple trigonometric Fourier series, convergence and divergence everywhere and almost everywhere, linear transformations, rotation group.

1. Discussion of the Problem

In the theory of Fourier expansions the following problem plays an important role: how properties of Fourier expansions are affected by modifying the function that generates these expansions?

In the one-dimensional case to this range of problems, for example, the following result belongs obtained in 1940 by D.E.Men'shov [1] (for trigonometric Fourier series): any measurable function finite almost everywhere on $\mathbb{T}^1 = [-\pi, \pi)$ (in particular, any continuous function f, $f \in \mathbb{C}(\mathbb{T}^1)$), can be changed on a set of

This work was supported by grant 05-01-00206 of the Russian Foundation for Fundamental Research.

arbitrary small measure so that the obtained function has the uniformly convergent Fourier series.

Let us also note the classical problem posed by N.N.Luzin: does a continuous function exist such that, after the continuous transformation of variable, it becomes a function with absolutely convergent Fourier series. As it is known the answer to this question turned out to be negative: in 1981 A.M.Olevskii [2] proved the existence of a function f, $f \in \mathbb{C}(\mathbb{T}^1)$, such that for any homeomorphism $\varphi : \mathbb{T}^1 \to \mathbb{T}^1$, – the Fourier series of superposition $(f \circ \varphi)(x) = f(\varphi(x))$ is not absolutely convergent. Let us mention, as well, the result of 1935 by H.Bohr [3], who proved that for any continuous function f there exists a homeomorphism $\varphi : \mathbb{T}^1 \to \mathbb{T}^1$, such that the Fourier series of superposition $f \circ \varphi$ is uniformly convergent. (The detailed survey of the concerning results in the one-dimensional case see in the papers of J.P.Kahane [4] and A.M.Olevskii [5, 6].)

As for the multiple case, in 1998 A.A.Saakyan [7], generalizing the result of H.Bohr, proved that for any function $f \in \mathbb{C}(\mathbb{T}^N)$, $\mathbb{T}^N = [-\pi, \pi)^N, N \geq 2$ (and therefore, for the continuous function with trigonometric Fourier series rectangularly divergent everywhere on $\mathbb{T}^N$ – see the example of Ch.Fefferman [8]), there exists a homeomorphism $\varphi : \mathbb{T}^N \to \mathbb{T}^N$ such that trigonometric Fourier series of superposition $f \circ \varphi$ uniformly rectangularly converges. The same year S.Galstyan and G.Karagulyan [9] proved an "opposite" (in a certain sense) result, namely: for any function $f \in \mathbb{C}(\mathbb{T}^N)$, $N \geq 2$ (which has no intervals of constancy in $\mathbb{T}^N$) there exists a homeomorphism $\varphi : \mathbb{T}^N \to \mathbb{T}^N$ such that the Fourier series of $f \circ \varphi$ rectangularly diverges almost everywhere (a.e.).

In 2000 O.S. Dragoshanskii [10] published the following result: there exists a function $f \in \mathbb{C}(\mathbb{T}^2)$ (whose support belongs to the square $[\frac{1}{2}, \frac{3}{4}]^2$) such that the double trigonometric Fourier series of f converges rectangularly a.e. on $\mathbb{T}^2$, while the same series but of the function $f \circ \tau$, where τ is a rotation of the coordinate system $\mathbb{R}^2$ on an angle $\frac{\pi}{4}$ diverges rectangularly on its support. In the same paper it was proved that rotation on the angle $\frac{\pi}{4}$ can "spoil", as well, the uniform convergence of the series under consideration.

We [11] in 2002 studied the problem concerning convergence everywhere and a.e. of multiple trigonometric Fourier series (summed over rectangles) of the function $f \circ \tau$, when $f \in L_1(\mathbb{T}^N)$, $N \geq 2$, $f(x) = 0$ on some subset (of positive measure) of $\mathbb{T}^N$, and τ is a rotation of the coordinate system $\mathbb{R}^N$ on an arbitrary angle.

In its turn, the results earlier obtained by us (see, e.g., [12]– [18]) which describe *the structural and geometric characteristics* (**SGC**) of sets of convergence and divergence a.e. and everywhere for multiple trigonometric Fourier series, multiple Walsh-Fourier series (summed over rectangles) and multiple Fourier integrals of functions f from various functional spaces $\mathcal{A}$ (e.g., L_1, Orlicz classes $L(\log^+ L)^s$, $s > 1$, the classes L_p, $1 < p < \infty$, $\mathbb{C}$, H^ω, etc.), f equals zero on some set $\mathfrak{A}$ of positive measure, permit to make some conclusions concerning convergence a.e. and everywhere of multiple Fourier expansions of the superposition $f \circ \psi$, when $f \in \mathcal{A}$, $f(x) = 0$ on $\mathfrak{A}$, and ψ belongs to some class Ψ of linear (e.g., orthogonal)

transformations of $\mathbb{R}^N$, $\Psi \subset \mathfrak{M}$, where $\mathfrak{M}$ is the set of (all) linear transformations of $\mathbb{R}^N$.

It is a matter of interest to find (describe) all those classes of transformations Ψ, which for the given space $\mathcal{A}$ "change" the sets of convergence and divergence everywhere or a.e. of the multiple Fourier expansion of a function f in the space $\mathcal{A}$ ($f(x) = 0$ on some set of positive measure), i.e. to give description of pairs $(\mathcal{A}, \Psi)$.

2. Notation

Consider the N–dimensional Euclidean space $\mathbb{R}^N$, whose elements will be denoted as $x = (x_1, \ldots, x_N)$, and set $kx = k_1x_1 + \cdots + k_Nx_N$, $|x| = (x_1^2 + \ldots + x_N^2)^{1/2}$.

Let $\mathbb{Z}^N$, $\mathbb{Z}^N \subset \mathbb{R}^N$ be a set of all vectors with integer coordinates, let us also define the set $\mathbb{Z}_\alpha^N = \{n = (n_1, \ldots, n_N) \in \mathbb{Z}^N : n_j \geq \alpha,\ j = 1, \ldots, N\}$, $\alpha \in \mathbb{Z}^1$.

Let $S_n(x; f)$, $n \in \mathbb{Z}_1^N$, $N \geq 1$ be the rectangular partial sum of trigonometric Fourier series of a function $f \in L_1(\mathbb{T}^N)$, $\mathbb{T}^N = [-\pi, \pi)^N$, whose particular case is the square partial sum $S_{n_0}(x; f)$, when $n_1 = \ldots = n_N = n_0$. Let $\mathcal{A} = \mathcal{A}(\mathbb{T}^N)$ be some linear subspace of the space $L_1(\mathbb{T}^N)$, $\mathfrak{A}$ – an arbitrary measurable set, $\mathfrak{A} \subset \mathbb{T}^N$, $\mu\mathfrak{A} > 0$ ($\mu = \mu_N$ is the N-dimensional Lebesgue measure), and let $f(x) = 0$ on $\mathfrak{A}$.

We investigate how does the behavior of $S_n(x; f)$ as $n \to \infty$, i.e. $\min\limits_{1 \leq j \leq N} n_j \to \infty$ (or $S_{n_0}(x; f)$ as $n_0 \to \infty$) on $\mathbb{T}^N$ depend on the smoothness of the function f (i.e. on the type of the space $\mathcal{A}$), on the "modification" of the function f, and, finally, on *the structural and geometric characteristics* of the set $\mathfrak{A}$ ($\mathbf{SGC}(\mathfrak{A})$).

3. Definition of the System of Functional Spaces

Denote as $\mathbb{F} = \mathbb{F}_N = \left\{\mathcal{A}_k^{(j)}\right\}_{k,j}$ a matrix $N \times 6$, whose elements are functional spaces $\mathcal{A}_k^{(j)} = \mathcal{A}_k^{(j)}(\mathbb{T}^N)$, $k = 1, \ldots, N$; $N \geq 1$ and $j \in \{0\} \bigcup J$, where $J = \{1, 2, \ldots, 5\}$. The spaces $\mathcal{A}_k^{(j)}$ will be defined as follows. For $k = 1, 2$ we set:

$$\mathcal{A}_1^{(j)} = \mathcal{A}_1^{(0)} = L_1\,,\ j \in J\,; \quad \mathcal{A}_2^{(0)} = \mathcal{A}_2^{(1)} = L_\infty\,; \quad \mathcal{A}_2^{(2)} = \mathcal{A}_2^{(3)} = L_2\,;$$
$$\mathcal{A}_2^{(4)} = L_p\,,\ 1 < p < 2; \quad \mathcal{A}_2^{(5)} = L(\log^+ L)^2. \quad (3.1)$$

For $k = 3, \ldots, N$ we set:

$$\mathcal{A}_k^{(0)} = H^{\overline{\omega}^{(k)}},$$

where $\overline{\omega}^{(k)}(\delta)$ is the modulus of continuity $\overline{\omega}^{(k)}(\delta) = \overline{\omega}_\lambda^{(k)}(\delta) = \lambda(\delta) \cdot \left(\log \frac{1}{\delta}\right)^{-\left[\frac{k}{2}\right]}$, where $[\xi]$ is the integral part of ξ, and $\lambda(\delta)$ is a function increasing to $+\infty$ as $\delta \to +0$ and $\lambda(\delta) = o(\log\log \frac{1}{\delta})$, $\delta \to +0$;

$$\mathcal{A}_k^{(1)} = H^{\omega^{(k-1)}} \quad \text{and} \quad \mathcal{A}_k^{(2)} = H_2^{\omega^{(k-1)}},$$

where $\omega^{(k-1)}(\delta) = \omega_{\varepsilon}^{(k-1)}(\delta) = (\log \frac{1}{\delta})^{-\frac{k-1}{2}-\varepsilon},\ 0 < \varepsilon < \frac{1}{2}$;[1]

$$\mathcal{A}_k^{(3)} = \left\{ f \in L_2(\mathbb{T}^N) : \sum_{n \in \mathbb{Z}^N} |c_n|^2 \cdot \max_{1 \le j_1 < \ldots < j_{k-1} \le N} \prod_{s=1}^{k-1} \log(|n_{j_s}| + 2) < +\infty \right\},$$

where $c_n = c_n(f)$ are Fourier coefficients of function f; and, besides, we set

$$\mathcal{A}_3^{(4)} = \left\{ f \in L_2(\mathbb{T}^N) : \sum_{n \in \mathbb{Z}^N} |c_n|^2 \log^2[\max_{s,l=1,2,\ldots,N} \min_{s \ne l}(|n_s|, |n_l|) + 2] < +\infty \right\},$$

$$\mathcal{A}_3^{(5)} = H^{\omega^{(1)}}, \quad \text{where} \quad \omega^{(1)}(\delta) = o([\log \frac{1}{\delta} \log\log\log \frac{1}{\delta}]^{-1}), \quad \delta \to +0.$$

For $k = 4, \ldots, N$ we set:

$$\mathcal{A}_k^{(4)} = \mathcal{A}_k^{(5)} = \mathcal{A}_k^{(1)}.$$

Let us note that "smoothness" of functions $f \in \mathcal{A}_k^{(j)}(\mathbb{T}^N)$ certainly "increases" with the growth of the number k, i.e. $\mathcal{A}_k^{(j)} \supset \mathcal{A}_{k+1}^{(j)}$, $j \in \{0\} \bigcup J$, $k = 1 \ldots, N-1$.

Let us also note that the classes $\mathcal{A}_k^{(j)}(\mathbb{T}^N)$, $j \in J$ have the following property: in the case $k > 1$ for any function $f \in \mathcal{A}_k^{(j)}(\mathbb{T}^{k-1})$ convergence of $(k-1)$ -multiple trigonometric Fourier series summed over rectangles takes place a.e. on $\mathbb{T}^{k-1}$ (see results of L.Carleson [19], R.Hunt [20] ($k = 2$); K.I.Oskolkov [21], P.Sjölin [22] ($k = 3$); L.V.Zhizhiashvili [23] and [24], F.Móricz [25] ($k \ge 4$)).

The indicated ("functional") matrix $\mathbb{F}$ was introduced by us in the paper [26].

4. Definition of the Classes of Linear Transformations of $\mathbb{R}^N$

Let $\mathfrak{M}$ be a class of (all) linear transformations of $\mathbb{R}^N$, $N \ge 1$. Denote as Ψ_1, $\Psi_1 \subset \mathfrak{M}$ the class of linear nonsingular transformations, whose inverse transformations have matrices $\mathbb{A} = \{a_{l,m}\}_{l,m=1}^N$, satisfying condition: there exists s, $1 \le s \le N$ such that

$$\max_{1 \le l \le N} |a_{l,s}| < 1. \tag{4.1}$$

Further, in the case of dimension of the space $N \ge 2$, we define the following N subsets of Ψ_1.

First, for any k, $2 \le k \le N$, we define the class of transformations Ψ_k: $\psi \in \Psi_k$ if the matrix $\mathbb{A}$ of inverse (to ψ) transformation ψ^{-1} satisfies condition: there exist $m_1, \ldots, m_k$, $1 \le m_1 < \ldots < m_k \le N$ such that

$$\max_{1 \le l \le N} \{|a_{l,m_1}| + \ldots + |a_{l,m_k}|\} < 1. \tag{4.2}$$

For classes of transformations $\Psi_1, \ldots, \Psi_N$, the embeddings are obvious: $\Psi_1 \supset \Psi_2 \supset \ldots \supset \Psi_N$.

[1] Note that $\mathcal{A}_k^{(0)} \subset \mathcal{A}_k^{(1)}$ if k is even, $k \ge 4$.

Second, for $N \geq 2$ we define the class of transformations $\Psi_0 \subset \Psi_1$. Let $\mathcal{F}$ be a group of rotations of $\mathbb{R}^N$ about the origin, and let $\mathcal{F}_0$ be a set of rotations from $\mathcal{F}$, that are compositions of rotations in all the two-dimensional coordinate planes by angles which are integer multiple of $\frac{\pi}{2}$. Set[2]

$$\Psi_0 = \mathcal{F} \setminus \mathcal{F}_0. \tag{4.3}$$

5. Setting of the Problem and Approaches to Its Solution

We pose and study the problem: how are the sets of convergence and divergence (everywhere or a.e.) of trigonometric Fourier series (in case $N \geq 2$ summed over rectangles) of function f, belonging to one of the spaces $\mathcal{A}$ (elements of the matrix $\mathbb{F}$) and vanishing on some measurable set $\mathfrak{A} \subset \mathbb{T}^N$, $0 < \mu\mathfrak{A} < (2\pi)^N$, $N \geq 1$, ($\mu = \mu_N$ is the Lebesgue measure) changed (if changed) in dependence on the transformation $\psi \in \Psi$, where $\Psi = \Psi_k$, $0 \leq k \leq N$? Thus, we want to "describe" a pair $(\mathcal{A}, \Psi)$.

Further, for any set $E \subset \mathbb{R}^N$ and any $\mathfrak{m} \in \mathfrak{M}$ we define the set $\mathfrak{m}(E) = \{y \in \mathbb{R}^N : y = \mathfrak{m}(x),\ x \in E\}$. Analogously the set $\mathfrak{m}^{-1}(E)$ is defined, where transformation $\mathfrak{m}^{-1}$ is such that: $\mathfrak{m}^{-1} \cdot \mathfrak{m} = 1$ (if $\mathfrak{m}^{-1}$ exists). It is obvious that for any $E \subset \mathbb{T}^N$ there exists $\mathfrak{m} \in \mathfrak{M}$ such that $\mathfrak{m}(E) \not\subset \mathbb{T}^N$.

Thus, taking into account that (in the present paper) we consider 2π-periodic functions $f(x)$, the question arises: how the Fourier series should be understood for the function $(f \circ \mathfrak{m})(x) = f(\mathfrak{m}(x))$, e.g., for rotation (of the coordinate system of $\mathbb{R}^N$), i.e. when $\mathfrak{m} = \tau \in \mathcal{F}$.[3]

Analogously to the paper [11], where we considered the group of rotations $\mathcal{F}$, we shall formulate two variants how the Fourier series of function $f \circ \mathfrak{m}$, $\mathfrak{m} \in \mathfrak{M}$ can be understood.

Let us fix an arbitrary $\mathfrak{m} \in \mathfrak{M}$. For any function $f \in L_1(\mathbb{T}^N)$[4] we define 2π-periodic (for $N \geq 2$ — in each argument) functions $g^{(l)}_{\mathfrak{m}}(x)$, $l = 1, 2$, so that on $\mathbb{T}^N$ these functions are defined by equalities:

$$g^{(1)}_{\mathfrak{m}}(x) = (f \circ \mathfrak{m})(x) = f(\mathfrak{m}(x)), \quad x \in \mathbb{T}^N, \tag{5.1}$$

$$g^{(2)}_{\mathfrak{m}}(x) = (f \circ \mathfrak{m})(x) = f(\mathfrak{m}(x)) \cdot \chi_{\mathbb{T}^N}(\mathfrak{m}(x)), \quad x \in \mathbb{T}^N, \tag{5.2}$$

where $\chi_{\mathbb{T}^N}(\cdot)$ is the characteristic function of the cube $\mathbb{T}^N$.

Thus, the posed above problem is decomposed into two problems in dependence on the regard to Fourier series of function $f \circ \mathfrak{m}$. Further in the text: for $l = 1$ – the problem 1, and for $l = 2$ – the problem 2.

Earlier we have investigated [12]–[18] (see also [26]) the problem concerning changes of the structure and geometry of sets of convergence and divergence a.e.

[2]It is obvious that rotations $\tau \in \mathcal{F}_0$ can not change the sets of convergence or divergence of multiple Fourier expansions.

[3]Let us note that for Fourier integrals $\int_{\mathbb{R}^N} \widehat{h}(\xi) e^{ix\xi}\, d\xi$, $x \in \mathbb{R}^N$, of function $h \in L_1(\mathbb{R}^N)$ the problem "in this sense" does not arise.

[4]Naturally, the function $f(x)$ is 2π -periodic in each argument.

and everywhere for (multiple) trigonometric Fourier series (for $N \geq 2$ summed over rectangles) of functions f in $\mathcal{A}_k^{(j)}(\mathbb{T}^N)$, $k = 1, \ldots, N$, $j \in \{0\} \bigcup J$, $f(x) = 0$ on some measurable set $\mathfrak{A} \subset \mathbb{T}^N$, in dependence on changes of structure and geometry of the set $\mathfrak{A}$. So, the both posed problems are reduced (in fact) to the study of the question concerning changes of structure and geometry of sets $\psi^{-1}(\mathfrak{A}) \cap \mathbb{T}^N$ and $\mathbb{T}^N \setminus supp(f \circ \psi)$, in dependence on $\psi \in \Psi_k$, $0 \leq k \leq N$.[5]

Let us note that problem 1, being a more complicated problem, is, at the same time, a more natural one for trigonometric Fourier series even in the study of such "unnatural" for these series "problem of rotations".

Let us show some particular solutions of problem 2, whose results give the description of the pairs $(\mathcal{A}, \Psi)$, more exactly, let us formulate the results describing (some) relation between the "smoothness" (in terms of the matrix $\mathbb{F}$) of the function f ($f(x) = 0$ on $\mathfrak{A}$) and the transformation ψ (in terms of the classes Ψ_k).

6. The Set of Transformations Ψ_k, $k = 1, \ldots, N$. Solution of Problem 2

Two following theorems give description of the pair $(\mathcal{A}_1^{(j)}, \Psi_1)$, $j \in \{0\} \bigcup J$, i.e., taking account of (3.1), – the pair (L_1, Ψ_1) (for $N = 1$ and for $N > 1$, respectively).

Theorem 6.1. *For any $\psi \in \Psi_1$ and ε, $0 < \varepsilon < 2\pi$, there exist the measurable sets $\Omega = \Omega(\varepsilon, \psi) \subset \mathbb{T}^1$, $\mathfrak{A} = \mathfrak{A}(\varepsilon, \psi) \subset \mathbb{T}^1 : \mu\Omega > 0$, $\mu\mathfrak{A} > 2\pi - \varepsilon$ and a function $f = f_{\varepsilon, \psi} \in L_1(\mathbb{T}^1)$, $f(x) = 0$ on $\mathfrak{A}$, such that*

1. $$\overline{\lim_{n \to \infty}} |S_n(x; f)| = +\infty \quad \text{in each point} \quad x \in \mathbb{T}^1, \tag{6.1}$$
2. $$\lim_{n \to \infty} S_n(x; f \circ \psi) = 0 \quad \text{in each point} \quad x \in \Omega. \tag{6.2}$$

Here the notation $f \circ \psi$ is understood in the sense of equality (5.2), i.e. $f \circ \psi = g_\psi^{(2)}$.

Theorem 6.2. *Let $N > 1$. For any $\psi \in \Psi_1$ and ε, $0 < \varepsilon < (2\pi)^N$, there exist the open sets $\Omega = \Omega(\varepsilon, \psi)$, $\mathfrak{A} = \mathfrak{A}(\varepsilon, \psi) : \Omega \subset \mathfrak{A} \subset \mathbb{T}^N$, $\mu\mathfrak{A} > (2\pi)^N - \varepsilon$, $0 < \mu\Omega < \mu\mathfrak{A}$ such that*

1. *There exists a function $f^{(0)} = f_{\varepsilon, \psi}^{(0)} \in L_1(\mathbb{T}^N)$, $f^{(0)}(x) = 0$ on $\mathfrak{A}$, and*
$$\overline{\lim_{n_0 \to \infty}} |S_{n_0}(x; f^{(0)})| = +\infty \quad \text{in each point} \quad x \in \mathbb{T}^N. \tag{6.3}$$
2. *For any function $f \in L_1(\mathbb{T}^N)$, $f(x) = 0$ on $\mathfrak{A}$,*
$$\lim_{n \to \infty} S_n(x; f \circ \psi) = 0 \quad \text{in each point} \quad x \in \Omega. \tag{6.4}$$

Here the notation $f \circ \psi$ is understood in the sense of equality (5.2), i.e. $f \circ \psi = g_\psi^{(2)}$.

Analogous results are obtained for other pairs $(\mathcal{A}_r^{(j)}, \Psi_k)$, where $k \leq r \leq N$, $j \in \{0\} \bigcup J$ for $k = r = N$, if $N = 2$, and for $1 \leq k \leq 2 \cdot \left[\frac{N-1}{2}\right]$, if $N \geq 3$, namely, the following theorems are true

[5] Note that for singular transformations $\mathfrak{m} \in \mathfrak{M}$ the discussed problem becomes trivial.

Theorem 6.3. *For any $\psi \in \Psi_2$ and $\varepsilon,\ 0 < \varepsilon < (2\pi)^2$, there exist the measurable sets $\Omega = \Omega(\varepsilon, \psi) \subset \mathbb{T}^2$, $\mathfrak{A} = \mathfrak{A}(\varepsilon, \psi) \subset \mathbb{T}^2 : \mu\Omega > 0$, $\mu\mathfrak{A} > (2\pi)^2 - \varepsilon$ and a function $f = f_{\varepsilon,\,\psi} \in L_\infty(\mathbb{T}^2)$, $f(x) = 0$ on $\mathfrak{A}$, such that*

1. $$\overline{\lim_{n\to\infty}} |S_n(x; f)| = +\infty \quad \textit{for almost all} \quad x \in \mathbb{T}^2, \tag{6.5}$$

2. $$\lim_{n\to\infty} S_n(x; f \circ \psi) = 0 \quad \textit{for almost all} \quad x \in \Omega. \tag{6.6}$$

Here the notation $f \circ \psi$ is understood in the sense of equality (5.2)*, i.e. $f \circ \psi = g_\psi^{(2)}$.*

Theorem 6.4. *Let $N \geq 3$. For any integer k and $r : 1 \leq k \leq 2 \cdot \left[\frac{N-1}{2}\right],\ k \leq r \leq N$, and any $\psi,\ \varepsilon :\ \psi \in \Psi_k$ and $0 < \varepsilon < (2\pi)^N$, there exist the open sets $\mathfrak{A} = \mathfrak{A}_k(\varepsilon, \psi)$, $\Omega = \Omega_{k,\,r}(\varepsilon, \psi) : \Omega \subset \mathfrak{A} \subset \mathbb{T}^N$, $\mu\mathfrak{A} > (2\pi)^N - \varepsilon$, $0 < \mu\Omega < \mu\mathfrak{A}$ such that*

1. *There exists a function $f^{(0)} = f^{(0)}_{k,\,\varepsilon,\,\psi} \in \mathcal{A}_k^{(0)}(\mathbb{T}^N)$, $f^{(0)}(x) = 0$ on $\mathfrak{A}$, and*

$$\overline{\lim_{n\to\infty}} |S_n(x; f^{(0)})| = +\infty \quad \textit{for almost all} \quad x \in \mathbb{T}^N. \tag{6.7}$$

2. *For any $j \in J$ and for any function $f \in \mathcal{A}_r^{(j)}(\mathbb{T}^N)$, $f(x) = 0$ on $\mathfrak{A}$,*

$$\lim_{n\to\infty} S_n(x; f \circ \psi) = 0 \quad \textit{for almost all} \quad x \in \Omega. \tag{6.8}$$

Here the notation $f \circ \psi$ is understood in the sense of equality (5.2)*, i.e. $f \circ \psi = g_\psi^{(2)}$ and $[\xi]$ is the integral part of ξ.*

Remark 6.5. Taking into account the embeddings: $\mathcal{A}_k^{(j)} \supset \mathcal{A}_r^{(j)}$, $j \in \{0\} \bigcup J$ for all k and $r : k \leq r \leq N$, and embeddings $\mathcal{A}_k^{(0)} \subset \mathcal{A}_k^{(1)}$ for even k, $k \geq 4$, we can make a conclusion that the 2-nd point in theorem 6.4 (see estimate (6.8)) is true, as well, (in case of even k, $k \geq 4$) for the function $f^{(0)} \in \mathcal{A}_k^{(0)}$, defined in point 1 of this theorem (see estimate (6.7)).

Further, in theorems 6.1– 6.4 the function f (in estimates (6.1), (6.2), (6.5) and (6.6)) and the function $f^{(0)}$ (in estimates (6.3) and (6.7)) depended on the transformation $\psi,\ \psi \in \Psi_k$ (i.e. for each transformation ψ its own function f was found (the function $f^{(0)}$)). So the question naturally arises: is it possible to construct a "universal" function f ($f \in \mathcal{A}_k^{(j)}$, with arbitrary small support), whose Fourier series unrestrictedly diverges (everywhere or a.e.) on $\mathbb{T}^N$, and, at the same time, the same series, but already of the function $f \circ \psi$, for any $\psi \in \Psi_k$ converges (everywhere or a.e.) on some subset (of positive measure) of $\mathbb{T}^N$?

For the class of transformations $\Psi_0 \subset \mathcal{F}$, where $\mathcal{F}$ is a group of rotations of $\mathbb{R}^N$ about the origin (see condition (4.3)), the answer to the posed question appears to be positive in many cases, and this fact is connected (partially) with the definite "specific character" of the problem (considered in the present paper) for transformations in $\mathcal{F}$.

7. The Group of Rotations of $\mathbb{R}^N$ About the Origin

Denote as

$$\mathbb{B}(O,\pi)=\{x\in\mathbb{R}^N:|x|<\pi\} \tag{7.1}$$

a ball inscribed into the cube $\mathbb{T}^N$. It is obvious that for any rotation $\tau,\ \tau\in\mathcal{F}$ and for any set $E\subset\mathbb{B}(O,\pi)$ – the set $\tau(E)\subset\mathbb{T}^N$.

Note that for $\tau\in\mathcal{F}$ the set $\tau^{-1}(\mathbb{T}^N)\setminus\mathbb{T}^N$ (and, moreover, the set $\{x\in\mathbb{R}^N:|x|\le\sqrt{N}\cdot\pi\}\setminus\mathbb{T}^N$) in the definition of functions $g_\tau^{(l)}$, $l=1,2$ (see (5.1), (5.2)) – (in general) "vanishes". The last is natural for the problem under consideration for Fourier series. However, this "vanishing" can be avoided in the problem 2 if we consider a more "narrow" class of functions $f(x)$, namely, f: $supp\,(f\cdot\chi_{_{\mathbb{T}^N}})\subset\mathbb{B}(O,\pi)$.[6]

7.1. The Set of Transformations Ψ_0. Solution of Problem 2. Functions in L_1

Theorem 7.1. *Let $\mathcal{F}$ be a group of rotations of $\mathbb{R}^2$ and let Ψ_0, $\Psi_0\subset\mathcal{F}$ satisfy condition (4.3). For any $\varepsilon,\ 0<\varepsilon<(2\pi)^2$, there exists an open set $\mathfrak{A}=\mathfrak{A}_\varepsilon\subset\mathbb{T}^2$, $\mu\mathfrak{A}>(2\pi)^2-\varepsilon$ such that*

1. *There exists a function $f^{(0)}=f_\varepsilon^{(0)}\in L_1(\mathbb{T}^2)$ such that $f^{(0)}(x)=0$ on $\mathfrak{A}$, $supp\,(f^{(0)}\cdot\chi_{_{\mathbb{T}^2}})\subset\mathbb{B}(O,\pi)$ (see (7.1)) and*

$$\overline{\lim_{n_0\to\infty}}\,|S_{n_0}(x;f^{(0)})|=+\infty\quad\text{in each point}\quad x\in\mathbb{T}^2.$$

2. *For any $\tau\in\Psi_0$ there exists an open (nonempty) set $\Omega=\Omega_\varepsilon(\tau)\subset\mathfrak{A}$ such that for any function $f\in L_1(\mathbb{T}^2):f(x)=0$ on $\mathfrak{A}$, $supp\,(f\cdot\chi_{_{\mathbb{T}^2}})\subset\mathbb{B}(O,\pi)$,*

$$\lim_{n\to\infty}S_n(x;f\circ\tau)=0\quad\text{in each point}\quad x\in\Omega.$$

Here the notation $f\circ\tau$ is understood in the sense of equality (5.2), i.e. $f\circ\tau=g_\tau^{(2)}$.

Concerning the case $N\ge3$, a "weaker", to some extent, result is true, for example, the following theorem holds.

Theorem 7.2. *Let $\mathcal{F}$ be a group of rotations of $\mathbb{R}^N$, $N\ge3$, and let Ψ_0, $\Psi_0\subset\mathcal{F}$ satisfy condition (4.3). For any $j,\ 1\le j\le N$, and any $\varepsilon,\ 0<\varepsilon<(2\pi)^N$, there exists an open set $\mathfrak{A}=\mathfrak{A}_{\varepsilon,j}\subset\mathbb{T}^N$, $\mu\mathfrak{A}>(2\pi)^N-\varepsilon$ such that*

1. *There exists a function $f^{(0)}=f_\varepsilon^{(0)}\in L_1(\mathbb{T}^N)$ such that $f^{(0)}(x)=0$ on $\mathfrak{A}$, $supp\,(f^{(0)}\cdot\chi_{_{\mathbb{T}^N}})\subset\mathbb{B}(O,\pi)$ (see (7.1)) and*

$$\overline{\lim_{n_0\to\infty}}\,|S_{n_0}(x;f^{(0)})|=+\infty\quad\text{in each point}\quad x\in\mathbb{T}^N. \tag{7.2}$$

[6] In the problem 1 (for $\tau\in\mathcal{F}$) this "vanishing" can be also avoided by choosing a "smaller" $supp\,(f\cdot\chi_{_{\mathbb{T}^N}})$ but (as it is not difficult to calculate) only for $N=2$ and $N=3$.

2. *For any* $\tau \in \Psi_0$ (*except rotations about the axes containing the coordinate axis* Ox_j) *there exists an open* (*nonempty*) *set* $\Omega = \Omega_{\varepsilon,\,j}(\tau) \subset \mathfrak{A}$ *such that for any function* $f \in L_1(\mathbb{T}^N) : f(x) = 0$ *on* $\mathfrak{A}$, $supp\,(f \cdot \chi_{_{\mathbb{T}^N}}) \subset \mathbb{B}(O, \pi)$,

$$\lim_{n\to\infty} S_n(x; f \circ \tau) = 0 \quad \textit{in each point} \quad x \in \Omega.$$

Here the notation $f \circ \tau$ *is understood in the sense of equality* (5.2), *i.e.* $f \circ \tau = g_\tau^{(2)}$.

We formulated Theorem 7.2 where we excluded rotations about the axes which are s-dimensional manifolds ($1 \le s \le N-2$) containing some (fixed) coordinate axis. Note that divergence of the "original" Fourier series (of function f, $f = f^{(0)}$ such that the support of the function $supp\,(f \cdot \chi_{_{\mathbb{T}^N}})$ in $\mathbb{B}(O, \pi)$) takes place on the whole cube $\mathbb{T}^N$(see (7.2)). If in the research of the posed problem (problem 2) we have no aim to have divergence of the (original) Fourier series on the whole cube $\mathbb{T}^N$, but we want to "remain" in the class of functions $\{f \in L_1 :\ supp\,(f \cdot \chi_{_{\mathbb{T}^N}}) \subset \mathbb{B}(O, \pi)\}$, we can obtain the following results.

Theorem 7.3. *Let* $\mathcal{F}$ *be a group of rotations of* $\mathbb{R}^N$, $N \ge 3$, *and let* Ψ_0, $\Psi_0 \subset \mathcal{F}$ *satisfy condition* (4.3). *For any* ε *and* $\alpha : 0 < \varepsilon < (2\pi)^N$, $0 < \alpha < (2\pi)^N$, *there exist the open sets* $\Omega_0 = \Omega_0(\varepsilon,\, \alpha)$, $\mathfrak{A} = \mathfrak{A}_{\varepsilon,\,\alpha} : \Omega_0 \subset \mathfrak{A} \subset \mathbb{T}^N$, $\mu\mathfrak{A} > (2\pi)^N - \varepsilon$, $0 < \mu\Omega_0 < \min(\alpha,\, \mu\mathfrak{A})$ *such that*

1. *There exists a function* $f^{(0)} = f^{(0)}_{\varepsilon,\,\alpha} \in L_1(\mathbb{T}^N)$ *such that* $f^{(0)}(x) = 0$ *on* $\mathfrak{A}$, $supp\,(f^{(0)} \cdot \chi_{_{\mathbb{T}^N}}) \subset \mathbb{B}(O, \pi)$ (*see* (7.1)) *and*
   a) $\overline{\lim\limits_{n_0\to\infty}} |S_{n_0}(x; f^{(0)})| = +\infty \quad$ *in each point* $\quad x \in \mathbb{T}^N \setminus \Omega_0$,
   b) $\lim\limits_{n\to\infty} S_n(x; f^{(0)}) = 0 \quad$ *in each point* $\quad x \in \Omega_0$.
2. *For any* $\tau \in \Psi_0$ *there exists an open set* $\Omega_1 = \Omega_1(\tau,\, \varepsilon,\, \alpha) \subset \mathfrak{A}$ *such that* $\Omega_0 \subset \Omega_1$, $\mu\Omega_0 < \mu\Omega_1$ *and for any function* $f \in L_1(\mathbb{T}^N) : f(x) = 0$ *on* $\mathfrak{A}$, $supp\,(f \cdot \chi_{_{\mathbb{T}^N}}) \subset \mathbb{B}(O, \pi)$,

$$\lim_{n\to\infty} S_n(x; f \circ \tau) = 0 \quad \textit{in each point} \quad x \in \Omega_1.$$

Here the notation $f \circ \tau$ *is understood in the sense of equality* (5.2), *i.e.* $f \circ \tau = g_\tau^{(2)}$.

7.2. The Set of Transformations Ψ_0. Solution of Problem 2. Functions in L_p, $p > 1$

Let us fix an arbitrary δ, $0 < \delta < 1$ and define the following set of "small oscillations (small rotations)" $\Psi_0(\delta)$, $\Psi_0(\delta) \subset \Psi_0$:

$$\Psi_0(\delta) = \left\{\tau \in \Psi_0 :\ |\tau x - x| < \delta \quad \text{for any} \quad x \in \mathbb{T}^N\right\}. \tag{7.3}$$

Theorem 7.4. *Let* $\mathcal{F}$ *be a group of rotations of* $\mathbb{R}^3$, *and let* Ψ_0, $\Psi_0 \subset \mathcal{F}$ *satisfy condition* (4.3). *There exist the open sets* Ω_0, $\mathfrak{A} : \Omega_0 \subset \mathfrak{A} \subset \mathbb{T}^3$, $\mu\mathfrak{A} > (2\pi)^3 - \varepsilon$, $0 < \mu\Omega_0 < \mu\mathfrak{A}$ *such that*

1. *There exists a function* $f^{(0)} \in L_\infty(\mathbb{T}^3)$, *such that* $f^{(0)}(x) = 0$ *on* $\mathfrak{A}$, $supp\,(f^{(0)} \cdot \chi_{_{\mathbb{T}^3}}) \subset \mathbb{B}(O, \pi)$ (*see* (7.1)) *and*

a) $\overline{\lim\limits_{n\to\infty}} |S_n(x; f^{(0)})| = +\infty$ *for almost all* $x \in \mathbb{T}^3 \setminus \Omega_0$,

b) $\lim\limits_{n\to\infty} S_n(x; f^{(0)}) = 0$ *for almost all* $x \in \Omega_0$.

2. *There exists* $\delta > 0$ *such that for any* $\tau \in \Psi_0(\delta) \subset \Psi_0$ (*see* (7.3)) *there exists an open set* $\Omega_1 = \Omega_1(\tau) \subset \mathfrak{A}$ *such that* : $\Omega_0 \cap \Omega_1 \neq \emptyset$, $\mu\Omega_0 < \mu\Omega_1$ *and for any function* $f \in L_\infty(\mathbb{T}^3) : f(x) = 0$ *on* $\mathfrak{A}$, *supp* $(f \cdot \chi_{_{\mathbb{T}^3}}) \subset \mathbb{B}(O, \pi)$,

$$\lim_{n\to\infty} S_n(x; f \circ \tau) = 0 \quad \textit{for almost all} \quad x \in \Omega_1.$$

Here the notation $f \circ \tau$ *is understood in the sense of equality* (5.2), *i.e.* $f \circ \tau = g_\tau^{(2)}$.

7.3. The Set of Transformations Ψ_0. Solution of Problem 1

An analog of Theorem 7.1 is true, exactly

Theorem 7.5. *Let* $\mathcal{F}$ *be a group of rotations of* $\mathbb{R}^2$, *and let* Ψ_0, $\Psi_0 \subset \mathcal{F}$ *satisfy condition* (4.3). *For any* ε, $0 < \varepsilon < (2\pi)^2$ *there exist an open set* $\mathfrak{A} = \mathfrak{A}_\varepsilon \subset \mathbb{T}^2$, $\mu\mathfrak{A} > (2\pi)^2 - \varepsilon$ *such that*

1. *There exists a function* $f^{(0)} = f_\varepsilon^{(0)} \in L_1(\mathbb{T}^2)$ *such that* $f^{(0)}(x) = 0$ *on* $\mathfrak{A}$, *supp* $(f^{(0)} \cdot \chi_{_{\mathbb{T}^2}}) \not\subset \mathbb{B}(O, \pi)$ (*see* (7.1)) *and*

$$\overline{\lim_{n_0\to\infty}} |S_{n_0}(x; f^{(0)})| = +\infty \quad \textit{in each point} \quad x \in \mathbb{T}^2.$$

2. *For any* $\tau \in \Psi_0$ *there exists an open* (*nonempty*) *set* $\Omega = \Omega_\varepsilon(\tau) \subset \mathfrak{A}$ *such that for any function* $f \in L_1(\mathbb{T}^2) : f(x) = 0$ *on* $\mathfrak{A}$, *supp* $(f \cdot \chi_{_{\mathbb{T}^2}}) \not\subset \mathbb{B}(O, \pi)$,

$$\lim_{n\to\infty} S_n(x; f \circ \tau) = 0 \quad \textit{in each point} \quad x \in \Omega.$$

Here the notation $f \circ \tau$ *is understood in the sense of equalities* (5.1), *i.e.* $f \circ \tau = g_\tau^{(1)}$.

Remark 7.6. The results of theorems 7.1, 7.2 and 7.5 in somewhat "more weak variant", where the 2-nd point was "formulated for the function $f^{(0)}$", were proved by us in [11].

Remark 7.7. The result of theorem 7.4 is valid as well for continuous functions and, moreover, for continuous functions with some modulus of continuity.

Remark 7.8. In theorems 6.2, 6.4, 7.1–7.3, and 7.5 the sets of convergence (to zero) are a finite collection of open rectangles (for $N \geq 3$ - parallelepipeds) with sides ($N \geq 3$ - edges) parallel to the coordinate axes.

References

[1] D. E. Men'shov, *Sur les Sértes de Fourier des Fonctions Continues.* Mat. Sb. **8** (1940), 493–518.

[2] A. M. Olevskii, *Change of Variable and Absolute Convergence of Fourier Series.* Dokl.Akad. Nauk USSR **256** (1981),284–287; English transl. in Soviet Math. Dokl. **23** (1981),284–287.

[3] H.Bohr, *Über einen Satz von J.Pal.* Acta Sci. Math. **7**(1935), 129-135.

[4] J. P. Kahane, *Quatre Lecons sur les Homeomorphismes du Cercle et les Series de Fourier.* Roma: Proc. Sem. Torino and Milano **2** (1983), 955–990.

[5] A. M. Olevskii, *Modifications of Functions and Fourier Series.* Uspekhi-Mat.-Nauk **40** (1985) 157–193; English transl. in Russ. Math. Surv. **40** (1985);

[6] A. M. Olevskii, *Homeomorphisms of the Circle, Modifications of Functions and Fourier Series.* Proc. Internat. Congr. Math., Berkley. **2** (1986), 976-989; Amer. Math. Soc. Transl. **2** (1990), 51–64.

[7] A. A. Saakyan, *On Bohr's Theorem for Multiple Fourier Series.* Mat. Zametki. **64** (1998), 913–924; English transl. in Math. Notes **64**(1998).

[8] Ch. Fefferman, *On the Divergence of Multiple Fourier Series.* Bull. Amer. Math. Soc. **77** (1971), 191–195.

[9] S. Sh. Galstyan, G. A. Karagulyan, *Divergence Almost Everywhere of Rectangular Partial Sums of Multiple Fourier Series of Bounded Functions.* Mat. Zametki. **64** (1998), 24–36; English transl. in Math. Notes **64** (1998).

[10] O. S. Dragoshanskii, *On Convergence of Double Fourier Series of Functions on T^2 and $\mathbb{R}^2$ Under Rotations of the System of Coordinates* Mat. Sb. **191** (2000), 87-110; English transl. in: Math. USSR Sb. **191** (2000).

[11] I. L. Bloshanskii, *A Criterion for Weak Generalized Localization in the Class L_1 for Multiple Trigonometric Fourier Series from the Viewpoint of Isometric Transformations.* Mat. Zametki. **71** (2002), 508–521; English transl. in: Math. Notes **71**(2002).

[12] I. L. Bloshanskii, *Some Problems of Multidimensional Harmonic Analysis.* Author's summary of Doctoral dissertation, Steklov Math. Inst. Acad. Sci. USSR, Moscow, 1991. (Russian)

[13] I. L. Bloshanskii, *On Convergence and Localization of Multiple Fourier Series and Integrals.* Author's summary of Candidate's dissertation, Moscow State Univ., Moscow, 1978. (Russian)

[14] I. L. Bloshanskii, *On Geometry of Measurable Sets in $N-$ dimensional Space, on which the Generalized Localization is True for Multiple Trigonometric Fourier Series of Functions in L_p, $p > 1$.* Mat. Sb. **121**(1983), 87–110; English transl. in Math. USSR-Sb. **49**(1984).

[15] I. L. Bloshanskii, *Two Criteria for Weak Generalized Localization for Multiple Trigonometric Fourier Series of Functions in L_p, $p \geq 1$.* Izv. Akad. Nauk SSSR. Ser. Mat. **49** (1985), 243–282; English transl. in Math. USSR Izv. **26** (1986).

[16] I. L. Bloshanskii, *On Some Questions of Square Convergence of Multiple Fourier Series and Integrals of Functions in L_1.* Dokl.Akad. Nauk USSR **294** (1987), 15–18; English transl. in Sov. Math. Dokl. **35** (1987).

[17] I. L. Bloshanskii, *The Structure and Geometry of Maximal Sets of Convergence and Unbounded Divergence Almost Everywhere of Multiple Fourier Series of Functions in L_1 Vanishing on a Given Set.* Izv. Akad. Nauk SSSR. Ser. Mat. **53** (1989), 675–707; English transl. in Math. USSR Izv. **35** (1990).

[18] I. L. Bloshanskii, O. K. Ivanova, T. Yu. Roslova, *Generalized Localization and Equiconvergence of Expansions in Double Trigonometric Fourier Series and Fourier Integral of Functions in $L(ln^+L)^2$*, Mat. Zametki. **60** (1996), 437–441; English transl. in: Math. Notes **60**(1996).

[19] L. Carleson, *On Convergence and Growth of Partial Sums of Fourier Series.* Acta Math. **116** (1966), 135–157.

[20] R. Hunt, *On the Convergence of Fourier Series.* Not. Amer. Math. Soc. **14** (1967), 537.

[21] K. I. Oskolkov, *Estimate of Degree of Approximation of Continuous Function and its Conjugate by Fourier Sums on the Set of Full Measure.* Izv. Akad. Nauk SSSR Ser. Mat. **38** (1974), 1339–1407; English transl. in Math. USSR Izv. **8** (1974).

[22] P. Sjölin, *Convergence Almost Everywhere of Certain Singular Integrals and Multiple Fourier Series.* Arkiv Matem. **9** (1971), 65–90.

[23] L. V. Zhizhiashvili, *Convergence of Multiple Trigonometric Fourier Series.* Bull. Acad.Sci. Georgian SSR, **80** (1975), 17–19.

[24] L. V. Zhizhiashvili, *Trigonometric Series and Their Conjugates.* Kluwer Acad. Publ. (1996).

[25] F. Móricz, *Lebesque Functions and Multiple Function Series.* I, Acta Math. Acad Sci. Hungar. **37** (1981), 481–496.

[26] I.L.Bloshanskii, *Structural and Geometric Characteristics of Sets of Convergence and Divergence of Multiple Fourier Series of Functions which Equal Zero on Some Set.* Intern. J. of Wavelets, Multiresolution and Inform. Processing **2** (2004), 187–195.

I.L. Bloshanskii
Moscow State Regional University 10 a, Radio Street
Moscow
105005, Russia
e-mail: `i.bloshn@g23.relcom.ru`

Wavelet Analysis and Applications
Tao Qian, Mang I. Vai and Xu Yuesheng, Eds.
Applied and Numerical Harmonic Analysis, 25–33

Sidon Type Inequalities for Wavelets

N.A. Sheikh

Abstract. In 1938, S.Sidon [9] proved an inequality for the complex trigonometric system on interval [0, 1) known as Sidon type inequality. This inequality was generalized by Bojanic and Stanojevic [1]. The Walsh case was investigated by Moricz and Schipp [7]. Another generalization for trigonometric case was given by Buntinas and Tanovic-Miller [2]. Here in this paper we proved it for wavelet case and also obtained the convergence of wavelet series in L^1 norm.

Mathematics Subject Classification (2000). Primary 41A17; Secondary 42C15.

Keywords. Sidon inequality, trigonometric system, wavelets, convergence in L^1 - norm, Hardy spaces.

1. Introduction

Denote $u = \{u_n, n \in N \, or \, n \in Z\}$ an orthonormal system defined on interval I, where N is the set of non-negative integers and Z is the set of integers. The Dirchlet kernels with respect to this system are denoted by

$$D_n = D_n^u = \sum_{|k|<n} u_k \qquad (n \in p = N \backslash \{0\})$$

If $U = T$ is the complex trigonometric system on [0,1) i.e., $U_n(x) = e_n(x) = e^{2\Pi i x}$ $(x \in I, n \in Z)$ then for every sequence $a = \{a_n, n \in P\}$

$$M_n(a, U) = \frac{1}{n} \int_I \left| \sum_{k=0}^{n-1} a_k D_k(x) \right| dx \leq C \max_{0 \leq k < n} |a_k|, \tag{1.1}$$

holds with an absolute constant $C > 0$. This was proved by S.Sidon in 1938 [9] . Concerning the history and elegant proof see Telyakovskii [10].

A generalization of (1.1) is the following inequality

$$M_n(a,U) \leq C_p \left(\frac{1}{n}\sum_{k=0}^{n-1}|a_k|^p\right)^{1/p} \quad (p>1,\ n\in P), \tag{1.2}$$

where C_p depends only on p.

For the trigonometric system it was proved by Bojanic and Stanojevic [1]. The same holds for complex trigonometric system $T = (e_n,\ n \in N)$ with non- negative indices which can be proved in the same way . The Walsh case was investigated by Moricz and Schipp [7] and (1.2) is proved for the Walsh - Paley system with constant $C_p = \frac{2.05p}{(p-1)}$.

Another generalization for the trigonometric case is given by Buntinas and Tanovic - Miller [2] namely, if $1 \leq p < 2$ and $\frac{1}{p}+\frac{1}{q}=1$, then

$$\frac{1}{n}\int_I \left|\sum_{k=0}^{n-1} a_k D_k(x)\right| dx \leq K_p \left\langle \left(\frac{\log\alpha}{n}\right)\sum_{k=1}^{n}|a_k| + \alpha^{-\frac{1}{q}}\left(\frac{1}{n}\sum_{k=1}^{n}|a_k|^p\right)^{1/p}\right\rangle$$

for all $\alpha \geq 1$ where $K_p = 2\left(1+e^{1/q}\right)(p-1)^{-1/p}$.

Let X be normed subspace of $L^1 = L^1[0,1)$ containing the dyadic step function, i.e., the function of the form

$$A_n = \sum_{k=0}^{2^n-1} a_k \chi[k2^{-n},(k+1)\ 2^{-n}) \tag{1.3}$$

where χ_j denotes the characteristic function of the set 'j' and $a_0 = 0$. The norm in X is denoted by $\|a\|_X$. If $X = L^p$ $(1 \leq p \leq \infty)$ then we denote L^p - norm by $\|.\|_p$. By means of this norm we introduce a sequence norm setting

$$\|a\|_X = \sup_{n\in N}\|A_n\|_X, \tag{1.4}$$

where the functions A_n are defined by (1.3). We denote by X^0 the set of sequences $a = \{a_k\}$ satisfying $\|a\|_X < \infty$. Using this notion (1.2) can be written in the form

$$M_n(a,U) = \sup_{n\in N} M_{2^n}(a,U) \leq C_p\|a\|_p \quad (1\leq p\leq\infty),$$

where $\|.\|_p$ denotes the sequence norm induced by the usual L^p -norm.

The dyadic Hardy space H^p can be defined by means of dyadic maximal function

$$f^*(x) = \sup_{n\in N}\frac{1}{|I_n(x)|}\int_{I_n(x)}|f(t)\ dt| \quad (x\in[0,1),\ f\in L^1)$$

Where $I_n(x)$ is the dyadic interval of the form $[k2^{-n},(k+1)2^{-n})$ containing x and $|I_n(x)| = 2^{-n}$ is the length of $I_n(x)$. The dyadic Hardy space H^p $(1 < p < \infty)$ is the collection of function $f \in L^1$ such that

$$\|f\|_{H^p} = \|f^*\|_p < \infty .$$

It is clear that $\|f\|_1 \leq \|f\|_{H^1}$ and H^1 is a complete proper subspace of L^1. It is known (see [7]) that for $p > 1$

$$\|f\|_p \leq \|f^*\|_p \leq \frac{p}{p-1} \|f\|_p$$

and consequently $H^p = L^p \; if \; 1 < p < \infty$ and in this case the L^p-norm and H^p-norms are equivalent.

The dyadic Hardy space $H = H^1$ has atomic characterization [8]. A function $\beta \in L^\infty$ is called dyadic atom if either $\beta = 1$ or there exists dyadic interval $J \subseteq [0,1)$ such that

(i) $\{\beta \neq 0\} = \{x \in [0,1) \; : \; \beta(x) \neq 0\} \subseteq J$
(ii) $\|\beta\|_\infty = |J|^{-1}$
(iii) $\int_0^1 \beta(t)\, dt = 0$

A function $f \in L^1$ belongs to H if and only if there exist dyadic atom $\beta_0, \beta_1, - - -$ and a sequence $\{a_n \, , n \in N\}$ such that

$$f = \sum_{n=0}^{\infty} a_n \beta_n, \quad \|a\|_{l^1} = \sum_{n=0}^{\infty} |a_n| < \infty , \tag{1.5}$$

furthermore,

$$\|f\|_H \leq \inf \|a\|_{l^1} \leq 25 \|f\|_H ,$$

where infimum is taken over all sequences $a \in l^1$ such that (1.5) holds for some atoms $\beta_0, \beta_1, - - -$.

The classical Hardy space consists of functions f, analytic on unit disc, which satisfy

$$\sup_{0 \leq r < 1} \left(\frac{1}{2\pi} \int_0^{2\pi} \left| F(re^{i\theta}) \right|^p \right)^{1/p} < \infty .$$

By taking real part of the boundary functions

$$\lim_{r \uparrow 1} F\left(re^{i\theta}\right) (0 < \theta < 2\pi)$$

and identifying the boundary of the unit disc with the interval [-1,1), one generates the classical non periodic Hardy space S^p on [0,1) , $(1 \leq p < \infty)$. As in the dyadic case S^p and L^p are isomorphic for $1 < p < \infty$, and $S = S^1$ is a proper Subspace of L^1. Moreover S has an atomic characterization just like that of H. The essential difference is that an atom for S can be supported on non dyadic intervals. Thus every dyadic atom for H can be supported on non dyadic intervals. Thus every dyadic atom is an atom for S but not conversely. Hence $H \subseteq S$

To obtain conditions on the series $\sum_{k=0}^{\infty} a_k u_k$ sufficient to L^1 - convergence. We introduce a class of sequences induced by norm $\|.\|_X$. For a sequence $b = \{b_n, n \in P\}$, set

$$B^n = \sum_{k=2^{n-1}}^{2^n-1} a_k \chi \left[k2^{-n}, (k+1)\ 2^{-n}\right) , \quad (n \in P),$$

and introduce the sequence norm

$$\|b\|_X = \sum_{n=0}^{\infty} 2^n \| \, |B|^n \|_X .$$

If $X = L^p$ we obtain the class of sequences introduced by Fomin [3].

Obviously

$$\|b\|_{L^1} \leq \|b\|_H \leq \|b\|_{L^p} \quad (1 < p \leq \infty)$$

A summation by parts yields that the nth partial sum of the above series can be written in the form

$$S_n = \sum_{k=0}^{n-1} a_k u_k = \sum_{k=1}^{n} \Delta a_k D_k + a_n D_n \quad (n \in P)$$

where $\Delta a_k = a_{k-1} - a_k$. $(k \in P)$.

The convergence of wavelets has been investigated by many authors. Y Meyer [6.ch.2] was among the first to study the convergence of wavelet expansions. He showed that if the mother wavelet is r- regular, the orthogonal wavelet expansion of a function will converge to it in the sense of $L^p(\Re)$, $1 \leq p < \infty$, and in the sense of some Sobolov spaces as well. G.Walter [10] proved that the orthogonal wavelet expansion of a function $f \in L^1 \bigcap L^2$ converges to f pointwise at every point of continuity of f and uniformly on compact subsets of any interval (a, b) on which f is continuous. Later, he relaxed this condition and assumed that the scaling function ϕ satisfies the condition $|\phi(x)| \leq \frac{C}{(1+|x|)^3}$. In [4, 5], S. Kelly, M. Kon, and L. Raphael improved Walter's result by proving pointwise convergence of orthogonal wavelet expansions not only under less stringent conditions, but also by extending them to n-dimensions.

2. Definitions and Notations

Wavelet analysis of a function $f \in L^2(\Re)$ basically consists in the decomposition of 'f' as a sum of wavelets

$$\psi_{b.a} = |a|^{\frac{-1}{2}} \psi \left(\frac{x-b}{a}\right) ,$$

where $\psi_{b,a}$ are dilated and translated copies of mother wavelet ψ and these functions are scaled so that their $L^2(\Re)$ norms are independent of 'a'.

For any $j, k \in Z$, we have

$$\left\| f\left(2^j . - k\right) \right\|_2 = \left[\int_{-\infty}^{\infty} \left| f\left(2^j x - k\right) \right|^2 dx \right]^{1/2} = 2^{-j/2}$$

Hence if a function $\psi \in L^2(\Re)$ has a unit length, then all the functions $\psi_{j,k}$ defined by

$$\psi_{j,k}(x) = 2^{j/2}\, \psi\left(2^j x - k\right), \quad j, k \in Z, \tag{2.1}$$

also have a unit length i.e.,

$$\|\psi_{j,k}\|_2 = \|\psi\|_2 = 1, j, k \in Z.$$

A function $\psi \in L^2(\Re)$ is called an orthogonal wavelet (o.n wavelet), if the family $\{\psi_{j.k}\}$, as defined in (2.1) is an orthonormal basis of $L^2(\Re)$, i.e.,

$$\langle \psi_{j,k}, \psi_{l,m} \rangle = \delta_{j,l}\, \delta_{k,m}, \quad j, k, l, m \in Z$$

where

$$\delta_{j,k} = \begin{cases} 0, & when\ j \neq k \\ 1, & when\ j = k \end{cases}$$

is the Kronecker delta defined on $Z \times Z$. Moreover, every $f \in L^2(\Re)$ can be written as

$$f(x) = \sum_{j,k=-\infty}^{\infty} c_{j,k} \psi_{j,k}(x) \tag{2.2}$$

This series representation of 'f' is called wavelet series. Analogous to the notion of Fourier coefficients the wavelet coefficient $c_{j,k}$ are given by

$$c_{j,k} = \langle f, \psi_{j,k} \rangle = \int_{-\infty}^{\infty} f(x)\, \overline{\psi_{j,k}(x)}\, dx. \tag{2.3}$$

That is, if we define an integral wavelet transform W_ψ on $L^2(\Re)$ by

$$(W_\psi f)(b, a) = |a|^{-1/2} \int_{-\infty}^{\infty} f(x)\, \psi\left(\overline{\frac{x-b}{a}}\right) dx, \quad f \in L^2(\Re)$$

The wavelet coefficient in (2.2) and (2.3) become

$$c_{j,k} = (W_\psi f)\left(\frac{k}{2^j}, \frac{1}{2^j}\right).$$

Denote $\psi = \{\psi_{j,k}, j, k \in Z\}$ an orthonormal wavelet system defined on $I = [0, 1]$. The Dirchlet kernels with respect to orthonormal wavelet system ψ are denoted by

$$D_{m,n} = \sum_{\substack{|j| < m \\ |k| < n}} \psi_{j,k}, (m, n \in P = N/0)$$

Let us also denote

$$M_{m,n}(c,\psi) = \frac{1}{mn}\int_I \left|\sum_{j=0}^{m-1}\sum_{k=0}^{n-1} c_{j,k}D_{j,k}(x)\right| dx$$

where $c=(c_{j,k})$ are wavelet coefficients of the wavelet series,

$$\sum_{j,k=-\infty}^{\infty} c_{j,k}\psi_{j,k}. \tag{2.4}$$

The partial sum of (2.4) is written as

$$S_{p,q} = \sum_{j=-p}^{q}\sum_{k=-p}^{q} c_{j,k}\psi_{j,k}.$$

Set

$$B^{m,n} = \sum_{j=2^{m-1}}^{2^m-1}\sum_{k=2^{n-1}}^{2^n-1} c_{j,k}\chi[j2^{-m},(j+1)2^{-m}]\chi[k2^{-n},(k+1)2^{-n}],$$

and introduce a norm

$$\|c\|_X = \sum_{m,n=0}^{\infty} 2^{m+n}\||B^{m+n}|\|_X.$$

3. Main Results

In this section we will prove Sidon type inequalities for wavelets and convergence of wavelet series in L^1- norm.

Theorem 3.1. *Suppose that for wavelet system* $\psi=\{\psi_{j,k}\, j,k\in Z\}$

$$M_{m,n}(c,\psi) = \frac{1}{mn}\int_I \left|\sum_{j=0}^{m-1}\sum_{k=0}^{n-1} c_{j,k}D_{j,k}(x)\right| dx$$

$$M(c,\psi) = \sup_{m,n} M_{m,n}(c,\psi) \le C\|c\|_\infty \tag{3.1}$$

is satisfied with constant $C>0$ *independent of wavelet coefficients* $c=\{c_{j,k}\}$

(i) *If for every* $m,n,i,t\in N$, $|\psi_{m,n}|=1$, *and*

$$D_{(m+i,n+t)} - D_{(m,n)} = \psi_{m,n}D_{i.t}\,, \tag{3.2}$$

then

$$M(c,\psi) \le C_1\ \|c\|_S\,, \tag{3.3}$$

for all $c=\{c_{j,k}\}$, *where* $C_1>0$ *is constant independent of* c.

(ii) *If for every* $l, r, s \in N$ *and* $0 \leq j, k < 2^s$, $\left|\psi_{(j,k)2^s}\right| = 1$, *where* $\psi_{(j,k)2s} = \psi_{j2^s,k2^s}$ *and*

$$D_{(l,r)2^s+(j,k)} - D_{(l,r)2^s} = \psi_{(l,r)2^s} D_{j,k}, \tag{3.4}$$

then

$$M(c,\psi) \leq C_2 \|c\|_H \tag{3.5}$$

for all $c = \{c_{j,k}\}$, *where* $C_2 > 0$ *is constant independent of* c, *and*

$$D_{(l,r)2^s+(j,k)} = D_{(l2^s+j,r2^s+k)}$$

Theorem 3.2. *Let* ψ *be a wavelet system. If*

$$\|D_{p,q}\| = 0(\log pq) \text{ as } p, q \to \infty, \tag{3.6}$$

then the wavelet series converges in L^1- *norm.*

Proof of Theorem 3.1: First we show that for every $m, n \in N$ and every $c = \{c_{j,k}\}$

$$M_{m,n}(c,\psi) \leq C_1 \|A_{m,n}\|_S . \tag{3.7}$$

where $A_{m,n} = \sum_{j=0}^{m-1} \sum_{k=0}^{n-1} c_{j,k} \chi[j,(j+1))\, \chi[k,(k+1))$.

To prove (3.7) let the sequence c of wavelet coefficients $c = \{c_{j,k}\}$ be such that the corresponding function $A_{m,n}$ is a atom supported in $J = [l,(l+1))$ and $k = [r,(r+1))$. Set $m = l$ and $n = r$. In this case

(a) $c_{j,k} = 0 \left(\begin{array}{l} j \notin [l,(l+1)) \\ k \notin [r,(r+1)) \end{array} \right.$

(b) $\sum_{j=o}^{l-1} \sum_{k=0}^{r-1} c_{j,k} = 0$

(c) $|c_{j,k}| \leq l\, r\,, \quad 0 \leq j < m, \quad 0 \leq k < n\,.$

Thus

$$M_{m,n}(c,\psi) = \frac{1}{m\,n} \int_I \left| \sum_{j=0}^{m-1} \sum_{k=0}^{n-1} c_{j,k} D_{j,k}(t) \right| dt$$

$$= \frac{1}{m\,n} \int_I \left| \sum_{j=0}^{m-1} \sum_{k=0}^{n-1} c_{(l,r)+(j,k)} \left(D_{(l,r)+(j,k)}(t) \right) - D_{(l,r)}(t) \right| dt$$

From (3.2) we get, $= \frac{1}{m\,n} \int_I \left| \sum_{j=0}^{m-1} \sum_{k=0}^{n-1} c_{(l,r)+(j,k)} D_{j,k}(t) \right| dt$

Since by (3.1) $\int_I \left| \sum_{j=0}^{m-1} \sum_{k=0}^{n-1} c_{(l,r)+(j,k)} D_{j,k}(t) \right| dt \leq \max_{\substack{l < i\,(r+1) \\ r < m < (r+1)}} |c_{i,m}|$

By (c) we get

$$M_{m,n}(c,\psi) \leq \frac{1}{m\,n}\, l\, r = 1$$

Replacing atomic decomposition by dyadic atomic decomposition (ii) can be proved in a similar way.

Remark: For every $c = \{c_{j,k}\}$ and $1 < p \leq \infty$, then

$$M(c, \psi) \leq C\|c\|_H \leq C\frac{p}{p-1}\|c\|_p,$$

where $C > 0$ is an absolute constant? □

Proof of Theorem 3.2: If we choose $p < l$ and $q < r$ where $2^{m-1} < l, r < 2^m$ and $2^{n-1} < p, q < 2^n$. Then

$$\|S_{p,q} - S_{l-1,r-1}\|_1 \leq \left\|\sum_{i=l}^{p}\sum_{j=r}^{q} \Delta\, b_{i,j} D_{i,j}\right\|_1 + |c_{l-1,r-1}|\ \|D_{l-1,r-1}\|_1 + |c_{p,q}|\ \|D_{p,q}\|_1$$

where $\Delta\, b_{i,j} = b_{i,j} - b_{i+1,j} - b_{i,j+1} + b_{i+1,j+1}$. On the basis of $\|D_{p,q}\| = 0\ (\log p\, q)$ as $p, q \to \infty$, the second and third term tends to zero as $p, q, l, r \to \infty$. On the basis of above remark the first term is estimated and is equivalent to

$$\left\|\sum_{i=l}^{p}\sum_{j=r}^{q} \Delta\, b_{i,j} D_{i,j}\right\|_1 \leq 2^{m+n}\, \|B^{m,n}\|_1 + \sum_{I_1=m+1}^{\infty}\sum_{I_2=n+1}^{\infty} 2^{(I_1+I_2)}\ \left\|\, |B^{I_1,I_2}|\, \right\|_H + 2^{m+n}\, \|\, |B^{m,n}|\, \|_H$$

which tends to zero as $p, q, l, r \to \infty$. □

References

[1] R. Bojanic and V.Stanojevic, *A class of L^1 -Convergence*, Trans.Amer.Math.Soc. 269 (1982), 577-683.

[2] M. Buntinas and N.Tanovic-Miller, *New Integrability and L^1 -Convergence for an even trigonometric Series*, Radovi Mathematicki, 6 (1990), 149-170.

[3] G.A. Fomin, *Obodnoi klase Trignometriceskih Math.*, Zametki, 23 (1978), 213-222.

[4] S.Kelly, M.Kon, and L. Raphael, *pointwise convergence of wavelet expansions*, Bull. Amer. Math. soc., vol.30 (1994), pp.87-94

[5] ———————, *local convergence for wavelet expansions*, J. Funct. Anal.,Vol.126 (1994), pp.102-138

[6] Y. Meyer, Ondelletes, Herman, Paris (1990).

[7] F. Moricz and F. Schipp, *on integrability and L^1 -convergence of Walsh Series*, J.Math.Anal.App. 146 (1990), 99-109.

[8] F. Schipp, W.R.Wade, P.Simon and J. Pal, *An introduction to dyadic Harmonic Analysis*, Adam Hilger, Bristol, New York, 1990.

[9] S. Siddon, *Über Fourier-Koeffizienten*, J. Lond. Math. Soc., 13 (1938), 181-183.

[10] S.S.Telyakovskii, *On a sufficient condition of Sidon inequality for integrability of trigonometric series*, Mat. Zametki, 14 (1973), 317-328.

[11] G. Walter, *pointwise convergence of wavelet expansions*, J. Approx. Theory, Vol. 80 (1995), pp. 108-118.

N.A. Sheikh
Department of Mathematics
National Institute of Technology Hazratbal Srinagar Kashmir-190006
India
e-mail: neyaznit@yahoo.co.in

Wavelet Analysis and Applications
Tao Qian, Mang I. Vai and Xu Yuesheng, Eds.
Applied and Numerical Harmonic Analysis, 35–42

Almansi Decomposition for Dunkl-Helmholtz Operators

Guangbin Ren and Helmuth R. Malonek

Abstract. We consider the iterated Dunkl-Helmholtz equation $(\Delta_h - \lambda)^n f = 0$ for nonzero λ in a domain of $\mathbb{R}^N$. Here $\Delta_h = \sum_{j=1}^N \mathcal{D}_j^2$ is the Dunkl Laplacian, and $\mathcal{D}_j$ is the Dunkl operator attached to the Coxeter group G associated with the reduced root system R,

$$\mathcal{D}_j f(x) = \frac{\partial f}{\partial x_j}(x) + \sum_{v \in R_+} \kappa_v \frac{f(x) - f(\sigma_v x)}{\langle x, v \rangle} v_j,$$

where κ_v is a multiplicity function on R and σ_v is the reflection with respect to the root v.

We prove that any solution f of the iterated Dunkl-Helmholtz equation has a decomposition of the form

$$f(x) = f_0(x) + R_\mu f_1(x) + \cdots + R_\mu^{n-1} f_{n-1}(x), \qquad \forall\, x \in \Omega,$$

where f_j are annihilated by $\Delta_h - \lambda$, μ is a fixed but arbitrary complex number, and $R_\mu^n = (R_\mu)^n$ are given by $R_\mu = \mu I + R_0$, with I the identity operator and R_0 the Euler operator.

Mathematics Subject Classification (2000). Primary 33C52; Secondary 31A30, 35C10.

Keywords. Dunkl operators, Helmholtz equation, Almansi decomposition.

1. Introduction

Polyharmonic theory is a powerful tool in many fields. As extension of polynomials, polyharmonic functions play a key role in multivariate approximation [1]. The polyharmonic theory has its roots in the theory of elasticity [2] and in radar imaging [3]. The fundamental result in the theory of polyharmonic functions is the

The first author was partially supported by the NNSF of China (No. 10471134), the SRFDP 20050358052, and NCET. The second author was partially supported by the R&D unit *Matemática a Aplicações* (UIMA) of the University of Aveiro, through the Portuguese Foundation for Science and Technology (FCT), co-financed by the European Community fund FEDER.

celebrated Almansi theorem [4, 5], which shows that for any polyharmonic function f of degree n in a starlike domain Ω in $\mathbb{R}^N$ with respect to 0, i.e., $\Delta^n f = 0$, there exist unique harmonic functions $f_0, \ldots, f_{n-1}$ such that

$$f(x) = f_0(x) + |x|^2 f_1(x) + \cdots + |x|^{2(n-1)} f_{n-1}(x), \qquad \forall\ x \in \Omega.$$

We refer to [6] for the applications of the Almansi decomposition in partial differential equations.

As same as the iterated Laplacian, the iterated Helmholtz operators $(\Delta - \lambda)^n$, $\lambda \in \mathbb{C} \setminus \{0\}$, have also gained considerable interest in mathematical physics [7]. These operators can be further considered in the setting of the Dunkl theory. The Dunkl theory is an extension of the classical harmonic theory. In 1989, Dunkl [8] constructed for each Coxeter group a family of commutative differential-difference operators $\mathcal{D}_j$, called Dunkl operators, which can be considered as perturbations of the usual partial derivatives by reflection parts. These operators stem from the analysis of quantum many body system of Calogero-Moser-Sutherland type [9] in mathematical physics. They also have their root in the theory of special functions [10]. With Dunkl operators substituted for partial derivatives $\frac{\partial}{\partial x_j}$, one can define the Laplacian in the Dunkl setting, which is a parametrized operator and invariant under reflection groups. These parametrized Laplacian underlies the Dunkl theory [11]. The Helmholtz operators in the setting of the Dunkl theory are called the Dunkl-Helmholtz operators.

The purpose of this article is to extend Almansi's theorem from Laplacian to the Dunkl-Helmholtz operators. A new phenomena shall arise that the auxiliary function jumps from $|x|^2$ to the Euler operator as λ being away from zero in the Almansi decompositions for $\Delta - \lambda$.

2. Main Theorem

For a nonzero vector $v \in \mathbb{R}^N$, the reflection σ_v in the hyperplane orthogonal to v is defined by

$$\sigma_v x := x - 2\frac{\langle x, v\rangle}{|v|^2} v, \qquad x \in \mathbb{R}^N,$$

where the symbol $\langle x, y\rangle$ denotes the usual Euclidean inner product and $|x|^2 = \langle x, x\rangle$.

A root system R is a finite set of nonzero vectors in $\mathbb{R}^N$ such that $\sigma_v R = R$ and $R \cap \mathbb{R}v = \{\pm v\}$ for all $v \in R$.

The Coxeter group G (or the finite reflection group) generated by the root system R is the subgroup of the orthogonal group $O(N)$ generated by $\{\sigma_u : u \in R\}$.

The positive subsystem R_+ is a subset of R such that $R = R_+ \cup (-R_+)$, where R_+ and $-R_+$ are separated by a hyperplane through the origin.

A multiplicity function κ_v is a G-invariant complex valued function defined on R, i.e, $\kappa_v = \kappa_{gv}$ for all $g \in G$.

The Dunkl operators $\mathcal{D}_j$, associated with the Coxeter group G and the multiplicity function κ, are the first order differential-difference operator

$$\mathcal{D}_j f(x) = \frac{\partial}{\partial x_j} f(x) + \sum_{v \in R_+} \kappa_v \frac{f(x) - f(\sigma_v x)}{\langle x, v \rangle} v_j.$$

The remarkable property of Dunkl operators is commutativity

$$\mathcal{D}_i \mathcal{D}_j = \mathcal{D}_j \mathcal{D}_i.$$

The Dunkl Laplacian is defined as

$$\Delta_h = \mathcal{D}_1^2 + \ldots + \mathcal{D}_N^2.$$

Let Ω be a G-invariant convex domain in $\mathbb{R}^N$ including 0, i.e, $G(\Omega) \subset \Omega$, $0 \in \Omega$, and $tx + (1-t)y \in \Omega$ for all $t \in [0,1]$ and $x, y \in \Omega$. A function $f : \Omega \longrightarrow \mathbb{C}$ in $C^{2n}(\Omega)$ is *Dunkl polyharmonic* of degree n if $(\Delta_h)^n f = 0$.

In [12], the Almansi decomposition theorem is established for Dunkl operators:

Theorem 2.1. *Assume that*

$$\mathrm{Re} \sum_{v \in R_+} \kappa_v > -N/2. \tag{2.1}$$

Let Ω be a G-invariant convex domain in $\mathbb{R}^N$ including 0, where G is the Coxeter group in $\mathbb{R}^N$. If f is a Dunkl polyharmonic function in Ω of degree n, then there exist unique Dunkl harmonic functions $f_0, \ldots, f_{n-1}$ such that

$$f(x) = f_0(x) + |x|^2 f_1(x) + \cdots + |x|^{2(n-1)} f_{n-1}(x), \qquad \forall\ x \in \Omega. \tag{2.2}$$

Conversely, the sum in (2.2)*, with $f_0, \ldots, f_{n-1}$ Dunkl harmonic in Ω, defines a Dunkl polyharmonic function in Ω of degree n.*

In this article we consider the decomposition theorem for the iterated Dunkl-Helmholtz operator.

Definition 2.2. The Dunkl-Helmholtz operator is given by

$$\Delta_{h,\lambda} := \Delta_h - \lambda$$

for any $\lambda \in \mathbb{C} \setminus \{0\}$.

When $\kappa_v = 0$, the Dunkl-Helmholtz operator is just the Helmholtz operator.

We fix $\mu \in \mathbb{C}$ throughout the paper. Let I be the identity operator. For any smooth function f in Ω, we denote the Euler operator

$$R_0 f(x) = \sum_{j=1}^{n} x_j \frac{\partial f}{\partial x_j}(x), \qquad x \in \Omega,$$

and denote

$$R_\mu = \mu I + R_0.$$

For simplicity, we write the iterated operators

$$\Delta_{h,\lambda}^n := (\Delta_{h,\lambda})^n, \qquad R_\mu^n := (R_\mu)^n.$$

For $\lambda \in \mathbb{C} \setminus \{0\}$, we denote

$$c_k = c_{k,\lambda} := \frac{1}{k!(2\lambda)^k}.$$

Our main result is contained in the following theorem.

Theorem 2.3. *Let $\kappa : R \to \mathbb{C}$ be an arbitrary multiplicity function on R, Ω be a G-invariant domain in $\mathbb{R}^N$, $\lambda \in \mathbb{C} \setminus \{0\}$, and $\mu \in \mathbb{C}$. If $f \in C^{2n}(\Omega)$ satisfies*

$$\Delta_{h,\lambda}^n f = 0. \tag{2.3}$$

for some positive integer n, then there exist unique functions $f_0, \ldots, f_{n-1}$ annihilated by the Dunkl-Helmholtz operator $\Delta_{h,\lambda}$ such that

$$f(x) = f_0(x) + R_\mu f_1(x) + \cdots + R_\mu^{n-1} f_{n-1}(x), \qquad \forall\ x \in \Omega. \tag{2.4}$$

Moreover the functions $f_0, \ldots, f_{n-1}$ are given by the following formulae:

$$\begin{aligned}
f_0 &= (I - c_1 R_\mu \Delta_{h,\lambda})(I - c_2 R_\mu^2 \Delta_{h,\lambda}^2) \cdots (I - c_{n-1} R_\mu^{n-1} \Delta_{h,\lambda}^{n-1}) f(x) \\
f_1 &= c_1 \Delta_{h,\lambda}(I - c_2 R_\mu^2 \Delta_{h,\lambda}^2) \cdots (I - c_{n-1} R_\mu^{n-1} \Delta_{h,\lambda}^{n-1}) f(x) \\
&\vdots \\
f_{n-2} &= c_{n-2} \Delta_{h,\lambda}^{n-2} (I - c_{n-1} R_\mu^{n-1} \Delta_{h,\lambda}^{n-1}) f(x) \\
f_{n-1} &= c_{n-1} \Delta_{h,\lambda}^{n-1} f(x).
\end{aligned}$$

Conversely, the sum in (2.4)*, with $f_0, \ldots, f_{n-1}$ annihilated by the Dunkl-Helmholtz operator $\Delta_{h,\lambda}$ in Ω with nonzero λ, defines a function f in Ω satisfying* (2.3).

Remark 2.4. Comparing the Almansi decompositions for the Dunkl operator and the Dunkl-Helmholtz operator, we find the auxiliary function $|x|^2$ in (2.2) changed to R_μ in (2.4) which causes a big difference. The Almansi decomposition for the Dunkl-Helmholtz operator puts no restriction to the multiplicity function κ, in contrast to the case for Dunkl operators. In the literature, it is generally assumed that $\kappa_v \geq 0$ (see [11]).

3. Some Lemmas

We first recall some basic facts in the theory of Dunkl harmonics; see [11].

Let R be a root system in $\mathbb{R}^N$ and G the associated Coxeter group. Fix a positive subsystem R_+ of R. Let $\kappa : R \to \mathbb{C}$ be a fixed multiplicity function $v \mapsto \kappa_v$ on R. The Dunkl operators $\mathcal{D}_j$, associated with the Coxeter group G and the multiplicity function κ, are the first order differential-difference operator. They enjoy the regularity property: If $f \in C^m(\Omega)$ with $m \geq 1$, then $\mathcal{D}_i f \in C^{m-1}(\Omega)$. This follows immediately from the formula

$$\frac{f(x) - f(\sigma_v x)}{\langle x, v \rangle} = \int_0^1 \langle \nabla f(t\sigma_v x + (1-t)x), \frac{2v}{|v|^2} \rangle dt \tag{3.1}$$

for $f \in C^1(\Omega)$ and $v \in R$. Here ∇ is the usual gradient operator.

The Dunkl Laplacian $\Delta_h = \sum_{j=1}^N \mathcal{D}_j^2$ can be written as (see [11]),

$$\Delta_h f(x) = \Delta f(x) + 2\sum_{v\in R_+} \kappa_v \frac{\langle \nabla f(x), v\rangle}{\langle x, v\rangle} - 2\sum_{v\in R_+} \kappa_v \frac{f(x) - f(\sigma_v x)}{\langle x, v\rangle^2}|v|^2.$$

Here Δ is the ordinary Laplacian operator. When $\kappa = 0$, the Dunkl Laplacian Δ_h is just the Laplacian Δ.

By the regularity of Dunkl operators, Δ_h is a regular operator in any G-invariant convex domain. Namely, if $f \in C^m(\Omega)$ with $m \geq 2$, then $\Delta_h f \in C^{m-2}(\Omega)$.

Consider the natural action of $O(N)$ on functions $f : \mathbb{R}^N \to \mathbb{C}$, given by $gf(x) = f(g^{-1}x)$. The Dunkl Laplacian Δ_h is G-invariant, i.e.,

$$g \circ \Delta_h = \Delta_h \circ g, \qquad \forall\ g \in G.$$

Example. In the one-dimensional case $N = 1$, the root system R is of type A_1, the reflection group $G = \mathbb{Z}_2$, and the multiplicity function is given by a single parameter $\kappa \in \mathbb{C}$. The Dunkl operator $\mathcal{D} := \mathcal{D}_1$ and the Dunkl-Helmholtz Laplacian $\Delta_{h,\lambda}$ are given respectively by

$$\begin{aligned} \mathcal{D}f(x) &= f'(x) + \kappa\frac{f(x) - f(-x)}{x}, \\ \Delta_{h,\lambda} f(x) &= f''(x) + 2\kappa\frac{f'(x)}{x} - 2\kappa\frac{f(x) - f(-x)}{x^2} - \lambda f(x). \end{aligned}$$

If f is an even function, then the third term in the formula of $\Delta_{h,\lambda} f$ vanishes, while the sum of the first two items provides a singular Sturm-Liouville operator.

With the regularity of Dunkl operator in hand, we can establish some lemmas. Recall our assumption that Ω is a G-invariant domain in $\mathbb{R}^N$, $\lambda \in \mathbb{C} \setminus \{0\}$, and $\mu \in \mathbb{C}$.

Let $s \in \mathbb{C}$ such that Re $s > 0$, and denote

$$I_s f(x) = \int_0^1 f(tx) t^{s-1} dt.$$

If Ω is a G-invariant domain in $\mathbb{R}^N$ and Re $s > 0$, then as operators on $C^2(\Omega)$ (see [12])

$$\begin{aligned} \Delta_h I_s &= I_{s+2}\Delta, \\ R_s I_s &= I_s R_s = I. \end{aligned}$$

Lemma 3.1. *If $f \in C^2(\Omega)$ and $\mu \in \mathbb{C}$, then*

$$R_{\mu+2}\Delta_h f = \Delta_h R_\mu f. \tag{3.2}$$

Proof. If Re $s > 0$, then $R_{s+2}\Delta_h = R_{s+2}\Delta_h I_s R_s = R_{s+2} I_{s+2}\Delta_h R_s = \Delta_h R_s$, so that $R_{\mu+2}\Delta_h = (R_{s+2} + (\mu - s)I)\Delta_h = \Delta_h R_s + \Delta_h((\mu - s)I) = \Delta_h R_\mu$. □

As a result, we find that if f is Dunkl harmonic, then so is $R_\mu f$.

Lemma 3.2. *Let $f \in C^2(\Omega)$ be such that $\Delta_{h,\lambda} f = 0$. Then for any $\mu \in \mathbb{C}$ and $n \in \mathbb{N}$*

$$c_n \Delta_{h,\lambda}^n R_\mu^n f = f. \tag{3.3}$$

Proof. We prove the identity by induction on n. As $\Delta_h R_0 = (2I + R_0)\Delta_h$, a simple calculation shows that

$$\Delta_{h,\lambda} R_\mu = R_\mu \Delta_{h,\lambda} + 2\Delta_{h,\lambda} + 2\lambda I. \tag{3.4}$$

The assertion (3.3) with $n = 1$ follows from (3.4). Now we assume the validity of (3.3) for the case $n = r$ and prove the case $n = r + 1$. Let $f \in \ker \Delta_{h,\lambda}$, then by assumption

$$\Delta_{h,\lambda}^{r+1} R_\mu^r f = 0. \tag{3.5}$$

Therefore from (3.4)

$$\Delta_{h,\lambda}^{r+1} R_\mu^{r+1} f = \Delta_{h,\lambda}^r (R_\mu \Delta_{h,\lambda} + 2\Delta_{h,\lambda} + 2\lambda) R_\mu^r f.$$

Denote $C_n = 1/c_n = n!2^n$. Applying (3.5) and the induction hypothesis, we have

$$\Delta_{h,\lambda}^{r+1} R_\mu^{r+1} f = \Delta_{h,\lambda}^r R_\mu \Delta_{h,\lambda} R_\mu^r f + 2\lambda C_r f.$$

It is seen that an additional factor appears after having interchanged R_μ with $\Delta_{h,\lambda}$. Continue in this way we obtain

$$\begin{aligned} \Delta_{h,\lambda}^{r+1} R_\mu^{r+1} f &= \Delta_{h,\lambda}^{r-1} R_\mu \Delta_{h,\lambda}^2 R_\mu^r f + 4\lambda C_r f \\ &= \cdots \\ &= R_\mu \Delta_{h,\lambda}^{r+1} R_\mu^r + 2(r+1)\lambda C_r f. \end{aligned}$$

From (3.5), we see that (3.3) holds for $n = r + 1$. This completes the proof. □

4. Proof of the Main Theorem

Now we come to the proof of our main theorem.

Proof of Theorem 2.3. Let $n \in \mathbb{N}$ and denote $H_n = \{f \in C^{2n}(\Omega) : \Delta_{h,\lambda}^n f = 0\}$. For shorthand, we write

$$T_n = (R_\mu)^n.$$

It is sufficient to show that

$$H_n = H_{n-1} + T_{n-1} H_1, \quad n \in \mathbb{N}.$$

Notice that Lemma 3.2 states that in H_1

$$c_n \Delta_{h,\lambda}^n T_n = I. \tag{4.1}$$

We split the proof into two parts.

(i) $H_n \supset H_{n-1} + T_{n-1} H_1$.

As $H_{n-1} \subset H_n$, we only need to show that $T_{n-1} H_1 \subset H_n$. For any $g \in H_1$, it follows from (4.1) that

$$\Delta_{h,\lambda}^n (T_{n-1} g) = c_{n-1}^{-1} \Delta_{h,\lambda} (c_{n-1} \Delta_{h,\lambda}^{n-1} T_{n-1}) g = c_{n-1}^{-1} \Delta_{h,\lambda} g = 0.$$

(ii) $H_n \subset H_{n-1} + T_{n-1}H_1$.

For any $f \in H_n$, we have the decomposition

$$f = (I - c_{n-1}T_{n-1}\Delta_{h,\lambda}^{n-1})f + T_{n-1}(c_{n-1}\Delta_{h,\lambda}^{n-1}f).$$

It is evident that the function between brackets in the second term belongs to H_1. We only need to show that also the first term is in H_{n-1}. This can be verified directly. Indeed

$$\begin{aligned}\Delta_{h,\lambda}^{n-1}(I - c_{n-1}T_{n-1}\Delta_{h,\lambda}^{n-1})f &= (\Delta_{h,\lambda}^{n-1} - (c_{n-1}\Delta_{h,\lambda}^{n-1}T_{n-1})\Delta_{h,\lambda}^{n-1})f \\ &= (\Delta_{h,\lambda}^{n-1} - \Delta_{h,\lambda}^{n-1})f = 0,\end{aligned}$$

as desired.

This proves that $H_n = H_{n-1} + T_{n-1}H_1$. By induction, we can easily deduce that $H_n = H_1 + T_1H_1 + \cdots + T_{n-1}H_1$.

Next we prove that for any $f \in H_n$ the decomposition

$$f = g + T_{n-1}f_{n-1}, \quad g \in H_{n-1},\ f_{n-1} \in H_1$$

is unique. In fact, for such a decomposition, applying $\Delta_{h,\lambda}^{n-1}$ on both sides we obtain

$$\begin{aligned}\Delta_{h,\lambda}^{n-1}f &= \Delta_{h,\lambda}^{n-1}g + \Delta_{h,\lambda}^{n-1}T_{n-1}f_{n-1} \\ &= c_{n-1}^{-1}f_{n-1}.\end{aligned}$$

Therefore

$$f_{n-1} = c_{n-1}\Delta_{h,\lambda}^{n-1}f,$$

so that

$$g = f - T_{n-1}f_{n-1} = (I - c_{n-1}T_{n-1}\Delta_{h,\lambda}^{n-1})f.$$

Thus the uniqueness follows by induction.

To prove the converse, we see from (3.3) that, for any $n \in \mathbb{N}$, $\Delta_{h,\lambda}^{n+1}R_\mu^n H_1 = 0$. Replacing n by j, we have

$$\Delta_{h,\lambda}^{n}R_\mu^j H_1 = 0$$

for any $n > j$. So $R_\mu^j H_1 \subset H_n$ for any $j < n$, as desired. □

References

[1] Kounchev, O. I., *Multivariate Polysplines: Applications to Numerical and Wavelet Analysis*, San Diego: Academic Press 2001.

[2] Lurie, S. A. and Vasiliev, V. V., *The Biharmonic Problem in the Theory of Elasticity*, Amsterdam: Gordon and Breach Publ. 1995.

[3] Andersson, L. E., Elfving, T., and Golub G. H., *Solution of biharmonic equations with application to radar imaging*, J. Comput. Appl. Math. 94 (1998), 153–180.

[4] Aronszajn, N. and Creese T. M., Lipkin, L. J., *Polyharmonic Functions*, New York: The Clarendon Press, Oxford University Press 1983.

[5] Malonek, H. R. and Ren, G. B., *Almansi-type theorems in Clifford analysis*, Math. Methods Appl. Sci. 25 (2002), 1541–1552.

[6] Obolashvili, E., *Higher Order Partial Differential Equations in Clifford Analysis, Effective Solutions to Problems*, Progress in Mathematical Physics 28, Boston: Birkhäuser Boston Inc. 2003.

[7] Courant, R. and Hilbert, D., *Methods of Mathematical Physics, Vol. II: Partial Differential Equations*, New York-London: Interscience Publishers 1962.

[8] Dunkl, C. F., *Differential-difference operators associated to reflection groups*, Trans. Amer. Math. Soc. 311(1989), 167–183.

[9] van Diejen, J. F. and Vinet, L., *Calogero-Sutherland-Morser Models*, New York: Springer-Verlag 2000.

[10] Vilenkin, N. Ja. and Klimyk, A. U., *Representation of Lie Groups and Special Functions, Recent Advances*, Mathematics and its Applications 316, Dordrecht: Kluwer Academic Publishers Group 1995.

[11] Dunkl, C. F. and Xu, Y., *Orthogonal Polynomials of Several Variables*, Cambridge: Cambridge Univ. Press 2001.

[12] Ren, G. B., *Almansi decomposition for Dunkl operators*, Science in China Ser. A 48 (2005), 1541–1552.

Guangbin Ren
University of Science and Technology of China,
Department of Mathematics,
Hefei, Anhui 230026,
P.R. China
e-mail: `rengb@ustc.edu.cn`

Helmuth R. Malonek
Universidade de Aveiro,
Departamento de Matemática
P-3810-193 Aveiro, Portugal
e-mail: `hrmalon@mat.ua.pt`

Wavelet Analysis and Applications
Tao Qian, Mang I. Vai and Xu Yuesheng, Eds.
Applied and Numerical Harmonic Analysis, 43–46

An Uncertainty Principle for Operators

Michael G. Cowling and M. Sundari

Abstract. Hardy's Uncertainty Principle asserts that if f is a function on $\mathbb{R}^n$ such that $\exp(\alpha|\cdot|^2)f$ and $\exp(\beta|\cdot|^2)\hat{f}$ are bounded, where $\alpha\beta > \frac{1}{4}$, then $f = 0$. In this paper, we prove a version of Hardy's result for operators.

Perhaps the basic difficulty in Fourier analysis, which is evident in the theory of wavelets, is that nontrivial functions cannot be localised in time and frequency. One manifestation of this is Hardy's Uncertainty Principle: suppose that f is a function on $\mathbb{R}^n$ and that

$$|f(x)| \le C \exp(-\alpha|x|^2) \qquad \forall x \in \mathbb{R}^n$$
$$|\hat{f}(\xi)| \le C \exp(-\beta|\xi|^2) \qquad \forall \xi \in \mathbb{R}^n.$$

If moreover $\alpha\beta > 1/4$, then $f = 0$; if $\alpha\beta = 1/4$, then $f(x) = \exp(-\alpha|x|^2)$, up to a constant. In this theorem, and in the rest of this paper, the Fourier transform $\hat{f}$ of f is defined by

$$\hat{f}(\xi) = \int_{\mathbb{R}^n} f(x) \exp(-i\xi \cdot x)\, dx \qquad \forall \xi \in \mathbb{R}^n.$$

A proof of Hardy's Uncertainty Principle (with a different definition of the Fourier transform and therefore stated slightly differently) may be found in [2]. In this paper, we prove a version of Hardy's result for operators.

1. The Main Result

Suppose that K is an operator on $L^2(\mathbb{R}^n)$ which is given by a kernel k, that is,

$$Kf(x) = \int_{\mathbb{R}^n} k(x, y)\, f(y)\, dy \qquad \forall x \in \mathbb{R}^n$$

This paper was prepared at the University of New South Wales. The second-named author was supported by an ARC grant held by the first-named author. She wishes to express her thanks for this support.

for all f in $L^2(\mathbb{R}^n)$. We call K a kernel operator. Kernel operators may be given different partial orderings. We write $|K_1| \le |K_2|$ if

$$\|K_1 f\|_2 \le \|K_2 f\|_2 \qquad \forall f \in L^2(\mathbb{R}^n)$$

and $|k_1| \le |k_2|$ if

$$|k_1(x,y)| \le |k_2(x,y)| \qquad \forall x, y \in \mathbb{R}^n.$$

We may omit some of the absolute value signs if one of the operators is positive, or if one of the kernels is positive.

The heat semigroup provides an important family of operators on $L^2(\mathbb{R}^n)$. We define the heat kernel p_s by

$$p_s(x,y) = C(s) \exp\Big(-\frac{|x-y|^2}{4s}\Big) \qquad \forall x, y \in \mathbb{R}^n$$

where $C(s)$ depends on n and on s but its precise value is irrelevant, and define the heat operator P_s by

$$P_s f(x) = \int_{\mathbb{R}^n} p_s(x,y)\, f(y)\, dy \qquad \forall x \in \mathbb{R}^n$$

for all f in $L^2(\mathbb{R}^n)$. Often P_s is written as $\exp(s\Delta)$ or $\exp(-s\Delta)$, depending on how the Laplacian is normalised.

Here is our version of Hardy's theorem for operators. If K is a convolution operator, this boils down to the classical version of Hardy's Uncertainty Principle, but otherwise it is more general.

Theorem 1. *Suppose that K is the operator on $L^2(\mathbb{R}^n)$ associated to the kernel k, and that*

$$|k| \le C p_s$$
$$|K| \le C P_t$$
$$s < t.$$

Then $K = 0$.

Before we proceed to the proof, we note that if m is any bounded measurable function on $\mathbb{R}^n$ and $k(x,y) = m(x)\, p_s(x,y)$, then the first two inequalities of the theorem hold when $t = s$; but clearly k is more general than a Gaussian.

Proof. Take any smooth compactly supported function b on $\mathbb{R}^n$. We will show that $K^* b = 0$. Since b is arbitrary, this establishes that $K^* = 0$, and hence $K = 0$.

To do this, take s' such that $s < s' < t$. Then

$$\begin{aligned} |K^* b(x)| &= \Big| \int_{\mathbb{R}^n} \bar{k}(y,x)\, b(y)\, dy \Big| \\ &\le C(s) \int_{\mathbb{R}^n} \exp\Big(-\frac{|y-x|^2}{4s}\Big)\, |b(y)|\, dy \\ &\le C(s,s',b) \exp\Big(-\frac{|x|^2}{4s'}\Big) \qquad \forall x \in \mathbb{R}^n. \end{aligned}$$

On the other hand, for any nonnegative integer k,

$$\begin{aligned}
\|\Delta^k K^* b\|_2 &= \sup\big\{\big|\big\langle \Delta^k K^* b, g\big\rangle\big| : g \in C_c^\infty(\mathbb{R}^n),\ \|g\|_2 \le 1\big\} \\
&\le \|b\|_2 \sup\big\{\big\|K\Delta^k g\big\|_2 : g \in C_c^\infty(\mathbb{R}^n),\ \|g\|_2 \le 1\big\} \\
&\le C\,\|b\|_2 \sup\big\{\big\|P_t \Delta^k g\big\|_2 : g \in C_c^\infty(\mathbb{R}^n),\ \|g\|_2 \le 1\big\} \\
&= C\,\|b\|_2 \sup\big\{\exp(-t|\xi|^2)\,|\xi|^{2k} : \xi \in \mathbb{R}^n\big\} \\
&= C\Big(\frac{k}{et}\Big)^k \|b\|_2
\end{aligned}$$

(when $k = 0$, the right hand side is to be interpreted as $C\|b\|_2$). Now take t' such that $s' < t' < t$. As noted by Thangavelu [4],

$$\begin{aligned}
\|\exp(t'|\cdot|^2)(K^*b)\,\hat{}\,\|_2 &\le \sum_{k\in\mathbb{N}} \frac{1}{k!}\|(t'|\cdot|^2)^k (K^*b)\,\hat{}\,\|_2 \\
&\le C \sum_{k\in\mathbb{N}} \frac{(t')^k}{k!}\Big(\frac{k}{et}\Big)^k \|b\|_2 \\
&= C \sum_{k\in\mathbb{N}} \Big(\frac{t'}{t}\Big)^k \Big(\frac{k}{e}\Big)^k \frac{1}{k!}\,\|b\|_2 \\
&< \infty.
\end{aligned}$$

Now a form of Hardy's principle proved by Cowling and Price [1], which also follows from a result of Beurling proved in Hörmander [3], states that if

$$\begin{gathered}
\|\exp\Big(\frac{|\cdot|^2}{4s'}\Big) f\|_\infty < \infty \\
\|\exp(t'|\cdot|^2)\,\hat{f}\|_2 < \infty \\
s' \le t'
\end{gathered}$$

then $f = 0$. We apply this with K^*b in place of f to deduce the required result. □

References

[1] M.G. Cowling and J.F. Price, "Bandwidth versus time concentration: the Heisenberg–Pauli–Weyl inequality", *SIAM J. Math. Anal.* **15** (1984), 151–165.

[2] H. Dym and H.P. McKean, *Fourier series and integrals.* Academic Press, New York, London, 1972.

[3] L. Hörmander, "A uniqueness theorem of Beurling for Fourier transform pairs", *Ark. Mat.* **29** (1991), 237–240.

[4] S. Thangavelu, Conference presentation in Kerala, India, January 2005.

Michael G. Cowling
School of Mathematics and Statistics
University of New South Wales
UNSW Sydney 2052
Australia
e-mail: m.cowling@unsw.edu.au

M. Sundari
Department of Mathematics
IIT Roorkee
Roorkee 247 667
Uttaranchal
India
e-mail: sundafma@iitr.ernet.in

Wavelet Analysis and Applications
Tao Qian, Mang I. Vai and Xu Yuesheng, Eds.
Applied and Numerical Harmonic Analysis, 47–56

Uncertainty Principle for Clifford Geometric Algebras $Cl_{n,0}$, $n = 3 \pmod 4$ Based on Clifford Fourier Transform

Eckhard S.M. Hitzer and Bahri Mawardi

Soli Deo Gloria

Abstract. First, the basic concepts of the multivector functions, vector differential and vector derivative in geometric algebra are introduced. Second, we define a generalized real Fourier transform on Clifford multivector-valued functions ($f : \mathbb{R}^n \to Cl_{n,0},\ n = 3 \pmod 4$). Third, we introduce a set of important properties of the Clifford Fourier transform on $Cl_{n,0},\ n = 3 \pmod 4$ such as differentiation properties, and the Plancherel theorem. Finally, we apply the Clifford Fourier transform properties for proving a *directional* uncertainty principle for $Cl_{n,0},\ n = 3 \pmod 4$ multivector functions.

Mathematics Subject Classification (2000). Primary 15A66; Secondary 43A32.

Keywords. Vector derivative, multivector-valued function, Clifford (geometric) algebra, Clifford Fourier transform, uncertainty principle.

1. Introduction

In the field of applied mathematics the Fourier transform has developed into an important tool. It is a powerful method for solving partial differential equations. The Fourier transform provides also a technique for signal analysis where the signal from the original domain is transformed to the spectral or frequency domain. In the frequency domain many characteristics of the signal are revealed. With these facts in mind, we extend the Fourier transform in geometric algebra.

Brackx et al. [1] extended the Fourier transform to multivector valued function-distributions in $Cl_{0,n}$ with compact support. They also showed some properties of this generalized Fourier transform. A related applied approach for hypercomplex Clifford Fourier transformations in $Cl_{0,n}$ was followed by Bülow et al. [2].

Support by University of Fukui GEPIS 2004 program.

By extending the classical trigonometric exponential function $\exp(j\,\boldsymbol{x} * \boldsymbol{\xi})$ (where $*$ denotes the scalar product of $\boldsymbol{x} \in \mathbb{R}^m$ with $\boldsymbol{\xi} \in \mathbb{R}^m$, j the imaginary unit) in [3, 4], McIntosh et al. generalized the classical Fourier transform. Applied to a function of m real variables this generalized Fourier transform is holomorphic in m complex variables and its inverse is *monogenic* in $m+1$ real variables, thereby effectively extending the function of m real variables to a monogenic function of $m+1$ real variables (with values in a *complex* Clifford algebra). This generalization has significant applications to harmonic analysis, especially to singular integrals on surfaces in $\mathbb{R}^{m+1}$. Based on this approach Kou and Qian obtained a Clifford Payley-Wigner theorem and derived Shannon interpolation of band-limitted functions using the monogenic sinc function [5, and references therein]. The Clifford Payley-Wigner theorem also allows to derive left-entire (left-monogenic in the whole $\mathbb{R}^{m+1}$) functions from square integrable functions on $\mathbb{R}^m$ with compact support.

In this paper we adopt and expand[1] to $\mathcal{G}_n,\ n = 3\,(\mathrm{mod}\,4)$ the generalization of the Fourier transform in Clifford geometric algebra $\mathcal{G}_3$ recently suggested by Ebling and Scheuermann [7]. We introduce detailed properties of the real[2] Clifford geometric algebra Fourier transform (CFT), which we subsequently use to define and prove a general directional uncertainty principle for $\mathcal{G}_n$ multivector functions.

2. Clifford's Geometric Algebra $\mathcal{G}_n$ of $\mathbb{R}^n$

Let us consider now and in the following an orthonormal vector basis $\{\boldsymbol{e}_1, \boldsymbol{e}_2, \ldots, \boldsymbol{e}_n\}$ of the real n-dimensional Euclidean vector space $\mathbb{R}^n$ with $n = 3\,(\mathrm{mod}\,4)$. Each basis vector has unit square, i.e. $\boldsymbol{e}_k^2 = 1$, $1 \leq k \leq n$. The geometric algebra over $\mathbb{R}^n$ denoted by $\mathcal{G}_n$ then has the graded 2^n-dimensional basis

$$\{1, \boldsymbol{e}_1, \boldsymbol{e}_2, \ldots, \boldsymbol{e}_n, \boldsymbol{e}_{12}, \boldsymbol{e}_{31}, \boldsymbol{e}_{23}, \ldots, i_n = \boldsymbol{e}_1\boldsymbol{e}_2 \ldots \boldsymbol{e}_n\}. \tag{2.1}$$

For the simplest case of $n = 3$ the basis reduces to

$$\begin{aligned} & \{1, \boldsymbol{e}_1, \boldsymbol{e}_2, \boldsymbol{e}_3, \boldsymbol{e}_{23}, \boldsymbol{e}_{31}, \boldsymbol{e}_{12}, i_3 = \boldsymbol{e}_1\boldsymbol{e}_2\boldsymbol{e}_3\} \\ = \ & \{1, i_3, \boldsymbol{e}_1, i_3\boldsymbol{e}_1 = \boldsymbol{e}_{23}, \boldsymbol{e}_2, i_3\boldsymbol{e}_2 = \boldsymbol{e}_{31}, \boldsymbol{e}_3 = \boldsymbol{e}_2\boldsymbol{e}_{23}, \boldsymbol{e}_{12} = \boldsymbol{e}_{31}\boldsymbol{e}_{23}\} \\ \doteq \ & \{1, i_3, \boldsymbol{e}_{23}, i_3\boldsymbol{e}_{23} = -\boldsymbol{e}_1, \boldsymbol{e}_{31}, i_3\boldsymbol{e}_{31} = -\boldsymbol{e}_2, \boldsymbol{e}_{12} = \boldsymbol{e}_{31}\boldsymbol{e}_{23}, i_3\boldsymbol{e}_{12} = -\boldsymbol{e}_3\}. \end{aligned} \tag{2.2}$$

Equation (2.2) exemplifies for $n = 3$ the general isomorphisms

$$\mathcal{G}_n \approx \mathcal{G}_{n-1} \times \mathbb{C} \approx \mathcal{G}_{0,n-1} \times \mathbb{C}, \tag{2.3}$$

[1]For further details and proofs in the case of $n = 3$ compare [6]. In the geometric algebra literature [8] instead of the mathematical notation $Cl_{p,q}$ the notation $\mathcal{G}_{p,q}$ is widely in use. It is convention to abbreviate $\mathcal{G}_{n,0}$ to $\mathcal{G}_n$.

[2]The meaning of *real* in this context is, that we use the n-dimensional volume element $i_n = \boldsymbol{e}_1\boldsymbol{e}_2 \ldots \boldsymbol{e}_n$ of the geometric algebra $\mathcal{G}_n$ over the field of the reals $\mathbb{R}$ to construct the kernel of the Clifford Fourier transformation of definition 4.1. This i_n has a clear geometric interpretation. Note that $i_n^2 = -1$ for $n = 2, 3\,(\mathrm{mod}\,4)$.

which can be exploited to transfer results from a complexified Clifford algebra $\mathcal{G}_{0,n-1} \times \mathbb{C}$ to the real geometric algebra $\mathcal{G}_n$.

The *grade selector* is defined as $\langle M \rangle_k$ for the k-vector part of M, especially $\langle M \rangle = \langle M \rangle_0$. Then M can be expressed as

$$M = \langle M \rangle + \langle M \rangle_1 + \langle M \rangle_2 + \ldots + \langle M \rangle_n. \tag{2.4}$$

The *reverse* of M is defined by the anti-automorphism

$$\widetilde{M} = \sum_{k=0}^{k=n} (-1)^{k(k-1)/2} \langle M \rangle_k. \tag{2.5}$$

The *square norm* of M is defined by

$$\|M\|^2 = \langle M \widetilde{M} \rangle, \tag{2.6}$$

where

$$\langle M \widetilde{N} \rangle = M * \widetilde{N} = \sum_A \alpha_A \beta_A \tag{2.7}$$

is a real valued (inner) *scalar product* for any M, N in $\mathcal{G}_n$ with $M = \sum_A \alpha_A \boldsymbol{e}_A$ and $N = \sum_A \beta_A \boldsymbol{e}_A$, $A \in \{0, 1, 2, \ldots, n, 12, 31, 23, \ldots, 12 \ldots n\}$, $\alpha_A, \beta_A \in \mathbb{R}$, and $\boldsymbol{e}_A$ the basis elements of (2.1). Especially for vectors $\boldsymbol{a}, \boldsymbol{b} \in \mathbb{R}^n$ we get (using the costumary dot)

$$\boldsymbol{a} \cdot \boldsymbol{b} = \langle \boldsymbol{a}\boldsymbol{b} \rangle = \boldsymbol{a} * \boldsymbol{b} = \sum_{A=1}^{n} \alpha_A \beta_A \tag{2.8}$$

As a consequence we obtain the *multivector Cauchy-Schwarz inequality*

$$|\langle M \widetilde{N} \rangle|^2 \leq \|M\|^2 \, \|N\|^2 \quad \forall \, M, N \in \mathcal{G}_n. \tag{2.9}$$

3. Multivector Functions, Vector Differential and Vector Derivative

Let $f = f(\boldsymbol{x})$ be a multivector-valued function of a vector variable $\boldsymbol{x}$ in $\mathcal{G}_n$. For an arbitrary vector $\boldsymbol{a}$ we define[3] the *vector differential* in the $\boldsymbol{a}$ direction as

$$\boldsymbol{a} \cdot \nabla f(\boldsymbol{x}) = \lim_{\epsilon \to 0} \frac{f(\boldsymbol{x} + \epsilon \boldsymbol{a}) - f(\boldsymbol{x})}{\epsilon} \tag{3.1}$$

provided this limit exists and is well defined. The basis independent linear *vector derivative* ∇ defined in [8, 9] obeys equation (3.1) for all vectors $\boldsymbol{a}$ and can be expanded as

$$\nabla = \boldsymbol{e}_k \partial_k = \boldsymbol{e}_1 \partial_1 + \boldsymbol{e}_2 \partial_2 + \ldots + \boldsymbol{e}_n \partial_n, \tag{3.2}$$

For use in later sections we state a number of elementary properties of the vector differential and the vector derivative (compare [8, 9])

[3]Bracket convention: $A \cdot BC = (A \cdot B)C \neq A \cdot (BC)$ and $A \wedge BC = (A \wedge B)C \neq A \wedge (BC)$ for multivectors $A, B, C \in \mathcal{G}_{p,q}$. The vector variable index $\boldsymbol{x}$ of the vector derivative is dropped: $\boldsymbol{\nabla_x} = \boldsymbol{\nabla}$ and $\boldsymbol{a} \cdot \boldsymbol{\nabla_x} = \boldsymbol{a} \cdot \boldsymbol{\nabla}$, but not when differentiating with respect to a different vector variable (compare e.g. proposition 3.2).

Proposition 3.1 (Chain rule for $g \circ \lambda, \lambda \in \mathbb{R}$). *For* $f(\boldsymbol{x}) = g(\lambda(\boldsymbol{x}))$, $\lambda(\boldsymbol{x}) \in \mathbb{R}$,

$$\boldsymbol{a} \cdot \nabla f = \{\boldsymbol{a} \cdot \nabla \lambda(\boldsymbol{x})\} \frac{\partial g}{\partial \lambda}. \tag{3.3}$$

Proposition 3.2 (Derivative from differential).

$$\nabla f = \nabla_{\boldsymbol{a}} (\boldsymbol{a} \cdot \nabla f). \tag{3.4}$$

Differentiating twice with the vector derivative, we get the differential Laplacian operator ∇^2. We can write $\nabla^2 = \nabla \cdot \nabla + \nabla \wedge \nabla$. But for integrable functions $\nabla \wedge \nabla = 0$. In this case we have $\nabla^2 = \nabla \cdot \nabla$.

The following form of the product rule deviates from [8] insofar as we do not use the perhaps unfamiliar overdot notation of Hestenes and Sobczyk.

Proposition 3.3 (Product rule).

$$\nabla(fg) = (\nabla f)g + \nabla_{\boldsymbol{a}} f(\boldsymbol{a} \cdot \nabla g) = (\nabla f)g + \sum_{k=1}^{n} \boldsymbol{e}_k f(\partial_k g). \tag{3.5}$$

Note that the multivector functions f and g in (3.5) *do not necessarily commute.*

Proposition 3.4 (Integration by parts).

$$\int_{\mathbb{R}^n} g(\boldsymbol{x})[\boldsymbol{a} \cdot \nabla h(\boldsymbol{x})] d^n\boldsymbol{x} = \left[\int_{\mathbb{R}^{n-1}} g(\boldsymbol{x}) h(\boldsymbol{x}) d^{n-1}\boldsymbol{x}\right]_{a\cdot x=-\infty}^{a\cdot x=\infty} - \int_{\mathbb{R}^n} [\boldsymbol{a} \cdot \nabla g(\boldsymbol{x})] h(\boldsymbol{x}) d^n\boldsymbol{x}. \tag{3.6}$$

Remark 3.5. Proposition 3.4 reduces to the familiar coordinate form, if we insert for $\boldsymbol{a}$ the grade 1 basis vectors $\boldsymbol{e}_k, 1 \leq k \leq n$ of (2.1), because

$$\boldsymbol{e}_k \cdot \nabla = \partial_k \quad \text{and} \quad \boldsymbol{e}_k \cdot \boldsymbol{x} = x_k. \tag{3.7}$$

But since the introduction of a coordinate system is arbitrary, we can conversly always rotate every chosen coordinate vector into the direction of the vector $\boldsymbol{a}$ of proposition 3.4, which shows that the generalized form 3.4 for the integration by parts formula is valid. Proposition 3.4 is used in the proof of the directional uncertainty principle 5.1.

4. Clifford Fourier Transform (CFT)

Definition 4.1. The Clifford Fourier transform (CFT) of $f(\boldsymbol{x})$ is the function $\mathcal{F}\{f\}$: $\mathbb{R}^n \to \mathcal{G}_n$ given by

$$\mathcal{F}\{f\}(\boldsymbol{\omega}) = \int_{\mathbb{R}^n} f(\boldsymbol{x})\, e^{-i_n \boldsymbol{\omega} \cdot \boldsymbol{x}}\, d^n\boldsymbol{x}, \tag{4.1}$$

where we can write $\boldsymbol{\omega} = \omega_1 \boldsymbol{e}_1 + \omega_2 \boldsymbol{e}_2 + \ldots + \omega_n \boldsymbol{e}_n$, $\boldsymbol{x} = x_1 \boldsymbol{e}_1 + x_2 \boldsymbol{e}_2 + \ldots + x_n \boldsymbol{e}_n$ with $\boldsymbol{e}_1, \boldsymbol{e}_2, \ldots, \boldsymbol{e}_n$ the basis vectors of $\mathbb{R}^n$.

Note that

$$d^n\boldsymbol{x} = \frac{d\boldsymbol{x_1} \wedge d\boldsymbol{x_2} \wedge \ldots \wedge d\boldsymbol{x_n}}{i_n} \tag{4.2}$$

TABLE 1. Properties of the Clifford Fourier transform (CFT)

Property	Multivector Function	CFT
Linearity	$\alpha f(\boldsymbol{x})+\beta\, g(\boldsymbol{x})$	$\alpha\mathcal{F}\{f\}(\boldsymbol{\omega})+\ \beta\mathcal{F}\{g\}(\boldsymbol{\omega})$
Delay	$f(\boldsymbol{x}-\boldsymbol{a})$	$e^{-i_n\boldsymbol{\omega}\cdot\boldsymbol{a}}\mathcal{F}\{f\}(\boldsymbol{\omega})$
Shift	$e^{i_n\boldsymbol{\omega}_0\cdot\boldsymbol{x}}f(\boldsymbol{x})$	$\mathcal{F}\{f\}(\boldsymbol{\omega}-\boldsymbol{\omega}_0)$
Scaling	$f(a\boldsymbol{x})$, $a\in\mathbb{R}\setminus\{0\}$	$\frac{1}{\lvert a\rvert^n}\mathcal{F}\{f\}(\frac{\boldsymbol{\omega}}{a})$
Convolution	$(f\star g)(\boldsymbol{x})$	$\mathcal{F}\{f\}(\boldsymbol{\omega})\,\mathcal{F}\{g\}(\boldsymbol{\omega})$
Vec. diff.	$\boldsymbol{a}\cdot\nabla f(\boldsymbol{x})$	$i_n\ \boldsymbol{a}\cdot\boldsymbol{\omega}\mathcal{F}\{f\}(\boldsymbol{\omega})$
	$\boldsymbol{a}\cdot\boldsymbol{x}\ f(\boldsymbol{x})$	$i_n\ \boldsymbol{a}\cdot\nabla_{\boldsymbol{\omega}}\ \mathcal{F}\{f\}(\boldsymbol{\omega})$
	$\boldsymbol{x}f(\boldsymbol{x})$	$i_n\ \nabla_{\boldsymbol{\omega}}\ \mathcal{F}\{f\}(\boldsymbol{\omega})$
Vec. deriv.	$\nabla^m f(\boldsymbol{x})$	$(i_n\ \boldsymbol{\omega})^m\mathcal{F}\{f\}(\boldsymbol{\omega})$
Plancherel T.	$\int_{\mathbb{R}^n} f_1(\boldsymbol{x})\widetilde{f_2(\boldsymbol{x})}\,d^n\boldsymbol{x}$	$\frac{1}{(2\pi)^n}\int_{\mathbb{R}^n}\mathcal{F}\{f_1\}(\boldsymbol{\omega})\widetilde{\mathcal{F}\{f_2\}(\boldsymbol{\omega})}\,d^n\boldsymbol{\omega}$
sc. Parseval T.	$\int_{\mathbb{R}^n}\ \lVert f(\boldsymbol{x})\rVert^2\,d^n\boldsymbol{x}$	$\frac{1}{(2\pi)^n}\int_{\mathbb{R}^n}\ \lVert\mathcal{F}\{f\}(\boldsymbol{\omega})\rVert^2\,d^n\boldsymbol{\omega}$

is scalar valued ($d\boldsymbol{x_k}=dx_k\boldsymbol{e_k}$, $k=1,2,\ldots,n$, no summation). For the dimension $n=3(\mathrm{mod}\,4)$ the pseudoscalar i_n acts like a commutative[4] imaginary unit ($i_n^2=-1$), i.e. i_n commutes with every element of $\mathcal{G}_n$ (it is *central*), and hence the Clifford Fourier kernel $e^{-i_n\boldsymbol{\omega}\cdot\boldsymbol{x}}$ will also commute with every element of $\mathcal{G}_n$. We therefore have the isomorphism (2.3) [exemplified for $n=3$ in (2.2)]. And in consequence, we also have an isomorphism between the presented Fourier transform and the classical Fourier transform, which also provides a straighforward strategy for the proofs of the properties of the CFT listed in table 1. An alternative way would be to generalize the proofs for $n=3$ in [6] to $n=3(\mathrm{mod}\,4)$. Due to the isomorphism, the CFT of equation (4.2) can be broken down to a tupel of 2^{n-1} scalar complex Fourier transforms, which also permits for numerical applications to make use of well-established fast Fourier transform algorithms. This has already been exploited for $n=3$ in [7].

Theorem 4.2. *The Clifford Fourier transform* $\mathcal{F}\{f\}$ *of* $f\in L^2(\mathbb{R}^n,\mathcal{G}_n)$, $\int_{\mathbb{R}^n}\lVert f\rVert^2 d^n\boldsymbol{x}<\infty$ *is invertible and its inverse is calculated by*

$$\mathcal{F}^{-1}[\mathcal{F}\{f\}](\boldsymbol{x})=f(\boldsymbol{x})=\frac{1}{(2\pi)^n}\int_{\mathbb{R}^n}\mathcal{F}\{f\}(\boldsymbol{\omega})\,e^{i_n\boldsymbol{\omega}\cdot\boldsymbol{x}}\,d^n\boldsymbol{\omega}. \tag{4.3}$$

A number of properties of the CFT are listed in table 1. A related formula for polynomials of the vector derivative (compare line 9) can be found in [4]. The reverse of line 10 and the square norm of line 11 are defined in (2.5) and (2.6), respectively.

[4]It is possible to define the CFT for $n=2(\mathrm{mod}\,4)$ as well, but then care has to be taken of the general non-commutativity of i_n with the elements of $\mathcal{G}_n$.

5. Uncertainty Principle

The uncertainty principle plays an important role in the development and understanding of quantum physics. It is also central for information processing [10].

In quantum physics it states e.g. that particle momentum and position cannot be simultaneously known. The multivector function $f(\boldsymbol{x})$ would represent the spatial part of a separable wave function and its CFT $\mathcal{F}\{f\}(\boldsymbol{\omega})$ the same wave function in momentum space (compare [11, 12, 13]). The variance in space would then be calculated as $(k = 1, 2, 3)$

$$(\Delta x_k)^2 = \int_{\mathbb{R}^3} \langle f(\boldsymbol{x})(\boldsymbol{e}_k \cdot \boldsymbol{x})^2 \tilde{f}(\boldsymbol{x})\rangle \, d^3\boldsymbol{x} = \int_{\mathbb{R}^3} (\boldsymbol{e}_k \cdot \boldsymbol{x})^2 \|f(\boldsymbol{x})\|^2 \, d^3\boldsymbol{x},$$

where it is customary to set without loss of generality the mean value of $\boldsymbol{e}_k \cdot \boldsymbol{x}$ to zero [13]. The variance in momentum space would be calculated as $(l = 1, 2, 3)$

$$\begin{aligned}(\Delta\omega_l)^2 &= \frac{1}{(2\pi)^3} \int_{\mathbb{R}^3} \langle \mathcal{F}\{f\}(\boldsymbol{\omega})(\boldsymbol{e}_l \cdot \boldsymbol{\omega})^2 \widetilde{\mathcal{F}}\{f\}(\boldsymbol{\omega})\rangle \, d^3\boldsymbol{\omega} \\ &= \frac{1}{(2\pi)^3} \int_{\mathbb{R}^3} (\boldsymbol{e}_l \cdot \boldsymbol{\omega})^2 \, \|\mathcal{F}\{f\}(\boldsymbol{\omega})\|^2 d^3\boldsymbol{\omega}.\end{aligned}$$

Again the mean value of $\boldsymbol{e}_l \cdot \boldsymbol{\omega}$ is costumarily set to zero, it merely corresponds to a phase shift [13]. Using our mathematical units, the space-momentum uncertainty relation of quantum mechanics is then expressed by (compare e.g. with (4.9) of [12, page 86])

$$\Delta x_k \Delta\omega_l = \frac{1}{2} \, \delta_{k,l} F, \tag{5.1}$$

where $\delta_{k,l}$ is the usual Kronecker symbol. Note that we have not normalized the squares of the variances by division with $F = \int_{\mathbb{R}^3} \|f(\boldsymbol{x})\|^2 \, d^3\boldsymbol{x}$, therefore the extra factor F on the right side of (5.1). Further explicit examples from image processing can be found in [17].

In general in Fourier analysis such conjugate entities correspond to the variances of a function and its Fourier transform which cannot both be simultaneously sharply localized (e.g. [10, 14]). Material on the classical uncertainty principle for the general case of $L_2(\mathbb{R}^n)$ without the additional condition $\lim_{|x|\to\infty} |x|^2 |f(x)| = 0$ can be found in [15] and [16]. Felsberg [17] even notes for two dimensions: *In 2D however, the uncertainty relation is still an open problem. In* [18] *it is stated that there is no straightforward formulation for the 2D uncertainty relation.*

From the view point of geometric algebra an uncertainty principle gives us information about how the variance of a multivector valued function and the variance of its Clifford Fourier transform are related. We can shed the restriction to the parallel $(k = l)$ and orthogonal $(k \neq l)$ cases of (5.1) by looking at the $\boldsymbol{x} \in \mathbb{R}^n$ variance in an arbitrary but fixed direction $\boldsymbol{a} \in \mathbb{R}^n$ and at the $\boldsymbol{\omega} \in \mathbb{R}^n$ variance in an arbitrary but fixed direction $\boldsymbol{b} \in \mathbb{R}^n$. This leads to the following theorem.

Theorem 5.1 (Directional uncertainty principle). *Let f be a multivector valued function in $\mathcal{G}_n$, $n = 3 \pmod 4$, which has the Clifford Fourier transform $\mathcal{F}\{f\}(\boldsymbol{\omega})$.*

Assume $\int_{\mathbb{R}^n} \|f(\boldsymbol{x})\|^2\, d^n\boldsymbol{x} = F < \infty$, *then the following inequality holds for arbitrary constant vectors* $\boldsymbol{a}$, $\boldsymbol{b}$*:*

$$\int_{\mathbb{R}^n} (\boldsymbol{a}\cdot\boldsymbol{x})^2 \|f(\boldsymbol{x})\|^2\, d^n\boldsymbol{x}\, \frac{1}{(2\pi)^n} \int_{\mathbb{R}^n} (\boldsymbol{b}\cdot\boldsymbol{\omega})^2\, \|\mathcal{F}\{f\}(\boldsymbol{\omega})\|^2 d^n\boldsymbol{\omega} \;\geq\; (\boldsymbol{a}\cdot\boldsymbol{b})^2\, \frac{1}{4}\, F^2 \quad (5.2)$$

Proof. Applying the results stated so far we have[5]

$$\begin{aligned}
&\int_{\mathbb{R}^n} (\boldsymbol{a}\cdot\boldsymbol{x})^2\, \|f(\boldsymbol{x})\|^2\, d^n\boldsymbol{x}\, \frac{1}{(2\pi)^n} \int_{\mathbb{R}^n} (\boldsymbol{b}\cdot\boldsymbol{\omega})^2\, \|\mathcal{F}\{f\}(\boldsymbol{\omega})\|^2 d^n\boldsymbol{\omega} \\
&\overset{\text{table 1, line 6}}{=} \int_{\mathbb{R}^n} (\boldsymbol{a}\cdot\boldsymbol{x})^2\, \|f(\boldsymbol{x})\|^2\, d^n\boldsymbol{x}\, \frac{1}{(2\pi)^n} \int_{\mathbb{R}^n} \|\mathcal{F}\{\boldsymbol{b}\cdot\nabla f\}(\boldsymbol{\omega})\|^2\, d^n\boldsymbol{\omega} \\
&\overset{\text{sc. Parseval}}{=} \int_{\mathbb{R}^n} (\boldsymbol{a}\cdot\boldsymbol{x})^2\, \|f(\boldsymbol{x})\|^2\, d^n\boldsymbol{x} \int_{\mathbb{R}^n} \|\boldsymbol{b}\cdot\nabla f(\boldsymbol{x})\|^2\, d^n\boldsymbol{x} \\
&\overset{\text{footnote 5}}{\geq} \left(\int_{\mathbb{R}^n} \boldsymbol{a}\cdot\boldsymbol{x}\, \|f(\boldsymbol{x})\|\, \|\boldsymbol{b}\cdot\nabla f(\boldsymbol{x})\|\, d^n\boldsymbol{x}\right)^2 \\
&\overset{(2.9)}{\geq} \left(\int_{\mathbb{R}^n} \boldsymbol{a}\cdot\boldsymbol{x} |\langle \widetilde{f(\boldsymbol{x})}\, \boldsymbol{b}\cdot\nabla f(\boldsymbol{x})\rangle|\, d^n\boldsymbol{x}\right)^2 \\
&\geq \left(\int_{\mathbb{R}^n} \boldsymbol{a}\cdot\boldsymbol{x} \langle \widetilde{f(\boldsymbol{x})}\, \boldsymbol{b}\cdot\nabla f(\boldsymbol{x})\rangle\, d^n\boldsymbol{x}\right)^2 .
\end{aligned}$$

Because of (2.6) and (2.7)

$$(\boldsymbol{b}\cdot\nabla)\|f\|^2 = 2\langle \widetilde{f}\, (\boldsymbol{b}\cdot\nabla) f\rangle, \quad (5.3)$$

we furthermore obtain

$$\begin{aligned}
&\int_{\mathbb{R}^n} (\boldsymbol{a}\cdot\boldsymbol{x})^2\, \|f(\boldsymbol{x})\|^2\, d^n\boldsymbol{x}\, \frac{1}{(2\pi)^n} \int_{\mathbb{R}^n} (\boldsymbol{b}\cdot\boldsymbol{\omega})^2\, \|\mathcal{F}\{f\}(\boldsymbol{\omega})\|^2 d^n\boldsymbol{\omega} \\
&\quad\geq \left(\int_{\mathbb{R}^n} \boldsymbol{a}\cdot\boldsymbol{x}\, \frac{1}{2}\, (\boldsymbol{b}\cdot\nabla\|f\|^2)\, d^n\boldsymbol{x}\right)^2 \\
&\quad\overset{\text{Prop. 3.4}}{=} \frac{1}{4}\left(\left[\int_{\mathbb{R}^{n-1}} \boldsymbol{a}\cdot\boldsymbol{x}\|f(\boldsymbol{x})\|^2 d^{n-1}\boldsymbol{x}\right]_{b\cdot x=-\infty}^{b\cdot x=\infty} \right. \\
&\qquad\qquad \left. - \int_{\mathbb{R}^n} [(\boldsymbol{b}\cdot\nabla)(\boldsymbol{a}\cdot\boldsymbol{x})]\, \|f(\boldsymbol{x})\|^2\, d^n\boldsymbol{x}\right)^2 \\
&\quad= \frac{1}{4}\left(0 - \boldsymbol{a}\cdot\boldsymbol{b}\int_{\mathbb{R}^n} \|f(\boldsymbol{x})\|^2\, d^n\boldsymbol{x})\right)^2 \\
&\quad= (\boldsymbol{a}\cdot\boldsymbol{b})^2\, \frac{1}{4}\, F^2.
\end{aligned}$$

Choosing $\boldsymbol{b} = \pm\boldsymbol{a}$, i.e. $\boldsymbol{b} \parallel \boldsymbol{a}$, with $\boldsymbol{a}^2 = 1$ we get from theorem 5.1 the **uncertainty principle** for parallel variance directions [compare with case $k = l$ of (5.1)]:

[5] $\phi, \psi : \mathbb{R}^n \to \mathbb{C}$, $\int_{\mathbb{R}^n} |\phi(x)|^2 d^n x \int_{\mathbb{R}^n} |\psi(x)|^2 d^n x \geq (\int_{\mathbb{R}^n} \phi(x)\bar{\psi(x)}\, d^n x)^2$

$$\int_{\mathbb{R}^n} (\boldsymbol{a}\cdot\boldsymbol{x})^2 \|f(\boldsymbol{x})\|^2\, d^n\boldsymbol{x}\, \frac{1}{(2\pi)^n} \int_{\mathbb{R}^n} (\boldsymbol{a}\cdot\boldsymbol{\omega})^2\, \|\mathcal{F}\{f\}(\boldsymbol{\omega})\|^2 d^n\boldsymbol{\omega} \;\geq\; \frac{1}{4}\, F^2. \tag{5.4}$$

□

Remark 5.2. In (5.4) equality holds for *Gaussian* multivector valued functions

$$f(\boldsymbol{x}) = C_0\, e^{-k\,\boldsymbol{x}^2} \tag{5.5}$$

where $C_0 \in \mathcal{G}_n$ is an arbitrary but constant multivector, $0 < k \in \mathbb{R}$. The proof for this follows from the observation that we have for the f of (5.5)

$$-2k\, \boldsymbol{a}\cdot\boldsymbol{x}\; f = \boldsymbol{a}\cdot\nabla f. \tag{5.6}$$

Choosing orthogonal directions $\boldsymbol{a}, \boldsymbol{b} \in \mathbb{R}^n$ we get from theorem 5.1 the **uncertainty principle** for orthogonal variance directions [compare with case $k \neq l$ of (5.1)]:

Theorem 5.3. *For* $\boldsymbol{a}\cdot\boldsymbol{b} = 0$*, i.e.* $\boldsymbol{b} \perp \boldsymbol{a}$*, we get*

$$\int_{\mathbb{R}^n} (\boldsymbol{a}\cdot\boldsymbol{x})^2 \|f(\boldsymbol{x})\|^2\, d^n\boldsymbol{x}\, \frac{1}{(2\pi)^n} \int_{\mathbb{R}^n} (\boldsymbol{b}\cdot\boldsymbol{\omega})^2\, \|\mathcal{F}\{f\}(\boldsymbol{\omega})\|^2 d^n\boldsymbol{\omega} \;\geq\; 0. \tag{5.7}$$

Theorem 5.4. *Under the same assumptions as in theorem* 5.1*, we obtain*

$$\int_{\mathbb{R}^n} \boldsymbol{x}^{\boldsymbol{2}}\, \|f(\boldsymbol{x})\|^2\, d^n\boldsymbol{x}\, \frac{1}{(2\pi)^n} \int_{\mathbb{R}^n} \boldsymbol{\omega}^{\boldsymbol{2}}\, \|\mathcal{F}\{f\}(\boldsymbol{\omega})\|^2 d^n\boldsymbol{\omega} \;\geq\; \frac{n}{4}\, F^2. \tag{5.8}$$

Remark 5.5. For the proof of theorem 5.4 we first insert $\boldsymbol{x}^2 = \sum_{k=1}^n (\boldsymbol{e}_k\cdot\boldsymbol{x})^2, \boldsymbol{\omega}^2 = \sum_{l=1}^n (\boldsymbol{e}_l\cdot\boldsymbol{\omega})^2$. After that we apply (5.4) and (5.7) depending on the relative directions of the vectors $\boldsymbol{e}_k$ and $\boldsymbol{e}_l$.

6. Conclusions

The (real) Clifford Fourier transform extends the traditional Fourier transform on scalar functions to $\mathcal{G}_n$ multivector functions with $n = 3 \,(\mathrm{mod}\, 4)$. Basic properties and rules for differentiation, convolution, the Plancherel and Parseval theorems were introduced.[6] We then presented a general directional uncertainty principle in the geometric algebra $\mathcal{G}_n$, $n = 3 \,(\mathrm{mod}\, 4)$ which describes how the variances (in arbitrary but fixed directions) of a multivector-valued function and its Clifford Fourier transform relate. The formula of the uncertainty principle in $\mathcal{G}_n$, $n = 3 \,(\mathrm{mod}\, 4)$ can be extended to $\mathcal{G}_n$, $n = 2 \,(\mathrm{mod}\, 4)$ taking due care of the resulting general non-commutativity of i_n with the elements of $\mathcal{G}_n$.

It is known that the Fourier transform is successfully applied to solving equations in all of classical and quantum physics such as the heat equation, wave equations, etc. The same is true for applications of the Fourier transform to problems in image processing and signal theory. Therefore in the future, we can apply geometric algebra and the Clifford Fourier transform to solve such problems involving the whole range of k-vector fields ($k = 0, 1, 2, \ldots, n$) in geometric algebras $\mathcal{G}_n$ with $n = 3 \,(\mathrm{mod}\, 4)$ and study the inevitably remaining uncertainties of the solutions.

[6] Similar formulas for $n = 2$ are also given and applied in [7].

Acknowledgment

This research was financially supported by the Global Engineering Program for International Students 2004 of the University of Fukui. We thank A. Hayashi for his continuous support and O. Yasukura and his colleagues from the Department of Applied Physics of the University of Fukui for their comments. We thank U. Kähler for his hints and E.J. Bayro-Corrochano, H. Ishi, S. Kraushaar and G. Sommer for good discussions. We further thank the reviewers and the editor T. Qian for valuable corrections and suggestions. E. Hitzer wants to thank his wife and children for their patient support.

References

[1] F. Brackx, R. Delanghe, and F. Sommen, *Clifford Analysis*, Vol. 76 of Research Notes in Mathematics, Pitman Advanced Publishing Program, 1982.

[2] T. Bülow, M. Felsberg and G. Sommer, *Non-commutative Hypercomplex Fourier Transforms of Multidimensional Signals*, in G. Sommer (ed.), *Geom. Comp. with Cliff. Alg., Theor. Found. and Appl. in Comp. Vision and Robotics,* Springer, (2001), 187–207.

[3] C. Li, A. McIntosh and T. Qian, *Clifford Algebras, Fourier Transform and Singular Convolution Operators On Lipschitz Surfaces*, Revista Matematica Iberoamericana, **10 (3)**, (1994), 665–695.

[4] A. McIntosh, *Clifford Algebras, Fourier Theory, Singular Integrals, and Harmonic Functions on Lipschitz Domains*, chapter 1 of J. Ryan (ed.), Clifford Algebras in Analysis and Related Topics, CRC Press, Boca Raton, 1996.

[5] T. Qian, *Paley-Wiener Theorems and Shannon Sampling in the Clifford Analysis Setting* in R. Ablamowicz (ed.), Clifford Algebras - Applications to Mathematics, Physcis, and Engineering, Birkäuser, Basel, (2004), 115–124.

[6] B. Mawardi, E. Hitzer, *Clifford Fourier Transformation and Uncertainty Principle for the Clifford Geometric Algebra* $Cl_{3,0}$, Adv. App. Cliff. Alg., **16 (1)**, (2006), 41–61.

[7] J. Ebling and G. Scheuermann, *Clifford Fourier Transform on Vector Fields*, IEEE Transactions on Visualization and Computer Graphics, **11 (4)**, July/August (2005), 469–479.

[8] D. Hestenes, G. Sobczyk, *Clifford Algebra to Geometric Calculus*, Kluwer, 1984.

[9] E. Hitzer, *Vector Differential Calculus*, Mem. Fac. Eng. Fukui Univ. **49 (2)**, (2001), 283–298. http://sinai.mech.fukui-u.ac.jp/gcj/publications/vdercalc/vderc_abs.html

[10] J. M. Rassias, *On The Heisenberg-Weyl Inequality*, Jour. of Inequalities in Pure and Appl. Math., **6 (1)**, article 11, (2005), 1–18. http://www.primedu.uoa.gr/~jrasssias/

[11] C. Doran, A. Lasenby, *Geometric Algebra for Physicists*, CUP, Cambridge, 2003.

[12] F. Schwabl, *Quantenmechanik*, 2nd ed., Springer, Berlin, 1990.

[13] H. Weyl, *The Theory of Groups and Quantum Mechanics*, Dover, New York, 1950.

[14] J. G. Christensen, *Uncertainty Principles*, Master Thesis, University of Copenhagen, 2003.

[15] S. Mallat, *A wavelet tour of signal processing*, Academic Press, 2001.

[16] K. Gröchenig, *Foundations of Time-Frequency Analysis*, Birkhäuser, 2001.

[17] M. Felsberg, *Low-Level Image Processing with the Structure Multivector*, PhD thesis, Kiel, 2002.

[18] G.H. Granlund, H. Knutsson, *Signal Processing for Computer Vision*, Kluwer, Dordrecht, 1995.

Eckhard S.M. Hitzer
Dep. of App. Phys.
University of Fukui
Bunkyo 3-9-1
910-8507 Fukui
Japan
e-mail: `hitzer@mech.fukui-u.ac.jp`

Bahri Mawardi
Dep. of App. Phys.
University of Fukui
Bunkyo 3-9-1
910-8507 Fukui
Japan
e-mail: `mawardi@quantum.apphy.fukui-u.ac.jp`

Chapter 2: Construction of Wavelets and Frame Theory

Wavelet Analysis and Applications
Tao Qian, Mang I. Vai and Xu Yuesheng, Eds.
Applied and Numerical Harmonic Analysis, 59–66

Orthogonal Wavelet Vectors in a Hilbert Space

Huai-Xin Cao and Bao-Min Yu

Abstract. In a Hilbert space, some concepts, such as orthogonal wavelet vector, multiresolution analysis(MRA), scaling vector, unitary-shift operator, are introduced, the existence of scaling vectors and orthogonal wavelet vectors are proved, and the standard forms of them are also given. Our abstract arguments give a short and brief proof of the usual existence result of orthogonal wavelet in $L^2(\mathbb{R})$.

Mathematics Subject Classification (2000). Primary 46C99, 47B99; Secondary 2C40.

Keywords. Hilbert space; multiresolution analysis; orthogonal wavelet vector; scaling vector.

Wavelet Analysis has been widely used in applied subjects. Abstract Wavelet Analysis has been studied in papers [1-8]. The main aim of the applied Wavelet Analysis is to find wavelets and the usual multiresolution analysis (MRA) is a best way of constructing orthogonal wavelets [9-12]. In this paper, we want to discuss Abstract Multiresolution Analysis (AMAR), i.e., multiresolution analysis in an abstract Hilbert space, which gives a way of constructing orthogonal wavelet vectors. Throughout this paper, $\mathscr{H}$ denotes any separable complex Hilbert space over the complex field $\mathbb{C}$, $\mathscr{B}(\mathscr{H})$ denotes the C^*-algebra consisting of all bounded linear operators on $\mathscr{H}$. For $E \subset \mathscr{B}(\mathscr{H})$, let E' be the commutant of E in $\mathscr{B}(\mathscr{H})$, that is,

$$E' = \{T \in \mathscr{B}(\mathscr{H}) \,|\, TA = AT, \forall\, A \in E\}\,,$$

$\mathscr{U}(E)$ be the set of all unitary operators in E. The letter $\mathbb{Z}$ denotes the set of all integers, and $\ell^2(\mathbb{Z})$ denotes the Hilbert space consisting of all complex sequences $\{c_n\}_{n=-\infty}^{+\infty}$ such that $\sum\limits_{n=-\infty}^{+\infty} |c_n|^2 < +\infty$, $\langle x, y\rangle$ is the inner product of x and y, $\bigvee F$ stands for the closed linear space spanned by F.

Definition 1. If D and T are unitary operators on $\mathscr{H}$ such that $TD = DT^2$, then we call the pair (D, T) a pair of wavelet-operators on $\mathscr{H}$.

Supported by NNSFs of China (No. 10561113 and No. 19771056).

Example 1. (1) Let D be any unitary operator on $\mathscr{H}$, I be the identity operator on $\mathscr{H}$, then (D, I) is a pair of wavelet-operators on $\mathscr{H}$. Generally, if (D, T) is a pair of wavelet-operators on $\mathscr{H}$, then for each unitary U on $\mathscr{H}$, the pair (UDU^*, UTU^*) is also a pair of wavelet-operators on $\mathscr{H}$.

(2) Suppose $\mathscr{H} = L^2(\mathbb{R})$, define $(Df)(t) = \sqrt{2}\, f(2t), (Tf)(t) = f(t-1)$, then (D, T) is a pair of wavelet-operators on $\mathscr{H}$.

(3) Let

$$\mathscr{H} = L^2(\mathbb{R})^n = \{(f_1, f_2, \ldots, f_n) : f_k \in L^2(\mathbb{R})\}$$

be the n-copies of the Hilbert space $L^2(\mathbb{R})$ and (D, T) be as in (2). Define

$$D_n(f_1, f_2, \ldots, f_n) = (Df_1, Df_2, \ldots, Df_n),\ T_n(f_1, f_2, \ldots, f_n) = (Tf_1, Tf_2, \ldots, Tf_n),$$

then D_n, T_n are unitaries on $\mathscr{H}$. For any unitary U on the Hilbert space $\mathscr{H}$, it is easy to check that the pair (UD_nU^*, UT_nU^*) is a pair of wavelet-operators on $\mathscr{H}$.

In the following, we use the notation (D, T) to denote an arbitrary pair of wavelet-operators on $\mathscr{H}$. For any unit vector ψ in $\mathscr{H}$, write

$$\psi_{j,\,k} = D^j T^k \psi, \forall\, (j, k) \in \mathbb{Z}^2.$$

Definition 2. If the vectors $\{\psi_{j,k}\}_{j,k\in\mathbb{Z}}$ consists of an orthonormal basis for $\mathscr{H}$, then we say that ψ is a (D, T)-orthogonal wavelet vector in $\mathscr{H}$.

For example, let S be the bilateral shift on the Hilbert space $\ell^2(\mathbb{Z})$ and $\{e_n\}_{n\in\mathbb{Z}}$ be the canonical basis for $\mathscr{H} = \ell^2(\mathbb{Z})$. Then the vector e_0 is a (S, I)-wavelet vector in $\mathscr{H}$. Also, let h be the Haar wavelet:

$$h(x) = \begin{cases} 1, & \text{if } 0 \le x < \frac{1}{2}; \\ -1, & \text{if } \frac{1}{2} \le x < 1; \\ 0, & \text{otherwise,} \end{cases}$$

and (D, T) be as in (2) of Example 1. Then it is well-known that h is a (D, T)-orthogonal wavelet vector in $\mathscr{H}$.

Definition 3. Suppose that $\mathscr{M} = \{V_j \mid j \in \mathbb{Z}\}$ is a sequence of closed subspaces of $\mathscr{H}$ satisfying the following conditions:

(1) $V_n \subset V_{n+1}, \forall\, n \in \mathbb{Z}$,
(2) $\overline{\bigcup\limits_{n\in\mathbb{Z}} V_n} = \mathscr{H}$,
(3) $\bigcap\limits_{n\in\mathbb{Z}} V_n = \{0\}$,
(4) $TV_0 = V_0$,
(5) $D^n V_0 = V_n, \forall\, n \in \mathbb{Z}$,

then $\mathscr{M}$ is called a (D, T)-MRA for $\mathscr{H}$.

Definition 4. Let $\mathscr{M} = \{V_j \mid j \in \mathbb{Z}\}$ be a (D, T)-MRA for $\mathscr{H}$. If a unit vector $\varphi \in \mathscr{H}$ such that $\{T^n\varphi \mid n \in \mathbb{Z}\}$ consists of an orthonormal basis for V_0, then we say that φ is a (D, T)-scaling vector for $\mathscr{M}$.

Definition 5. Let A be a unitary operator on a Hilbert space $\mathscr{K}$. If there exists a unitary operator $U : \mathscr{K} \longrightarrow \ell^2(\mathbb{Z})$ such that $A = U^*SU$, where S is the bilateral shift on $\ell^2(\mathbb{Z})$, then A is called a U-shift operator on $\mathscr{K}$, shortly, a U-shift.

Proposition 1. *Let $\mathscr{M} = \{V_j \,|\, j \in \mathbb{Z}\}$ be a (D,T)-MRA for $\mathscr{H}$, $T|_{V_0}$ be a U-shift on V_0. Then $\varphi := U^*e_0$ is a (D,T)-scaling vector for $\mathscr{M}$, where $e_0 = \{\delta_{j,0}\}_{j\in\mathbb{Z}}$.*

Theorem 1. *If $\mathscr{M} = \{V_j \,|\, j \in \mathbb{Z}\}$ is a (D,T)-MRA for $\mathscr{H}$, $T|_{V_0}$ is a U-shift on V_0, φ is a unit vector, then φ is a (D,T)-scaling vector for $\mathscr{M}$ if and only if $\varphi \in U^*(\mathscr{U}(\{S\}')e_0)$, where $\mathscr{U}(\{S\}')e_0 = \left\{Ae_0 \,|\, A \in \mathscr{U}(\{S\}')\right\}$.*

Proof. Suppose $V \in \mathscr{U}(\{S\}')$, then $VS = SV$ and so $S = VSV^*$. Thus,

$$T|_{V_0} = U^*SU = U^*VSV^*U = (V^*U)^*S(V^*U),$$

which yields that $T|_{V_0}$ is a V^*U-shift. By Proposition 1, U^*Ve_0 is a (D,T)-scaling vector for $\mathscr{M}$.

Conversely, suppose that φ is a (D,T)-scaling vector for $\mathscr{M}$ and $\varphi_1 = U^*e_0$. From Proposition 1 we see that φ_1 is a (D,T)-scaling vector for $\mathscr{M}$. Since φ is also a (D,T)-scaling vector for $\mathscr{M}$, then $\{T^n\varphi_1 \,|\, n \in \mathbb{Z}\}$ and $\{T^n\varphi \,|\, n \in \mathbb{Z}\}$ all are orthonormal bases for Hilbert space V_0. Define $R(T^n\varphi_1) = T^n\varphi$, $\forall n \in \mathbb{Z}$, then we can get a unitary operator R on V_0. Clearly, $RT|_{V_0} = T|_{V_0}R$. Now, we put $V = URU^*$, then V is a unitary operator on $\ell^2(\mathbb{Z})$ and

$$VS = URU^*S = URT|_{V_0}U^* = UT|_{V_0}RU^* = SURU^* = SV,$$

hence $V \in \mathscr{U}(\{S\}')$. In addition, since $U^*Ve_0 = RU^*e_0 = R\varphi_1 = \varphi$, we have $\varphi \in U^*(\mathscr{U}(\{S\}')e_0)$. □

Corollary 1. *If $\mathscr{M} = \{V_j \,|\, j \in \mathbb{Z}\}$ is a (D,T)-MRA for $\mathscr{H}$, $T|_{V_0}$ is a U-shift on V_0, φ is a unit vector, then φ is a (D,T)-scaling vector for $\mathscr{M}$ if and only if $\varphi \in \mathscr{U}(\{T|_{V_0}\}')U^*e_0$.*

Proof. This follows immediately from $\mathscr{U}(\{T|_{V_0}\}')U^* = U^*\mathscr{U}(\{S\}')$. □

Lemma 1. *There exists a unitary operator C_1 on $\ell^2(\mathbb{Z})$ such that*

$$C_1^2 = -I,\ C_1J = JC_1,\ SC_1 = -C_1S^{-1}$$

and

$$|\langle C_1e_k, f\rangle| = |\langle e_{-k-1}, f\rangle| (\forall k \in \mathbb{Z}, \forall f \in \mathscr{H}),$$

where $J : \ell^2(\mathbb{Z}) \to \ell^2(\mathbb{Z})$ is the conjugate linear operator on $\ell^2(\mathbb{Z})$ defined by $J\{c_n\} = \{\overline{c_n}\}$.

Proof. Let $\{e_n \,|\, n \in \mathbb{Z}\}$ be the canonical orthonormal basis for $\ell^2(\mathbb{Z})$. It is easy to check that the map

$$C_1 : \sum_{n\in\mathbb{Z}} \lambda_n e_n \mapsto \sum_{n\in\mathbb{Z}} (-1)^{n+1}\ \lambda_{-n-1}\, e_n$$

is a unitary operator on $\ell^2(\mathbb{Z})$ satisfying the desired conditions. Especially, $C_1e_k = (-1)^k e_{-k-1}$. □

Remark 1. For any unitary C_1 on $\ell^2(\mathbb{Z})$ satisfying the four conditions in Lemma 1, let $C = JC_1$, then it can be proved that $C : \ell^2(\mathbb{Z}) \to \ell^2(\mathbb{Z})$ is a bounded conjugate linear operator and has the following properties:

(1) $C^2 = -I$;
(2) $\langle Cx, Cy\rangle = \langle y, x\rangle, \forall\, x, y \in l^2(\mathbb{Z})$;
(3) $Cx \perp x, \forall\, x \in \ell^2(\mathbb{Z})$;
(4) $S^n C = (-1)^n C S^{-n}, \forall\, n \in \mathbb{Z}$;
(5) $|\langle Ce_k, f\rangle| = |\langle e_{-k-1}, f\rangle| (\forall k \in \mathbb{Z}, \forall f \in \mathscr{H})$.

Lemma 2. $\{m - 2k \,|\, k \in \mathbb{Z}\} \cup \{2k - m - 1 \,|\, k \in \mathbb{Z}\} = \mathbb{Z}, \forall\, m \in \mathbb{Z}$.

Lemma 3. *If $\mathscr{M} = \{V_j \,|\, j \in \mathbb{Z}\}$ is a (D, T)-MRA for $\mathscr{H}$, $T|_{V_0}$ is a U-shift, φ is a (D, T)-scaling vector for $\mathscr{M}$, $f = UD^{-1}\varphi$, and C is any bounded conjugate linear operator satisfying the first four conditions in Remark 1, then*

(1) $\left\{S^{2l} f \,|\, l \in \mathbb{Z}\right\}$ is an orthonormal basis for UV_{-1}.
(2) $\mathscr{B} := \left\{S^{2l} f \,|\, l \in \mathbb{Z}\right\} \cup \left\{S^{2l} Cf \,|\, l \in \mathbb{Z}\right\}$ is an orthonormal subset of $\ell^2(\mathbb{Z})$.

Proof. Since

$$S^{2l} f = S^{2l} UD^{-1}\varphi = UT^{2l} D^{-1}\varphi = UD^{-1} T^l \varphi$$

and $\left\{T^l \varphi \,|\, l \in \mathbb{Z}\right\}$ is an orthonormal basis for V_0, then

$$\left\{S^{2l} f \,|\, l \in \mathbb{Z}\right\} = UD^{-1} \left\{T^l \varphi \,|\, l \in \mathbb{Z}\right\}$$

is an orthonormal basis for $UD^{-1}V_0 = UV_{-1}$. Hence (1) holds. Since φ is a unit vector and S and C all are isometry operators, then each element in $\mathscr{B}$ is a unit vector. Further, it follows from Lemma 1 that

$$S^{2k} Cf = CS^{-2k} f \,(k \in \mathbb{Z}),$$

and thus when $k \neq l$,

$$\left\langle S^{2k} Cf, S^{2l} Cf\right\rangle = \left\langle CS^{-2k} f, CS^{-2l} f\right\rangle = \left\langle S^{-2l} f, S^{-2k} f\right\rangle = 0.$$

Therefore $\left\{S^{2l} Cf \,|\, l \in \mathbb{Z}\right\}$ is an orthonormal subset. Moreover, since

$$S^{2k} Cf = S^{k+l} S^{k-l} Cf = (-1)^{k-l} S^{k+l} CS^{l-k} f$$

and by Remark 1, $S^{l-k} f \perp CS^{l-k} f = (-1)^{k-l} S^{k-l} Cf$, we get $S^{l-k} f \perp S^{k-l} Cf$. Since S^{l+k} is unitary, so

$$S^{2l} f = S^{k+l} S^{l-k} f \perp S^{k+l} S^{k-l} Cf = S^{2k} Cf.$$

It follows from part (1) that $\mathscr{B}$ is an orthonormal subset in $\ell^2(\mathbb{Z})$. □

Lemma 4. *If $E, F \subset \mathscr{H}$ and $E \perp F$, then $\bigvee(E \cup F) = \bigvee E \oplus \bigvee F$.*

Proposition 2. *Let $\mathscr{M} = \{V_j \,|\, j \in \mathbb{Z}\}$ be a sequence of closed linear subspaces of $\mathscr{H}$ satisfying the conditions (1)∼(3) in Definition 3, and $W_n = V_{n+1} \cap V_n^{\perp} = V_{n+1} \ominus V_n$. Then*

$$\mathscr{H} = \bigoplus_{n \in \mathbb{Z}} W_n = \left\{\sum_{n \in \mathbb{Z}} x_n \,|\, x_n \in W_n \text{ and } \sum_{n \in \mathbb{Z}} x_n \text{ is convergent}\right\}.$$

Now, we can give a method of constructing (D,T)-orthogonal wavelet vectors from a given (D,T)-MRA.

Theorem 2. *If $\mathscr{M}=\{V_j \mid j\in\mathbb{Z}\}$ is a (D,T)-MRA for $\mathscr{H}$, $T|_{V_0}$ is a U-shift on V_0, φ is a (D,T)-scaling vector for $\mathscr{M}$, then for each integer k, $\psi_k := DU^*S^{2k}CUD^*\varphi$ is a (D,T)-orthogonal wavelet vector in $\mathscr{H}$, where C is any bounded conjugate linear operator having the properties (1)-(5) in Remark 1.*

Proof. By Proposition 2, $\mathscr{H}=\bigoplus\limits_{n\in\mathbb{Z}} W_j$. It is easy to see that

$$W_j = V_{j+1}\cap V_j^{\perp} = (D^jV_1)\cap(D^jV_0)^{\perp} = D^j(V_1\cap V_0^{\perp}) = D^jW_0,$$

hence $\mathscr{H}=\bigoplus\limits_{j\in\mathbb{Z}} D^jW_0$. So it suffices to show that $\left\{T^l\psi_k \mid l\in\mathbb{Z}\right\}$ is an orthonormal basis for W_0. Put $f=UD^{-1}\varphi$, then

$$T^l\psi_k = T^lDU^*S^{2k}CUD^{-1}\varphi = DT^{2l}U^*S^{2k}CUD^{-1}\varphi = DU^*S^{2l+2k}Cf.$$

Thus, to prove that $\left\{T^l\psi \mid l\in\mathbb{Z}\right\}$ is an orthonormal basis for W_0, we only need to show that $\left\{U^*S^{2l}Cf \mid l\in\mathbb{Z}\right\}$ is an orthonormal basis for W_{-1} (because $DW_{-1}=W_0$). Further, because $U^*(UV_0\ominus UV_{-1})=V_0\ominus V_{-1}=W_{-1}$, it suffices to show that $\left\{S^{2l}Cf \mid l\in\mathbb{Z}\right\}$ is an orthonormal basis for $UV_0\ominus UV_{-1}$. By Lemma 3, the set

$$\mathscr{B} := \left\{S^{2l}f \mid l\in\mathbb{Z}\right\}\cup\left\{S^{2l}Cf \mid l\in\mathbb{Z}\right\}$$

is an orthonormal set in $\ell^2(\mathbb{Z})=UV_0$. Combining with Lemma 4, we see that

$$\bigvee\mathscr{B} = \bigvee\left\{S^{2l}f \mid l\in\mathbb{Z}\right\}\oplus\bigvee\left\{S^{2l}Cf \mid l\in\mathbb{Z}\right\} = UV_{-1}\oplus\bigvee\left\{S^{2l}Cf \mid l\in\mathbb{Z}\right\}.$$

Suppose that P is the orthogonal projection of $\ell^2(\mathbb{Z})$ onto $\bigvee\mathscr{B}$, and $f=\sum\limits_{n\in\mathbb{Z}}\lambda_n e_n$, then

$$\left|\left\langle e_m, S^{2l}f\right\rangle\right| = \left|\left\langle e_m, \sum_{n\in\mathbb{Z}}\lambda_{n-2l}\,e_n\right\rangle\right| = \left|\lambda_{m-2l}\right|,$$

$$\left|\left\langle e_m, S^{2l}Cf\right\rangle\right| = \left|\left\langle Ce_m, S^{-2l}f\right\rangle\right| = \left|\left\langle e_{-m-1}, S^{-2l}f\right\rangle\right| = \left|\lambda_{2l-m-1}\right|.$$

It follows from Lemma 2 that

$$\begin{aligned}\|Pe_m\|^2 &= \sum_{l\in\mathbb{Z}}\left|\left\langle e_m, S^{2l}f\right\rangle\right|^2 + \sum_{l\in\mathbb{Z}}\left|\left\langle e_m, S^{2l}Cf\right\rangle\right|^2\\ &= \sum_{l\in\mathbb{Z}}\left|\lambda_{m-2l}\right|^2 + \sum_{l\in\mathbb{Z}}\left|\lambda_{2l-m-1}\right|^2\\ &= \|f\|^2\\ &= 1.\end{aligned}$$

Hence $\|e_m-Pe_m\|^2=\|e_m\|^2-\|Pe_m\|^2=0$. This implies that $Pe_m=e_m$, $\forall m\in\mathbb{Z}$. Thus, $\ell^2(\mathbb{Z})=\bigvee\mathscr{B}$. Therefore

$$\bigvee\left\{S^{2l}Cf \mid l\in\mathbb{Z}\right\} = (UV_0)\cap(UV_{-1})^{\perp} = UV_0\ominus UV_{-1}.$$

This shows that $\left\{S^{2l}Cf \,|\, l \in \mathbb{Z}\right\}$ is an orthonormal basis for $UV_0 \ominus UV_{-1}$. Hence, from preceding arguments we can conclude that ψ_k is a (D,T)-orthogonal wavelet vector in $\mathscr{H}$. □

Next theorem gives a general form of (D,T)-orthogonal wavelet vectors.

Theorem 3. *Let ψ_0 be a (D,T)-orthogonal wavelet vector in $\mathscr{H}$, ψ be a unit vector in $\mathscr{H}$, then ψ is a (D,T)-orthogonal wavelet vector in $\mathscr{H}$ if and only if there exists $V \in \mathscr{U}(C_{\psi_0}\{D,T\})$ such that $\psi = V\psi_0$, where $C_{\psi_0}\{D,T\}$ stands for the set*

$$\{A \in \mathscr{B}(\mathscr{H}) \,|\, AB\psi_0 = BA\psi_0, \forall\, B \in \{D,T\}\}.$$

Proof. Suppose $V \in \mathscr{U}(C_{\psi_0}\{D,T\}), \psi = V\psi_0$, then

$$D\psi = DV\psi_0 = VD\psi_0,\ T\psi = TV\psi_0 = VT\psi_0.$$

Hence

$$\psi_{j,k} = D^jT^k\psi = VD^jT^k\psi_0 \text{ for } j,k \in \mathbb{Z}.$$

Since $\left\{D^jT^k\psi_0 \,|\, j,k \in \mathbb{Z}\right\}$ is an orthonormal basis for $\mathscr{H}$ and V is unitary, so $\{\psi_{j,\,k} \,|\, j,k \in \mathbb{Z}\}$ is an orthonormal basis for $\mathscr{H}$ and then ψ is a (D,T)-orthogonal wavelet vector in $\mathscr{H}$.

On the other hand, suppose that ψ is a (D,T)-orthogonal wavelet vector in $\mathscr{H}$, then $\left\{D^jT^k\psi_0 \,|\, j,k \in \mathbb{Z}\right\}$ and $\left\{D^jT^k\psi \,|\, j,k \in \mathbb{Z}\right\}$ all are orthonormal bases for $\mathscr{H}$. Define

$$V(D^jT^k\psi_0) = D^jT^k\psi\,(j,k \in \mathbb{Z}),$$

then we obtain a unitary operator V on $\mathscr{H}$ with $V\psi_0 = \psi$. Further, since

$$DV\psi_0 = D\psi = VD\psi_0,$$

$$TV\psi_0 = T\psi = VT\psi_0,$$

we see that $V \in \mathscr{U}(C_{\psi_0}\{D,T\})$ which satisfies $\psi = V\psi_0$. □

Example 2. Let $\mathscr{H}$ and (D,T) be as in part (2) of Example 1, define $\varphi_0 = \chi_{[0,1)}$, and

$$V_0 = \bigvee\{T^n\varphi_0 \,|\, n \in \mathbb{Z}\} = \bigvee\left\{\chi_{[n,n+1)} \,|\, n \in \mathbb{Z}\right\}, V_n = D^nV_0,$$

Then $\mathscr{M} = \{V_n \,|\, n \in \mathbb{Z}\}$ is a (D,T)-MRA for $\mathscr{H}$([11, Example 6.4.3]). Define $U : V_0 \longrightarrow \ell^2(\mathbb{Z})$ by $U(T^n\varphi_0) = e_n$, then U is a unitary operator with $UT|_{V_0} = SU$. So $T|_{V_0}$ is a U-shift on V_0. It is easy to check that φ_0 is a (D,T)-scaling vector for $\mathscr{M}$ and $\varphi_0 = U^*e_0$. By Theorem 2, $\psi = DU^*CUD^*\varphi_0 = \chi_{[-1/2,\,0)} - \chi_{[-1,-1/2)}$ is a (D,T)-orthogonal wavelet vector in $\mathscr{H}$. It is clear that $-T\psi$ is also a (D,T)-orthogonal wavelet vector in $\mathscr{H}$. Clearly, $-T\psi = \chi_{[0,1/2)} - \chi_{[1/2,1)}$, which is just the Haar wavelet.

By using our abstract result(Theorem 2), we can easily deduce the following standard result in traditional wavelet analysis, without using Fourier transformation.

Theorem 4. *Let $\mathscr{M} = \{V_n \mid n \in \mathbb{Z}\}$ be an MRA for the Hilbert space $L^2(\mathbb{R})$ with a scaling function φ that makes $\{\varphi_{0,k}\}_{k\in\mathbb{Z}}$ is an orthonormal basis for V_0. Then for every integer k, the function*

$$\psi_k = \sum_{n\in\mathbb{Z}} (-1)^{n+1} \langle \varphi_{1,-n-1}, \varphi \rangle \varphi_{1,n+2k}$$

is an orthogonal wavelet in $L^2(\mathbb{R})$, where $\varphi_{j,k}(t) = 2^{j/2}\varphi(2^j t - k)$.

Proof. Let $\mathscr{H} = L^2(\mathbb{R})$ and (D, T) be as in the part (2) of Example 1, then $\mathscr{M} = \{V_n \mid n \in \mathbb{Z}\}$ is a (D, T)-MRA for the Hilbert space $\mathscr{H}$ with a (D, T)-scaling vector φ. Define $U : V_0 \longrightarrow \ell^2(\mathbb{Z})$ by $U(T^n\varphi) = e_n$, then U is a unitary operator with $UT|_{V_0} = SU$. So $T|_{V_0}$ is a U-shift on V_0.

Let C_1 be the unitary operator given by the proof of Lemma 1, and $C = JC_1$, then

$$C\left(\sum_{n\in\mathbb{Z}} \lambda_n e_n\right) = \sum_{n\in\mathbb{Z}} (-1)^{n+1}\, \overline{\lambda_{-n-1}} e_n,$$

for all $\{\lambda_n\}_{n\in\mathbb{Z}}$. From Theorem 2, we see that $\psi_k = DU^*S^{2k}CUD^*\varphi$ is a (D, T)-orthogonal wavelet vector in $\mathscr{H}$ for every integer k. Since $D^*\varphi \in V_{-1} \subset V_0$ and $\{T^n\varphi\}_{n\in\mathbb{Z}}$ is an orthonormal basis for V_0, we see that

$$D^*\varphi = \sum_{n\in\mathbb{Z}} \langle D^*\varphi, T^n\varphi \rangle T^n\varphi.$$

Thus, an easy computation shows that

$$\psi_k = \sum_{n\in\mathbb{Z}} (-1)^{n+1} \langle DT^{-1-n}\varphi, \varphi \rangle DT^{n+2k}\varphi = \sum_{n\in\mathbb{Z}} (-1)^{n+1} \langle \varphi_{1,-n-1}, \varphi \rangle \varphi_{1,n+2k}.$$

This completes the proof. □

Remark 2. Under the assumptions of Theorem 4, since $T^kD = DT^{2k}$, we see that $\psi_k = T^k\psi_0$ for every integer k. Especially, the functions

$$\psi_0 = \sum_{n\in\mathbb{Z}} (-1)^{n+1} \langle DT^{-1-n}\varphi, \varphi \rangle DT^n\varphi \text{ (See [12], P. 135)}$$

and

$$\psi_1 = \sum_{n\in\mathbb{Z}} (-1)^{n+1} \langle DT^{-1-n}\varphi, \varphi \rangle DT^{n+2}\varphi = \sum_{n\in\mathbb{Z}} (-1)^{n-1} \langle DT^{1-n}\varphi, \varphi \rangle DT^n\varphi$$

are orthonormal wavelets in $L^2(\mathbb{R})$.

References

[1] X. Dai, D. R. Larson, *Wandering vectors for unitary systems and orthogonal wavelets*, Memoirs Amer. Math. Soc., 1998(134), No. 640.

[2] D. H. Han, D. R. Larson, *Frames, bases and group representations*, Memoirs Amer. Math. Soc., 2000(147), No. 697.

[3] D. R. Larson, *Von Neumann algebras and wavelets, Proceedings*, NATO Adv. Studies Institute on Operator Algebras and Applicationsa, 1997(495): 267-312.

[4] D. R. Larson, W. S. Tang, E. Weber, *Multiwavelets associated with countable groups of unitary operators in Hilbert spaces*, Int. J. Pure Appl. Math. 2003, 6(2),123-144.

[5] M. Michael, D. R. Larson, *Frames in Hilbert C^*-modules and C^*-algebras*, J. Operator Theory, 2002, 48(2),273-314.

[6] D. Han, D. R. Larson, M. Papadakis, Th. Stavropoulos, *Multiresolution analyses of abstract Hilbert spaces and wandering subspaces*, The functional and harmonic analysis of wavelets and frames (San Antonio, TX, 1999), 259-284, Contemp. Math., 247, Amer. Math. Soc., Providence, RI, 1999.

[7] O. Christensen, *A introduction to frames and Riesz bases*, Birkhäuser, Boston, 2003.

[8] H. X. Cao, *Bessel sequences in a Hilbert space*, J. Engineering Mathematics, 2000, 17(2): 92-98.

[9] C. K. Chui, *An introduction to Wavelets*, Academic Press, Boston, 1992.

[10] X. D. Dai, S. J. Lu, *Wavelets in Subspaces*, Michgan Math. J., 1996, 43(1): 81–98.

[11] M. A. Pinsky, *Introduction to Fourier Analysis and Wavelets*, Wadsworth Group, Books/Cole, 2002.

[12] I. Daubechies, *Ten Lectures on Wavelets*, SIAM, Philadelphia, 1992.

Huai-Xin Cao
College of Mathematics and Information Science, Shaanxi Normal University, Xi'an 710062, China
e-mail: caohx@snnu.edu.cn

Bao-Min Yu
College of Mathematics and Information Science, Shaanxi Normal University, Xi'an 710062, China

Wavelet Analysis and Applications
Tao Qian, Mang I. Vai and Xu Yuesheng, Eds.
Applied and Numerical Harmonic Analysis, 67–82

Operator Frames for $B(\mathcal{H})$

Chun-Yan Li and Huai-Xin Cao

Abstract. Operator frames for the space $B(\mathcal{H})$ of all bounded linear operators on a Hilbert space $\mathcal{H}$ are introduced and discussed. By introducing the concept of operator response of vectors in a Hilbert space, we establish a relationship between operator frames for $B(\mathcal{H})$ and usual frames for Hilbert space $\mathcal{H}$ and show that operator frames preserve so many properties of usual frames that we can say that the concept of operator frames is a generalization of frames for Hilbert spaces. In fact, a frame for a Hilbert space or a frame of subspaces for a Hilbert space may be considered as a special case of operator frames in certain sense.

Mathematics Subject Classification (2000). Primary 42C15; Secondary 46C99.

Keywords. Operator frame; operator Riesz basis; Hilbert space.

1. Introduction

In 1946, Gabor [12] discussed a decomposition of signals in terms of elementary signals. In 1952, Duffin and Schaeffer [11] generalized the Gabor's fundamental ideal and introduced the notion of frame in nonharmonic Fourier analysis. The work of Duffin and Schaeffer was not continued until 1986 when Daubechies, Grossman and Meyer [10] applied the theory of frame to wavelet and Gabor transform. After their work, the theory of frame began to be studied widely and deeply. Today, the theory of frame has been applied to signal processing, image processing, data compressing, and sampling theory and so on.

In this paper, let Λ be the set of all integral numbers or the set of all natural numbers, $\mathcal{F}(\Lambda)$ be the set of all nonempty finite subsets of Λ and $B(\mathcal{H},\mathcal{K})$ be the set of all bounded linear operators from a Hilbert space $\mathcal{H}$ into a Hilbert space $\mathcal{K}$. In the case where $\mathcal{K}=\mathcal{H}$, we write $B(\mathcal{H})=B(\mathcal{H},\mathcal{H})$.

This work was supported by the NNSFs of China(No. 10561113, No. 19971056).

A frame for a Hilbert space $\mathcal{H}$ is a sequence $\{f_i\}_{i\in\Lambda}$ of vectors in $\mathcal{H}$ satisfying the condition that there exist constants $A, B > 0$ such that

$$A\|x\|^2 \leq \sum_{i\in\Lambda} |\langle f_i, x\rangle|^2 \leq B\|x\|^2, \forall x \in \mathcal{H}.$$

Theory of frames for Hilbert spaces have been developed deeply. Many people have done momentous works in this field such as D. Han, D. Lason, R. Young, P. G. Casazza, O. Christensen and H. X. Cao(see [2,6,9,14,16]).

In 2004, P. G. Casazza introduced in [3] the notion of frames of subspaces. Let $\{v_i\}_{i\in\Lambda}$ be a family of weights, i.e. $v_i > 0$, $\forall i \in \Lambda$. A family of subspaces $\{W_i\}_{i\in\Lambda}$ of a Hilbert space $\mathcal{H}$ is a frame of subspaces with respect to $\{v_i\}_{i\in\Lambda}$ for $\mathcal{H}$, if there exist constants $A, B > 0$ such that

$$A\|x\|^2 \leq \sum_{i\in\Lambda} v_i^2 \|\pi_{W_i} x\|^2 \leq B\|x\|^2, \forall x \in \mathcal{H}, \tag{1.1}$$

where π_{W_i} is the projection from $\mathcal{H}$ onto $W_i, \forall i \in \Lambda$.

In 1990s, Grochenig, Aldroubi, Sung and Tang began to study the theory of frame in Banach spaces. They introduced two kinds of notions of frames in a Banach space: Banach frames and $p-$frames$(1 < p < \infty)$. A sequence $\{f_i^*\}_{i\in\Lambda}$ in the dual space X^* of a Banach space X is a $p-$frame for X if there exist constants $A, B > 0$ such that

$$A\|x\| \leq \|\{\langle x, f_i^*\rangle\}_{i\in\Lambda}\|_{l^p(\Lambda)} \leq B\|x\|, \forall, x \in X.$$

And a Banach frame with respect to the Banach space $l^p(\Lambda)$ for X is a $p-$frame for X with a reconstruction operator S(see[1,13]).

In this paper, a new notion of frames is introduced: operator frames. We will see that an operator frame is different from a frame for Hilbert spaces and a frame of subspaces. When we consider an operator frame as a sequence of elements in the dual space of space $L^1(\mathcal{H})$ of trace-class operators on a Hilbert space $\mathcal{H}$ (since $B(\mathcal{H}) = L^1(\mathcal{H})^*$(see[15])), it is not difficult to find out that an operator frame is also different from a Banach frame for $L^1(\mathcal{H})$. In Section 2, we will give the concepts of operator Bessel sequences, operator frames and operator Riesz bases and discuss some properties of them. It is well-known that if a Banach frame $\{T_i\}_{i\in\Lambda}$ for $L^1(\mathcal{H})$, has a dual, we can reconstruct every element in $L^1(\mathcal{H})$ and its dual space $B(\mathcal{H})$ immediately. Unluckily, a dual of a Banach frame does not always exist and so this reconstruction maybe not be realized. One can refer to References [1,4,5,7,13] for the theory of Banach frames. In Section 3, dual frames of an operator frame is defined. The advantages of an operator frame are shown by the following facts. First, a dual of an operator frame always exists; second, we can reconstruct not only elements of $\mathcal{H}$, but also elements of $B(\mathcal{H})$ pointwisely by using an operator frame and its dual frame. In order to establish a relationship between operator frames and frames for Hilbert spaces, we introduce the notion of operator response in Section 4. In this section, we shall see that, in some sense, the notion of operator frames can be viewed as a generalization of frames for Hilbert spaces.

2. Operator Frames

Definition 2.1. A family of bounded linear operators $\{T_i\}_{i\in\Lambda}$ on a complex Hilbert space $\mathcal{H}$ is an operator Bessel sequence in $B(\mathcal{H})$, if there exists a positive constant $M > 0$ such that

$$\sum_{i\in\Lambda} \|T_i x\|^2 \leq M\|x\|^2, \quad \forall x \in \mathcal{H},$$

M is called a bound for $\{T_i\}_{i\in\Lambda}$. Denote by $B_{\mathcal{H}}$ the set of all operator Bessel sequences in $B(\mathcal{H})\}$ indexed by Λ.

For any elements $T = \{T_i\}_{i\in\Lambda}$ and $S = \{S_i\}_{i\in\Lambda}$ of $B_{\mathcal{H}}$, we define

$$\lambda T + \mu S = \{\lambda T_i + \mu S_i\}_{i\in\Lambda}, \quad \forall \lambda, \mu \in \mathbb{C},$$

and

$$\|T\| = \sup_{\|x\|\leq 1} (\sum_{i\in\Lambda} \|T_i x\|^2)^{\frac{1}{2}}.$$

We can easily check that $(B_{\mathcal{H}}, \|\cdot\|)$ is a Banach space.

Let $\mathcal{H}$ be a Hilbert space. We denote that

$$S(\mathcal{H}) = \{\{x_i\}_{i\in\Lambda} : x_i \in \mathcal{H}\}$$

$$l^2(\mathcal{H}) = \{\{x_i\}_{i\in\Lambda} : x_i \in \mathcal{H}, \sum_{i\in\Lambda} \|x_i\|^2 < \infty\}.$$

and define an inner product

$$\langle \{x_i\}_{i\in\Lambda}, \{y_i\}_{i\in\Lambda} \rangle = \sum_{i\in\Lambda} \langle x_i, y_i \rangle.$$

Proposition 6.2 in [8] yields that $l^2(\mathcal{H})$ is a Hilbert space.

Let $T = \{T_i\}_{i\in\Lambda}$ be an operator Bessel sequence in $B(\mathcal{H})$ and the operator

$$R_T : \mathcal{H} \to l^2(\mathcal{H})$$

be defined by

$$R_T x = \{T_i x\}_{i\in\Lambda}, \quad \forall x \in \mathcal{H}.$$

Clearly, R_T is a bounded linear operator.

Define

$$\alpha(T) = R_T, \forall T \in B_{\mathcal{H}},$$

then we get a mapping α from $(B_{\mathcal{H}}, \|\cdot\|)$ to $B(\mathcal{H}, l^2(\mathcal{H}))$. It is clear that α is linear and isometric.

Let $\{e_i\}_{i\in\Lambda}$ be an orthonormal basis for $\mathcal{H}$ and A be an operator in $B(\mathcal{H}, l^2(\mathcal{H}))$. Assume that

$$Ae_i = \{f_j^i\}_{j\in\Lambda} \in l^2(\mathcal{H}), \forall i \in \Lambda,$$

then

$$Ax = A(\sum_{i\in\Lambda} c_i e_i) = \{\sum_{i\in\Lambda} c_i f_j^i\}_{j\in\Lambda} \in l^2(\mathcal{H}), \forall x = \sum_{i\in\Lambda} c_i e_i \in \mathcal{H}.$$

This shows that for any $x = \sum_{i\in\Lambda} c_i e_i$ in $\mathcal{H}$, $\sum_{i\in\Lambda} c_i f_j^i$ converges. Define a sequence of operators $T = \{T_j\}_{j\in\Lambda}$ by

$$T_j x = \sum_{i\in\Lambda} c_i f_j^i, \forall x = \sum_{i\in\Lambda} c_i e_i \in \mathcal{H}.$$

From [9, Theorem 1], we have that there exists $M > 0$ such that

$$\|T_j x\|^2 = \|\sum_{i\in\Lambda} c_i f_j^i\|^2 \leq M\|x\|^2.$$

Thus, $\{T_j\}_{j\in\Lambda} \subset B(\mathcal{H})$. For any $x = \sum_{i\in\Lambda} c_i e_i \in \mathcal{H}$, we get

$$\sum_{j\in\Lambda} \|T_j x\|^2 = \sum_{j\in\Lambda} \|\sum_{i\in\Lambda} c_i f_j^i\|^2 = \|Ax\|^2 \leq \|A\|^2\|x\|^2.$$

Hence, $T = \{T_j\}_{j\in\Lambda}$ is an operator Bessel sequence. Compute

$$R_T x = \{T_j x\}_{j\in\Lambda} = \{\sum_{i\in\Lambda} c_i f_j^i\}_{j\in\Lambda} = Ax, \forall x = \sum_{i\in\Lambda} c_i e_i \in \mathcal{H}.$$

This shows that $R_T = A$. Consequently, the space $B_{\mathcal{H}}$ and the operator space $B(\mathcal{H}, l^2(\mathcal{H}))$ are isometrically isomorphic. This fact will be used in our discussion on operator frames.

Definition 2.2. Let $T = \{T_i\}_{i\in\Lambda}$ be an operator Bessel sequence in $B(\mathcal{H})$, then the operator R_T is called the analysis operator of $T = \{T_i\}_{i\in\Lambda}$.

Lemma 2.3. *Let $T = \{T_i\}_{i\in\Lambda}$ be an operator Bessel sequence in $B(\mathcal{H})$. Then the adjoint of R_T is given by*

$$R_T^*(\{x_i\}_{i\in\Lambda}) = \sum_{i\in\Lambda} T_i^* x_i, \ \forall \{x_i\}_{i\in\Lambda} \in l^2(\mathcal{H}).$$

Proof. Assume that $T = \{T_i\}_{i\in\Lambda}$ is an operator Bessel sequence in $B(\mathcal{H})$ with a bound M_T. $\{x_i\}_{i\in\Lambda} \in l^2(\mathcal{H})$ means that $\sum_{i\in\Lambda} \|x_i\|^2$ converges i.e. $\forall \varepsilon > 0, \exists N \in \mathcal{F}(\Lambda)$ such that $\sum_{i\in L} \|x_i\|^2 < \varepsilon$, whenever $L \in \mathcal{F}(\Lambda)$ with $L \cap N = \emptyset$. For every $L \in \mathcal{F}(\Lambda)$ with $L \cap N = \emptyset$, we can find a unit vector $x_0 \in \mathcal{H}$ such that

$$\|\sum_{i\in L} T_i^* x_i\| = |\langle \sum_{i\in L} T_i^* x_i, x_0\rangle| = |\sum_{i\in L} \langle x_i, T_i x_0\rangle|.$$

Hence,

$$\begin{aligned} \|\sum_{i\in L} T_i^* x_i\|^2 &= |\sum_{i\in L} \langle x_i, T_i x_0\rangle|^2 \\ &\leq \sum_{i\in L} \|x_i\|^2 \cdot \sum_{i\in\Lambda} \|T_i x_0\|^2 \\ &\leq M_T \varepsilon. \end{aligned}$$

This shows that $\sum_{i\in\Lambda} T_i^* x_i$ converges. Thus, R_T^* is well-defined. Also, it is easy to check that the adjoint of R_T is defined as above. □

We call R_T^* the synthesis operator of $T = \{T_i\}_{i\in\Lambda}$.

Theorem 2.4. *Let $T = \{T_i\}_{i\in\Lambda}$ be a sequence of operators on $\mathcal{H}$, then the following statements are equivalent.*

(1) *$T = \{T_i\}_{i\in\Lambda}$ is an operator Bessel sequence in $B(\mathcal{H})$.*
(2) *There exists a positive constant M such that*

$$\|\sum_{i\in\Lambda} T_i^* x_i\|^2 \leq M\|\{x_i\}_{i\in\Lambda}\|^2, \quad \forall\{x_i\}_{i\in\Lambda} \in l^2(\mathcal{H}).$$

(3) *There exists a positive constant M such that*

$$\|\sum_{i\in L} T_i^* x_i\|^2 \leq M\sum_{i\in L}\|x_i\|^2, \quad \forall\{x_i\}_{i\in\Lambda} \in S(\mathcal{H}), \forall L \in \mathcal{F}(\Lambda).$$

(4) *For every $\{x_i\}_{i\in\Lambda} \in l^2(\mathcal{H})$, $\sum_{i\in\Lambda} T_i^* x_i$ converges.*

Proof. Clearly, (2) ⇔ (3) ⇔ (4) is always true.

Next, we prove (1) ⇔ (2). Assume that $T = \{T_i\}_{i\in\Lambda}$ is an operator Bessel sequence in $B(\mathcal{H})$ with analysis operator R_T. Put $M = \|R_T^*\|^2$, then

$$\begin{aligned}\|\sum_{i\in\Lambda} T_i^* x_i\|^2 &= \|R_T^*(\{x_i\}_{i\in\Lambda})\|^2 \\ &\leq \|R_T^*\|^2 \cdot \|\{x_i\}_{i\in\Lambda})\|^2 \\ &= M\|\{x_i\}_{i\in\Lambda})\|^2, \qquad \forall\{x_i\}_{i\in\Lambda} \in l^2(\mathcal{H}).\end{aligned}$$

Conversely, if (2) holds, we define an bounded linear operator $Q : l^2(\mathcal{H}) \to \mathcal{H}$ by $Q(\{x_i\}_{i\in\Lambda}) = \sum_{i\in\Lambda} T_i^* x_i$, and compute that

$$Q^* x = \{T_i x\}_{i\in\Lambda} \in l^2(\mathcal{H}), \quad \forall x \in \mathcal{H}.$$

Hence,

$$\sum_{i\in\Lambda}\|T_i x\|^2 = \|\{T_i x\}_{i\in\Lambda}\|^2 = \|Q^* x\|^2 \leq \|Q^*\|^2 \cdot \|x\|, \quad \forall x \in \mathcal{H}.$$

So $T = \{T_i\}_{i\in\Lambda}$ is an operator Bessel sequence in $B(\mathcal{H})$. □

Definition 2.5. A family of bounded linear operators $\{T_i\}_{i\in\Lambda}$ on a Hilbert space $\mathcal{H}$ is said to be an operator frame for $B(\mathcal{H})$, if there exist positive constants $A, B > 0$ such that

$$A\|x\|^2 \leq \sum_{i\in\Lambda}\|T_i x\|^2 \leq B\|x\|^2, \forall x \in \mathcal{H}.$$

Where A and B are called a lower bound and an upper bound for the operator frame, respectively. An operator frame $\{T_i\}_{i\in\Lambda}$ is said to be tight if the constants A and B can be chosen equally. It is called a Parseval operator frame if $A = B = 1$, and a self-adjoint operator frame if every operator T_i is self-adjoint, i.e. $T_i = T_i^*$.

Let $\{W_i\}_{i\in\Lambda}$ be a frame of subspaces with respect to $\{v_i\}_{i\in\Lambda}$ for $\mathcal{H}$. Put $T_i = v_i\pi_{W_i}, \forall i \in \Lambda$, then we get a sequence of operators $\{T_i\}_{i\in\Lambda}$. Clearly, the condition (1.1) implies that there exist constants $A, B > 0$ such that

$$A\|x\|^2 \leq \sum_{i\in\Lambda} \|T_i x\|^2 \leq B\|x\|^2, \quad \forall x \in \mathcal{H}.$$

Thus, the sequence $\{T_i\}_{i\in\Lambda}$ becomes an operator frame for $\mathcal{H}$. With this point of view, a frame of subspaces can be viewed as a special case of operator frames. Another relationship between operator frames and frames of subspaces is given in Theorem 3.6 below.

Example 2.6. Let $L^2(\mathbb{R})$ be the Hilbert space consisting of all Lebesgue measurable and square integrable functions on $\mathbb{R}$. For every $f \in L^2(\mathbb{R})$, we define operators V, U in $B(L^2(\mathbb{R}))$ in such a way that

$$(Vf)(x) = f(x-1), \ (Uf)(x) = 2^{\frac{1}{4}} f(2x).$$

Then for every fixed $k \in \mathbb{Z}$, the sequence $\{U^j V^k\}_{j\in\mathbb{N}}$ is a tight operator frame for $L^2(\mathbb{R})$.

Indeed, for any $f \in L^2(\mathbb{R})$, we have

$$\begin{aligned}
\sum_{j\in\mathbb{N}} \|U^j V^k f\|^2 &= \sum_{j\in\mathbb{N}} \int_{\mathbb{R}} |U^j V^k f(x)|^2 dx \\
&= \sum_{j\in\mathbb{N}} \int_{\mathbb{R}} |2^{\frac{j}{4}} f(2^j x - k)|^2 dx \\
&= \sum_{j\in\mathbb{N}} 2^{\frac{j}{2}} \int_{\mathbb{R}} |f(2^j x - k)|^2 dx \\
&= \sum_{j\in\mathbb{N}} 2^{-\frac{j}{2}} \int_{\mathbb{R}} |f(y)|^2 dy (y = 2^j x) \\
&= \sum_{j\in\mathbb{N}} 2^{-\frac{j}{2}} \|f\|^2 \\
&= \|f\|^2 \sum_{j\in\mathbb{N}} 2^{-\frac{j}{2}} \\
&= (2+\sqrt{2})\|f\|^2.
\end{aligned}$$

Theorem 2.7. *Assume that $\{T_i\}_{i\in\Lambda}$ is an operator Bessel sequence in $B(\mathcal{H})$. If $\{T_i\}_{i\in\Lambda}$ is a 2−frame for $L^1(\mathcal{H})$, then it is an operator frame for $B(\mathcal{H})$.*

Proof. Since $\{T_i\}_{i\in\Lambda}$ is a 2−frame for $L^1(\mathcal{H})$, there are constants $A, B > 0$ such that

$$A\|x\otimes x\|_1^2 \leq \sum_{i\in\Lambda} |\langle T_i, x\otimes x\rangle|^2 \leq B\|x\otimes x\|_1^2, \quad \forall x \in \mathcal{H}.$$

From the theory of trace-class operators, we can get

$$\begin{aligned}\sum_{i\in\Lambda}|\langle T_i, x\otimes x\rangle|^2 &= \sum_{i\in\Lambda}|\mathrm{tr}((x\otimes x)T_i)|^2\\ &= \sum_{i\in\Lambda}|\mathrm{tr}(x\otimes T_i^*x)|^2\\ &= \sum_{i\in\Lambda}|\langle T_ix, x\rangle|^2\\ &\leq \sum_{i\in\Lambda}\|T_ix\|^2\|x\|^2.\end{aligned}$$

Note that $\|x\otimes y\|_1 = \|x\|\|y\|$, we obtain that

$$A\|x\|^2 \leq \sum_{i\in\Lambda}\|T_ix\|^2.$$

Since $\{T_i\}_{i\in\Lambda}$ is an operator Bessel sequence, it is an operator frame for $B(\mathcal{H})$. □

Assume that $T = \{T_i\}_{i\in\Lambda}$ is an operator frame for $B(\mathcal{H})$ and R_T, R_T^* are the analysis operator and synthesis operator of $T = \{T_i\}_{i\in\Lambda}$, respectively, we define the frame operator S_T of $T = \{T_i\}_{i\in\Lambda}$ as $S_T = R_T^*R_T$.

Theorem 2.8. *Assume that S_T is the frame operator of an operator frame $T = \{T_i\}_{i\in\Lambda}$ for $B(\mathcal{H})$ with bounds A, B, then S_T is a positive invertible operator on $\mathcal{H}$ and $AI \leq S_T \leq BI$. Moreover, we have a reconstruction formula*

$$x = \sum_{i\in\Lambda} S_T^{-1}T_i^*T_ix, \quad \forall x\in\mathcal{H}.$$

Proof. It is clear that S_T is positive. For any $x \in \mathcal{H}$, since $T = \{T_i\}_{i\in\Lambda}$ is an operator frame with bounds A, B, we have

$$\langle Ax, x\rangle = A\|x\|^2 \leq \sum_{i\in\Lambda}\|T_ix\|^2 = \langle S_Tx, x\rangle \leq \langle Bx, x\rangle.$$

This shows that

$$AI \leq S_T \leq BI,$$

which implies that S_T is invertible. Further, for any $x \in \mathcal{H}$, we have

$$x = S_T^{-1}S_Tx = S_T^{-1}\sum_{i\in\Lambda}T_i^*T_ix = \sum_{i\in\Lambda}S_T^{-1}T_i^*T_ix.$$

□

Definition 2.9. A sequence $T = \{T_i\}_{i\in\Lambda}$ in $B(\mathcal{H})$ is said to be independent, if the following condition is satisfied:

$$\sum_{i\in\Lambda}T_i^*x_i = 0, \{x_i\}_{i\in\Lambda} \in S(\mathcal{H}) \Longrightarrow x_i = 0, \forall i\in\Lambda.$$

Theorem 2.10. *Let $T = \{T_i\}_{i\in\Lambda}$ be an operator Bessel sequence in $B(\mathcal{H})$, then*

(1) *$T = \{T_i\}_{i\in\Lambda}$ is an operator frame for $B(\mathcal{H})$ if and only if R_T is below bounded.*
(2) *$T = \{T_i\}_{i\in\Lambda}$ is an independent operator frame for $B(\mathcal{H})$ if and only if R_T is invertible.*

Proof. The proof of (1) is easy, so we omit it. Assume that $T = \{T_i\}_{i\in\Lambda}$ is independent, we now prove that R_T is invertible. On the one hand, from the condition and the definition of independent operator frame, we can know that R_T^* is injective, and so $R(R_T) = \ker(R_T^*) = \{0\}$. This shows that range of R_T is dense in $\mathcal{H}$. On the other hand, from (1), we know that R_T is below bounded and so $R(R_T)$ is closed. Hence R_T is invertible. Conversely, if R_T is invertible, then R_T is below bounded. Thus, $T = \{T_i\}_{i\in\Lambda}$ is an operator frame. Now, suppose that $T = \{T_i\}_{i\in\Lambda}$ is not independent, then there exist a non-zero sequence $\{x_i\}_{i\in\Lambda} \subset \mathcal{H}$ and some $i_0 \in \Lambda$ such that $x_{i_0} \neq 0$. Thus

$$T_{i_0}^* x_{i_0} = \sum_{i\neq i_0} T_i^* x_i. \tag{2.1}$$

Since R_T is also surjective, there exists $x \in \mathcal{H}$ such that $R_T x = \{T_j x\}_{j\in\Lambda} = \eta_{i_0} \in l^2(\mathcal{H})$, where $\eta_{i_0} = \{y_j\}_{j\in\Lambda}, y_{i_0} = x_{i_0}$ and $y_j = 0, j \neq i_0$. Hence, $T_{i_0} x = x_{i_0}$ and so $\langle x, T_{i_0}^* x_{i_0}\rangle = \langle T_{i_0} x, x_{i_0}\rangle = \|x_{i_0}\|^2 \neq 0$. But (2.1) can implies that

$$\langle x, T_{i_0}^* x_{i_0}\rangle = \langle x, \sum_{i\neq i_0} T_i^* x_i\rangle = \sum_{i\neq i_0} \langle x, T_i^* x_i\rangle = \sum_{i\neq i_0} \langle T_i x, x_i\rangle = 0.$$

a contradiction. This shows that $T = \{T_i\}_{i\in\Lambda}$ is independent. □

Definition 2.11. A family of operators $\{T_i\}_{i\in\Lambda}$ on $\mathcal{H}$ is called, if

$$\overline{\mathfrak{span}}\{T_i^*\}_{i\in\Lambda} = \mathcal{H},$$

where

$$\overline{\mathfrak{span}}\{T_i^*\}_{i\in\Lambda} = \text{the cloure of } \{\sum_{i\in L} T_i^* x_i : \{x_i\}_{i\in\Lambda} \in S(\mathcal{H}), \forall L \in \mathcal{F}(\Lambda)\}.$$

Definition 2.12. A operator sequence $T = \{T_i\}_{i\in\Lambda}$ on $\mathcal{H}$ is an operator Riesz basis for $B(\mathcal{H})$, if it satisfies:

1. $\overline{\mathfrak{span}}\{T_i^*\}_{i\in\Lambda} = \mathcal{H}$ and
2. there exist constants $C, D > 0$ such that

$$C\|\{x_i\}_{i\in\Lambda}\|^2 \leq \|\sum_{i\in\Lambda} T_i^* x_i\|^2 \leq D\|\{x_i\}_{i\in\Lambda}\|^2, \quad \forall \{x_i\}_{i\in\Lambda} \in l^2(\mathcal{H}). \tag{2.2}$$

Immediately, we know that every operator Riesz basis is always an operator frame from the following conclusion.

Theorem 2.13. *Let $T = \{T_i\}_{i\in\Lambda}$ be a sequence of operators on $\mathcal{H}$, then the following statements are equivalent.*

(1) *$T = \{T_i\}_{i\in\Lambda}$is an operator Riesz basis.*
(2) *$T = \{T_i\}_{i\in\Lambda}$ is an independent operator frame.*

Proof. If $T = \{T_i\}_{i\in\Lambda}$ is an operator Riesz basis, then R_T^* is below bounded by Theorem 2.10 and so the range of R_T^* is closed and denote $R(R_T^*)$. In addition, $\overline{\mathtt{span}}\{T_i^*\}_{i\in\Lambda} = R(R_T^*) = \mathcal{H}$. Thus, R_T^* is bijective. Applying the Banach Inverse Theorem, R_T^* is invertible and so R_T is also invertible. Hence, Theorem 2.4(2) and Theorem 2.10(2) imply that $T = \{T_i\}_{i\in\Lambda}$ is an independent operator frame.

Conversely, assume that $T = \{T_i\}_{i\in\Lambda}$ is an independent operator frame, then Theorem 2.10(2) shows that R_T is invertible. Thus R_T^* is invertible. For any $\{x_i\}_{i\in\Lambda} \in l^2(\mathcal{H})$, we have

$$\|\{x_i\}_{i\in\Lambda}\|^2 = \|R_T^{*-1}R_T^*(\{x_i\}_{i\in\Lambda})\|^2 \le \|R_T^{*-1}\|^2\|R_T^*(\{x_i\}_{i\in\Lambda})\|^2.$$

Put $C = \|R_T^{*-1}\|^{-2}, D = \|R_T^*\|^2$, then

$$\begin{aligned} C\|\{x_i\}_{i\in\Lambda}\|^2 &\le \|R_T^*(\{x_i\}_{i\in\Lambda})\|^2 = \|\sum_{i\in\Lambda} T_i^* x_i\|^2 \\ &\le D\|\{x_i\}_{i\in\Lambda}\|^2, \quad \forall\{x_i\}_{i\in\Lambda} \in l^2(\mathcal{H}). \end{aligned}$$

Thus, condition (2.2) holds. Since R_T^* is invertible, the condition (1) of Definition 2.12 holds. Hence $T = \{T_i\}_{i\in\Lambda}$ is an operator Riesz basis. □

3. Dual of Operator Frames

In this section, we will study reconstruction problem. Thus we need introduce the notion of dual frames of an operator frame.

Definition 3.1. Let $T = \{T_i\}_{i\in\Lambda}$ be an operator frame for $B(\mathcal{H})$. A family of operators $\widetilde{T} = \{\widetilde{T}_i\}_{i\in\Lambda}$ on $\mathcal{H}$ is called a dual of operator frame $T = \{T_i\}_{i\in\Lambda}$ if they satisfy

$$x = \sum_{i\in\Lambda} T_i^*\widetilde{T}_i x \quad \forall x \in \mathcal{H}. \tag{3.1}$$

Furthermore, we call $\{\widetilde{T}_i\}_{i\in\Lambda}$ a dual frame of the operator frame $T = \{T_i\}_{i\in\Lambda}$ if $\{\widetilde{T}_i\}_{i\in\Lambda}$ is also an operator frame for $B(\mathcal{H})$ and satisfies condition (3.1).

Theorem 3.2. *Every operator frame for $B(\mathcal{H})$ has a dual frame.*

Proof. If $T = \{T_i\}_{i\in\Lambda}$ is an operator frame for $B(\mathcal{H})$ with bounds A, B, then the operator sequence $\widetilde{T} = \{T_i S_T^{-1}\}_{i\in\Lambda}$ is a dual frame of $T = \{T_i\}_{i\in\Lambda}$. In fact, we have

$$x = S_T S_T^{-1} x = \sum_{i\in\Lambda} T_i^* T_i S_T^{-1} x = \sum_{i\in\Lambda} T_i^*\widetilde{T}_i x, \quad \forall x \in \mathcal{H}.$$

And $\widetilde{T} = \{T_i S_T^{-1}\}_{i\in\Lambda}$ satisfies

$$A\|S_T\|^{-2}\cdot\|x\|^2 \le \sum_{i\in\Lambda}\|\widetilde{T}_i x\|^2 = \sum_{i\in\Lambda}\|T_i S_T^{-1}x\|^2 \le B\|S_T^{-1}\|^2\cdot\|x\|^2, \quad \forall x \in \mathcal{H}.$$

Hence, $\{T_i S_T^{-1}\}_{i\in\Lambda}$ is called the canonical dual frame of $\{T_i\}_{i\in\Lambda}$. □

Remark 3.3. Assume that $T = \{T_i\}_{i\in\Lambda}$ is an operator frame for $B(\mathcal{H})$ with analytic operator R_T and $\widetilde{T} = \{\widetilde{T}_i\}_{i\in\Lambda}$ is a dual frame of T with analytic operator $R_{\widetilde{T}}$, Then for any x in $\mathcal{H}$, we have

$$x = \sum_{i\in\Lambda} T_i^* \widetilde{T}_i x = R_T^* R_{\widetilde{T}} x. \tag{3.2}$$

This shows that every element of $\mathcal{H}$ can be reconstructed with an operator frame for $B(\mathcal{H})$ and its dual frame.

Moreover, we also have another fact that for any operator A on $\mathcal{H}$, we get

$$Ax = \sum_{i\in\Lambda} T_i^* \widetilde{T}_i Ax, \quad \forall x \in \mathcal{H}. \tag{3.3}$$

That is, an association of operator frame and its dual frame can reconstruct pointwisely every operator on $\mathcal{H}$ and so we can write

$$A \doteq \sum_{i\in\Lambda} T_i^* \widetilde{T}_i A,$$

where $\sum\limits_{i\in\Lambda} T_i^* \widetilde{T}_i A$ converges strongly to A.

Lemma 3.4. *Let $T = \{T_i\}_{i\in\Lambda}$ be an operator frame for $B(\mathcal{H})$ with bounds A, B. If $Q = \{Q_i\}_{i\in\Lambda}$ is an operator Bessel sequence in $B(\mathcal{H})$ with a bound $M < \frac{A^2}{4B}$, then $T \pm Q = \{T_i \pm Q_i\}_{i\in\Lambda}$ is an operator frame for $B(\mathcal{H})$.*

Proof. We only prove the case that $T+Q = \{T_i+Q_i\}_{i\in\Lambda}$. The other case is similar.

For any $x \in \mathcal{H}$, we have

$$\begin{aligned}
\sum_{i\in\Lambda} \|(T_i+Q_i)x\|^2 &\le \sum_{i\in\Lambda} (\|T_i x\| + \|Q_i x\|)^2 \\
&= \sum_{i\in\Lambda} \|T_i x\|^2 + \sum_{i\in\Lambda} \|Q_i x\|^2 + 2\sum_{i\in\Lambda} \|T_i x\|\|Q_i x\| \\
&\le B\|x\|^2 + M\|x\|^2 + 2(\sum_{i\in\Lambda} \|T_i x\|^2)^{\frac{1}{2}} \cdot (\sum_{i\in\Lambda} \|Q_i x\|^2)^{\frac{1}{2}} \\
&\le (B+M)\|x\|^2 + 2\sqrt{B}\sqrt{M}\|x\|^2 \\
&\le (B+M+2\sqrt{B}\sqrt{M})\|x\|^2.
\end{aligned}$$

and

$$\begin{aligned}
\sum_{i\in\Lambda} \|(T_i+Q_i)x\|^2 &\ge \sum_{i\in\Lambda} (\|T_i x\| - \|Q_i x\|)^2 \\
&= \sum_{i\in\Lambda} \|T_i x\|^2 + \sum_{i\in\Lambda} \|Q_i x\|^2 - 2\sum_{i\in\Lambda} \|T_i x\|\|Q_i x\| \\
&\ge A\|x\|^2 + \sum_{i\in\Lambda} \|Q_i x\|^2 - 2(\sum_{i\in\Lambda} \|T_i x\|^2)^{\frac{1}{2}} \cdot (\sum_{i\in\Lambda} \|Q_i x\|^2)^{\frac{1}{2}}
\end{aligned}$$

$$\begin{aligned} &\geq A\|x\|^2 - 2(\sum_{i\in\Lambda}\|T_ix\|^2)^{\frac{1}{2}}\cdot(\sum_{i\in\Lambda}\|Q_ix\|^2)^{\frac{1}{2}} \\ &\geq (A-2\sqrt{B}\sqrt{M})\|x\|^2. \end{aligned}$$

Hence, $T+Q=\{T_i+Q_i\}_{i\in\Lambda}$ is an operator frame for $B(\mathcal{H})$. □

Theorem 3.5. *Let $T=\{T_i\}_{i\in\Lambda}$ be an operator frame for $B(\mathcal{H})$ with bounds A,B, then the following statements are equivalent.*

(1) *$T=\{T_i\}_{i\in\Lambda}$ is independent.*
(2) *$T=\{T_i\}_{i\in\Lambda}$ is an operator Riesz basis.*
(3) *$R(R_T)=l^2(\mathcal{H})$.*
(4) *$T=\{T_i\}_{i\in\Lambda}$ has a unique dual frame.*

Proof. Theorem 2.10 and Theorem 2.13 yield that (1) ⇔ (2) ⇔ (3). It need only prove (1) ⇔ (4).

(1) ⇒ (4) Suppose that independent operator frame $\{T_i\}_{i\in\Lambda}$ have two dual frames: $\widetilde{T}=\{\widetilde{T_i}\}_{i\in\Lambda}$ and $\widetilde{Q}=\{\widetilde{Q}_i\}_{i\in\Lambda}$, then $R_{\widetilde{T}}$ and $R_{\widetilde{Q}}$ are left inverses of R_T^* from (3.2). Thus $\widetilde{T}=\widetilde{Q}$.

(4) ⇒ (1) Assume that $T=\{T_i\}_{i\in\Lambda}$ has a unique dual frame $\widetilde{T}=\{\widetilde{T_i}\}_{i\in\Lambda}$. Suppose that $T=\{T_i\}_{i\in\Lambda}$ is not independent, then $R(R_T)\neq l^2(\mathcal{H})$, i.e. $R(R_T)^\perp\neq\{0\}$. Thus there exists a non-zero element $\{x_i\}_{i\in\Lambda}\in R(R_T)^\perp$ such that $\|\{x_i\}_{i\in\Lambda}\|<\frac{A}{2\sqrt{B}}$. Take a unit vector $e\in\mathcal{H}$, define a sequence of bounded linear operators $\widetilde{U}=\{\widetilde{U}_i\}_{i\in\Lambda}$ in such a way that $\widetilde{U}_ix=\langle x,e\rangle x_i,\forall x\in\mathcal{H}$. Put $\widetilde{Q}=\widetilde{U}+\widetilde{T}$, then for all x in $\mathcal{H}$,

$$\begin{aligned} \sum_{i\in\mathbb{L}}\|\widetilde{U}_ix\|^2 &= \sum_{i\in\Lambda}\|\langle x,e\rangle x_i\|^2\leq\sum_{i\in\Lambda}\|\langle x,e\rangle\|^2\|x_i\|^2 \\ &\leq \|x\|^2\sum_{i\in\Lambda}\|x_i\|^2. \end{aligned}$$

Thus, the sequence $\{\widetilde{U}_i\}_{i\in\Lambda}$ is an operator Bessel sequence with a Bessel bound less than $\frac{A^2}{4B}$. By Lemma 3.4 we know that $\widetilde{Q}$ is an operator frame for $B(\mathcal{H})$. For any $x\in\mathcal{H}$, since $\{\widetilde{U}_ix\}_{i\in\Lambda}=\{\langle x,e\rangle x_i\}_{i\in\Lambda}\in R(R_T)^\perp=\ker(R_T^*)$, we see that $R_T^*(\{\widetilde{U}_ix\}_{i\in\Lambda})=\sum\limits_{i\in\Lambda}T_i^*\widetilde{U}_ix=0$, and so

$$x=\sum_{i\in\Lambda}T_i^*\widetilde{T}_ix=\sum_{i\in\Lambda}T_i^*(\widetilde{T}_i+\widetilde{U}_i)x=\sum_{i\in\Lambda}T_i^*\widetilde{Q}_ix.$$

Thus $\widetilde{Q}$ is also a dual frame of $T=\{T_i\}_{i\in\Lambda}$. Clearly, $\widetilde{Q}\neq\widetilde{T}$. This contradicts the uniqueness of the dual frame of T. Hence, $T=\{T_i\}_{i\in\Lambda}$ is independent. □

For a frame of subspaces $\{W_i\}_{i\in\Lambda}$ with respect to the family of weights $\{v_i\}_{i\in\Lambda}$ for $\mathcal{H}$ with synthesis operator $T_{W,v}$, the sequence $\{u_i\}_{i\in\Lambda}=\{S_{W,v}^{-1}W_i\}_{i\in\Lambda}$ is called the dual frame of $\{W_i\}_{i\in\Lambda}$(see[3]), where the operator $S_{W,v}=T_{W,v}T_{W,v}^*$.

Theorem 3.6. *For a frame of subspaces $\{W_i\}_{i\in\Lambda}$ with respect to the family of weights $\{v_i\}_{i\in\Lambda}$ for $\mathcal{H}$, define $T_i = v_i S_{W,v}\pi_{W_i} S_{W,v}^{-1}$ and $Q_i = v_i \pi_{u_i} S_{W,v}^{-1}$, then $Q = \{Q_i\}_{i\in\Lambda}$ and $T = \{T_i\}_{i\in\Lambda}$ are all operator frames for $B(\mathcal{H})$, and Q is a dual frame of T.*

Proof. Assume that $\{W_i\}_{i\in\Lambda}$ has frame bounds A, B.

Claim 1. $T = \{T_i\}_{i\in\Lambda}$ is an operator frame for $B(\mathcal{H})$.

For any $x \in \mathcal{H}$, we have

$$\begin{aligned}\sum_{i\in\Lambda}\|T_i x\|^2 &= \sum_{i\in\Lambda}\|v_i S_{W,v}\pi_{W_i} S_{W,v}^{-1}x\|^2\\ &\le \|S_{W,v}\|^2 B\|S_{W,v}^{-1}x\|^2\\ &\le B\|S_{W,v}\|^2\|S_{W,v}^{-1}\|^2\|x\|^2.\end{aligned}$$

On the other hand,

$$\begin{aligned}\sum_{i\in\Lambda}\|T_i x\|^2 &= \sum_{i\in\Lambda}\|v_i S_{W,v}\pi_{W_i} S_{W,v}^{-1}x\|^2\\ &\ge \sum_{i\in\Lambda}\|S_{W,v}^{-1}\|^{-2}\|v_i\pi_{W_i} S_{W,v}^{-1}x\|^2\\ &\ge \|S_{W,v}^{-1}\|^{-2}A\|S_{W,v}^{-1}x\|^2\\ &\ge A\|S_{W,v}^{-1}\|^{-2}\|S_{W,v}\|^{-2}\|x\|^2.\end{aligned}$$

Thus $T = \{T_i\}_{i\in\Lambda}$ is an operator frame.

Claim 2. $Q = \{Q_i\}_{i\in\Lambda}$ is also an operator frame for $B(\mathcal{H})$. The proof is similar to Claim 1.

Claim 3. $T_{U,v} = S_{W,v}^{-1}T_{W,v}S_{W,v}, T_{U,v}^* = S_{W,v}^{-1}T_{W,v}^*S_{W,v}, S_{U,v} = S_{W,v}$.

It is easy to check that $\pi_{u_i} = S_{W,v}^{-1}\pi_{W_i}S_{W,v}$. Thus $T_{U,v} = S_{W,v}^{-1}T_{W,v}S_{W,v}$, $T_{U,v}^* = S_{W,v}^{-1}T_{W,v}^*S_{W,v}$ and so

$$\begin{aligned}S_{U,v} &= T_{U,v}T_{U,v}^*\\ &= S_{W,v}^{-1}T_{W,v}S_{W,v}S_{W,v}^{-1}T_{W,v}^*S_{W,v}\\ &= S_{W,v}^{-1}T_{W,v}T_{W,v}^*S_{W,v}\\ &= S_{W,v}^{-1}S_{W,v}S_{W,v}\\ &= S_{W,v}.\end{aligned}$$

Hence, for any $x \in \mathcal{H}$, we compute

$$\begin{aligned}\sum_{i\in\mathbb{L}} T_i^*Q_i x &= \sum_{i\in\Lambda} v_i S_{W,v}^{-1}\pi_{W_i}S_{W,v}\cdot v_i S_{W,v}^{-1}\pi_{W_i}S_{W,v}S_{W,v}^{-1}x\\ &= S_{W,v}^{-1}(\sum_{i\in\Lambda} v_i^2\pi_{W_i}x)\\ &= S_{W,v}^{-1}(S_{W,v}x)\\ &= x.\end{aligned}$$

This shows that $Q = \{Q_i\}_{i\in\Lambda}$ is an dual operator frame of the operator frame $T = \{T_i\}_{i\in\Lambda}$. □

In inequality (1.1), if $A = B$, we call $\{W_i\}_{i\in\Lambda}$ a Parseval frame of subspaces for $\mathcal{H}$.

Theorem 3.7. *Assume that $\{W_i\}_{i\in\Lambda}$ is a Parseval frame of subspaces for a Hilbert space $\mathcal{H}$, then $\{v_i\pi_{W_i}\}_{i\in\Lambda}$ is an operator frame for $B(\mathcal{H})$ and a dual frame of itself.*

Proof. When $\{W_i\}_{i\in\Lambda}$ is a Parseval frame of subspaces, $S_{W,v} = I$. Clearly, this theorem is a consequence of Theorem 3.6. □

4. Operator Responses

In order to show that the notion of operator frames is a generalization of usual frames for Hilbert spaces, we introduce the concept of operator responses of elements of Hilbert spaces.

Definition 4.1. Let $\mathcal{H}$ be a Hilbert space and e be a unit vector (i.e. $\|e\| = 1$) in $\mathcal{H}$. For every f in $\mathcal{H}$, put $T_f^e = e \otimes f$, that is,

$$T_f^e x = \langle x, f\rangle e, \forall x \in \mathcal{H}.$$

It is well know that T_f^e is a linear bounded operator on $\mathcal{H}$ of rank ≤ 1 and $T_f^{e*} = f \otimes e$. We call T_f^e the operator response of f with respect to e. The set $\mathcal{R}_e^{\mathcal{H}} = \{T_f^e : f \in \mathcal{H}\}$ is called the operator response space of $\mathcal{H}$ with respect to e.

Theorem 4.2. *Assume that $\{f_i\}_{i\in\Lambda}$ is a sequence in $\mathcal{H}$ and $\{e_i\}_{i\in\Lambda}$ is a sequence of unit vectors in $\mathcal{H}$, then the following statements are valid.*

(1) *$\{f_i\}_{i\in\Lambda}$ is complete, i.e. $\overline{span}\{f_i : i \in \Lambda\} = \mathcal{H}$ if and only if $\{T_{f_i}^e\}_{i\in\Lambda}$ is complete.*
(2) *$\{f_i\}_{i\in\Lambda}$ is a frame for Hilbert space $\mathcal{H}$ if and only if $\{T_{f_i}^{e_i}\}_{i\in\Lambda}$ is an operator frame for $B(\mathcal{H})$.*
(3) *$\{f_i\}_{i\in\Lambda}$ is a tight frame for Hilbert space $\mathcal{H}$ if and only if $\{T_{f_i}^{e_i}\}_{i\in\Lambda}$ is a tight operator frame for $B(\mathcal{H})$.*
(4) *$\{f_i\}_{i\in\Lambda}$ is a normalized tight frame for Hilbert space $\mathcal{H}$ if and only if $\{T_{f_i}^{e_i}\}_{i\in\Lambda}$ is a Parseval operator frame for $B(\mathcal{H})$.*
(5) *If $\{e_i\}$ is either not complete, or orthogonal, then $\{T_{f_i}^{e_i}\}_{i\in\Lambda}$ is not independent.*

Proof. If $\{f_i\}_{i\in\Lambda}$ is complete, then $\forall x \in \mathcal{H}, \forall \varepsilon > 0$, there exits a sequence $\{c_i\}_{i\in\Lambda} \in \mathbb{C}$ and a finite set $L \in \mathcal{F}(\Lambda)$ such that

$$\|\sum_{i\in L} c_i f_i - x\| < \varepsilon.$$

Take $x_i = c_i e_i (\forall i \in \Lambda$ then $\langle x_i, e_i\rangle = c_i, \forall i \in \Lambda$ and so

$$\|\sum_{i\in L} T_{f_i}^{e_i *} x_i - x\| = \|\sum_{i\in L} \langle x_i, e_i\rangle f_i - x\| = \|\sum_{i\in L} c_i f_i - x\| < \varepsilon.$$

Thus $\overline{\mathtt{span}}\{T_{f_i}^{e_i}\} = \mathcal{H}$, that is, $\{T_{f_i}^{e_i}\}_{i\in\Lambda}$ is complete.

On the other hand, if $\{T_{f_i}^{e_i}\}_{i\in\Lambda}$ is complete, then $\forall x \in \mathcal{H}, \forall \varepsilon > 0$, there exits a sequence $\{x_i\}_{i\in\Lambda} \in S(\mathcal{H})$ and a finite set $L \in \mathcal{F}(\Lambda)$ such that

$$\| \sum_{i\in L} T_{f_i}^{e_i *} x_i - x\| < \varepsilon.$$

That is,

$$\| \sum_{i\in L} \langle x_i, e_i\rangle f_i - x\| < \varepsilon.$$

Thus $\{f_i\}_{i\in\Lambda}$ is complete.

Moreover, for every $x \in \mathcal{H}$, we have

$$\sum_{i\in\Lambda} \|T_{f_i}^{e_i} x\|^2 = \sum_{i\in\Lambda} \|\langle x, f_i\rangle e_i\|^2 = \sum_{i\in\Lambda} |\langle x, f_i\rangle|^2. \tag{4.1}$$

Thus, (2) though (4) are valid.

Assume that $\{e_i\}$ is not complete, then $\{e_i : i \in \Lambda\}^\perp \neq \{0\}$. Take a nonzero sequence $\{x_i\}_{i\in\Lambda} \subset \{e_i : i \in \Lambda\}^\perp \setminus \{0\}$, then

$$\sum_{i\in\Lambda} T_{f_i}^{e_i *} x_i = \sum_{i\in\Lambda} \langle x_i, e_i\rangle f_i = 0. \tag{4.2}$$

This shows that the sequence $\{T_{f_i}^{e_i}\}_{i\in\Lambda}$ is not independent. Next, we suppose that $\{e_i\}$ is orthogonal.Take a mapping $\phi : \Lambda \to \Lambda$ such that $\phi(i) \neq i$ for all $i \in \Lambda$ and define $x_i = e_{\phi(i)}$, then

$$\sum_{i\in\Lambda} T_{f_i}^{e_i *} x_i = \sum_{i\in\Lambda} \langle e_{\phi(i)}, e_i\rangle f_i = 0. \tag{4.3}$$

Hence, the sequence $\{T_{f_i}^{e_i}\}_{i\in\Lambda}$ is not independent. □

Theorem 4.3. *Let $\{f_i\}_{i\in\Lambda} \subset \mathcal{H}$, $\{\widetilde{f}_i\}_{i\in\Lambda} \subset \mathcal{H}$ and $\{e_i\}_{i\in\Lambda}$ be a sequence of unit vectors in $\mathcal{H}$, then the following statements are equivalent.*

(1) *$\{f_i\}_{i\in\Lambda}$ and $\{\widetilde{f}_i\}_{i\in\Lambda}$ are a pair of dual frames for $\mathcal{H}$.*
(2) *$\{T_{\widetilde{f}_i}^{e_i}\}_{i\in\Lambda}$ and $\{T_{f_i}^{e_i}\}_{i\in\Lambda}$ are dual frames of each other.*

Proof. (1) $\Longrightarrow$ (2) Let (1) hold. Then Theorem 4.2 implies that $\{T_{f_i}^{e_i}\}_{i\in\Lambda}$ and $\{T_{\widetilde{f}_i}^{e_i}\}_{i\in\Lambda}$ are operator frames for $B(\mathcal{H})$.

Second, for any $x \in \mathcal{H}$, we may compute

$$\begin{aligned}\sum_{i\in\Lambda} T_{f_i}^{e_i *} T_{\widetilde{f}_i}^{e_i} x &= \sum_{i\in\Lambda} T_{f_i}^{e_i *} \langle x, \widetilde{f}_i\rangle e_i \\ &= \sum_{i\in\Lambda} \langle \langle x, \widetilde{f}_i\rangle e_i, e_i\rangle f_i \\ &= \sum_{i\in\Lambda} \langle x, \widetilde{f}_i\rangle \langle e_i, e_i\rangle f_i \\ &= \sum_{i\in\Lambda} \langle x, \widetilde{f}_i\rangle f_i \\ &= x.\end{aligned}$$

Hence, $\{T_{\widetilde{f}_i}^{e_i}\}_{i\in\Lambda}$ is a dual frame of the operator frame $\{T_{f_i}^{e_i}\}_{i\in\Lambda}$. Similarly, we can prove that $\{T_{f_i}^{e_i}\}_{i\in\Lambda}$ is a dual frame of the operator frame $\{T_{\widetilde{f}_i}^{e_i}\}_{i\in\Lambda}$.

(2) $\Longrightarrow$ (1) Suppose that $\{T_{\widetilde{f}_i}^{e_i}\}_{i\in\Lambda}$ and $\{T_{f_i}^{e_i}\}_{i\in\Lambda}$ are dual framed of each other, then we know from Theorem 4.2 that $\{f_i\}_{i\in\Lambda}$ and $\{\widetilde{f}_i\}_{i\in\Lambda}$ are frames for $\mathcal{H}$ and

$$\sum_{i\in\Lambda} T_{f_i}^{e_i *} T_{\widetilde{f}_i}^{e_i} x = x, \sum_{i\in\Lambda} T_{\widetilde{f}_i}^{e_i *} T_{f_i}^{e_i} x = x, \forall x \in \mathcal{H}.$$

Furthermore, for any $x \in \mathcal{H}$, we get

$$\begin{aligned} x &= \sum_{i\in\Lambda} T_{f_i}^{e_i *} T_{\widetilde{f}_i}^{e_i} x = \sum_{i\in\Lambda} T_{f_i}^{e_i *} \langle x, \widetilde{f}_i\rangle e_i \\ &= \sum_{i\in\Lambda} \langle \langle x, \widetilde{f}_i\rangle e_i, e_i\rangle f_i = \sum_{i\in\Lambda} \langle x, \widetilde{f}_i\rangle \langle e_i, e_i\rangle f_i \\ &= \sum_{i\in\Lambda} \langle x, \widetilde{f}_i\rangle f_i \end{aligned}$$

and

$$\begin{aligned} x &= \sum_{i\in\Lambda} T_{\widetilde{f}_i}^{e_i *} T_{f_i}^{e_i} x = \sum_{i\in\Lambda} T_{\widetilde{f}_i}^{e_i *} \langle x, f_i\rangle e \\ &= \sum_{i\in\Lambda} \langle \langle x, f_i\rangle e_i, e_i\rangle \widetilde{f}_i = \sum_{i\in\Lambda} \langle x, f_i\rangle \langle e_i, e_i\rangle \widetilde{f}_i \\ &= \sum_{i\in\Lambda} \langle x, f_i\rangle \widetilde{f}_i. \end{aligned}$$

Thus $\{f_i\}_{i\in\Lambda}$ and $\{\widetilde{f}_i\}_{i\in\Lambda}$ are a pair of dual frames for $\mathcal{H}$. □

From the discussion above, we can find that the concept of operator frames is a generalization of frames for Hilbert spaces. Operator responses of elements of a Hilbert space play an important role in studying the relation between operator frames and frames for Hilbert spaces.

References

[1] A. Aldroubi, Q. Sung and W. Tang, *p−frames and shift invariant subspaces of L^p*, J. Fourier Anal. Appl. **7** (2001), 1-22.

[2] P. G. Casazza, *The art of frame theory*, Taiwang J. of Math. **4(2)** (2000), 129-201.

[3] P. G. Casazza and G. Kutyniok, *Frame of subspaces*, Contemporary Mathematics (2000).

[4] P. G. Casazza, O. Christensen and D. Stoeva, *Frame expansions in separable Banach spaces*, J. Math. Anal. Appl. **1** (2005), 1-14.

[5] P. G. Casazza, D. Han and D. Larson, *Frames for Banach spaces*, Contemp. Math. **247** (1999), 149-182.

[6] O. Christensen, *An introduction to frames and Riesz bases*, Birkhäuser, Boston, 2003.

[7] O. Christensen and D. T. Stoeva, *p−frames in separable Banach spaces*, Adv. In Comp. Math. **18** (2003), 117-126.

[8] J. B. Conway, *A course in functional analysis*, Springer-Verlag, New York, 1985.

[9] H. X. Cao, *Bessel sequences in a Hilbert spaces*, J. Engineering Mathematics **117** (2000), 92-95.

[10] I. Daubechies, A. Grossmann and Y. Meyer, *painless nonorthogonal expansion*, J. Math. Ph. **27** (1986), 1271-1283.

[11] R. J. Duffin and A. C. schaeffer, *A class of nonharmonic Fourier serier*, Trans. Amer. Math. Soc. **72** (1952), 341-366.

[12] D. Gabor, *Theory of communications*, J. Inst. Elec. Engrg. **93** (1946), 429-457.

[13] K. Grochenig, *Describing functions: Atomic decompositions versus frames*, Monatsh. Math. **112** (1991), 1-41.

[14] D. Han and D. Larson, *Frame, bases and group representations*, Mem. Amer. Math. Soc. to appear.

[15] G. J. Murphy, *C^*-Algebras and Operators Theory*, Academic Press, Inc. 1990.

[16] R. Young, *An introduction to nonharmonic fourier series*, Academic Press, New York, 1980.

Chun-Yan Li
College of Mathematics and Information Science, Shaanxi Normal University, Xi'an 710062, P. R. China;
Department of Mathematics and Physics, Chongqing University of Science and Technology, Chongqing, 400042, P. R. China
e-mail: `lichunyan@stu.snnu.edu.cn`

Huai-Xin Cao
College of Mathematics and Information Science, Shaanxi Normal University, Xi'an 710062, P. R. China
e-mail: `caohx@snnu.edu.cn`

Wavelet Analysis and Applications
Tao Qian, Mang I. Vai and Xu Yuesheng, Eds.
Applied and Numerical Harmonic Analysis, 83–90

On the Stability of Multi-wavelet Frames

Gang Wang and ZhengXing Cheng

Abstract. Frame plays an important role in the theory of wavelet analysis. Frame theory and stability of frames are important topics of wavelet analysis. Recently, people pay more attention to multi-wavelet frames. Among literatures, Chui[2], for instance, give a complete characterization of multi-wavelet frames for arbitrary dilation factor $a > 1$. There, however, is relatively less results on the stability of multi-wavelet frames. This paper devotes to the study of stability of multi-wavelet frames based on functional analysis methods. The following meaningful results are obtained: firstly, multi-wavelet frames are stable by some kinds of linear operators action; Secondly, multi-wavelet frames are stable over some kinds of perturbations conditions on ψ.

Mathematics Subject Classification (2000). Primary 42C40; Secondary 65T60.

Keywords. Frames, Multi-wavelet Frames, Stability.

1. Introduction

We begin with wavelet frames. Let $a > 1$, $b > 0$ and let $\psi_{j,k}(x) = a^{\frac{j}{2}}\psi(a^j x - bk)$, then when ψ, a, b satisfy given conditions, $\{\psi_{j,k}(x) : j, k \in Z\}$ constitute the *wavelet frames of* $L^2(R)$, that is, there exists constant A, $B > 0$ so that $A\|f\|^2 \leq \sum_{j,k\in Z} |\langle f, \psi_{j,k}(x)\rangle|^2 \leq B\|f\|^2$, $\forall f \in L^2(R)$, where A and B are called *wavelet frame bounds*. However, for an arbitrary mother wavelet function $\Psi(x)$ and for an arbitrary dilation factor a and translation factor b, wavelet frames can not always be obtained. So, it is important to study the stability of wavelet frames. The wavelet frames $\{\psi_{j,k}(x)\}$ are called *stable*, when there is small perturbation on a, b, j, k or ψ, $\{\psi_{j,k}(x)\}$ are still wavelet frames. The stability of wavelet frames is needed in applications.

Many people pay attention to studying the stability of wavelet frames. In [5], Favier and Zalik study the stability of single-wavelet frame when there is perturbation conditions on k and ψ. In [1], Balan proves the stability of single-wavelet frame when there is perturbation conditions on b and ψ .

Recently, people pay more attention to multi-wavelet frames, such as: in [2], Chui studies multi-wavelet frames and establishes a complete characterization to multi-wavelet frames for an arbitrary dilation factor $a > 1$. But, there is relatively less results on the stability of multi-wavelet frames. In this paper, the stability of multi-wavelet frames are studied and some meaningful results are obtained.

2. Multi-wavelet Frames

Definition 2.1. [2] Let $1 < a < \infty$, and $b > 0$, A finite collection $\Psi_L(x) = \{\psi_1(x), \cdots, \psi_L(x)\}$ of functions in $L^2(R)$ is said to generate *an multi-wavelet frames*

$$F_a = \{\psi_{l,j,k}(x) = a^{\frac{j}{2}}\psi_l(a^j x - kb) : \\ j, k \in N;\ l = 1, \cdots, L\} \tag{2.1}$$

if there exist positive constant A and B, with $0 < A \le B < \infty$, so that for $\forall f \in L^2(R)$, we have

$$A\|f\|_2^2 \le \sum_{l=1}^{L}\sum_{j,k=1}^{\infty} |\langle f,\ \psi_{l,j,k}(x)\rangle|^2 \le B\|f\|_2^2,$$

where A and B are called *upper and lower multi-wavelet frame bounds* respectively.

In the paper, we also need the following:

Lemma[3] *Let X and Y be Banach space, $\lambda_1,\ \lambda_2 \in [0, 1)$, and $S,\ T: X \to Y$ are linear operators so that for $\forall x \in X$, there is $\|S(x) - T(x)\| \le \lambda_1\|S(x)\| + \lambda_2\|T(x)\|$, then there exists*

$$\mathrm{codim}_Y \overline{S(x)} = \mathrm{codim}_Y \overline{T(x)}.$$

3. The Stability of Multi-wavelet Frames

Theorem 3.1. *Let F_a defined in* (2.1) *be the multi-wavelet frames generated by*

$$\Psi_L(x) = \{\psi_1(x), \cdots, \psi_L(x)\},$$

let $T \in L(L^2(R),\ L^2(R))$ be surjection so that $T\psi_L(x) = \tilde{\psi}_L(x)$, $l = 1, \cdots, L$, then

$$\tilde{F}_a = \{\tilde{\psi}_{l,j,k}(x) = a^{\frac{j}{2}}\tilde{\psi}_l(a^j x - kb) : \\ j,\ k \in N,\ l = 1, \cdots, L\}$$

are the multi-wavelet frames of $L^2(R)$.

Proof. Since $F_a = \{\psi_{l,j,k}(x)\}_{l=1,\cdots,L;\ j,\ k\in N}$ is wavelet frames of $L^2(R)$, then for $\forall\ f \in L^2(R)$, there is

$$A\|f\|_2^2 \le \sum_{l=1}^{L}\sum_{j,k=1}^{\infty} |\langle f,\ \psi_{l,j,k}(x)\rangle|^2 \le B\|f\|_2^2.$$

By virtue of $T\psi_l(x) = \tilde{\psi}_l(x)$, $l = 1, \cdots, L$, there is

$$T\psi_{l,j,k}(x) = \tilde{\psi}_{l,j,k}(x), \quad j,\ k \in N;\ l = 1, \cdots, L.$$

In the following, we prove that for $\{\tilde{\psi}_{l,j,k}(x)\}_{j,\,k\in N;\,l=1,\cdots,L}$, the inequality of frames holds true,

$$\begin{aligned}\sum_{l=1}^{L}\sum_{j,k=1}^{\infty}\left|\left\langle g,\ \tilde{\psi}_{l,j,k}(x)\right\rangle\right|^2 &= \sum_{l=1}^{L}\sum_{j,k=1}^{\infty}\left|\langle g,\ T\psi_{l,j,k}(x)\rangle\right|^2\\ &= \sum_{l=1}^{L}\sum_{j,k=1}^{\infty}\left|\langle T^*g,\ \psi_{l,j,k}(x)\rangle\right|^2\\ &\le B\|T^*g\|_2^2 \le B\|T\|_2^2\|g\|_2^2\end{aligned}$$

and

$$\begin{aligned}\sum_{l=1}^{L}\sum_{j,k=1}^{\infty}\left|\left\langle g,\ \tilde{\psi}_{l,j,k}(x)\right\rangle\right|^2 &= \sum_{l=1}^{L}\sum_{j,k=1}^{\infty}\left|\langle g,\ T\psi_{l,j,k}(x)\rangle\right|^2\\ &= \sum_{l=1}^{L}\sum_{j,k=1}^{\infty}\left|\langle T^*g,\ \psi_{l,j,k}(x)\rangle\right|^2\\ &\ge A\|T^*g\|_2^2 \ge A\left\|(T^*)^{-1}\ |_{T^*(L^2(R))}\right\|_2^2\ \|g\|_2^2\end{aligned}$$

then $\tilde{F}_a = \{\tilde{\psi}_{l,j,k}(x)\}_{j,\,k\in N;\,l=1,\cdots,L}$ is the wavelet frames of $L^2(R)$. □

Theorem 3.2. *Let the collection of functions $F_a = \{\psi_{l,j,k}(x)\}_{j,\,k\in N;j=1,\cdots,L}$ defined in (2.1) be the multi-wavelet frames which are generated by $\Psi_L(x)$ and the frame bounds are A and B, let $M \ge 0$, $\lambda \ge 0$, $0 \le \beta \le 1$ and $(1-\lambda)\sqrt{A} > \sqrt{M}$, and let $\{\tilde{\psi}_{l,j,k}(x)\}_{j,\,k\in N;\,l=1,\cdots,L}$ be formed by $\tilde{\Psi}_L(x) = \{\tilde{\psi}_1(x), \cdots, \tilde{\psi}_L(x)\}$ by dilation and translation with the same dilation and translation parameters as $\{\psi_{l,j,k}(x)\}_{j,\,k\in N;\,l=1,\cdots L}$ by $\Psi_L(x)$ in (2.1), and $\{\tilde{\psi}_{l,j,k}(x)\}_{j,\,k\in N;\,l=1,\cdots,L}$ satisfies that for $l = 1, \cdots, L$; $j,\ k = 1, 2, \cdots$, and for every $C_{l,1,1}, \cdots, C_{l,j,k}$, there is*

$$\begin{aligned}\left\|\sum_{l=1}^{L}\sum_{j,k=1}^{\infty}C_{l,j,k}(\psi_{l,j,k}(x)-\tilde{\psi}_{l,j,k}(x))\right\|_2 &\le \lambda\left\|\sum_{l=1}^{L}\sum_{j,k=1}^{\infty}C_{l,j,k}\psi_{l,j,k}(x)\right\|_2\\ &\quad+\beta\left\|\sum_{l=1}^{L}\sum_{j,k=1}^{\infty}C_{l,j,k}\tilde{\psi}_{l,j,k}(x)\right\|_2\\ &\quad+\sqrt{M}\Big(\sum_{l=1}^{L}\sum_{j,k=1}^{\infty}|C_{l,j,k}|^2\Big)^{\frac{1}{2}}\end{aligned}\tag{3.1}$$

then $\{\tilde{\psi}_{l,j,k}(x)\}_{j,\,k\in N;\,l=1,\cdots,L}$ are multi-wavelet frames of $L^2(R)$, and the frame bounds are $\dfrac{[(1-\lambda)\sqrt{A}-\sqrt{M}]^2}{(1+\beta)^2}$ and $\dfrac{[(1+\lambda)\sqrt{B}-\sqrt{M}]^2}{(1-\beta)^2}$.

Proof. For $j,\ k = 1, 2, \cdots;\ l = 1, \cdots, L$ and every $C_{l,1,1},\ C_{l,1,2}, \cdots,\ C_{l,n,n}$, from (3.1) there is

$$\Big\|\sum_{l=1}^{L}\sum_{j,k=1}^{n} C_{l,j,k}\tilde{\psi}_{l,j,k}(x)\Big\|_2 \le \frac{1+\lambda}{1-\beta}\Big\|\sum_{l=1}^{L}\sum_{j,k=1}^{n} C_{l,j,k}\psi_{l,j,k}(x)\Big\|_2 + \frac{\sqrt{M}}{1-\beta}\Big(\sum_{l=1}^{L}\sum_{j,k=1}^{n}|C_{l,j,k}|^2\Big)^{\frac{1}{2}}$$

By virtue of the Hahn-Banach Theorem, there exist $x^* \in (L^2(R))^* = L^2(R)$, with $\|x^*\|_2 = 1$, so that

$$\begin{aligned}\Big\|\sum_{l=1}^{L}\sum_{j,k=1}^{n} C_{l,j,k}\psi_{l,j,k}(x)\Big\|_2 &= x^*\Big(\sum_{l=1}^{L}\sum_{j,k=1}^{n} C_{l,j,k}\psi_{l,j,k}(x)\Big)\\ &\le \Big(\sum_{l=1}^{L}\sum_{j,k=1}^{n}|C_{l,j,k}|^2\Big)^{\frac{1}{2}}\\ &\quad\times\Big(\sum_{l=1}^{L}\sum_{j,k=1}^{n}|x^*(\psi_{l,j,k}(x))|^2\Big)^{\frac{1}{2}}\\ &\le \sqrt{B}\Big(\sum_{l=1}^{L}\sum_{j,k=1}^{n}|C_{l,j,k}|^2\Big)^{\frac{1}{2}}.\end{aligned}$$

So, there is

$$\Big\|\sum_{l=1}^{L}\sum_{j,k=1}^{n} C_{l,j,k}\tilde{\psi}_{l,j,k}(x)\Big\|_2 \le \frac{1}{1-\beta}\Big(\sqrt{B}(1+\lambda)+\sqrt{M}\Big)\times\Big(\sum_{l=1}^{L}\sum_{j,k=1}^{n}|C_{l,j,k}|^2\Big)^{\frac{1}{2}}$$

For every $y^* \in (L^2(R))^* = L^2(R)$, from the above formula, there is

$$\begin{aligned}\sum_{l=1}^{L}\sum_{j,k=1}^{n}|y^*\Big(\tilde{\psi}_{l,j,k}(x)\Big)|^2 &= y^*\Big(\sum_{l=1}^{L}\sum_{j,k=1}^{n}\frac{|y^*(\tilde{\psi}_{l,j,k}(x)|^2}{y^*(\tilde{\psi}_{l,j,k}(x))}\tilde{\psi}_{l,j,k}(x)\Big)\\ &\le \frac{\|y^*\|_2}{1-\beta}\big[\sqrt{B}(1+\lambda)+\sqrt{M}\big]\\ &\quad\times\Big(\sum_{l=1}^{L}\sum_{j,k=1}^{n}|y^*(\tilde{\psi}_{l,j,k}(x)|^2\Big)^{\frac{1}{2}}\end{aligned}$$

So, we have

$$\Big(\sum_{l=1}^{L}\sum_{j,k=1}^{n}\Big|y^*(\tilde{\psi}_{l,j,k}(x))\Big|^2\Big)^{\frac{1}{2}} \le \frac{\|y^*\|_2}{1-\beta}[\sqrt{B}(1+\lambda)+\sqrt{M}]$$

Let $n \to \infty$, then we have

$$\sum_{l=1}^{L}\sum_{j,k=1}^{\infty}\Big|y^*(\tilde{\psi}_{l,j,k}(x))\Big|^2 \le \|y\|_2^2\frac{[\sqrt{B}(1+\lambda)+\sqrt{M}]^2}{(1-\beta)^2}.$$

That is, for $\forall\, f \in L^2(R)$, there is

$$\sum_{l=1}^{L}\sum_{j,k=1}^{\infty}\Big|\Big\langle f,\ \tilde{\psi}_{l,j,k}(x)\Big\rangle\Big|^2 \le \|f\|_2^2\frac{[\sqrt{B}(1+\lambda)+\sqrt{M}]^2}{(1-\beta)^2}$$

In the following, we are to prove the lower frame bound of $\{\tilde{\psi}_{l,j,k}(x)\}_{j,\,k\in N;\,l=1,\cdots,L}$ is $\dfrac{[(1-\lambda)\sqrt{A}-\sqrt{M}]^2}{(1+\beta)^2}$.

Let $T : L^2(R) \to l_2$ be

$$T(x) = \{\langle x,\ \psi_{l,j,k}(x)\rangle\}_{j,\,k\in N;\,l=1,\cdots,L},$$

then there is

$$\sqrt{A}\|x\|_2^2 \le \|T(x)\|_2^2 \le \sqrt{B}\|x\|_2^2,\ \forall\, x \in L^2(R).$$

Let $V = T(L^2(R))$, then T^{-1} is linear homeomorphism and $\|T^{-1}\| \le \sqrt{A^{-1}}$, and V is the closed subspace of l_2, so we can let $P : l_2 \to V$ be orthogonal projection.

Let $S = T^{-1}P : l_2 \to L^2(R)$, then there is

$$\|S\| \le \|T^{-1}\| \cdot \|P\| \le \sqrt{A^{-1}}.$$

Let $S^* : L^2(R) \to l_2$ be the conjugate operator of S, and let

$$S^*(x) = \{C_{l,j,k}(x)\}_{j,\,k\in N;l=1,\cdots,L},$$

then there is

$$\begin{aligned}\Big(\sum_{l=1}^{L}\sum_{j,k=1}^{\infty}|C_{l,j,k}(x)|^2\Big)^{\frac{1}{2}} &\le \|S\| \cdot \|x\|_2\\ &\le \sqrt{A^{-1}}\|x\|_2\end{aligned} \tag{3.2}$$

For every $y \in L^2(R)$, there is

$$\begin{aligned}\Big\langle\sum_{l=1}^{L}\sum_{j,k=1}^{\infty}C_{l,j,k}(x)\psi_{l,j,k}(x),\ y\Big\rangle &= \sum_{l=1}^{L}\sum_{j,k=1}^{\infty}C_{l,j,k}(x)\,\langle\psi_{l,j,k}(x),\ y\rangle\\ &= \langle S^*(x),\ T(y)\rangle = \langle x,\ ST(y)\rangle\\ &= \langle x,\ T^{-1}PT(y)\rangle = \langle x,\ y\rangle\end{aligned}$$

So we have

$$x = \sum_{l=1}^{L} \sum_{j,k=1}^{\infty} C_{l,j,k}(x)\psi_{l,j,k}(x).$$

Let $L(x) = \sum\limits_{l=1}^{L} \sum\limits_{j,k=1}^{\infty} C_{l,j,k}(x)\tilde{\psi}_{l,j,k}(x)$. From (3.1) and(3.2), the linear operator $L: L^2(R) \to L^2(R)$ which satisfies that for $\forall\, x \in L^2(R)$, there is

$$\|x - L(x)\|_2 \le (\lambda + \frac{\sqrt{M}}{\sqrt{A}})\|x\|_2 + \beta\|L(x)\|_2$$

and

$$\begin{aligned}\frac{(1-\lambda)\sqrt{A} - \sqrt{M}}{(1+\beta)\sqrt{A}}\|x\|_2 &\le \|L(x)\|_2 \\ &\le \frac{(1+\lambda)\sqrt{A} + \sqrt{M}}{(1-\beta)\sqrt{A}}\|x\|_2.\end{aligned}$$

So, L is one to one and bounded linear operator, and $L(L^2(R))$ is closed subspace. By virtue of the Lemma, we can conclude that L is surjection. Therefore, L is invertible bounded linear operator and

$$\|L^{-1}\| \le \frac{(1+\beta)\sqrt{A}}{[(1-\lambda)\sqrt{A} - \sqrt{M}]}$$

For every x, $y \in L^2(R)$, there is

$$\begin{aligned}|\langle x,\ L^*(y)\rangle| = |\langle L(x),\ y\rangle| &= \left|\sum_{l=1}^{L}\sum_{j,k=1}^{\infty} C_{l,j,k}(x)\left\langle \tilde{\psi}_{l,j,k}(x),\ y\right\rangle\right| \\ &\le \Big(\sum_{l=1}^{L}\sum_{j,k=1}^{\infty}|C_{l,j,k}(x)|^2\Big)^{\frac{1}{2}} \\ &\quad \times \Big(\sum_{l=1}^{L}\sum_{j,k=1}^{\infty}\left|\left\langle y,\ \tilde{\psi}_{l,j,k}(x)\right\rangle\right|^2\Big)^{\frac{1}{2}} \\ &\le \sqrt{A^{-1}}\|x\|_2\Big(\sum_{l=1}^{L}\sum_{j,k=1}^{\infty}\left|\left\langle y,\ \tilde{\psi}_{l,j,k}(x)\right\rangle\right|^2\Big)^{\frac{1}{2}}\end{aligned}$$

So, there is

$$\begin{aligned}\|L^*(y)\|_2 &= \sup_{\|x\|\le 1}|\langle x,\ L^*(y)\rangle| \\ &\le \sqrt{A^{-1}}\Big(\sum_{l=1}^{L}\sum_{j,k=1}^{\infty}|\langle y,\ \tilde{\psi}_{l,j,k}(x)\rangle|^2\Big)^{\frac{1}{2}}\end{aligned}$$

So, there is

$$\begin{aligned}\|y\|_2 = \|(L^*)^{-1}L^*(y)\|_2 &\le \|L^{-1}\| \cdot \|L^*(y)\|_2 \\ &\le \frac{(1+\beta)\sqrt{A}}{(1-\lambda)\sqrt{A}-\sqrt{M}}\sqrt{A^{-1}} \\ &\quad \times \Big(\sum_{l=1}^{L}\sum_{j,k=1}^{\infty}\Big|\langle y,\ \tilde{\psi}_{l,j,k}(x)\rangle\Big|^2\Big)^{\frac{1}{2}}\end{aligned}$$

That is, for $\forall\, f \in L^2(R)$, there is,

$$\sum_{l=1}^{L}\sum_{j,k=1}^{\infty}\Big|\langle f,\ \tilde{\psi}_{l,j,k}(x)\rangle\Big|^2 \quad \ge \|f\|_2^2\Big(\frac{(1-\lambda)\sqrt{A}-\sqrt{M}}{1+\beta}\Big)^2$$

□

As the result of Theorem 2*, we have the following:*

Theorem 3.3. *Let* $\{\psi_{l,j,k}(x)\}_{j,\,k\in N;\,l=1,\cdots,L}$ *be the multi-wavelet frames generated by* $\Psi_L(x)$ *in* (2.1)*, the upper and lower bounds are* A *and* B*, and let*

$$\{\tilde{\psi}_{l,j,k}(x)\}_{j,\,k\in N;\,l=1,\cdots,L} \subseteq L^2(R)$$

be formed by $\tilde{\Psi}_L(x) = \{\tilde{\psi}_1(x),\cdots,\tilde{\psi}_L(x)\}$ *by dilation and translation with the same dilation and translation parameters as* $\{\psi_{l,j,k}(x)\}_{j,\,k\in N;\,l=1,\cdots,L}$ *by* $\Psi_L(x)$ *in* (2.1)*. If there exist* $R < A$*, so that for* $\forall\, f \in L^2(R)$*, we have*

$$\sum_{l=1}^{L}\sum_{j,k=1}^{\infty}\Big|\Big\langle f,\ \psi_{l,j,k}(x)-\tilde{\psi}_{l,j,k}(x)\Big\rangle\Big|^2 \le R\|f\|_2^2,$$

then $\{\tilde{\psi}_{l,j,k}(x)\}_{j,\,k\in N;\,l=1,\cdots,L}$ *are multi-wavelet frames of* $L^2(R)$*, and the upper and lower frame bounds are* $(\sqrt{A}-\sqrt{M})^2$ *and* $(\sqrt{B}+\sqrt{M})^2$*.*

References

[1] R. Balan, *Stability Theorems for fourier frames and wavelet Riesz bases*, to appear in Journal of Fourier Analysis and applications.

[2] C. K. Chui, *Orthonormal wavelets and Tight Frames with arbitrary real dilations*, Applied and Computational Harmonic Analysis, **9**(2000), 243-264.

[3] P.G.Casazza, N.J.Katon, *Generalizing the Paley-Wiener perturbation theory for Banach space*, Proc. Amer. Math. Soc, **127(2)**(1999), 519-527.

[4] I. Daubechies, Ten Lectures On Wavelets, CBMS-NSF Regional Conference in Applied Mathematics, SIAM Publ, Philadelphia,(1992), 56-106.

[5] S. Favier, R. Zalik, *On the stability of frames and Riesz bases*, Applied and Computational Harmonic Analysis, **2(2)**(1995), 160-173.

[6] Y. N. Guo, J. Y. Zhou, *On the stability and perturbation of Riesz Frames*, Acta Mathematica Sinica, **46(4)**(2003), 673-682.

[7] Y.C. Zhu, *On the stability of q-Frames and p-Riesz bases in Banach space*, Chinese Annals of Mathematics, **22A(3)**(2001), 359-364.

Gang Wang
School of Math-Physics and Information Science, XinJiang Normal University, Urumqi, XinJiang, 830054, P.R.China
e-mail: angelayy@sina.com

ZhengXing Cheng
Faculty of Science, Xi'an JiaoTong University, Xi'an, Shaanxi, 710049, P.R.China
e-mail: zhengxingch@163.com

Wavelet Analysis and Applications
Tao Qian, Mang I. Vai and Xu Yuesheng, Eds.
Applied and Numerical Harmonic Analysis, 91–98

Biorthogonal Wavelets Associated with Two-Dimensional Interpolatory Function

Jianwei Yang, Yuan Yan Tang, Zhengxing Cheng and Xinge You

Abstract. To construct biorthogonal wavelets from two-dimensional interpolatory function, a large amount of computation is involved in traditional method. In this paper, a method is developed for constructing the biorthogonal wavelets. Masks of the biorthogonal wavelets are given explicitly. Neither the Gram-Schmidt processing nor the inverse of a nonsingular polynomial matrix is needed.

Mathematics Subject Classification (2000). Primary 42C15; Secondary 65T60.

Keywords. Interpolatory function, biorthogonal wavelet system, wavelet, mask.

1. Introduction

During the past few years, the construction of interpolatory scaling function has become of increasing interest (see, e.g. [1, 2, 3, 4]). However, there still does not exist a simple method to construct biorthogonal wavelets from the associated two-dimensional interpolatory function. In this paper, a method is presented for constructing biorthogonal wavelets from two-dimensional interpolatory function. Biorthogonal wavelet masks can be constructed explicitly.

Let $\phi(\mathbf{x}) \in L^2(R^2)$, which satisfies the following refinable equation

$$\phi(\mathbf{x}) = \sum_{\alpha \in Z^2} p_\alpha \phi(2\mathbf{x} - \alpha), \tag{1.1}$$

and let

$$V_0 = \mathrm{Span}_{L^2(R^2)}\{\phi(\mathbf{x} - \alpha),\ \alpha \in Z^2\},\ V_k = \{f(2^k\mathbf{x} - \alpha),\ f \in V_0,\ \alpha \in Z^2\}.$$

If $\hat{\phi}(0) \neq 0$, it was shown in [5] (see also [6]) that $\{V_k\}_{k\in Z}$, the sequence of subspace of $L^2(R^2)$, satisfies

$$\overline{\bigcup_{k\in Z} V_k} = L^2(R^2), \quad \bigcap_{k\in Z} V_k = \{0\}.$$

If $\phi(\mathbf{x})$ and its shifts form a Riesz basis of V_0, the sequence of the subspaces $\{V_k\}_{k\in Z}$ forms a multiresolution analysis (MRA) of $L^2(R^2)$. $\phi(\mathbf{x})$ is called a scaling function.

If $\phi(\mathbf{x})$ is a continuous two-dimensional scaling function, which satisfies

$$\phi(\alpha) = \delta_{0,\alpha},\ \alpha \in Z^2, \tag{1.2}$$

we say that $\phi(\mathbf{x})$ is an interpolatory scaling function.

In practical image processing, images are often first represented by sampling space V_k. When the pixel values of an image f are given, an image is normally (or easily) represented by

$$f_k = 2^k \sum_{\alpha\in Z^2} f(\frac{\alpha}{2^k})\phi(2^k\mathbf{x} - \alpha)$$

for a certain dilation level k. However, to apply the decomposition and reconstruction algorithm, one should use the function [3]

$$\sum_{\alpha\in Z^2} < f_k, 2^k\tilde{\phi}(2^k\mathbf{x} - \alpha) > 2^k\phi(2^k - \alpha).$$

This function is not the function f_k, unless the refinable function ϕ satisfies the condition (1.2). Hence, by using the sampling space generated by interpolatory refinable function, one simplifies (or reduces the errors of) the first step of the decomposition and reconstruction algorithm (see [3]). During the past few years, some excellent results on the construction of interpolatory functions have been published. For any positive integers N and $\tilde{N}$ with $N \leq \tilde{N}$, J. Kovačević and Sweldens [7] constructed an interpolatory mask satisfying sum rules of order $\tilde{N}$ and its dual mask satisfying sum rules of order N. In [2], H. Ji *et al* proposed a convolution method to construct refinable functions of arbitrary regularity which are dual to an interpolatory scaling function. For an interpolatory mask, B. Han [1] has provided an CBC algorithm to construct the dual masks which satisfy sum rules of any given order. However, up to now, there is still no simple method to construct the two-dimensional biorthogonal wavelets from the interpolatory refinable function. The method provided by H. Ji *et al*. [2] needs not only the Gram-Schmidt processing but also the computation of the inverse of a Laurent matrix. In this paper, we provide a method for constructing the two-dimensional biorthogonal wavelets from the interpolatory refinable function. The wavelet masks are given explicitly.

The two-dimensional biorthogonal wavelet system is introduced in Section 2. In Section 3, formulas are provided for constructing biorthogonal wavelet masks from two-dimensional interpolatory function. Example is also given to demonstrate this method. Finally, the conclusion is given in Section 4.

2. Two-Dimensional Biorthogonal Wavelet System

We call $\Delta = \{\alpha : p_\alpha \neq 0\}$ the support of $\{p_\alpha\}_{\alpha\in Z^2}$. For $\omega = (\omega_1, \omega_2) \in R^2$, $\alpha = (\alpha_1, \alpha_2) \in Z^2$, we denote $z_1 = e^{-i\omega_1}$, $z_2 = e^{-i\omega_2}$, $\mathbf{z}^\alpha = z_1^{\alpha_1} z_2^{\alpha_2}$. Let

$$P(\mathbf{z}) = P(z_1, z_2) = \frac{1}{4}\sum_{\alpha\in Z^2} p_\alpha \mathbf{z}^\alpha = \frac{1}{4}\sum_{\alpha\in Z^2} p_\alpha z_1^{\alpha_1} z_2^{\alpha_2}.$$

For scaling function $\phi(\mathbf{x})$, if there exists $\tilde{\phi}(\mathbf{x})$ such that

$$\tilde{\phi}(\mathbf{x}) = \sum_{\alpha\in Z^2} \tilde{p}_\alpha \tilde{\phi}(2\mathbf{x} - \alpha), \text{ and } < \phi(\mathbf{x}), \tilde{\phi}(\mathbf{x} - \alpha >= \delta_{\alpha,0},$$

then we call $\tilde{\phi}(\mathbf{x})$ the dual of $\phi(\mathbf{x})$. We denote $\tilde{P}(\mathbf{z}) = \sum_{\alpha\in Z^2} \tilde{p}_\alpha \mathbf{z}^\alpha$.

Suppose that $\psi^j(\mathbf{x})$, $\tilde{\psi}^j(\mathbf{x})$ $(j = 1, 2, 3)$ are biorthogonal wavelets associated with $\phi(\mathbf{x}), \tilde{\phi}(\mathbf{x})$, which satisfy

$$\psi^j(\mathbf{x}) = \sum_{\alpha\in Z^2} q_\alpha^j \phi(2\mathbf{x} - \alpha), \ \tilde{\psi}^j(\mathbf{x}) = \sum_{\alpha\in Z^2} \tilde{q}_\alpha^j \tilde{\phi}(2\mathbf{x} - \alpha),$$

then

$$< \psi^j(\mathbf{x}), \tilde{\phi}(\mathbf{x} - \alpha) >=< \phi(\mathbf{x}), \tilde{\psi}^j(\mathbf{x} - \alpha) >= 0,$$
$$< \psi^{j_1}(\mathbf{x}), \tilde{\psi}^{j_2}(\mathbf{x} - \alpha) >= \delta_{\alpha,0}\delta_{j_1,j_2},$$

where $j, j_1, j_2 = 1, 2, 3$. We call $Q^j(\mathbf{z}) = \sum_{\alpha\in Z^2} q_\alpha^j \mathbf{z}^\alpha$ and $\tilde{Q}^j(\mathbf{z}) = \sum_{\alpha\in Z^2} \tilde{q}_\alpha^j \mathbf{z}^\alpha$ the wavelet masks. For convenience, we denote

$$m(\omega) = P(\mathbf{z}), \ \tilde{m}(\omega) = \tilde{P}(\mathbf{z}), \ m^j(\omega) = Q^j(\mathbf{z}), \ \tilde{m}^j(\omega) = \tilde{Q}^j(\mathbf{z}).$$

Let $\mu_0 = (0, 0), \mu_1 = (1, 0), \mu_2 = (0, 1), \mu_3 = (1, 1)$. By [4], we know that

$$\sum_{k=0}^{3} m(\omega + \mu_k\pi)\overline{\tilde{m}(\omega + \mu_k\pi)} = 1, \tag{2.1}$$

$$\sum_{k=0}^{3} m(\omega + \mu_k\pi)\overline{\tilde{m}^j(\omega + \mu_k\pi)} = 0, \tag{2.2}$$

$$\sum_{k=0}^{3} m^j(\omega + \mu_k\pi)\overline{\tilde{m}(\omega + \mu_k\pi)} = 0, \tag{2.3}$$

$$\sum_{k=0}^{3} m^{j_1}(\omega + \mu_k\pi)\overline{\tilde{m}^{j_2}(\omega + \mu_k\pi)} = \delta_{j_1,j_2}, \ j, j_1, j_2 = 1, 2, 3. \tag{2.4}$$

If (2.2)$\sim$(2.4) are satisfied, we call $\{q_\alpha^j\}_{\alpha\in Z^2}$, $\{\tilde{q}_\alpha^j\}_{\alpha\in Z^2} (j = 1, 2, 3)$ the biorthogonal wavelet filters associated with $\{p_\alpha\}_{\alpha\in Z^2}$, $\{\tilde{p}_\alpha\}_{\alpha\in Z^2}$. If (2.1)$\sim$(2.4) are satisfied, we say that $\{p_\alpha\}_{\alpha\in Z^2}$,$\{\tilde{p}_\alpha\}_{\alpha\in Z^2}$, $\{q_\alpha^j\}_{\alpha\in Z^2}$,$\{\tilde{p}_\alpha^j\}_{\alpha\in Z^2}$ form a two-dimensional biorthogonal wavelet system [8].

3. Construction of Biorthogonal Wavelets

We adopt the following notations

$$E_{0k} = \frac{1}{2}\sum_{\alpha\in Z^2} p_{2\alpha+\mu_k}\mathbf{z}^{2\alpha},\ E_{jk} = \frac{1}{2}\sum_{\alpha\in Z^2} q^j_{2\alpha+\mu_k}\mathbf{z}^{2\alpha},$$
$$\tilde{E}_{0k} = \frac{1}{2}\sum_{\alpha\in Z^2} \tilde{p}_{2\alpha+\mu_k}\mathbf{z}^{2\alpha},\ \tilde{E}_{jk} = \frac{1}{2}\sum_{\alpha\in Z^2} \tilde{q}^j_{2\alpha+\mu_k}\mathbf{z}^{2\alpha},\ R(z_1,z_2) = (1,z_1,z_2,z_1z_2)^T,$$

where $k = 0,1,2,3,\ j = 1,2,3$. It follows that

$$P(\mathbf{z}) = \frac{1}{2}(E_{00},E_{01},E_{02},E_{03})R(z_1,z_2), \tag{3.1}$$
$$\tilde{P}(\mathbf{z}) = \frac{1}{2}(\tilde{E}_{00},\tilde{E}_{01},\tilde{E}_{02},E_{03})R(z_1,z_2), \tag{3.2}$$
$$Q^j(\mathbf{z}) = \frac{1}{2}(E_{j0},E_{j1},E_{j2},E_{j3})R(z_1,z_2), \tag{3.3}$$
$$\tilde{Q}^j(\mathbf{z}) = \frac{1}{2}(\tilde{E}_{j0},\tilde{E}_{j1},\tilde{E}_{j2},E_{03})R(z_1,z_2), \tag{3.4}$$

where $j = 1,2,3,\ k = 0,1,2,3$. We call $E_{0k},\tilde{E}_{0k},E_{jk},\tilde{E}_{jk}$ the polyphase factors of $P(\mathbf{z})$, $\tilde{P}(\mathbf{z})$, $Q^j(\mathbf{z})$, and $\tilde{Q}^j(\mathbf{z})$ respectively. Hence, the necessary condition for $\{p_\alpha\}_{\alpha\in Z^2}$, $\{\tilde{p}_\alpha\}_{\alpha\in Z^2}$, $\{q^j_\alpha\}_{\alpha\in Z^2}$, $\{\tilde{p}^j_\alpha\}_{\alpha\in Z^2}$ to form a biorthogonal wavelet system is that the following equation holds

$$E(\mathbf{z})\tilde{E}(\mathbf{z})^* = I_4, \tag{3.5}$$

where

$$E(\mathbf{z}) = \begin{pmatrix} E_{00} & E_{01} & E_{02} & E_{03} \\ E_{10} & E_{11} & E_{12} & E_{13} \\ E_{20} & E_{21} & E_{22} & E_{23} \\ E_{30} & E_{31} & E_{32} & E_{33} \end{pmatrix},\ \tilde{E}(\mathbf{z}) = \begin{pmatrix} \tilde{E}_{00} & \tilde{E}_{01} & \tilde{E}_{02} & \tilde{E}_{03} \\ \tilde{E}_{10} & \tilde{E}_{11} & \tilde{E}_{12} & \tilde{E}_{13} \\ \tilde{E}_{20} & \tilde{E}_{21} & \tilde{E}_{22} & \tilde{E}_{23} \\ \tilde{E}_{30} & \tilde{E}_{31} & \tilde{E}_{32} & \tilde{E}_{33} \end{pmatrix}.$$

The matrixes $E(\mathbf{z})$, $\tilde{E}(\mathbf{z})$ are called the polyphase matrixes of biorthogonal wavelet system. Therefore, in order to construct the biorthogonal wavelets associated with $\phi(\mathbf{x})$ and $\tilde{\phi}(\mathbf{x})$, we only need to extend $E(\mathbf{z})$, $\tilde{E}(\mathbf{z})$ by their first rows so that Eq.(3.5) is satisfied.

Now we provide the formulas for constructing biorthogonal wavelet masks from two-dimensional interpolatory function.

Theorem 3.1. Suppose that $\phi(\mathbf{x})$ is an interpolatory scaling function, $\tilde{\phi}(\mathbf{x})$ is a dual of $\phi(\mathbf{x})$, E_{0k}, $\tilde{E}_{0k}$ $(k = 0,1,2,3)$ are polyphase factors of $P(\mathbf{z})$, and $\tilde{P}(\mathbf{z})$. Then the biorthogonal wavelet masks $Q^j(\mathbf{z})$ and $\tilde{Q}^j(\mathbf{z})$ can be given as follows

$$Q^j(\mathbf{z}) = \frac{1}{2}(e_j^T - \overline{\tilde{E}_{0j}}(E_{00}\ E_{01}\ E_{02}\ E_{03}))R(z_1, z_2), \tag{3.6}$$

$$\tilde{Q}^j(\mathbf{z}) = \frac{1}{2}(e_j^T - (\overline{2E_{0j}}, 0, 0, 0))R(z_1, z_2), \tag{3.7}$$

where $j = 1, 2, 3$, and $e_1 = (0, 1, 0, 0)^T, e_2 = (0, 0, 1, 0)^T, e_3 = (0, 0, 0, 1)^T$.

Proof. By [4], we only need to prove that $Q^j(\mathbf{z})$ and $\tilde{Q}^j(\mathbf{z})$, which are given in (3.6) and (3.7), satisfy the conditions (2.2)$\sim$(2.4).

For $j = 1, 2, 3$, let

$$(E_{j0}, E_{j1}, E_{j2}, E_{j3}) = e_j^T - \overline{\tilde{E}_{0j}}(E_{00}\ E_{01}\ E_{02}\ E_{03}), \tag{3.8}$$

$$(\tilde{E}_{j0}, \tilde{E}_{j1}, \tilde{E}_{j2}, \tilde{E}_{j3}) = e_j^T - (\overline{2E_{0j}}, 0, 0, 0). \tag{3.9}$$

We note that $R(z_1, z_2)^T\overline{R(z_1, z_2)} = 4$. By (3.1)$\sim$(3.4), we only need to prove that $E_{jk}, \tilde{E}_{jk}$ $(k = 0, 1, 2, 3,\ j = 1, 2, 3)$, which are given in (3.8) and (3.9), satisfy the condition (3.5). Note that $\phi(\mathbf{x})$ is an interpolatory filter, by equation (1.2), we know that $p_{2\alpha} = \delta_{0,\alpha}$. It follows that $E_{00} = \frac{1}{2}$. Hence,

$$\begin{aligned} & (E_{j0}, E_{j1}, E_{j2}, E_{j3})(\tilde{E}_{j0}, \tilde{E}_{j1}, \tilde{E}_{j2}, \tilde{E}_{j3})^* \\ = \ & (e_j^T - \overline{\tilde{E}_{0j}}(E_{00}\ E_{01}\ E_{02}\ E_{03}))(e_j^T - (2E_{0j}, 0, 0, 0))^T \\ = \ & \delta_{jl} - \overline{\tilde{E}_{0j}}E_{0l} + 2E_{00}E_{0l}\overline{\tilde{E}_{0j}} = \delta_{jl}, \end{aligned}$$

where $j, l = 0, 1, 2, 3$. This completes the proof. □

Example. We consider the interpolatory filter and its dual filter in Example 6.5 of [1]. The mask of the interpolatory function is supported on $[-1, 1] \cap Z^2$ and given by

$$\begin{bmatrix} 1/4 & 1/2 & 1/4 \\ 1/2 & 1 & 1/2 \\ 1/4 & 1/2 & 1/4 \end{bmatrix}$$

The mask of its dual is supported on $[-4, 4] \cup Z^2$ and given by

$$\begin{bmatrix} 0 & 0 & 0 & \frac{3}{128} & \frac{3}{64} & \frac{3}{128} & 0 & 0 & 0 \\ 0 & 0 & 0 & -\frac{3}{64} & -\frac{3}{32} & -\frac{3}{64} & 0 & 0 & 0 \\ 0 & 0 & -\frac{1}{16} & -\frac{1}{8} & -\frac{3}{8} & -\frac{1}{8} & \frac{1}{16} & 0 & 0 \\ \frac{3}{128} & -\frac{3}{64} & -\frac{1}{8} & \frac{11}{32} & \frac{51}{64} & \frac{11}{32} & -\frac{1}{8} & -\frac{3}{64} & \frac{3}{128} \\ \frac{3}{64} & -\frac{3}{32} & -\frac{3}{8} & \frac{51}{64} & \frac{33}{16} & \frac{51}{64} & -\frac{3}{8} & -\frac{3}{32} & \frac{3}{64} \\ \frac{3}{128} & -\frac{3}{64} & -\frac{1}{8} & \frac{11}{32} & \frac{51}{64} & \frac{11}{32} & -\frac{1}{8} & -\frac{3}{64} & \frac{3}{128} \\ 0 & 0 & -\frac{1}{16} & -\frac{1}{8} & -\frac{3}{8} & -\frac{1}{8} & \frac{1}{16} & 0 & 0 \\ 0 & 0 & 0 & -\frac{3}{64} & -\frac{3}{32} & -\frac{3}{64} & 0 & 0 & 0 \\ 0 & 0 & 0 & \frac{3}{128} & \frac{3}{64} & \frac{3}{128} & 0 & 0 & 0 \end{bmatrix}$$

By Theorem 3.1, the biorthogonal wavelet filters can be given as follows:

- $\{q_\alpha^1\}_{\alpha\in Z^2}$, $\{q_\alpha^2\}_{\alpha\in Z^2}$, $\{q_\alpha^3\}_{\alpha\in Z^2}$, their support are in $[-5,5]$, which can be given as follows

$$\begin{bmatrix}
0 & 0 & 0 & 0 & 0 & 0 & 0 & 0 & 0 & 0 & 0\\
0 & 0 & 0 & 0 & 0 & 0 & 0 & 0 & 0 & 0 & 0\\
0 & 0 & 0 & 0 & \frac{3}{128} & \frac{3}{64} & 0 & 0 & 0 & 0 & 0\\
0 & 0 & 0 & 0 & \frac{3}{32} & \frac{3}{32} & \frac{3}{64} & 0 & 0 & 0 & 0\\
-\frac{3}{256} & -\frac{3}{256} & \frac{1}{32} & \frac{1}{16} & -\frac{51}{256} & -\frac{45}{128} & \frac{7}{128} & \frac{1}{16} & -\frac{3}{512} & -\frac{3}{256} & 0\\
-\frac{3}{256} & -\frac{3}{128} & \frac{13}{256} & \frac{1}{8} & -\frac{43}{128} & -\frac{51}{64} & -\frac{43}{128} & \frac{1}{8} & \frac{13}{256} & -\frac{3}{128} & -\frac{3}{256}\\
-\frac{3}{512} & -\frac{3}{128} & \frac{13}{512} & \frac{1}{8} & -\frac{43}{256} & \frac{13}{64} & -\frac{35}{256} & \frac{1}{8} & \frac{13}{512} & -\frac{3}{128} & -\frac{3}{512}\\
-\frac{3}{256} & -\frac{3}{128} & \frac{13}{256} & \frac{1}{8} & -\frac{43}{128} & -\frac{51}{64} & -\frac{43}{128} & \frac{1}{8} & \frac{13}{256} & -\frac{3}{128} & -\frac{3}{256}\\
0 & -\frac{3}{256} & -\frac{3}{512} & \frac{1}{16} & \frac{7}{128} & -\frac{45}{128} & -\frac{51}{256} & \frac{1}{16} & \frac{1}{32} & -\frac{3}{256} & -\frac{3}{512}\\
0 & 0 & 0 & 0 & \frac{3}{64} & \frac{3}{32} & \frac{3}{64} & 0 & 0 & 0 & 0\\
0 & 0 & 0 & 0 & 0 & \frac{3}{64} & \frac{3}{128} & 0 & 0 & 0 & 0
\end{bmatrix}$$

$$\begin{bmatrix}
0 & 0 & 0 & 0 & -\frac{3}{512} & -\frac{3}{256} & -\frac{3}{512} & -\frac{3}{256} & 0 & 0 & 0\\
0 & 0 & 0 & 0 & -\frac{3}{256} & -\frac{3}{128} & -\frac{3}{128} & -\frac{3}{128} & -\frac{3}{256} & 0 & 0\\
0 & 0 & 0 & 0 & \frac{1}{32} & \frac{13}{256} & \frac{13}{512} & \frac{13}{256} & -\frac{3}{512} & 0 & 0\\
0 & 0 & 0 & 0 & \frac{1}{16} & \frac{1}{8} & \frac{1}{8} & \frac{1}{8} & \frac{1}{16} & 0 & 0\\
0 & 0 & \frac{3}{128} & \frac{3}{64} & -\frac{51}{256} & -\frac{43}{128} & -\frac{43}{256} & -\frac{43}{128} & \frac{7}{128} & \frac{3}{64} & 0\\
0 & 0 & \frac{3}{64} & \frac{3}{32} & -\frac{45}{128} & -\frac{51}{64} & \frac{13}{64} & -\frac{5}{64} & -\frac{45}{128} & \frac{3}{32} & \frac{3}{64}\\
0 & 0 & 0 & \frac{3}{64} & \frac{7}{128} & -\frac{43}{128} & -\frac{43}{256} & -\frac{43}{128} & -\frac{51}{256} & \frac{3}{64} & \frac{3}{128}\\
0 & 0 & 0 & 0 & \frac{1}{16} & \frac{1}{8} & \frac{1}{8} & \frac{1}{8} & \frac{1}{16} & 0 & 0\\
0 & 0 & 0 & 0 & -\frac{3}{512} & \frac{13}{256} & \frac{13}{512} & \frac{13}{256} & \frac{1}{32} & 0 & 0\\
0 & 0 & 0 & 0 & -\frac{3}{256} & -\frac{3}{128} & -\frac{3}{128} & -\frac{3}{128} & -\frac{3}{256} & 0 & 0\\
0 & 0 & 0 & 0 & 0 & -\frac{3}{256} & -\frac{3}{512} & -\frac{3}{256} & -\frac{3}{512} & 0 & 0
\end{bmatrix}$$

$$\begin{bmatrix}
0 & 0 & 0 & 0 & 0 & 0 & 0 & 0 & 0 & 0 & 0\\
0 & 0 & 0 & 0 & 0 & 0 & 0 & 0 & 0 & 0 & 0\\
0 & 0 & 0 & 0 & \frac{3}{256} & \frac{3}{128} & \frac{3}{256} & \frac{3}{128} & 0 & 0 & 0\\
0 & 0 & 0 & 0 & \frac{3}{128} & \frac{3}{64} & \frac{3}{64} & \frac{3}{64} & \frac{3}{128} & 0 & 0\\
0 & 0 & \frac{3}{256} & \frac{3}{128} & -\frac{11}{128} & -\frac{19}{128} & -\frac{19}{256} & -\frac{19}{128} & \frac{3}{128} & \frac{3}{128} & 0\\
0 & 0 & \frac{3}{128} & \frac{3}{64} & -\frac{19}{128} & -\frac{11}{32} & -\frac{11}{32} & -\frac{11}{32} & -\frac{19}{128} & \frac{3}{64} & \frac{3}{128}\\
0 & 0 & \frac{3}{256} & \frac{3}{64} & -\frac{19}{256} & -\frac{11}{32} & \frac{53}{64} & -\frac{11}{32} & -\frac{19}{256} & \frac{3}{64} & \frac{3}{256}\\
0 & 0 & \frac{3}{128} & \frac{3}{64} & -\frac{19}{128} & -\frac{11}{32} & -\frac{11}{32} & -\frac{11}{32} & -\frac{19}{128} & \frac{3}{64} & \frac{3}{128}\\
0 & 0 & 0 & \frac{3}{128} & \frac{3}{128} & -\frac{19}{128} & -\frac{19}{256} & -\frac{19}{128} & -\frac{11}{128} & \frac{3}{128} & \frac{3}{256}\\
0 & 0 & 0 & 0 & \frac{3}{128} & \frac{3}{64} & \frac{3}{64} & \frac{3}{64} & \frac{3}{128} & 0 & 0\\
0 & 0 & 0 & 0 & 0 & \frac{3}{128} & \frac{3}{256} & \frac{3}{128} & \frac{3}{256} & 0 & 0
\end{bmatrix}$$

- $\{\tilde{q}^1_\alpha\}_{\alpha\in Z^2}$, $\{\tilde{q}^1_\alpha\}_{\alpha\in Z^2}$, $\{\tilde{q}^1_\alpha\}_{\alpha\in Z^2}$, their support are all in $[0,3]^2$, which can be given as follows

$$\begin{bmatrix} -\frac{1}{2} & 1 & -\frac{1}{2} \\ 0 & 0 & 0 \\ 0 & 0 & 0 \end{bmatrix}, \begin{bmatrix} 0 & 0 & 0 \\ -\frac{1}{2} & 1 & -\frac{1}{2} \\ 0 & 0 & 0 \end{bmatrix}, \begin{bmatrix} 0 & 0 & 0 \\ 0 & 0 & 0 \\ -\frac{1}{2} & 1 & -\frac{1}{2} \end{bmatrix}$$

Remark 3.2. In the construction of multi-dimensional wavelets, to improve the properties of the wavelets, the support of the scaling function may be enlarged. As a result, the nonzero coefficients in $\{p_\alpha\}_{\alpha\in Z^2}$ and $\{\tilde{p}_\alpha\}_{\alpha\in Z^2}$ will increase drastically. If the biorthogonal wavelets are constructed by the method given in [2], not only the Gram-Schmidt processing but also the inverse of a nonsingular polynomial matrix is needed. In our method, the biorthogonal wavelet masks are given explicitly (see the formulas (3.6) and (3.7)). Hence, the procedure for constructing two-dimensional biorthogonal wavelets from an interpolatory function is similar to that of one-dimensional biorthogonal wavelets. When compared with [2], our method results in significant amount of computational saving.

Remark 3.3. In this paper, we only consider the construction of two-dimensional biorthogonal wavelets associated with the dilation matrix $2I$. In fact, Theorem 3.1 can be generalized to the case of multidimensional and arbitrary dilation matrix.

4. Conclusion

For a pair of two-dimensional dual refinable functions, when one of them is interpolatory, we provide formulas for constructing the associated biorthogonal wavelet masks. Neither the Gram-Schmidt processing nor the computation of the inverse of a Laurent matrix is needed.

References

[1] B. Han, *Analysis and construction of optimal multivariate biorthogonal wavelets with compact support*, SIAM J. Math. Anal. **30** (2000), 274–304.

[2] H. Ji, S. D. Riemenschneider, and Z. Shen, *Multivariate compactly supported fundamental refinables,duals, and biorthogonal wavelets*, Studies in Appl. Math. **102** (1999), 173–204.

[3] H. Ji and Z. Shen, *Compactly supported (bi)orthogonal wavelets generated by interpolatory refinable functions*, Advances in Comp. Math. **11** (1999), 81–104.

[4] R. Long, *High-dimensional wavelet analysis*, World Scientific, Beijing, 1995.

[5] Z. Shen, *Refinable function vectors*, SIAM J. Math. Anal. **28** (1998), 235–250.

[6] R. Q. Jia and Z. Shen, *Multiresolution and wavelets*, Pro. Edinburgh Math. Soc. **37** (1994), 271–300.

[7] J. Kovačević and W. Sweldens, *Wavelet families of increasing order in arbitrary dimensions*, IEEE Trans. Image Proc. **9** (2000), no. 3, 480–496.

[8] D. Chen, B. Han, and S. D. Riemenschneider, *Construction of multivariate biorthogonal wavelets with arbitrary vanishing moments*, Advances in Comp. Math. **13** (2000), 131–165.

Jianwei Yang
Department of Computer Science
Henan Institute of Finance and Economics
Zhengzhou 450002
P. R. China
e-mail: yjianw2002@yahoo.com.cn

Yuan Yan Tang
Department of Computer Science
Chongqing University
Chongqing, 400044
P. R. China
e-mail: yytang@comp.hkbu.edu.hk

Zhengxing Cheng
School of Science
Xi'an Jiaotong University
Xi'an 710049
P. R. China

Xinge You
Faculty of Mathematics & Computer Science
Hubei University
Wuhan,430062,
P. R. China
e-mail: xyou@comp.hkbu.edu.hk

Wavelet Analysis and Applications
Tao Qian, Mang I. Vai and Xu Yuesheng, Eds.
Applied and Numerical Harmonic Analysis, 99–106

Parameterization of Orthogonal Filter Bank with Linear Phase

Xiaoxia Feng, Zhengxing Cheng and Zhongpeng Yang

Abstract. For the M-channel FIR orthogonal filter bank with linear phase, a complete parameterization is obtained by applying the singular value decomposition of matrices related to the corresponding polyphase matrix. In the obtained parameterization forms, the number of the required parameters is reduced to $(N+2)\binom{\frac{M}{2}}{2}$.

Mathematics Subject Classification (2000). Primary 42C40; Secondary 15A23.

Keywords. paraunitary matrix; linear phase; filter bank; singular value decomposition.

1. Introduction

In some applications, particularly in image processing, it is desirable that each individual filter in a paraunitary system is of linear phase. Paraunitary FIR filter banks can perform an orthogonal transformation to the data without phase distortion, and this symmetric property(linear phase) can be used for efficient implementation[1], so we only discuss the paraunitary FIR filter banks with linear phase in this paper.

For general paraunitary filter banks, Vaidyanathan et. al. proposed a complete and minimal structure[2][3], which shows that any parauintary system of McMillan degree N can be factorized into a product of N degree-one paraunitary building blocks and an unitary matrix. In practice, we care more about the filter length than the degree of the system. In this case, it is expected to have a parameterization form for paraunitary systems with given order[4].

In order to get the parameterization of a paraunitary system with linear phase and order N, by applying the theory of the balanced vectors, [5] obtained the form (3.9) which requires $2(N+2)\binom{M/2}{2}$ parameters; applying the singular

The paper is supported by the scientific research "fifteen" layout item of the educational office in Jilin, 2004.

value decomposition of the matrices, [4] obtained the form (9) which requires $2(N+1)\binom{M/2}{2}$ parameters, moreover, by using the method similar to the cosine-sine decomposition of a general unitary matrix, [4] further factorized this system into the form (47) which requires $(N+2)\binom{M/2}{2}$ parameters.

Motivated by [6], we propose a complete parameterization of a paraunitary system with order N, only by applying the singular value decomposition of the matrices related to the coefficient matrices of this system. Our aim is such that the required parameters representing this system is as small as possible by a more efficient method.

In addition, in M-band orthogonal wavelet systems, there are $M-1$ wavelet filters, and they are not uniquely determined by the scaling filter, it is very difficult to construct these wavelet filters, the parameterization of the filter bank is an important method to construct these wavelet filters. And the complete parameterization of the filter bank often provides an efficient structure for optimal design and fast implementation too, thus the research on the complete parameterization of the paraunitary filter bank with linear phase is very important too.

2. Prepared Knowledge

A filter $H_0(z)$ is called an M-band orthogonal scaling filter if it satisfies the condition

$$\sum_{k=0}^{M-1} \left|H_0(e^{i(\frac{\omega+2k\pi}{M})})\right|^2 = 1. \tag{2.1}$$

Given a scaling filter, the associated scaling function $\psi_0(x)$ is the solution of the following two-scale refinement equation

$$\psi_0(x) = \sum_n h_0(n)\psi_0(Mx-n). \tag{2.2}$$

A sufficient condition for (2.2) to have a solution in $L^1(R)$ is that the scaling filter $H_0(z)$ satisfies the linear constraint

$$H_0(1) = 1, \tag{2.3}$$

and

$$H_0(e^{i\omega}) \neq 0, \quad \forall\, \omega \in [-\frac{\omega}{M}, \frac{\omega}{M}], \tag{2.4}$$

the associated scaling function generates an orthogonal basis.

Corresponding to the scaling filter $H_0(z)$, there are $M-1$ wavelet filters $H_l(z)$, and they satisfy

$$\sum_{k=0}^{M-1} H_p(e^{i(\frac{\omega+2k\pi}{M})})H_q^*(e^{i(\frac{\omega+2k\pi}{M})}) = \delta_{p-q}, \quad 0 \le p \le M-1,\ 1 \le q \le M-1, \tag{2.5}$$

the corresponding wavelet functions are defined by

$$\widehat{\psi}_l(\omega) = H_l(e^{i\omega/M})\,\widehat{\phi}(\omega/M),\ l = 1, 2, \cdots, M-1.$$

We call $\mathcal{H}(z) = [H_0(z), H_1(z), \cdots, H_{M-1}(z)]^T$ the filter bank of the M-band wavelet system. When $H_l(z)(0 \le l \le M-1)$ satisfies (2.1) and (2.5), we say that $\mathcal{H}(z)$ is orthogonal. Here, we only discuss real FIR causal filter bank and M is even.

If every filter of the filter bank $\mathcal{H}(z)$ is either symmetric or antisymmetric about the same center of symmetry $(M(N+1)-1)/2$, i.e.,

$$h_k(M(N+1)-1-n) = s_k h_k(n), \tag{2.6}$$

where $s_k = 1$ or -1, $0 \le n \le M(N+1)-1$, $0 \le k \le M-1$, then we call $\mathcal{H}(z)$ to have linear phase.

The filter bank $\mathcal{H}(z)$ can also be represented by its polyphase matrix $P(z)$ as follows

$$\mathcal{H}(z) = \frac{1}{\sqrt{M}} P(z^M) \begin{bmatrix} 1 \\ z^{-1} \\ \vdots \\ z^{-(M-1)} \end{bmatrix}, \tag{2.7}$$

where

$$P(z) = \begin{bmatrix} H_{0,0}(z) & H_{0,1}(z) & \cdots & H_{0,M-1}(z) \\ \cdots & \cdots & \cdots & \cdots \\ H_{M-1,0}(z) & H_{M-1,1}(z) & \cdots & H_{M-1,1}(z) \end{bmatrix},$$

$$H_k(z) = \frac{1}{\sqrt{M}} \sum_{l=0}^{M-1} H_{k,l}(z^m) z^{-k}, \quad H_{k,l}(z) = \sqrt{M} \sum_{n=0}^{N} h_k(Mn+l) z^{-n}.$$

Then the filter bank $\mathcal{H}(z)$ is orthogonal if and only if the corresponding polyphase matrix $P(z)$ is paraunitary[6], i.e., $P(z)$ satisfies

$$P(z^{-1})^T P(z) = I_M,$$

meanwhile, $P(z)$ is said to form a paraunitary system.

Since the polyphase representation is useful not only for theoretical study of filter banks but also for their efficient implementation, it is reasonable to require the symmetries of filters to conform to the polyphase structure. In other words, in order to obtain the parameterization of paraunitary filter banks with linear phase, we first need to obtain the characterization of its polyphase matrix which reflects the linear phase property of the individual filters. By the simple computation, we can obtain the following lemma[5]

Lemma 2.1. *Let $P(z)$ be the polyphase matrix of the filter bank $\mathcal{H}(z)$, then the filter $h_l(k)$($0 \le l \le M-1$) has linear phase if and only if $P(z)$ satisfies the following condition*

$$P(z) = z^{-N} D P(z^{-1}) J_M, \tag{2.8}$$

where $D = \mathrm{diag}(s_0, s_1, \cdots, s_{M-1})$, J_M is $M \times M$ antidiagonal matrix, N is the order of $P(z)$, i.e., the highest power of z^{-1} in $P(z)$.

We can obtain the parameterization of another paraunitary matrix $E_N(z)$ that is a transform of $P(z)$ by applying the singular value decomposition of matrices, so does the one of $P(z)$ by the relation between $P(z)$ and $E_N(z)$.

3. Main Results

In this section, we shall give the parameterization of the orthogonal filter bank $\mathcal{H}(z)$ with linear phase, by the method of the singular value decomposition of matrices, here, the corresponding polyphase matrix $P(z)$ satisfies (2.8).

Let the unitary matrix

$$R = \frac{\sqrt{2}}{2}\begin{bmatrix} I_{M/2} & J_{M/2} \\ J_{M/2} & -I_{M/2} \end{bmatrix},$$

then

$$R^T J_M R = \operatorname{diag}(I_{M/2}, -I_{M/2}). \tag{3.1}$$

From [5], we know that there are $M/2$ symmetric, and $M/2$ antisymmetric filters in the filter bank $\mathcal{H}(z)$ when M is even, thus the half of the diagonal elements of D are 1, and the others are -1, so there exists a $M \times M$ permutation matrix Q such that

$$QDQ^T = \operatorname{diag}(I_{M/2}, -I_{M/2}). \tag{3.2}$$

Take

$$E_N(z) = QP(z)R, \tag{3.3}$$

by (2.8), (3.1) and (3.2), we have

$$E_N(z) = z^{-N}\operatorname{diag}(I_{M/2}, -I_{M/2})E_N(z^{-1})\operatorname{diag}(I_{M/2}, -I_{M/2}), \tag{3.4}$$

it follows that $E_N(z)$ is paraunitary by the paraunitarity of $P(z)$ and unitarity of R and Q.

Theorem 3.1. *A causal FIR matrix $E_N(z)$ is paraunitary and satisfies* (3.4) *if and only if $E_N(z)$ can be parameterized as*

$$E_N(z) = V_N(z)V_{N-1}(z)\cdots V_1(z)\operatorname{diag}(w, u), \tag{3.5}$$

where $V_i(z)(1 \le i \le N)$ has the following form

$$V_i(z) = \frac{1}{2}\begin{bmatrix} I_{M/2} & -v_i \\ -v_i^T & I_{M/2} \end{bmatrix} + \frac{1}{2}\begin{bmatrix} I_{M/2} & v_i \\ v_i^T & I_{M/2} \end{bmatrix} z^{-1}, \tag{3.6}$$

v_i, w and u are $\frac{M}{2} \times \frac{M}{2}$ orthogonal matrices.

Proof. Assume that

$$E_N(z) = e_0 + e_1 z^{-1} + e_2 z^{-2} + \cdots + e_N z^{-N}$$

be paraunitary and satisfy (3.4). It follows that

$$e_N = \operatorname{diag}(I_{M/2}, -I_{M/2})\, e_0 \operatorname{diag}(I_{M/2}, -I_{M/2}). \tag{3.7}$$

Since $E_N(z)$ is paraunitary, then

$$e_N^T e_0 = 0. \tag{3.8}$$

By (3.7) and (3.8), we obtain that

$$e_0^T \operatorname{diag}(I_{M/2}, -I_{M/2})\, e_0 = 0. \tag{3.9}$$

Partitioning e_0 as $e_0 = \begin{bmatrix} B_1 \\ B_2 \end{bmatrix}$, where both B_1 and B_2 are $\frac{M}{2} \times M$ matrices, thereby by (3.9), we have

$$e_0^T \operatorname{diag}(I_{M/2}, -I_{M/2})\, e_0 = \left[B_1^T, B_2^T\right] \operatorname{diag}(I_{M/2}, -I_{M/2}) \begin{bmatrix} B_1 \\ B_2 \end{bmatrix} = 0,$$

furthermore,

$$B_1^T B_1 = B_2^T B_2. \tag{3.10}$$

Therefore, both B_1 and B_2 have the same singular values. Let $\sigma_1, \sigma_2, \cdots, \sigma_n$ be their nonzero singular values, then $\sigma_i (1 \le i \le n)$ is positive. Furthermore, there exists an $M \times M$ orthogonal matrix G such that

$$B_1^T B_1 = B_2^T B_2 = G \operatorname{diag}(\Lambda_n^2, 0)\, G^T, \tag{3.11}$$

where $\Lambda_n = \operatorname{diag}(\sigma_1, \sigma_2, \cdots, \sigma_n)$.

From (3.11), it follows that

$$\operatorname{rank} B_1 = \operatorname{rank} B_1^T B_1 = \operatorname{rank} B_2 = \operatorname{rank} B_1^T B_1 = n \le \frac{M}{2},$$

and there are two $\frac{M}{2} \times \frac{M}{2}$ orthogonal matrices G_1, G_2 such that

$$B_1 B_1^T = G_1 \operatorname{diag}(\Lambda_n^2, 0)\, G_1^T; \quad B_2 B_2^T = G_2 \operatorname{diag}(\Lambda_n^2, 0)\, G_2^T. \tag{3.12}$$

Thereby by means of (3.11), (3.12) and the theory of singular value decomposition(see [8]: 144-147), we can derive that the singular value decompositions of B_1, B_2 are

$$B_1 = G_1 \operatorname{diag}(\Lambda_n, 0)\, G^T; \quad B_2 = G_2 \operatorname{diag}(\Lambda_n, 0)\, G^T, \tag{3.13}$$

then

$$B_1 = (G_1 G_2^T)\, G_2 \operatorname{diag}(\Lambda_n, 0)\, G^T = -v_N B_2, \tag{3.14}$$

where $v_N = -G_1 G_2^T$.

According to the orthogonal properties of G_1 and G_2, we obtain

$$v_N^T v_N = (-G_1 G_2^T)^T (-G_1 G_2^T) = I_{M/2},$$

namely, v_N is orthogonal and satisfies

$$[I_{M/2}, v_N] e_0 = [I_{M/2}, v_N] \begin{bmatrix} B_1 \\ B_2 \end{bmatrix} = [I_{M/2}, v_N] \begin{bmatrix} -v_N B_2 \\ B_2 \end{bmatrix} = 0. \tag{3.15}$$

Moreover,

$$\left[v_N^T, I_{M/2}\right] e_0 = \left[v_N^T, I_{M/2}\right] \begin{bmatrix} -v_N B_2 \\ B_2 \end{bmatrix} = -v_N^T v_N B_2 + B_2 = 0,$$

so

$$\begin{bmatrix} I_{M/2} & v_N \\ v_N^T & I_{M/2} \end{bmatrix} e_0 = 0. \tag{3.16}$$

By (3.7) and (3.16), we have

$$\begin{aligned} &\begin{bmatrix} I_{M/2} & -v_N \\ -v_N^T & I_{M/2} \end{bmatrix} e_N \\ &= \begin{bmatrix} I_{M/2} & -v_N \\ -v_N^T & I_{M/2} \end{bmatrix} \operatorname{diag}(I_{M/2}, -I_{M/2})\, e_0 \operatorname{diag}(I_{M/2}, -I_{M/2}) \\ &= \begin{bmatrix} I_{M/2} & v_N \\ -v_N^T & -I_{M/2} \end{bmatrix} e_0 \operatorname{diag}(I_{M/2}, -I_{M/2}) \\ &= \operatorname{diag}(I_{M/2}, -I_{M/2}) \begin{bmatrix} I_{M/2} & v_N \\ v_N^T & I_{M/2} \end{bmatrix} e_0 \operatorname{diag}(I_{M/2}, -I_{M/2}) \\ &= 0. \end{aligned} \tag{3.17}$$

Take the order-one matrix $V_N(z)$ as (3.6), by the direct computation, we have that $V_N(z)$ satisfies the following properties:

$$i) \quad V_N(z)\, V_N(z^{-1}) = I_M; \tag{3.18}$$

$$ii) \quad V_N(z^{-1}) \operatorname{diag}(I_{M/2}, -I_{M/2})\, V_N(z^{-1}) = z \operatorname{diag}(I_{M/2}, -I_{M/2}). \tag{3.19}$$

Take

$$E_N(z) = V_N(z) E_{N-1}(z). \tag{3.20}$$

Since both $E_N(z)$ and $V_N(z)$ are paraunitary, then $E_{N-1}(z)$ is *paraunitary*. It is clear that $E_{N-1}(z)$ has *order* $\mathbf{N-1}$ in virtue of (3.17).

From (3.6), (3.18) and (3.20), it follows that

$$\begin{aligned} E_{N-1}(z) &= V_N(z^{-1}) E_N(z) \\ &= \frac{1}{2} \begin{bmatrix} I_{M/2} & -v_N \\ -v_N^T & I_{M/2} \end{bmatrix} E_N(z) + \frac{1}{2} z \begin{bmatrix} I_{M/2} & v_N \\ v_N^T & I_{M/2} \end{bmatrix} E_N(z). \end{aligned} \tag{3.21}$$

The second term on the right-hand side of (3.21) is responsible for the non-causality, but we select v_N such that (3.16) holds, therefore $E_N(z)$ is *causal*.

Substitute (3.20) into (3.4), we have

$$z^{-N} \operatorname{diag}(I_{M/2}, -I_{M/2})\, V_N(z^{-1})\, E_{N-1}(z^{-1}) \operatorname{diag}(I_{M/2}, -I_{M/2}) = V_N(z)\, E_{N-1}(z),$$

namely,

$$\begin{aligned} &z^{-N} \big(V_N(z^{-1}) \operatorname{diag}(I_{M/2}, -I_{M/2}) V_N(z^{-1}) \big)\, E_{N-1}(z^{-1}) \operatorname{diag}(I_{M/2}, -I_{M/2}) \\ &= E_{N-1}(z), \end{aligned}$$

by (3.19), we know

$$z^{-(N-1)} \operatorname{diag}(I_{M/2}, -I_{M/2})\, E_{N-1}(z^{-1}) \operatorname{diag}(I_{M/2}, -I_{M/2}) = E_{N-1}(z),$$

therefore $E_{N-1}(z)$ satisfies (3.4), i.e., the corresponding filter bank has *linear phase*.

In a word, $E_{N-1}(z)$ is paraunitary, and has linear phase. At the moment, there is a reduction in order by 1, thereby for a paraunitary matrix $E_N(z)$ satisfying (3.4), this process is guaranteed to terminate in N steps. Similar to the above process, there exist $\frac{M}{2} \times \frac{M}{2}$ orthogonal matrices $v_{N-1}, \cdots, v_1$ such that $V_{N-1}(z), \cdots, V_1(z)$ defined by (3.6) satisfy the properties (3.18) and (3.19). Then $E_N(z)$ can be written as

$$E_N(z) = V_N(z)E_{N-1}(z) = V_N(z)\,V_{N-1}(z)E_{N-2}(z) = V_N(z)\cdots V_1(z)E_0, \quad (3.22)$$

where

$$E_0^T E_0 = I_M, \quad E_0 = \mathrm{diag}(I_{M/2}, -I_{M/2})\,E_0\,\mathrm{diag}(I_{M/2}, -I_{M/2}),$$

it follows that E_0 has the form $E_0 = \mathrm{diag}(w, u)$, w, u are $\frac{M}{2} \times \frac{M}{2}$ orthogonal matrices. Substitute E_0 into (3.22), we have that the necessity holds.

For the sufficiency, by (3.18), (3.19) and the hypothesis, it follows that $E_N(z)$ satisfying (3.5) is causal, paraunitary and satisfies (3.4). □

By the theorem 3.1 and (3.3), we derive

Corollary 3.2. *Let $P(z)$ be the corresponding polyphase matrix of the filter bank $\mathcal{H}(z)$. Then $P(z)$ is paraunitary and satisfies* (2.8) *if and only if $P(z)$ can be parameterized as*

$$P(z) = Q^T V_N(z)V_{N-1}(z)\cdots V_1(z)\,\mathrm{diag}(w, u)R^T \quad (3.23)$$

Through (2.7) and the corollary 3.2, we derive the following theorem

Theorem 3.3. *When M is even, a causal FIR filter bank $\mathcal{H}(z)$ is orthogonal and satisfies* (2.6) *if and only if it can be parameterized as*

$$\mathcal{H}(z) = \frac{1}{\sqrt{M}} Q^T V_N(z)V_{N-1}(z)\cdots V_1(z)\mathrm{diag}(w, u)\cdot R^T \begin{bmatrix} 1 \\ z^{-1} \\ \vdots \\ z^{-(M-1)} \end{bmatrix}. \quad (3.24)$$

By the parameterization form (3.24) of the filter bank $\mathcal{H}(z)$, we can design many scaling filters with different properties, and let they satisfy the conditions (2.3) and (2.4), then we derive scaling functions and the corresponding wavelets.

4. Comment

For our results, the parameterization form (3.23) of $P(z)$ requires $(N+2)\binom{M}{2}$ parameters, which is less than that of (3.9) in [5] and (9) in [4], and is equal to that of (47) in [4]. But we only use singular values decomposition of matrices to get the parameterization of $P(z)$ with the same parameters, out of question, not only this method decrease computing complexity, but it is simpler and more effective as well.

References

[1] P. P. Vaidyanathan, *Multirate Systems and Filter banks*, Prentice Hall, Englewood Cliffs, 1993.

[2] Z. Doganata, P. P. Vaidyanathan and T. Q. Nguyen, *General synthesis procedure for FIR lossless transfer matrices, for perfect-reconstruction multirate filter bank application*, IEEE Trans. Acoustics, Speech, and Signal Processing, 36(10)(1988), 1561-1574.

[3] P. P. Vaidyanathan, T. Q. Nguyen, Z. Doganata and T. Saramaki, *Improved technique for design of perfect reconstruction FIR QMF banks with lossless polyphase matrices*, IEEE Trans. Acoustics, Speech, and Signal Processing, 37(7)(1989), 1042-1056.

[4] X. Q. Gao, T. Q. Nguyen and G. Strang, *On factorization of M-channel paraunity filter banks*, IEEE Trans. Signal Processing, 49(2001), 1433-1446.

[5] A. K. Soman, P. P. Vaidyanathan, T. Q. Nguyen, *Linear phase paraunitary filter banks: theory, factorizations and designs*, IEEE Trans. Signal Processing, 41(12)(1993), 3480-3496.

[6] Q. T. Jiang, *Parameterization of m-channel orthogonal multifilter banks*, Advances in Computational Mathematics, 12(2000), 189-211.

[7] P. Steffen, P. N. Heller, R. A. Gopinath, and C. S. Burrus, *Theory of regular M-band wavelet bases*, IEEE Trans. Signal Processing, 41(12)(1993), 3497-3510.

[8] R. A. Horn and C. R. Johnson, *Topics in matrix analysis[M]*, Cambridge U. P., Cambridge U. K., 1991, 144-147.

Xiaoxia Feng
Faculty of Science
Xi'an Jiaotong University
Xi'an, Shaanxi, 710049
P. R. China;
Department of Mathematics.
Beihua University
Jilin, Jilin, 132013
P. R. China
e-mail: `jlfengxx@sohu.com`

Zhengxing Cheng
Faculty of Science
Xi'an Jiaotong University
Xi'an, Shaanxi, 710049
P. R. China
e-mail: `zhengxingch@163.com`

Zhongpeng Yang
Department of Mathematics
Putian College
Putian, Fujian, 351100
P. R. China
e-mail: `yangzhongpeng@126.com`

Wavelet Analysis and Applications
Tao Qian, Mang I. Vai and Xu Yuesheng, Eds.
Applied and Numerical Harmonic Analysis, 107–121

On Multivariate Wavelets with Trigonometric Vanishing Moments

Ying Li, Zhi-Dong Deng and Yan-Chun Liang

Abstract. Wavelets with trigonometric vanishing moments are studied for the first time. A practical construction algorithm of multivariate orthonormal wavelets with trigonometric vanishing moments is proposed. Based on such construction algorithm, a tight frame of $L^2(\mathbb{R}^d)$ can be obtained even at the worst case. An example of construction of bivariate orthonormal wavelets providing concrete trigonometric vanishing moments is presented.

Keywords. Non-tensor product, trigonometric vanishing moment, tight framework, vanishing moment, trigonometric polynomial.

1. Introduction

Wavelets have been a rapidly developed branch in mathematics, which become a powerful tool for many applications such as signal processing, function approximation, image processing and computational molecule biology. With the remarkable increase of processing problems, it is very desirable to design wavelets possessing various properties such as orthonormality or symmetry or compact support or vanishing moments.

The order of vanishing moments is one of the most important factors for success of wavelets in various applications such as image compression and singularity detection. In particular, vanishing moments are necessary for smoothness of wavelets (see [1]) and guarantee the approximation order (see [2]).

It is well known that trigonometric polynomials can also accomplish the same outstanding approximation behavior compared with algebra polynomials. In this paper, trigonometric vanishing moments are studied. Wavelets with trigonometric vanishing moments are orthogonal to trigonometric polynomials. Such wavelets not only inherit the excellence of wavelets with vanishing moments, but also keep the good features of exponential (trigonometric) function basis, such as periodicity and specific frequency information.

For multivariate non-tensor product compactly supported orthonormal wavelets providing trigonometric vanishing moments, a practical construction algorithm is found. In addition, a tight frame of $L^2(\mathbb{R}^d)$ can be obtained even at the worst case utilizing our proposed construction algorithm. An example of construction of bivariate orthonormal wavelets providing concrete trigonometric vanishing moments is presented.

2. Notations and Preliminaries

A compactly supported multivariate function $f(x), x \in \mathbb{R}^d$ is refinable with mask c if it satisfies the following refinement equation:

$$f(x) = \sum_{j \in \mathbb{Z}^d} c_j f(2x - j) \tag{1}$$

where $c = \{c_j\}_{\mathbb{Z}^d}$ is a finitely supported sequence on $\mathbb{Z}^d$. If c satisfies $\sum_{j \in \mathbb{Z}^d} c_j = 2^d$, there exists a unique compactly supported function $f(x)$ such that the refinement equation holds [3]. Define $C(w)$ as a mask symbol of c in the following:

$$C(w) = \sum_{j \in \mathbb{Z}^d} c_j e^{-iwj}, w \in \mathbb{R}^d.$$

By δ we denote the Dirac sequence on $\mathbb{Z}^d$ defined by $\delta_0 = 1$ and $\delta_k = 0$ for all $k \in \mathbb{Z}^d \backslash \{0\}$. $l(\mathbb{Z}^d)$ denote the linear space of all sequences defined on $\mathbb{Z}^d$. Let $l^2(\mathbb{Z}^d)$ be a space of all sequences $\{a_l\}_{l \in \mathbb{Z}^d}$ which satisfy $\sum_{l \in Z^2} |a_l|^2 < +\infty$. Let $\mathbf{E}$ denote the 2^d vertexes set of the d-dimension hypercube. $\mathbf{F} = \mathbf{E} \backslash \{0\}$. The elements of $\mathbf{E}$ beginning with zero are sorted in order. Define $\delta_{\nu,\mu} = 1, \text{if } \nu = \mu; \text{otherwise } \delta_{\nu,\mu} = 0$. Let $|\alpha| = \sum_{i=1}^{d} |\alpha_i|$ be the length of $\alpha = (\alpha_1, \cdots, \alpha_d) \in \mathbb{Z}^d$.

Define a shift operator $E^y, y \in \mathbb{R}^d$ as follows

$$E^y g(x) = g(x + y) \tag{2}$$

where g is a function on $\mathbb{R}^d$.

For any nonnegative integer N, denote T^d_{N-1} as the space of all d-dimension trigonometric polynomials of total degree less than N. Let $T^d_{-1} = 0$.

A compactly supported function $f \in L^1(\mathbb{R}^d)$ has N order vanishing moments if

$$\int_{\mathbb{R}^d} f(x)p(x)dx = 0, \qquad \forall p \in \Pi_{N-1} \tag{3}$$

where Π_{N-1} is the set of all polynomials of total degree less than N.

Compared with vanishing moments, the definition of N order trigonometric vanishing moments is proposed in the following.

Definition 2.1. *A compactly supported function $f \in L^1(\mathbb{R}^d)$ has N order trigonometric vanishing moments if*

$$\int_{\mathbb{R}^d} f(x)p(x)dx = 0, \qquad \forall p \in T^d_{N-1} \tag{4}$$

To avoid confusions, we emphasize that the wavelets with vanishing moments are orthogonal to polynomials.

3. Construction of Orthonormal Wavelets with Trigonometric Vanishing Moments

Let compactly supported functions ϕ and $\psi^\mu, \mu \in \mathbf{F}, \in L^2(\mathbb{R}^d)$ be scaling function and wavelet functions respectively, trigonometric polynomial functions $H(w) = \frac{1}{2^d}\sum_{n\in\mathbb{Z}^d} h_n e^{-iwn}$ and $G^\mu(w) = \frac{1}{2^d}\sum_{n\in\mathbb{Z}^d} g^\mu_n e^{-iwn}, \mu \in \mathbf{F}$, are the corresponding refinement filter symbols. So we have:

$$\hat{\phi}(w) = H(w/2)\hat{\phi}(w/2) \tag{5}$$

$$\hat{\psi}^\mu(w) = G^\mu(w/2)\hat{\phi}(w/2), \qquad \mu \in \mathbf{F} \tag{6}$$

For d-dimension orthonormal wavelets, the following necessary conditions are easily obtained.

$$H(0) = 1, \qquad \textstyle\sum_{\tau\in\mathbf{E}} |H(\pi\tau + w)|^2 = 1 \tag{7}$$

$$\begin{array}{l} \textstyle\sum_{\tau\in\mathbf{E}} H(\pi\tau + w)\overline{G^\mu(\pi\tau + w)} = 0 \\ \textstyle\sum_{\tau\in\mathbf{E}} G^\nu(\pi\tau + w)\overline{G^\mu(\pi\tau + w)} = \delta_{\nu,\mu},\ \nu, \mu \in \mathbf{F} \end{array} \tag{8}$$

When the scaling filter symbol $H(w)$ satisfies the formula (7), we call that $H(w)$ is orthonormal. The key of construction of orthonormal wavelets is to solve $H(w)$ and $G^\mu, \mu \in \mathbf{F}$, satisfying (7) and (8).

If the wavelets provides trigonometric vanishing moments, we can easily deduce the following conclusions.

Theorem 3.1. *The wavelet functions $\psi^\mu, \mu \in \mathbf{F}$, have N order trigonometric vanishing moments if only and if* $\hat{\psi}^\mu(k) = 0, |k| < N, k \in \mathbb{Z}^d,\ \mu \in \mathbf{F}$.

Lemma 3.1. *For $\mu \in \mathbf{F}$, let trigonometric polynomial $G^\nu(w)$ be the corresponding refinement filter symbol of the wavelet function ψ^μ. If $G^\nu(w), \nu \in \mathbf{F}$, satisfy*

$$G^\nu(k/2) = 0, |k| < N,\ k \in \mathbb{Z}^d, \nu \in \mathbf{F} \tag{9}$$

then the wavelet functions $\psi^\mu, \mu \in \mathbf{F}$ have N order trigonometric vanishing moments.

From lemma 3.1, a sufficient condition of wavelets with trigonometric vanishing moments is achieved. We need solve $H(w)$ and $G^{\mu}, \mu \in \mathbf{F}$ satisfying (7), (8) and (9) in order to the construction of d-dimension orthonormal wavelets with N order trigonometric vanishing moments. Due to a large of unknown parameters, there are many difficulties in directly solving (7), (8) and (9). Under the condition of (7) and (8), we establish an equivalent condition of (9) which is imposed on the scale symbol $H(w)$ in the following theorem.

Theorem 3.2. *Let trigonometric polynomial functions $H(w)$ and $G^{\nu}(w), \nu \in \mathbf{F}$ satisfy respectively* (7)*, and* (8)*,then* (9) *is equivalent to*

$$E^{k/2}H(\pi\tau) = 0, \tau \in \mathbf{F}, |k| < N, \ k \in \mathbb{Z}^d. \tag{10}$$

We will prove this theorem after the following lemma.

Lemma 3.2. *Let $n \times n$ matrix B satisfy $BB^* = B^*B$. If the elements of the r-th row of B except for the diagonal element are all zeros, then the elements of the r-th column of B except for the diagonal element are also all zeros.*

Proof. Suppose $B = (a_{i,j})_{1\le i,j\le n}$ and $B^* = (b_{i,j})_{1\le i,j\le n}$. Obviously, $b_{i,j} = \overline{a}_{j,i}$. The r-th diagonal element of BB^* is $\sum_{j=1}^{n} a_{r,j}b_{j,r} = \sum_{j=1}^{n} a_{r,j}\overline{a}_{j,r}$, and the element of the r-th diagonal element of B^*B is $\sum_{k=1}^{n} b_{r,k}b_{k,r} = \sum_{k=1}^{n} \overline{a}_{k,r}a_{k,r} = \sum_{k=1}^{n} |a_{k,r}|^2$. For $a_{r,j} = 0, r \neq j$, we have $|a_{r,r}|^2 = \sum_{k=1}^{n} |a_{k,r}|^2$. Then

$$\sum_{k\neq r, 1\le k\le n} |a_{k,r}|^2 = 0 \Longrightarrow a_{k,r} = 0, \qquad k \neq r, 1 \le k \le n.$$

So the conclusion is true. □

For convenience, denote $G^0(w) = H(w)$. Let $2^d \times 2^d$ matrix A be

$$A = [G^{\mu}(w + \tau\pi)]_{\mu,\tau\in\mathbf{E}} \tag{11}$$

where μ and τ are taken strictly according to the order of the elements of E, the subscript μ and superscript τ show the row change and column change respectively.

Proof of Theorem 3.2. From (7) and (8), $AA^* = I$, where A is defined by (11) and A^* denotes the conjugate transpose of A. So A is a unitary matrix and $A^*A = I$. From lemma 3.2, it is obvious that the theorem 3.2 holds. □

Using the equivalent condition of the theorem 3.2, we can firstly solve the scaling symbol $H(w)$ satisfying (7) and (10), independent of $G^{\nu}(w), \nu \in \mathbf{F}$. Then we can obtain $G^{\nu}(w), \nu \in \mathbf{F}$, satisfying (8) by other method such as matrix extension in [7]. After the computation of the scaling filter symbol $H(w)$ and wavelet filter symbols $G^{\nu}(w), \nu \in \mathbf{F}$, define the compactly supported scaling function ϕ as follows

$$\hat{\phi}(w) = \prod_{j=1}^{\infty} H(2^{-j}w), \qquad w \in \mathbb{R}^d \tag{12}$$

and the corresponding wavelet functions $\psi^\mu, \mu \in \mathbf{F}$, are defined by (6). From lemma 3.1 and theorem 3.2, such wavelet functions $\psi^\mu, \mu \in \mathbf{F}$, have N order trigonometric vanishing moment. Our proposed construction method is practical and flexible.

Additionally, we put forward another equivalent form of (10) for computation easy.

Lemma 3.3. *Let the trigonometric polynomial function* $H(w) = \frac{1}{2^d} \sum\limits_{k \in \mathbb{Z}^d} h_k e^{-iwk}$, $w \in \mathbb{R}^d$, *satisfy* $H(0) = 1$. *Then for* $\mu \in \mathbb{Z}^d$, *the following conditions are equivalent:*
(a) $E^{\mu/2} H(\pi\tau) = 0$, *for all* $\tau \in \mathbf{F}$.
(b) $\sum_{l \in \mathbb{Z}^d} h_{2l+\eta} e^{-i(2l+\eta)\cdot \frac{\mu}{2}} = \sum_{l \in \mathbb{Z}^d} h_{2l} e^{-il\cdot\mu}$, *for all* $\eta \in \mathbf{E}$.

Proof. An element $k \in \mathbb{Z}^d$ can be written uniquely as $2l+\gamma$ with $l \in \mathbb{Z}^d$ and $\gamma \in \mathbf{F}$.

$$E^{\mu/2} H(\pi\tau) = H(\mu/2 + \pi\tau) = \tfrac{1}{2^d} \textstyle\sum_{k \in \mathbb{Z}^d} h_k e^{-ik\pi\tau} e^{-ik\frac{\mu}{2}}$$
$$= \tfrac{1}{2^d} \sum_{\gamma \in \mathbf{E}} \sum_{l \in \mathbb{Z}^d} h_{2l+\gamma} e^{-i2l\pi\tau} e^{-i\pi\tau\gamma} e^{-i(2l+\gamma)\frac{\mu}{2}} = \tfrac{1}{2^d} \sum_{\gamma \in \mathbf{E}} e^{-i\pi\tau\gamma} e^{-i\gamma\frac{\mu}{2}}$$
$$\times \sum_{l \in \mathbb{Z}^d} h_{2l+\gamma} e^{-il\mu}$$

Hence $E^{\mu/2} H(\pi\tau) = \frac{1}{2^d} \sum_{\gamma \in \mathbf{E}} b(\gamma) e^{-i(\pi\tau + \frac{\mu}{2})\gamma}$ where $b(\gamma) = \sum_{l \in \mathbb{Z}^d} h_{2l+\gamma} e^{-il\mu}$.

The condition (a) implies

$$\sum_{\gamma \in \mathbf{E}} b(\gamma) e^{-i(\pi\tau + \frac{\mu}{2})\gamma} = 0, \forall \tau \in \mathbf{F}.$$

Let $\eta \in \mathbf{E}$,then

$$\sum_{\tau \in \mathbf{E}} e^{i\pi\eta\tau} \sum_{\gamma \in \mathbf{E}} b(\gamma) e^{-i(\pi\tau + \frac{\mu}{2})\gamma} = \sum_{\gamma \in \mathbf{E}} b(\gamma) e^{-i\frac{\mu}{2}\gamma} \sum_{\tau \in \mathbf{E}} e^{i\pi(\eta-\gamma)\tau}.$$

Since

$$\sum_{\tau \in \mathbf{E}} e^{i\pi(\eta-\gamma)\tau} = \begin{cases} 2^d, & \eta = \gamma \\ 0, & \eta \neq \gamma \end{cases}$$

Therefore,

$$\sum_{\tau \in \mathbf{E}} e^{i\pi\eta\tau} \sum_{\gamma \in \mathbf{E}} b(\gamma) e^{-i(\pi\tau + \frac{\mu}{2})\gamma} = 2^d b(\eta) e^{-i\frac{\mu}{2}\eta}.$$

On the other hand,

$$\sum_{\tau \in \mathbf{E}} e^{i\pi\eta\tau} \sum_{\gamma \in \mathbf{E}} b(\gamma) e^{-i(\pi\tau + \frac{\mu}{2})\gamma} = \sum_{\gamma \in \mathbf{E}} b(\gamma) e^{-i\frac{\mu}{2}\gamma} + \sum_{\tau \in \mathbf{F}} e^{i\pi\eta\tau} \sum_{\gamma \in \mathbf{E}} b(\gamma) e^{-i(\pi\tau + \frac{\mu}{2})\gamma}$$
$$= \sum_{\gamma \in \mathbf{E}} b(\gamma) e^{-i\frac{\mu}{2}\gamma}$$

So we have

$$2^d b(\eta) e^{-i\frac{\mu}{2}\eta} = \sum_{\gamma \in \mathbf{E}} b(\gamma) e^{-i\frac{\mu}{2}\gamma}, \text{for all } \eta \in \mathbf{E}.$$

Thereby,

$$2^d b(\eta) e^{-i\frac{\mu}{2}\eta} = 2^d b(0) e^{-i\frac{\mu}{2}0} = 2^d b(0).$$

So $\sum_{l \in \mathbb{Z}^d} h_{2l+\eta} e^{-i(2l+\eta)\cdot\frac{\mu}{2}} = \sum_{l \in \mathbb{Z}^d} h_{2l} e^{-il\cdot\mu}, \forall\ \eta \in \mathbf{E}$. $(a) \Longrightarrow (b)$ holds.

Conversely, from the condition (b), we have $b(\eta)e^{-i\frac{\mu}{2}\eta} = b(0), \forall \eta \in \mathbf{E}$. Hence, there exists

$$E^{\mu/2}H(\pi\tau) = H(\mu/2 + \pi\tau) = \frac{1}{2^d}\sum_{\gamma\in\mathbf{E}} b(\gamma)e^{-i(\pi\tau+\frac{\mu}{2})\gamma}$$
$$= \frac{1}{2^d}\sum_{\gamma\in\mathbf{E}} b(0)e^{-i\pi\tau\gamma} = \frac{1}{2^d}b(0)\sum_{\gamma\in\mathbf{E}} e^{-i\pi\tau\gamma} = \frac{1}{2^d}b(0)\sum_{\gamma\in\mathbf{E}}(-1)^{\tau\gamma}$$

In addition,

$$\sum_{\gamma\in\mathbf{E}}(-1)^{\tau\gamma} = \sum_{\gamma\in\mathbf{E}} e^{-i\pi\tau\gamma} = 0, \forall\ \tau \in \mathbf{F}$$

So $E^{\mu/2}H(\pi\tau) = 0, \forall\ \tau \in \mathbf{F}$ holds. □

On the other hand, it is well known that $\sum_{\tau\in\mathbf{E}} |H(\pi\tau + w)|^2 = 1$ equals to $\sum_{l\in\mathbb{Z}^d} h_l h_{l+2m} = 2^d\delta_{m,0}, m \in \mathbb{Z}^d$.

Based on the lemma 3.3 and the above formulation, $H(w)$ can be solved. But (12) is the only possible candidate for the compactly supported scaling function corresponding to the trigonometric polynomial $H(w)$ constructed. Therefore we should check whether ϕ satisfies some basic requirements for a scaling function, which are $\phi \in L^2(\mathbb{R}^d)$ and the orthonormality of the shifts of the scaling function ϕ.

If the trigonometric polynomial $H(w)$ satisfies (7), then the corresponding scaling function $\phi \in L^2(\mathbb{R}^d)$ can be guaranteed. But it is incapable of making sure the orthonormality of $\{\phi(x-k), x \in \mathbb{R}^d, k \in \mathbb{Z}^d\}$. So the orthonormal filter symbol $H(w)$ is not always coming into being the orthonormal scaling function.

The sufficient and necessary condition of orthonormal wavelets is othonormalityof the shifts of the scaling function ϕ. But it need additional conditions imposed on the scale symbol $H(w)$. Before we go into conditions on $H(w)$, which ensure that ϕ is orthonormal, it is interesting to know what the functions $\psi^\mu, \mu \in \mathbf{F}$, defined by (6) would be even if ϕ is not orthonormal.

For the case of 1-dimension, $\psi(x) = \frac{1}{2}\sum_{n\in\mathbb{Z}}(-1)^n\overline{h_{1-n}}\phi(2x-n)$ when $H(w)$ is orthonormal. Even if the shifts $\{\phi(x-k), x \in \mathbb{R}^d, k \in \mathbb{Z}^d\}$ of the scaling function ϕ are not othonormal, $\psi(x)$ at least can constitute a tight frame of $L^2(\mathbb{R})$ in [4]. Through the similar derivation of 1-dimension case, we generalize this conclusion for d-dimension on the condition of $H(w)$ and $G^\mu(w), \mu \in \mathbf{F}$, satisfying (7) and (8).

The frame is provided with practical signification, which can also be used to accomplish series expansion for any function belonging to $L^2(\mathbb{R}^d)$ and the approximation of such expansion is numerical stability. In detail, a little disturbance of the function will only result in a little disturbance of the coefficients and vice versa, which is just the equivalence between the L^2-norm of the function and the l^2-norm of the expanding coefficients. At this point, the frame is consistent with *Riesz* basis and orthonormal basis. But the distinctness among them is that the elements involved in the frame are correlative, which make the information of the expanding coefficients redundant. Nevertheless, in some practical application fields, such redundancy would be beneficial.

Denote

$$\phi_{j,k} = 2^{\frac{jd}{2}}\phi(2^j x - k), \quad \psi^{\mu}_{j,k} = 2^{\frac{jd}{2}}\psi^{\mu}(2^j x - k), j \in \mathbb{Z}, k \in \mathbb{Z}^d, \mu \in \mathbf{F}.$$

Theorem 3.3. *Let trigonometric polynomials $H(w)$ and $G^{\nu}(w), \nu \in \mathbf{F}, w \in \mathbb{R}^d$ satisfy* (7) *and* (8) *respectively, and let ϕ and $\psi^{\mu}, \mu \in \mathbf{F}$ be the compactly supported functions defined by* (12) *and* (6)*. Then for all $f \in L^2(\mathbb{R}^d)$,there exists*

$$\sum_{\mu\in\mathbf{F}}\sum_{j\in\mathbb{Z}}\sum_{k\in\mathbb{Z}^d} |< f, \psi^{\mu}_{j,k} >|^2 = ||f||^2 \tag{13}$$

i.e.$\{\psi^{\mu}_{j,k}, j \in \mathbb{Z}, k \in \mathbb{Z}^d, \mu \in \mathbf{F}\}$ *constitute a tight frame of $L^2(\mathbb{R}^d)$.*

From theorem 3.3, we already have a tight frame of $L^2(\mathbb{R}^d)$ without any extra conditions on $H(w)$ except for satisfying (7) and (10),

Next we will discuss what additional conditions are necessary to make ensure that the scaling function ϕ is orthonormal shifts. W. Lawton [6] gives a sufficient and necessary condition to check whether the refinable function ϕ have orthonormal shifts. Here we use this condition to check the orthonormality of the shifts of our constructed function ϕ.

Let a finite sequence $h = \{h_k\}_{k\in\mathbb{Z}^d}$ supported in $[0, J-1]^d, J > 0$, whose symbol is $H(w)$. Define

$$B = (2^d h^{au}_{2p-q})_{p,q\in[-J+1,J-1]^d} \tag{14}$$

where the sequence h^{au} is called the autocorrelation of the sequence h and defined as follows:

$$h^{au}_k = \sum_{l\in\mathbb{Z}^d} h_{k-l}\overline{h}_{-l}, \qquad k \in \mathbb{Z}^d \tag{15}$$

If $H(0) = 1$, and the refinable function ϕ generated by h belongs to $L^2(\mathbb{R}^d)$, from [6], ϕ is orthonormal if and only if the sequence δ is a unique eigenvector of the matrix B defined by (14) corresponding to the simple eigenvalue 1.

Furthermore, we generalize the matrix extension [7] to d-dimension space. Thus the corresponding wavelets are obtained. The following theorem is easily proved based on the above discuss and the MRA of $L^2(\mathbb{R})$ (see [8]).

Theorem 3.4. *Let trigonometric polynomials $H(w)$ and $G^{\nu}(w), \nu \in \mathbf{F}, w \in \mathbb{R}^d$ satisfy* (7) *and* (8) *respectively,and for nonnegative integer N, $H(w)$ satisfies* (10)*. If the compactly supported function ϕ defined by* (12) *is orthonormal. Then the wavelets $\psi^{\mu}, \mu \in \mathbf{F}$ defined by* (6) *have N order trigonometric vanishing moments and $\{\psi^{\mu}_{j,k}, j \in \mathbb{Z}, k \in \mathbb{Z}^d, \mu \in \mathbf{F}\}$ forms an orthonormal basis of $L^2(\mathbb{R}^d)$.*

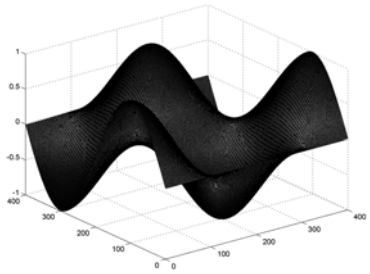

FIGURE 1. The original figure of $sinx_1 sinx_2$

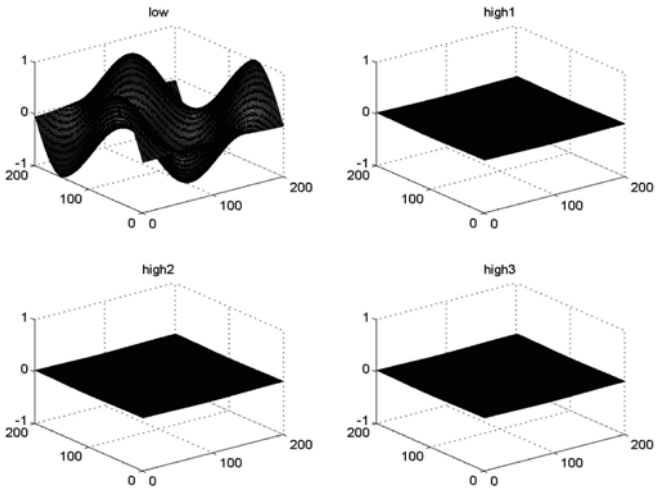

FIGURE 2. The figure of the wavelet decomposition of $f(x) = sinx_1 sinx_2$

4. Numerical Example

Given $N = 2, 3$, we construct bivariate compactly supported non-tensor product orthonormal wavelets with N order trigonometric vanishing moments based on the above algorithm. The corresponding filters that we constructed are listed in Appendix. In the following an numerical example is presented to validate the trigonometric vanishing moment property of the constructed wavelets.

Let $f(x) = f(x_1, x_2) = sinx_1 sinx_2$. First make a discrete process for $f(x)$. Then decompose the discrete $f(x)$ using our constructed wavelets with 3 trigonometric vanishing moments. The original figure of $f(x)$ and the figure of wavelet decomposition are given in figure 1 and figure 2 respectively. From figure 2 it is

clear that the high frequencies of $f(x)$ are almost zeros, which is determined by the order of trigonometric vanishing moments.

5. Acknowledgements

The authors are grateful acknowledge Yu-Jing Guan for his useful discussion. This work is supported by the National Natural Science Foundation of China (60321002).

Appendix

For N=2: the low frequency H is

$$\left[\ A_2, B_2\ \right]$$

where

$$A_2 = \begin{bmatrix} 0.000877068502070000 & -0.00217017555027750 & -0.00160256955152750 \\ -0.00217017551704250 & 0.00446449664686000 & 0.00497124245399000 \\ -0.00160256950883500 & 0.00497124236596250 & 0.00869834985493750 \\ 0.00993380679413000 & -0.0204902519736525 & -0.0328592454723625 \\ 0.0177477598035825 & -0.0390325921033750 & -0.0565521908910750 \\ 0.00925857226745500 & -0.0202053237481550 & -0.0215681033651525 \end{bmatrix}$$

and

$$B_2 = \begin{bmatrix} 0.00993380688379500 & 0.0177477598463825 & 0.00925857221062500 \\ -0.0204902520504250 & -0.0390325922237225 & -0.0202053236719875 \\ -0.0328592454946325 & -0.0565521909327750 & -0.0215681032553600 \\ 0.0990133898600425 & 0.176474322895575 & 0.0750252470885100 \\ 0.176474322829218 & 0.321239655148145 & 0.144993330308675 \\ 0.0750252471651375 & 0.144993330361885 & 0.0778642975881325 \end{bmatrix}$$

the according high frequency filter $G^{(0,1)}$:

$$\left[\ A_2^{(0,1)}, B_2^{(0,1)}\ \right]$$

where

$$A_2^{(0,1)} = \begin{bmatrix} 0 & 0 & 0.00115895898017562 \\ 0 & 0 & -0.00286767156510306 \\ 0.0232400686562530 & 0.0194049573093637 & 0.0197255013320486 \\ -0.0499333461371130 & -0.0415114250914843 & -0.0336810400578003 \\ 0.0331676197772188 & 0.0198257538275190 & 0.00672983173232021 \\ -0.00377744451366267 & 0.00952362785687292 & 0.137759846989406 \\ -0.140867172341056 & -0.00903378390012367 & 0 \\ -0.0980902399371456 & -0.0243986686292091 & 0 \end{bmatrix}$$

and

$$B_2^{(0,1)} = \begin{bmatrix} -0.00286767160901982 & -0.00114093124812466 & 0.0107098277591408 \\ 0.00589938923656547 & 0.00415229141552820 & -0.0221041614680812 \\ 0.0224376140096577 & 0.0362826223006250 & 0.0254207290294945 \\ -0.0611084782654006 & -0.0836749554255576 & -0.0245975332921892 \\ 0.0785772415558306 & -0.0881703240078017 & 0.239523468582971 \\ -0.267440921656210 & 0.108470183105057 & 0.153259078849674 \\ 0 & 0 & 0 \\ 0 & 0 & 0 \end{bmatrix}$$

the according high frequency filter $G^{(1,0)}$:

$$\begin{bmatrix} A_2^{(1,0)}, B_2^{(1,0)} \end{bmatrix}$$

where

$$A_2^{(1,0)} = \begin{bmatrix} -0.00418367167599627 & 0.00274989339942355 & 0.00470186679707548 \\ 0.00860667155090754 & -0.00486498126847825 & -0.00977752356726717 \\ 0.0315305834135352 & -0.0226968594109252 & -0.0413147922667280 \\ -0.0922346339059928 & 0.0698749036239389 & 0.0795775265427353 \\ -0.118050062204540 & 0.0357086820868361 & 0.0242711625840596 \\ -0.0698354941072250 & -0.0429297840800764 & 0.00121370379275128 \\ 0 & 0 & 0 \\ 0 & 0 & 0 \end{bmatrix}$$

where

$$B_2^{(1,0)} = \begin{bmatrix} 0 & 0 & 0.00169081558842072 \\ 0 & 0 & -0.00418367161192572 \\ 0.0214581504037808 & 0.0891485253457010 & 0.125375417747959 \\ -0.0369870231948183 & -0.185992252041450 & -0.268609131522267 \\ 0.0259558227120533 & 0.112208320729640 & 0.217681409922140 \\ -0.0183151193075948 & 0.0516903387289760 & 0.00541826615540679 \\ -0.0191061362661868 & -0.0827098967736900 & 0 \\ 0.00663966282013075 & -0.0332239854720385 & 0 \end{bmatrix}$$

the according high frequency filter $G^{(1,1)}$:

$$\begin{bmatrix} A_2^{(1,1)}, B_2^{(1,1)} \end{bmatrix}$$

where

$$A_2^{(1,1)} = \begin{bmatrix} 0 & 0 & -0.000435000892690504 \\ 0 & 0 & 0.00107634498899520 \\ -0.0133689968687221 & 0.0180659030214254 & 0.0359062140148005 \\ 0.0325728063788420 & -0.0366941425919970 & -0.0842543794721133 \\ -0.0000359525928575965 & 0.0180368366377682 & -0.0155410753412477 \\ -0.0498000453140100 & 0.0266824945690023 & 0.124655750027269 \\ 0.198098462178410 & -0.0532242431472339 & 0 \\ 0.0568425500394516 & -0.0371584022445480 & 0 \end{bmatrix}$$

and

$$B_2^{(1,1)} = \begin{bmatrix} 0.00107634500547880 & 0.00246395592796380 & -0.00905689124923250 \\ -0.00221426265133720 & -0.00659560115914500 & 0.0186588515823477 \\ 0.00152634915830774 & -0.0283531646738812 & -0.0240326834819606 \\ -0.000160425218156222 & 0.0770481698281840 & 0.0164197093731460 \\ 0.139024776016093 & -0.0229278286852003 & -0.246489256613581 \\ -0.224365982484507 & 0.165613926931721 & -0.0791089408851653 \\ 0 & 0 & 0 \\ 0 & 0 & 0 \end{bmatrix}$$

For N=3: the low frequency H is

$$\begin{bmatrix} A_3, B_3 \end{bmatrix}$$

where

$$A_3 = \begin{bmatrix} 0.001050692925 & -0.00137842057500000 & 0.00139268210000000 \\ -0.00137842235000000 & 0.00069228217500000 & -0.00195368947500000 \\ 0.00139268157500000 & -0.00195368792500000 & -0.0000792107125000000 \\ 0.00025638770000000 & 0.00068942635000000 & 0.00246802950000000 \\ -0.00160885055000000 & 0.00324114650000000 & -0.00182845547500000 \\ -0.00227104322500000 & 0.00155689295000000 & 0.00358252100000000 \\ 0.00425046050000000 & -0.00554880800000000 & -0.00681163550000000 \\ 0.00697939625000000 & -0.0109051725000000 & -0.0129694105000000 \\ 0.00313570675000000 & -0.0127158987500000 & 0.00279534200000000 \\ 0.00463437275000000 & -0.0103890985000000 & 0.00434127150000000 \end{bmatrix}$$

$$\begin{bmatrix} 0.000256384350000000 & -0.00160884990000000 \\ 0.000689427600000000 & 0.00324114825000000 \\ 0.00246803027500000 & -0.00182845650000000 \\ 0.000256788825000000 & -0.00459710175000000 \\ -0.00459710275000000 & -0.000462449500000000 \\ -0.0100955242500000 & 0.00456146450000000 \\ 0.0136214717500000 & 0.0135751950000000 \\ 0.0412290350000000 & 0.00137962290000000 \\ 0.0307611950000000 & -0.0111617912500000 \\ 0.0104302502500000 & -0.00607148625000000 \end{bmatrix}$$

and

$$B_3 = \begin{bmatrix} -0.00227104110000000 & 0.00425045850000000 & 0.00697939675000000 \\ 0.00155689372500000 & -0.00554880775000000 & -0.0109051757500000 \\ 0.00358251875000000 & -0.00681163400000000 & -0.0129694082500000 \\ -0.0100955255000000 & 0.0136214702500000 & 0.0412290375000000 \\ 0.00456146675000000 & 0.0135751960000000 & 0.00137962135000000 \\ 0.0298400175000000 & -0.0238858877500000 & -0.0910682975000000 \\ -0.0238858880000000 & -0.0211511487500000 & 0.0155957102500000 \\ -0.0910683000000000 & 0.0155957120000000 & 0.204004107500000 \\ -0.0667274600000000 & 0.00540489375000000 & 0.186497255000000 \\ -0.0149734900000000 & -0.00451472125000000 & 0.0542229025000000 \end{bmatrix}$$

$$\begin{bmatrix} 0.00313570775000000 & 0.00463437175000000 \\ -0.0127158972500000 & -0.0103890972500000 \\ 0.00279534225000000 & 0.00434126950000000 \\ 0.0307611925000000 & 0.0104302515000000 \\ -0.0111617927500000 & -0.00607148425000000 \\ -0.0667274575000000 & -0.0149734922500000 \\ 0.00540489400000000 & -0.00451472050000000 \\ 0.186497252500000 & 0.0542229025000000 \\ 0.252354425000000 & 0.114713485000000 \\ 0.114713485000000 & 0.0738123575000000 \end{bmatrix}$$

the according high frequency filter $G^{(0,1)}$ is:

$$\left[\begin{array}{c} A_3^{(0,1)}, B_3^{(0,1)} \end{array}\right]$$

where

$$A_3^{(0,1)} = \left[\begin{array}{ccc}
0 & 0 & 0.00210840782875476 \\
0 & 0 & -0.00276605695624201 \\
0.0210640847478962 & 0.0239720546536162 & 0.0131150873136822 \\
-0.0464101621157653 & -0.0448324338217457 & -0.0320238453236112 \\
0.0464162170281967 & 0.0342848595744440 & 0.0441620346722871 \\
-0.0148847999076046 & 0.00558033305273670 & -0.0338041163047813 \\
0.00814260818561114 & -0.0467154701828439 & 0.0208972745311624 \\
-0.0122524301445535 & -0.0277486433152704 & 0.00819210561724972 \\
0.00802790788749712 & 0.0559304402919023 & 0.0143104249569804 \\
0.00129227299604935 & 0.0185563991312259 & 0.0114159327303982 \\
-0.206251674975683 & 0.0691297388438068 & 0 \\
-0.193077118358503 & 0.0662377517001263 & 0
\end{array}\right.$$

$$\left.\begin{array}{cc}
-0.00276605339437938 & 0.00510130627173317 \\
0.00138919100219254 & -0.00694654982345029 \\
-0.0106968956519990 & 0.00904161115774829 \\
-0.000441982968770556 & 0.0116405843638888 \\
0.0398536934610097 & -0.0186153897889095 \\
-0.0618297001230756 & -0.000633047687830840 \\
0.0602966585303838 & -0.0184132686843876 \\
0.00453166517810013 & 0.00233666403745157 \\
-0.0376787773122579 & -0.0611862857745323 \\
-0.0846968836587366 & 0.102230930632226 \\
0 & 0 \\
0 & 0
\end{array}\right]$$

and

$$B_3^{(0,1)} = \left[\begin{array}{ccc}
-0.00251162793698928 & -0.00160582481643785 & -0.00211208163645764 \\
0.00290326168142947 & 0.00409726174582719 & 0.00369236672183579 \\
-0.0169691525097504 & 0.00404201086011464 & 0.0274648207425377 \\
0.0257533412886414 & -0.0135314398683656 & -0.0420702015213052 \\
-0.0288626918641360 & -0.0198264224147336 & 0.0136726789155425 \\
0.00196291399059760 & 0.0505422469291780 & 0.0633784737497883 \\
0.0229723914952898 & -0.0159993737401931 & -0.0839929469402634 \\
0.0268533934244109 & -0.000404415328536778 & -0.0428119683006598 \\
-0.00193214541579107 & 0.0519817785838869 & 0.00215710728953622 \\
0.0489520963648001 & -0.127552161343852 & -0.00636118519334368 \\
0 & 0 & 0 \\
0 & 0 & 0
\end{array}\right.$$

$$\left.\begin{array}{cc}
0.00334974713300377 & 0.00833610915872498 \\
-0.00168486130951536 & -0.0192392800184229 \\
0.00146510165211751 & 0.0167474491346390 \\
-0.0273373179241198 & -0.0212388943774148 \\
0.0211677460966716 & 0.0458074455546473 \\
-0.00300918041169930 & -0.0236528277884549 \\
0.00344015453596420 & -0.0107884246449990 \\
-0.0123470593739111 & 0.0147725523291714 \\
-0.0240772304498232 & 0.175450513818964 \\
-0.000017236262707745 1 & 0.164324582631381 \\
0 & 0 \\
0 & 0
\end{array}\right]$$

the according high frequency filter $G^{(1,0)}$:

$$\left[\begin{array}{c} A_3^{(1,0)}, B_3^{(1,0)} \end{array}\right]$$

where

$$A_3^{(1,0)} = \begin{bmatrix} 0 & 0 & 0.00527501632690025 \\ 0 & 0 & -0.00692038580312525 \\ 0.0430562982764235 & 0.0722381944359635 & 0.0453505977199668 \\ -0.0989103424833070 & -0.129100408313870 & -0.110105039768344 \\ 0.0668934862281779 & 0.0987500468818425 & 0.0934888354547117 \\ -0.00588318033685025 & 0.0292508074529420 & -0.000349213984559003 \\ -0.0243240357491118 & -0.181905200127919 & 0.0418438381667381 \\ 0.0430266661144508 & 0.0106705182233941 & -0.0560909736703448 \\ 0.00296329023210645 & 0.0367078054522158 & 0.0961414981891572 \\ 0.0725077035388635 & -0.0459545384210097 & 0.0178594039299865 \\ 0.0301893868652180 & -0.0504379463992989 & 0 \\ 0.0533163698587758 & -0.0400877033020673 & 0 \end{bmatrix}$$

$$\begin{bmatrix} -0.00692037689171673 & 0.0143677147287506 \\ 0.00347561089358910 & -0.0194848799859822 \\ 0.00801511296858635 & 0.0440175780522542 \\ -0.0661907094112600 & -0.0376050794668453 \\ 0.0747452316247861 & 0.00982383934527517 \\ -0.0446881750163803 & 0.0354779660428747 \\ 0.0925469247517093 & -0.114456588994710 \\ -0.0415160281163310 & 0.0227697014669532 \\ -0.0559230352386463 & 0.0607176374983685 \\ 0.0115554018164617 & -0.0396891818500721 \\ 0 & 0 \\ 0 & 0 \end{bmatrix}$$

and

$$B_3^{(1,0)} = \begin{bmatrix} -0.00838916560067383 & 0.00214620015224831 & -0.0101884144998694 \\ 0.00832101688545020 & 0.00197114509328672 & 0.0129506154039823 \\ -0.0195083882136818 & -0.0154883109392574 & -0.00305671986155127 \\ 0.0280373673851783 & 0.0224757608820818 & -0.0000075692304474095 9 \\ 0.00926564511043194 & -0.0591162021033808 & 0.0365382965870718 \\ -0.0214335324120101 & 0.0473008267916477 & -0.0523073283567794 \\ -0.0463560021493588 & 0.0561947145729417 & 0.0253719840027164 \\ 0.0575023135618419 & -0.0290097964681611 & 0.0186544213384738 \\ -0.0281928196286481 & -0.0680297108965943 & 0.0488977765058992 \\ 0.0242942780057384 & 0.0288790436164232 & -0.00434344578020062 \\ 0.0301893868652180 & -0.0504379463992989 & 0 \\ 0 & 0 & 0 \end{bmatrix}$$

$$\begin{bmatrix} 0.00989630705822832 & 0.0201798532694428 \\ -0.00496345833052713 & -0.0440157637577756 \\ -0.0172234277064309 & 0.0245364382262692 \\ 0.0207626529509143 & 0.0155710585771673 \\ -0.0143124664652826 & 0.0140955645965111 \\ -0.0552466436221325 & 0.0348047014923097 \\ 0.0728430848486414 & -0.0816048144015882 \\ -0.0528568157392743 & 0.0141506515007110 \\ 0.0214290414095881 & -0.0663656994848438 \\ -0.00646421647363700 & -0.0292035934395572 \\ 0 & 0 \\ 0 & 0 \end{bmatrix}$$

the according high frequency filter $G^{(1,1)}$:

$$\left[\; A_3^{(1,1)}, B_3^{(1,1)} \; \right]$$

where

$$A_3^{(1,1)} = \begin{bmatrix} 0 & 0 & 0.000117374244555254 \\ 0 & 0 & -0.000153985315937410 \\ 0.0165581192613890 & 0.0192771703500114 & -0.00688264884627795 \\ -0.0250834224646992 & -0.0228401509344430 & -0.00351453831942513 \\ 0.0375587904487678 & 0.0437987753887888 & -0.0284995953515754 \\ -0.0267179685329450 & 0.0330009626043208 & 0.0394850794761708 \\ 0.00109617310856942 & -0.00930279220410017 & 0.0868316949686014 \\ 0.0648440384668865 & -0.00307729660865373 & 0.0468852775112540 \\ -0.108009329679053 & 0.0781799357487619 & -0.0637692840819434 \\ -0.0670890385413101 & -0.0649439483839269 & 0.120268713309136 \\ 0.0891689395944439 & -0.00188578160672728 & 0 \\ 0.0452606821151232 & -0.0489688158222072 & 0 \end{bmatrix}$$

$$\begin{bmatrix} -0.000153985117649902 & 0.00221910132792689 \\ 0.000773357232891733 & -0.00292542095530328 \\ -0.0121652358804233 & 0.0191928042147786 \\ 0.00472002971601547 & -0.00572637127319008 \\ -0.00779304103223451 & 0.0238324075469179 \\ -0.0592245039644389 & -0.0216842582050344 \\ 0.0389316512106280 & 0.0834535265849850 \\ -0.0295526682147306 & -0.0820283152110427 \\ 0.0966001541477489 & -0.0982751213673698 \\ -0.162743091596802 & 0.167760599575571 \\ 0 & 0 \\ 0 & 0 \end{bmatrix}$$

and

$$B_3^{(1,1)} = \begin{bmatrix} -0.00267852730807130 & 0.000707617420121361 & 0.00267403038060246 \\ 0.00143663407655740 & -0.00105069814653051 & 0.000310430245042659 \\ 0.00658053803554283 & 0.00890992585869000 & 0.0346484234976300 \\ -0.0165262691330678 & -0.0434796922709317 & -0.0392359562564319 \\ 0.0183227228402569 & 0.0139265178328942 & 0.0613361594339826 \\ 0.0479171815501325 & -0.00219586602067572 & -0.0735708287261825 \\ -0.0211485776565514 & -0.0576433485215772 & -0.0221614678478543 \\ 0.0464606868315364 & 0.0311295336982669 & -0.0184089302371874 \\ 0.0966108277321110 & -0.0471218886770148 & -0.00615051575903280 \\ -0.0776615355776033 & -0.0342254988622366 & 0.0576556953214200 \\ 0 & 0 & 0 \\ 0 & 0 & 0 \end{bmatrix}$$

$$\begin{bmatrix} -0.00127230194216365 & -0.00919792524374074 \\ 0.00411508193941002 & 0.00317149071267714 \\ -0.00140929351645181 & -0.0374351916890777 \\ -0.0000762170152020060 & -0.00171730766476417 \\ -0.000579469780395569 & -0.0533961102368122 \\ 0.0143176725285066 & 0.102737600816209 \\ 0.0647896358857432 & -0.0655311476616241 \\ 0.0244688620170385 & 0.0214227520262634 \\ 0.00934674967705861 & 0.00549748808290365 \\ -0.0206149532815089 & -0.0464746259449390 \\ 0 & 0 \\ 0 & 0 \end{bmatrix}$$

References

[1] R. Q. Jia, Approximation properties of multivariate wa wavelets, Math. Comp. 67(1998)647-655.

[2] M. Bownik, The construction of r-regular wavelets for arbitrary dilation, J.Fourier Anal. Appl. 7(2001)489-506.

[3] A.S.CavarettaW.Dahmen and C.A.Micchelli, Stationary subdivision, Memoir Amer. Math. Soc.93 (1991), 1-186.

[4] Daubechies, Ten lecture on wavelets, CBMS-Conference Lecture Notes, v.61(1992), SIAM Philadelphia.

[5] Long Ruilin, the wavelet analysis of high dimension,Word books publishing company,1995.

[6] W. Lawton, S.L. Lee, Zuowei Shen,*Convergence of multivariateal cascade algorithm*, Numerische Mathematik, 78 (1998) 3, 427-438.

[7] W. Lawton, S. L. Lee and Z. W. Shen, An algorithm for matrix extension and wavelet construction, Mathematics of Computations, 65, pp.723-737,1996

[8] S.G.Mallat, Multiresolution approximations and wavelet orthogonal bases of $L^2(\mathbb{R})$, Trans. Amer. Math. Society 315, pp. 69-87, 1989.

Ying Li
Department of Computer Science and Technology
State Key Laboratory of Intelligent Technology and Systems
Tsinghua University, Beijing 100084, P.R. China
College of Computer Science and Technology
Jilin University, Changchun 130021, P.R. China.
e-mail: `liyingqh@mail.tsinghua.edu.cn`

Zhi-Dong Deng
Department of Computer Science and Technology
State Key Laboratory of Intelligent Technology and Systems
Tsinghua University, Beijing 100084, P.R. China
e-mail: `michael@tsinghua.edu.cn`

Yan-Chun Liang
College of Computer Science and Technology
Key Laboratory of Symbol Computation and Knowledge Engineering of Ministry of Education
Jilin University, Changchun 130021, P.R. China
e-mail: `ycliang@jlu.edu.cn`

Wavelet Analysis and Applications
Tao Qian, Mang I. Vai and Xu Yuesheng, Eds.
Applied and Numerical Harmonic Analysis, 123–142

Directional Wavelet Analysis with Fourier-Type Bases for Image Processing

Zhen Yao, Nasir Rajpoot and Roland Wilson

Abstract. Motivated by the fact that in natural images, there is usually a presence of local strongly oriented features such as directional textures and linear discontinuities, a representation which is both well-localised in frequency and orientation is desirable to efficiently describe those oriented features. Here we introduce a family of multiscale trigonometric bases for image processing using Fourier-type constructions, namely, the multiscale directional cosine transform and the multiscale Fourier transform. We also show that by seeking an adaptive basis locally, the proposed bases are able to capture both oriented harmonics as well as discontinuities, although the complexity of such adaptiveness varies significantly. We conducted denoising experiments with the proposed bases and the results show great promise of the proposed directional wavelet bases.

Keywords. Directional wavelets, curvelets, Fourier transform, cosine transform, denoising, restoration.

1. Introduction

The application of transforms in image processing is often based on a separable construction. Rows and columns in an image are treated independently and the two-dimensional basis functions are simply tensor products of the corresponding one-dimensional functions. Such method keeps simplicity in terms of design and computation, but is not capable of capturing properly all the interesting features of an image. For example, the orthonormal separable wavelet transform [5] in higher dimensions is seriously limited in its ability to efficiently represent higher dimensional features such as lines. Furthermore, the lack of frequency selectivity remains an elusive problem with most techniques operating in the wavelet domain.

Edges and textures in an image can exist at all possible locations, orientations, and scales. The ability to efficiently analyse and describe directional patterns is thus of fundamental importance for image analysis and image compression. The

idea that biological visual systems might analyse image along dimensions such as orientation, scale and frequency (ie. bandpass) dates back to the work by Hubel and Wiesel [19] in the 1960's. In the computational vision literature, the idea of analysing images along multiple orientations appears at the beginning of the seventies with the Binford-Horn's line-finder [119, 120] and later work by Granlund [121]. Many edge-based image representations have then been elaborated [97, 98] with different edge detection procedures and image approximations using jump models along these edges. To refine these models, multiscale edge representations using wavelet maxima [99] or an edge-adapted multiresolution representation [100] have also been studied. Edge based image representations with complete orthonormal families of foveal wavelets in [101] and footprints [102] have been introduced and studied to reconstruct the main image edge structures. To stabilize the edge detection, global optimization procedures have also been elaborated by Donoho [103], Shukla et al. [104] and Wakin et al. [105]. The optimal configuration of edges is then calculated with an image segmentation over dyadic squares using fast dynamic programming algorithms over quadtrees. Instead of describing the image geometry through edges, which are most often ill-defined, Le Pennec and Mallat later proposed a basis named *"bandelets"* [106] which characterises the image geometry with a geometric flow of vectors. Recently, Peyré and Mallat presented the *second generation bandelets* [122]. The decomposition is computed first by the standard wavelet transform, followed by adaptive geometric orthogonal filters. The compression results are significantly better than wavelet-based coders.

All the approaches previously discussed are *adaptive* representations, in the sense that the bases are adapted to the signal/image contents. Meanwhile, from a different heuristic principle, a number of researchers have been working on developing *fixed* directional representation bases for natural images. The idea of curvelets [64] is to represent a curve as a superposition of functions of various lengths and widths obeying the scaling law $width \approx length^2$. Several different methods were proposed to construct the curvelets. A digital implementation for the curvelet transform, more commonly referred as the *curvelet-99* was used in [88] for noise removal by Starck et al. The transform first decomposes the image into subbands, i.e., separating the object into a series of disjoint scales, using the *algorithme á trous* wavelet transform. Each scale is then analysed by means of a local windowed ridgelet [54] transform. The proposed transform is $16J+1$ times redundant, with J being the number of scales for decomposition. The same authors later proposed a combined approach with curvelets and wavelets in denoising [89]. Such joint sparse representation idea is related to the idea of *Matching Pursuit* (MP) and *Basis Pursuit* (BP) [92], and another application in image deconvolution was presented in [90].

While the redundancy certainly is a advantage in the area of image restoration, it is by no means an ideal transform for compression and other tasks. In order to construct a form of discrete curvelet frame with less redundancy, Do and Vetterli [66, 67] pioneered the *"contourlet"* transform by marrying the Laplacian pyramid and a directional filter bank. Such approach is called *"double filter bank"*

structure. The Laplacian pyramid mainly is used for separating isotropic features into different resolutions, then the directional filter links the point discontinuities into linear structures. This allows contourlets to efficiently approximate a smooth contour at different scales. The double filter bank design certainly allows the contourlet to be flexibly constructed. In [111], Lu and Do developed a critically sampled contourlet transform called *"CRISP-contourlet* using a combined iterated non-separable filter bank for both multiscale and directional decomposition. A non-subsampled contourlet transform was recently proposed [110]. The Laplacian pyramid was substituted with a 2-channel non-subsampled 2D filter bank which is similar to the *á trous* wavelet expansion. However, with J levels of decomposition, it has $J + 1$ redundancy. By contrast, the 2-D *á trous* algorithm by tensor product has $3J + 1$ redundancy. The whole transform has $1 + \sum_{j=1}^{J} 2^{l_j}$, where l_j denotes the number of levels in the transform at the j-th scale. Experimental results suggest that the transform compares favourably to other existing denoising and enhancement methodds reported in literature.

The curvelets can also be conveniently constructed from a frequency tiling approach. Such idea later adopted by Candés and Donoho [65] in constructing *second generation curvelets* which do not require ridgelets. Such tight frame can be computed more efficiently than the previous curvelet-99 implementation. A recent report [8] details its implementation using unequally-spaced fast Fourier transforms (USFFT) and the wrapping of specially selected Fourier samples. Both implmentations are improved in the sense that they are conceptually simpler, faster and far less redundant. The same strategy was used in constructing a 3D curvelet transform [7] whose basis functions are planar patches. These digital implementations can be found in the `CurveLab` distribution.

However, the assumption that natural images are characterised solely by linear edges is not true. Evidently we have seen attempts to separate the image into additive ingredients [3] - usually one is textural and the other is piecewisely smooth. This suggests that there is usually a presence of local strongly oriented harmonics (textures) separated by curvilinear edges. Sparse representations which are both well-localised in frequency and orientation is desirable to efficiently describe such oriented harmonic features. Also, it would be ideal to accommodate both directional linear features as well as directional periodic textures in a unified manner according to the *"image=texture+edge"* model. In this paper, we show that directional wavelet analysis can be performed with directional trigonometric transforms localised in a multiscale framework. We introduce the *Multiscale Directional Cosine Bases* in section 2 which can efficiently represent local oriented harmonics, and with a local directional cosine packet analysis, we can accommodate both directional periodic ridges and ridgelets which is a dual basis to the ridgelet packets. In section 3, we show that directional singularities and harmonics can also be captured by the *Multiresolution Fourier transform* using a Gaussian model of its magnitude spectrum with less computational burden. Next we show some results from our denoising experiments with both transforms and compare

them with other wavelet transforms in section 4. The paper concludes with a summary in section 5.

2. The Multiscale Directional Cosine Transform

Like the 2D orthonormal wavelet transform, the discrete cosine transform (DCT) in 2D is also formed by tensor product, resulting in basis functions which look like "chessboard" patterns. Therefore we need to define a directional cosine operator in order to bring the orientation parameter into the transform. Also, we will need to localise the basis spatially in order to capture local features. This section describes the construction of the Multiscale Directional Cosine Transform (MDCT).

2.1. The Directional Cosine Basis

First we define the parametric space $\Gamma = \{\gamma = (k, \vec{\theta})\}$ where $k \in [0, 2\pi), \vec{\theta} \in \mathbf{S}^{d-1}$, $\vec{\theta}$ is on the unit sphere $\mathbf{S}^{d-1}$ in dimension d which indicates orientation and k indicates the frequency. Consider a family of orthonormal trigonometric basis for $L^2([0,1])$, derived from Fourier transform $\hat{f}(\xi) = \int e^{-ix\xi} f(x)dx$.

1. $\{\sqrt{2}\sin(\frac{2k+1}{2}\pi x)\}$, $k = 0, 1, 2, 3, ...$
2. $\{\sqrt{2}\sin(k\pi x)\}$, $k = 1, 2, 3, ...$
3. $\{\sqrt{2}\cos(\frac{2k+1}{2}\pi x)\}$, $k = 0, 1, 2, 3, ...$
4. $\{1, \sqrt{2}\cos(k\pi x)\}$, $k = 1, 2, 3, ...$

We denote such a trigonometric basis as $c_k(x)$, and the corresponding transform can be written as $\langle f, c_k \rangle$. Now we define the continuous directional trigonometric transform on a multi-variate function $f(\mathbf{x}), \mathbf{x} \in \mathbb{R}^d$:

$$\mathcal{C}_\gamma(\mathbf{x}) = c_k(\vec{\theta} \cdot \mathbf{x}) \tag{1}$$

Since $\langle f, c_k \rangle$ is essentially a Fourier transform, we have the admissibility condition

$$K_\mathcal{C} = \int \frac{|\hat{\mathcal{C}}(\xi)|^2}{|\xi|^d} d\xi < \infty \tag{2}$$

and the reconstruction is

$$f = \int \langle f, \mathcal{C}_\gamma \rangle \mathcal{C}_\gamma \mu(d\gamma) \tag{3}$$

The Parseval relation holds

$$\|f\|_2^2 = \int |\langle f, \mathcal{C}_\gamma \rangle|^2 \mu(d\gamma) \tag{4}$$

For a general image representation, we choose the $c_k = \{1, \sqrt{2}\cos(k\pi x)\}$, known as the cosine II basis, which has faster decay on interval $[0, 1]$ than the Fourier transform. We then have the directional 2D basis

$$\mathcal{C}_{k,\theta} = \lambda_k \cos(\pi k(x\cos\theta + y\sin\theta)) \tag{5}$$

where $\lambda_k = \begin{cases} 1 & \text{if } k = 0 \\ \sqrt{2} & \text{if } x \neq 0. \end{cases}$

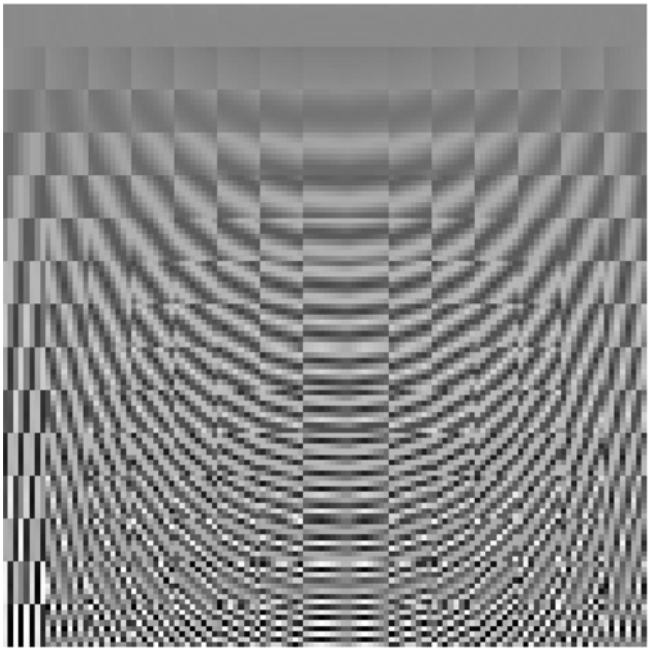

FIGURE 1. The 8×8 directional cosine basis vectors

The directional 2D continuous cosine transform is defined as

$$\begin{aligned} \mathcal{C}f(k,\theta) &= \langle f, \mathcal{C}_{k,\theta} \rangle \\ &= \int_{\mathbb{R}^2} \lambda_k f(x,y) \cos(\pi k(x\cos\theta + y\sin\theta)) dxdy \end{aligned}$$

The directional cosine basis vectors are indexed by frequency k and direction θ, as can be seen in Figure 1. It is obvious that the basis vectors look similar to the Fourier basis despite the fact that the directional cosine transform is real-to-real instead of real-to-complex and its approximation error decays more rapidly than the Fourier counterpart, due to its symmetrical boundary extension.

2.2. Directional Cosine Packets

Smooth local trigonometric bases proposed by Coifman and Meyer [1] and by Malvar [2] use smooth window functions to split the signal and to fold overlapping parts back into the pieces so that the orthogonality is preserved. Therefore, the folded signal is suited for representation by a trigonometric basis. At its simplest, a typical local cosine basis function has the form :

$$\phi_{n,k}(x) = b_n(x)\cos(k + \frac{1}{2})\pi x. \tag{6}$$

where b_n is a smooth window or a *bell function*.

The usefulness of applying smooth local trigonometric bases to focus on local interesting properties of a signal is well studied, and their applications such as MP3 audio compression have been demonstrated to be successful. As we have discussed, image usually consists regions of homogenous textures separated by linear edges and contours. It is then natural to consider applying local cosine basis on Radon projected slices in order to represent both periodic patterns and some linear singularities. In this work, we use the Coifman-Wickerhauser's entropy-based best basis algorithm [45] to look for the best local cosine basis with dyadic interval. The resulting adaptive basis is similar to one possible "*ridgelet packets*" construction mentioned in [32]. We will thereafter refer to such dictionary of bases in the Radon domain as the *"directional cosine packets"*.

2.3. Multiscale Digital Implementation

For an image representation basis to be useful, the basis vectors should be localised both in space and frequency, and they should have certain orientation selectivity. More importantly, to capture patterns of interest at different scales, the basis need to be multiresolution. A prototypical MDC function has the form

$$\psi_{k,\theta,s,\mathbf{t}}(\mathbf{x}) = b\left(\frac{\mathbf{x}-\mathbf{t}}{s}\right)\mathcal{C}_{k,\theta}\left(\frac{\mathbf{x}-\mathbf{t}}{s}\right). \tag{7}$$

where k, θ, $\mathbf{t}$ and s denotes the frequency, orientation, location and scale parameters of the function respectively and $b(\cdot)$ is the smooth bell function chosen along with the sampling interval to ensure invertibility of the discrete form of the transform.

The discrete implementation of MDCT is similar to the digital curvelet-99 construction. While the discrete cosine transform and discrete Radon transform [55] are well studied in the literature, a combination of these two transforms gives us the discrete directional cosine operator. Unlike curvelet-99 which is very redundant, the multiresolution property of the MDC transform is given by the well-known decimated Laplacian pyramid [35]. The discrete MDC of a 2D vector $\mathbf{x}$, at scale s is given by

$$\mathbf{X}_s = \mathcal{C}_n(\mathbf{I} - \mathbf{G}_{s,s+1}\mathbf{G}_{s+1,s})\mathbf{x}_s. \tag{8}$$

where $\mathbf{X}_s$ denotes the transform at scale s, $\mathcal{C}_n$ is the discrete directional cosine transform operator with window size $n \times n$, $\mathbf{I}$ is the identity operator, $\mathbf{x}_s$ is the Gaussian pyramid representation of $\mathbf{x}$ at scale s

$$\mathbf{x}_s = \prod_{l=0}^{s-1} \mathbf{G}_{l+1,l}\mathbf{x}. \tag{9}$$

and $\mathbf{G}_{s,s+1}, \mathbf{G}_{s+1,s}$ are the raising and lowering operators associated with transitions between levels in the Gaussian pyramid. We certainly have the choice of using the directional cosine packets as the transform operator $\mathcal{C}_n$ by substituting the cosine transform by a cosine packet operator ψ_n, forming a semi-adaptive basis. In this way, the MDC packet basis is able to capture a wide range of directional features at different resolutions.

3. The Multiresolution Fourier Transform

The MDCT is similar to the curvelet-99 transform, only the wavelet ridge function is replaced by the cosine basis. With the local cosine analysis on Radon slices, the MDC packet bases fits well to the *" image = edges + textures"* model.

However, the proposed bases have two limitations. The first problem is that best basis for local cosine packets has to be sought on every Radon slice, making the computation extremely expensive. Secondly, the Radon transform is a redundant transform and its inverse introduces some numerical errors. One might note that the Radon transform is directly related to the Fourier transform by the Fourier Slice Theorem, briefly stated as below:

Theorem 1. (Fourier Slice Theorem). *The 1D Fourier transform with respect to t of the projection $Rf(t,\theta)$ is equal to a central slice, at angle θ, of the 2D Fourier transform of the function $f(x,y)$, that is,*

$$\hat{Rf}(t,\theta) = \hat{f}(\xi\cos\theta, \xi\sin\theta). \tag{10}$$

where

$$\hat{f}(\xi_1,\xi_2) = \int\int f(x,y)e^{-2\pi i(x\xi_1+y\xi_2)}dxdy.$$

is the 2D Fourier transform of $f(x,y)$.

Since many discrete Radon transform are implemented via this theorem, it suggests that we may be able to perform such directional analysis using the standard Fourier transform.

3.1. The MFT Implementation

The *Multiresolution Fourier Transform* (MFT) [42, 44] has been proposed as a combination of STFT and wavelet methods, which inherits many of the desired features of both. With the windowing function $g(t)$, the transform of a function $f \in L^2(\mathbb{R})$ at position u frequency ξ and scale s is defined as:

$$Mf(u,\xi,s) = \frac{1}{\sqrt{s}}\int_{-\infty}^{+\infty} f(t)g(s(t-u))e^{-i\xi t}dt. \tag{11}$$

In effect, it is simply a stack of windowed Fourier transforms, in which the scale of the analysis window is varied systematically with the stack index. As a general image analysis tool, it has been applied in feature extraction and segmentation with music and image analysis, such as music note segmentation and extracting boundary curves in a multiresolution fashion [44]. It has also been used in texture synthesis and analysis [17] and many other areas.

The discrete implementation of MFT can take many forms. Similar to the construction of the digital MDCT described before. We build the MFT on top of the Laplacian pyramid, then on each level of the pyramid, windowed Fourier transform is performed with the same window size regardless of the scale. The discrete MFT of a 2D vector $\mathbf{x}$, at scale s is given by

$$\hat{\mathbf{x}}_s = \mathcal{F}_n(\mathbf{I} - \mathbf{G}_{s,s+1}\mathbf{G}_{s+1,s})\mathbf{x}_s. \tag{12}$$

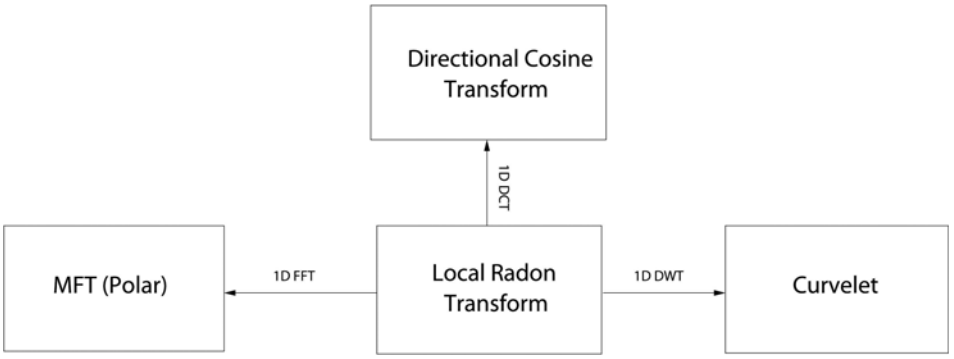

FIGURE 2. The relationships between MFT, Radon, Curvelet and directional cosine basis

where $\mathcal{F}_n$ is the discrete Fourier transform operator with window size $n \times n$. The closeness of the Burt and Adelson filter to a Gaussian function gives the pyramid virtually isotropic behavior, which can be well exploited by the high frequency resolution of the Fourier basis. The whole transform is some 5.33 times redundant if overlapping window is used.

We can see that the only difference between MFT and the MDCT is that the operator used here is just a Fourier transform. In fact, the polar separablity of the Fourier transform suggests that it is also a directional trigonometric transform and Radon transform was implemented via the Fourier-slice theorem by inverse Fourier transform on Fourier polar slices. The relations between MFT, MDCT, Radon and curvelet transform can be illustrated in Figure 2. It is obvious that it requires an inverse Fourier transform and a cosine transform to convert the Fourier domain into the directional cosine domain. Although it has some advantage in approximation convergence, the extra computation is 2 times more than the conventional Fourier transform.

3.2. Gaussian Modelling of Fourier Spectrum

The Fourier basis is a natural representation for directional periodic patterns, although it decays slower than a cosine basis in terms of approximation. In order to perform some sort of *"curvelet"* analysis, we need a model for linear features in the Fourier domain. Fortunately, such model is not difficult to derive, since a line in the spatial domain will be transformed into another line in its Fourier domain perpendicular to its direction.

The magnitude intensity of the local Fourier spectrum can be modelled as a single 2D Gaussian function with its centroid fixed at the origin, which means the Gaussian is zero-mean :

$$G(\mathbf{x}) = \frac{1}{2\pi} \exp\left(\frac{-\mathbf{x}^T C^{-1} \mathbf{x}}{2}\right). \tag{13}$$

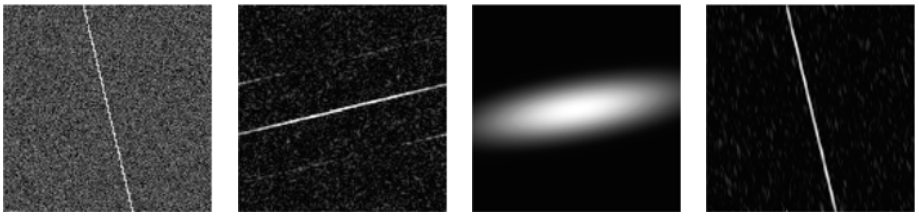

(a) (b) (c) (d)

FIGURE 3. (a) a noisy line, (b) the Fourier transform of the noisy line, (c) The Gaussian filter estimated from inertia tensor, (d) the denoised line.

The covariance matrix C of the Gaussian $G(\cdot)$ can be obtained from the inertia tensor of the spectrum.

$$C = \sum_{\vec{\omega}} |\hat{f}(\vec{\omega})|^2 \vec{\omega}\vec{\omega}^T. \tag{14}$$

where the $\hat{f}(\vec{\omega})$ denotes the Fourier coefficients. With the covariance matrix C, the shape and the orientation of the Gaussian is determined. The centroid of the feature $\mathbf{x}_0$ can then be estimated by taking the pairwise average correlations between neighbouring coefficients in each of the horizontal and vertical directions:

$$\mathbf{x}_0 = \frac{B}{2\pi} \arg\left(\sum_{\vec{\omega}} \hat{f}(\vec{\omega} - 1)\hat{f}(\vec{\omega})^* \right). \tag{15}$$

where B is the windowing size.

The choice of using the Gaussian function is due to several reasons. First, the uncertainty principle states that the Gaussian function can achieve optimal spread in space and frequency, and it is smooth in both domains. Secondly, the shape of the 2D Gaussian function can be both isotropic and anisotropic. When the covariance matrix gives an anisotropic Gaussian distribution, this suggests that the spatial feature is a linear shape. In other cases, the Gaussian blobs will tend to be isotropic. A simple measure of the anisotropy can be obtained by performing the Principal Components Analysis (PCA) on the covariance matrix C, yielding two eignvalues λ_1 and λ_2, where $\lambda_1 \leq \lambda_2$. The measure is simply:

$$\mathcal{A} = \left| \frac{\lambda_1 - \lambda_2}{\lambda_1 + \lambda_2} \right| \tag{16}$$

To test the effectiveness of our model, we use a simple linear feature with Gaussian white noise. The noisy line (see Figure 3.(a)) is transformed into its Fourier domain (see Figure 3.(b)). In order to suppress noise, we can use the $G(\mathbf{x})$ as a frequency filter in the Fourier domain. However, the problem is that the inertia

TABLE 1. The comparative image denoising results in SNR

Image	Noise (dB)	TIWP	Curvelet	MDCT	MDC Packet	MFT
barbara	0	14.75	14.59	14.89	**15.19**	14.80
	5	16.08	15.93	16.42	16.85	**17.10**
	10	18.00	17.64	18.44	18.85	**19.68**
	15	21.12	19.64	20.34	20.71	**22.46**
	20	24.92	21.41	21.88	22.10	**24.65**
lena	0	17.06	17.10	17.24	**17.75**	16.63
	5	18.96	18.82	18.99	**19.63**	19.02
	10	21.08	20.83	21.05	**21.89**	21.60
	15	23.49	23.10	23.35	24.26	**24.43**
	20	26.15	25.35	25.60	26.31	**26.94**
grain	0	12.93	13.06	13.10	**13.22**	12.85
	5	13.81	13.66	13.84	**14.29**	14.01
	10	15.87	15.01	15.51	16.18	**16.30**
	15	18.72	17.28	18.00	18.84	**19.66**
	20	22.02	20.05	20.56	21.38	**22.82**

tensor itself is easily affected by noise. Our solution is to apply thresholding on the noisy transformed data as a stage of pre-processing, in order to suppress the noise energy. The inertia tensor C then can be more reliably estimated from the thresholded data. Therefore, the resulting Gaussian frequency filter is estimated from a thresholded version of Figure 3.(b). The inversion is a clean line image without most of the noise energy. In this way, we have achieved a directional *ridgelet*-like analysis with the Fourier basis, based on the single-feature hypothesis. While the assumption is not realistic for a natural image, such library of wave packets will work well locally in a multiresolution setting. A combination of this model to the MFT allows us to analyse the signal adaptively, so that many features including contours and textures can be captured effectively.

4. Image Denoising Experiments

Good bases for reprensenting images should be able to capture important features of interest, so that the reconstruction requires as few basis functions as possible. The bases' effectiveness can be tested by performing denoising experiments by simple thresholding in the transformed domain. For the MDCT and MDC packet transform, the denoising experiments are performed in such settings:

- The Laplacian pyramid is decomposed at 5 levels of subbands.
- The window size n is chosen at 16×16, modulated with a squared cosine.
- The windows are overlapped by 50%.

The thresholding we use is a form of the universal thresholding proposed in [76], multiplied by an extra constant a, $\Theta = a\sqrt{2\log N}\sigma/1.23^L$, where $N = n^2 = 256$ here and L denotes the level of decomposition, while $L = 0$ corresponds to the highest frequency subband. For directional cosine denoising, $a = 0.08$ was found to give satisfactory result. For the directional local cosine packets, $a = 0.062$ was used. The lowpass subband is left intact.

The settings for the MFT are generally the same as for the MDCT, only with a little sophistication on estimating the filter and $a = 0.8$

1. Within each Fourier transformed block $\hat{B}$, we apply the threshold $8\sqrt{2\log 256}\sigma$ on that to obtain $\hat{B}_T$, from which the inertia tensor C will be estimated.
2. If $\mathcal{A}_C > 0.43$, which means there is a strong directional feature present, the Gaussian filter generated from C will apply on the original noisy spectrum $\hat{B}$ to obtain $\hat{B}_G$, the inverse Fourier transform is taken on $(\hat{B}_G + \hat{B}_T)/2$ as the denoised block.
3. Otherwise, we take the $\hat{B}_T$ as the denoised block.

The Fourier-type transforms are compared with two algorithms. The first is a wavelet-packet based wavelet shrinkage algorithm which is described in [15], called $\mathcal{S}$-Bayes in which the thresholding function is a modified version of the *BayesShrink* [80]. The best wavelet packet basis is sought by using the Shannon entropy function and cycle-spinning [81] is used to suppress the pseudo-Gibbs artifact. Essentially such treatment gives the translation invariance to the wavelet packet basis, which is known to be good in representing periodic signals as well as discontinuities.

The second is a modified version of curvelet. The curvelet-99 implementation reported in [88], which uses a much more redundant overcomplete wavelet frame than our MDCT and MFT, is a "specialised" transform to perform denoising task instead of general-purpose image processing. Therefore, here the local ridgelets are placed on the Laplacian pyramid as in our setting, in order to carry out a fair comparison.

We have conducted experiments on a wide range of natural images. Three of them present some typical characteristics: `barbara` contains some directional and non-directional periodic textures; `lena`, which can be regarded as one of the "curvelet-friendly" image, since it mainly consists of linear discontinuities at different scales; the `grain` image is a texture image which was considered to be very difficult to compress. It contains many directional components, however very irregular.

Table 1 gives denoising results in SNR by those five bases, where the best numbers are stressed in bold. We see that the best results are always among the MDC packet and the MFT, while the MDC packet seems to be more effective in more noisy situations. This is due to the fact that the Gaussian filters are estimated from the noise-sensitive inertia tensor. When the spectrum are dominated by the noise energy, a simple thresholding would fail to preserve the signal information. However, the MFT can be considered as the overall winner: it compares well with

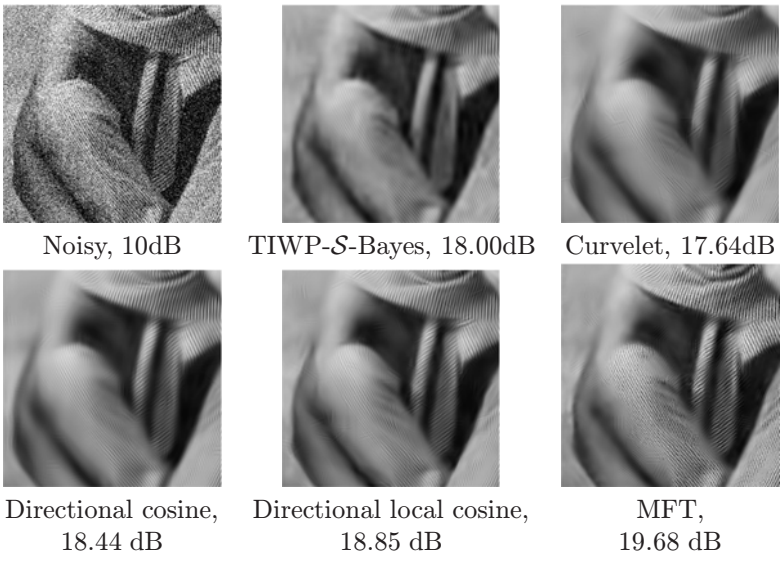

FIGURE 4. Detailed comparative denoising results on `barbara`

other denoising methods and its computational cost is much lower than the rest of the methods. We also notice that TIWP-S-BayesShrink sometimes outperforms at some low noise levels, since the BayesShrink tends to optimise the MSE output. However, the visual qualities of other candidates are more pleasing, preserving important directional features on the image.

A detailed head-to-head comparison is presented in Figure 4 on `barbara`. It is obvious that from the TIWP-$\mathcal{S}$-BayesShrink thresholded image, the diagonal strips are absent on the cloth in the middle, although a few of such patterns can be seen on the trousers. The curvelet is able to recover some of those directional patterns, but incomplete nonetheless. These features are restored almost completely by our proposed methods.

Since the directional cosine packets can be regarded as a generalisation of the curvelets and directional cosine bases, it is not suprising to see it gives better results than these two counterparts. However, it introduces considerable amount of extra computations, since the best basis has to be sought for each of the Radon slices. Also, the inverse Radon transform from incomplete data introduces numerical errors in the reconstruction. Although visually MFT and MDC packet both captured linear and oscillating patterns, MFT's reconstruction is much sharper and outperforms by quite a margin in SNR. On the other hand, the best-basis search ensures that the denoised image from MDC packet is smoother and almost "artifact-free". Considering the visual/statistical performance and the complexity, the MFT with Gaussian filter is the overall winner.

5. Conclusions

In this paper, we have reviewed a growing literature body on directional wavelets' construction, analysis and their applications. The contribution of this paper is to introduce sets of Fourier-type bases which have localisation in space and frequency, orientation selectivity, and employing a multiresolution pyramidal framework allowing analyses of images at different scales.

In a sense, the Fourier-type bases qualify as geometrical wavelets and share a lot of similarities with other directional wavelet bases proposed previously. But the semi-adaptiveness allows us to capture local directional texture patches and linear features at ease and we have shown that by a simple Gaussian frequency filter model of magnitude spectrum intensity, analysis of directional harmonics and linear features can be carried out much more efficiently than any other directional wavelet bases proposed to date. It can be considered as a parametric curvelet representation, or a *generalised directional wavelet packets* and the simple inertia tensor method has demonstrated to be a good substitute for the Cartesian-polar conversion. More importantly, its computational cost is a big advantage, since it does not involve a notion of Radon transform, nor the best-basis search as in some adaptive representations.

The effectiveness of the proposed bases was tested against the state-of-the-art translation-invariant wavelet packet based shrinkage method and the curvelets. The new bases demonstrated a strong potential in the experiments, outperforming the opponents by quite a margin. While producing much visually pleasant output than the wavlet packets with optimal threshold, the MDC bases seems to be able to capture a wider range of directional features than the curvelet, even without the local cosine treatment.

The denoising experiments show the effectiveness of conducting multiresolution analysis with these bases. A wide variation on the theme is possible, for example using variable sized windows on the original image might be another possibility, or to use the *algorithme á trous* subband decomposition for better denoising results. The usage of the Gaussian frequency filter and its parameter estimation in noisy environments are still under investigation. It is our intention to put forward these bases in a general way in this work to popularise their usage in various kinds of image processing tasks.

References

[1] R. Coifman and Y. Meyer, *Remarques sur l'analyse de Fourier à fenêtre* C.R. Acad. Sci. Paris Sér. I Math. (1991), Vol 1, No. 312, 259-261.

[2] H.S. Malvar, *Lapped transforms for efficient transform/subband coding*, IEEE Trans. Acoust. Speech Signal Processing, (1990), vol 38, 969-978

[3] F. Meyer and A. Averbuch and R. Coifman, *Multilayered image representation: Application to image compression*, IEEE Transactions on Image Processing, (2002), vol 11, 1072-1080

[4] D.L. Donoho and M. Duncan, *Digital curvelet transform: Strategy, implementation, and expe riments*, Proceedings of Aerosense, Wavelet Applications VII, SPIE, (2000), pp4056

[5] S. Mallat, *A Theory for Multiresolution Signal Decomposition: The Wavelet Representation*, IEEE Trans. on Pattern Analysis and Machine Intelligence, July, 1989, vol 11, 674-693

[6] A.P. Dempster and N.M. Laird and D.B. Rubin, *Maximum-Likelihood from incomplete data via the EM algorithm*, Journal of Royal Statistic Society Ser. B, (1977), vol 39

[7] L. Ying and L. Demanet and E.J. Candés, *3D Discrete Curvelet Transform*, Proceedings SPIE Wavelet XI, Jul-Aug,2005, vol 5914

[8] E. Candés and L. Demanet and D. Donoho and L. Ying, *Fast Discrete Curvelet Transforms*, California Institute of Technology, July 2005

[9] M. Choi and R.Y. Kim and M.G. Kim, *The Curvelet Transform for Image Fusion*, Proceedings ISPRS Congress, Istanbul, July 2004, 59-64

[10] R. Eslami and H. Radha, *On Low Bit-Rate Coding using the Contourlet TransforOn Low Bit-Rate Coding using the Contourlet Transform*, Proceedings Asilomar Conference on Signals Systems and Computers, Pacific Grove, CA, Nov 2003, 1524-1528

[11] J.M Feng and T. Hsu and J.L. Kuo, *Texture analysis based on affine transform coding*, Proceedings IEEE ICIP, 1999, vol 1, 153-157

[12] A.D. Calway, *Image Representation Based on the Affine Symmetry Group*, Proceedings IEEE ICIP, 1996, 189-192xs

[13] A. Bhalerao and R. Wilson, *Affine Invariant Image Segmentation*, Proceedings British Machine Vision Conference, 2004

[14] I.K. Levy and R. Wilson, *Three-Dimensional Wavelet Transform Video Coding Using Symmetric Codebook Vector Quantization*, IEEE Transactions on Image Processing, March 2001, vol 10, no 3, 470-475

[15] N. Rajpoot and Z. Yao and R. Wilson, *Adaptive Wavelet Restoration of Noisy Video Sequences*, Proceedings IEEE ICIP 2004, Singapore, 2004, to appear

[16] Z. Yao and N. Rajpoot, *Radon/Ridgelet signature for image authentication*, Proceedings IEEE ICIP 2004, Singapore, 2004, to appear

[17] T.I. Hsu and R.G. Wilson, *A Two-Component Model Of Texture For Analysis And Synthesis*, IEEE Transactions on Image Processing, 1998, vol 7, 1466-1476

[18] N. Rajpoot and R. Wilson and Z Yao, *Planelets: A New Analysis Tool for Planar Feature Extraction*, Proceedings 5th International Workshop on Image Analysis for Multimedia Interactive Services (WIAMIS'2004), Lisbon,n Portugal,n April 2004,

[19] D.H. Hubel and T.N. Wiesel, *Receptive fields,n binocular interaction and functional architecture in the cat's visual cortex*, Journal of Physiology, 1962, vol 160, 106-154

[20] I. Daubechies, *Ten lectures on wavelets*, SIAM, 1992, Philadelphia

[21] A. E. Jacquin, *Fractal Image Coding: A Review*, Proceedings of the IEEE, Oct 1993, vol 81, no 10,n 1451-1465

[22] F. Lefebvre and J. Czyz and B. Macq, *A Robust Soft Hash Algorithm for Digital Image Signature*, Proc. of ICIP, Barcelona, Sep 2003,n vol II, 495-498

[23] C.Y. Lin and S.F. Chang, *A Robust Image Authentication Method Distinguishing JPEG Compression from Malicious Manipulation*, IEEE Trans. on Curcuits and Systems for Video Technology, Feb 2001, vol 11,n no 2, 153-168

[24] C.S. Lu and H.Y.M. Liao,n *Structural Digital Signature for Image Authentication: An Incidental Distortion Resistant Scheme*, IEEE Trans. on Multimedia, 2003, vol 5, no 2, 161-173

[25] C. E. Shannon, *Communication theory of secrecy systems*, Bell Syst. Tech. J., Oct 1949, vol 28,n 656-715

[26] M. Schneider and S.F. Chang,n *A Robust Content Based Digital Signature for Image Authentication*, Proc. of ICIP, 1996, vol 3, 227-230

[27] G.L. Friedman, *The Trustworthy Digital Camera: Restoring Credibility to the P hotographic Image*, IEEE Trans. on Consumer Electronics, Nov 1993, vol 39, no 4, 905-910

[28] N.Holliman and N. Memon, *Counterfeiting Attacks on Oblivious Block-wise Independent Invisible Watermarking Schemes*, IEEE Trans. on Image Processing, Mar 2000, vol 9,no 3, 432-441

[29] J. Fridrich and M. Goljan and R. Du, *Lossless data embedding - new paradigm in digital watermarking* , EURASIP Journ. Appl. Sig. Proc., Feb 2002, vol 2002, no 2, 185-196

[30] E.T. Lin and E.J. Delp, *A Review of Fragile Image Watermarks*, Proc. of ACM Multimeida & Security Workshop, Orlando, 1999, 25-29

[31] A. Averbuch and R. Coifman and D. Donoho and M. Israeli and J. Walden, *The pseudopolar FFT and its applications*, University of Yale, YaleU/DCS/RR-1178, 1999

[32] A.G. Flesia and H. Hel-Or and A. Averbuch and E.J. Candés and R.R. Coifman and D.L. Donoho, *Digital Implementation of Ridgelet Packets*, Beyond Wavelets, Academic Press, Sep 2003, 31-60

[33] A. Bhalerao and R. Wilson, *A Fourier Approach to 3D Local Feature Estimation from Volume Data*, Proc. British Machine Vision Conference (BMVC), Sep 2001, vol 2, 461-470

[34] A. Papoulis, *Signal Analysis*, McGraw-Hill, 1984

[35] P.J. Burt and E.H. Adelson, *The Laplacian pyramid as a compact image code*, IEEE Transactions on Communications, 1983, vol 31, 532-540

[36] N.G. Kingsbury, *Image processing with complex wavelets*, Phil. Trans. Royal Society. A, 1999

[37] A. Pizurica and V. Zlokolika and W. Philips, *Combined wavelet domain and temporal video denoising*, Proceedings of IEEE International Conference on Advanced Video and Signal Based Surveillance (AVSS), Jul 2003

[38] P.R. Meulemans, *Hierarchical Image Sequence Analysis and Segmentation*, University of Warwick, United Kingdom, May 2001

[39] P.R. Meulemans and R.G. Wilson, *Image motion analysis using a generalised wavelet transform*, Proceedings IEEE International Conference on image Processing (ICIP), Santa Barbara, US, 1997

[40] I.W. Selesnick and K.Y. Li, *Video denoising using 2D and 3D dual-tree complex wavelet transforms*, Proceedings of SPIE Wavelets X, Aug 2003

[41] D. Gabor, *Theory of communication*, Journal of IEE, 1946, vol 93 429-457

[42] A. Calway, *The Multiresolution Fourier Transform: A General Purpose Tool for Image Analysis*, University of Warwick, 1989

[43] A.R. Davies, *Image feature analysis using the Multiresolution Fourier Transform*, University of Warwick, 1993

[44] R. Wilson and A.D. Calway and E.R.S. Pearson, *A generalized wavelet transform for Fourier analysis: the multiresolution Fourier transform and its application to image and audio signal analysis*, IEEE Trans. on Information Theory, 1992, vol 38, 674-690

[45] R.R. Coifman and M.V. Wickerhauser, *Entropy-based algorithms for best basis selection*, IEEE Trans. on Information Theory, 1992, vol 38, no 2, 713-718

[46] P. Auscher and G. Weiss and M.V. Wickerhauser, *Local sine and Cosine bases of Coifman and Meyer and the Construction of Smooth Wavelets*, Wavelets: A Tutorial in Theory and Applications, Academic Press, San Diego, 1992, 237-256

[47] R.R. Coifman and Y. Meyer, *Orthonormal Wave Packet Bases*, Dept. of Mathematics, Yale University, New Haven, 1990

[48] G. Aharoni and A. Averbuch, R. Coifman and M. Israeli, *Local cosine transform - A method for the reduction of the blocking effect in JPEG*, J. Math. Imag. Vision, 1993, vol 3, 7-38

[49] K. Ramchandran and M. Vetterli, *Best Wavelet packet bases in a rate distortion sense*, IEEE Trans. on Image Processing, Apr 1993, vol 2, no 2, 160-175

[50] F.G. Meyer and A.Z. Averbuch and J-O. Strömberg, *Fast adaptive wavelet packet image compression*, IEEE Trans. on Image Processing, 2000, 792-800

[51] N.M. Rajpoot and R.G. Wilson and F.G. Meyer and R.R. Coifman, *Adaptive Wavelet Packet Basis Selection for Zerotree Image Coding*, IEEE Trans. on Image Processing, Dec 2003, vol 12, no 12, 1460-1472

[52] F.G. Meyer, *Image Compression With Adaptive Local Cosines: A Comparative Study*, IEEE Trans. Image Processing, Jun 2002, vol 11, no 6, 616-629

[53] Minh N. Do and Martin Vetterli, *The Finite Ridgelet Transform for Image Representation*, IEEE Trans. Image Processing, Jan 2003, vol 12, no 1, 16-28

[54] E.J. Candés, *Ridgelets: Theory and applications*, Dept. of Stats, Stanford Univ., Stanford, CA, 1998

[55] A. Averbuch and R. Coifman and D.L. Donoho and M. Israeli, *Fast Slant Stack: A notion of Radon transform for data in a Cartesian grid which is rapidly computible, algebraically exact, geometrically faithful and invertible*, to appear in SIAM Scientific Computing

[56] S.R. Deans, *The Radon Transform and Some of Its Applications*, Wiley, New York, 1983

[57] R.A. Zuidwijk, *Directional and Time-Scale Wavelet Analysis*, SIAM Journal of Mathematical Analysis, 2000, vol 31, no 2, 416-430

[58] R.A. Zuidwijk, *The wavelet X-ray transform*, Centre Math. Computer Sci., 1997, PNA-R9703, ISSN 1386-3711

[59] B.Sahiner and A.E. Yagle, *Iterative inversion of the Radon transform using image adaptive wavelet constraints*, Proceedings of ICIP 98, 1998, vol 2, 709-713

[60] T. Olson and J. DeStefano, *Wavelet localization of the Radon transform*, IEEE Transactions on Signal Processing, 1994, vol 42, no 8, 2055-2067

[61] S. Zhao and G. Welland and G. Wang, *Wavelet sampling and localization schemes for the Radon transform in two dimensions*, SIAM Journal of Applied MAthematics, 1997, vol 57, no 6, 1749-1762

[62] D.L. Donoho, *Ridge Functions and Orthonormal Ridgelets*, Journal of Approximation Theory, Aug 2001, vol 111, no 2, 143-179

[63] D.L. Donoho, *Orthonormal Ridgelets and Linear singularities*, SIAM Journal on Mathematical Analysis, 2000, vol 31, no 5, 1062-1099

[64] E.J. Candés and D.L. Donoho, *Curvelets - a suprisingly effective nonadaptive representation for objects with edges*, Curves and Surfaces, Vanderbilt University Press, Nashville, TN, 2000, 105-120

[65] E.J. Candés and D.L. Donoho, *New tight frames of curvelets and optimal representations of objects with C^2 smooth singularities*, Department of Statistics, Stanford University, 2002, submitted

[66] M.N. Do and M. Vetterli, *Contourlet*, Beyond Wavelets, Academic Press, 2003

[67] M.N. Do and M. Vetterli, *The contourlet transform: an efficient directional multiresolution image representation*, Submitted to IEEE Transactions Image Processing, 2003

[68] S.R. Deans, *The Radon Transform and Some of Its Applications*, Krieger Publishing Company,Revised edition, 1993

[69] G.T. Herman, *Image reconstruction from projections: The Fundamental of Computerized Tomography*, Academic Press, New York, 1980

[70] G. Beylkin, *Discrete Radon transform*, IEEE Transactions on Acoustics and Speech Signal Processing, 1987, vol 35, 162-172

[71] M.L. Brady, *A fast discrete approximation algorithm for the Radon transform*, SIAM Journal of Computing, 1998, vol 27, no 1, 107-119

[72] A. Brandt and J. Mann and M. Brodski and M. Galun, *A fast and accurate Multilevel inversion of the Radon transform*, SIAM journal of Applied Mathematics, 2000, vol 60, no 2, 437-462

[73] W.A. Götze and H.J. Druckmüller, *A fast digital Radon transform - an efficient means for evaluating the Hough transform*, Pattern Recognition, 1995, vol 28, no 12, 1985-1992

[74] F. Matúš and J. Flusser, *Image representation via a finite Radon transform*, IEEE Transactions on Pattern Analysis and Machine Intelligence, Oct 1993, vol 15, no 10, 996-1006

[75] D.L. Donoho, *De-noising by soft-thresholding*, IEEE Transactions on Information Theory, May 1995, vol 41, 613-627

[76] D.L. Donoho and I.M. Johnstone, *Ideal Spatial Adaptation via Wavelet Shrinkage*, Biometrika, 1994, vol 81, 425-455

[77] M. Jansen, *Noise Reduction by Wavelet Thresholding*, Springer-Verlag,2001

[78] C.M. Stein, *Estimation of the mean of a multivariate normal distribution*, Ann. Statist., 1981, vol 9, no 6, 1135-1151

[79] D.L. Donoho and I.M. Johnstone, *Adapting to unknown smoothness via wavelet shrinkage*, Journal of the American Statistical Association, Dec 1995, vol 90, no 432, 1200-1224

[80] S.G. Chang and B. Yu and M. Vetterli, *Adaptive wavelet thresholding for image denoising and compression*, IEEE Transaction on Image Processing, Sep 2000, vol 9, no 9, 1532-1546

[81] R.R. Coifman and D.L. Donoho, *Translation invariant denoising*, Wavelets in Statistics, Springer,New York,1995,125-150

[82] A.G. Bruce and H-Y. Gao and W. Stuetzle, *Subset-selection and ensemble methods for wavelet de-noising*, Statistica Sinica, 1999, vol 9, 167-182

[83] D.B. Percival and A.T. Walden, *Wavelet Methods for Time Series Analysis*, Cambridge University Press,Cambridge, 2000

[84] T.P.Y. Yu and A. Stoschek and D.L. Donoho, *Translation- and direction-invariant denoising of 2D and 3D images: experience and algorithms*, Proceedings of the SPIE, Wavelet Applications in Signal and Image Processing IV, 1996, vol 2825, 608-619

[85] A. Chambolle and B.J. Lucier, *Interpreting translation-invariant wavelet shrinkage as a new image smoothing scale space*, IEEE Transactions on Image Processing, Jul 2001, vol 10, no 7, 993-1000

[86] R. Eslami and H. Radha, *The contourlet transform for image de-noising using cycle spinning*, Proceedings of the 37th Asilomar Conference on Signals, Systems and Computers, Nov 2003, vol 2, 1982-1986

[87] L.R. Varshney, *Despeckling Synthetic Aperture Radar Imagery using the Contourlet Transform*, Applications of Signal Processing (Spring 2004), Apr 2004

[88] J. Starck and E.J. Candés and D.L. Donoho, *The curvelet transform for image denoising*, IEEE Transactions on Image Processing, Jun 2002, vol 11, no 6, 670-684

[89] J. Starck and D.L. Donoho and E.J., *Very high quality image restoration by combining wavelets and curvelets*, Proceedings of SPIE Wavelets: Applications in Signal and Image Processing IX, 2001, vol 4478, 9-19

[90] J. Starck and M.K. Nguyen and F. Murtagh, *Wavelets and curvelets for image deconvolution: a combined approach*, Signal Processing, 2003, vol 83, 2279-2283

[91] P. Carre and D. Helbert and E. Andres, *3-D Fast Ridgelet Transform*, Proceedings IEEE International Conference on Image Processing (ICIP), Sep 2003, vol I, 1021-1024

[92] S. Mallat and Z. Zhang, *Atomic decomposition by basis pursuit*, IEEE Transactions on Signal Processing, 1993, vol 41, no 12, 3397-3415

[93] N.M. Rajpoot, *Local Discriminant Wavelet Packet Basis for Texture Classification,*, Proceedings SPIE Wavelets X, San Diego, California, Aug 2003

[94] Z. Yao and R. Wilson, *Hybrid 3D Fractal Coding with Neighbourhood Vector Quantisation*, EURASIP Journal on Applied Signal Processing, Special Issue on Nonlinear Signal and Image Processing, Part II, Nov 2004, vol 2004, no 16, 2571-2579

[95] Z. Yao and N. Rajpoot, *Image Denoising Using Multiscale Directional Cosine Bases*, Proceedings IEEE ICIP 2005, Genova, Italy, Sep 2005

[96] S. Carlsson, *Sketch based coding of gray level images*, IEEE Transactions on Image Processing, Jan 1988, vol 15, no 1, 57-83

[97] J. Elder, *Are edges imcomplete?*, International Journal Computer Vision, 1999, vol 34, no 2/3, 97-122

[98] X. Xue and X. Wu, *Image compression based on multi-scale edge compensation*, Proceedings IEEE ICIP, 1999, vol 3, 560-564

[99] S. Mallat and S.S. Zhong, *Wavelet transform maxima and multiscale edges*, Wavelets and their applications,Jones and Bartlett,1992

[100] A. Cohen and B. Matei, *Nonlinear subdivisions schemes: Applications to image processing*, Tutorial on Multiresolution in Geometric Modelling, Springer, New York, 2002

[101] E. Le Pennec and S. Mallat, *Image compression with geometrical wavelets*, presented at IEEE ICIP, Vancouver, BC, Canada, Sep 2000

[102] M. Dragotti and M. Vetterli, *Wavelet footprints: Theory, algorithm and applications*, IEEE Transactions on Signal Processing, May 2003, vol 51, no 5, 1306-1323

[103] D. Donoho, *Wedgelets: Nearly-minimax estimation of edges*, Ann. Stat., 1999, vol 27, 353-382

[104] R. Shukla and P.L. Dragotti and M.N. Do and M. Vetterli, *Rate-distortion optimized tree structured compression algorithms*, IEEE Transactions on Image Processing, to be published

[105] M. Wakin and J. Romberg and H. Choi and R. Baraniuk, *Rate-distortion optimized image compression using wedgelets*, Proceedings IEEE ICIP, 2002, vol 3, 237-240

[106] E. Le Pennec and S. Mallat, *Sparse Geometric Image Representations with Bandelets*, IEEE Transactions on Image Processing, Apr 2005, vol 14, no 4,423-438

[107] D. Wang and L. Zhang and A. Vincent and F. Speranza, *Curved Wavelet Transform for Image Coding*, Technical Report, Moving Picture Experts Group, Nov 2004

[108] P. Campisi and D. Kundur and A. Neri, *Robust Digital Watermarking in the ridgelet domain*, IEEE Signal Processing Letters, Oct 2004,vol 11, no 10, 826-830

[109] H. Le Borgne and N. O'Connor, *Ridgelet-based signatures for natural image classification*, Proceedings 2nd Conference on Information Retrieval and Its Applications, Grenoble, France, 2005

[110] A.L. Cunha and J. Zhou and M.N. Do, *The Nonsubsampled Contourlet Transform:Theory, Design and Applications*, IEEE Transactions on Image Processing, 2005, submitted

[111] Y. Lu and M.N. Do, *CRISP-contourlet: a critically sampled directional multiresolution image representation*, Proceedings SPIE conference on Wavelet Applications in Signal and Image Processing,San Diego,Aug 2003

[112] R. Eslami and H. Radha, *Wavelet-based Contourlet Packet Image Coding*, Proceedings Conference on Information Science and Systems, The Johns Hopkins University, Mar 2005

[113] R. Eslami and H. Radha, *Wavelet-based Contourlet Transform and Its Application to Image Coding*, Proceedings IEEE ICIP,Singapore,Oct 2004

[114] D.D. Po and M.N. Do, *Directional Multiscale Modeling of Images using the Contourlet Transform*, IEEE Transactions on Image Processing,2003

[115] F.G. Meyer and R.R. Coifman, *Brushlets: Steerable Wavelet Packets*, Beyond Wavelets,Academic Press Inc.,2001,1-25

[116] F.G. Meyer and R.R. Coifman, *Brushlets: a tool for directional image analysis and image compression*, Applied and Computational Harmonic Analysis, 1997, 147-187

[117] Y. Meyer, *Wavelets and operators*, Cambridge University Press, 1993

[118] H. F. Smith, *A Parametrix Construction for Wave Equantions with $C^{1,1}$ Coefficients*, Ann. Inst. Fourier, Grenoble, 1998, vol 48, no 3, 797-835

[119] T. Binford, *Inferring surfaces from images*, Artificial Intelligence, 1981, vol 17, 205-244

[120] B. Horn, *The Binford-Horn linefinder*, MIT AI Lab, Memo 284, 1971

[121] G.H. Granlund, *In search of a general picture processing operator*, Computer Graphics and Image Processing, 1978, vol 8, 155-173

[122] G. Peyré and S. Mallat, *Discrete Bandelets with Geometric Orthogonal Filters*, Proceedings IEEE ICIP, Genova, Italy, 2005, submitted

[123] A.D. Calway and R. Wilson, *Curve extraction in Images Using a multiresolution framework*, CVGIP: Image Understanding, May 1994, vol 59, no 3, 349-366

[124] C.T. Li, *Multiresolution Image Segmentation Integrating Gibbs Sampler and Region Merging Algorithm*, Signal Processing, 2003, vol 83, no 1, 609-620

Zhen Yao
Department of Computer Science
University of Warwick, CV4 7AL
United Kingdom
e-mail: yao@dcs.warwick.ac.uk

Nasir Rajpoot
Department of Computer Science
University of Warwick, CV4 7AL
United Kingdom
e-mail: nasir@dcs.warwick.ac.uk

Roland Wilson
Department of Computer Science
University of Warwick, CV4 7AL
United Kingdom
e-mail: rgw@dcs.warwick.ac.uk

Wavelet Analysis and Applications
Tao Qian, Mang I. Vai and Xu Yuesheng, Eds.
Applied and Numerical Harmonic Analysis, 143–171

Unitary Systems and Wavelet Sets

David R. Larson

Abstract. A wavelet is a special case of a vector in a separable Hilbert space that generates a basis under the action of a system of unitary operators defined in terms of translation and dilation operations. We will describe an operator-interpolation approach to wavelet theory using the local commutant of a unitary system. This is an application of the theory of operator algebras to wavelet theory. The concrete applications to wavelet theory include results obtained using specially constructed families of wavelet sets. The main section of this paper is section 5, in which we introduce the interpolation map σ induced by a pair of wavelet sets, and give an exposition of its properties and its utility in constructing new wavelets from old. The earlier sections build up to this, establishing terminology and giving examples. The main theoretical result is the Coefficient Criterion, which is described in Section 5.2.2, and which gives a matrix valued function criterion specificing precisely when a function with frequency support contained in the union of an interpolation family of wavelet sets is in fact a wavelet. This can be used to derive Meyer's famous class of wavelets using an interpolation pair of Shannon-type wavelet sets as a starting point. Section 5.3 contains a new result on interpolation pairs of wavelet sets: a proof that every pair of sets in the generalized Journe family of wavelet sets is an interpolation pair. We will discuss some results that are due to this speaker and his former and current students. And we finish in section 6 with a discussion of some open problems on wavelets and frame-wavelets.

Mathematics Subject Classification (2000). Primary 46L99; Secondary 42C15, 46H25.

Keywords. Wavelet, wavelet set, unitary system, frame.

1. Introduction

A wavelet is a special case of a vector in a separable Hilbert space that generates a basis under the action of a collection, or "system", of unitary operators defined in

This research was supported by a grant from the NSF.

terms of translation and dilation operations. This approach to wavelet theory goes back, in particular, to earlier work of Goodman, Lee and Tang [10] in the context of multiresolution analysis. We will begin by describing the operator-interpolation approach to wavelet theory using the local commutant of a system that was worked out by the speaker and his collaborators a few years ago. This is really an abstract application of the theory of operator algebras, mainly von Neumann algebras, to wavelet theory. The concrete applications of operator-interpolation to wavelet theory include results obtained using specially constructed families of wavelet sets. In fact X. Dai and the speaker had originally developed our theory of wavelet sets [5] specifically to take advantage of their natural and elegant relationships with these wavelet unitary systems. We will also discuss some new results and open questions.

The main idea in *operator-theoretic interpolation* of wavelets (and frames) is that new wavelets can be obtained as linear combinations of known ones using *coefficients* which are *operators* (in fact, *Fourier multipliers*) in a certain class. Both the ideas and the essential computations extend naturally to more general unitary systems and *wandering vectors*. Many of the methods work for more involved systems that are important to applied harmonic analysis, such as Gabor and generalized Gabor systems, and various types of *frame* unitary systems.

1.1. Terminology

The set of all bounded linear operators on a Hilbert space H will be denoted by $B(H)$. A *bilateral shift* U on H is a unitary operator U for which there exists a closed linear subspace $E \subset H$ with the property that the family of subspaces $\{U^n E : n \in \mathbb{Z}\}$ are orthogonal and give a direct-sum decomposition of H. The subspace E is called a *complete wandering subspace* for U, and the *multiplicity* of U is defined to be the dimension of E. The *strong operator topology* on $B(H$ is the topology of pointwise convergence, and the *weak operator topology* is the weakest topology such that the vector functionals $\omega_{x,y}$ on $B(H)$ defined by $A \mapsto \langle Ax, y\rangle$, $A \in B(H)$, $x, y \in H$, are all continuous. An *algebra of operators* is a linear subspace of $B(H)$ which is closed under multiplication. An *operator algebra* is an algebra of operators which is *norm-closed*. A subset $\mathcal{S} \subset B(H)$ is called *selfadjoint* if whenever $A \in \mathcal{S}$ then also $A^* \in \mathcal{S}$. A *C^*-algebra* is a self-adjoint operator algebra. A *von Neumann algebra* is a C^*-algebra which is closed in the weak operator topology. For a unital operator algebra, it is well known that being closed in the weak operator topology is equivalent to being closed in the closed in the strong operator topology. The *commutant* of a set $\mathcal{S}$ of operators in $B(H)$ is the family of all operators in $B(H)$ that *commute* with every operator in $\mathcal{S}$. It is closed under addition and multiplication, so is an algebra. And it is clearly closed in both the weak operator topology and the strong operator topology. We use the standard *prime* notation for the commutant. So the commutant of a subset $\mathcal{S} \subset B(H)$ is denoted: $\mathcal{S}' := \{A \in B(H) : AS = SA,\ S \in \mathcal{S}\}$. The commutant of a selfadjoint set of operators is clearly a von Neumann algebra. Moreover, by a famous theorem of Fuglede every operator which commutes with a normal operator N also commutes with its adjoint N^*, and hence the commutant of any set of *normal* operators is also

a von Neumann algebra. So, of particular relevance to this work, the commutant of any set of *unitary* operators is a von Neumann algebra.

1.1.1. Frames and Operators. A sequence of vectors $\{f_j\}$ in a separable Hilbert space H is a *frame* (or *frame sequence*) if there exist constants $C_1, C_2 > 0$ such that

$$C_1\|f\|_2^2 \leq \sum_j |< f, f_j >|^2 \leq C_2\|f\|_2^2$$

for all $f \in H$. If $C_1 = C_2$ the frame is called *tight*, and if $C_1 = C_2 = 1$, $\{f_j\}$ is called a *P*arseval frame. (The term *normalized tight* has also been used for this (cf [14]). A vector ξ is called a *f*rame vector for a unitary system $\mathcal{U}$ if the set of vectors $\mathcal{U}\xi$ is a frame for H.

A Riesz basis for a Hilbert space is a bounded unconditional basis. Frames sequences are generalizations of Riesz bases. A number of the basic aspects of a geometric, or operator-theoretic, approach to discrete frame theory on Hilbert space arises from the fact that a frame sequence is simply an "inner" direct summand of a Riesz basis. The basic principle is that a Hilbert space frame sequence can be dilated to a Riesz basis for larger Hilbert space. We call this the *Frame Dilation Theorem*. In other words, for a given frame sequence there is a larger Hilbert space and a Riesz basis for the larger space such that the orthogonal projection from the larger space onto the smaller space compresses the Riesz basis to the frame sequence. We proved this at the beginning of [14], and used it to prove the other results [14], and subsequently to prove some applications to Hilbert C*-module theory jointly with M. Frank. We proved it first for Parseval frames, and then for general frames. (We remark that this type of dilation result for frames was also independently known and used independently by several others in different contexts.)

It is interesting to note that the Parseval frame case of the Frame Dilation Theorem can be derived easily from the purely atomic case of a well known theorem of Naimark on projection valued measures. We thank Chandler Davis for pointing this out to us at the Canadian Operator Algebras Symposium in 1999. We (Han and I) basically proved this special case of Naimark's theorem implicitely in the first section of [14] without recognizing it was a special case of Naimark's theorem, and then we proved the appropriate generalization we needed for general (non-tight) frames. Naimark's Dilation Theorem basically states that a suitable positive operator valued measure on a Hilbert space *dilates* to a projection valued measure on a larger Hilbert space. That is, there is a projection valued measure [PVM] on a larger Hilbert space such that the orthogonal projection from the larger space unto the smaller space compresses the [PVM] to the [POVM]. In the discrete (i.e. purely atomic measure) case, it can be interpreted as stating that a suitable sequence of positive operators dilates to a sequence of projections. The dilation theorem for a Parseval frame follows easily from Naimark's Theorem applied to the [POVM] obtained by replacing each vector x_i in the frame sequence with the elementary tensor operator $x_i \otimes x_i$, obtaining the atoms for a [POVM] defined on all subsets of the index set for the frame. The dilation theorem for a general (non-tight) frame

does not seem to follow directly from Naimark's theorem – but it may follow from a generalization of it. We remark that some other generalizations of the frame dilation theorem have been recently worked out, notably by W. Czaja.

1.1.2. Unitary Systems, Wandering Vectors, and Frame Vectors. We define a *unitary system* to be simply a countable collection of unitary operators $\mathcal{U}$ acting on a Hilbert space H which contains the identity operator. The *interesting* unitary systems all have additional structural properties of various types. (For instance, wavelet systems and Gabor systems are both "ordered products" of two abelian groups: the dilation and translation groups in the wavelet case, and the modulation and translation groups in the Gabor case.) We will say that a vector $\psi \in H$ is *wandering* for $\mathcal{U}$ if the set

$$\mathcal{U}\psi := \{U\psi : U \in \mathcal{U}\} \tag{1}$$

is an orthonormal set, and we will call ψ a *complete wandering vector* for $\mathcal{U}$ if $\mathcal{U}\psi$ spans H. This (abstract) point of view can be useful. Write $\mathcal{W}(\mathcal{U})$ for the set of complete wandering vectors for $\mathcal{U}$. Further, a *Riesz vector* for $\mathcal{U}$ is a vector ψ such that $\mathcal{U}\psi$ is a Riesz basis for H (indexed by the elements of $\mathcal{U}$), and a *frame vector* is a vector ψ such that $\mathcal{U}\psi$ is a frame sequence for H (again using $\mathcal{U}$ as its index set), and we adopt similar terminology for Parseval frame vectors and Bessel vectors. We use $\mathcal{R}W(\mathcal{U})$, $\mathcal{F}(\mathcal{U})$, $\mathcal{P}F(\mathcal{U})$, $\mathcal{B}(\mathcal{U})$ to denote, respectively, the sets of Riesz vectors, frame vectors, Parseval frame vectors, and Bessel vectors for $\mathcal{U}$.

One of the main tools in this work is the *local commutant* of a system of unitary operators (see section 3.2). This is a natural generalization of the commutant of the system, and like the commutant it is a linear space of operators which is closed in the weak and the strong operator topologies, but unlike the commutant it is usually not selfadjoint, and is usually not closed under multiplication. It contains the commutant of the system, but can be much larger than the commutant. The local commutant of a wavelet unitary system captures all the information about the wavelet system in an essential way, and this gives the *flavor* of our approach to the subject.

1.1.3. Normalizers. If U is a unitary operator and $\mathcal{A}$ is an operator algebra, then U is said to *normalize* $\mathcal{A}$ if $U^\star \cdot \mathcal{A} \cdot U = \mathcal{A}$. In the most interesting cases of operator-theoretic interpolation: that is, for those cases that yield the strongest structural results, the relevant unitaries in the local commutant of the system normalize the commutant of the system.

1.2. Acknowledgement

This article was written in response to an invitation by the organizers of the 4th International Conference on Wavelet Analysis and its Applications, Macau, China, December 2005 [WAA2005] to be a keynote speaker. We thank the organizers for their kind invitation to present these notes.

2. Wavelets

For simplicity of presentation, much of the work in this article will deal with one-dimensional wavelets, and in particular, the dyadic case. The other cases: non-dyadic wavelets and wavelets in higher dimensions, are at least notationally more complicated.

2.1. One Dimension

A *dyadic orthonormal* wavelet in one dimension is a unit vector $\psi \in L^2(\mathbb{R}, \mu)$, with μ Lebesgue measure, with the property that the set

$$\{2^{\frac{n}{2}}\psi(2^n t - l) : n, l \in \mathbb{Z}\} \tag{2}$$

of all integral translates of ψ followed by dilations by arbitrary integral powers of 2, is an orthonormal basis for $L^2(\mathbb{R}, \mu)$. The term *dyadic* refers to the dilation factor "2". The term *mother wavelet* is also used in the literature for ψ. Then the functions

$$\psi_{n,l} := 2^{\frac{n}{2}}\psi(2^n t - l)$$

are called elements of the wavelet basis generated by the "mother". The functions $\psi_{n,l}$ will not themselves be mother wavelets unless $n = 0$.

Let T and D be the translation (by 1) and dilation (by 2) unitary operators in $B(L^2(\mathbb{R})$ given by $(Tf)(t) = f(t-1)$ and $(Df)(t) = \sqrt{2}f(2t)$. Then

$$2^{\frac{n}{2}}\psi(2^n t - l) = (D^n T^l \psi)(t)$$

for all $n, l \in \mathbb{Z}$. Operator-theoretically, the operators T, D are *bilateral shifts* of *infinite multiplicity*. It is obvious that $L^2([0,1])$, considered as a subspace of $L^2(\mathbb{R})$, is a complete wandering subspace for T, and that $L^2([-2,-1] \cup [1,2])$ is a complete wandering subspace for D.

Let $\mathcal{U}_{D,T}$ be the unitary system defined by

$$\mathcal{U}_{D,T} = \{D^n T^l : n, l \in \mathbb{Z}\} \tag{3}$$

where D and T are the operators defined above. Then ψ is a dyadic orthonormal wavelet if and only if ψ is a complete wandering vector for the unitary system $\mathcal{U}_{D,T}$. This was our original motivation for developing the abstract unitary system theory. Write

$$\mathcal{W}(D,T) := \mathcal{W}(\mathcal{U}_{D,T}) \tag{4}$$

to denote the set of all dyadic orthonormal wavelets in one dimension.

An abstract interpretation is that, since D is a bilateral shift it has (many) complete wandering subspaces, and a wavelet for the system is a vector ψ whose translation space (that is, the closed linear span of $\{T^k : k \in \mathbb{Z}\}$ is a complete wandering subspace for D. Hence ψ must generate an orthonormal basis for the entire Hilbert space under the action of the unitary system.

In one dimension, there are non-dyadic orthonormal wavelets: i.e. wavelets for all possible dilation factors besides 2 (the dyadic case). We said "possible", because the scales $\{0, 1, -1\}$ are excluded as scales because the dilation operators they would introduce are not bilateral shifts. All other real numbers for scales yield wavelet theories. In [5, Example 4.5 (x)] a family of examples is given of

three-interval wavelet sets (and hence wavelets) for all scales $d \geq 2$, and it was noted there that such a family also exists for dilation factors $1 < d \leq 2$. There is some recent (yet unpublished) work that has been done, by REU students and mentors, building on this, classifying finite-interval wavelet sets for all possible real (positive and negative scale factors). I will mention this work, in passing, in my talk.

2.2. N-Dimensions

2.2.1. Expansive Dilations. Let $1 \leq m < \infty$, and let A be an $n \times n$ real matrix which is *expansive* (equivalently, all (complex) eigenvalues have modulus > 1). By a *dilation - A regular-translation orthonormal wavelet* we mean a function $\psi \in L^2(\mathbb{R}^n)$ such that

$$\{|det(A)|^{\frac{n}{2}} \psi(A^n t - (l_1, l_2, ..., l_n)^t) : n, l \in \mathbb{Z}\} \tag{5}$$

where $t = (t_1, ..., t_n)^t$, is an orthonormal basis for $L^2(\mathbb{R}^n; m)$. (Here m is product Lebesgue measure, and the superscript "t" means transpose.)

If $A \in M_n(\mathbb{R})$ is invertible (so in particular if A is expansive), then it is very easy to verify that the operator defined by

$$(D_A f)(t) = |detA|^{\frac{1}{2}} f(At) \tag{6}$$

for $f \in L^2(\mathbb{R}^n)$, $t \in \mathbb{R}^n$, is *unitary.* For $1 \leq i \leq n$, let T_i be the unitary operator determined by translation by 1 in the i^{th} coordinate direction. The set (5) above is then

$$\{D_A^k T_1^{l_1} \cdots T_n^{l_n} \psi : k, l_i \in \mathbb{Z}\} \tag{7}$$

If the dilation matrix A is expansive, but the translations are along some oblique lattice, then there is an invertible real $n \times n$ matrix T such that conjugation with D_T takes the entire wavelet system to a regular-translation expansive-dilation matrix. This is easily worked out, and was shown in detail in [18] in the context of working out a complete theory of unitary equivalence of wavelet systems. Hence the wavelet theories are equivalent.

2.2.2. Non-expansive Dilations. Much work has been accomplished concerning the existence of wavelets for dilation matrices A which are not expansive. Some of the original work was accomplished in the Ph.D. theses of Q. Gu and D. Speegle, when they were together finishing up at Texas A&M. Some significant additional work was accomplished by Speegle and also by others. In [18], with Ionascu and Pearcy we proved that if an *nxn* real invertible matrix A is not similar (in the nxn complex matrices) to a unitary matrix, then the corresponding dilation operator D_A is in fact a bilateral shift of infinite multiplicity. If a dilation matrix were to admit any type of wavelet (or frame-wavelet) theory, then it is well-known that a necessary condition would be that the corresponding dilation operator would have to be a bilateral shift of infinite multiplicity. I am happy to report that in very recent work [23], with E. Schulz, D. Speegle, and K. Taylor, we have succeeded in showing that this minimal condition is in fact sufficient: such a matrix, with regular translation lattice, admits a (perhaps infinite) tuple of functions, which collectively generates a frame-wavelet under the action of this unitary system.

3. More General Unitary Systems

3.1. Some Restrictions

We note that *most* unitary systems $\mathcal{U}$ do not have complete wandering vectors. For $\mathcal{W}(\mathcal{U})$ to be nonempty, the set $\mathcal{U}$ must be very special. It must be *countable* if it acts separably (i.e. on a separable Hilbert space), and it must be *discrete* in the strong operator topology because if $U, V \in \mathcal{U}$ and if x is a wandering vector for $\mathcal{U}$ then

$$\|U - V\| \geq \|Ux - Vx\| = \sqrt{2}$$

Certain other properties are forced on $\mathcal{U}$ by the presence of a wandering vector. (Or indeed, by the nontriviality of any of the sets $\mathcal{W}(\mathcal{U})$, $\mathcal{RW}(\mathcal{U})$, $\mathcal{F}(\mathcal{U})$, $\mathcal{PF}(\mathcal{U})$, $\mathcal{B}(\mathcal{U})$.) One purpose of [5] was to investigate such properties. Indeed, it was a matter of some surprise to us to discover that such a theory is viable even in some considerable generality. For perspective, it is useful to note that while $\mathcal{U}_{D,T}$ has complete wandering vectors, the reversed system

$$\mathcal{U}_{T,D} = \{T^l D^n : n, l \in \mathbb{Z}\}$$

fails to have a complete wandering vector. (A proof of this was given in the introduction to [5].)

3.2. The Local Commutant

3.2.1. A Special Case: The System $\mathcal{U}_{D,T}$. Computational aspects of operator theory can be introduced into the wavelet framework in an elementary way. Here is the way we originally did it: Fix a wavelet ψ and consider the set of all operators $A \in B(L^2(\mathbb{R}))$ which *commute* with the *action* of dilation and translation on ψ. That is, require

$$(A\psi)(2^n t - l) = A(\psi(2^n t - l)) \tag{8}$$

or equivalently

$$D^n T^l A\psi = AD^n T^l \psi \tag{9}$$

for all $n, l \in \mathbb{Z}$. Call this the *local commutant of the wavelet system $\mathcal{U}_{D,T}$ at the vector ψ*. (In our first preliminary writings and talks we called it the *point commutant* of the system.) Formally, the local commutant of the dyadic wavelet system on $L^2(\mathbb{R})$ is:

$$\mathcal{C}_\psi(\mathcal{U}_{D,T}) := \{A \in B(L^2(\mathbb{R})) : (AD^n T^l - D^n T^l A)\psi = 0, \forall n, l \in \mathbb{Z}\} \tag{10}$$

This is a linear subspace of $B(H)$ which is closed in the strong operator topology, and in the weak operator topology, and it clearly contains the *commutant* of $\{D, T\}$.

A motivating example is that if η is any other wavelet, let $V := V_\psi^\eta$ be the unitary (we call it the *interpolation unitary*) that takes the basis $\psi_{n,l}$ to the basis $\eta_{n,l}$. That is, $V\psi_{n,l} = \eta_{n,l}$ for all $n, l \in \mathbb{Z}$. Then $\eta = V\psi$, so $VD^n T^l \psi = D^n T^l V\psi$ hence $V \in \mathcal{C}_\psi(\mathcal{U}_{D,T})$.

In the case of a pair of complete wandering vectors ψ, η for a general unitary system $\mathcal{U}$, we will use the same notation V_ψ^η for the unitary that takes the vector $U\psi$ to $U\eta$ for all $U \in \mathcal{U}$.

This simple-minded idea is reversible, so for every unitary V in $\mathcal{C}_\psi(\mathcal{U}_{D,T})$ the vector $V\psi$ is a wavelet. This correspondence between unitaries in $\mathcal{C}_\psi(D,T)$ and dyadic orthonormal wavelets is one-to-one and onto (see Proposition 3.1). This turns out to be useful, because it leads to some new formulas relating to decomposition and factorization results for wavelets, making use of the *linear* and *multiplicative* properties of $\mathcal{C}_\psi(D,T)$.

It turns out (a proof is required) that the entire local commutant of the system $\mathcal{U}_{D,T}$ at a wavelet ψ is *not* closed under multiplication, but it also turns out (also via a proof) that for *most* (and perhaps *all*) wavelets ψ the local commutant at ψ contains many noncommutative operator algebras (in fact von Neumann algebras) as subsets, and their unitary groups *parameterize* norm-arcwise-connected families of wavelets. Moreover, $\mathcal{C}_\psi(D,T)$ is closed under *left multiplication* by the commutant $\{D,T\}'$, which turns out to be an abelian nonatomic von Neumann algebra. The fact that $\mathcal{C}_\psi(D,T)$ is a *left module* under $\{D,T\}'$ leads to a method of obtaining new wavelets from old, and of obtaining connectedness results for wavelets, which we called *operator-theoretic interpolation* of wavelets in [5], (or simply *operator-interpolation*).

3.2.2. General Systems. More generally, let $\mathcal{S} \subset B(H)$ be a set of operators, where H is a separable Hilbert space, and let $x \in H$ be a nonzero vector, and *formally* define the *local commutant* of $\mathcal{S}$ at x by

$$\mathcal{C}_x(\mathcal{S}) := \{A \in B(H) : (AS - SA)x = 0, S \in \mathcal{S}\}$$

As in the wavelet case, this is a weakly and strongly closed linear subspace of $B(H)$ which contains the commutant $\mathcal{S}'$ of $\mathcal{S}$. If x is *cyclic* for $\mathcal{S}$ in the sense that $\text{span}(\mathcal{S}x)$ is dense in H, then x *separates* $\mathcal{C}_x(\mathcal{S})$ in the sense that for $S \in \mathcal{C}_x(\mathcal{S})$, we have $Sx = 0$ iff $x = 0$. Indeed, if $A \in \mathcal{C}_x(\mathcal{S})$ and if $Ax = 0$, then for any $S \in \mathcal{S}$ we have $ASx = SAx = 0$, so $A\mathcal{S}x = 0$, and hence $A = 0$.

If $A \in \mathcal{C}_x(\mathcal{S})$ and $B \in \mathcal{S}'$, let $C = BA$. Then for all $S \in \mathcal{S}$,

$$(CS - SC)x = B(AS)x - (SB)Ax = B(SA)x - (BS)Ax = 0$$

because $ASx = SAx$ since $A \in \mathcal{C}_x(\mathcal{S})$, and $SB = BS$ since $B \in \mathcal{S}'$. Hence $\mathcal{C}_x(\mathcal{S})$ is closed under left multiplication by operators in $\mathcal{S}'$. That is, $\mathcal{C}_x(\mathcal{S}$ is a *left module* over $\mathcal{S}'$.

It is interesting that, if in addition $\mathcal{S}$ is a multiplicative semigroup, then in fact $\mathcal{C}_x(\mathcal{S})$ is identical with the commutant $\mathcal{S}'$ so in this case the commutant is not a new structure. To see this, suppose $A \in \mathcal{C}_x(\mathcal{S})$. Then for each $S, T \in \mathcal{S}$ we have $ST \in \mathcal{S}$, and so

$$AS(Tx) = (ST)Ax = S(ATx) = (S)Tx$$

So since $T \in \mathcal{S}$ was arbitrary and $\text{span}(\mathcal{S}x) = H$, it follows that $AS = SA$.

Proposition 3.1. *If $\mathcal{U}$ is any unitary system for which $\mathcal{W}(\mathcal{U}) \neq \emptyset$, then for any $\psi \in \mathcal{W}(\mathcal{U})$*

$$\mathcal{W}(\mathcal{U}) = \{U\psi : U \text{ is a unitary operator in } \mathcal{C}_\psi(\mathcal{U})\}$$

and the correspondence $U \to U\psi$ is one-to-one.

Proposition 3.2. *Let $\mathcal{U}$ be a unitary system on a Hilbert space H. If ψ is a complete wandering vector for $\mathcal{U}$, then:*

(i) $\mathcal{RW}(\mathcal{U}) = \{A\psi : A \text{ is an operator in } \mathcal{C}_\psi(\mathcal{U}) \text{ that is invertible in } B(H)\}$;
(ii) $\mathcal{F}(\mathcal{U}) = \{A\psi : A \text{ is an operator in } \mathcal{C}_\psi(\mathcal{U}) \text{ that is surjective}\}$;
(ii) $\mathcal{PF}(\mathcal{U}) = \{A\psi : A \text{ is an operator in } \mathcal{C}_\psi(\mathcal{U}) \text{ that is a co-isometry}\}$;
(ii) $\mathcal{B}(\mathcal{U}) = \{A\psi : A \text{ is an operator in } \mathcal{C}_\psi(\mathcal{U})\}$

3.3. Operator-Theoretic Interpolation

Now suppose $\mathcal{U}$ is a unitary system, such as $\mathcal{U}_{D,T}$, and suppose $\{\psi_1, \psi_2, \ldots, \psi_m\} \subset \mathcal{W}(\mathcal{U})$. (In the case of $\mathcal{U}_{D,T}$, this means that $(\psi_1, \psi_2, \ldots, \psi_n)$ is an n-tuple of wavelets.

Let $(A_1, A_2, \ldots, A_n)$ be an n-tuple of operators in the commutant $\mathcal{U}'$ of $\mathcal{U}$, and let η be the vector

$$\eta := A_1\psi_1 + A_2\psi_2 + \cdots + A_n\psi_n \ .$$

Then

$$\begin{aligned} \eta &= A_1\psi_1 + A_2V_{\psi_1}^{\psi_2}\psi_1 + \ldots A_nV_{\psi_1}^{\psi_n}\psi_1 \\ &= (A_1 + A_2V_{\psi_1}^{\psi_2} + \cdots + A_nV_{\psi_1}^{\psi_n})\psi_1 \ . \end{aligned} \tag{11}$$

We say that η is obtained by *operator interpolation* from $\{\psi_1, \psi_2, \ldots, \psi_m\}$. Since $\mathcal{C}_{\psi_1}(\mathcal{U})$ is a left $\mathcal{U}'$ - module, it follows that the operator

$$A := A_1 + A_2V_{\psi_1}^{\psi_2} + \ldots A_nV_{\psi_1}^{\psi_n} \tag{12}$$

is an element of $\mathcal{C}_{\psi_1}(\mathcal{U})$. Moreover, if B is another element of $\mathcal{C}_{\psi_1}(\mathcal{U})$ such that $\eta = B\psi_1$, then $A - B \in \mathcal{C}_{\psi_1}(\mathcal{U})$ and $(A-B)\psi_1 = 0$. So since ψ_1 separates $\mathcal{C}_{\psi_1}(\mathcal{U})$ it follows that $A = B$. Thus A is the *unique* element of $\mathcal{C}_{\psi_1}(\mathcal{U})$ that takes ψ_1 to η. Let $\mathcal{S}_{\psi_1,\ldots,\psi_n}$ be the family of all finite sums of the form

$$\sum_{i=0}^{n} A_iV_{\psi_1}^{\psi_i} \ .$$

This is the left module of $\mathcal{U}'$ generated by $\{I, V_{\psi_1}^{\psi_2}, \ldots, V_{\psi_1}^{\psi_n}\}$. It is the $\mathcal{U}'$*-linear span* of $\{I, V_{\psi_1}^{\psi_2}, \ldots, V_{\psi_1}^{\psi_n}\}$.

Let

$$\mathcal{M}_{\psi_1,\ldots,\psi_n} := (\mathcal{S}_{\psi_1,\ldots,\psi_n})\psi_1 \tag{13}$$

So

$$\mathcal{M}_{\psi_1,\ldots,\psi_n} \ = \ \left\{ \sum_{i=0}^{n} A_i\psi_i \ : \ A_i \in \mathcal{U}' \right\} \ .$$

We call this the *interpolation space* for $\mathcal{U}$ generated by $(\psi_1, \ldots, \psi_n)$. From the above discussion, it follows that for every vector $\eta \in \mathcal{M}_{\psi_1,\psi_2,\ldots,\psi_n}$ there exists a unique operator $A \in \mathcal{C}_{\psi_1}(\mathcal{U})$ such that $\eta = A\psi_1$, and moreover this A is an element of $\mathcal{S}_{\psi_1,\ldots,\psi_n}$.

3.3.1. Normalizing the Commutant. In certain essential cases (and we are not sure how general this type of case is) one can prove that an interpolation unitary V_ψ^η *normalizes* the commutant $\mathcal{U}'$ of the system in the sense that $V_\eta^\psi \mathcal{U}' V_\psi^\eta = \mathcal{U}'$. (Here, it is easily seen that $(V_\psi^\eta)^* = V_\eta^\psi$.) Write $V := V_\psi^\eta$. If V normalizes $\mathcal{U}'$, then the algebra, before norm closure, generated by $\mathcal{U}'$ and V is the set of all finite sums (trig polynomials) of the form $\sum A_n V^n$, with coefficients $A_n \in \mathcal{U}'$, $n \in \mathbb{Z}$. The closure in the strong operator topology is a von Neumann algebra. Now suppose further that *every power* of V is contained in $\mathcal{C}_\psi(\mathcal{U})$. This occurs only in special cases, yet it occurs frequently enough to yield some general methods. Then since $\mathcal{C}_\psi(\mathcal{U})$ is a SOT-closed linear subspace which is closed under left multiplication by $\mathcal{U}'$, this von Neumann algebra is contained in $\mathcal{C}_\psi(\mathcal{U})$, so its unitary group parameterizes a norm-path-connected subset of $\mathcal{W}(\mathcal{U})$ that contains ψ and η via the correspondence $U \to U\psi$.

In the special case of *wavelets*, this is the basis for the work that Dai and I did in [5, Chapter 5] on operator-theoretic interpolation of wavelets. In fact, we specialized there and *reserved* the term *operator-theoretic interpolation* to refer explicitly to the case when the interpolation unitaries normalize the commutant. In some subsequent work, we *loosened* this restriction yielding our more general definition given in this article, because there are cases of interest in which we weren't able to prove normalization. However, it turns out that if ψ and η are s-elementary wavelets (see section 4.4), then indeed V_ψ^η normalizes $\{D, T\}'$. (See Proposition 5.3.) Moreover, V_ψ^η has a very special form: after conjugating with the Fourier transform, it is a composition operator with a symbol σ that is a natural and very computable measure-preserving transformation of $\mathbb{R}$. In fact, it is precisely this special form for V_ψ^η that allows us to make the computation that it normalizes $\{D, T\}'$. On the other hand, we know of no pair (ψ, η) of wavelets for which V_ψ^η fails to normalize $\{D, T\}'$. The difficulty is simply that in general it is very hard to do the computations. This is stated as Problem 2 in the final section on *Open Problems*.

In the wavelet case $\mathcal{U}_{D,T}$, if $\psi \in \mathcal{W}(D, T)$ then it turns out that $\mathcal{C}_\psi(\mathcal{U}_{D,T})$ is in fact *much larger* than $(\mathcal{U}_{D,T})' = \{D, T\}'$, underscoring the fact that $\mathcal{U}_{D,T}$ is NOT a group. In particular, $\{D, T\}'$ is abelian while $\mathcal{C}_\psi(\mathcal{D}, \mathcal{T})$ is nonabelian for every wavelet ψ. (The proof of these facts are contained in [5].)

3.3.2. Interpolation Pairs of Wandering Vectors. In some cases where a pair ψ, η of vectors in $\mathcal{W}(\mathcal{U})$ are given it turns out that the unitary V in $\mathcal{C}_\psi(\mathcal{U})$ with $V\psi = \eta$ happens to be a *symmetry* (i.e. $V^2 = I$). Such pairs are called *interpolation pairs* of wandering vectors, and in the case where $\mathcal{U}$ is a wavelet system, they are called interpolation pairs of wavelets. Interpolation pairs are more prevalent in the theory, and in particular the wavelet theory, than one might expect. In this case (and in more complex generalizations of this) certain linear combinations of complete wandering vectors are themselves complete wandering vectors – not simply complete Riesz vectors.

Proposition 3.3. *Let $\mathcal{U}$ be a unitary system, let $\psi, \eta \in \mathcal{W}(\mathcal{U})$, and let V be the unique operator in $\mathcal{C}_\psi(\mathcal{U})$ with $V\psi = \eta$. Suppose*

$$V^2 = I.$$

Then

$$\cos\alpha \cdot \psi \, + i \sin\alpha \cdot \eta \in \mathcal{W}(\mathcal{U})$$

for all $0 \leq \alpha \leq 2\pi$.

The above result can be thought of as the *prototype* of our operator-theoretic interpolation results. It is the second most elementary case. (The most elementary case is described in the context of the exposition of Problem 4 in the final section.) More generally, the scalar α in Proposition 3.3 can be replaced with an appropriate *self-adjoint operator* in the commutant of $\mathcal{U}$. In the wavelet case, after conjugating with the Fourier transform, which is a unitary operator, this means that α can be replaced with a wide class of nonnegative dilation-periodic (see definition below) bounded measurable functions on $\mathbb{R}$.

4. Wavelet Sets

Wavelet sets belong to the theory of wavelets via the Fourier Transform. We will do most of this section in a tutorial-style, to make the concepts more accessible to students and colleagues who are not already familiar with them.

4.1. Fourier Transform

We will use the following form of the Fourier–Plancherel transform $\mathcal{F}$ on $\mathcal{H} = L^2(\mathbb{R})$, which is a form that is *normalized* so it is a unitary transformation, a property that is desirable for our treatment.

If $f, g \in L^1(\mathbb{R}) \cap L^2(\mathbb{R})$ then

$$(\mathcal{F}f)(s) := \frac{1}{\sqrt{2\pi}} \int_{\mathbb{R}} e^{-ist} f(t) dt := \hat{f}(s), \tag{14}$$

and

$$(\mathcal{F}^{-1}g)(t) = \frac{1}{\sqrt{2\pi}} \int_{\mathbb{R}} e^{ist} g(s) ds. \tag{15}$$

We have

$$(\mathcal{F}T_\alpha f)(s) = \frac{1}{\sqrt{2\pi}} \int_{\mathbb{R}} e^{-ist} f(t-\alpha) dt = e^{-is\alpha}(\mathcal{F}f)(s).$$

So $\mathcal{F}T_\alpha\mathcal{F}^{-1}g = e^{-is\alpha}g$. For $A \in \mathcal{B}(\mathcal{H})$ let $\hat{A}$ denote $\mathcal{F}A\mathcal{F}^{-1}$. Thus

$$\widehat{T_\alpha} = M_{e^{-i\alpha s}}, \tag{16}$$

where for $h \in L^\infty$ we use M_h to denote the multiplication operator $f \to hf$. Since $\{M_{e^{-i\alpha s}} : \ \alpha \in \mathbb{R}\}$ generates the m.a.s.a. $\mathcal{D}(\mathbb{R}) := \{M_h : \ h \in L^\infty(\mathbb{R})\}$ as a von Neumann algebra, we have

$$\mathcal{F}\mathcal{A}_T\mathcal{F}^{-1} = \mathcal{D}(\mathbb{R}).$$

Similarly,

$$\begin{aligned}(\mathcal{F}D^n f)(s) &= \frac{1}{\sqrt{2\pi}}\int_{\mathbb{R}} e^{-ist}(\sqrt{2})^n f(2^n t)dt \\ &= (\sqrt{2})^{-n}\cdot\frac{1}{\sqrt{2\pi}}\int_{\mathbb{R}} e^{-i2^{-n}st}f(t)dt \\ &= (\sqrt{2})^{-2}(\mathcal{F}f)(2^{2^{-n}}s) = (D^{-n}\mathcal{F}f)(s).\end{aligned}$$

So $\widehat{D}^n = D^{-n} = D^{*n}$. Therefore,

$$\widehat{D} = D^{-1} = D^*. \tag{17}$$

If f is an $L^2(\mathbb{R})$ function, as usual we write $\widehat{f}(s) = (\mathcal{F}(f))(s)$. If $\rho(s)$ is a real-valued function such that $\widehat{f}(s) = e^{i\rho(s)}|\widehat{f}(s)|$, we call $\rho(s)$ the *phase* of f. The phase is well defined *a.e.* modulo 2π-translation.

4.2. The Commutant of $\{D, T\}$

We have $\mathcal{F}\{D,T\}'\mathcal{F}^{-1} = \{\widehat{D},\widehat{T}\}'$. It turns out that $\{\widehat{D},\widehat{T}\}'$ has an elementary characterization in terms of Fourier multipliers:

Theorem 4.1.

$$\{\widehat{D},\widehat{T}\}' = \{M_h\colon\ h\in L^\infty(\mathbb{R})\ \textit{and}\ h(s) = h(2s)\ \textit{a.e.}\}.$$

Proof. Since $\widehat{D} = D^*$ and D is unitary, it is clear that $M_h \in \{\widehat{D},\widehat{T}\}'$ if and only if M_h commutes with D. So let $g \in L^2(\mathbb{R})$ be arbitrary. Then (a.e.) we have

$$\begin{aligned}(M_h Dg)(s) &= h(s)(\sqrt{2}\ g(2s)), \quad \text{and} \\ (DM_h g)(s) &= D(h(s)g(s)) = \sqrt{h}(2s)g(2s).\end{aligned}$$

Since these must be equal a.e. for arbitrary g, we must have $h(s) = h(2s)$ a.e. □

Now let $E = [-2,-1)\cup[1,2)$, and for $n\in\mathbb{Z}$ let $E_n = \{2^n x\colon\ x\in E\}$. Observe that the sets E_n are disjoint and have union $\mathbb{R}\backslash\{0\}$. So if g is any uniformly bounded function on E, then g extends uniquely (a.e.) to a function $\tilde{g}\in L^\infty(\mathbb{R})$ satisfying

$$\tilde{g}(s) = \tilde{g}(2s), \qquad s\in\mathbb{R},$$

by setting

$$\tilde{g}(2^n s) = g(s), \qquad s\in E, n\in\mathbb{Z},$$

and $\tilde{g}(0) = 0$. We have $\|\tilde{g}\|_\infty = \|g\|_\infty$. Conversely, if h is any function satisfying $h(s) = h(2s)$ a.e., then h is uniquely (a.e.) determined by its restriction to E. This 1-1 mapping $g\to M_{\tilde{g}}$ from $L^\infty(E)$ onto $\{\widehat{D},\widehat{T}\}'$ is a $*$-isomorphism.

We will refer to a function h satisfying $h(s) = h(2s)$ a.e. as a 2-*dilation periodic function*. This gives a simple algorithm for computing a large class of wavelets from a given one, by simply modifying the *phase* (see also section 4.7):

$$\begin{aligned} &\textit{Given } \psi,\textit{, let } \widehat{\psi} = \mathcal{F}(\psi)\textit{, choose a real-valued function } h \in L^\infty(E) \\ &\textit{arbitrarily, let } g = \exp(ih)\textit{, extend to a 2-dilation periodic} \\ &\textit{function } \tilde{g} \textit{ as above, and compute } \psi_{\tilde{g}} = \mathcal{F}^{-1}(\tilde{g}\widehat{\psi}). \end{aligned} \tag{18}$$

In the description above, the set E could clearly be replaced with $[-2\pi, -\pi) \cup [\pi, 2\pi)$, or with any other "dyadic" set $[-2a, a) \cup [a, 2a)$ for some $a > 0$.

4.3. The Shannon Wavelet

We now give an account of s-elementary and MSF-wavelets. The two most elementary dyadic orthonormal wavelets are the well-known *Haar wavelet* and *Shannon's wavelet* (also called the Littlewood–Paley wavelet). The Shannon set is the prototype of the class of wavelet sets.

Shannon's wavelet is the $L^2(\mathbb{R})$-function with Fourier transform $\widehat{\psi}_S = \frac{1}{\sqrt{2\pi}}\chi_{E_0}$ where

$$E_0 = [-2\pi, -\pi) \cup [\pi, 2\pi). \tag{19}$$

The argument that $\widehat{\psi}_S$ is a wavelet is in a way even more transparent than for the Haar wavelet. And it has the advantage of generalizing nicely. For a simple argument, start from the fact that the exponents

$$\{e^{i\ell s} \colon\ n \in \mathbb{Z}\}$$

restricted to $[0, 2\pi]$ and normalized by $\frac{1}{\sqrt{2\pi}}$ is an orthonormal basis for $L^2[0, 2\pi]$. Write $E_0 = E_- \cup E_+$ where $E_- = [-2\pi, -\pi)$, $E_+ = [\pi, 2\pi)$. Since $\{E_- + 2\pi, E_+\}$ is a partition of $[0, 2\pi)$ and since the exponentials $e^{i\ell s}$ are invariant under translation by 2π, it follows that

$$\left\{ \frac{e^{i\ell s}}{\sqrt{2\pi}}\Big|_{E_0} \colon\ n \in \mathbb{Z} \right\} \tag{20}$$

is an orthonormal basis for $L^2(E_0)$. Since $\widehat{T} = M_{e^{-is}}$, this set can be written

$$\{\widehat{T}^\ell \widehat{\psi}_s \colon\ \ell \in \mathbb{Z}\}. \tag{21}$$

Next, note that any "dyadic interval" of the form $J = [b, 2b)$, for some $b > 0$ has the property that $\{2^n J \colon\ n \in \mathbb{Z}\}$, is a partition of $(0, \infty)$. Similarly, any set of the form

$$\mathcal{K} = [-2a, -a) \cup [b, 2b) \tag{22}$$

for $a, b > 0$, has the property that

$$\{2^n \mathcal{K} \colon\ n \in \mathbb{Z}\}$$

is a partition of $\mathbb{R}\backslash\{0\}$. It follows that the space $L^2(\mathcal{K})$, considered as a subspace of $L^2(\mathbb{R})$, is a complete wandering subspace for the dilation unitary $(Df)(s) = \sqrt{2}\ f(2s)$. For each $n \in \mathbb{Z}$,

$$D^n(L^2(\mathcal{K})) = L^2(2^{-n}\mathcal{K}). \tag{23}$$

So $\bigoplus_n D^n(L^2(\mathcal{K}))$ is a direct sum decomposition of $L^2(\mathbb{R})$. In particular E_0 has this property. So

$$D^n\left\{\frac{e^{i\ell s}}{\sqrt{2\pi}}\Big|_{E_0}:\ \ell\in\mathbb{Z}\right\}=\left\{\frac{e^{2^n i\ell s}}{\sqrt{2\pi}}\Big|_{2^{-n}E_0}:\ \ell\in\mathbb{Z}\right\} \tag{24}$$

is an orthonormal basis for $L^2(2^{-n}E_0)$ for each n. It follows that

$$\{D^n\widehat{T}^\ell\widehat{\psi}_s:\ n,\ell\in\mathbb{Z}\}$$

is an orthonormal basis for $L^2(\mathbb{R})$. Hence $\{D^nT^\ell\psi_s:\ n,\ell\in\mathbb{Z}\}$ is an orthonormal basis for $L^2(\mathbb{R})$, as required.

For our work, in order to proceed with developing an operator-algebraic theory that had a chance of directly impacting concrete function-theoretic wavelet theory we needed a large supply of examples of wavelets which were elementary enough to work with. First, we found another "Shannon-type" wavelet in the literature. This was the Journe wavelet, which we found described on p. 136 in Daubechies book [8]. Its Fourier transform is $\widehat{\psi}_J=\frac{1}{\sqrt{2\pi}}\chi_{E_J}$, where

$$E_J=\left[-\frac{32\pi}{7},-4\pi\right)\cup\left[-\pi,-\frac{4\pi}{7}\right)\cup\left[\frac{4\pi}{7},\pi\right)\cup\left[4\pi,\frac{32\pi}{7}\right).$$

Then, thinking the old adage "where there's smoke there's fire!", we painstakingly worked out many more examples. So far, these are the basic building blocks in the *concrete* part of our theory. By this we mean the part of our theory that has had some type of direct impact on function-theoretic wavelet theory.

4.4. Definition of Wavelet Set

We define a *wavelet set* to be a measurable subset E of $\mathbb{R}$ for which $\frac{1}{\sqrt{2\pi}}\chi_E$ is the Fourier transform of a wavelet. The wavelet $\widehat{\psi}_E:=\frac{1}{\sqrt{2\pi}}\chi_E$ is called *s-elementary* in [5].

It turns out that this class of wavelets was also discovered and systematically explored completely independently, and in about the same time period, by Guido Weiss (Washington University), his colleague and former student E. Hernandez (U. Madrid), and his students X. Fang and X. Wang. Two of the papers of this group are [9] and [17], in which they are called MSF (minimally supported frequency) wavelets. In signal processing, the parameter s, which is the independent variable for $\widehat{\psi}$, is the *frequency* variable, and the variable t, which is the independent variable for ψ, is the *time* variable. It is not hard to show that no function with support a subset of a wavelet set E of strictly smaller measure can be the Fourier transform of a wavelet. (Here, the support of a measurable function is defined to be the set of points at which it does not vanish.) In other words, an MSF wavelet has *minimal* possible support in the frequency domain. However, the problem of whether the support set of any wavelet necessarily contains a wavelet set remains open. It was raised by this author (Larson) in a talk about ten years ago, and has been open for several years. We include it as Problem 3 in the final section of this article. A natural subproblem, which was posed in the same talk, asks whether a

wavelet with minimal possible support in the frequency domain is in fact an MSF wavelet; or equivalently, is its support a wavelet set?

4.4.1. The Spectral Set Condition. From the argument above describing why Shannon's wavelet is, indeed, a wavelet, it is clear that *sufficient* conditions for E to be a wavelet set are

(i) the normalized exponential $\frac{1}{\sqrt{2\pi}}e^{i\ell s}$, $\ell \in \mathbb{Z}$, when restricted to E should constitute an orthonormal basis for $L^2(E)$ (in other words E is a *spectral set* for the integer lattice $\mathbb{Z}$),

and

(ii) The family $\{2^n E\colon\ n \in \mathbb{Z}\}$ of dilates of E by integral powers of 2 should constitute a measurable partition (i.e. a partition modulo null sets) of $\mathbb{R}$.

These conditions are also necessary. In fact if a set E satisfies (i), then for it to be a wavelet set it is obvious that (ii) must be satisfied. To show that (i) must be satisfied by a wavelet set E, consider the vectors

$$\widehat{D}^n \widehat{\psi}_E = \frac{1}{\sqrt{2\pi}} \chi_{2^{-n}E}, \qquad n \in \mathbb{Z}.$$

Since $\widehat{\psi}_E$ is a wavelet these must be orthogonal, and so the sets $\{2^n E\colon\ n \in \mathbb{Z}\}$ must be disjoint modulo null sets. It follows that $\{\frac{1}{\sqrt{2\pi}} e^{i\ell s}|_E\colon\ \ell \in \mathbb{Z}\}$ is not only an orthonormal set of vectors in $L^2(E)$, it must also *span* $L^2(E)$.

It is known from the theory of *spectral sets* (as an elementary special case) that a measurable set E satisfies (i) if and only if it is a generator of a measurable partition of $\mathbb{R}$ under translation by 2π (i.e. iff $\{E + 2\pi n\colon\ n \in \mathbb{Z}\}$ is a measurable partition of $\mathbb{R}$). This result generalizes to spectral sets for the integral lattice in $\mathbb{R}^n$. For this elementary special case a direct proof is not hard.

4.5. Translation and Dilation Congruence

We say that measurable sets E, F are *translation congruent modulo* 2π if there is a measurable bijection $\phi\colon\ E \to F$ such that $\phi(s) - s$ is an integral multiple of 2π for each $s \in E$; or equivalently, if there is a measurable partition $\{E_n\colon\ n \in \mathbb{Z}\}$ of E such that

$$\{E_n + 2n\pi\colon\ n \in \mathbb{Z}\} \tag{25}$$

is a measurable partition of F. Analogously, define measurable sets G and H to be *dilation congruent modulo* 2 if there is a measurable bijection $\tau\colon\ G \to H$ such that for each $s \in G$ there is an integer n, depending on s, such that $\tau(s) = 2^n s$; or equivalently, if there is a measurable partition $\{G_n\}_{-\infty}^{\infty}$ of G such that

$$\{2^n G\}_{-\infty}^{\infty} \tag{26}$$

is a measurable partition of H. (Translation and dilation congruency modulo other positive numbers of course make sense as well.)

The following lemma is useful.

Lemma 4.2. *Let $f \in L^2(\mathbb{R})$, and let $E = \operatorname{supp}(f)$. Then f has the property that*

$$\{e^{ins} f\colon\ n \in \mathbb{Z}\}$$

is an orthonormal basis for $L^2(E)$ if and only if

(i) *E is congruent to $[0, 2\pi)$ modulo 2π, and*
(ii) *$|f(s)| = \frac{1}{\sqrt{2\pi}}$ a.e. on E.*

If E is a measurable set which is 2π-translation congruent to $[0, 2\pi)$, then since

$$\left\{ \frac{e^{i\ell s}}{\sqrt{2\pi}}\Big|_{[0,2\pi)}\colon\ \ell \in \mathbb{Z} \right\}$$

is an orthonormal basis for $L^2[0, 2\pi]$ and the exponentials $e^{i\ell s}$ are 2π-invariant, as in the case of Shannon's wavelet it follows that

$$\left\{ \frac{e^{i\ell s}}{\sqrt{2\pi}}\Big|_{E}\colon\ \ell \in \mathbb{Z} \right\}$$

is an orthonormal basis for $L^2(E)$. Also, if E is 2π-translation congruent to $[0, 2\pi)$, then since

$$\{[0, 2\pi) + 2\pi n\colon\ n \in \mathbb{Z}\}$$

is a measurable partition of $\mathbb{R}$, so is

$$\{E + 2\pi n\colon\ n \in \mathbb{Z}\}.$$

These arguments can be reversed.

We say that a measurable subset $G \subset \mathbb{R}$ is a 2-*dilation generator* of a *partition* of $\mathbb{R}$ if the sets

$$2^n G := \{2^n s\colon\ s \in G\}, \qquad n \in \mathbb{Z} \tag{27}$$

are disjoint and $\mathbb{R} \setminus \cup_n 2^n G$ is a null set. Also, we say that $E \subset \mathbb{R}$ is a 2π-*translation generator of a partition* of $\mathbb{R}$ if the sets

$$E + 2n\pi := \{s + 2n\pi\colon\ s \in E\}, \qquad n \in \mathbb{Z}, \tag{28}$$

are disjoint and $\mathbb{R} \setminus \cup_n (E + 2n\pi)$ is a null set.

Lemma 4.3. *A measurable set $E \subseteq \mathbb{R}$ is a 2π-translation generator of a partition of $\mathbb{R}$ if and only if, modulo a null set, E is translation congruent to $[0, 2\pi)$ modulo 2π. Also, a measurable set $G \subseteq \mathbb{R}$ is a 2-dilation generator of a partition of $\mathbb{R}$ if and only if, modulo a null set, G is a dilation congruent modulo 2 to the set $[-2\pi, -\pi) \cup [\pi, 2\pi)$.*

4.6. A Criterion

The following is a useful criterion for wavelet sets. It was published independently by Dai–Larson in [5] and by Fang–Wang (who were students of Guido Weiss) in [9] at about the same time (in December, 1994). In fact, it is amusing that the two papers had been submitted within two days of each other; only much later did we even learn of each other's work on wavelets and of this incredible timing.

Proposition 4.4. *Let $E \subseteq \mathbb{R}$ be a measurable set. Then E is a wavelet set if and only if E is both a 2-dilation generator of a partition (modulo null sets) of $\mathbb{R}$ and a 2π-translation generator of a partition (modulo null sets) of $\mathbb{R}$. Equivalently, E is a wavelet set if and only if E is both translation congruent to $[0, 2\pi)$ modulo 2π and dilation congruent to $[-2\pi, -\pi) \cup [\pi, 2\pi)$ modulo 2.*

Note that a set is 2π-translation congruent to $[0, 2\pi)$ iff it is 2π-translation congruent to $[-2\pi, \pi) \cup [\pi, 2\pi)$. So the last sentence of Proposition 4.4 can be stated: A measurable set E is a wavelet set if and only if it is both 2π-translation and 2-dilation congruent to the Littlewood–Paley set $[-2\pi, -\pi) \cup [\pi, 2\pi)$.

4.7. Phases

If E is a wavelet set, and if $f(s)$ is any function with support E which has constant modulus $\frac{1}{\sqrt{2\pi}}$ on E, then $\mathcal{F}^{-1}(f)$ is a wavelet. Indeed, by Lemma 4.2 $\{\widehat{T}^{\ell} f\colon \ \in \mathbb{Z}\}$ is an orthonormal basis for $L^2(E)$, and since the sets $2^n E$ partition $\mathbb{R}$, so $L^2(E)$ is a complete wandering subspace for $\widehat{D}$, it follows that $\{\widehat{D}^n \widehat{T}^{\ell} f\colon \ n, \ell \in \mathbb{Z}\}$ must be an orthonormal basis for $L^2(\mathbb{R})$, as required. In [9, 17] the term MSF-wavelet includes this type of wavelet. So MSF-wavelets can have arbitrary phase and s-elementary wavelets have phase 0. If ψ is a wavelet we say [5] that a real-valued function $\rho(s)$ is *attainable* as a phase of ψ if the function $e^{i\rho(s)}|\psi(s)|$ is also the Fourier transform of a wavelet. So *every* phase is *attainable* in this sense for an MSF or s-elementary wavelet. Attainable phases of wavelets have been studied in [5] and [26], in particular.

4.8. Some Examples of One-Dimensional Wavelet Sets

It is usually easy to determine, using the dilation-translation criteria, in Proposition 4.4, whether a given finite union of intervals is a wavelet set. In fact, to verify that a given "candidate" set E is a wavelet set, it is clear from the above discussion and criteria that it suffices to do two things.

1. Show, by appropriate partitioning, that E is 2-dilation-congruent to a set of the form $[-2a, -a) \cup [b, 2b)$ for some $a, b > 0$. and
2. Show, by appropriate partitioning, that E is 2π-translation-congruent to a set of the form $[c, c + 2\pi)$ for some real number c.

On the other hand, wavelet sets suitable for testing hypotheses can be quite difficult to construct. There are very few "recipes" for wavelet sets, as it were. Many families of such sets have been constructed for reasons including perspective, experimentation, testing hypotheses, etc., including perhaps the pure enjoyment of doing the computations − which are somewhat "puzzle-like" in nature. In working with the theory it is nice (and in fact we find it necessary) to have a large supply of wavelets on hand that permit relatively simple analysis.

For this reason we take the opportunity here to present for the reader a collection of such sets, mainly taken from [5], leaving most of the work in verifying that they are indeed wavelet sets to the reader.

We refer the reader to [6] for a proof of the existence of wavelet sets in $\mathbb{R}^{(n)}$, and a proof that there are sufficiently many to generate the Borel structure of

$\mathbb{R}^{(n)}$. These results are true for arbitrary expansive dilation factors. Some concrete examples in the plane were subsequently obtained by Soardi and Weiland, and others were obtained by Gu and by Speegle in their thesis work at A&M. Two had also been obtained by Dai for inclusion in the revised concluding remarks section of our Memoir [5].

In these examples we will usually write intervals as half-open intervals $[\,\cdot\,,\,)$ because it is easier to verify the translation and dilation congruency relations (1) and (2) above when wavelet sets are written thus, even though in actuality the relations need only hold modulo null sets.

(i) As mentioned above, an example due to Journe of a wavelet which admits no multiresolution analysis is the s-elementary wavelet with wavelet set

$$\left[-\frac{32\pi}{7}, -4\pi\right) \cup \left[-\pi, \frac{4\pi}{7}\right) \cup \left[\frac{4\pi}{7}, \pi\right) \cup \left[4\pi, \frac{32\pi}{7}\right).$$

To see that this satisfies the criteria, label these intervals, in order, as J_1, J_2, J_3, J_4 and write $J = \cup J_i$. Then

$$J_1 \cup 4J_2 \cup 4J_3 \cup J_4 = \left[-\frac{32\pi}{7}, -\frac{16\pi}{7}\right) \cup \left[\frac{16\pi}{7}, \frac{32\pi}{7}\right).$$

This has the form $[-2a, a) \cup [b, 2b)$ so is a 2-dilation generator of a partition of $\mathbb{R}\backslash\{0\}$. Then also observe that

$$\{J_1 + 6\pi, J_2 + 2\pi, J_3, J_4 - 4\pi\}$$

is a partition of $[0, 2\pi)$.

(ii) The Shannon (or Littlewood–Paley) set can be generalized. For any $-\pi < \alpha < \pi$, the set

$$E_\alpha = [-2\pi + 2\alpha, -\pi + \alpha) \cup [\pi + \alpha, 2\pi + 2\alpha)$$

is a wavelet set. Indeed, it is clearly a 2-dilation generator of a partition of $\mathbb{R}\backslash\{0\}$, and to see that it satisfies the translation congruency criterion for $-\pi < \alpha \leq 0$ (the case $0 < \alpha < \pi$ is analogous) just observe that

$$\{[-2\pi + 2\alpha, 2\pi) + 4\pi, [-2\pi, -\pi + \alpha) + 2\pi, [\pi + \alpha, 2\pi + 2\alpha)\}$$

is a partition of $[0, 2\pi)$. It is clear that ψ_{E_α} is then a continuous (in $L^2(\mathbb{R})$-norm) path of s-elementary wavelets. Note that

$$\lim_{\alpha \to \pi} \widehat{\psi}_{E_\alpha} = \frac{1}{\sqrt{2\pi}} \chi_{[2\pi, 4\pi)}.$$

This is *not* the Fourier transform of a wavelet because the set $[2\pi, 4\pi)$ is not a 2-dilation generator of a partition of $\mathbb{R}\backslash\{0\}$. So

$$\lim_{\alpha \to \pi} \psi_{E_\alpha}$$

is not an orthogonal wavelet. (It is what is known as a Hardy wavelet because it generates an orthonormal basis for $H^2(\mathbb{R})$ under dilation and translation.) This example demonstrates that $\mathcal{W}(D, T)$ is *not* closed in $L^2(\mathbb{R})$.

(iii) Journe's example above can be extended to a path. For $-\frac{\pi}{7} \leq \beta \leq \frac{\pi}{7}$ the set

$$J_\beta = \left[-\frac{32\pi}{7}, -4\pi + 4\beta\right) \cup \left[-\pi + \beta, -\frac{4\pi}{7}\right) \cup \left[\frac{4\pi}{7}, \pi + \beta\right) \cup \left[4\pi + 4\beta, 4\pi + \frac{4\pi}{7}\right)$$

is a wavelet set. The same argument in (i) establishes dilation congruency. For translation, the argument in (i) shows congruency to $[4\beta, 2\pi + 4\beta)$ which is in turn congruent to $[0, 2\pi)$ as required. Observe that here, as opposed to in (ii) above, the limit of ψ_{J_β} as β approaches the boundary point $\frac{\pi}{7}$ *is* a wavelet. Its wavelet set is a union of 3 disjoint intervals.

(iv) Let $A \subseteq [\pi, \frac{3\pi}{2})$ be an arbitrary measurable subset. Then there is a wavelet set W, such that $W \cap [\pi, \frac{3\pi}{2}) = A$. For the construction, let

$$\begin{aligned} B &= [2\pi, 3\pi) \backslash 2A, \\ C &= \left[-\pi, -\frac{\pi}{2}\right) \backslash (A - 2\pi) \\ \text{and} \quad D &= 2A - 4\pi. \end{aligned}$$

Let

$$W = \left[\frac{3\pi}{2}, 2\pi\right) \cup A \cup B \cup C \cup D.$$

We have $W \cap [\pi, \frac{3\pi}{2}) = A$. Observe that the sets $[\frac{3\pi}{2}, 2\pi)$, A, B, C, D, are disjoint. Also observe that the sets

$$\left[\frac{3\pi}{2}, 2\pi\right), A, \frac{1}{2}B, 2C, D,$$

are disjoint and have union $[-2\pi, -\pi) \cup [\pi, 2\pi)$. In addition, observe that the sets

$$\left[\frac{3\pi}{2}, 2\pi\right), A, B - 2\pi, C + 2\pi, D + 2\pi,$$

are disjoint and have union $[0, 2\pi)$. Hence W is a wavelet set.

(v) Wavelet sets for arbitrary (not necessarily integral) dilation factors other then 2 exist. For instance, if $d \geq 2$ is arbitrary, let

$$\begin{aligned} A &= \left[-\frac{2d\pi}{d+1}, -\frac{2\pi}{d+1}\right), \\ B &= \left[\frac{2\pi}{d^2-1}, \frac{2\pi}{d+1}\right), \\ C &= \left[\frac{2d\pi}{d+1}, \frac{2d^2\pi}{d^2-1}\right) \end{aligned}$$

and let $G = A \cup B \cup C$. Then G is d-wavelet set. To see this, note that $\{A + 2\pi, B, C\}$ is a partition of an interval of length 2π. So G is 2π-translation-congruent to $[0, 2\pi)$.

Also, $\{A, B, d^{-1}C\}$ is a partition of the set $[-d\alpha, -\alpha) \cup [\beta, d\beta)$ for $\alpha = \frac{2\pi}{d^2-1}$, and $\beta = \frac{2\pi}{d^2-1}$, so from this form it follows that $\{d^n G\colon\ n \in \mathbb{Z}\}$ is a partition of $\mathbb{R}\backslash\{0\}$. Hence if $\psi := \mathcal{F}^{-1}(\frac{1}{\sqrt{2\pi}}\chi_G)$, it follows that $\{d^{\frac{n}{2}}\psi(d^n t - \ell)\colon\ n, \ell \in \mathbb{Z}\}$ is orthonormal basis for $L^2(\mathbb{R})$, as required.

5. Operator-Theoretic Interpolation for Wavelet Sets

Operator-theoretic interpolation takes a particularly natural form for the special case of s-elementary (or MSF) wavelets that facilitates hands-on computational techniques in investigating its properties. Let E, F be a pair of wavelet sets. Then for (a.e.) $x \in E$ there is a unique $y \in F$ such that $x - y \in 2\pi\mathbb{Z}$. This is the *translation congruence* property of wavelet sets. Also, for (a.e.) $x \in E$ there is a unique $z \in F$ such that $\frac{x}{z}$ is an integral power of 2. This is the *dilation congruence* property of wavelet sets. (See section 2.5.6.)

There is a natural *closed-form algorithm* for the *interpolation unitary* $V_{\psi_E}^{\psi_F}$ which maps the wavelet basis for $\widehat{\psi}_E$ to the wavelet basis for $\widehat{\psi}_F$. Indeed, using both the translation and dilation congruence properties of $\{E, F\}$, one can explicitly compute a (unique) measure-preserving transformation $\sigma := \sigma_E^F$ mapping $\mathbb{R}$ onto $\mathbb{R}$ which has the property that $V_{\psi_E}^{\psi_F}$ is identical with the *composition operator* defined by:

$$f \mapsto f \circ \sigma^{-1}$$

for all $f \in L^2(\mathbb{R})$. With this formulation, compositions of the maps σ between different pairs of wavelet sets are not difficult to compute, and thus products of the corresponding interpolation unitaries can be computed in terms of them.

5.1. The Interpolation Map σ

Let E and F be arbitrary wavelet sets. Let $\sigma\colon\ E \to F$ be the 1-1, onto map implementing the 2π-translation congruence. Since E and F both generated partitions of $\mathbb{R}\backslash\{0\}$ under dilation by powers of 2, we may extend σ to a 1-1 map of $\mathbb{R}$ onto $\mathbb{R}$ by defining $\sigma(0) = 0$, and

$$\sigma(s) = 2^n \sigma(2^{-n}s) \quad \text{for} \quad s \in 2^n E, \quad n \in \mathbb{Z}. \tag{29}$$

We adopt the notation σ_E^F for this, and call it the *interpolation map* for the ordered pair (E, F).

Lemma 5.1. *In the above notation, σ_E^F is a measure-preserving transformation from $\mathbb{R}$ onto $\mathbb{R}$.*

Proof. Let $\sigma := \sigma_E^F$. Let $\Omega \subseteq \mathbb{R}$ be a measurable set. Let $\Omega_n = \Omega \cap 2^n E$, $n \ni \mathbb{Z}$, and let $E_n = 2^{-n}\Omega_n \subseteq E$. Then $\{\Omega_n\}$ is a partition of Ω, and we have $m(\sigma(E_n)) = m(E_n)$ because the restriction of σ to E is measure-preserving. So

$$\begin{aligned} m(\sigma(\Omega)) &= \sum_n m(\sigma(\Omega_n)) = \sum_n m(2^n \sigma(E_n)) \\ &= \sum_n 2^n m(\sigma(E_n)) = \sum_n 2^n m(E_n) \\ &= \sum_n m(2^n E_n) = \sum_n m(\Omega_n) = m(\Omega). \end{aligned}$$ □

A function $f: \mathbb{R} \to \mathbb{R}$ is called 2-*homogeneous* if $f(2s) = 2f(s)$ for all $s \in \mathbb{R}$. Equivalently, f is 2-homogeneous iff $f(2^n s) = 2^n f(s)$, $s \in \mathbb{R}$, $n \in \mathbb{Z}$. Such a function is completely determined by its values on any subset of $\mathbb{R}$ which generates a partition of $\mathbb{R}\backslash\{0\}$ by 2-dilation. So σ_E^F is the (unique) 2-homogeneous extension of the 2π-transition congruence $E \to F$. The set of all 2-homogeneous measure-preserving transformations of $\mathbb{R}$ clearly forms a group under composition. Also, the composition of a 2-dilation-periodic function f with a 2-homogeneous function g is (in either order) 2-dilation periodic. We have $f(g(2s)) = f(2g(s)) = f(g(s))$ and $g(f(2s)) = g(f(s))$. These facts will be useful.

5.1.1. An Algorithm for the Interpolation Unitary. Now let

$$U_E^F := U_{\sigma_E^F}, \tag{30}$$

where if σ is any measure-preserving transformation of $\mathbb{R}$ then U_σ denotes the composition operator defined by $U_\sigma f = f \circ \sigma^{-1}$, $f \in L^2(\mathbb{R})$. Clearly $(\sigma_E^F)^{-1} = \sigma_F^E$ and $(U_E^F)^* = U_F^E$. We have $U_E^F \widehat{\psi}_E = \widehat{\psi}_F$ since $\sigma_E^F(E) = F$. That is,

$$U_E^F \widehat{\psi}_E = \widehat{\psi}_E \circ \sigma_F^E = \frac{1}{\sqrt{2\pi}} \chi_E \circ \sigma_F^E = \frac{1}{\sqrt{2\pi}} \chi_F = \widehat{\psi}_F.$$

Proposition 5.2. *Let E and F be arbitrary wavelet sets. Then $U_E^F \in \mathcal{C}_{\widehat{\psi}_E}(\widehat{D}, \widehat{T})$. Hence $\mathcal{F}^{-1} U_E^F \mathcal{F}$ is the interpolation unitary for the ordered pair (ψ_E, ψ_F).*

Proof. Write $\sigma = \sigma_E^F$ and $U_\sigma = U_E^F$. We have $U_\sigma \widehat{\psi}_E = \widehat{\psi}_F$ since $\sigma(E) = F$. We must show

$$U_\sigma \widehat{D}^n \widehat{T}^l \widehat{\psi}_E = \widehat{D}^n \widehat{T}^l U_\sigma \widehat{\psi}_E, \quad n, l \in \mathbb{Z}.$$

We have

$$\begin{aligned} (U_\sigma \widehat{D}^n \widehat{T}^l \widehat{\psi}_E)(s) &= (U_\sigma \widehat{D}^n e^{-ils} \widehat{\psi}_E)(s) \\ &= U_\sigma 2^{-\frac{n}{2}} e^{-il2^{-n}s} \widehat{\psi}_E(2^{-n}s) \\ &= 2^{-\frac{n}{2}} e^{-il2^{-n}\sigma^{-1}(s)} \widehat{\psi}_E(2^{-n}\sigma^{-1}(s)) \\ &= 2^{-\frac{n}{2}} e^{-il\sigma^{-1}(2^{-n}s)} \widehat{\psi}_E(\sigma^{-1}(2^{-n}s)) \\ &= 2^{-\frac{n}{2}} e^{-il\sigma^{-1}(2^{-n}s)} \widehat{\psi}(2^{-n}s). \end{aligned}$$

This last term is nonzero iff $2^{-n}s \in F$, in which case $\sigma^{-1}(2^{-n}s) = \sigma_F^E(2^{-n}s) = 2^{-n}s + 2\pi k$ for some $k \in \mathbb{Z}$ since σ_F^E is a 2π-translation-congruence on F. It follows that $e^{-il\sigma^{-2}(2^{-n}s)} = e^{-il2^{-n}s}$. Hence we have

$$\begin{aligned}(U_\sigma \widehat{D}^n \widehat{T}^l \widehat{\psi}_E)(s) &= 2^{-\frac{n}{2}} e^{-ils^{-2^n}s} \widehat{\psi}_F(2^{-n}s) \\ &= (\widehat{D}^n \widehat{T}^l \widehat{\psi}_F)(s) \\ &= (\widehat{D}^n \widehat{T}^l U_\sigma \widehat{\psi}_E)(s).\end{aligned}$$

We have shown $U_E^F \in \mathcal{C}_{\widehat{\psi}_E}(\widehat{D}, \widehat{T})$. Since $U_E^F \widehat{\psi}_E = \widehat{\psi}_F$, the uniqueness part of Proposition 3.1 shows that $\mathcal{F}^{-1} U_E^F \mathcal{F}$ must be the interpolation unitary for (ψ_E, ψ_F). □

5.2. The Interpolation Unitary Normalizes the Commutant

Proposition 5.3. *Let E and F be arbitrary wavelet sets. Then the interpolation unitary for the ordered pair (ψ_E, ψ_F) normalizes $\{D, T\}'$.*

Proof. By Proposition 5.2 we may work with U_E^F in the Fourier transform domain. By Theorem 6, the generic element of $\{\widehat{D}, \widehat{T}\}'$ has the form M_h for some 2-dilation-periodic function $h \in L^\infty(\mathbb{R})$. Write $\sigma = \sigma_E^F$ and $U_\sigma = U_E^F$. Then

$$U_\sigma^{-1} M_h U_\sigma = M_{h \circ \sigma^{-1}}. \tag{31}$$

So since the composition of a 2-dilation-periodic function with a 2-homogeneous function is 2-dilation-periodic, the proof is complete. □

5.2.1. $\mathcal{C}_\psi(D, T)$ Is Nonabelian. It can also be shown ([5, Theorem 5.2 (iii)]) that if E, F are wavelet sets with $E \neq F$ then U_E^F is not contained in the double commutant $\{\widehat{D}, \widehat{T}\}''$. So since U_E^F and $\{\widehat{D}, \widehat{T}\}'$ are both contained in the local commutant of $\mathcal{U}_{\widehat{D},\widehat{T}}$ at $\widehat{\psi}_E$, this proves that $\mathcal{C}_{\widehat{\psi}_E}(\widehat{D}, \widehat{T})$ is nonabelian. In fact (see [5, Proposition 1.8]) this can be used to show that $\mathcal{C}_\psi(D, T)$ is nonabelian for every wavelet ψ. We suspected this, but we could not prove it until we discovered the "right" way of doing the needed computation using s-elementary wavelets.

The above shows that a pair (E, F) of wavelets sets (or, rather, their corresponding s-elementary wavelets) admits operator-theoretic interpolation if and only if Group$\{U_E^F\}$ is contained in the local commutant $\mathcal{C}_{\widehat{\psi}_E}(\widehat{D}, \widehat{T})$, since the requirement that U_E^F normalizes $\{\widehat{D}, \widehat{T}\}'$ is automatically satisfied. It is easy to see that this is equivalent to the condition that for each $n \in \mathbb{Z}$, σ^n is a 2π-congruence of E in the sense that $(\sigma^n(s) - s)/2\pi \in \mathbb{Z}$ for all $s \in E$, which in turn implies that $\sigma^n(E)$ is a wavelet set for all n. Here $\sigma = \sigma_E^F$. This property hold trivially if σ is *involutive* (i.e. $\sigma^2 = \text{identity}$).

5.2.2. The Coefficient Criterion. In cases where "torsion" is present, so $(\sigma_E^F)^k$ is the identity map for some finite integer k, the von Neumann algebra generated by $\{\widehat{D}, \widehat{T}\}'$ and $U := U_E^F$ has the simple form

$$\left\{ \sum_{n=0}^{k} M_{h_n} U^n : \ h_n \in L^\infty(\mathbb{R}) \text{ with } h_n(2s) = h_n(s), \quad s \in \mathbb{R} \right\},$$

and so each member of this "interpolated" family of wavelets has the form

$$\frac{1}{\sqrt{2\pi}} \sum_{n=0}^{k} h_n(s) \chi_{\sigma^n(E)} \tag{32}$$

for 2-dilation periodic "coefficient" functions $\{h_n(s)\}$ which satisfy the necessary and sufficient condition that the operator

$$\sum_{n=0}^{k} M_{h_n} U^n \tag{33}$$

is unitary.

A standard computation shows that the map θ sending $\sum_0^k M_{h_n} U^n$ to the $k \times k$ function matrix (h_{ij}) given by

$$h_{ij} = h_{\alpha(i,j)} \circ \sigma^{-i+1} \tag{34}$$

where $\alpha(i,j) = (i+1)$ modulo k, is a $*$-isomorphism. This matricial algebra is the cross-product of $\{D,T\}'$ by the $*$-automorphism $ad(U_E^F)$ corresponding to conjugation with U_E^F. For instance, if $k=3$ then θ maps

$$M_{h_1} + M_{h_2} U_E^F + M_{h_3} (U_E^F)^2$$

to

$$\begin{pmatrix} h_1 & h_2 & h_3 \\ h_3 \circ \sigma^{-1} & h_1 \circ \sigma^{-1} & h_2 \circ \sigma^{-1} \\ h_2 \circ \sigma^{-2} & h_3 \circ \sigma^{-2} & h_1 \circ \sigma^{-2} \end{pmatrix}. \tag{35}$$

This shows that $\sum_0^k M_{h_n} U^n$ is a unitary operator iff the scalar matrix $(h_{ij})(s)$ is unitary for almost all $s \in \mathbb{R}$. Unitarity of this matrix-valued function is called the *Coefficient Criterion* in [5], and the functions h_i are called the interpolation coefficients. This leads to formulas for families of wavelets which are new to wavelet theory.

5.3. Interpolation Pairs of Wavelet Sets

For many interesting cases of note, the interpolation map σ_E^F will in fact be an *involution* of $\mathbb{R}$ (i.e. $\sigma \circ \sigma = id$, where $\sigma := \sigma_E^F$, and where id denotes the identity map). So torsion *will* be present, as in the above section, and it will be present in an essentially simple form. The corresponding interpolation unitary will be a *symmetry* in this case (i.e. a selfadjoint unitary operator with square I).

It is curious to note that verifying a simple operator equation $U^2 = I$ directly by matricial computation can be extremely difficult. It is much more computationally feasible to verify an equation such as this by pointwise (a.e.) verifying explicitly the relation $\sigma \circ \sigma = id$ for the interpolation map. In [5] we gave a number of examples of interpolation pairs of wavelet sets. We give below a collection of examples that has not been previously published: Every pair sets from the Journe family is an interpolation pair.

5.4. Journe Family Interpolation Pairs

Consider the parameterized path of *generalized Journe* wavelet sets given in Section 4.8 Item (iii). We have

$$J_\beta = \left[-\frac{32\pi}{7}, -4\pi - 4\beta\right) \cup \left[-\pi + \beta, -\frac{4\pi}{7}\right) \cup \left[\frac{4\pi}{7}, \pi + \beta\right) \cup \left[4\pi + 4\beta, 4\pi + \frac{4\pi}{7}\right)$$

where the set of parameters β ranges $-\frac{\pi}{7} \leq \beta \leq \frac{\pi}{7}$.

Proposition 5.4. *Every pair* $(J_{\beta_1}, J_{\beta_2})$ *is an interpolation pair.*

Proof. Let $\beta_1, \beta_2 \in \left[-\frac{\pi}{7}, \frac{\pi}{7}\right)$ with $\beta_1 < \beta_2$. Write $\sigma = \sigma_{J_{\beta_2}}^{J_{\beta_1}}$. We need to show that

$$\sigma^2(x) = x \tag{*}$$

for all $x \in \mathbb{R}$. Since σ is 2-homogeneous, it suffices to verify (*) only for $x \in J_{\beta_1}$. For $x \in J_{\beta_1} \cap J_{\beta_2}$ we have $\sigma(x) = x$, hence $\sigma^2(x) = x$. So we only need to check (*) for $x \in (J_{\beta_1} \backslash J_{\beta_2})$. We have

$$J_{\beta_1} \backslash J_{\beta_2} = [-\pi + \beta_1, -\pi + \beta_2) \cup [4\pi + 4\beta_1, 4\pi + 4\beta_2).$$

It is useful to also write

$$J_{\beta_2} \backslash J_{\beta_1} = [-4\pi + 4\beta_1, -4\pi + 4\beta_2) \cup [\pi + \beta_1, \pi + \beta_2).$$

On $[-\pi + \beta_1, -\pi + \beta_2)$ we have $\sigma(x) = x + 2\pi$, which lies in $[\pi + \beta_1, \pi + \beta_2)$. If we multiply this by 4, we obtain $4\sigma(x) \in [4\pi + 4\beta_1, 4\pi + 4\beta_2) \subset J_{\beta_1}$. And on $[4\pi + 4\beta_1, 4\pi + 4\beta_2)$ we clearly have $\sigma(x) = x - 8\pi$, which lies in $[-4\pi + 4\beta_1, -4\pi + 4\beta_2)$.

So for $x \in [-\pi + \beta_1, -\pi + \beta_2)$ we have

$$\sigma^2(x) = \sigma(\sigma(x)) = \frac{1}{4}\sigma(4\sigma(x)) = \frac{1}{4}[4\sigma(x) - 8\pi] = \sigma(x) - 2\pi = x + 2\pi - 2\pi = x.$$

On $[4\pi + 4\beta_1, 4\pi + 4\beta_2)$ we have $\sigma(x) = x - 8\pi$, which lies in $[-4\pi + 4\beta_1, -4\pi + 4\beta_2)$. So $\frac{1}{4}\sigma(x) \in [-\pi + \beta_1, -\pi + \beta_2)$. Hence

$$\sigma\left(\frac{1}{4}\sigma(x)\right) = \frac{1}{4}\sigma(x) + 2\pi$$

and thus

$$\sigma^2(x) = 4\sigma\left(\frac{1}{4}\sigma(x)\right) = 4\left[\frac{1}{4}\sigma(x) + 2\pi\right] = \sigma(x) + 8\pi = x - 8\pi + 8\pi = x$$

as required.

We have shown that for all $x \in J_{\beta_1}$ we have $\sigma^2(x) = x$. This proves that $(J_{\beta_1}, J_{\beta_2})$ is an interpolation pair.

□

6. Some Open Problems

We will discuss four problems on wavelets that we have investigated from an operator-theoretic point of view over the past ten years, together with some related problems. The set of orthonormal dyadic one-dimensional wavelets is a set of vectors in the unit sphere of a Hilbert space $H = L^2(\mathbb{R})$. It is natural to ask what are the topological properties of $\mathcal{W}(D, T)$ as a subset of the metric space H? This type of question is interesting from a pure mathematical point of view, speaking as an operator theorist, and it just may have some practical consequences depending on the nature and the degree of depth of solutions.

Problem 1: [Connectedness] This was the first global problem in wavelets that we considered from an operator-theoretic point of view. In [5] we posed a number of open problems in the context of the memoir. The first problem we discussed was Problem A (in [5]) which conjectured that $\mathcal{W}(D, T)$ is norm-arcwise-connected. It turned out that this conjecture was also formulated independently by Guido Weiss and his group (see [9], [17, [26]) from a harmonic analysis point of view (our point of view was purely functional analysis), and this problem (and related problems) was the primary stimulation for the creation of the WUTAM CONSORTIUM – a team of 14 researchers based at Washington University and Texas A&M University. (See [26], for the first publication of this group.) This *connectedness conjecture* was answered yes in [26] for the special case of the family of dyadic orthonormal MRA wavelets in $L^2(\mathbb{R})$, but still remains open for the family of *arbitrary* dyadic orthonormal wavelets in $L^2(\mathbb{R})$, as well as for the family of orthonormal wavelets for any fixed n and any dilation matrix in $\mathbb{R}^n$. A natural related problem which also remains open, is whether the set of Riesz wavelets is connected. An intermediate problem, which is also open, asks whether given two orthonormal wavelets is there a continuous path connecting them consisting of Riesz wavelets? (Some evidence for a positive answer to this problem is given by Proposition 6.1 below, which easily shows that every point on the convex path connecting two wavelets (i.e. $(1-t)\psi + t\eta$)is a Riesz wavelet *except* for perhaps the midpoint corresponding to $t = 0.5$. Thus this problem has an easy positive solution for many pairs of orthonormal wavelets, but no way has been found to get around the midpoint obstruction to show that all pairs are connected, perhaps by some exotic type of path.) A subproblem is the same problem but for the set of *frame-wavelets* $\mathcal{F}(D, T)$ (now widely called *framelets*). Is the set of all frame-wavelets connected?; or more specifically–is the set of all Parseval frame wavelets connected? The reader can easily deduce some *frame versions* of Proposition 6.1 using elementary spectral theory of operators which provides some quick-and-easy partial results on paths of frames. These are tantalizing, but the main problems still remain open.

All of these connectivity problems have counterparts for other unitary systems. For wavelet systems, they remain open (to our knowledge) for all dimensions n and all expansive matrix dilation factors. And for other systems, in particular in [14], we showed that for a fixed choice of modulation and translation parameters (necessarily, of course, with product ≤ 1) the set of Weyl-Heisenberg (or Gabor) frames is connected in this sense, and also it is norm-dense in $L^2(\mathbb{R})$ in the sense

of Problem 2 below. Although the Weil-Heisenberg (aka Gabor) unitary systems are of a simpler operator-theoretic structure than the wavelet systems, and this permits the use of some techniques which do not work so well in the wavelet theory, even so this perhaps is another reason to think that general connectedness results are possible within the wavelet theory.

Problem 2: [Density] Is the set $\mathcal{RW}(D,T)$ of all Riesz wavelets *dense* in the norm topology in the Hilbert space $L^2(\mathbb{R})$? This was posed as a conjecture by Larson in a talk in August 1996 in a NATO conference held in Samos, Greece. It was posed in the same spirit as the connectivity problem above, in the sense that it asks about the topological nature of $\mathcal{RW}(D,T)$ as a subset of the metric space $L^2(\mathbb{R})$. Like the connectivity problem it is a *global* type of problem. A positive answer might be useful for applications if it could be given a some type of *quantitative interpretation*. A subproblem of this, which was discussed in several subsequent talks, is the same density problem but for the set of frame-wavelets $\mathcal{F}(D,T)$. (Of course a positive answer for wavelets would imply it for framelets.) Like the connectivity problem, this problem makes sense for the family of Riesz wavelets for any fixed n and any dilation matrix in $\mathbb{R}^n$.

One of the reasons for thinking that this conjecture may be positive is the following result, which we think is the most *elementary* application of operator-theoretic interpolation. It is abstracted from Chapter 1 of [5], although the form in [5] is a bit different.

Proposition 6.1. *Let $\mathcal{U}$ be a unitary system on a Hilbert space H. If ψ_1 and ψ_2 are in $\mathcal{W}(\mathcal{U})$, then*

$$\psi_1 + \lambda\psi_2 \in \mathcal{RW}(\mathcal{U})$$

for all complex scalars λ with $|\lambda| \neq 1$. More generally, if ψ_1 and ψ_2 are in $\mathcal{RW}(\mathcal{U})$ then there are positive constants $b > a > 0$ such that $\psi_1 + \lambda\psi_2 \in \mathcal{RW}(\mathcal{U})$ for all $\lambda \in \mathbb{C}$ with either $|\lambda| < a$ or with $|\lambda| > b$.

Proof. If $\psi_1, \psi_2 \in \mathcal{W}(\mathcal{U})$, let V be the unique unitary in $\mathcal{C}_{\psi_2}(\mathcal{U})$ given by Proposition 3.1 such that $V\psi_2 = \psi_1$. Then

$$\psi_1 + \lambda\psi_2 = (V + \lambda I)\psi_2.$$

Since V is unitary, $(V + \lambda I)$ is an invertible element of $\mathcal{C}_{\psi_2}(\mathcal{U})$ if $|\lambda| \neq 1$, so the first conclusion follows from Proposition 3.2. Now assume $\psi_1, \psi_2 \in \mathcal{RW}(\mathcal{U})$. Let A be the unique invertible element of $\mathcal{C}_{\psi_2}(\mathcal{U})$ such that $A\psi_2 = \psi_1$, and write $\psi_1 + \lambda\psi_2 = (A + \lambda I)\psi_2$. Since A is bounded and invertible there are $b > a > 0$ such that

$$\sigma(A) \subseteq \{z \in \mathbb{C} : a < |z| < b\}$$

where $\sigma(A)$ denotes the spectrum of A, and the same argument applies.

□

The above proposition indicates that Riesz wavelets are plentiful. As mentioned above, by writing $(1-t)\psi_2 + t\psi_1 = ((1-t)V + tI)\psi_1$, and using the fact that the local commutant is a linear space so contains $(1-t)V + tI$, it follows

that a convex combination of orthonormal wavelets is a Riesz wavelet except possibly for the mid-point corresponding to $t = 0.5$. So, if ψ and η are orthonormal wavelets, the line in the vector space $L^2(\mathbb{R})$ containing the pair ψ, η is in the norm closure of the set of Riesz wavelets. Operator theoretic interpolation shows that more general linear combinations of finite families of Riesz wavelets are very often Riesz wavelets. And if one considers a finite family of wavelet sets $\mathcal{C}$, with union $\mathcal{S}$, then the restricted sets of Riesz wavelets, or orthonormal wavelets, or Parseval framelets, or framelets, which are restricted in the sense that they have their frequency support contained in $\mathcal{S}$, is always connected if the family of wavelet sets is an *interpolation family*, and these restricted sets of wavelets are very often connected even if the interpolation family criterion fails for $\mathcal{C}$. (In fact, it is a conjecture that these restricted sets of wavelets are *always* connected.) Moreover, these restricted sets are *dense* in $L^2(S)$ (considered as a subspace of $L^2(\mathbb{R})$) if the family $\mathcal{C}$ is an interpolation family, and it is yet another conjecture that they are *always* dense in $L^2(S)$. It is also known (see [5] for instance) that the linear span $\mathcal{W}(D,T)$ is dense in $L^2(\mathbb{R})$. So these facts together suggest that it is probably true that the set of Riesz wavelets $\mathcal{RW}(D,T)$ is dense in $L^2(\mathbb{R})$. However, the problem remains open. Also, as mentioned above under the *connectivity* problem, one can easily deduce some *frame versions* of Proposition 6.1 using elementary spectral theory of operators which provides some quick-and-easy partial results on density of Riesz wavelets and framelets. However, the general problem for Riesz wavelets remains open. (For the density problem for framelets, we mention that Marcin Bownick has recently obtained a significant positive result! It appears that he has solved the problem positively for *framelets*. But apparently it remains open for Riesz wavelets.)

As with the connectedness problem, all of these problems have counterparts for other unitary systems. For wavelet systems, they remain open (to our knowledge) for all dimensions n and all expansive matrix dilation factors (except for the recent interesting framelet density result of Bownick mentioned above). And for other systems, as mentioned in the context of Problem 1, in [14] we showed that for a fixed choice of modulation and translation parameters with product ≤ 1 the set of Weyl-Heisenberg (or Gabor) frames is dense in $L^2(\mathbb{R})$ in this sense. This is another reason to think that general density results might be possible within the wavelet theory.

Problem 3: [Frequency Support] (See section 4.4.) [Must the support of the Fourier transform of a wavelet contain a wavelet set?] This conjecture was posed about 10 years ago, by Larson, and the problem still remains open for the case of dimension 1 and dilation factor 2. It makes sense for any finite dimension n and any matrix dilation, and it apparently remains unsolved in any case. It has been studied by several researchers, and Z. Rzeszotnik, in particular, has made some progress on the problem. A related problem, also posed by Larson, (see section 4.4) asks whether a wavelet which has minimal support in the frequency domain is necessarily an MSF wavelet. (In other words: Is a minimal support set in the frequency domain necessarily a wavelet set).

Problem 4: [Normalization] (See section 3.3.1.) If $\{\psi, \eta\}$ is a pair of dyadic orthonormal wavelets, does the interpolation unitary V_ψ^η normalize $\{D, T\}'$? As mentioned above, the answer is yes if ψ and η are s-elementary wavelets. This problem makes sense for orthonormal wavelets in higher dimensions for matrix dilation factors, and for other scalar dilations in one dimension. We know of no counterexample for any of these cases. However, the problem might just lie in the fact that in most cases, other than for wavelet sets, we have no reasonable techniques for doing the computations. This problem was also discussed in context in Section 3.3.1, and it could be the most important problem remaining in the direction of further development of the unitary system approach to wavelet theory.

References

[1] E. A. Azoff, E. J. Ionascu, D. R. Larson, and C. M. Pearcy, *Direct Paths of Wavelets.* Houston J. Math. **29** (2003), no. 3, 737–756.

[2] L. Baggett, H. Medina, and K. Merrill, *Generalized Multi-resolution Analyses and a Construction Procedure for all Wavelet Sets in R^n.* J. Fourier Anal. Appl. **5** (1999).

[3] J. J. Benedetto and M. Leon, *The Construction of Single Wavelets in D-dimensions.* J. Geom. Anal. **11** (2001), no. 1, 1–15.

[4] X. Dai, Y. Diao, Q. Gu and D. Han, *Wavelets with Frame Multiresolution Analysis.* J. Fourier Analysis and Applications **9** (2003), 39–48.

[5] X. Dai and D. Larson, *Wandering Vectors for Unitary Systems and Orthogonal Wavelets.* Mem. Amer. Math. Soc. **134** (1998).

[6] X. Dai, D. Larson and D. Speegle, *Wavelet Sets in R^n.* J. Fourier Anal. Appl. **3** (1997), no. 4, 451–456.

[7] X. Dai, D. Larson, and D. Speegle, *Wavelet Sets in R^n - II.* Contemp. Math **216** (1998), 15–40.

[8] I. Daubechies, *Ten Lectures on Wavelets.* SIAM Philadelphia, PA, 1992.

[9] X. Fang and X. Wang, *Construction of Minimally-supported Frequencies Wavelets.* J. Fourier Anal. Appl. 2 (1996), 315–327.

[10] T. N. T. Goodman, S. L. Lee and W. S. Tang, *Wavelets in Wandering Subspaces.* Transactions AMS **338** (1993), 639–654.

[11] Q. Gu, *On Interpolation Families of Wavelet Sets.* Proc. Amer. Math. Soc. **128** (2000), 2973–2979.

[12] D. Han, *Wandering Vectors for Irrational Rotation Unitary Systems.* Transactions AMS **350** (1998), 309–320.

[13] D. Han, J-P. Gabardo, and D. R. Larson, *Gabor Frames and Operator Algebras.* Wavelet Appl. in Signal and Image Proc., Proc. SPIE 4119 (2000), 337–345.

[14] D. Han and D. R. Larson, *Frames, Bases and Group Representations.* Memoirs AMS **697** (2000).

[15] D. Han and D. R. Larson, *Wandering Vector Multipliers for Unitary Groups.* Transactions AMS **353** (2001), 3347–3370.

[16] C. Heil, P. E. T. Jorgensen, and D. R. Larson (eds.), *Wavelets, Frames and Operator Theory, Contemp. Math., 345*. AMS, Providence, RI, 2004, College Park, MD, Jan. 15–21, 2003.

[17] E. Hernandez, X. Wang and G. Weiss, *Smoothing Minimally Supported Frequency (MSF) Wavelets: Part I*. J. Four. Anal. Appl. 2 (1996), 329–340.

[18] E. Ionascu, D. Larson, and C. Pearcy, *On the Unitary Systems Affiliated with Orthonormal Wavelet Theory in n-dimensions*. J. Funct. Anal. **157** (1998), no. 2, 413–431.

[19] R. Kadison and J. Ringrose, *Fundamentals of the Theory of Operator Algebras, Vol. I and II*. Academic Press, Inc. 1983 and 1985.

[20] K. Kornelson and D. Larson, *Rank-one Decomposition of Operators and Construction of Frames. Wavelets, Frames, and Operator Theory, Contemp. Math., 345*. AMS, 2004, pp. 203–214.

[21] D. R. Larson, *Von Neumann Algebras and Wavelets. Operator Algebras and Applications (Samos, 1996), 267–312*. NATO Adv. Sci. Inst. Ser. C Math. Phys. Sci., 495, Kluwer Acad. Publ., Dordrecht, 1997.

[22] D. R. Larson, *Frames and Wavelets from an Operator-theoretic Point of View, Operator Algebras and Operator Theory (Shanghai, 1997), 201–218*. Contemp. Math., 228, AMS, Providence, RI, 1998.

[23] D. R. Larson, E. Schulz, D. Speegle, and K. Taylor, *Explicit Cross Sections of Singly Generated Group Actions*, to appear.

[24] D. R. Larson, W. S. Tang, and E. Weber, *Multiwavelets Associated with Countable Groups of Unitary Operators in Hilbert Spaces*. Int. J. Pure Appl. Math. **6** (2003), no. 2, 123–144.

[25] D. Speegle, *The s-elementary Wavelets are Path-connected*. Proc. Amer. Math. Soc. **132** (2004), 2567–2575

[26] Wutam Consortium, *Basic Properties of Wavelets*. J. Four. Anal. Appl. **4** (1998), 575–594.

David R. Larson
Department of Mathematics
Texas A&M University
College Station, TX 77843-3368, U.S.A.
e-mail: `larson@math.tamu.edu`

Wavelet Analysis and Applications
Tao Qian, Mang I. Vai and Xu Yuesheng, Eds.
Applied and Numerical Harmonic Analysis, 173–184

Clifford Analysis and the Continuous Spherical Wavelet Transform

Paula Cerejeiras, Milton Ferreira and Uwe Kähler

Abstract. We present a group-theoretical approach for the continuous wavelet transform on the sphere S^{n-1}, based on the Lorentz group $\mathrm{Spin}(1,n)$ (the conformal group of the unit sphere). We introduce transformations on the sphere based on the decomposition of the group $\mathrm{Spin}(1,n)$ into the maximal compact subgroup of rotations ($\mathrm{Spin}(n)$) and the set of Möbius transformations in $\mathbb{R}^n$ of the form $\varphi_a(x) = (x-a)(1+ax)^{-1}, |a| < 1$. This approach presents an advantage of allowing the full use of the whole of the conformal group $\mathrm{Spin}(1,n)$, and in such way, it is a generalization of the continuous wavelet transform defined by J. P. Antoine and P. Vandergheynst (see [1], [2]). We will give an account of the influence of the parameter a arising in the definition of dilatations / contractions on the sphere. Finally we give different representations (with different properties) for the Hilbert space $L_2(S^{n-1})$ and the Hardy space H^2.

Mathematics Subject Classification (2000). Primary 30G35; Secondary: 42C40.
Keywords. Continuous Spherical Wavelet Transform, Möbius transformations.

1. Introduction

Wavelet analysis as proven useful in a myriad of applications due to the ability of wavelets to resolve localized signal content in both scale and space (see [3]). Many of these applications, however, are restricted to data defined in Euclidean space: the 1-dimensional line (signal processing), the 2-dimensional plane (image processing) and, occasionally, higher dimensions. Nevertheless, data are often measured or

The research of the first author was supported by *Fundação para a Ciência e a Tecnologia (FCT)*, sabbatical grant SFRH/BSAB/495/2005; the research of the second author was supported by *Fundação para a Ciência e a Tecnologia (FCT)*, grant SFRH/BD/12744/2003. Research (partially) supported by *Unidade de Investigação Matemática e Aplicações* of University of Aveiro, through *Programa Operacional "Ciência, Tecnologia, Inovação"* (POCTI) of the *Fundação para a Ciência e a Tecnologia (FCT)*, cofinanced by the European Community fund FEDER.

defined on other manifolds, such as the sphere. A number of attempts have been made to extend wavelets to the sphere, mainly via stereographic projection. Those are not really satisfactory, due to the disregard of the spherical geometry and the difficulty of defining dilatations on the sphere. Nevertheless it is possible to introduce local dilatations on the sphere if one uses the conformal group, that is, the Lorentz group $SO(1,n)$. In [1] the authors use, for the 2-sphere case, the Iwasawa decomposition of $SO_0(1,3)$ (or KAN decomposition, where K is the maximal compact subgroup, $A = SO_0(1,1) \cong \mathbb{R} \cong \mathbb{R}_*^+$ is the subgroup of Lorentz boosts in the $z-$direction and $N \cong \mathbb{C}$ is a two dimensional abelian subgroup). They use the parameter space $X \cong SO_0(1,3)/N \cong SO(3) \cdot \mathbb{R}_*^+$, i.e., the product of $SO(3)$ for motions and $\mathbb{R}_*^+$ for dilatations on S^2. We want to remark that when we impose this parameter space then some information is lost, since we do not make full use of the whole conformal group.

Here we want to define a continuous wavelet transform on the unit sphere which makes full use of the whole conformal group of the sphere. For that purpose we use some well known facts in Clifford analysis, where the study of the invariance group of null solutions of the Euclidean Dirac operator is of major importance (see [4], [5]). In the case of the sphere this group coincides with the group of Möbius transformations leaving the unit ball invariant [6]. One possible description of this group is in terms of a projective identification of the points in the Euclidean space $\mathbb{R}^n$ with the rays in the null cone in $\mathbb{R}^{1,n+1}$ (see [7], [8], [9]). Hence, the Möbius group is identified with the group $\mathrm{Spin}(1,n+1)$. This identification has been the main theme of several works on Clifford analysis (see [8], [10]). Also related with this approach is the study of the Clifford Analysis on hyperbolic spaces, and this due to the fact that the subgroup $\mathrm{Spin}(1,n)$ of Möbius transformations leaving the unit sphere invariant is the isometry group of these non-Euclidean geometries. For an overview of the function theory in the hyperbolic unit ball we refer the work of D. Eelbode ([10]). Furthermore, for the connection between wavelet theory and Clifford analysis we also would like to refer to [11], [12], [13] and [14].

2. Preliminaries

Let $\mathbb{R}^{p,q}$ denote the $n-$dimensional vectorial space over $\mathbb{R}$ $(n = p+q)$ endowed with an orthonormal basis $e_i, i = 1, ..., n$, and with signature (p,q) induced by the non-degenerate bilinear form $B(x,y)$ such that $B(e_i,e_i) = -1$ for $1 \leq i \leq p$ and $B(e_i,e_i) = 1$ for $p < i \leq n$. We define $\mathbb{R}_{p,q}$ as the universal real algebra generated by $\mathbb{R}^{p,q}$ which preserves the bilinear form $B(x,y)$. Hence we have $e_i^2 = -B(e_i,e_i), i = 1, \ldots, n$ and $e_ie_j + e_je_i = 0, i \neq j$. For a vector x we have that $x^2 = -B(x,x)$ is real valued. A vector is said to be invertible if and only if it is non-isotropic. In $\mathbb{R}^{0,n}$ we have that each non-zero vector y is invertible

We define the Clifford conjugation $a \mapsto \overline{a}$ by $\overline{ab} = \overline{b}\overline{a}$, $\overline{e_i} = -e_i$, and $\overline{1} = 1$. As a consequence, the inverse of a vector y is given by $y^{-1} = \overline{y}/|y|^2$. We remark that due to the non-commutative character of Clifford algebras, the inverse at

left is in general different from the inverse at right. Usually we denote by $\frac{x}{y}$ the product xy^{-1}, there is, by means of the right-hand side inverse. The particular linear combination of basic elements $e_{i_1} \dots e_{i_k}$, $(1 \leq i_1 < \dots < i_k \leq n)$, with equal length k is designated a $k-$vector and we shall denote by $[x]_k$ the k-vector part of $x \in \mathbb{R}_{p,q}$. The linear subspace over $\mathbb{R}$ spanned by the elements of equal length k is to be called $\mathbb{R}^k_{p,q}$ the space of $k-$vectors.

We introduce the Spin group $\mathrm{Spin}(p,q)$ of all even finite products of invertible vectors s such that $s\overline{s} = \pm 1$. For each $s \in \mathrm{Spin}(p,q)$ we have that the mapping $\chi(s) : x \mapsto \chi(s)x = sxs'^{-1}$ is a special orthogonal transformation, thus setting $\mathrm{Spin}(p,q)$ as a double covering of $SO(p,q)$.

3. Conformal Group of the Unit Sphere

Let us now take a look into the special case of the conformal group over the sphere. We can parameterize this group in the form $M(B^n) \sim SO(n) \times B^n$ where $SO(n)$ is the maximal compact subgroup of $M(B^n)$ and B^n is isomorphic to a group of Möbius transformations acting on the unit ball (see [8]). We consider the set of Möbius transformations

$$\varphi_a(x) = (x-a)(1+ax)^{-1}, \quad |a| < 1 \tag{3.1}$$

which maps the unit ball onto itself and also the sphere onto the sphere.

The composition of two such Möbius transformations is again (up to a rotation) a Möbius transformation $\varphi_a \circ \varphi_b(x) = q\varphi_{(1-ab)^{-1}(a+b)}(x)\overline{q}$, where $q = \frac{1-ab}{|1-ab|}$. We denote by $a \times b = (1-ab)^{-1}(a+b)$ the symbol of the new Möbius transformation. The symbol satisfies the relation $(1-ab)^{-1}(a+b) = (a+b)(1-ba)^{-1}$. We notice that the neutral element under this group operation is $\varphi_0 \equiv Id$ while for an inversion we have $\varphi_a^{-1}(x) = \varphi_{-a}(x)$. We have that $G = (M(B^n), \circ)$ is a (non-abelian) locally compact group. There exists a natural isomorphism between this group and the group of points $G^* = (B^n, \times)$ by means of an identification of each $\varphi_a \leftrightarrow a \in B^n$ and $\varphi_a \circ \varphi_b \leftrightarrow a \times b$.

Of special importance for this paper are the following two types of subgroups.

Example. **Subgroups of dimension $n-1$:** let $\omega \in S^{n-1}$. We consider the hyperplane $< \omega, x >= 0$ and we define the ball B^{n-1} as the intersection of the unit ball with this hyperplane. Then we have:

Proposition 3.1. *(see* [15]*) The set of points $a \in B^{n-1}$ together with the group operation $\times$ forms a subgroup of G^*.*

Example. **Subgroups of dimension one:** let L be the segment resulting from the intersection of the unit ball with the straight line passing by the origin and spanned by ω. Then we have:

Proposition 3.2. *(see* [15]*) The set of points $a \in L$ together with the group operation $\times$ forms a subgroup of G^* of dimension one.*

We remark that for each $a \in B^n$ the points $a/|a|$ and $-a/|a|$ are the fixed points of φ_a.

4. Hyperbolic Model

For the construction of a theory of wavelets the study of dilatations is of foremost importance. In the case of the sphere these dilatations are not given by simple Euclidean dilatations through inverse stereographic projection, but by hyperbolic rotations. In what follows we consider the Clifford Algebra $\mathbb{R}_{1,n}$, together with the special identification $\epsilon := e_{n+1}$, the vector that spans the time-axis.

A pure boost is viewed as a transformation $\mathcal{B}(\omega)$ which belongs to the Lie algebra generated by the bi-vectors of the form $\epsilon\omega$, with $\omega \in S^{n-1}$. It has the general form

$$s = \cosh\frac{\alpha}{2} + \epsilon\omega \sinh\frac{\alpha}{2}, \alpha \in \mathbb{R}, \omega \in S^{n-1} \tag{4.1}$$

and it acts on space-time vectors according to the transformation rules $X \to Y = sX\overline{s}$, and on functions via the (Spin-invariant) $L-$representation $F(X) \to L(s)F(X) = sF(\overline{s}Xs)$, or $H-$representation $F(X) \to H(s)F(X) = sF(\overline{s}Xs)\overline{s}$.

Proposition 4.1. *Let $\xi = \sum_{i=1}^{n} \xi_i e_i$ be a point on the sphere and s be of the form (4.1).*

Then the boost $s\xi\overline{s}$ yields the point on the sphere

$$\xi' = \sum_{i=1}^{n} \frac{\xi_i + ((\cosh\alpha - 1) < \xi, \omega > - \sinh\alpha)\omega_i}{\cosh\alpha - \sinh\alpha < \xi, \omega >} e_i \tag{4.2}$$

We can relate transformations (3.1) and (4.2) in the following way:

Proposition 4.2 (see [8]**).** *We assume, in* (3.1)*, $a = t\omega$, with $-1 < t < 1$, and $\omega \in S^{n-1}$. Then transformations (3.1) and (4.2) are related by means of*

$$\alpha = \ln\left(\frac{1+t}{1-t}\right) \quad \text{and} \quad t = \frac{e^{\alpha}-1}{e^{\alpha}+1} = \tanh\left(\frac{\alpha}{2}\right).$$

As a result we obtain an isomorphism between the subgroup of Lorentz boosts in a fixed direction $\omega \in S^{n-1}$ and the subgroup of Möbius transformations of dimension one mentioned in proposition 3.2. Moreover, a pure boost $\mathcal{B}(\omega)$ can always be described as the composition $R(e_n, \omega) \circ \mathcal{B}(e_n) \circ R(\omega, e_n)$, where $R(\omega, \xi)$ stands for the rotation mapping $\omega \in S^{n-1}$ into $\xi \in S^{n-1}$. Therefore it is sufficient to consider pure boosts in the e_n-direction. We will consider the subgroup Spin$(1,1)$ as the subgroup of Lorentz boosts in the e_n-direction. Its action on a given point $\omega = \{\theta_j, \phi\}_{j=1}^{n-2}$ of S^{n-1} is fully determined by

$$\omega \mapsto \omega_\alpha = \{(\theta_j)_\alpha, \phi_\alpha\}_{j=1}^{n-2}, \tag{4.3}$$

where

$$(\theta_j)_\alpha = \theta_j \quad \text{and} \quad \tan\frac{\phi_\alpha}{2} = \mathrm{e}^{\alpha}\tan\frac{\phi}{2}. \tag{4.4}$$

This action corresponds to a pure dilatation on the sphere and it is exactly the usual Euclidean dilatation lifted on S^{n-1} by inverse stereographic projection (see [2]). We will show in the next section that the local dilatation around the North Pole depends on two parameters (not only one as in [2]) if we use the whole conformal group of the sphere.

It is well known that the group $\mathrm{SO}(1,n)$ has two different decompositions, the so-called Iwasawa decomposition (or KAN-decomposition) and the Cartan decomposition (or KAK-decomposition) (see [16] and [17]). We now show how to obtain the KAK-decomposition for the $\mathrm{Spin}(1,n)$ group. We consider the following elements of $\mathrm{Spin}(n)$

$$\begin{aligned} s_i &= \cos\frac{\theta_i}{2} + e_1 e_{i+1}\sin\frac{\theta_i}{2}, \\ s_{n-1} &= \cos\frac{\phi}{2} + e_n e_1 \sin\frac{\phi}{2}, \end{aligned}$$

with $0 \le \theta_i < 2\pi, i = 1,\ldots,n-2$, and $0 \le \phi \le \pi$. We identify the element $s = s_1 \ldots s_{n-2}s_{n-1}$ with the element $\xi(\theta_1,\ldots,\theta_{n-2},\phi) \in S^{n-1} = \mathrm{Spin}(n)/\mathrm{Spin}(n-1)$. Then we obtain the following polar decomposition.

Lemma 4.3. *For s like above we have $\varphi_a(x) = \varphi_{sre_n\overline{s}}(x) = s\varphi_{re_n}(\overline{s}xs)\overline{s}$, where $r = |a| \in [0,1[$.*

Thus, a Möbius transformation can be described in terms of a point $a \in x_n^+ - \mathrm{axis} \cap B^n$ and a convenient rotation induced by s. If we apply to the right-hand side of this identity the rotation present in the usual $\mathrm{Spin}(1,n)$ decomposition (see [8]) we derive the KAK decomposition for an arbitrary element of the group $\mathrm{Spin}(1,n)$.

5. Influence of the Parameter a on Spherical Calottes

In this section we describe the influence of the parameter $a \in B^n$ on the generation of the new spherical calotte obtained by the application of a Möbius transformation φ_a to a given calotte. Without loss of generality we consider a spherical calotte $\mathcal{U}_h = \{x \in S^{n-1} : x_n \ge h\}$ centered at the North Pole, given in polar coordinates by

$$\left\{\begin{array}{rcl} x_1 &=& \cos(\theta_1')\cos(\theta_2')\cdots\cos(\theta_{n-2}')\sin(\phi') \\ x_2 &=& \sin(\theta_1')\cos(\theta_2')\cdots\cos(\theta_{n-2}')\sin(\phi') \\ x_3 &=& \sin(\theta_2')\cos(\theta_3')\cdots\cos(\theta_{n-2}')\sin(\phi') \\ &\vdots& \\ x_{n-1} &=& \sin(\theta_{n-2}')\sin(\phi') \\ x_n &=& \cos(\phi') \end{array}\right.$$

with $\theta_1' \in [0,2\pi[$, $\theta_i' \in [0,\pi[$, $i \in \{2,\ldots,n-2\}$ and $\phi' \in [0,\phi_0]$, for a fixed $\phi_0 \in [0,\pi]$, with $h = \cos(\phi_0)$.

Consider now the sphere S^{n-2} in the hyperplane $x_n = h$

$$\begin{cases} x_1^2 + x_2^2 + ... + x_{n-1}^2 &= 1 - h^2 \\ x_n &= h \end{cases} .$$

We will consider this sphere as the *support of the spherical calotte* $\mathcal{U}_h$. Obviously $\varphi_a(S^{n-2})$ is a new sphere (say, S_*^{n-2}) and it stands for the support of the new spherical calotte. For a complete description of the new spherical calottes obtained see [15].

Definition 5.1. The image of the North Pole under the action of φ_a will be called **attractor point** and it will be denoted by **A**. It is given by:

$$A = \begin{bmatrix} \frac{2a_1(a_n-1)}{1+|a|^2-2a_n} \\ \vdots \\ \frac{2a_{n-1}(a_n-1)}{1+|a|^2-2a_n} \\ \frac{(1-|a|^2+2a_n(a_n-1)}{1+|a|^2-2a_n} \end{bmatrix} . \tag{5.1}$$

Given an initial spherical calotte $\mathcal{U}_h$, its image $\varphi_a(\mathcal{U}_h)$ is a new spherical calotte, say $\mathcal{U}_{h,a}$, centered in general at a different point on the unit sphere, whose distance to its support hyperplane is given by

$$dist = \frac{2r\cos\phi - h(1+r^2)}{\sqrt{k}} + 1 \tag{5.2}$$

where $a \equiv a(r, \theta_1, \theta_2, \ldots, \theta_{n-2}, \phi)$, $k = 4r^2(r\cos\phi - h)^2 \sin^2\phi + (1 - r^2 + 2r\cos\phi\ (r\cos\phi - h))^2$, that is, this distance only depends on the parameters r and ϕ. Then we obtain a local analysis on the sphere given by the family of neighborhoods $\{\mathcal{U}_{h,r,\phi}^{\theta_1,\cdots,\theta_{n-2}} : r \in [0,1[, \theta_1 \in [0, 2\pi[, \theta_2, \ldots, \theta_{n-2}, \phi \in [0, \pi]$. These neighborhoods correspond to dilatations or contractions of the original calotte $\mathcal{U}_h$ under consideration. We illustrate this with an example in $\mathbb{R}^3$:

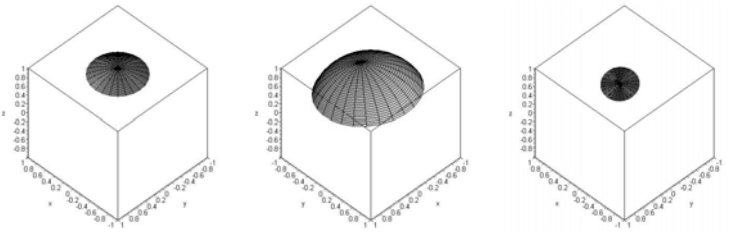

1 2 3

FIGURE 1. Spherical calotte for $h = \cos(\pi/6) = \sqrt{3}/2$: **1** - $\mathcal{U}_h$, **2** - $r = 1/2, \theta = 5\pi/3, \phi = \pi/6$, **3** - $r = 3/10, \theta = 5\pi/3, \phi = 7\pi/9$.

We have the advantage of having a preferable contraction inside the calotte given by the position of the *attractor point*. The parameters $\theta_1, \ldots, \theta_{n-2}$ contribute to the localization of the attractor point.

It is possible to define for each fixed $h \in [-1, 1]$ two different regions on the unit ball that will be called *dilatation* and *contraction regions*, respectively. These two regions are separated by a surface $\mathcal{S}$ generated by a revolution of the arc $\overrightarrow{\gamma}(r) = (r(1-(hr)^2)^{1/2}, 0, \ldots, 0, r^2h), r \in [0, 1[$ in turn of the x_n-axis. The dilatation region corresponds to the region in the unit ball above the surface $\mathcal{S}$ while the contraction region corresponds to the region below the surface $\mathcal{S}$. We remark that $\varphi_a(\mathcal{U}_h), a \in \mathcal{S}$, have all equal area. They only differ by the localization of the attractor point.

The particular case of [1] and [2] is obtained assuming the values $\phi = 0$ (x_n^+-axis $\cap B^n$ - dilatation region) and $\phi = \pi$ (x_n^--axis $\cap B^n$ - contraction region). These two half axis can be used to generate/construct a sequence of approximation spaces. However it is possible to choose other domains for the parameter's variation and thus we would obtain different sequences of approximation spaces.

6. The Continuous Spherical Wavelet Transform

We will consider two different Hilbert spaces. The first is the usual space of square integrable functions on the sphere, namely, the space $L_2(S^{n-1})$ and the second is the monogenic Hardy space $H^2 \subset L_2(S^{n-1})$, which means the functions which can be considered as boundary values of monogenic functions on the unit ball.

On the space $L_2(S^{n-1})$ we use the following inner product and norm

$$< f, g >= \int_{S^{n-1}} \overline{f(x)} g(x) dS(x), \tag{6.1}$$

and

$$||f||^2 = 2^n \int_{S^{n-1}} [\overline{f(x)} f(x)]_0 dS(x), \tag{6.2}$$

where $[\lambda]_0$ denotes the real part of the Clifford number λ and $dS(x)$ is the normalized $Spin(n)-$invariant measure on S^{n-1}. We consider the following unitary operators

$$R_1(s)f(x) = f(\overline{s}xs), \ s \in \mathrm{Spin}(n) \tag{6.3}$$

and

$$D_1(a)f(x) = \left(\frac{1-|a|^2}{|1-ax|^2}\right)^{\frac{n-1}{2}} f(\varphi_{-a}(x)), \, a \in B^n. \tag{6.4}$$

We remark that in the case of $a = re_n$, with $r \in]-1, 1[$, via the change of variables $r = \frac{u-1}{u+1}$, $u > 0$, we obtain the operator

$$D_1(u)f(x) = \lambda_1(u, \phi) f(\omega_{1/u}), \tag{6.5}$$

where

$$\lambda_1(u, \phi) = \left(\frac{4u^2}{((u^2-1)\cos\phi + (u^2+1))^2}\right)^{\frac{n-1}{4}}$$

and $\omega_{1/u}$ is the notation used in (4.3) with $\alpha = \ln(1/u)$. This operator is the same operator used in [2].

Based on the two operators defined above we consider the representation

$$\pi_1(s,a)f(x) = R_1(s) \circ D_1(a)f(x) = \\ = \left(\frac{1-|a|^2}{|1-a\overline{s}xs|^2}\right)^{\frac{n-1}{2}} f(\varphi_{-a}(\overline{s}xs)) \tag{6.6}$$

which can be proved to be equivalent to the representation

$$\tilde{\pi}_1(s,b) = \left(\frac{1-|b|^2}{|1-bx|^2}\right)^{\frac{n-1}{2}} f(\overline{s}\varphi_{-b}(x)s) \tag{6.7}$$

with $b = sa\overline{s}$ and the group operation $(s_1,a_1)\circ(s_2,a_2) = (s_1s_2, (s_1a_2\overline{s_1}) \times a_1)$, where $s_1, s_2 \in \mathrm{Spin}(n)$ and $a_1, a_2 \in B^n$.

By the results obtained in section 5 and lemma 4.3 we can restrict the point $a \in B^n$ to the bidimensional parameter $d = (r\sin\phi, 0, \cdots, 0, r\cos\phi)$, with $r \in [0,1[$ and $\phi \in [0,\pi]$. In fact we can describe an arbitrary point $a \in B^n$ in terms of a point of the form d and a convenient rotation, as e.g.

$$\begin{aligned} a &= s_1 \cdots s_{n-2}s_{n-1}\, r\, \mathrm{e}_n\, \overline{s_{n-1}}\, \overline{s_{n-2}} \cdots \overline{s_1} \\ &= \hat{s}d\overline{\hat{s}}, \end{aligned} \tag{6.8}$$

with $\hat{s} = s_1 \cdots s_{n-2} \in \mathrm{Spin}(n)$ and $d = s_{n-1}\, r\, \mathrm{e}_n\, \overline{s_{n-1}}$ (cf. lemma (4.3)). We remark that, as seen before, the parameters $\theta_1, \ldots, \theta_{n-2}$ only give us information about the localization of the attractor point and this information can also be obtained by the action of the Spin group.

In this way, $D_1(d)$ is our dilatation operator, which will be used from now on.

With respect to the square integrability of our representation we have the following theorem (see [15])

Theorem 6.1. *A function $\psi \in L_2(S^{n-1}, \mathbb{R}_{0,n})$ is admissible if there exists a finite constant $c > 0$ such that*

$$\sum_m \int_0^\pi \int_0^1 |a_k^{(m)}(d)|_0^2 \frac{r}{(1-r^2)^n} dr d\phi < c \tag{6.9}$$

where $a_k^{(m)}(d) =< H_k^{(m)}, D_1(d)\psi >$ denotes the Fourier coefficients associated to the orthonormal basis of spherical harmonics $\{H_k^{(i)}, i = 1, \cdots, N(n,k)\}_{k=0}^{\infty}$.

As a necessary (and almost sufficient) condition for the admissibility we have (see [15]):

Proposition 6.2. *Let $\psi \in L_2(S^{n-1})$ be a function with support on a given spherical calotte $\mathcal{U}_h$. If ψ is an admissible function then it necessarily satisfies the condition*

$$\int_{\mathcal{U}_h} \frac{\psi(y)}{(1+\sin\phi\, y_1 + \cos\phi\, y_n)^{\frac{n-1}{2}}}\, dS_y = 0, \tag{6.10}$$

$\forall\, \phi \in [\arccos(h), \pi]$.

It is difficult to prove the existence of wavelets if we consider the bidimensional parameter d. However we can fix an angle $\phi \in [0, \pi/2]$ and consider the one dimensional subgroup of Möbius transformations obtained by the parameter $d_\phi = (t\sin\phi, 0, \ldots, 0, t\cos\phi)$, with $-1 < t < 1$. Then we can reformulate our admissibility condition (6.9).

Theorem 6.3. *A function $\psi \in L_2(S^{n-1}, \mathbb{R}_{0,n})$ is admissible if there exists a finite constant $c > 0$ such that*

$$\sum_m \int_{-1}^{1} |a_k^{(m)}(d_\phi)|_0^2 \frac{dt}{(1-t^2)^n} < c \tag{6.11}$$

where $a_k^{(m)}(d_\phi) =< H_k^{(m)}, D_1(d_\phi)\psi >$ denotes the Fourier coefficients.

Also the necessary condition (6.10) can now be stated as

$$\int_{\mathcal{U}_h} \frac{\psi(y)}{(|1-\omega y|^2)^{\frac{n-1}{2}}} dS_y = 0 \tag{6.12}$$

where $\omega = (\sin\phi, 0, \ldots, 0, \cos\phi)$ and $\mathcal{U}_h$ is chosen such that $-\cos\phi < h < \cos\phi$. With this condition on the calotte the operator $D_1(d_\phi)$ is a conformal dilatation/contraction operator on the sphere (see [15]). This is a zero mean condition and in the case $\phi = 0$ we obtain the same necessary condition considered in [2], $\int_{S^{n-1}} \frac{\psi(y)}{(1+y_n)^{\frac{n-1}{2}}} dS_y = 0$, which is the exact equivalent of the usual necessary condition for Euclidean wavelets, $\int \psi(x) d^{n-1}x = 0$ (see [2]). One simple way to construct wavelets to our case is to consider a function ψ with compact support on $\mathcal{U}_h$ such that $\int_{U_h} \psi(y) dS_y = 0$. Then the function $\psi_1(y) = (|1-\omega y|^2)^{\frac{n-1}{2}} \psi(y)$, $y \in \mathcal{U}_h$ is an (almost) admissible function i.e., a wavelet.

For an admissible function ψ and $f \in L_2(S^{n-1})$ we define the continuous wavelet transform on the sphere as

$$V_\psi f(s, d_\phi) :=< \tilde{\pi}_1(s, d_\phi)\psi, f >_{L_2} .$$

Thus V_ψ can be inverted on its range by its adjoint V_ψ^* given by

$$V_\psi^* F(x) =$$

$$\int_{Spin(n)} \int_{-1}^{1} \big(\tilde{\pi}_1(s, d_\phi)\psi\big)(x) F(s, d_\phi)\, d\mu(s) \frac{dt}{(1-t^2)^n}$$

In the case of the Hardy space H^2 we consider two different operators that preserve the monogenicity of the function, namely,

$$R_2(s)f(x) = sf(\overline{s}xs), \ s \in \mathrm{Spin}(n) \tag{6.13}$$

and

$$D_2(a)f(x) =$$

$$(1-|a|^2)^{\frac{n-1}{2}} \frac{1-xa}{|1-ax|^n} f(\varphi_{-a}(x)). \tag{6.14}$$

Therefore we have the representation

$$\pi_2(s,a)f(x) = R_2(s) \circ D_2(a)f(x) =$$

$$= (1-|a|^2)^{\frac{n-1}{2}} s \frac{1-\overline{s}xsa}{|1-a\overline{s}xs|^n} f(\varphi_{-a}(\overline{s}xs)) \tag{6.15}$$

This representation is equivalent to

$$\tilde{\pi}_2(s,b)f(x) = (1-|a|^2)^{\frac{n-1}{2}} \frac{1-xb}{|1-bx|^n} sf(\overline{s}\varphi_{-b}(x)s) \tag{6.16}$$

with $b = sa\overline{s}$.

Once again we restrict the parameter a to a parameter d_ϕ in order to have a conformal dilatation/contraction operator on the sphere.

By considering an orthonormal basis of inner spherical monogenics $(P(k)f)_{k\in\mathbb{N}}$ for the Hardy space H^2 we can derive an admissibility condition for wavelets in this space.

Theorem 6.4. *A function $\psi \in H^2$ is admissible if there exists a finite constant $c > 0$ such that*

$$\sum_m \int_{-1}^{1} |a_k^{(m)}(d_\phi)|_0^2 \frac{dt}{(1-t^2)^n} < c \tag{6.17}$$

where $a_k^{(m)}(d_\phi) =< P_k^{(m)}, D_2(d_\phi)\psi >_{L_2}$ are the Fourier coefficients of $D_2(d_\phi)\psi$.

In the case of the Hardy space our necessary condition reads as follows.

Proposition 6.5. *Let $\psi \in H^2$ be a function with compact support, i.e. ψ lives on a spherical calotte $\mathcal{U}_h$ such that $-\cos(\phi) < h < \cos(\phi)$. If ψ is an admissible function then necessarily it satisfies the condition*

$$\int_{\mathcal{U}_h} \frac{1-\omega y}{|1-\omega y|^n} \psi(y) dS_y = 0, \tag{6.18}$$

where $\omega = (\sin\phi, 0, \ldots, 0, \cos\phi)$.

Finally we define for an admissible $\psi \in H^2$ and $f \in H^2$ the continuous wavelet transform as

$$W_\psi f(s, d_\phi) :=< \tilde{\pi}_2(s, d_\phi)\psi, f >_{H_2} .$$

Let us remark that in this case $W_\psi f$ is monogenic in the unit ball.

We would like to remark that although $\psi \equiv 1$ is not an admissible function if we use it in this CWT we recover the Cauchy integral formula in Clifford Analysis up to a constant factor.

References

[1] Antoine, J. P., and P. Vandergheynst: *Wavelets on the 2-sphere: A group-Theoretical Approach*, Applied and Computational Harmonic Analysis **7** (1999), 262-291.

[2] Antoine, J. P., and Vandergheynst P.: *Wavelets on the n-sphere and other manifolds*, J. Math. Physics **39** 8 (1998), 3987-4008.

[3] Daubechies, I.: *Ten Lectures on Wavelets*, SIAM, Philadelphia, PA (1992).

[4] Brackx, F., Delanghe, R., and F. Sommen: *Clifford Analysis* (Research Notes in Mathematics: Vol. 76), Boston: Pitman-Longman 1982.

[5] Delanghe, R., Sommen, F., and V. Souček: *Clifford analysis and spinor-valued functions: a function theory for the Dirac operator*, Math. and its Appl. **53**, Dordrecht: Kluwer Acad. Publ. 1992.

[6] Ahlfors, L. V.: *Möbius transformations in several dimensions*, Ordway Professorship Lectures in Mathematics (1981).

[7] Loo-Keng Hua: *Starting with the unit circle*, Springer-Verlag: New-York Inc., 1981.

[8] Cnops, J. : *Hurwitz pairs and applications of Möbius transformations*, Habilitation dissertation, Universiteit Gent, Faculteit van de Wetenschappen, 1994.

[9] Cerejeiras, P., Kähler, U., and F. Sommen: *Clifford Analysis on Projective Hyperbolic Space*, Journal of Natural Geometry **22** (2002), N.o 1-2, 19-34.

[10] Eelbode, D., *Clifford Analysis on the Hyperbolic Unit Ball*, Thesis, Universiteit Gent, Department Wiskunde, 2004.

[11] Brackx, F., and F. Sommen: *Clifford–Bessel wavelets in Euclidean space*, Math. Meth. Appl. Sci. **25** (2002), No.16-18, 1479-1491.

[12] Brackx, F., and F. Sommen: *Benchmarking of three-dimensional Clifford wavelet functions*. Complex Variables, Theory Appl. **47** (2002), No.7, 577-588.

[13] Cnops, J.: *The wavelet transform in Clifford Analysis*, Comput. Meth. Funct. Theory **1** (2001) 2, 353-374.

[14] Cnops, J., and V. Kisil: *Monogenic functions and representations of nilpotent Lie groups in quantum mechanics*, Math. Meth. Appl. Sci. **22** (1999) 4, 353-373.

[15] Cerejeiras, P., Ferreira, M., and U. Khler: *Continuous wavelet transform on the sphere using Clifford Analysis*, in preparation.

[16] Knapp, A.W.: *Lie groups beyond an introduction*, Birkhäuser (1996).

[17] Takahashi, R.: *Sur les reprsentations unitaires des groupes de Lorentz gnraliss*, Bulletin de la Soc. Math. France **tome 91** (1963), 289-433.

Paula Cerejeiras
Departamento de Matemática
Universidade de Aveiro
P-3810-193, Aveiro
Portugal
e-mail: pceres@mat.ua.pt

Milton Ferreira
Departamento de Matemática
Universidade de Aveiro
P-3810-193, Aveiro
Portugal
e-mail: mferreira@mat.ua.pt

Uwe Kähler
Departamento de Matemática
Universidade de Aveiro
P-3810-193, Aveiro
Portugal
e-mail: uwek@mat.ua.pt

Wavelet Analysis and Applications
Tao Qian, Mang I. Vai and Xu Yuesheng, Eds.
Applied and Numerical Harmonic Analysis, 185–198

Clifford-Jacobi Polynomials and the Associated Continuous Wavelet Transform in Euclidean Space

Fred Brackx, Nele De Schepper and Frank Sommen

Abstract. Specific wavelet kernel functions for a continuous wavelet transform in Euclidean space are presented within the framework of Clifford analysis. These multi-dimensional wavelets are constructed by taking the Clifford-monogenic extension to $\mathbb{R}^{m+1}$ of specific functions in $\mathbb{R}^m$ generalizing the traditional Jacobi weights. The notion of Clifford-monogenic function is a direct higher dimensional generalization of that of holomorphic function in the complex plane. Moreover, crucial to this construction is the orthogonal decomposition of the space of square integrable functions into the Hardy space $H^2(\mathbb{R}^m)$ and its orthogonal complement. In this way a nice relationship is established between the theory of the Clifford Continuous Wavelet Transform on the one hand, and the theory of Hardy spaces on the other hand. Furthermore, also new multi-dimensional polynomials, the so-called Clifford-Jacobi polynomials, are obtained.

Mathematics Subject Classification (2000). 42B10; 44A15; 30G35.

Keywords. Continuous Wavelet Transform; Clifford analysis.

1. Introduction

The wavelet transform has become quite a standard tool in numerous research and application domains and its popularity has increased rapidly over the last decades (see e.g. [1, 2, 3]).
Wavelets on the real line constitute a family of functions $\psi_{a,b}$ derived from one single function ψ, called the mother wavelet, by change of scale a (i.e. by dilation) and by change of position b (i.e. by translation):

$$\psi_{a,b}(x) = \frac{1}{\sqrt{a}}\,\psi\left(\frac{x-b}{a}\right) \quad , \quad a > 0 \quad , \quad b \in \mathbb{R} \quad .$$

In wavelet theory some conditions on the mother wavelet ψ have to be imposed. We request ψ to be an L_2-function (finite energy signal) which is well localized both in the time domain and in the frequency domain. Moreover ψ has to satisfy the so-called admissibility condition:

$$C_\psi := \int_{-\infty}^{+\infty} \frac{|\widehat{\psi}(u)|^2}{|u|}\, du < +\infty \quad ,$$

where $\widehat{\psi}$ denotes the Fourier transform of ψ. In the case where ψ is also in L_1, this admissibility condition implies

$$\int_{-\infty}^{+\infty} \psi(x)\, dx = 0 \quad .$$

In other words: ψ must be an oscillating function, which explains its qualification as "wavelet".
In practice, applications impose additional requirements, among which a given number of vanishing moments:

$$\int_{-\infty}^{+\infty} x^n\ \psi(x)\, dx = 0 \quad , \quad n = 0, 1, \ldots, N \quad .$$

This means that the corresponding Continuous Wavelet Transform (abbreviated CWT):

$$F(a,b) = < \psi_{a,b}, f > = \frac{1}{\sqrt{a}} \int_{-\infty}^{+\infty} \overline{\psi}\left(\frac{x-b}{a}\right)\ f(x)\, dx$$

will filter out polynomial behaviour of the signal f up to degree N, making it adequate at detecting singularities.
When considering two L_2-functions f and g with respective CWT-images F and G, the following inner product in the space of transforms may be introduced:

$$[F, G] = \frac{1}{C_\psi} \int_{-\infty}^{+\infty} \int_0^{+\infty} \overline{F}(a,b)\ G(a,b)\ \frac{da}{a^2}\, db \quad .$$

Taking into account the above mentioned admissibility condition for the mother wavelet ψ, the corresponding Parseval formula is readily obtained:

$$[F, G] = < f, g > \quad .$$

In other words, as a consequence of the admissibility condition the CWT is an isometry from the space of signals into the space of transforms.
The CWT may be extended to higher dimensions while still enjoying the same properties as in the one dimensional case. These higher dimensional CWTs typically originate as tensor products of one dimensional phenomena. However also the non-separable treatment of two dimensional wavelets should be mentioned (see [4]).

The classical wavelet theory can be extended to the Clifford analysis setting. Clifford analysis may be regarded as a direct and elegant generalization to higher dimension of the theory of the holomorphic functions in the complex plane, centred

around the notion of monogenic function, i.e. a null solution of the Dirac operator (Section 2).
The first step in the construction of multi-dimensional Clifford-wavelets, is the introduction of new polynomials, generalizing classical orthogonal polynomials on the real line to the Clifford analysis setting. Their construction rests upon a specific Clifford analysis technique, the so-called Cauchy-Kowalewskaia extension of a real-analytic function in $\mathbb{R}^m$ to a monogenic function in $\mathbb{R}^{m+1}$. One starts from a real-analytic function in an open connected domain in $\mathbb{R}^m$, as an analogue of the classical weight function. The new Clifford algebra-valued polynomials are then generated by the Cauchy-Kowalewskaia extension of this weight function. For these polynomials a recurrence relation and a Rodrigues formula are established. This Rodrigues formula together with Stokes's theorem lead to an orthogonality relation of the new Clifford-polynomials. From this orthogonality relation we select candidates for mother wavelets and show that these candidates indeed may serve as kernel functions for a multi-dimensional continuous wavelet transform if they satisfy certain conditions (see [5]).
We have applied the above technique and have constructed in this way Clifford-wavelets on the basis of Clifford generalizations of the Hermite polynomials, the Laguerre polynomials and the Gegenbauer polynomials (see [6, 7, 8, 9, 10]).

In this paper the remaining class of Clifford algebra-valued basic wavelet functions is presented, namely the one based on a Clifford generalization of the classical Jacobi polynomials on the real line. As a Clifford generalization of the Jacobi weight function, we take the Clifford algebra-valued function $F(\underline{x}) = (1+\underline{x})^{\alpha}\ (1-\underline{x})^{\beta}$ with $\alpha, \beta \in \mathbb{R}$. The Cauchy-Kowalewskaia extension of this weight function generates the so-called general Clifford-Jacobi polynomials (Section 3). For these polynomials a recurrence relation and a Rodrigues formula are established, but no orthogonality relation can be derived. However the special case $\alpha = \beta + 1$ does yield orthogonal polynomials, which are called the special Clifford-Jacobi polynomials (subsection 4.1). These polynomials are the appropriate building blocks for the so-called Clifford-Jacobi wavelets (subsection 4.2). However, these wavelets do not satisfy the mother wavelet conditions established in [5]. Nevertheless we are able to use them as kernel functions for a multi-dimensional Clifford CWT. To that end we are forced to use the orthogonal decomposition of the space of square integrable functions into the Hardy space $H^2(\mathbb{R}^m)$ and its orthogonal complement (subsection 4.3). In this way a nice relationship is established between the theory of the Clifford CWT on the one hand, and the theory of Hardy spaces on the other hand.

2. The Clifford Toolbox

Clifford analysis (see e.g. [11] and [12]) offers a function theory which is a higher dimensional analogue of the theory of the holomorphic functions of one complex variable. Consider functions defined in $\mathbb{R}^m$ $(m > 1)$ and taking values in the

Clifford algebra $\mathbb{R}_m$ or its complexification $\mathbb{C}_m$. If $(e_1, \ldots, e_m)$ is an orthonormal basis of $\mathbb{R}^m$, then a basis for $\mathbb{R}_m$ or $\mathbb{C}_m$ is given by $(e_A \ : \ A \subset \{1, \ldots, m\})$ where $e_\emptyset = 1$ is the identity element.
The non-commutative multiplication in the Clifford algebra is governed by the rules:

$$e_j e_k + e_k e_j = -2\ \delta_{j,k} \quad , \quad j,k = 1, \ldots, m \quad .$$

Conjugation is defined as the anti-involution for which

$$\overline{e_j} = -e_j \quad , \quad j = 1, \ldots, m \quad .$$

In the case of $\mathbb{C}_m$, the Hermitian conjugate of an element $\lambda = \sum_A \lambda_A\ e_A$ $(\lambda_A \in \mathbb{C})$ is defined by

$$\lambda^\dagger = \sum_A \lambda_A^c\ \overline{e_A}$$

where λ_A^c denotes the complex conjugate of λ_A.

In what follows $\mathbb{R}_m^k$ denotes the subspace of k-vectors, i.e. the space spanned by the products of k different basis vectors.

The Euclidean space $\mathbb{R}^m$ is embedded in the Clifford algebras $\mathbb{R}_m$ and $\mathbb{C}_m$ by identifying $(x_1, \ldots, x_m)$ with the vector variable $\underline{x}$ given by

$$\underline{x} = \sum_{j=1}^m e_j x_j \quad ,$$

whereas the Euclidean space $\mathbb{R}^{m+1}$ is identified with $\mathbb{R}_m^0 \oplus \mathbb{R}_m^1$ by identifying $(x_0, x_1, \ldots, x_m)$ with the paravector $x_0 + \underline{x}$.

The Spin-group

$$Spin(m) = \left\{ s = \underline{\omega}_1 \ldots \underline{\omega}_{2\ell}\ ;\ \underline{\omega}_j \in S^{m-1},\ j = 1, \ldots, 2\ell,\ \ell \in \mathbb{N} \right\} \quad ,$$

where S^{m-1} denotes the unit sphere in $\mathbb{R}^m$, is a two-fold covering group of the rotation group $SO(m)$. For each $T \in SO(m)$ there exists $s \in Spin(m)$ such that $T(\underline{x}) = s\underline{x}\overline{s} = (-s)\ \underline{x}\ (-\overline{s})$, for all $\underline{x} \in \mathbb{R}^m$.

An $\mathbb{R}_m$- or $\mathbb{C}_m$-valued function $F(x_1, \ldots, x_m)$, respectively $G(x_0, x_1, \ldots, x_m)$, is called left monogenic in an open region of $\mathbb{R}^m$, respectively $\mathbb{R}^{m+1}$, if in that region:

$$\partial_{\underline{x}} F = 0 \quad , \quad \text{respectively} \quad (\partial_{x_0} + \partial_{\underline{x}})G = 0 \quad .$$

Here $\partial_{\underline{x}}$ is the Dirac operator in $\mathbb{R}^m$:

$$\partial_{\underline{x}} = \sum_{j=1}^m e_j \partial_{x_j} \quad ,$$

whereas $\partial_{x_0} + \partial_{\underline{x}}$ is the Cauchy-Riemann operator in $\mathbb{R}^{m+1}$.
The notion of right monogenicity is defined in a similar way by letting act the Dirac operator, or the Cauchy-Riemann operator, from the right.

A left, respectively right, monogenic homogeneous polynomial P_k of degree k ($k \geq 0$) in $\mathbb{R}^m$ is called a left, respectively right, inner spherical monogenic of order k.

If $\underline{\Omega} \subset \mathbb{R}^m$ is open, then an open neighbourhood Ω of $\underline{\Omega}$ in $\mathbb{R}^{m+1}$ is said to be x_0-normal, if for each $x \in \Omega$ the line segment $\{x + t \ ; \ t \in \mathbb{R}\} \cap \Omega$ is connected and contains exactly one point in $\underline{\Omega}$.
Considering $\mathbb{R}^m$ as the hyperplane $x_0 = 0$ in $\mathbb{R}^{m+1}$, a real-analytic function $f(\underline{x})$ in an open connected domain $\underline{\Omega}$ in $\mathbb{R}^m$ can be uniquely extended to a monogenic function $f^*(x_0, \underline{x})$ in an open connected and x_0-normal neighbourhood Ω of $\underline{\Omega}$ in $\mathbb{R}^{m+1}$. This so-called Cauchy-Kowalewskaia (CK-) extension of $f(\underline{x})$ is given by

$$f^*(x_0, \underline{x}) = \sum_{\ell=0}^{\infty} (-1)^\ell \ \frac{x_0^\ell}{\ell!} \ \partial_{\underline{x}}^\ell f(\underline{x}) \quad . \tag{2.1}$$

Introducing the fundamental solution E of the Cauchy-Riemann operator, given by

$$E(x_0, \underline{x}) = \frac{1}{A_{m+1}} \frac{x_0 - \underline{x}}{|x_0 + \underline{x}|^{m+1}}$$

where A_{m+1} stands for the area of the unit sphere S^m in $\mathbb{R}^{m+1}$, we may define for a square integrable function $f \in L_2(\mathbb{R}^m, dV(\underline{x}))$, its Cauchy integral in the half spaces $\mathbb{R}_{\pm}^{m+1} = \{(x_0, \underline{x}) \in \mathbb{R}^{m+1} \ : \ x_0 \underset{<}{\geq} 0\}$ by

$$\mathcal{C}[f](x_0, \underline{x}) = E(x_0, \ . \ ) * f(\ . \ )(\underline{x}) = \int_{\mathbb{R}^m} E(x_0, \underline{x} - \underline{y}) \ f(\underline{y}) \ dV(\underline{y}) \quad ,$$

for $x_0 \neq 0$, where $dV(\underline{y})$ stands for the Lebesgue measure on $\mathbb{R}^m$. This Cauchy integral is a linear isomorphism between $L_2(\mathbb{R}^m, dV(\underline{x}))$ and the Hardy space $H^2(\mathbb{R}_+^{m+1})$ (see for e.g. [13]).
Two projection operators may be defined by considering the $L_2(\mathbb{R}^m, dV(\underline{x}))$ non-tangential boundary values for $x_0 \to 0+$ and $x_0 \to 0-$ of the Cauchy integral:

$$\mathbb{P}^+[f] = \lim_{x_0 \underset{>}{\to} 0} \mathcal{C}[f](x_0, \underline{x}) = \frac{1}{2} f(\underline{x}) + \frac{1}{2} H[f](\underline{x})$$

and

$$\mathbb{P}^-[f] = -\lim_{x_0 \underset{<}{\to} 0} \mathcal{C}[f](x_0, \underline{x}) = \frac{1}{2} f(\underline{x}) - \frac{1}{2} H[f](\underline{x}) \quad ,$$

where $H[f]$ denotes the Hilbert transform of the function f. This yields the orthogonal decomposition of the space of square integrable functions into the Hardy space $H^2(\mathbb{R}^m)$ and its orthogonal complement:

$$L_2(\mathbb{R}^m, dV(\underline{x})) = H^2(\mathbb{R}^m) \oplus H^2(\mathbb{R}^m)^\perp \quad .$$

In the sequel, the Fourier transform of f will be denoted by $\mathcal{F}[f]$; it is defined by

$$\mathcal{F}[f](\underline{\xi}) = (2\pi)^{-m/2} \int_{\mathbb{R}^m} \exp\left(-i < \underline{x}, \underline{\xi} >\right) \ f(\underline{x}) \ dV(\underline{x}).$$

The Fourier transform of the Hilbert transform is given by

$$\mathcal{F}\big[H[f]\big](\underline{\xi}) = i\underline{\eta}\ \mathcal{F}[f](\underline{\xi})$$

where we have used spherical co-ordinates in frequency space given by

$$\underline{\xi} = \rho\ \underline{\eta}\ \ ,\ \ \rho = |\underline{\xi}| \in [0, +\infty[\ \ ,\ \ \underline{\eta} \in S^{m-1}\ \ .$$

Hence, the orthogonal decomposition of an $L_2(\mathbb{R}^m, dV(\underline{x}))$ - function f :

$$f = \mathbb{P}^+[f] + \mathbb{P}^-[f]$$

reads in frequency space

$$\mathcal{F}[f] = \frac{1}{2}(1 + i\underline{\eta})\ \mathcal{F}[f] + \frac{1}{2}(1 - i\underline{\eta})\ \mathcal{F}[f]\ \ .$$

Here the so-called Clifford-Heaviside functions

$$P^+ = \frac{1}{2}\left(1 + i\underline{\eta}\right)\quad ,\quad P^- = \frac{1}{2}\left(1 - i\underline{\eta}\right)\quad ,\quad \underline{\eta} \in S^{m-1}\quad ,$$

appear; they were introduced independently by Sommen in [14] and McIntosh in [15] and [16]. They are self-adjoint mutually orthogonal idempotents:

$$P^+ + P^- = 1\ ;\ P^+P^- = P^-P^+ = 0\ ;\ (P^+)^2 = P^+\ ;\ (P^-)^2 = P^-\ \ . \tag{2.2}$$

Furthermore, they satisfy

$$i\underline{\xi}\ P^\pm = \pm|\underline{\xi}|\ P^\pm\ \text{ or }\ \underline{\xi}\ P^\pm = \mp i\ |\underline{\xi}|\ P^\pm\ \ . \tag{2.3}$$

3. The General Clifford-Jacobi Polynomials

As a generalization to Clifford analysis of the classical Jacobi weight function, we take the Clifford algebra-valued weight function $F(\underline{x}) = (1 + \underline{x})^\alpha(1 - \underline{x})^\beta$ with $\alpha, \beta \in \mathbb{R}$. Keeping in mind the properties (2.2) and (2.3) of the Clifford-Heaviside functions, we define the factor $(1 + \underline{x})^\alpha$ as follows:

$$(1 + \underline{x})^\alpha := (1 - ir)^\alpha\ P^+ + (1 + ir)^\alpha\ P^-$$

with $r = |\underline{x}|$. Note that both terms $(1 \pm ir)^\alpha$ are well-defined for each $r \in [0, +\infty[$. Indeed, the complex-valued function $(1 + z)^\alpha$ $(\alpha \in \mathbb{R})$ is defined in the whole complex plane except for a branch cut, which can be chosen along the negative real axis from -1 to $-\infty$.
Similarly, we define

$$(1 - \underline{x})^\beta := (1 + ir)^\beta\ P^+ + (1 - ir)^\beta\ P^-\ \ .$$

This method for defining the factors $(1 + \underline{x})^\alpha$ and $(1 - \underline{x})^\beta$ was also used in [15] and [17].
Hence, the weight function may also be written as

$$F(\underline{x}) = (1 - ir)^\alpha\ (1 + ir)^\beta\ P^+ + (1 + ir)^\alpha\ (1 - ir)^\beta\ P^-\ \ .$$

Note that the second term is the complex conjugate of the first one, which is in accordance with the fact that $F(\underline{x})$ takes its values in the real Clifford algebra $\mathbb{R}_m$.

The general Clifford-Jacobi polynomials, denoted by $J^+_{\ell,\alpha,\beta}(\underline{x})$ and $J^-_{\ell,\alpha,\beta}(\underline{x})$, are generated by the CK-extension $F^*(x_0,\underline{x})$ of the weight function $F(\underline{x})$:

$$\begin{aligned} & F^*(x_0,\underline{x}) \\ = & \sum_{\ell=0}^{\infty}(-1)^\ell \ \frac{x_0^\ell}{\ell!} \ \partial_{\underline{x}}^\ell F(\underline{x}) \\ = & \sum_{\ell=0}^{\infty} \frac{x_0^\ell}{\ell!}(1-ir)^{\alpha-\ell}(1+ir)^{\beta-\ell}r^{-\ell} \ \left[J^+_{\ell,\alpha,\beta}(\underline{x}) \ P^+ + J^-_{\ell,\alpha,\beta}(\underline{x}) \ P^-\right] \\ & + \ \sum_{\ell=0}^{\infty} \frac{x_0^\ell}{\ell!}(1+ir)^{\alpha-\ell}(1-ir)^{\beta-\ell}r^{-\ell} \ \left[(J^-_{\ell,\alpha,\beta}(\underline{x}))^c \ P^+ + (J^+_{\ell,\alpha,\beta}(\underline{x}))^c \ P^-\right] \ . \end{aligned}$$

By definition, we have

$$F^*(0,\underline{x}) = (1+\underline{x})^\alpha \ (1-\underline{x})^\beta \ ,$$

which yields

$$J^+_{0,\alpha,\beta}(\underline{x}) = 1 \quad \text{and} \quad J^-_{0,\alpha,\beta}(\underline{x}) = 0 \ .$$

Furthermore, the monogenicity of $F^*(x_0,\underline{x})$ leads to the recurrence relation:

$$\begin{aligned} & J^+_{\ell+1,\alpha,\beta}(\underline{x}) \ P^+ + J^-_{\ell+1,\alpha,\beta}(\underline{x}) \ P^- \\ = & \ i\big((\alpha-\ell)(1+ir) - (\beta-\ell)(1-ir)\big) \ \underline{x} \ \big(J^+_{\ell,\alpha,\beta}(\underline{x}) \ P^+ + J^-_{\ell,\alpha,\beta}(\underline{x}) \ P^-\big) \\ & + i\ell(1+|\underline{x}|^2) \ \big(-J^+_{\ell,\alpha,\beta}(\underline{x}) \ P^+ + \ J^-_{\ell,\alpha,\beta}(\underline{x}) \ P^-\big) \\ & - \ (1+|\underline{x}|^2) \ r \ \partial_{\underline{x}}\big(J^+_{\ell,\alpha,\beta}(\underline{x}) \ P^+ + J^-_{\ell,\alpha,\beta}(\underline{x}) \ P^-\big) \ , \end{aligned}$$

from which the general Clifford-Jacobi polynomials can be computed recursively. It appears that $J^\pm_{\ell,\alpha,\beta}(\underline{x})$ is a polynomial of degree 2ℓ in the variable $\underline{x}$.
One also has the Rodrigues formula:

$$\begin{aligned} & \partial_{\underline{x}}^\ell\big((1+\underline{x})^\alpha(1-\underline{x})^\beta\big) \\ = & \ (-1)^\ell r^{-\ell} \ \Big((1-ir)^{\alpha-\ell}(1+ir)^{\beta-\ell} \ \big(J^+_{\ell,\alpha,\beta}(\underline{x}) \ P^+ + J^-_{\ell,\alpha,\beta}(\underline{x}) \ P^-\big) \\ & + \ (1+ir)^{\alpha-\ell} \ (1-ir)^{\beta-\ell} \ \big(J^+_{\ell,\alpha,\beta}(\underline{x}) \ P^+ + J^-_{\ell,\alpha,\beta}(\underline{x}) \ P^-\big)^c\Big) \ . \end{aligned}$$

Remark 3.1. Combining the above Rodrigues formula with Stokes's theorem does not yield an orthogonality relation for the general Clifford-Jacobi polynomials w.r.t. the weight function $F(\underline{x})$. However, it is possible to construct orthogonal polynomials in the special case where $\alpha = \beta + 1$ (see next section).

4. The Special Clifford-Jacobi Polynomials and Associated CWT

4.1. The Special Clifford-Jacobi Polynomials

In this section we consider the special case where $\alpha = \beta + 1$ ($\beta \in \mathbb{R}$), i.e. we consider the Clifford algebra-valued weight function:

$$\begin{aligned} F(\underline{x}) &= (1+\underline{x})^{\beta+1}\ (1-\underline{x})^{\beta} \\ &= (1+\underline{x})\ (1+|\underline{x}|^2)^{\beta} \quad . \end{aligned}$$

Natural powers of the Dirac operator acting on the weight function can be written as

$$\partial_{\underline{x}}^{\ell}\Big((1+|\underline{x}|^2)^{\beta}\ (1+\underline{x})\Big) = (1+|\underline{x}|^2)^{\beta-\ell}\ (1+\underline{x})\ J_{\ell,\beta}(\underline{x})$$

with $J_{\ell,\beta}(\underline{x})$ a polynomial of degree ℓ in the vector variable $\underline{x}$. The CK-extension of $F(\underline{x})$ then takes the form

$$F^*(x_0,\underline{x}) = \sum_{\ell=0}^{\infty} \frac{x_0^{\ell}}{\ell!}\ (1+|\underline{x}|^2)^{\beta-\ell}\ (1+\underline{x})\ J_{\ell,\beta}(\underline{x}) \quad .$$

Remark 4.1. Note that if we take more generally $\alpha = \beta + n$ ($n \in \mathbb{N} \setminus \{1\}$), i.e. we consider the weight function

$$G(\underline{x}) = (1+\underline{x})^{n}\ (1+|\underline{x}|^2)^{\beta} \quad , \quad n = 2,3,4,\ldots$$

then we can also write

$$\partial_{\underline{x}}^{\ell}\big((1+|\underline{x}|^2)^{\beta}\ (1+\underline{x})^{n}\big) = (1+|\underline{x}|^2)^{\beta-\ell}\ (1+\underline{x})\ J_{\ell,\beta,n}(\underline{x})$$

with $J_{\ell,\beta,n}(\underline{x})$ a polynomial of degree $n+\ell-1$ in $\underline{x}$.
However in order to obtain, by means of the CK-extension technique, orthogonal polynomials w.r.t. the weight function $G(\underline{x})$ we should have had a relation of the form

$$\partial_{\underline{x}}^{\ell}\big((1+|\underline{x}|^2)^{\beta}\ (1+\underline{x})^{n}\big) = (1+|\underline{x}|^2)^{\beta-\ell}\ (1+\underline{x})^{n}\ J^*_{\ell,\beta,n}(\underline{x})$$

with $J^*_{\ell,\beta,n}(\underline{x})$ a polynomial of degree ℓ in $\underline{x}$.
Hence, the case $\alpha = \beta+1$ is the only case where the CK-extension technique leads to orthogonal polynomials w.r.t. the weight function.
Note that the same situation occurred when studying the generalized Clifford-Jacobi polynomials on the open unit ball $B(1)$ of Euclidean space (see [18]). These Clifford algebra-valued polynomials, which were constructed by means of a different approach, are orthogonal in $B(1)$ w.r.t. the weight function $(1+i\underline{x})^{\alpha}\ (1-i\underline{x})^{\beta}$ ($\alpha, \beta > -1$). There the case $\beta = \alpha+1$ is also special. Indeed, only when $\beta = \alpha+1$, it is possible to obtain an explicit recurrence relation for the generalized Clifford-Jacobi polynomials.

From the monogenicity relation of $F^*(x_0,\underline{x})$, we derive the recurrence relation:

$$J_{\ell+1,\beta}(\underline{x}) = 2(\ell-\beta)\underline{x}\ J_{\ell,\beta}(\underline{x}) + \ (\underline{x}-1)\ \partial_{\underline{x}}\big((1+\underline{x})\ J_{\ell,\beta}(\underline{x})\big) \quad .$$

As $J_{0,\beta}(\underline{x}) = 1$, we thus obtain

$$\begin{aligned} J_{1,\beta}(\underline{x}) &= m - (2\beta + m)\underline{x} \\ J_{2,\beta}(\underline{x}) &= -2\beta m - 4\beta\underline{x} + 2\beta(2\beta + m)\underline{x}^2 \\ J_{3,\beta}(\underline{x}) &= -2\beta m(m+2) + 2\beta(2\beta m + 4\beta - 4 + m^2)\underline{x} \\ &\quad +2\beta(-4 + 4\beta + 2\beta m + m^2)\underline{x}^2 + 2\beta(2\beta + m)(2 - 2\beta - m)\underline{x}^3 \\ &\quad \text{and so on.} \end{aligned}$$

From the explicit formula (2.1) for the CK-extension, we obtain the Rodrigues formula:

$$J_{\ell,\beta}(\underline{x}) = (-1)^{\ell}\ (1 + |\underline{x}|^2)^{\ell-\beta}\ (1 + \underline{x})^{-1}\ \partial_{\underline{x}}^{\ell}\Big((1 + \underline{x})\ (1 + |\underline{x}|^2)^{\beta}\Big)$$

which together with Stokes's theorem yields the following orthogonality relation.

Theorem 4.2. *Whenever $\ell < t < (-2\beta - m)/2$, one has the orthogonality relation*

$$\int_{\mathbb{R}^m} J^{\dagger}_{\ell,\beta+\ell}(\underline{x})\ J_{t,\beta+t}(\underline{x})\ (1 + \underline{x})\ (1 + |\underline{x}|^2)^{\beta}\ dV(\underline{x}) = 0 \quad .$$

4.2. The Clifford-Jacobi Wavelets

Note that Theorem 4.2 implies that for $0 < t < (-2\beta - m)/2$

$$\int_{\mathbb{R}^m} J_{t,\beta+t}(\underline{x})\ (1 + \underline{x})\ (1 + |\underline{x}|^2)^{\beta}\ dV(\underline{x}) = 0 \quad .$$

Consequently, the $L_1 \cap L_2$-functions

$$\begin{aligned} \psi_{t,\beta}(\underline{x}) &= J_{t,\beta+t}(\underline{x})\ (1 + \underline{x})\ (1 + |\underline{x}|^2)^{\beta} \\ &= (-1)^{t}\ \partial_{\underline{x}}^{t}\Big((1 + \underline{x})\ (1 + |\underline{x}|^2)^{\beta+t}\Big) \end{aligned}$$

have zero momentum. In Section 4.3 we will show that they can be used as mother wavelets; we call them the Clifford-Jacobi wavelets. Note that the condition $0 < t < (-2\beta - m)/2$ forces us to make the restriction $\beta < -m/2$.

These Clifford-Jacobi wavelets are invariant under the rotation group $Spin(m)$, which means that

$$s\ \psi_{t,\beta}(\overline{s}\underline{x}s)\ \overline{s} = \psi_{t,\beta}(\underline{x}) \quad , \quad s \in Spin(m) \quad .$$

Furthermore, the wavelets $\psi_{t,\beta}(\underline{x})$ have vanishing moments if the condition $2\beta < -m - t - 1$ is fulfilled, as is shown in the next proposition.

Proposition 4.3. *If $2\beta < -m - t - 1$, the Clifford-Jacobi wavelet $\psi_{t,\beta}(\underline{x})$ has vanishing moments:*

$$\int_{\mathbb{R}^m} \underline{x}^j\ \psi_{t,\beta}(\underline{x})\ dV(\underline{x}) = 0$$

for $0 \le j < -m - t - 2\beta - 1$ and $j < t$.

Moreover, the Fourier transform of the Clifford-Jacobi wavelets takes the form:

$$\begin{aligned}\mathcal{F}[\psi_{t,\beta}](\underline{\xi}) &= (-i)^t \frac{2^{\beta+t+1}}{\Gamma(-\beta-t)}\ |\underline{\xi}|^{-m/2-\beta-t-1}\underline{\xi}^t \\ &\quad \left\{ |\underline{\xi}|\ K_{m/2+\beta+t}(|\underline{\xi}|) - i\ K_{m/2+\beta+t+1}(|\underline{\xi}|)\ \underline{\xi} \right\} \end{aligned} \tag{4.1}$$

with $K_\nu(t)$ the modified Bessel function of the second kind, also called Macdonald function.

4.3. The Clifford-Jacobi CWT

The Clifford-Jacobi wavelets do not satisfy the mother wavelet conditions of the general Clifford CWT theory established in [5]. Indeed, in view of (4.1) we see that

$$\begin{aligned}&\mathcal{F}[\psi_{t,\beta}](\underline{\xi})\ \left(\mathcal{F}[\psi_{t,\beta}](\underline{\xi})\right)^\dagger \\ &= \left(\frac{2^{\beta+t+1}}{\Gamma(-\beta-t)}\right)^2 |\underline{\xi}|^{-m-2\beta}\left(\left(K_{m/2+\beta+t}(|\underline{\xi}|)\right)^2 + \left(K_{m/2+\beta+t+1}(|\underline{\xi}|)\right)^2\right) \\ &\quad - 2i\left(\frac{2^{\beta+t+1}}{\Gamma(-\beta-t)}\right)^2 |\underline{\xi}|^{-m-2\beta} K_{m/2+\beta+t+1}(|\underline{\xi}|)\ K_{m/2+\beta+t}(|\underline{\xi}|)\ \frac{\underline{\xi}}{|\underline{\xi}|} \end{aligned} \tag{4.2}$$

which is in fact not radial symmetric (i.e. only depending on $|\underline{\xi}|$) as it should be.

Nevertheless we are able to use the Clifford-Jacobi wavelets as kernel functions for a multi-dimensional Clifford CWT. For this purpose, we are forced to decompose each square integrable function $f \in L_2(\mathbb{R}^m, dV(\underline{x}))$ into its Hardy components (see Section 2)

$$f = \mathbb{P}^+[f] + \mathbb{P}^-[f]$$

with

$$\mathbb{P}^+[f] = \frac{1}{2}(f + H[f]) \in H^2(\mathbb{R}^m)$$

and

$$\mathbb{P}^-[f] = \frac{1}{2}(f - H[f]) \in H^2(\mathbb{R}^m)^\perp \quad .$$

In what follows, we briefly denote $f^\pm = \mathbb{P}^\pm[f]$.
In this way we define, still for $0 < t < (-2\beta - m)/2$, the 'half' Clifford-Jacobi CWTs by

$$\begin{aligned} T^\pm_{t,\beta}[f^\pm](a,\underline{b}) &= F^\pm_{t,\beta}(a,\underline{b}) \\ &= < \psi^{a,\underline{b}}_{t,\beta}\ ,\ f^\pm > \\ &= \int_{\mathbb{R}^m} \left(\psi^{a,\underline{b}}_{t,\beta}(\underline{x})\right)^\dagger\ f^\pm(\underline{x})\ dV(\underline{x})\ , \end{aligned}$$

where the continuous family of wavelets

$$\psi^{a,\underline{b}}_{t,\beta}(\underline{x}) = \frac{1}{a^{m/2}}\ \psi_{t,\beta}\left(\frac{\underline{x}-\underline{b}}{a}\right) \quad ,$$

with $a \in \mathbb{R}_+$ and $\underline{b} \in \mathbb{R}^m$ originates from the mother wavelet $\psi_{t,\beta}$ by dilation and translation.
The definition of the 'half' Clifford-Jacobi CWTs can be rewritten in frequency space as

$$F^{\pm}_{t,\beta}(a,\underline{b}) = (2\pi)^{m/2}\ a^{m/2}\ \mathcal{F}\left[\left(\mathcal{F}[\psi_{t,\beta}](a\underline{\xi})\right)^{\dagger}\mathcal{F}[f^{\pm}](\underline{\xi})\right](-\underline{b}) \quad . \tag{4.3}$$

We now prove that the 'half' Clifford-Jacobi CWT $T^{+}_{t,\beta}$, respectively $T^{-}_{t,\beta}$, maps the Hardy space $H^2(\mathbb{R}^m)$, respectively $H^2(\mathbb{R}^m)^{\perp}$, isometrically into a weighted L_2-space on $\mathbb{R}_+ \times \mathbb{R}^m$.
To that end we calculate

$$\int_{\mathbb{R}^m}\int_0^{+\infty} \left(F^{\pm}_{t,\beta}(a,\underline{b})\right)^{\dagger}\ G^{\pm}_{t,\beta}(a,\underline{b})\ \frac{da}{a^{m+1}}\ dV(\underline{b}) \quad . \tag{4.4}$$

In view of (4.3) and the Parseval formula, we obtain

$$\int_{\mathbb{R}^m}\int_0^{+\infty} \left(F^{\pm}_{t,\beta}(a,\underline{b})\right)^{\dagger}\ G^{\pm}_{t,\beta}(a,\underline{b})\ \frac{da}{a^{m+1}}\ dV(\underline{b}) \ =$$
$$(2\pi)^m \int_{\mathbb{R}^m} \left(\mathcal{F}[f^{\pm}](\underline{\xi})\right)^{\dagger}\left(\int_0^{+\infty} \mathcal{F}[\psi_{t,\beta}](a\underline{\xi})\ \left(\mathcal{F}[\psi_{t,\beta}](a\underline{\xi})\right)^{\dagger}\ \frac{da}{a}\right)\mathcal{F}[g^{\pm}](\underline{\xi})\ dV(\underline{\xi}) \quad .$$

By means of the substitution

$$\underline{\xi} = \frac{r}{a}\ \underline{\eta} \quad , \quad \underline{\eta} \in S^{m-1} \quad ,$$

the integral between brackets becomes

$$\int_0^{+\infty} \mathcal{F}[\psi_{t,\beta}](a\underline{\xi})\ \left(\mathcal{F}[\psi_{t,\beta}](a\underline{\xi})\right)^{\dagger}\ \frac{da}{a} = \int_0^{+\infty} \mathcal{F}[\psi_{t,\beta}](r\underline{\eta})\ \left(\mathcal{F}[\psi_{t,\beta}](r\underline{\eta})\right)^{\dagger}\ \frac{dr}{r} \, .$$

Next, using expression (4.2) we find

$$\int_0^{+\infty} \mathcal{F}[\psi_{t,\beta}](a\underline{\xi})\ \left(\mathcal{F}[\psi_{t,\beta}](a\underline{\xi})\right)^{\dagger}\ \frac{da}{a} = c_1 + c_2\ \underline{\eta}$$

with

$$c_1 = \left(\frac{2^{\beta+t+1}}{\Gamma(-\beta-t)}\right)^2 \int_0^{+\infty} r^{-m-2\beta-1}\left(\left(K_{m/2+\beta+t}(r)\right)^2 + \left(K_{m/2+\beta+t+1}(r)\right)^2\right) dr$$

and

$$c_2 = -2i\ \left(\frac{2^{\beta+t+1}}{\Gamma(-\beta-t)}\right)^2 \int_0^{+\infty} r^{-m-2\beta-1} K_{m/2+\beta+t+1}(r)\ K_{m/2+\beta+t}(r)\ dr \quad .$$

Note that c_1 and c_2 are finite constants, since the modified Bessel functions of the second kind K_ν with $\mathrm{Im}(\nu) = 0$, have the following limiting behaviour:

$$K_\nu(x) \approx \frac{\pi}{2\sin(\pi|\nu|)}\left(\frac{1}{-|\nu|!}\right)\left(\frac{2}{x}\right)^{|\nu|} \quad \text{for } x \to 0$$

and

$$K_\nu(x) \approx \left(\frac{\pi}{2x}\right)^{1/2} \exp(-x) \quad \text{for } x \to \infty \quad ,$$

and since moreover we consider $0 < t < (-2\beta - m)/2$.
Consequently, the integral (4.4) becomes

$$\begin{aligned} &\int_{\mathbb{R}^m} \int_0^{+\infty} \left(F^{\pm}_{t,\beta}(a,\underline{b})\right)^{\dagger} \, G^{\pm}_{t,\beta}(a,\underline{b}) \, \frac{da}{a^{m+1}} \, dV(\underline{b}) \\ &= \quad (2\pi)^m \, c_1 < \mathcal{F}[f^{\pm}], \mathcal{F}[g^{\pm}] > \\ &\qquad + (2\pi)^m \, c_2 \int_{\mathbb{R}^m} \left(\mathcal{F}[f^{\pm}](\underline{\xi})\right)^{\dagger} \, \underline{\eta} \, \mathcal{F}[g^{\pm}](\underline{\xi}) \, dV(\underline{\xi}) \quad . \end{aligned}$$

As

$$\begin{aligned} \underline{\eta} \, \mathcal{F}[g^{\pm}](\underline{\xi}) &= \underline{\eta} \, P^{\pm} \, \mathcal{F}[g](\underline{\xi}) \\ &= \mp i \, P^{\pm} \, \mathcal{F}[g](\underline{\xi}) \\ &= \mp i \, \mathcal{F}[g^{\pm}](\underline{\xi}) \quad , \end{aligned}$$

this integral can be further simplified to

$$\begin{aligned} &\int_{\mathbb{R}^m} \int_0^{+\infty} \left(F^{\pm}_{t,\beta}(a,\underline{b})\right)^{\dagger} \, G^{\pm}_{t,\beta}(a,\underline{b}) \, \frac{da}{a^{m+1}} \, dV(\underline{b}) \\ &= \quad (2\pi)^m \, (c_1 \mp i c_2) < f^{\pm}, g^{\pm} > \quad . \end{aligned}$$

Hence we can define the following inner products on the spaces of transforms

$$[F^{\pm}_{t,\beta}, G^{\pm}_{t,\beta}] = \frac{1}{C^{\pm}} \int_{\mathbb{R}^m} \int_0^{+\infty} \left(F^{\pm}_{t,\beta}(a,\underline{b})\right)^{\dagger} G^{\pm}_{t,\beta}(a,\underline{b}) \, \frac{da}{a^{m+1}} \, dV(\underline{b})$$

with

$$C^{\pm} = (2\pi)^m \, (c_1 \mp i c_2) \quad .$$

These inner products satisfy the Parseval formulae:

$$[F^{\pm}_{t,\beta}, G^{\pm}_{t,\beta}] = < f^{\pm}, g^{\pm} >$$

which implies that the 'half' Clifford-Jacobi CWTs $T^{\pm}_{t,\beta}$ are isometries, as it should be.

The twin transforms $T^{\pm}_{t,\beta}$ may be combined into a 'complete' Clifford-Jacobi CWT acting on $L_2(\mathbb{R}^m, dV(\underline{x}))$. Indeed, for $f \in L_2(\mathbb{R}^m, dV(\underline{x}))$ we put

$$\begin{aligned} T_{t,\beta}[f](a,\underline{b}) &= F_{t,\beta}(a,\underline{b}) \\ &= < \psi^{a,\underline{b}}_{t,\beta} \, , \, f > \\ &= < \psi^{a,\underline{b}}_{t,\beta} \, , \, f^{+} > + < \psi^{a,\underline{b}}_{t,\beta} \, , \, f^{-} > \\ &= F^{+}_{t,\beta}(a,\underline{b}) + F^{-}_{t,\beta}(a,\underline{b}) \quad . \end{aligned}$$

Remark 4.4. The CK-extension technique also works for the more general weight function

$$G(\underline{x}) = (1+\underline{x})\ (1+|\underline{x}|^2)^{\beta}\ P_k(\underline{x}) \quad , \quad \beta \in \mathbb{R}$$

with $P_k(\underline{x})$ an arbitrary but fixed left inner spherical monogenic of order k. In this way, one obtains the so-called generalized special Clifford-Jacobi polynomials $J_{t,\beta,k}(\underline{x})$ $(t = 0, 1, 2, \ldots)$ which are the appropriate building blocks for the generalized Clifford-Jacobi wavelets given by

$$\begin{aligned} \psi_{t,\beta,k}(\underline{x}) &= (1+|\underline{x}|^2)^{\beta}\ (1+\underline{x})\ J_{t,\beta+t,k}(\underline{x})\ P_k(\underline{x}) \\ &= (-1)^t\ \partial_{\underline{x}}^t \Big((1+|\underline{x}|^2)^{\beta+t}\ (1+\underline{x})\ P_k(\underline{x}) \Big) \ . \end{aligned}$$

Naturally, these wavelets are not invariant under the rotation group $Spin(m)$. Hence this group must be taken into consideration when defining the associated CWT.

References

[1] C. K. Chui, An Introduction to Wavelets. Academic Press, Inc., San Diego, 1992.

[2] I. Daubechies, Ten Lectures on Wavelets. SIAM, Philadelphia, 1992.

[3] G. Kaiser, A Friendly Guide to Wavelets. Birkhäuser Verlag (Boston, 1994).

[4] J.-P. Antoine, R. Murenzi, P. Vandergheynst and Syed Twareque Ali, Two-Dimensional Wavelets and their Relatives, Cambridge University Press, Cambridge, 2004.

[5] F. Brackx, N. De Schepper and F. Sommen, New multivariable polynomials and their associated Continuous Wavelet Transform in the framework of Clifford Analysis. In: L.H. Son, W. Tutschke, S. Jain (eds.), Methods of Complex and Clifford Analysis (Proceedings of ICAM Hanoi 2004), SAS International Publication, Delhi, 2006, 275-294.

[6] F. Brackx and F. Sommen, Clifford-Hermite Wavelets in Euclidean Space, *Journal of Fourier Analysis and Applications* **6**, no. 3 (2000), 299-310.

[7] F. Brackx and F. Sommen, The Generalized Clifford-Hermite Continuous Wavelet Transform, *Advances in Applied Clifford Algebras* **11(S1)**, 2001, 219-231.

[8] F. Brackx, N. De Schepper and F. Sommen, The Bi-axial Clifford-Hermite Continuous Wavelet Transform, *Journal of Natural Geometry* **24** (2003), 81-100.

[9] F. Brackx, N. De Schepper and F. Sommen, The Clifford-Laguerre Continuous Wavelet Transform, *Bull. Belg. Math. Soc. - Simon Stevin* **11**(2), 2004, 201-215.

[10] F. Brackx, N. De Schepper and F. Sommen, The Clifford-Gegenbauer Polynomials and the Associated Continuous Wavelet Transform, *Integral Transform. Spec. Funct.* **15** (2004), no. 5, 387-404.

[11] F. Brackx, R. Delanghe and F. Sommen, Clifford Analysis, Pitman Publ., Boston, London, Melbourne, 1982.

[12] R. Delanghe, F. Sommen and V. Souček, Clifford Algebra and Spinor-Valued Functions. Kluwer Acad. Publ., Dordrecht, 1992.

[13] J. Gilbert and M. Murray, Clifford Algebras and Dirac operators in harmonic analysis, Cambridge: University Press 1991.

[14] F. Sommen, Some connections between complex analysis and Clifford analysis. *Complex Variables: Theory and Application* **1** (1982), 97-118.

[15] C. Li, A. McIntosh and T. Qian, Clifford algebras, Fourier transforms and singular convolution operators on Lipschitz surfaces, *Revista Matematica Iberoamericana* **10** (1994), no. 3, 665-721.

[16] A. McIntosh, Clifford Algebras, Fourier Theory, Singular Integrals and Harmonic Functions on Lipschitz Domains. In: J. Ryan (ed.), Clifford Algebras in Analysis and Related Topics, CRC Press, Boca Raton, 1996, 33-87.

[17] J. Peetre and T. Qian, Möbius covariance of iterated Dirac operators, *J. Austral. Math. Soc. (Series A)* **56** (1994), 1-12.

[18] F. Brackx, N. De Schepper and F. Sommen, Clifford algebra-valued orthogonal polynomials in the open unit ball of Euclidean Space, *International Journal of Mathematics and Mathematical Sciences* **52** (2004), 2761-2772.

Fred Brackx
Clifford Research Group, Department of Mathematical Analysis,
Faculty of Engineering, Ghent University,
Galglaan 2, B-9000 Gent,
Belgium
e-mail: `fb@cage.ugent.be`

Nele De Schepper
Clifford Research Group, Department of Mathematical Analysis,
Faculty of Engineering, Ghent University,
Galglaan 2, B-9000 Gent,
Belgium
e-mail: `nds@cage.ugent.be`

Frank Sommen
Clifford Research Group, Department of Mathematical Analysis,
Faculty of Sciences, Ghent University,
Galglaan 2, B-9000 Gent,
Belgium
e-mail: `fs@cage.ugent.be`

Chapter 3: Fractal and Multifractal Theory, Wavelet Algorithm, Wavelet in Numerical Analysis

Wavelet Analysis and Applications
Tao Qian, Mang I. Vai and Xu Yuesheng, Eds.
Applied and Numerical Harmonic Analysis, 201–246

Wavelet Leaders in Multifractal Analysis

Stéphane Jaffard, Bruno Lashermes and Patrice Abry

Abstract. The properties of several multifractal formalisms based on wavelet coefficients are compared from both mathematical and numerical points of view. When it is based directly on wavelet coefficients, the multifractal formalism is shown to yield, at best, the increasing part of the weak scaling exponent spectrum. The formalism has to be based on new multiresolution quantities, the wavelet leaders, in order to yield the entire and correct spectrum of Hölder singularities. The properties of this new multifractal formalism and of the alternative weak scaling exponent multifractal formalism are investigated. Examples based on known synthetic multifractal processes are illustrating its numerical implementation and abilities.

1. Introduction

The purpose of multifractal analysis is to study functions or signals whose pointwise Hölder regularity may change widely from point to point. In such situations, the determination of the pointwise regularity at each point is numerically unstable; usually, it is quite meaningless since the exact regularity at a particular point usually does not carry a useful information. Therefore, one rather wishes to derive some information concerning the size of the sets of points where the pointwise regularity exponent takes a given value H. This "size" is mathematically formalized as the Hausdorff dimension. These dimensions define a function of the exponents H referred to as the spectrum of singularities (or multifractal spectrum) of f and denoted $d_f(H)$. Therefore, **performing the multifractal analysis of a function (or of a signal) f means to determine (or to estimate) its spectrum of singularities** $d_f(H)$. When working on real-life signals, the spectrum $d_f(H)$ cannot be computed by first determining the regularity exponent at each point, since it was precisely introduced as a substitute for this quantity; hence the necessity to introduce a method that yields this spectrum from numerically computable quantities derived from the signal. This is precisely the goal of "multifractal formalisms" and the purpose of the present work is to introduce a new multifractal formalism, based on new multiresolution quantities, the wavelet leaders.

However before introducing wavelet techniques, we will first examine how such formalisms were introduced in the setting of measures and functions; indeed a careful inspection of these more simple settings will be the key to a good understanding of what the alternative wavelet extensions yield.

In this paper, we first provide the reader with a description of the different multifractal formalisms which have been introduced in the setting of measures (Section 2) and in the setting of functions (Section 3). The first wavelet-based formulas are presented in Section 4; we will discuss the pertinence of these wavelet-based formulas and show that they lead to numerically unstable computations. The way to overcome these problems is to give up basing the multifractal formalism directly on wavelet coefficients but rather on wavelet leaders. This is developed in Section 5. Finally, In Section 6 we show that the previous multifractal formalism based on wavelet coefficients can be (partly) interpreted as yielding the spectrum of singularities based on another pointwise regularity exponent: The weak scaling exponent.

This paper is partly a review paper and partly a research paper. Its main novelty is twofold:

- We show that, both numerically **and** theoretically, a wavelet-based multifractal formalism yields more accurate results if it is built on wavelet leaders rather than directly on wavelet coefficients. The particular examples supplied by Brownian motion and fractional Brownian motions are investigated in details and the performances of the different multifractal formalisms are compared both theoretically and numerically on these examples.
- We show that a multifractal formalism based on wavelet coefficients can only be expected to yield the *weak scaling spectrum* (see Definition 19), and therefore it can yield the spectrum of singularities only in the particular cases where the two spectra coincide.

The numerical data shown in this paper only involve synthetic signals (Fractional Brownian Motions and multiplicative cascades) whose spectra are knowm exactly, since they thus supply reliable benchmarks in order to compare the different methods under investigation. Let us mention, however, that multifractal analysis is now successfully used in many fields of science (turbulence, clouds modelling, physiological signals and images, traffic data, rough interfaces...), see [1, 4, 13, 23, 34, 48, 58] and references therein. Inside mathematics, multifractal measures or functions were also shown to be relevant in many different areas, such as analytic number theory, Diophantine approximation, Peano-type functions, dynamical systems, stochastic processes,..., see [29, 30, 34] and references therein.

2. Multifractal Analysis of Measures

2.1. Mathematical Notions

We start by introducing the mathematical tools that are needed in the multifractal analysis of measures. The first one is the definition of Hausdorff dimension (see e.g., [20]).

Definition 1. **Hausdorff dimension:** Let $A \subset \mathbb{R}^d$. If $\varepsilon > 0$ and $\delta \in [0, d]$, we denote

$$M_\varepsilon^\delta = \inf_R \left(\sum_i |A_i|^\delta \right),$$

where R is an ϵ-covering of A, i.e. a covering of A by a countable collection of bounded sets $\{A_i\}_{i\in\mathbb{N}}$ of diameters $|A_i| \leq \varepsilon$. The infimum is therefore taken on all ϵ-coverings. For any $\delta \in [0, d]$, the δ-dimensional Hausdorff measure of A is

$$mes_\delta(A) = \lim_{\epsilon\to 0} M_\epsilon^\delta;$$

note that the limit exists (it can take the value $+\infty$) since M_ϵ^δ is a decreasing function of ϵ. There exists $\delta_0 \in [0, d]$ such that

$$\forall \delta < \delta_0, \quad mes_\delta(A) = +\infty; \quad \text{and } \forall \delta > \delta_0, \quad mes_\delta(A) = 0.$$

This critical δ_0 is called the Hausdorff dimension of A.

Multifractal analysis is relevant for measures whose regularity changes from point to point. Therefore we need to introduce the following notion of pointwise regularity of measures.

Definition 2. **Hölder exponent:** Let $x_0 \in \mathbb{R}^d$ and let $\alpha \geq 0$. A nonnegative measure μ defined on $\mathbb{R}^d$ belongs to $C^\alpha(x_0)$ if there exists a constant $C > 0$ such that, in a neighbourhood of x_0,

$$\mu(B(x_0, r)) \leq Cr^\alpha,$$

where $B(x_0, r)$ denotes the open ball of center x_0 and radius r. Let x_0 belong to the support of μ; then the Hölder exponent of μ at x_0 is

$$h_\mu(x_0) = \sup\{\alpha : \mu \in C^\alpha(x_0)\}.$$

Definition 3. **Singularity (or multifractal) spectrum:** Let $E_\mu(H)$ denote the set of points where the Hölder exponent of μ takes the value H. (Note that $E_\mu(H)$ is included in the support of μ.) The spectrum of singularities of μ (denoted by $d_\mu(H)$) is the Hausdorff dimension of $E_\mu(H)$.

Remarks: In the previous definition, when $E_\mu(H) = \emptyset$, then its dimension is $-\infty$. This is actually more than a simple convention. Indeed, the multifractal formalism that is studied below is expected to yield $-\infty$ for the values of H for which $E_\mu(H) = \emptyset$.

The Hölder exponent of a measure is called the "local dimension" by some authors.

We will need to be able to deduce the Hölder exponent at every point from a "discretized version" of μ, i.e. from the values of μ on a countable collection of sets. A possible choice for this collection of sets is supplied by the dyadic cubes which are defined as follows.

Definition 4. **Dyadic cube:** A dyadic cube of scale j is a cube of the form

$$\lambda = \left[\frac{k_1}{2^j}, \frac{k_1+1}{2^j}\right) \times \cdots \times \left[\frac{k_d}{2^j}, \frac{k_d+1}{2^j}\right),$$

where $k = (k_1, \ldots k_d) \in \mathbb{Z}^d$.

Each point $x_0 \in \mathbb{R}^d$ is contained in a unique dyadic cube of scale j, denoted by $\lambda_j(x_0)$.

The cube $3\lambda_j(x_0)$ is the cube of same center as $\lambda_j(x_0)$ and three times wider; i.e. it is the cube

$$\lambda = \left[\frac{k_1-1}{2^j}, \frac{k_1+2}{2^j}\right) \times \cdots \times \left[\frac{k_d-1}{2^j}, \frac{k_d+2}{2^j}\right).$$

The following lemma is a key ingredient in the derivation of the multifractal formalism for measures.

Lemma 2.1. *Let μ be a nonnegative measure defined on $\mathbb{R}^d$. Then*

$$h_\mu(x_0) = \liminf_{j \to +\infty} \left(\frac{\log\left(\mu[3\lambda_j(x_0)]\right)}{\log(2^{-j})}\right). \tag{2.1}$$

Proof. By definition of the Hölder exponent,

$$\forall \epsilon > 0,\ \exists r > 0,\ \forall r \leq R, \quad \mu(B(x,r)) \leq r^{H-\epsilon};$$

but $3\lambda_j(x_0) \subset B(x_0, 3\sqrt{d}2^{-j})$, so that

$$\mu(3\lambda_j(x_0)) \leq (3\sqrt{d})^{H-\epsilon} 2^{-j(H-\epsilon)},$$

and it follows that

$$h_\mu(x_0) \leq \liminf_{j \to +\infty} \left(\frac{\log\left(\mu(3\lambda_j(x_0))\right)}{\log(2^{-j})}\right).$$

On the other hand, if $h_\mu(x_0) = H$, then there exists a sequence of balls $B_n = B(x_0, r_n)$ and $\epsilon_n > 0$ such that $r_n \to 0$, $\epsilon_n \to 0$ and $r_n^{H+\epsilon_n} \leq \mu(B_n) \leq r_n^{H-\epsilon_n}$. Let j_n be such that $\frac{1}{2}2^{-j_n} < r_n \leq 2^{-j_n}$; then $B_n \subset 3\lambda_{j_n}(x_0)$ so that $\mu(B_n) \leq \mu(3\lambda_{j_n}(x_0))$, which implies the lower bound for the Hölder exponent. □

Remark: This lemma relies heavily on the fact that the measure μ is nonnegative, and therefore is an increasing set function; indeed, if μ is no more assumed to be a nonnegative measure, then one easily checks that (2.1) is no more valid. This property will play a key-role in the following, therefore we introduce the following terminology.

Definition 5. **Hierarchical set functions:** A function μ defined on a collection of sets is called hierarchical if it is nonnegative and increasing, i.e. satisfies

$$A \subset B \Longrightarrow \mu(A) \leq \mu(B);$$

The first example of multifractal measures studied were multiplicative cascades, which were introduced by B. Mandelbrot for modelling the distribution of energy in fully developed turbulence, see [45]; their mathematical properties were investigated by J.-P. Kahane and J. Peyrière in [36]. The purpose of the multifractal formalism is to derive the spectrum of singularities from global quantities which are effectively computable in practice. Such formulas were initially introduced by G. Parisi and U. Frisch in the context of fully developed turbulence in order to interpret the nonlinearity of the scaling function associated with the increments of the velocity field, see [55]; in the measure setting, and more precisely for invariant measures of dynamical systems they were introduced by T. Halsey, M. Jensen, L. Kadanoff, I. Procaccia and B. Shraiman in [23]. There exists several variants for the mathematical formulation of the multifractal formalism, see [12, 54] for instance, and we present the one given by R. Riedi in [56], because it presents a very good compromise between effective computability and numerical stability, as will be shown below.

2.2. Derivation of the Multifractal Formalism

Since Lemma 2.1 shows that the pointwise Hölder exponents can be derived from the quantities $\mu(3\lambda)$, it is natural to base a multifractal formalism on these quantities. We now assume that μ is compactly supported.

Definition 6. **Measure (or box-aggregated) structure functions and scaling functions:** Let Λ_j denote the collection of dyadic cubes of scale j. The structure function of the measure μ is

$$\Sigma_\mu(p,j) = 2^{-dj} \sum_{\lambda\in\Lambda_j}{}^{*} \mu(3\lambda)^p, \tag{2.2}$$

where the notation Σ^* means that the sum is only taken on the cubes λ such that $\mu(\lambda) \neq 0$.

The scaling function of μ is defined for $p \in \mathbb{R}$ by

$$\eta_\mu(p) = \liminf_{j\to+\infty} \left(\frac{\log\left(\Sigma_\mu(p,j)\right)}{\log(2^{-j})} \right).$$

Let us now show why the spectrum of singularities is expected to be recovered from the scaling function. The definition of the scaling function roughly means that $\Sigma_\mu(p,j) \sim 2^{-\eta_\mu(p)j}$. Let us estimate the contribution to $\Sigma_\mu(p,j)$ of the cubes λ that cover the points of $E_\mu(H)$. Lemma 2.1 asserts that they satisfy $\mu(3\lambda) \sim 2^{-Hj}$; since we need about $2^{-d_\mu(H)j}$ such cubes to cover $E_\mu(H)$, the corresponding contribution roughly is

$$2^{-dj} 2^{d_\mu(H)j} 2^{-Hpj} = 2^{-(d-d_\mu(H)j+Hp)j}.$$

When $j \to +\infty$, the dominant contribution comes from the smallest exponent, so that

$$\eta_\mu(p) = \inf_H (d - d_\mu(H) + Hp). \tag{2.3}$$

Proposition 1. For any compactly supported Borelian measure μ, the scaling function $\eta_\mu(p)$ is a concave function on $\mathbb{R}$.

Remark: We state this concavity result only for the first scaling function that we meet. However, the same proof applies to *all* scaling functions defined in the paper: All of them are concave.

Proposition 1 is a consequence of the following lemma of [24].

Lemma 2.2. *Let $(a_i)_{i=1,\dots,N}$ be a finite collection of positive real numbers. Then the function $\omega : \mathbb{R} \longrightarrow \mathbb{R}$ defined by*

$$\omega(p) = \log\left(\sum_{i=1}^{N} a_i^p\right)$$

is a convex function on $\mathbb{R}$.

Proof of Lemma 2.2**:** The function $\omega(p)$ clearly is a continuous function defined on the whole $\mathbb{R}$. Thus, in order to prove that $\omega(p)$ is convex, it is sufficient to check that

$$\forall p, q \in \mathbb{R}, \qquad \omega\left(\frac{1}{2}(p+q)\right) \leq \frac{1}{2}(\omega(p) + \omega(q)). \tag{2.4}$$

Consider the vectors in $\mathbb{R}^N$

$$A = (a_1^{p/2}, \dots a_N^{p/2}) \quad \text{and} \quad B = (a_1^{q/2}, \dots a_N^{q/2});$$

The Cauchy-Schwartz inequality applied to these vectors yields

$$\sum_{i=1}^{N} a_i^{(p+q)/2} \leq \left(\sum_{i=1}^{N} a_i^p\right)^{1/2} \left(\sum_{i=1}^{N} a_i^p\right)^{1/2}.$$

Taking the logarithm on both sides of this inequality yields exactly (2.4).

Proof of Proposition 1**:** For each j, we will apply Lemma 2.2 to the collection of $(\mu(3\lambda))_{\lambda\in\Lambda_j}$ such that $\mu(\lambda) \neq 0$ (and therefore $\mu(3\lambda) \neq 0$); this collection is finite, since μ is assumed to be compactly supported; it follows that, for any j, the function

$$p \to \log\left(\sum_{\lambda\in\Lambda_j}{}^{*} \mu(3\lambda)^p\right)$$

is convex; therefore, when divided by $\log(2^{-j})$, it is concave; Proposition 1 follows because concavity is preserved under taking infimums and pointwise limits, and therefore under taking liminfs.

Proposition 1 is in agreement with the fact that the right-hand side of (2.3) necessarily is a concave function (as an infimum of a family of linear functions) no matter whether $d_\mu(H)$ is concave or not. However, if the spectrum also is a concave function, then the Legendre transform in (2.3) can be inverted (as a consequence of general result on the duality of convex functions, see for instance Chapter 1.3 of [11]), which justifies the following definition.

Definition 7. A measure μ follows the multifractal formalism for measures if its spectrum of singularities satisfies

$$d_\mu(H) = \inf_{p\in\mathbb{R}}(d - \eta_\mu(p) + Hp). \tag{2.5}$$

Let us now explain the reason for the convention in the definition of Σ^* used in (2.2); indeed structure functions are often defined using $\mu(\lambda)$ instead of $\mu(3\lambda)$, and with the convention that the sum is taken only on the nonvanishing terms. One easily checks that this simpler way to define the structure function actually yields the same values of $\eta_\mu(p)$ for positive p; however, it is no more the case if p is negative for the following reason: It may happen that the cube λ barely intersects the support of the measure; then $\mu(\lambda)$ does not vanish, but may be arbitrarily small and, when raised to a negative power, it will therefore lead to totally unstable computations; the convention for the Σ^* used above turns this drawback: When $\mu(\lambda) \neq 0$, the cube 3λ "widely" intersects the support of the measure.

The derivation exposed above is not a mathematical proof, and the determination of the range of validity of (2.5) (and of its variants) is one of the main mathematical problems concerning the multifractal analysis of measures. Nonetheless, let us stress the fact that the justification of this derivation relies heavily on (2.1), i.e. on the fact that the Hölder exponent of a measure can be estimated from the set of values that it takes on dyadic cubes. The formulation of the multifractal formalism given by (2.5) combines two advantages:

- It is based on quantities that are effectively computable in practice: By contrast with alternative formulas proposed by some mathematicians, the structure function is not based on the consideration of a non-countable collection of coverings of the support of μ.
- The scaling function has "good" mathematical properties, see [38, 56] (for instance it is invariant under bi-Lipschitz deformations of the measure, which is a natural requirement since the spectrum of singularities has this invariance property).

This last remark points the way towards the kind of criteria that we will use in order to select multifractal formalisms: In situations where the validity of several possible multifractal formalisms cannot be justified in all generality, a weaker benchmark in order to compare them will be to determine which ones satisfy invariance properties which are obvious for the spectrum of singularities. Such properties will be reffered to as *robustness properties* in the following. For instance, if the scaling function is defined through wavelet coefficients, we will require that it is independent of the (smooth enough) wavelet basis chosen. Note also that, in several applications, it happens that the spectrum of singularities itself has no direct scientific interpretation and multifractal analysis is only used as a classification tool in order to discriminate between several types of signals; then, one is no more concerned with the validity of (2.5) but only with having its right-hand side defined in a meaningful way; therefore, in such cases, robustness

criteria are the only mathematical requirements which remain in order to compare the pertinence or several possible scaling functions.

3. Multifractal Analysis of Functions: Increments vs. Oscillations

Let us now consider the multifractal analysis of functions. We will start by recalling the corresponding relevant definitions in this context. Multifractal analysis is relevant for functions whose regularity changes from point to point. Therefore we introduce the following notion of pointwise regularity of functions, which is the most widely used. (Note however that in some specific settings, other pointwise regularity exponents of functions can be used: The weak scaling exponent, see Section 6 and the T_u^p exponent, see [32] and references therein.)

Definition 8. **Hölder exponent:** Let $x_0 \in \mathbb{R}^d$ and let $\alpha \geq 0$. A locally bounded function $f : \mathbb{R}^d \to \mathbb{R}$ belongs to $C^\alpha(x_0)$ if there exists a constant $C > 0$ and a polynomial P satisfying $deg(P) < \alpha$ and such that, in a neighbourhood of x_0,

$$|f(x) - P(x - x_0)| \leq C|x - x_0|^\alpha.$$

The Hölder exponent of f at x_0 is

$$h_f(x_0) = \sup\{\alpha : f \in C^\alpha(x_0)\}.$$

Definition 9. **Singularity (or multifractal) spectrum:** Let f be a locally bounded function, and let $E_f(H)$ denote the set of points where the Hölder exponent of f takes the value H. The spectrum of singularities of f (denoted by $d_f(H)$) is the Hausdorff dimension of $E_f(H)$.

Remarks: If $h_f(x_0) < 1$ (which is often the case in signal processing), then the polynomial $P(x - x_0)$ boils down to $f(x_0)$.

The function $h_f(x_0)$ may take the value $+\infty$.

If $0 < h_f(x_0) < 1$, then the Hölder exponent expresses how "spiky" the graph of f is at x_0. For instance the Hölder exponent of $f(x) = |x - x_0|^\alpha$ is α at x_0 and $+\infty$ elsewhere (if α is not an even integer).

3.1. Comparison of Multifractal Formalisms

The numerical determination of the spectrum of singularities of a signal meets the same problem as for measures. The multifractal formalism in this context was introduced by G. Parisi and U. Frisch; they proposed to derive it from the estimation of the L^p norm of increments of the signal [55]: Let us assume that the function f considered is a one-variable function. A structure function based on increments is

$$\Sigma_f^1(p, j) = 2^{-j} \sum_k{}^* \left| f\left(\frac{k+1}{2^j}\right) - f\left(\frac{k}{2^j}\right)\right|^p \tag{3.1}$$

where the $\sum^*$ means that the sum is taken only on non vanishing terms. The scaling function of f is defined for $p \in \mathbb{R}$ by

$$\eta_f^1(p) = \liminf_{j \to +\infty} \left(\frac{\log\left(\Sigma_f^1(p,j)\right)}{\log(2^{-j})} \right). \tag{3.2}$$

The same arguments as for the derivation of the multifractal formalism for measures lead to

$$d_f(H) = \inf_{p \in \mathbb{R}} (1 - \eta_f^1(p) + Hp) \tag{3.3}$$

(recall that we deal with functions of one variable here, so that d is replaced by 1 in this formula). Since (3.1) involves only first order differences, one expects (3.3) to yield the spectrum of singularities of f only if all Hölder exponents take values less than 1.

A first problem which is met here is that there is no formula corresponding to (2.1) and based on increments of f: For instance, if $0 < \alpha < 1$; the function

$$x^\alpha \sin\left(\frac{2\pi}{x}\right)$$

vanishes at the points 2^{-j} but its Hölder exponent at 0 is not $+\infty$ but α. A second problem is that this structure function does not clearly extend to the several dimensional setting. (Which increments should be preferred on a cube?)

Let us now describe an alternative point of view which solves these difficulties. The function f is defined on $\mathbb{R}^d$, and we assume for the sake of simplicity that $0 < h_f(x) < 1$; then the local quantity based on dyadic cubes which is considered is the *oscillation* of f.

Definition 10. **Oscillations:** The oscillation of a function f over a set K is

$$Osc_f(K) = \sup_{x \in K} f(x) - \inf_{x \in K} f(x).$$

The motivation for basing the study of pointwise Hölder regularity on the oscillation is that it is a hierarchical notion in the sense of Definition 5: Indeed, clearly,

$$\mu \subset \nu \Longrightarrow Osc_f(\mu) \leq Osc_f(\nu)$$

and therefore the Hölder exponent at each point can be derived from the knowledge of the oscillation on the countable collection of dyadic cubes, as shown by the following lemma.

Lemma 3.1. *Let $f : \mathbb{R}^d \to \mathbb{R}$ be a locally bounded function satisfying $h_f(x_0) = H$, with $0 < H < 1$; then*

$$H = \liminf_{j \to +\infty} \left(\frac{\log\left(Osc_f(3\lambda_j(x_0))\right)}{\log(2^{-j})} \right). \tag{3.4}$$

This lemma corresponds to Lemma 2.1 in the context of functions; its proof is very similar, so that we leave it. Let us just insist on the fact that it holds because the oscillation is a hierarchical notion, when increments are not.

Following the same arguments as in the case of positive measures, one can base a multifractal formalism on this lemma by introducing the structure function

$$\Sigma_f^2(p,j) = 2^{-dj} \sum_{\lambda\in\Lambda_j}{}^{*} \left(Osc_f(3\lambda)\right)^p ;$$

following in this function setting the idea of [56], the Σ^* means that the sum is restricted to the cubes λ for which $Osc_f(\lambda) \neq 0$. The corresponding *scaling function* of f is

$$\eta_f^2(p) = \liminf_{j\to+\infty} \left(\frac{\log\left(\Sigma_f^2(p,j)\right)}{\log(2^{-j})} \right). \tag{3.5}$$

The same arguments as above lead to the formula

$$d_f(H) = \inf_{p\in\mathbb{R}} (d - \eta_f^2(p) + Hp), \tag{3.6}$$

which we expect to hold only when the spectrum of singularities of f is supported inside the interval $(0,1)$ (i.e. if there are no Hölder exponents larger than 1 in the signal).

3.2. Examples: Brownian Motion and Fractional Brownian Motions

We do not intend to investigate in details the properties of the multifractal formalisms supplied by (3.3) and (3.6), because our main motivation is to focus on wavelet-based formulas, which will be shown to possess better mathematical and numerical properties. However, we will only illustrate them by simple examples supplied by Brownian motion and by fractional Brownian motions (hereafter F.B.M.). Such examples provide us with theoretical and numerical benchmarks on which alternative formalisms can as well be tested.

Recall that Brownian motion is the only stochastic process (or random function) $(B_t)_{t\geq 0}$ with stationary independent increments (i.e. satisfying if $t > s$, $B_t - B_s$ is independent of B_s and has the same law as B_{t-s}) and with continuous sample paths. (Uniquenes is implied by the normalization $E(|B_t|^2) = 1$.)

Fractional Brownian motion of index γ $(0 < \gamma < 1)$ is the only Gaussian random process $(B_t^\gamma)_{t\geq 0}$ satisfying

$$E(|B_t^\gamma - B_s^\gamma|^2) = |t-s|^{2\gamma}.$$

One can show that Brownian motion is precisely $B_t^{1/2}$. The key role played by fractional Brownian motions in signal processing comes from the fact that they supply the most simple one parameter family of stochastic processes with stationary increments, and therefore are widely used in modelling. We will use the following important feature: F.B.M. of index γ can be deduced from Brownian motion by a sample path by sample path fractional integration of order $\gamma - 1/2$ if $\gamma > 1/2$, and by a sample path by sample path fractional derivation of order $(1/2) - \gamma$ if $\gamma < 1/2$.

Recall that, with probability 1, a sample path of Brownian motion has everywhere the Hölder exponent 1/2, so that its spectrum of singularities is

$$\left.\begin{array}{ll} d(H) & = 1 \qquad \text{if } H = \frac{1}{2} \\ & = -\infty \quad \text{else,} \end{array}\right\} \tag{3.7}$$

see for instance [1, 35].

The following theorem illustrates the superiority of the multifractal formalism based on oscillations (as opposed to increments).

Theorem 3.2. *Let B_t be a generic sample path of Brownian motion; then, with probability 1, the multifractal formalism based on increments* (3.3) *yields that a.s.*

$$\begin{array}{ll} \inf\limits_{p\in\mathbb{R}}(d - \eta^1_B(p) + Hp) & = \frac{3}{2} - H \quad \textit{if } H \in \left[\frac{1}{2}, \frac{3}{2}\right] \\ & = -\infty \qquad \textit{else,} \end{array}$$

whereas the multifractal formalism based on oscillations (3.6) *yields the correct spectrum given by* (3.7).

The proof of Theorem 3.2 is given in the Appendix where, in particular, we will show that a.s.

$$\left.\begin{array}{ll} \eta^1_B(p) & = p/2 \qquad \text{if } p \geq -1 \\ & = 1 + 3p/2 \quad \text{else,} \end{array}\right\} \tag{3.8}$$

and a.s. $\forall p \in \mathbb{R}$, the *lim inf* in (3.2) is a true limit, which clearly implies the first part of Theorem 3.2. The fact that this *lim inf* actually is a limit is important when one wants to double check numerically this result in simulation, since, in practice, only true limits can be estimated. Note that we will give another proof of the second part of Theorem 3.2 in the more general setting supplied by F.B.M.; however, we prefer to separate the case of Brownian motion which will be treated completely by elementary means, whereas the F.B.M. case requires the use of more sophisticated tools derived from the so-called *small ball estimates*.

Let us consider a generic sample path of Brownian motion B_t on $[0, 1]$ (by scaling invariance, the particular choice of interval is irrelevant). The increments $B_{(k+1)/2^j} - B_{k/2^j}$ are I.I.D. random variables of common law $2^{-j/2}\chi_{j,k}$, where the $\chi_{j,k}$ are standard Gaussians; thus, in order to estimate (3.1) for Brownian motion, we have to estimate the order of magnitude of

$$A(p, j) = \sum_{k=1}^{2^j} |\chi_{j,k}|^p, \tag{3.9}$$

and the structure function will be

$$\Sigma^1_B(p, j) = 2^{-j(1+p/2)} A(p, j).$$

(With probability one, a non-degenerate Gaussian random variable does not vanish so that, in all computations that will be performed in this section and in the following concerning Brownian motion or F.B.M., the $\sum^*$ sums are just usual sums.)

Note at this point that the problem of estimation of the $A(p,j)$ is not the same as estimating moments of order p of a Gaussian variable, since the computations here are performed sample path by sample path, and not in expectation; indeed, if such a process models a given observed signal, then the "rule of the game" is that one sample path is observed, and not averages over a large number of realizations. This remark is particularly relevant fo large negative values of p where the two approaches lead to different results (moments diverge if $p < -1$, whereas the order of magnitude of $A(p,j)$) can always be estimated for any negative value of p).

Let us now consider the fractional Brownian case. With probability 1, a sample path of F.B.M. of order β has everywhere the Hölder exponent β so that its spectrum of singularities is

$$\left.\begin{array}{ll} d(H) & = 1 \quad \text{if } H = \beta \\ & = -\infty \quad \text{else,} \end{array}\right\} \tag{3.10}$$

see for instance [1, 35].

Theorem 3.3. *Let $\beta \in (0,1)$ and $B_\beta(t)$ be a generic sample path of F.B.M. of order β; then, with probability 1,*

$$\forall p \in \mathbb{R}, \quad \eta^2_{B_\beta}(p) = \beta p \tag{3.11}$$

and the lim inf *in* (3.5) *is a true limit.*

The multifractal formalism based on oscillations (3.6) *yields the correct spectrum* (3.10) *for the F.B.M..*

Proof of Theorem 3.3**:** First we recall a well-known result concerning the uniform modulus of continuity of the sample paths of F.B.M. of order β [35]: With probability 1, there exists $C > 0$ such that

$$\sup_t \left(\sup_{h \le 1} \frac{|B_\beta(t+h) - B_\beta(t)|}{|h|^\beta |\log h|} \right) \le C$$

It follows that, with probability 1, all oscillations

$$Osc_{B_\beta}(I_{j,k}) = \sup_{s \in I_{j,k}} B_\beta(s) - \inf_{s \in I_{j,k}} B_\beta(s)$$

are bounded by $CN^{-\beta} \log N$ (where $N = 2^j$ is the number of intervals considered).

'Small ball estimates' for a random process X_t are concerned with the estimation of

$$\mathbb{P}\left(\sup_{0 \le s \le t} |X_s| \le \epsilon \right)$$

Lower bounds for the oscillation are a consequence of the small ball estimates for the F.B.M.; indeed

$$\sup_{0 \le s \le t} B_\beta(s) - \inf_{0 \le s \le t} B_\beta(s) \le 2 \sup_{0 \le s \le t} |B_\beta(s)|$$

and, by Theorem 2.1 of [53], if $\epsilon \leq t^{\beta}$,

$$\mathbb{P}\left(\sup_{0\leq s\leq t}|B_{\beta}(s)|\leq\epsilon\right)\leq\exp\left(-Ct\epsilon^{-1/\beta}\right).$$

Since all oscillations have the same law it follows that, for a given N, all oscillations $Osc_{B_\beta}(I_{j,k})$ are larger than $2N^{-\beta}(\log N)^{-2\beta}$ with probability at least $1-N\exp(-C(\log N)^2)$. As above, a direct application of the Borel-Cantelli Lemma shows that the multifractal formalism based on oscillations yields the correct spectrum (3.6) for a.e. sample path of the F.B.M.

As mentioned above, our purpose in this section was only to illustrate the two multifractal formalisms based on increments and oscillations on the particular examples provided by Brownian motion and F.B.M.. However, the proof of Theorem 3.3 clearly shows that results on the multifractal formalism based on oscillations immediately follow from small ball estimates for the process considered (such estimates for Gaussian processes can be found in [41, 42, 53] for instance), so that general results of validity of the multifractal formalism supplied by (3.6) could clearly be easily proved for general Gaussian processes.

4. Multifractal Analysis of Functions: Wavelet Based Formulas

Lemma 3.1 can be generalized to higher Hölder exponents by using higher order differences in the definition of the oscillation, see [29], however, it leads to rather complicated quantities for the computation of structure functions, and it presents strong instabilities under the presence of noise. Therefore, once wavelet techniques were available, alternative formulas were proposed; they were based either on the continuous wavelet transform of the signal (by Arneodo et al., see [4, 6] and references therein) or on its coefficients on an orthonormal wavelet basis, see [27, 29] and references therein. The starting point of all these methods is a wavelet characterization of the Hölder exponent. Let us start by recalling basic definitions concerning wavelet expansions. Though formulas based on the discrete wavelet coefficients were introduced later than those based on the continuous wavelet transform, we start by describing the discrete ones, since they are in spirit very close to the dyadic partitionings we introduced in the measure setting, and they pave the way to the wavelet leaders technique of Section 5.

4.1. Wavelet Bases

We now recall the definition of wavelet bases. Let $r \in \mathbb{N}$; an r-smooth wavelet basis of $\mathbb{R}^d$ is composed of 2^d-1 wavelets $\psi^{(i)}$ which belong to C^r and satisfy the following properties:

- $\forall i,\ \ \forall\alpha$ such that $|\alpha|\leq r,\quad \partial^{\alpha}\psi^{(i)}$ has fast decay,
- The set of functions $2^{dj/2}\psi^{(i)}(2^jx-k)$, $j\in\mathbb{Z}$, $k\in\mathbb{Z}^d$, $i\in\{1,...,2^d-1\}$ is an orthonormal basis of $L^2(\mathbb{R})^d$.

The wavelet basis is ∞-smooth if it is r-smooth for any $r \in \mathbb{R}$, in which case all wavelets $\psi^{(i)}$ belong to the Schwartz class.

Thus any function f in $L^2(\mathbb{R}^d)$ can be written

$$f(x) = \sum c_{j,k}^{(i)} \psi^{(i)}(2^j x - k) \tag{4.1}$$

where

$$c_{j,k}^{(i)} = 2^{dj} \int f(x) \psi^{(i)}(2^j x - k) dx.$$

(Note that, in (4.1), wavelets are not normalized for the L^2 norm but for the L^∞ norm, which avoids an extra factor $2^{dj/2}$ in all mathematical results concerning Hölder regularity.) Let us note at this point that it is often relevant to use a slight generalization based on biorthogonal wavelets, the definition of which we now recall.

A *Riesz basis* of an Hilbert space H is a collection of vectors (e_n) such that the finite linear expansions $\sum_{n=1}^N a_n e_n$ are dense in H and

$$\exists C, C' > 0 : \quad \forall N, \forall a_n, \quad C \sum_{n=1}^N |a_n|^2 \leq \left|\left| \sum_{n=1}^N a_n e_n \right|\right|_H^2 \leq C' \sum_{n=1}^N |a_n|^2.$$

Two collections of functions (e_n) and (f_n) form *biorthogonal bases* if each collection is a Riesz basis, and if $\langle e_n | f_m \rangle = \delta_{n,m}$. When such is the case, any element $f \in H$ can be written

$$f = \sum_{n=1}^{\infty} \langle f | f_n \rangle e_n.$$

Biorthogonal wavelet bases are couples of bases of the form $2^{dj/2} \tilde{\psi}^{(i)}(2^j x - k)$ and $2^{dj/2} \psi^{(i)}(2^j x - k)$, $j \in \mathbb{Z}$, $k \in \mathbb{Z}^d$, $i \in \{1, ..., 2^d - 1\}$ which are biorthogonal (for the L^2 norm).

The relevance of biorthogonal wavelet bases is due to two reasons: On one hand their construction is more flexible and, for instance, allows for wavelets which have some symmetry properties, which is an important requirement in image processing, see [15]; on the other hand, for theoretical purposes, this setting is often more adapted to derive the properties of some random processes; we will see the example of Brownian motion and of F.B.M. in Sections 4.3 and 5.4 where a decomposition on well chosen biorthogonal wavelet bases allows to decorrelate the wavelet coefficients of these processes (the wavelet coefficients become independent random variables), and therefore greatly simplifies their analysis.

Wavelets will be indexed by dyadic cubes as follows: Since i takes $2^d - 1$ values, we can consider that i takes values among all dyadic subcubes λ_i of $[0,1)^d$ of width $1/2$ except for $[0, 1/2)^d$; thus, the set of indices (i, j, k) can be relabelled using dyadic cubes as follows: λ denotes the cube $\{x : \ 2^j x - k \in \lambda_i\}$; we note $\psi_\lambda(x) = \psi^{(i)}(2^j x - k)$ (an L^∞ normalization is used), and $c_\lambda = 2^{dj} \int \psi_\lambda(x) f(x) dx$. We will use the notations $c_{j,k}^{(i)}$ or c_λ indifferently for wavelet coefficients. Note that the index λ gives an information on the localization and the scale of the corresponding wavelet; for instance, if the wavelets $\psi^{(i)}$ are compactly supported

then $\exists C : supp(\psi_\lambda) \subset C\lambda$ where $C\lambda$ denotes the cube of same center as λ and C times larger; thus the indexation by the dyadic cubes is more than a simple notation: The wavelet ψ_λ is "essentially" localized around the cube λ. Finally, Λ_j will denote the set of dyadic intervals λ of width 2^{-j}.

4.2. Hölder Regularity and Derivation of the Multifractal Formalism

The wavelet characterization of the Hölder exponent requires the following regularity hypothesis, which is slightly stronger than continuity.

Definition 11. **Uniform Hölder function:** A function f is a uniform Hölder function if there exists $\epsilon > 0$ such that $f \in C^\epsilon(\mathbb{R}^d)$, i.e.

$$\exists C > 0 \quad \text{such that } \forall x, y \in \mathbb{R}, \ |f(x) - f(y)| \leq C|x - y|^\epsilon.$$

The following proposition was proved in [25].

Proposition 2. Let $\alpha > 0$. If f is $C^\alpha(x_0)$, then there exists $C > 0$ such that the wavelet coefficients of f satisfy

$$\forall j \geq 0, \qquad |c_{j,k}| \leq C2^{-\alpha j}(1 + |2^j x_0 - k|)^\alpha. \tag{4.2}$$

Conversely, if (4.2) holds and if f is uniform Hölder, then $\exists C > 0$ and a polynomial P satisfying $deg(P) < \alpha$ and such that, in a neighbourhood of x_0,

$$|f(x) - P(x - x_0)| \leq C|x - x_0|^\alpha |\log(1/|x - x_0|).$$

The *influence cone above* x_0 is the set of dyadic cubes which are of the form $\lambda_j(x_0)$ and their $3^d - 1$ immediate neighbours at the same scale, i.e. the dyadic cubes λ of scale j such that $dist(\lambda, \lambda_j(x_0)) = 0$. Note that it is composed of the cubes of scale j included in $3\lambda_j(x_0)$. The regularity criterium supplied by Lemma 2 has often been loosely interpreted as stating that the wavelet coefficients decay like $2^{-\alpha j}$ in the influence cone; indeed, it is the case for *cusp-like* singularities which behave like

$$A + B|x - x_0|^\alpha$$

in the neighbourhood of x_0; such functions are characterized by the fact that there are no strong oscillations in the neighbourhood of x_0. Let us assume for the moment that, indeed, the function considered exhibits only this type of pointwise singularities, and therefore, the Hölder exponent at x_0 is given by

$$h_f(x_0) = \lim_{j \to +\infty} \left(\frac{\log(|c_{\lambda_n}|)}{\log(2^{-j_n})} \right), \tag{4.3}$$

where the λ_n are dyadic cubes of scale j_n in the influence cone above x_0. Following the same arguments as above, we introduce the structure function

$$W_f^1(p, j) = 2^{-dj} \sum_{\lambda \in \Lambda_j}{}^* |c_\lambda|^p, \tag{4.4}$$

where the $\sum^*$ means here that the sum is taken on the nonvanishing wavelet coefficients. The corresponding *scaling function* of f is

$$\zeta_f^1(p) = \liminf_{j\to+\infty} \left(\frac{\log\left(W_f^1(p,j)\right)}{\log(2^{-j})} \right).$$

One is therefore led to the following multifractal formalism

$$d_f(H) = \inf_{p\in\mathbb{R}} (d - \zeta_f^1(p) + Hp). \tag{4.5}$$

Several criticisms can be addressed to this multifractal formalism:

1. It implicitely assumes that the only singularities met are *cusp-like* singularities. This is of course an assumption which is impossible to check on a signal. Let us briefly mention other types of singularities which can be met. On the opposite from cusp singularities are the *chirp-like* singularities which display very strong oscillations in the neighbourhood of x_0, such as

$$C_{\alpha,\beta}(x) = |x - x_0|^\alpha \sin\left(\frac{1}{|x - x_0|^\beta}\right), \tag{4.6}$$

   where $\alpha > 0$ and $\beta > 0$. Such functions are counterexamples to (4.3); indeed their wavelet coefficients display a much stronger decay in the influence cone: They decay faster than 2^{-Nj} for any $N > 0$. They have indeed large wavelet coefficients which make (4.2) optimal for them too, but these large coefficients are situated far away from the influence cone: They correspond to indices (j,k) such that $|2^j x_0 - k| \sim 2^{-j/(1+\beta)}$, see [33] for precise statements. This is illustrated numerically in Fig. 1, top row.
2. The quantity

$$\liminf_{j\to+\infty} \left(\frac{\log\left(|c_{\lambda_j(x_0)}|\right)}{\log(2^{-j})} \right) \tag{4.7}$$

   on which the corresponding exponent is based does not define a quantity which is independent of the wavelet basis chosen.
3. Wavelet coefficients can be extremely small by chance, so that we expect the structure function defined in (4.4) to be completely unstable for $p < 0$.
4. One can show that the scaling function $\zeta_f^1(p)$ is independent of the (smooth) wavelet basis chosen when $p > 0$ but it is not the case any longer if $p < 0$.

We will address these problems in a detailed way in the following: In Section 5 we will introduce a multifractal formalism based on alternative quantities that will have the required robustness properties; and in Section 6 we will show that the wavelet-based formula (4.5) actually is a multifractal formalism adapted (for $p > 0$) to another exponent, the *weak-scaling exponent*, and we will extend this multifractal formalism in a robust way for $p < 0$.

4.3. Examples: Brownian Motion and Fractional Brownian Motions

We now show that, even when the signal only displays cusp-like singularities, then (4.5) does not necessarily yield the right spectrum of singularities. This pathology already appears on the particularly striking examples supplied by the sample paths of Brownian motion, and of F.B.M. (we treat only the F.B.M. case since Brownian motion is the subcase corresponding to the Hurst exponent $\beta = 1/2$).

An important result of Paul Lévy states that, if (e_n) is an orthogonal basis of $L^2(\mathbb{R})$, and if f_n denotes a primitive of e_n, then Brownian motion can be decomposed on the f_n in the following particularly simple way

$$B_t = \sum \chi_n (f_n(t) - f_n(0))$$

where the χ_n are independent identically distributed (i.i.d.) standard Gaussians. Let us apply this result using an orthonormal wavelet basis for the e_n. A primitive of ψ is supplied by the function ψ_1 whose Fourier transform is given by $\hat{\psi}_1(\xi) = \hat{\psi}(\xi)/\xi$. The primitive of $2^{j/2}\psi(2^j x - k)$ is $2^{-j/2}\psi_1(2^j x - k)$, therefore

$$B_t = \sum_{j,k} \chi_{j,k}(\psi_{j,k}(t) - \psi_{j,k}(-k)).$$

The contributions of the terms corresponding to $j < 0$ and the constant terms belongs to C^∞ (if the wavelet used is C^∞), therefore one can write

$$B_t = \sum_{j \geq 0,k} \chi_{j,k}\psi_{j,k}(t) + R(t),$$

where $R(t)$ is a C^∞ process. We can apply the same argument in order to obtain a wavelet decomposition of F.B.M. since, as mentioned already, F.B.M. of index γ can be deduced from Brownian motion by a sample path by sample path fractional integration of order $\gamma - 1/2$ if $\gamma > 1/2$, or a fractional derivation of order $(1/2) - \gamma$ if $\gamma < 1/2$. (We refer the reader to [2, 51] where the wavelet decomposition of F.B.M. is investigated in details and, in particular, the remainders $R(t)$ and $R^\alpha(t)$ are given an explicit form which allows for accurate simulations of the long range dependence.) Let

$$\hat{\psi}_\alpha(\xi) = \frac{1}{|\xi|^\alpha}\hat{\psi}(\xi) \tag{4.8}$$

(ψ_α is the fractional integral of ψ of order α). If the wavelet ψ has enough vanishing moments, then ψ_α is a wavelet and the $2^{j/2}\psi_\alpha(2^j x - k)$ and the $2^{j/2}\psi_{-\alpha}(2^j x - k)$ form biorthogonal bases, see [29, 49]; the point of using these bases in order to analyze F.B.M. is that, as a consequence of the previous remarks, the coefficients of F.B.M. are decorrelated on it. More precisely, if $t \in [0, 1]$ then

$$B_\beta(t) = \sum_{j=0}^{\infty} \sum_{k \in \mathbb{Z}} 2^{-\beta j} \xi_{j,k}\, \psi_{\beta+1/2}(2^j t - k) + R(t) \tag{4.9}$$

where $R(t)$ is a C^∞ random process, and the $\xi_{j,k}$ are I.I.D. standard centered Gaussians, see [2, 51]. Therefore

$$W^1_{B_\beta}(p,j) = 2^{-\beta p j} \sum_{k=1}^{2^j} |\chi_{j,k}|^p,$$

which, up to the factor $2^{-(1+\beta p)j}$ has exactly the same expression as $A(p,j)$ defined by (3.9). Therefore the computation performed in Section 3.2 yields the following result.

Proposition 3. Let $B_\beta(t)$ be a generic sample path of F.B.M. of order $\beta \in (0,1)$, and assume that the wavelet used is C^2. Then, with probability 1, the wavelet multifractal formalism (4.5) applied to $B_\beta(t)$ yields

$$\left.\begin{array}{ll} \inf\limits_{p\in\mathbb{R}} (d - \zeta^1_{B_\beta}(p) + Hp) & = \beta + 1 - H \quad \text{if } H \in [\beta, \beta+1] \\ & = -\infty \qquad\quad \text{else,} \end{array}\right\} \tag{4.10}$$

and the lim inf in the definition of the scaling function $\zeta^1_{B_\beta}(p)$ is a limit.

5. Wavelet Leaders

In this section, we exhibit quantities d_λ called the wavelet leaders which are based on the wavelet coefficients, and such that the formula corresponding to (4.7) yields an exponent which is independent of the wavelet basis chosen, and which, under a very mild uniform regularity assumption, actually is the Hölder exponent. We investigate the properties of the multifractal formalism based on these quantities and, in particular, the stability of the structure function for $p < 0$.

5.1. Pointwise Hölder Regularity Conditions

We saw that the Hölder exponent of a function f is not necessarily given by (4.7). Another indication that (4.7) is not the right quantity to consider in the derivation of the multifractal formalism is that the necessity to base a multifractal formalism on a quantity which is "hierarchical" (in the sense of Definition 5) was put into light several times in previous sections. A simple quantity which is larger than $|c_\lambda|$ and is hierarchical is supplied by the wavelet leaders, which are defined as follows.

Definition 12. **Wavelet Leaders:** Let f be a bounded function; the wavelet leaders of f are

$$d_\lambda = \sup_{\lambda' \subset 3\lambda} |c_{\lambda'}|. \tag{5.1}$$

If x_0 is a given point, then

$$d_j(x_0) = d_{\lambda_j(x_0)}.$$

Note that since $f \in L^\infty$,

$$|c_\lambda| \le 2^{dj} \int |f(x)||\psi_\lambda(x)|dx \le C \sup |f(x)|,$$

so that $\forall\lambda$, $d_\lambda \leq C \parallel f \parallel_\infty$, and therefore the wavelet leaders are finite. We will usually assume in the following that the function studied is bounded, so that the wavelet leaders are finite. Note however that wavelet leaders are well defined under the weaker assumption that f belongs to the *Bloch space* which coincides with the Besov space $B^{0,\infty}_\infty$ and is characterized by the condition

$$\exists C > 0, \ \ \forall\lambda, \ \ |c_\lambda| \leq C$$

(see Chap. 6.8 of [49] and references therein for properties of this function space).

The following proposition allows to characterize the pointwise regularity by a decay condition of the $d_j(x_0)$ when $j \to +\infty$.

Proposition 4. Let $f \in L^\infty(\mathbb{R}^d)$ and $\alpha > 0$. The condition

$$\forall j \geq 0, \qquad d_j(x_0) \leq C 2^{-\alpha j} \tag{5.2}$$

is equivalent to (4.2). (This is illustrated numerically in Fig. 1, bottom row.)

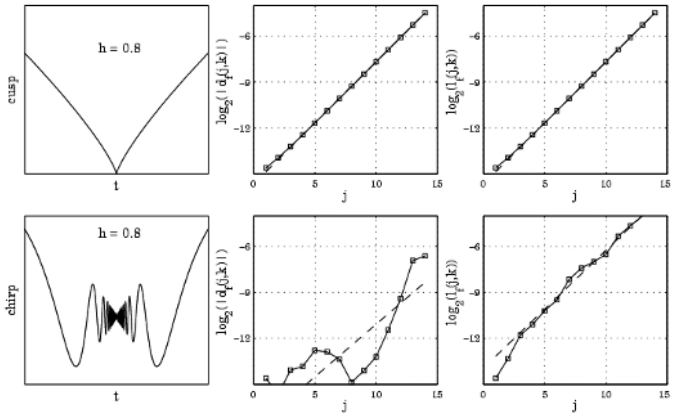

FIGURE 1. **Cusp vs Chirp singularity.** Left column, cusp singularity $|x - x_0|^h$ (top row) versus chirp singularity (bottom row) $|x - x_0|^h \sin(\frac{1}{|x-x_0|^\beta})$ with $\beta = 1$. Central column, wavelet coefficients, c_λ for λ such that $2^{-j}k = t_0$, right column, wavelet leaders, d_λ for λ such that $2^{-j}k = t_0$. One sees that while the decrease along scales j of the wavelet coefficients correctly characterizes the Hölder exponent cusp singularities, it does not for chirp-type ones. The decrease along scales j of the wavelet leaders do accurately characterize all type of singularities, as in Eq. 5.2.

Proof of Proposition 4: We first prove that (4.2) implies (5.2). Let $j \geq 0$ and assume that $\lambda' \subset 3\lambda_j(x_0)$. Since

$$|c_{\lambda'}| \leq C2^{-\alpha j'}(1 + |2^{j'}x_0 - k'|)^{\alpha}, \quad j' \geq j-1 \quad \text{and} \quad |k'2^{-j'} - x_0| \leq 4d2^{-j},$$

it follows that $|c_{\lambda'}| \leq C2^{-\alpha j}$, so that $d_j(x_0) \leq C2^{-\alpha j}$.

Let us now prove the converse result. If λ' is a cube of side $2^{-j'}$, denote by λ $(= \lambda(\lambda'))$ the dyadic cube defined by

- If $\lambda' \subset 3\lambda_{j'}(x_0)$, then $\lambda = \lambda_{j'}(x_0)$,
- else, if $j = \sup\{l : \lambda' \subset 3\lambda_l(x_0)\}$, then $\lambda = \lambda_j(x_0)$, and it follows that

$$2^{-j-1} \leq |k'2^{-j'} - x_0| \leq 4d2^{-j}.$$

In the first case, by hypothesis, $|c_{\lambda'}| \leq d_{j'}(x_0) \leq C.2^{-\alpha j'}$. In the second case,

$$|c_{\lambda'}| \leq d_j(x_0) \leq C2^{-\alpha j} \leq C|x_0 - k'2^{-j'}|^{\alpha},$$

so that (4.2) holds in both cases.

Note that, as a consequence of Proposition 4 and Theorem 3 of [26], it follows that Condition (5.2) is independent of the wavelet basis which is chosen, if the wavelets are r-smooth with $r > \alpha$.

5.2. Multifractal Formalisms

The reader will have noticed the striking similarity between Lemma 2.1 and Proposition 4: Both provide a characterization of pointwise Hölder regularity by a condition on hierarchical quantities considered in the influence cone. Therefore one can derive the multifractal formalism for functions exactly in the same manner as was done previously for measures. It is therefore natural to use a structure function based on wavelet leaders, i.e. which is of the form

$$2^{-dj} \sum_{\lambda \in \Lambda_j}{}^{*} (d_\lambda)^p;$$

however, obtaining the correct definition for the $\sum^*$ in this setting is much more delicate than in the measure setting of Section 2; the problem for measures was to find a way to keep the contribution of a cube in the structure function only if it did include an important amount of the support of the measure. When one tries to reproduce this feature in the wavelet setting one meets three problems:

- The size of the support of the wavelet changes with the wavelet used, so that formulas based on the consideration that the support of the function analyzed intersects "widely" the support of the wavelet cannot be universal, but have to be taylored to the particular wavelet basis used.
- Such considerations become irrelevant if the support of the wavelet is the whole $\mathbb{R}^d$, which is the case if the wavelet used belongs to the Schwartz class.
- If the wavelets used have a finite smoothness and a finite number of vanishing moments, then they cannot analyze smoother parts of the function. If such smoother parts occur on a set of dimension d, the multifractal formalism can yield incorrect results for the largest Hs (which may be infinite); since

the multifractal formalism yields a concave function, this error can make the whole decreasing part of the spectrum wrong (which is the part obtained for $p < 0$ in the Legendre transform formula).

We are confronted with a deadlock: $\sum^*$ formulas make sense only if the wavelet is compactly supported, hence has a finite smoothness, in which case, the $p < 0$ part of the scaling function may be completely unstable, since it can be changed by adding an arbitrarily small and smooth perturbation on the function.

Therefore, there is no universal formula without any drawback; However, this discussion shows that one may use the following "rule of thumb": On one hand, it is reasonable to use a $\sum^*$ formula based on compactly supported wavelets when analyzing compactly supported functions which are not arbitrarily smooth inside their support; on the other hand, one should rather use wavelets in the Schwartz class when analyzing functions with full support, in which case wavelet leaders are not expected to vanish (this could only happen for "toy examples", i.e. for artificial functions which are defined through their wavelet coefficients on the precise wavelet basis which is used for the analysis); and, in that case, we do not need to eliminate vanishing wavelet leaders in the definition of the structure function. Therefore, we separate two cases depending on whether the wavelets are compactly supported or belong to the Schwartz class.

First case: Compactly supported wavelets

Definition 13. **Leader based Multifractal Formalism 1:** Let f be a uniform Hölder function and assume that the wavelets used are compactly supported. The extended wavelet leaders are

$$e_\lambda = \sup_{supp(\psi_{\lambda'}) \subset 3supp(\psi_\lambda)} |c_{\lambda'}|,$$

where $supp(\psi_\lambda)$ stands for the support of the wavelet ψ_λ, i.e., the closure of the set of points x such that $\psi_\lambda(x) \neq 0$.
The wavelet structure function $W_f^2(p, j)$ is defined for $p \in \mathbb{R}$ by

$$W_f^2(p, j) = 2^{-dj} \sum_{\lambda \in \Lambda_j}^{*} (e_\lambda)^p,$$

where the $\sum^*$ means that the sum is taken on all λ' such that

$$\sup_{supp(\psi_{\lambda'}) \subset supp(\psi_\lambda)} |c_{\lambda'}| \neq 0.$$

The scaling function of f is defined by

$$\zeta_f^2(p) = \liminf_{j \to +\infty} \left(\frac{\log\left(W_f^2(p, j)\right)}{\log(2^{-j})} \right).$$

Second case: Wavelets in the Schwartz class

Definition 14. **Leader based Multifractal Formalism 2:** Let f be a uniform Hölder function. The wavelet structure function $W_f^3(p,j)$ is defined for $p \in \mathbb{R}$ by

$$W_f^3(p,j) = 2^{-dj} \sum_{\lambda \in \Lambda_j} (d_\lambda)^p.$$

The scaling function of f is defined by

$$\zeta_f^3(p) = \liminf_{j \to +\infty} \left(\frac{\log\left(W_f^3(p,j)\right)}{\log(2^{-j})} \right).$$

Note that we can consider $\zeta_f^3(p)$ even if the wavelets do not belong to the Schwartz class.

In both cases, the same argument as above yields the following multifractal formalism based on the wavelet leaders

$$d_f(H) = \inf_{p \in \mathbb{R}} (d - \zeta_f(p) + Hp), \tag{5.3}$$

where $\zeta_f(p)$ stands either for $\zeta_f^2(p)$ or $\zeta_f^3(p)$ depending on the type of wavelet basis which is used.

Numerically, the determination of the scaling functions $\zeta_f^2(p)$ or $\zeta_f^3(p)$ requires the knowledge of the wavelet coefficients on more scales than the function $\zeta_f^1(p)$; indeed, in order to be trustable, the computation of a wavelet leader at a given scale requires the computation of the wavelet coefficients on several scales below. In the second case, the heuristic argument used in the derivation of the multifractal formalism is backed by mathematical results: It is proved in [29] that the scaling function $\zeta_f^3(p)$ is independent of the wavelet basis (in the Schwartz class) which is chosen and, if f is a uniform Hölder function, then

$$d_f(H) \leq \inf_{p \in \mathbb{R}} (d - \zeta_f^3(p) + Hp). \tag{5.4}$$

One pitfall of using (5.3) in applications is that, as mentioned already, the right-hand side of (5.3) is, by construction, a concave function. Since, in practice, using a Legendre transform of a scaling function is the only way to estimate numerically spectrums of singularities of signals, this may give the (perhaps erroneous) feeling that all spectrums of singularities of signals are concave functions, and therefore that mathematical models that yield concave spectrums are the only relevant ones (this remark also applies to all the variants of the multifractal formalisms that were mentioned above). Let us just mention at this point very simple models of random wavelet series with wavelet coefficients correlated through a Markov chain on the dyadic tree; such models have been proposed to model signals and images; however, they have recently been shown to yield non concave spectrums, see [19] and references therein.

5.3. Robustness for Wavelet-Based Quantities

Let us be more specific concerning the requirement of independence of the wavelet basis, since it is related to our previous discussion on robustness criteria. The scaling functions ζ_f^2 and ζ_f^3 are defined by conditions on the wavelet coefficients. Since the left-hand side of (5.3) is defined independently of any wavelet basis, the multifractal formalism will have no chance to hold if the scaling function depends on the wavelet basis chosen. Naïvely, in order to check this independence, one should first dispose of a description of all possible wavelet bases, which is not realistic. In practice, one checks a stronger (but simpler) requirement which implies that the scaling function considered has some additional stability; indeed, the matrix of the operator which maps an orthonormal wavelet basis onto another orthonormal wavelet basis is invariant under the action of infinite matrices which belong to algebras $\mathcal{M}^\gamma$ that are defined below; therefore, one can check that the scaling function is also invariant under this action, which is the purpose of Corollary 1 and Proposition 6.

Definition 15. **Algebras $\mathcal{M}^\gamma$:** Let $\gamma > 0$; an infinite matrix $A(\lambda, \lambda')$ indexed by the dyadic cubes belongs to $\mathcal{M}^\gamma$ if

$$|A(\lambda, \lambda')| \leq \frac{C\, 2^{-(\frac{d}{2}+\gamma)(j-j')}}{(1+(j-j')^2)(1+2^{\inf(j,j')} dist(\lambda, \lambda'))^{d+\gamma}}.$$

Matrices of operators which map a smooth wavelet basis onto another one belong to these algebras. It is proved in [49] that the matrix which maps an r-smooth wavelet basis onto another r-smooth wavelet basis belongs to $\mathcal{M}^\gamma$ for any $\gamma < r$, and that the spaces $\mathcal{M}^\gamma$ are algebras. More generally, matrices (on wavelet bases) of pseudodifferential operators of order 0, such as the Hilbert transform in dimension 1, or the Riesz transforms in higher dimensions, belong to these algebras (for any $\gamma > 0$ if the wavelets are C^∞). We denote by $\mathcal{O}p(\mathcal{M}^\gamma)$ the space of operators whose matrix on a wavelet basis belongs to $\mathcal{M}^\gamma$. The following result is proved in [29].

Proposition 5. Let $p > 0$ and $A \in \mathcal{O}p(\mathcal{M}^\gamma)$ for a $\gamma > 0$. If $\zeta_f^3(p) < p\gamma$, then

$$\zeta_{A(f)}^3(p) \geq \zeta_f^3(p).$$

Applying this proposition to the operator that maps an r-smooth wavelet basis onto another r-smooth wavelet basis, and also to the inverse of this operator, shows that, under the hypotheses of Proposition 5, the scaling function $\zeta_f^3(p)$ is independent of the wavelet basis.

Another important remark is that $\zeta_f^2(p)$ and $\zeta_f^3(p)$ clearly coincide as long as $p > 0$ and $\zeta_f^3(p) < pr$. This follows from the fact, that by definition of d_λ and e_λ, one has,

$$W_f^3(p, j) \leq W_f^2(p, j) \leq 3^d W_f^3(p, j).$$

Thus the following result holds.

Corollary 1. Assume that the wavelet basis used is r-smooth; if $p > 0$ and $\zeta_f^3(p) < pr$, then the scaling function $\zeta_f^3(p)$ is independent of the wavelet basis used and $\zeta_f^2(p) = \zeta_f^3(p)$.

Note that, if the wavelets belong to the Schwartz class, then the previous result holds on the whole range $p > 0$.

Unfortunately, the case $p < 0$ leads to strongly different conclusions (and therefore justifies the introduction of two different scaling functions). In order to state the results in that case, we will need here a different requirement than the one used in Proposition 5.

Definition 16. **Quasidiagonal infinite matrix:** An infinite matrix $A(\lambda, \lambda')$ is quasidiagonal if A is invertible, and if A and A^{-1} belong to $\mathcal{M}^\gamma$ for any $\gamma > 0$.

Let $C = \{c_\lambda\}_{\lambda \in \Lambda}$ be a collection of coefficients indexed by the dyadic cubes. A property $\mathcal{P}$ is **robust** if the following condition holds: If $\mathcal{P}(C)$ holds then, for any quasidiagonal operator $\mathbf{M}$, $\mathcal{P}(\mathbf{M}C)$ holds.

The matrix of an operator which maps a wavelet basis in the Schwartz class onto another one is quasidiagonal, see [49]. Therefore, in order to check that a condition defined on the wavelet coefficients is independent of the wavelet basis (in the Schwartz class) used, one can check the stronger property that it is invariant under the action of quasidiagonal matrices. The following result is proved in [29].

Proposition 6. If $p < 0$, then $\zeta_f^3(p)$ is independent of the wavelet basis in the Schwartz class which is used.

5.4. Illustrations and Examples

5.4.1. Fractional Brownian Motion. The following result shows that both multifractal formalisms based on wavelet leaders yield the correct spectrum of singularities for F.B.M.

Theorem 5.1. *Let $\beta \in (0,1)$ and $B_\beta(t)$ be a generic sample path of F.B.M. of order β. Assume that the wavelet used belongs to the Schwartz class, then, with probability 1,*

$$\forall p \in \mathbb{R}, \quad \zeta_{B_\beta}^3(p) = \beta p \tag{5.5}$$

and the liminfs in the definitions of the scaling functions are true limits; the wavelet leaders based multifractal formalism (5.3) *yields the correct spectrum* (3.10).

Proof of Theorem 5.1**:** First, we note that the previous robustness results of Section 5.3 for $\zeta_f^3(p)$ imply that the results do not depend of the wavelet basis in the Schwartz class which is used, and, in particular, we can use the biorthogonal basis generated by the wavelets (4.8) which leads to the decomposition (4.9). Then

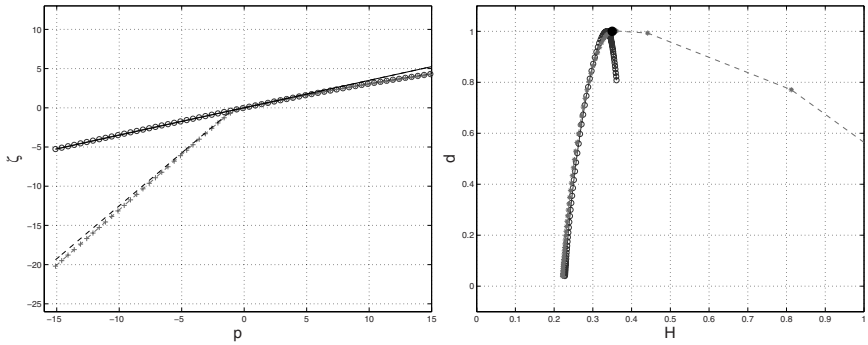

FIGURE 2. **Fractional Brownian Motion.** From a single sample path of fractional Brownian motion synthetized numerically (using the Circulant embedding Matrix technique[8]) with $\beta = 0.35$ (number of sampling points: 2^{18}), one obtains: Left, solid (black) line: theoretical $\zeta_f(p)$, dashed (black) line corresponds to Eq. 3.8, solid (blue) line with 'o': $\zeta_f^3(p)$, dashed (red) line with '+': $\zeta_f^1(p)$. Right, large full (black) dot, theoretical $d(H)$, solid (blue) line with 'o': $d^3(H)$, dashed (red) line with '+': $d^1(H)$. While the wavelet based and leader based formalisms both yield the correct $\zeta_f(p)$s for positive ps, the leader based one only is able to correctly measure the $\zeta_f(p)$s for negative ps. The corresponding Legendre transform (solid (blue) line with 'o':) concentrates around the theoretical $d(H)$. Its extension around the correct value gives us an idea of the accuracy of the numerical procedure.

$$\begin{aligned}
\mathbb{P}(d_\lambda \leq j^{-4\beta}2^{-\beta j}) &= \prod_{\lambda' \subset 3\lambda} \mathbb{P}\left(|c_{\lambda'}| \leq j^{-4\beta}2^{-\beta j}\right) \\
&= \prod_{\lambda' \subset 3\lambda} \mathbb{P}\left(2^{-\beta j'}|\chi_{\lambda'}| \leq j^{-4\beta}2^{-\beta j}\right) \\
&\leq \prod_{\lambda' \subset 3\lambda} j^{-4\beta}2^{\beta(j'-j)}.
\end{aligned}$$

We pick the scale $j' = j + \left[\frac{2\log j}{\log 2}\right] + 1$, and we note that the number of subintervals of scale j' which are subintervals of λ is larger than j^2, so that

$$\mathbb{P}(d_\lambda \leq j^{-4\beta}2^{-\beta j}) \leq \left(j^{-4\beta}2^{\beta(j'-j)}\right)^{j^2},$$

and one easily checks that this quantity is bounded by e^{-j^2} for j large enough. Since $\sum_j \sum_{k=0}^{2^j} e^{-j^2}$ is finite, the Borel-Cantelli lemma implies that for j large enough, all the d_λ are larger than $j^{-4\beta}2^{-\beta j}$. On the other hand, we already saw that, with probability one, for j large enough, all the $|\chi_\lambda|$ indexed by a dyadic subinterval of $[0,1]$ are bounded by j, and (5.5) follows from these two estimates.

Fig. 2 compares the wavelet and leader based multifractal formalisms practically applied to a sample path of fractional Brownian motion produced numerically using the so called *Circulant embedding Matrix* synthesis procedure [8]. One clearly sees that the wavelet formalism cannot reach the negative p part of $\zeta(p)$ and hence fails to measure correctly $d(H)$, while the the leader based formalism accurately analyzes both $\zeta(p)$ and $d(H)$. Moreover, it is interesting to note that the wavelet based formalism follows for negative ps the prediction derived from Eq. 4.10 in Proposition 3 (dashed black line).

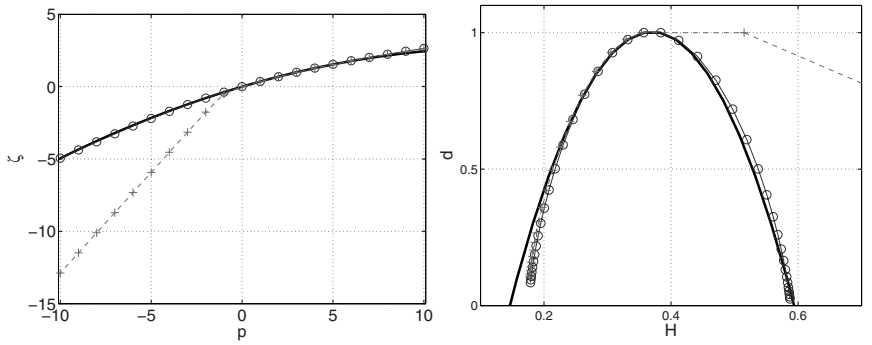

FIGURE 3. **Multiplicative Random Wavelet Cascades.** From (an average of 500 realizations of) a log-normal RWC produced numerically (number of samples: 2^{17}), one obtains: Left, solid (black) line: theoretical $\zeta_f(p)$, solid (blue) line with 'o': $\zeta_f^3(p)$, dashed (red) line with '+': $\zeta_f^1(p)$. Right, solid (black) line, theoretical $d(H)$, solid (blue) line with 'o': $d^3(H)$, dashed (red) line with '+': $d^1(H)$. While the wavelet based and leader based formalisms both yield the correct $\zeta_f(p)$s for positive ps, the leader based one only is able to correctly measure the $\zeta_f(p)$s for negative ps. The corresponding Legendre transforms yield correct measure of $d(H)$ for the lowest hs while only the leader based approach accurately measures the largest hs.

5.4.2. Multiplicative Cascades. The second example is based on random multiplicative cascades (or martingales). Instead of the celebrated cascades construction developed by Mandelbrot [45] and studied theoretically by Kahane and Peyrière

[36] that produce multifractal measures, we chose to illustrate the multifractal formalisms on multiplicative random wavelet cascades (RWC), introduced by Arneodo et al., as they provide us with well defined synthetic multifractal functions or processes (cf. [7]).
RWC are defined through their wavelet coefficient expansion on an orthonormal wavelet basis as:

$$f(x) = \sum_{j\in\mathbb{Z}} \sum_{k\in\mathbb{Z}} d_f(j,k)\psi(2^j x - k).$$

Following original constructions, the wavelet coefficients $d_f(j,k)$ entering the definition of RWCs are obtained as a product of (positive) multipliers $W_{j,k}$, which consist of mean one independent and identically distributed random variables:

$$d_{rwc}(j,k) = z_{j,k} \prod_{j'=1..j,\ k'/\lambda(j,k)\subset\lambda(j',k')} W_{j',k'}.$$

The $z_{j,k}$ are random variables taking value $+1$ or -1 with equal probability and ensuring that the wavelet coefficients are randomly chosen positive or negative.

It is known that such constructions yield multifractal processes whose $\zeta(p)$ and hence $d_f(H)$ are entirely determined from the function $-\log_2 \mathbb{E}W^p$ (see [7] for details). For instance, one commonly chose log-normal multipliers, i.e., $-\log_2 \mathbb{E}W^p = mp - \sigma^2 \ln 2 p^2/2$, m and σ being two parameters to be chosen.

In Fig. 3, the wavelet based and leader based multifractal formalisms are compared using 500 synthetic realizations of sample paths (number of samples: 2^{17}) of a log-normal RWC. One clearly sees that the wavelet based multifractal formalism fails to measure $\zeta(p)$ for negative ps and $d(H)$ for the largest Hs, while the leader based multifractal formalism produces a correct analysis over the entire spectrum.

5.4.3. Two-Dimensional Multiplicative Mandelbrot's Cascades. The third example aims at showing the leader based mutifractal formalism at work in higher dimension. We chose to use here 2-dimensional (log normal) multiplicative Mandelbrot's cascades, whose standard definition not recalled here can be found in [45] or e.g., [4, 7, 39]. The corresponding measure is then (fractionally) integrated to produce a 2D function [4]. Fig. 4 compares the wavelet based and leader multifractal formalisms applied to this 2D function. Fig. 4 is obtained from a log normal cascade, with fractional integration of order 1/2, number of sampling points $= 2^{10} \times 2^{10}$, see [40] for details on the synthesis procedure. Again, the wavelet based multifractal formalism yields an incorrect determination of the scaling exponents for negative ps and of $D(h)$ for its upper (or right) part while the leader based one produces a relevant measure over the entire spectrum. This validates the theoretical and practical straightforward extension of the leader based multifractal formalism to higher dimensions.

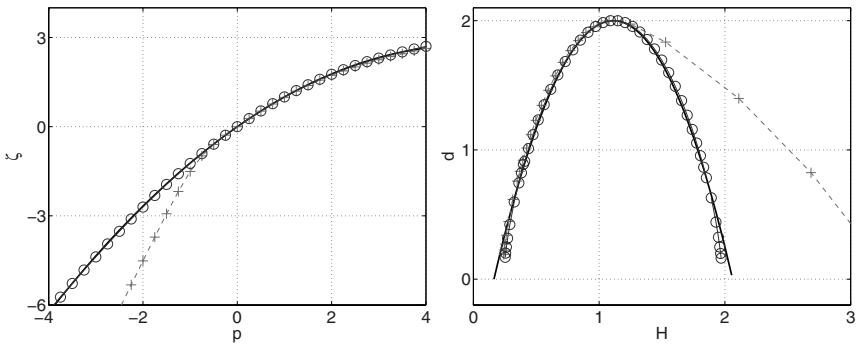

FIGURE 4. **Two-Dimensional Multiplicative Random Mandelbrot Cascades.** From (500 realizations of) a two-dimensional log-normal (fractionally integrated) Mandelbrot's binomial multiplicative cascade produced numerically (number of samples: $2^{10} \times 2^{10}$), one obtains: Left, solid (black) line: theoretical $\zeta_f(p)$, solid (blue) line with 'o': $\zeta_f^3(p)$, dashed (red) line with '+': $\zeta_f^1(p)$. Right, solid (black) line, theoretical $d(H)$, solid (blue) line with 'o': $d^3(H)$, dashed (red) line with '+': $d^1(H)$. While the wavelet based and leader based formalisms both yield the correct $\zeta_f(p)$s for positive ps, the leader based one only is able to correctly measure the $\zeta_f(p)$s for negative ps. The corresponding Legendre transforms yield correct measure of $d(H)$ for the lowest hs while only the leader based approach accurately measures the largest hs. This illustrates that the leader based formalism works efficiently and easily in higher dimensions.

5.5. Further Comments, Analysis and Synthesis Routines

At this stage, a number of comments are in order:

In the numerical examples presented here, we have implemented the formalism corresponding to Definition 14, with Daubechies wavelets (i.e., with wavelets that do not belong to the Schwartz class). The numerical results above show that this theoretical requirement can probably be weakened. Moreover in the present numerical implementation, digitalization has two major practical impacts. It implies a finite number of vanishing moments for the mother wavelet so that its belonging to the Schwartz class remains at a theoretical level. The same holds for the theoretical possible choice of a C^∞ mother wavelet. This is under further current investigations.

In numerous papers more focused on practical multifractal analysis (see for instance [3, 39, 40]), the convention $a = 2^j$ is preferred to $a = 2^{-j}$ chosen in the present text. This implies that the limit in the equations defining the ζ_f are taken for $j \to -\infty$.

All the procedures used in the present work to synthesize processes and signals and to implement multifractal formalism analysis were developed by ourselves[1] in MATLAB or C.

5.6. Practical and Numerical Multifractal Analysis: Comparisons Against Other Multifractal Formalisms and Against the Wavelet Transform Modulus Maxima Approach

5.6.1. Practical and Historical Implementations of Multifractal Formalisms. Because multifractal analysis was first applied to characterize strange attractors in the field of chaos (see e.g., [23]) and dissipation field in hydrodynamic turbulence (see e.g., [58, 48]), the earliest formalism actually used in applications was based on the computation of structure functions based on measures:

$$\forall p \in \mathbb{R},\ \Sigma_\mu(p,j) = 2^{-dj} \sum_{\lambda \in \Lambda_j} \mu(\lambda)^p,$$

a formula that closely resembles that of Definition 6 proposed here.

In hydrodynamic turbulence, one is not only interested in dissipation fields, but also in velocity ones, i.e., in functions. This is why Parisi and Frisch [55] proposed to define a formalism based on the increments $f((k+1)/2^j) - f(k/2^j)$ of the function f under analysis:

$$p > 0,\ \Sigma^1_f(p,j) = 2^{-j} \sum_k \left| f\left(\frac{k+1}{2^j}\right) - f\left(\frac{k}{2^j}\right)\right|^p$$

Immediately after they appeared, wavelet were read as generalizations both for box-aggregation and increments. For instance, the increments are commonly referred to as the *poor man's wavelet* and the historical Haar wavelet can be seen as a difference of averaged (or aggregated) quantities (see e.g., [34, 50]). Therefore, wavelets act as increments of higher orders and hence generalize the usual increments. Moreover, multiplicative cascades have been used as a standard for the synthesis of multifractal measure [45]. Box aggregation yield a correct multifractal spectrum only for the special class of conservative cascades (see e.g., [37]). This is why both continuous and discrete wavelet transforms have been involved in multifractal analysis since their earlier times, mainly to study turbulence velocity and dissipation fields (see e.g., [47, 13, 4]).

However, it has immediately been observed that most of the early-proposed multifractal formalisms failed to work for negative values of p, a major drawback as the analysis of the full multifractal spectrum theoretically involves the use of both positive an negative ps. To overcome this difficulty, Arneodo and co-authors introduced the use of the *wavelet transform modulus maxima* method (**WTMM**). To date, it remains one of the most widely used tool for empirical multifractal analysis performed in actual applications. The wavelet leader multifractal formalism

[1]The authors wish to thank Stéphane Roux, Physics Lab., ENS de Lyon, for having made available to them his codes implementing the wavelet transform modulus maxima technique

proposed here provides us with a new, relevant and efficient multifractal analysis framework.

In the section below, we briefly describe the **WTMM** tool and propose elements of comparisons between the two approaches with no aim to cover a full and detailed analysis of the difference between them.

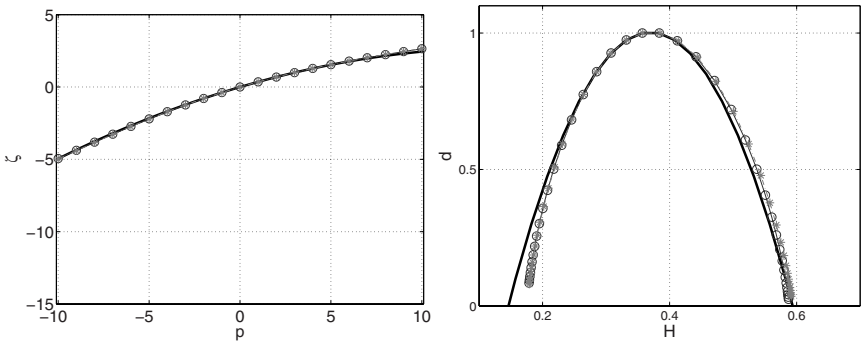

FIGURE 5. **leaders vs WTMM multifractal formalisms.** On the same set of synthetic data as the one used to obtain Fig. 3 (Multiplicative Random Wavelet Cascades), ones obtains: Left, solid (black) line: theoretical $\zeta_f(p)$, solid (blue) line with 'o': $\zeta_f^3(p)$, mixed (magenta) line with '*': $\zeta_f(p)$, produced by the **WTMM** approach. Right, solid (black) line, theoretical $d(H)$, solid (blue) line with 'o': $d^3(H)$, mixed (magenta) line with '*': $d^1(H)$, produced by the **WTMM** approach. Both formalisms are yielding very close and equivalent results at the price, however, of a very different computational cost though.

5.6.2. Wavelet Transform Modulus Maxima. The use of d_λ is reminiscent of the **WTMM** initially introduced by S. Mallat in [44] and developed by A. Arneodo E. Bacry and J.-F. Muzy in the context of multifractal analysis, see [4, 6] and references therein: Assume that ψ is a wavelet, i.e. a well localized function with enough vanishing moments (in practice a derivative, or a second derivative of a Gaussian is often used). One computes the continuous wavelet tranform of f

$$C_f(a,b) = a \int f(x)\psi\left(\frac{x-b}{a}\right) dx$$

which is a function defined in the upper half plane $\{(a,b) : \ a > 0, \ b \in \mathbb{R}\}$. For each scale a, one spots the local maxima of the functions $b \to C_f(a,b)$. These local maxima are connected through scales, thus yielding the *wavelet skeleton*. At each local maximum located at position (a,b) in the time scale plane, one associates the supremum of the wavelet transform on the sub-skeleton issued from (a,b) (i.e.

the maximum on the part of the skeleton which is linked to (a, b) and corresponds to values of the scale parameter smaller than a). The $\zeta(p)$ are then obtained using formulas such as those in Definitions 13 and 14, the partition function being computed only with the supremum skeleton values (see, e.g., [4, 5, 6] for details).

Practical results obtained with the **WTMM** approach are illustrated in Fig. 5 (on the same set of synthetic data as the one used to produce Fig. 3) and compared to those produced with the leader based multifractal formalism. One sees that both approaches yield equivalent results. Their merits are further compared below.
Historically, the **WTMM** has been the first and remained for a long time the only multifractal formalism yielding correct results for negative ps. Also, it enabled the first attempts to analyze chirp type singularities [5]. However, a number of important differences between the wavelet leaders and **WTMM** approaches can be pointed out.

From a mathematical point of view, the main differences are the following: The wavelet leader based multifractal formalism now benefits of well established theoretical mathematical results as described in previous sections. The situation is much different for the case of the **WTMM**. In the wavelet maxima method, the spacing between the local maxima need not be of the order of magnitude of the scale a or even be regularly spaced; therefore, the scaling function thus obtained can be different from $\zeta_f^3(p)$ (see [27] where counterexamples are constructed). It follows that, up to now, no mathematical results have been proved to hold for the wavelet maxima method. For instance, theoretical results such as the independence of the scaling function with the analyzing wavelet, or the fact that the Legendre transform of the scaling function yields an upper bound for the spectrum of singularities, are not available so far. This is because, as seen before, operators that map a wavelet basis on another one belong to classes of infinite matrices which are easy to describe. On the opposite, a wavelet transform belongs to a specific subspace of $L^2(dadb/a^2)$: The so-called *"Reproducing Kernel Hilbert Spaces"*, which depend on the wavelet, see [22]. Therefore describing specific classes of operators that act on these spaces is much more difficult to handle.

On the computational side, an important drawback of the **WTMM** lies in its computational cost. It is based on the computation of a full continuous wavelet transform followed by the skeletization and maxima tracking procedures. The leaders approach is based on the coefficients on an orthogonal wavelet decomposition and hence benefits from fast decomposition algorithms (cf. [43]). It implies that the wavelet leaders approach can be used for signals of arbitrary length while the **WTMM** is often restricted to much shorter ones.

Along the same line, while the wavelet leaders approach is straightforwardly and without extra difficulties extended to arbitrary higher dimensions (cf. Fig. 4), the definition of the **WTMM** needs to be significantly modified to a more complex procedure before extension to higher dimensions. Those further complications strongly impair the mathematical analysis of the method and substantially increase the corresponding computational cost (see e.g., [37] for discussions).

The statistical performance of the estimators for the $\zeta(p)$ exponents based on these two different approaches are being investigated and compared (see for instance [57]).

Numerical results regarding the leader based analysis of processes containing chirp-type singularities are been proposed in [3, 40] and show that the wavelet leader based formalism correctly measures the corresponding multifractal spectra. This will be further developed in forthcoming works.

6. The Weak-Scaling Exponent

In this section, we investigate whether we can expect (4.5) to yield the spectrum associated with some alternative pointwise exponent. We will show that, though the scaling function $\zeta_f^1(p)$ may depend on the wavelet basis chosen if $p < 0$, nonetheless it is independent of the wavelet basis for $p > 0$ and, when the infimum in (4.5) is reached for $p > 0$, then (4.5) is expected to yield the spectrum of singularities based on the *weak scaling exponent*, which was introduced by Y. Meyer in [50]. This weak scaling exponent coincides with the Hölder exponent in the case of cusp-like singularities, and this will explain why the multifractal formalism based on (4.5) yields the correct increasing part of the spectrum for signals such as Brownian motion. This interpretation will thus allow us to give a new interpretation to the computations done in previous papers which were based on (4.5).

6.1. Characterizations of the Weak Scaling Exponent

Before giving a precise definition, let us first give a feeling on the nature of the information supplied by the weak-scaling exponent. The weak-scaling exponent was introduced as a substitute for the Hölder exponent, which displays a better behaviour under integration: Let $f : \mathbb{R} \longrightarrow \mathbb{R}$ be a function, and denote by $f^{(-1)}$ a primitive of f. It may happen that $h_{f^{(-1)}}(x_0) \neq h_f(x_0) + 1$ as might be expected. A typical example where $h_{f^{(-1)}}(x_0)$ is strictly larger than $h_f(x_0) + 1$ is supplied by the chirp $C_{\alpha,\beta}$ defined in (4.6), when $\beta > 0$; indeed its Hölder exponent at x_0 is α and its Hölder exponent is increased by $1 + \beta$ after one primitivation, as shown immediately by writing

$$C_{\alpha,\beta}^{(-1)}(x) = \int_{x_0}^{x} \left(\frac{|t - x_0|^{\alpha+\beta+1}}{\beta} \right) \beta |t - x_0|^{-\beta-1} \sin\left(\frac{1}{|t - x_0|^{\beta}} \right) dt$$

and integrating by parts.

This phenomenon is the source of many difficulties and, in particular, it is one of the causes of failure of the multifractal formalism based on wavelet coefficients, see [5]. Indeed, as already mentioned, counterexamples to the heuristic which led to (4.5) are supplied by functions such as $C_{\alpha,\beta}$. Therefore it is natural to wonder if there is an alternative exponent endowed with the additional property that the exponent of a primitive is just the exponent of the function shifted by 1, and that would be "close" to the Hölder exponent (for instance, they would coincide for cusps such as $|x - x_0|^{\alpha}$). This is precisely the *weak-scaling exponent* $h_f^{ws}(x_0)$

which has been discovered by Y. Meyer, see [50], and can be characterized by the following properties:

- $h_f^{ws}(x_0) \geq h_f(x_0)$.
- $h_{f(-1)}^{ws}(x_0) = h_f^{ws}(x_0) + 1$
- $h_f^{ws}(x_0)$ is the smallest exponent satisfying the two previous conditions.

These three requirements are not easy to use directly in order to compute the weak-scaling exponent of a function; in practice, one uses a characterization on the wavelet coefficients supplied by Theorem 1.2 of [50].

First, we have to introduce the $\Gamma^s(x_0)$ smoothness criterium.

Definition 17. Let f be a tempered distribution; f belongs to $\Gamma^s(x_0)$ if and only if there exists $s' > 0$ such that f belongs to the two-microlocal space $C^{s,-s'}(x_0)$, which means that the wavelet coefficients of f (taken on a wavelet basis in the Schwartz class) satisfy

$$|c_{j,k}| \leq C2^{-sj}(1 + |2^j x_0 - k|)^{s'}. \tag{6.1}$$

Note that (4.2) already consisted of a two-microlocal condition.

Definition 18. Let f be a tempered distribution; the weak-scaling exponent of f is

$$h_f^{ws}(x_0) = \sup\{s : \ f \in \Gamma^s(x_0)\}. \tag{6.2}$$

This definition is independent of the wavelet basis chosen and it coincides with the informal definition given above, see [50].

Definition 19. **Weak scaling exponent spectrum:** We denote by $E_f^{ws}(H)$ the set of points where the weak-scaling exponent of a distribution f takes the value H. The weak-scaling spectrum of f (denoted by $d_f^{ws}(H)$) is the Hausdorff dimension of $E_f^{ws}(H)$.

In order to derive the multifractal formalism for the weak scaling exponent, the following alternative characterization will be useful (Note that it slightly differs from the wavelet characterization obtained in [32]).

Definition 20. **ϵ-leader:** Let $\epsilon > 0$. The ϵ-cone of scale j above x_0 is

$$C_j^\epsilon(x_0) = \{\lambda' \subset 3\lambda_j(x_0) \quad \text{such that} \ \ j' \leq (1+\epsilon)j\}.$$

The ϵ-leader of scale j above x_0 is

$$d_j^\epsilon(x_0) = \sup_{\lambda' \in C_j^\epsilon(x_0)} |c_{\lambda'}|.$$

It is worth noting that the limit $\epsilon \to +\infty$ corresponds to the definition of the wavelet leaders (cf. Definition 12) while in the limit $\epsilon \to 0$ one recovers the usual wavelet coefficients.

Proposition 7. Let f be a tempered distribution. The weak scaling exponent of f at x_0 is the supremum of the values of H satisfying

$$\forall \epsilon > 0, \ \ \exists J \ \ \forall j \geq J \quad d_j^\epsilon(x_0) \leq C2^{-(H-\epsilon)j}. \tag{6.3}$$

Proof of Proposition 7: Suppose that there exists $s' > 0$ such that (6.1) holds. Let $\epsilon > 0$; then

$$d_j^\epsilon(x_0) \leq \sup_{\lambda' \in C_j^\epsilon(x_0)} 2^{-sj'}(1 + |2^{j'}x_0 - k'|)^{s'} \leq 2^{-sj}2^{(j'-j)s'} \leq 2^{-sj}2^{s'\epsilon j}.$$

Since ϵ can be chosen arbitrarily small, (6.3) holds for $H = s$.

Conversely, suppose that (6.3) holds. Since f is a finite order distribution, it follows that

$$\exists u \in \mathbb{R}, \ \exists C > 0, \ \forall j, k \quad |c_{j,k}| \leq C.2^{-uj}. \tag{6.4}$$

We can of course assume that u satisfies $H - 1 - u > 0$.

First, if λ' belongs to an ϵ-cone of scale j above x_0, then

$$j \geq j'/(1 + \epsilon)$$

so that

$$|c_{\lambda'}| \leq C.2^{-j'(H-\epsilon)/(1+\epsilon)}$$

and (6.3) holds for an s arbitrarily close to H and $s' = 0$.

Else, if λ' does not belong to an ϵ-cone of scale j above x_0 then, in particular, it is outside the ϵ-cone of scale $= j'/(1 + \epsilon)$ above x_0, so that

$$|2^{j'}x_0 - k'| \geq 2^{j'}2^{-j} \geq 2^{j'\epsilon/(1+\epsilon)}.$$

It follows that

$$|c_{\lambda'}| \leq C.2^{-uj'} \leq C.2^{-Hj'}2^{-(u-H)j'} \leq C.2^{-Hj'}|2^{j'}x_0 - k'|^{(H-u)(1+\epsilon)/\epsilon},$$

and (6.3) holds for $s = H$ and $s' = (H - u)(1 + \epsilon)/\epsilon$.

6.2. Multifractal Formalism for the Weak Scaling Exponent

Proposition 7 states that the weak scaling exponent at x_0 is given by the order of magnitude of the the ϵ-leaders above x_0. Therefore, the following structure and scaling functions are naturally associated with the weak scaling exponent.

Definition 21. **Weak scaling exponent Multifractal formalism:** Let f be a temperate distribution and assume that the wavelets used belong to the Schwartz class. If $p \in \mathbb{R}$, let

$$d_\lambda^\epsilon = \sup_{\lambda' \subset 3\lambda, \ j' \leq (1+\epsilon)j} |c_{\lambda'}|,$$

$$W_f^4(p, \epsilon, j) = 2^{-dj} \sum_{\lambda \in \Lambda_j} (d_\lambda^\epsilon)^p,$$

and

$$\zeta_f^4(p, \epsilon) = \liminf_{j \to +\infty} \left(\frac{\log\left(W_f^4(p, \epsilon, j)\right)}{\log(2^{-j})} \right). \tag{6.5}$$

The weak scaling function of f is defined by

$$\zeta_f^4(p) = \lim_{\epsilon \to 0} \zeta_f^4(p, \epsilon). \tag{6.6}$$

Note that, when $\epsilon \to 0$, the ϵ-leaders are defined by a supremum over a decreasing set, and therefore, they decrease; it follows that, if $p > 0$, then $W_f^4(p, \epsilon, j)$ decreases when $\epsilon \to 0$, and, if $p < 0$, then $W_f^4(p, \epsilon, j)$ increases when $\epsilon \to 0$, which implies that the limit exists in (6.6) in all cases.

The same arguments as for the derivation of the previous multifractal formalisms lead to the following multifractal formalism for the weak scaling exponent:

$$d_f^{ws}(H) = \inf_{p \in \mathbb{R}} (d - \zeta_f^4(p) + Hp) \tag{6.7}$$

The following result shows that the Legendre transform of the scaling function yields an upper bound for the weak-scaling spectrum without any uniform regularity assumption, see [32].

Theorem 6.1. *Let f be a tempered distribution. Then its weak scaling spectrum satisfies*

$$d_f^{ws}(H) \leq \inf_{p \in \mathbb{R}} \left(Hp - \zeta_f^4(p) + d \right). \tag{6.8}$$

Let us now study more precisely the scaling function $\zeta_f^4(p)$.

Proposition 8. Let $p > 0$. If the wavelets are r-smooth with $r > p\zeta_f^1(p)$, then

$$\zeta_f^4(p) = \zeta_f^1(p).$$

This result implies that the increasing part of the Legendre transforms in (4.5) and (6.8) coincide. This is important in practice since $\zeta_f^1(p)$ is much easier to obtain numerically (because it is not defined as a double limit). Furthermore Proposition 8 shows that the multifractal formalism given by (4.5) is expected to yield the increasing part of the weak scaling spectrum, as announced.

Proof of Proposition 8**:** Let $p > 0$; since $(d_\lambda^\epsilon)^p \geq |c_{\lambda'}|^p$, it follows that $\zeta_f^4(p) \leq \zeta_f^1(p)$. Conversely,

$$(d_\lambda^\epsilon)^p \leq \sum_{\lambda' \subset 3\lambda,\ j' \leq (1+\epsilon)j} |c_{\lambda'}|^p$$

so that

$$w_f^4(p, \epsilon, j) \leq w_f^1(p, \epsilon, j) + 2^d w_f^1(p, \epsilon, j+1) + \cdots + 2^{d\epsilon j} w_f^1(p, \epsilon, (1+\epsilon)j);$$

therefore

$$\zeta_f^4(p, \epsilon) \geq (d+1)\epsilon + \zeta_f^1(p, \epsilon).$$

Since this is true $\forall \epsilon > 0$, it follows that $\zeta_f^4(p) \geq \zeta_f^1(p)$.

Let us now give a function space interpretation to $\zeta_f^1(p)$ (hence to $\zeta_f^4(p)$) when $p > 0$. Recall that f belongs to the homogeneous Besov space $\dot{B}_p^{s,\infty}(\mathbb{R}^d)$ if

$$\exists C,\ \forall j \quad 2^{(sp-d)j} \sum_{\lambda \in \Lambda_j} |c_\lambda|^p \leq C. \tag{6.9}$$

It follows that

$$\zeta_f^1(p) = \sup\{s : \quad f \in \dot{B}_p^{s/p,\infty}(\mathbb{R}^d)\}.$$

Since (6.9) holds as soon as the wavelets are r-smooth with $s > r$, it follows that $\zeta_f^4(p)$ is independent of the r-smooth wavelet basis as soon as $r > p\zeta_f^4(p)$.

If $p < 0$, then $\zeta_f^4(p)$ cannot be given any more a function space interpretation; however, one can prove that it is still independent of the wavelet basis (in the Schwartz class), by using the same arguments as those developed in [29] in order to prove that $\zeta_f^3(p)$ is robust.

One may wonder if $\zeta_f^1(p)$ and $\zeta_f^4(p)$ still coincide for $p < 0$. The example of F.B.M., which we now consider, shows that it is not the case.

6.3. Examples: The weak Scaling Spectrum of Fractional Brownian Motions

First, let us determine the weak scaling exponent of F.B.M. at every point. We use the characterization supplied by Proposition 7, which is independent of the wavelet basis chosen (because it is equivalent to the two-microlocal characterization (6.1), which defines a robust condition, as shown in [26]). Furthermore, using again this robustness property, we can use the decomposition (4.9) on biorthogonal wavelets adapted to F.B.M.. Therefore the wavelet coefficients are $2^{-\beta j}\chi_{j,k}$ where the $\chi_{j,k}$ are I.I.D. standard centered Gaussians. Then, the proof of Theorem 5.1 shows that, for j large enough, the ϵ-leaders are larger than $j^{-4\beta}2^{-\beta j}$ (because, in the proof, the supremum in the definition of the wavelet leaders is extracted only in the range of scales between j and $j + \left[\frac{2\log j}{\log 2}\right] + 1$, which is smaller than $j + \epsilon j$ for j large enough). Therefore, the Borel-Cantelli lemma implies that a.s. for j large enough, all the d_λ^ϵ stand between $j^{-4\beta}2^{-\beta j}$ and $j2^{-\beta j}$. Thus, the following theorem holds.

Theorem 6.2. *Let $\beta \in (0,1)$ and $B_\beta(t)$ be a generic sample path of F.B.M. of order β. Assume that the wavelet used is C^2; then, with probability 1, the weak scaling exponent of B_β is everywhere β,*

$$\forall p \in \mathbb{R}, \quad \zeta_{B_\beta}^4(p) = \beta p \tag{6.10}$$

and the liminfs in the definitions of the scaling functions are true limits.

The multifractal formalism (5.3) *yields the correct weak scaling spectrum of singularities of F.B.M..*

One can note that by inverting the two limits $\epsilon \to 0$ and $j \to +\infty$ in Definition 21 and (6.5) and (6.6), one recovers the wavelet coefficient based multifractal formalism, which was shown in Section 4 to yield an incorrect measure of the multifractal spectrum of F.B.M. Hence, F.B.M. provides us with a pedagogical example to emphasize how much the order of the limits matters in multifractal analysis.

7. Conclusion

We conclude this paper by some comments concerning the comparison of the three wavelet-based multifractal formalisms given by (4.5), (5.3) and (6.7), why they may coincide or differ, and how this is related to the presence of "oscillating singularities", as opposed to "cusp-singularities".

Let us first discuss what is usually understood by these two types of singularities. As mentioned already, a typical example of a cusp at x_0 is supplied by the function $|x - x_0|^\alpha$ (where α is positive and is not an even integer so that the function is not C^∞ at x_0). This is usually opposed to chirps such a the functions $C_{\alpha,\beta}$ defined in (4.6). These particular examples do not supply us with a general mathematical definition; they can only give some clues in this direction. Unfortunately, there is no general agreement as to what should be the right definition of a chirp. Actually, several definitions have been proposed (see [5, 14, 28, 33, 52]) and simple models of random wavelet series have been shown to display such behaviors, see [9]. Furthermore, C. Melot and A. Fraysse showed that such oscillatory behaviors are not exceptional but "generic" among the functions which have a given scaling function $\zeta_f^1(p)$, see [21, 46]. We won't compare the merits of these definitions here, but rather discuss the opposite point of view: When can one say that a function displays cusps, since this is the case where we expect the different multifractal formalisms to coincide. The clue for a possible answer lies again in the comparison between the properties of the cusps $|x - x_0|^\alpha$ and the chirps $C_{\alpha,\beta}$: Recall that the Hölder exponent of both functions at x_0 is α, but the weak scaling exponent of the cusp is α whereas it is $+\infty$ for the chirps; following this remark, Y. Meyer proposed in [50] the following general definition for a cusp.

Definition 22. **Cusp singularity:** Let f be a function which is bounded in a neighbourhod of x_0, and such that $h_f(x_0) < \infty$; f has a cusp singularity at x_0 if

$$h_f(x_0) = h_f^{ws}(x_0).$$

Note that this definition does not involve the wavelet coefficients of f: however, in order to understand its implications in multifractal analysis, it is necessary to check what it implies for the wavelet leaders. The characterizations supplied by Propositions 4 and 7 show that, if f has a cusp singularity at x_0, then we can expect that, for any $\epsilon > 0$, the supremum in the quantity $\sup_{\lambda' \subset 3\lambda_j(x_0)} |c_{\lambda'}|$ is actually reached for a λ' whose scale j' satisfies $j \leq j' \leq (1+\epsilon)j$ (if j is large enough). A typical example of this behavior is supplied by F.B.M.: Indeed, in Section 5.4, we estimated these suprema and actually showed that a.s. every point is a cusp singularity (since everywhere the Hölder exponent and the weak scaling exponent both take the value β). We can wonder why the first multifractal formalism yields a different spectrum, see Proposition 3. A close inspection of the proof of this proposition compared with the proof of Theorem 5.1 shows that, though the suprema of wavelet coefficients on very small subtrees of the form

$$\{\lambda' \subset \lambda : \quad j' \leq (1+\epsilon)j\}$$

are of the order of magnitude of $2^{-\beta j}$ with a probability extremely close to 1, nonetheless, single wavelet coefficients have a Gaussian distribution and therefore can take very small values with a much larger probability, which becomes non negligeable when one considers simultaneously a large number of coefficients (2^j in the present case).

Is it nonetheless possible that (4.5), (5.3) and (6.7) yield the same result? Since the scaling function $\zeta_f^1(p)$ is not robust, this can only be the consequence of a very particular choice of the wavelet basis. In practice, this only happens if an algorithm is used to define the coefficients of the function (or of the stochastic process) on a given wavelet basis, and *the same wavelet basis* is used also in the analysis procedure. Such models have been currently proposed, all of them verifying the following hierarchical property:

$$\lambda' \subset \lambda \quad \Longrightarrow |c_{\lambda'}| \leq |c_\lambda|. \tag{7.1}$$

Typical examples of wavelet series satisfying this property can be constructed starting with a probability measure μ defined on $\mathbb{R}^d$ and picking, for an $\alpha \geq 0$ and $q > 0$,

$$c_\lambda = 2^{-\alpha j}[\mu(\lambda)]^q,$$

see [10, 7] and references therein. Because of (7.1), all wavelet multifractal formalisms trivially yield the same result but again, under the very artificial assumption that one picks the same synthesizing and analyzing wavelets, since (7.1) will not remain valid if the wavelets are changed. Note that, if the synthesizing and analyzing wavelets differ, then the last two multifractal formalisms will still coincide (because there exists a wavelet basis for which it is the case, and the corresponding scaling functions are robust); by contrast, numerical results show that the first multifractal formalism yields a different spectrum: The decreasing part of the Legendre transform is artificially raised, as in the F.B.M. case (see Proposition 3), because of very small wavelet coefficients whose influence in the structure function is not eliminated by taking suprema of coefficients, as in the wavelet leaders case. (Note that experimentalists are aware of this pitfall: Even if they study "artificial signals" defined through their wavelet coefficients, they take only for granted results which have been validated by using several different wavelet bases.)

8. Appendix: Proof of Theorem 3.2

Let us first prove (3.8). We start by two elementary remarks. If χ is a standard Gaussian, then

$$\mathbb{P}(|\chi| \geq j) \leq e^{-j^2/2};$$

it follows from the Borel-Cantelli Lemma that, with probability 1,

$$\exists J, \ \ \forall j \geq J, \ \ \forall k = 1, ..., 2^j, \quad |\chi_{j,k}| \leq j,$$

hence,

$$\text{if } \ p > 0, \quad \text{ then } \ A(p, j) \leq 2^{-pj/2} j^p. \tag{8.1}$$

On the other hand,

$$\mathbb{P}\left(|\xi| \leq j^{-2}2^{-j}\right) \leq \sqrt{\frac{2}{\pi}} j^{-2}2^{-j};$$

it follows that, for a given j, one of the 2^j Gaussians $\xi_{j,k}$ will be smaller than $j^{-2}2^{-j}$ with probability at most j^{-2}. Thus, by the Borel-Cantelli lemma, with probability 1,

$$\exists J, \quad \forall j \geq J, \quad \forall k \quad |\xi_{j,k}| \geq j^{-2}2^{-j}. \tag{8.2}$$

In order to obtain precise estimates on $A(j,p)$, we can use estimates for the distribution of the $|\xi_{j,k}|$ in the neighbourhood of 0; up to a smooth change of variable, it is the same as the distribution of 2^j I.I.D. random variables x_k distributed with the Lebesgue measure on $[0,1]$ and therefore the estimate of $A(p,j)$ will be the same in both cases. Recall that the *empirical process* is defined as follows: Points $(x_n)_{n\in\mathbb{N}}$ are drawn independently with the Lebesgue measure on $[0,1]$; therefore the estimates on $A(j,p)$ will be the same in both cases, up to a constant term. The empirical process is the collection of random processes

$$P_t^N = \sum_{n=1}^{N} 1_{[0,x_n)}(t).$$

Estimates on the joint distribution of the x_n are usually expressed in terms of

$$\alpha_t^N = \sqrt{N}\left(\frac{P_t^N}{N} - t\right)$$

which is the "correct" renormalization of the empirical process since it converges to a non-trivial limit (a Brownian bridge), see [18, 59] and references therein. The increments of the empirical process can be estimated using the following result which is a particular case of Lemma 2.4 of [59].

Lemma 8.1. *There exist two positive constants C_1' and C_2' such that, if $0 < l < 1/8$, $Nl \geq 1$ and $8 \leq A \leq C_1'\sqrt{Nl}$,*

$$\mathbb{P}\left(\sup_{|t-s|\leq l} |\alpha_t^N - \alpha_s^N| > A\sqrt{l}\right) \leq \frac{C_2'}{l} e^{-A^2/64}. \tag{8.3}$$

Note that the condition

$$\sup_{|t-s|\leq l} |\alpha_t^N - \alpha_s^N| \leq A\sqrt{l}$$

implies that the number of points $(x_n)_{n\leq N}$ that fall in the interval $[s,t]$ differs from $N|t-s|$ by at most $A\sqrt{NL}$.

In the following, we will use Lemma 8.1 repeatedly with intervals of different lengths and positions; however, each time, we will pick $N = 2^j$ and $A = j$; this last choice will allow use to obtain such small probabilities of the opposite events that we can apply the Borel-Cantelli lemma to their complement at the end. First we estimate the number of points that fall in the interval $[9/10, 1]$, so that $l = 1/10$; it follows that, with probability larger than $1 - Ce^{-j^2/64}$, this number differs from

$(1/10)2^j$ by at most $j2^{j/2}\sqrt{10}$. On one hand, if $p > 0$, then $A(p,j) \geq C(p)2^j$ and (3.8) for $p > 0$ follows from this estimate together with (8.1). On the other hand it follows that

$$\text{if } p < 0, \text{ then } \quad A(p,j) \geq C2^j. \tag{8.4}$$

Let us now apply Lemma 8.1 on the interval $[0, j^3 2^{-j}]$, so that $l = j^3 2^{-j}$. With probability larger than $1 - Ce^{-j^2/64}2^j/j^3$, the number of points in this interval is larger than $j^3 - j\sqrt{j^3 2^{-j} 2^j} \geq j^3/2$, so that

$$\text{if } p < 0, \text{ then } \quad A(p,j) \geq \frac{1}{2} j^{3+3p} 2^{-pj}. \tag{8.5}$$

Let us now obtain upper bounds for $A(p,j)$ when $p < 0$. Let m be a fixed, large integer, and let

$$a_0 = 0, \text{ and } a_k = 2^{-(1-k/m)j} \text{ for } k = 1, \ldots, m-1, \text{ and } l_k = a_k - a_{k-1}.$$

We first apply Lemma 8.1 in the first interval $[0, a_1]$. With probability larger than $1 - C2^j e^{-j^2/64}$, the number of points in this interval is bounded by $a_1 2^j + j2^{j/2}\sqrt{a_1}$, taking into account the value of a_1 and (8.2), it follows that the contribution to $A(p,j)$ of the points that fall in this interval is bounded by

$$2 \cdot 2^{j/m} j^{-2p} 2^{-pj}. \tag{8.6}$$

We now apply Lemma 8.1 on the remaining intervals. We obtain that $\forall k = 1, \ldots, m-1$, with probability larger than $C_2' 2^j e^{-j^2/64}$ the number of points that fall in the interval $[a_{k-1}, a_k)$ differs from $l_k 2^j$ by at most $j2^{j/2}\sqrt{l_k}$. It follows that, if $p > 0$ then, with probability at most $C_2' m 2^j e^{-j^2/64}$ the contribution of each interval $[a_{k-1}, a_k)$ to $A(p,j)$ is bounded by

$$2^{-j} l_k 2^j a_k^p + j2^{j/2}\sqrt{l_k} a_{k-1}^p$$

which is bounded by

$$2^{-pj}\left(2^{(p+1)jk/m} + 2^{(p+1/2)jk/m} 2^{-pj/m}\right).$$

If $p < -1$ then each of these terms is bounded by (8.6), and if $-1 \leq p < 0$ then each is bounded by $C2^j$; therefore (3.8) follows in all cases for $p < 0$.

We now prove the second part of Theorem 3.2, i.e. that, in the case of a sample path of Brownian motion, a.s.

$$\forall p \in \mathbb{R}, \quad \eta_B^2 = p/2, \tag{8.7}$$

and that the *lim inf* in (3.5) is a true limit, which will imply the second assertion of Theorem 3.2.

Let $I_{j,k}$ denote the interval $[k2^{-j}, (k+1)2^{-j})$. The oscillations

$$Osc_B(I_{j,k}) = \sup_{s \in I_{j,k}} B_s - \inf_{x \in I_{j,k}} B_s \quad (k = 0, \ldots, 2^j - 1)$$

are 2^j i.i.d. random variables, and we have to estimate

$$\sum_k \left(Osc_B(I_{j,k})\right)^p$$

Proposition 9. Let $O_t = \sup_{s\in[0,t]} B_s - \inf_{x\in[0,t]} B_s$. The law of O_t satisfies

$$\text{if} \quad a \le \sqrt{t}, \quad \mathbb{P}\{O_t \le a\} \le \frac{1}{2\pi} \exp\left(-\frac{\pi^2 t}{a^2}\right)$$

and

$$\text{if} \quad a \ge \sqrt{t}, \quad \mathbb{P}\{O_t \ge a\} \le \frac{4a}{\sqrt{2\pi t}} \exp\left(-\frac{a^2}{8t}\right).$$

Proof of Proposition 9: Let $B_t^* = \sup_{[0,t]} |B_s|$. We can reduce the problems of estimations of the oscillation to estimations on B_t^*, since

$$B_t^* \le \sup_{[0,t]} B_s - \inf_{[0,t]} B_s \le 2B_t^*.$$

We will need two estimations for the law of the random variable B_t^*. We start by recalling (see [16] Proposition 8.4.27) that

$$\mathbb{P}\left(B_t^* \le a\right) = \frac{1}{\sqrt{2\pi t}} \sum_{k\in\mathbb{Z}} (-1)^k \int_{(2k-1)a}^{(2k+1)a} \exp\left(-\frac{u^2}{2t}\right) du \tag{8.8}$$

so that the density of B_t^* is

$$g_t(a) = \frac{2}{\sqrt{2\pi t}} \sum_{k\in\mathbb{Z}} (-1)^k (2k+1) \exp\left(-\frac{(2k+1)^2 a^2}{2t}\right).$$

Let $u = a/\sqrt{t}$ and $f(x) = x\exp(-x^2/2)$, then

$$g_t(a) = \frac{2}{a\sqrt{2\pi}} \sum_{k\in\mathbb{Z}} (-1)^k f\left((2k+1)u\right).$$

Since f is in the Schwartz class, the Poisson summation formula yields

$$\sum_{n\in\mathbb{Z}} f(x+an) = \sum_{k\in\mathbb{Z}} \frac{1}{a} \hat{f}\left(\frac{2\pi k}{a}\right) e^{-2i\pi kx/a}.$$

Applying this formula with $2a$ and substracting, we obtain

$$\sum_{n\in\mathbb{Z}} (-1)^n f(x+an) = \frac{1}{a} \sum_{k \text{ odd}} \hat{f}\left(\frac{\pi k}{a}\right) e^{i\pi kx/a}.$$

We use this formula with $x = u$, $a = 2u$ and $f(x) = x\exp(-x^2/2)$, whose Fourier transform is $-i\xi\sqrt{2\pi}\exp(-\xi^2/2)$; it follows that

$$\begin{aligned} g_t(a) &= \frac{-\pi}{2u^2 a}\sum_{k\ odd} i^{k+1}k\exp\left(-\frac{\pi^2k^2}{8u^2}\right) \\ &= \frac{\pi}{4u^2a}\sum_{l=0}^{\infty}(-1)^l(2l+1)\exp\left(-\frac{\pi^2(2l+1)^2}{8u^2}\right). \end{aligned}$$

Therefore

$$\begin{aligned} \mathbb{P}\left(B_t^* \le a\right) &= \int_0^a g_t(x)dx = \sum_{l=0}^{\infty}\frac{(-1)^l}{2\pi(2l+1)}\exp\left(-\frac{\pi^2(2l+1)^2t}{a^2}\right) \\ &\le \frac{1}{2\pi}\exp\left(-\frac{\pi^2 t}{a^2}\right), \end{aligned}$$

so that

$$\mathbb{P}\left\{O_t \le a\right\} \le \mathbb{P}\left\{B_t^* \le a\right\} \le \frac{1}{2\pi}\exp\left(-\frac{\pi^2 t}{a^2}\right).$$

Separating the term $k = 1$ from the others in (8.8) it follows that

$$\begin{aligned} \mathbb{P}\left(B_t^* \ge a\right) &= \frac{2}{\sqrt{2\pi t}}\int_a^{\infty}\exp\left(-\frac{u^2}{2t}\right)du \\ &\quad -\frac{2}{\sqrt{2\pi t}}\sum_{k=1}^{\infty}(-1)^k\int_{(2k-1)a}^{(2k+1)a}\exp\left(-\frac{u^2}{2t}\right)du \end{aligned}$$

which is bounded by $\dfrac{8a}{\sqrt{2\pi t}}\exp\left(-\dfrac{a^2}{2t}\right)$. Therefore

$$\mathbb{P}\left\{O_t \ge a\right\} \le \mathbb{P}\left\{B_t^* \ge a/2\right\} \le \frac{4a}{\sqrt{2\pi t}}\exp\left(-\frac{a^2}{8t}\right),$$

hence the second point of Proposition 9 holds.

Let j be fixed and $N = 2^j$. It follows that the event

$$\{\textit{One of the oscillations } \mathrm{Osc}_B(I_{j,k}) \textit{ is smaller than } 1/(\sqrt{N}\log N)\}$$

has probability less than $Ne^{-\pi(\log N)^2}$; and similarly the event

$$\{\textit{One of the oscillations } \mathrm{Osc}_B(I_{j,k}) \textit{ is larger than } \log N/\sqrt{N}\}$$

has probability less than $2N(\log N)e^{-\pi(\log N)^2}$. The structure function can be estimated just as in the increments case, but the computations are much easier because the distribution of the suprema decays very strongly near 0, and a direct application of the Borel-Cantelli Lemma shows that (8.7) holds, so that the multifractal formalism yields now the correct spectrum for a.e. sample path of Brownian motion.

References

[1] P. Abry, P. Goncalves and J. Lévy-Véhel *Lois d'échelle, Fractales et ondelettes,* Vol. 1 and 2, Hermes (2002).

[2] P. Abry and F. Sellan, *The wavelet-based synthesis for fractional Brownian motion proposed by F. Sellan and Y. Meyer: Remarks and fast implementation,* Appl. Comput. Harmon. Anal. 3, No.4, pp. 377–383 (1996).

[3] P. Abry, S. Jaffard, and B. Lashermes. Revisiting scaling, multifractal, and multiplicative cascades with the wavelet leader lens. In *Optic East, Wavelet Applications in Industrial Applications II, Vol. 5607*, pages 103–117, Philadelphia, USA, 2004.

[4] A. Arneodo, B. Audit, N. Decoster, J.-F. Muzy, C. Vaillant, *Wavelet-based multifractal formalism: applications to DNA sequences, satellite images of the cloud structure and stock market data,* in: The Science of Disasters; A. Bunde, J. Kropp, H. J. Schellnhuber eds., Springer pp. 27–102 (2002).

[5] A. Arneodo, E. Bacry, S. Jaffard, J-F. Muzy, *Oscillating singularities on Cantor sets: A grandcanonical multifractal formalism,* J. Statist. Phys., vol. 87 pp. 179–209 (1997)

[6] A. Arneodo, E. Bacry, J-F. Muzy, *The thermodynamics of fractals revisited with wavelets,* Physica A Vol.213 p.232-275 (1995).

[7] A. Arneodo, E. Bacry, and J.-F. Muzy. Random cascades on wavelet dyadic trees. *J. Math Phys.*, 39(8):4142–4164, 1998.

[8] J.-M. Bardet, G. Lang, G. Oppenheim, A. Philippe, and M. S. Taqqu. Generators of long-range dependent processes: a survey. In P. Doukhan, G. Oppenheim, and M. S. Taqqu, editors, *Long-Range Dependence: Theory and Applications*, pages 579–623, Boston, 2003. Birkhäuser.

[9] J.-M. Aubry and S. Jaffard *Random wavelet series* Comm. Math. Phys., vol. 227, pp. 483–514 (2002).

[10] J. Barral and S. Seuret, *From multifractal measures to multifractal wavelet series,* preprint (2005).

[11] H. Brezis, *Analyse fonctionelle*, Masson (1983).

[12] G. Brown, G. Michon et J. Peyrière, *On the multifractal analysis of measures,* J. Statist. Phys., vol. 66 pp. 775-790 (1992).

[13] A. B. Chhabra and C. Meneveau and R. V. Jensen and K. R. Sreenivasan, Direct determination of the $f(\alpha)$ singularity spectrum and its application to fully developed turbulence, Physical Review A, 40(9), 1989, 5284–5294.

[14] E. Chassande-Mottin and P. Flandrin, *On the time-frequency detection of chirps,* Appl. Comput. Harmon. Anal., Vol. 6 pp. 252–281 (1999).

[15] A. Cohen and R. Ryan, *Wavelets and multiscale signal processing*, Chapman & Hall (1995).

[16] D. Dacunha-Castelle and M. Duflo *Probabilités et Statistiques Vol. 2* Masson (1993)

[17] I. Daubechies. *Orthonormal bases of compactly supported wavelets,* Comm. Pure and App. Math. Vol. 41, pp. 909–996 (1988).

[18] P. Deheuvels and D. M. Mason *Functional laws of the iterated logarithm for the increments of empirical and quantile processes,* Ann. of Proba., Vol. 20 pp. 1248–1287 (1992).

[19] A. Durand *Random wavelet series with correlated coefficients*, preprint (2005).

[20] K. Falconer *Fractal geometry,* John Wiley and sons (1990).

[21] A. Fraysse, *Résultats de généricité en analyse multifractale,* Thèse de l'Université Paris XII (2005).

[22] A. Grossmann, J. Morlet and T. Paul *Transforms associated to square integrable group representations. I. General results,* J. Math. Phys Vol 26 (10) pp. 2473-2479 (1985) .

[23] T. Halsey, M. Jensen, L. Kadanoff, I. Procaccia and B. Shraiman, *Fractal measures and their singularities: The characterization of strange sets,* Phys. Rev. A, vol. 33 pp. 1141–1151 (1986)

[24] G.H. Hardy, J. E. Littlewood, and G. Pólya *Inequalities,* Cambridge University Press (1952).

[25] S. Jaffard, *Exposants de Hölder en des points donnés et coefficients d'ondelettes,* C. R. Acad. Sci. Sér. I Math., vol. 308 pp. 79–81 (1989).

[26] S. Jaffard *Pointwise smoothness, two-microlocalization and wavelet coefficients, Publ. Mat.* **35** *(1991), 155–168.*

[27] S. Jaffard, *Multifractal formalism for functions. Part 1: Results valid for all functions and Part 2: Selfsimilar functions,* SIAM J. Math. Anal. **28** (1997), 944–998.

[28] S. Jaffard, *Oscillation spaces: Properties and applications to fractal and multifractal functions,* J. Math. Phys., vol. 39 pp. 4129–4141 (1998)

[29] S. Jaffard, *Wavelet techniques in multifractal analysis,* Fractal Geometry and Applications: A Jubilee of Benoît Mandelbrot, M. Lapidus et M. van Frankenhuijsen Eds., Proceedings of Symposia in Pure Mathematics, AMS, Vol. 72 Part 2 pp. 91–152 (2004).

[30] S. Jaffard, *On Davenport expansions,* Fractal Geometry and Applications: A Jubilee of Benoît Mandelbrot, M. Lapidus et M. van Frankenhuijsen Eds., Proceedings of Symposia in Pure Mathematics, AMS, Vol. 72 Part 1 pp. 273–303 (2004).

[31] S. Jaffard, *Pointwise regularity associated with function spaces and multifractal analysis,* Approximation and Probability, T. Figiel and A. Kamont Eds., Banach Center Pub. Vol. 72 pp. 93–110 (2006).

[32] S. Jaffard and C. Melot, *Wavelet analysis of fractal Boundaries, Part 1: Local regularity and Part 2: Multifractal formalism*, Comm. Math. Phys., Vol. 258 n. 3, pp. 513–565 (2005).

[33] S. Jaffard and Y. Meyer. *Wavelet methods for pointwise regularity and local oscillation of functions,* Mem. Am. Math. Soc. **123** (1996), 587.

[34] S. Jaffard, Y. Meyer and R. Ryan *Wavelets: Tools for Science and Technology,* S.I.A.M., (2001)

[35] J.-P. Kahane, Some Random Series of Functions, Cambridge University Press, 1985.

[36] J.-P. Kahane, and J. Peyrière, *Sur certaines martingales de Benoit Mandelbrot,* Adv. Math., vol. 22, pp. 131–145 (1976).

[37] P. Kestener and A. Arneodo, Three-dimensional wavelet-based multifractal method: The need for revisiting the multifractal description of turbulence dissipation data, Physical Review Letters Vol 91 p. 194501, (2003).

[38] K.-S. Lau, Ka-Sing and S.-M. Ngai, *Multifractal measures and a weak separation condition,* Adv. Math. 141, No.1, 45-96 (1999).

[39] B. Lashermes, P. Abry, and P. Chainais. New insights into the estimation of scaling exponents. *Int. J. of Wavelets, Multiresolution and Information Processing*, 2(4):497–523, 2004.

[40] B. Lashermes, S. Jaffard, and P Abry. Wavelet Leader based Multifractal Analysis. In *Proc. of the Int. Conf. on Acoust. Speech and Sig. Proc.*, 2005.

[41] W. Li, *Small ball probabilities for Gaussian Markov processes under the L_p-norm,* Stoch. Proc. Appl. Vol. 92, pp. 87–102 (2001).

[42] W. Li and Q.-M. Shao, *Gaussian processes: Inequalities, small ball probabilities and applications,* D. N. Shanbhag et al. ed., Stochastic processes: Theory and methods. Amsterdam: North-Holland/ Elsevier. Handb. Stat. Vol. 19, pp. 533–597 (2001).

[43] S. Mallat *A Wavelet tour of signal processing,* Academic Press (1998)

[44] S. Mallat and W. L. Hwang *Singularity detection and processing with wavelets,* IEEE Trans. Info. Theo. Vol. 38 pp. 617–643 (1992)

[45] B. Mandelbrot, *Intermittent turbulence in selfsimilar cascades: divergence of high moments and dimension of the carrier,* J. Fluid Mech., vol. 62 pp. 331–358 (1974).

[46] C. Melot, *Oscillating singularities in Besov spaces*, J. Math. Pures Appl., Vol. 9, . Ser. 83, pp. 367–416 (2004).

[47] C. Meneveau, Analysis of turbulence in the orthonormal wavelet representation, J. Fluid Mech., 232, 469–520, 1991.

[48] C. Meneveau and K. R. Sreenivasan, The multifractal spectrum of the dissipation field in turbulent flows, Nuclear Physics B, 2, 49–76, 1987.

[49] Y. Meyer, *Ondelettes et opérateurs.* Hermann, 1990.

[50] Y. Meyer, *Wavelets, Vibrations and Scalings*, CRM Ser. AMS Vol. 9, *Presses de l'Université de Montréal* (1998).

[51] Y. Meyer, F. Sellan and M. Taqqu, *Wavelets, generalized white noise and fractional integration: The synthesis of fractional Brownian motion,* J. Fourier Anal. Appl. 5, No.5, pp. 465–494 (1999)

[52] Y. Meyer and H. Xu. *Wavelet analysis and chirps,* Appl. Comput. Harmon. Anal. Vol. 4, pp. 366–379 (1997).

[53] D. Monrad and H. Rootzén *Small values of Gaussian processes and functional laws of the iterated logarithm,* Proba. Theo. Rel. Fields Vol. 101 p. 173-192 (1995).

[54] L. Olsen, *A multifractal formalism,* Adv. Math., vol. 116 pp. 92–195 (1995).

[55] G. Parisi and U. Frisch, *On the singularity structure of fully developed turbulence;* appendix to *Fully developed turbulence and intermittency,* by U. Frisch; Proc. Int. Summer school Phys. Enrico Fermi, 84-88 North Holland (1985).

[56] R. Riedi, *An improved multifractal formalism and self-similar measures,* J. Math. Anal. Appl. Vol. 189, No.2, pp. 462–490 (1995).

[57] S. Roux, B. Lashermes, P. Abry and S. Jaffard, Contributions l'étude des performances statistiques des estimateurs multifractals, XXIème colloque GRETSI, Louvain- la-Neuve, belgium, 2005.

[58] K.R. Sreenivasan, *Fractals and multifractals in turbulence*, Ann. Rev. Fluid Mech.,23, 1991, 539–600.

[59] W. Stute, *The oscillation behavior of empirical processes,* Ann. Proba. Vol. 10, pp. 86–107 (1982).

Stéphane Jaffard
Laboratoire d'Analyse et de Mathématiques Appliquées, Université Paris XII,
61 Avenue du Général de Gaulle,
94010 Créteil Cedex, France
and Institut Universitaire de France.
e-mail: jaffard@univ-paris12.fr

Bruno Lashermes
Laboratoire de Physique / École Normale Supérieure de Lyon and CNRS UMR 5672,
46, allée d'Italie,
69364 Lyon cedex, France
e-mail: Bruno.Lashermes@ens-lyon.fr

Patrice Abry
Laboratoire de Physique / École Normale Supérieure de Lyon and CNRS UMR 5672,
46, allée d'Italie,
69364 Lyon cedex, France
e-mail: Patrice.Abry@ens-lyon.fr

Wavelet Analysis and Applications
Tao Qian, Mang I. Vai and Xu Yuesheng, Eds.
Applied and Numerical Harmonic Analysis, 247–254

Application of Fast Wavelet Transformation in Parametric System Identification

Klaus Markwardt

Abstract. This work deals with discrete embedding of system operators in identification models on basis of Fast Wavelet Transformation (FWT). In particular for FWT-models of linear dynamic systems the missing variables can be calculated with the help of connection coefficients. The application of connection coefficients provides the direct projection of the system operators into the corresponding wavelet space. Here a class of operators is introduced, which satisfies certain permutability relations with respect to dilations and translations. This class contains especially derivation and integration operators and some special convolution operators, like the Hilbert-transform. Such a definition allows the systematic determination of generalized connection coefficients. It gives so the possibility to realize identification procedures for different models and their implementations in a unified pattern. The method can be used for all biorthogonal wavelet systems whose synthesis functions are in the domain of the system operators.

Keywords. FWT, biorthogonal wavelets, connection coefficients, system identification.

1. Biorthogonal Wavelet Systems

Every vector $c \in \mathbb{R}^{\mathbb{Z}}$ with finite many entries is here shortly called a (finite discrete) filter. With appropriate indices $s, u \in \mathbb{Z}$ it can be written in the form

$$c = \big(\cdots, \quad 0, \quad 0, \quad c_s, \quad \cdots, \quad c_u, \quad 0, \quad 0, \quad \cdots \big) . \tag{1.1}$$

Let's assume that $\{h, \tilde{h}, g, \tilde{g}\}$ is a system of four filters with the following properties

$$\sum_k h_k \, \tilde{h}_{k+2l} = \delta_{l0} , \qquad \sum_k g_k \, \tilde{g}_{k+2l} = \delta_{l0} , \tag{1.2}$$

$$\sum_k \tilde{h}_k \, g_{k+2l} = 0 , \qquad \sum_k h_k \, \tilde{g}_{k+2l} = 0 , \tag{1.3}$$

$$\sum_k h_k = \sum_k \tilde{h}_k = \sqrt{2} , \qquad \sum_k g_k = \sum_k \tilde{g}_k = 0 . \tag{1.4}$$

The two integers s, u are chosen such that all four filters can be written in the form (1.1) with the same minimal $[s, u] \subset \mathbb{Z}$. It follows

$$\sum_k (-1)^k h_k = 0 \quad \text{and} \quad \sum_k (-1)^k \tilde{h}_k = 0. \tag{1.5}$$

Further conclusions and relations to other biorthogonal filter representations are given in [5], cp. [2], [3], and for the special orthogonal case in [1], [4]. If this filters fulfill some further properties, which are related to the eigenvalues of two Lawton matrices, then by

$$\varphi(t) = \sqrt{2} \sum_k h_k \, \varphi(2t-k)\,, \qquad \psi(t) = \sqrt{2} \sum_k g_k \, \varphi(2t-k) \tag{1.6}$$

$$\tilde{\varphi}(t) = \sqrt{2} \sum_k \tilde{h}_k \, \tilde{\varphi}(2t-k) \qquad \tilde{\psi}(t) = \sqrt{2} \sum_k \tilde{g}_k \, \tilde{\varphi}(2t-k) \tag{1.7}$$

$$\int_{-\infty}^{\infty} \varphi(t)\, dt = \int_{-\infty}^{\infty} \tilde{\varphi}(t)\, dt = 1\,. \tag{1.8}$$

scaling functions $\varphi, \tilde{\varphi} \in L^2(\mathbb{R})$ and wavelets $\psi, \tilde{\psi} \in L^2(\mathbb{R})$ are determined uniquely. They have compact support, such that with the above defined s, u

$$supp(\varphi) \subset [s, u]\,, \qquad supp(\tilde{\varphi}) \subset [s, u] \tag{1.9}$$

is valid. The deduced variants $\varphi_{j,k}(t) = \sqrt{2^{-j}}\, \varphi(2^{-j}\, t - k)$, $\cdots\cdots$
for $i, j, k, l \in \mathbb{Z}$ satisfy the biorthogonal relations

$$\langle \varphi_{j,k} \, , \, \tilde{\varphi}_{j,l} \rangle = \delta_{k,l} \tag{1.10}$$

$$\langle \varphi_{i,k} \, , \, \tilde{\psi}_{j,l} \rangle = \langle \tilde{\varphi}_{i,k} \, , \, \psi_{j,l} \rangle = 0 \quad \text{for} \quad i \geq j \tag{1.11}$$

$$\langle \psi_{i,k} \, , \, \tilde{\psi}_{j,l} \rangle = \delta_{i,j} \cdot \delta_{k,l}\,. \tag{1.12}$$

In particular $\{\psi_{i,k}\}, \{\tilde{\psi}_{i,k}\}$ builds a pair of biorthogonal Riesz bases in $L^2(\mathbb{R})$, cp.[2] and [3]. Using $\tilde{\varphi}$, $\tilde{\psi}$ in the synthesis and φ, ψ in the analysis we get for the projection on the level J

$$(\tilde{\mathbf{P}}_J f)(t) = \sum_k S_{Jk} \, \tilde{\varphi}_{J,k}(t) \qquad with \qquad S_{Jk} = \langle f \, , \, \varphi_{J,k} \rangle\,. \tag{1.13}$$

Let f_s be a sampled signal. After suitable dilation it can be approximated by (1.13) on the level $J = 0$ using wavelet sampling approximation or an preprocessing method for getting the basic coefficients S_{0k}, cp.[5]. Successive applying of the decomposition formulas (FWT)

$$S_{l+1,k} = \sum_r h_{r-2k}\, S_{l,r}\,, \qquad W_{l+1,k} = \langle f \, , \, \psi_{l+1,k} \rangle = \sum_r g_{r-2k}\, S_{l,r} \tag{1.14}$$

gives the representation with the wavelet coefficients W_{lk}

$$(\tilde{\mathbf{P}}_0 f)(t) = \sum_k S_{Lk} \, \tilde{\varphi}_{L,k} + \sum_{l=1}^{L} \left\{ \sum_k W_{lk} \, \tilde{\psi}_{l,k} \right\}. \tag{1.15}$$

With increasing l the frequency center of the inner sums decreases step by step by the factor 0.5. Using wavelet packets induced by appropriate $\{h, \tilde{h}, g, \tilde{g}\}$ you get trees with the possibility of stronger locally frequency resolution, cp.[10].
The inverse formula of (1.14) is known as

$$S_{l,k} \;=\; \sum_r \tilde{h}_{k-2r}\, S_{l-1,r} \;+\; \sum_r \tilde{g}_{k-2r}\, W_{l-1,r}\,. \tag{1.16}$$

2. Connection Coefficients for D-homogeneous Operators

The parameter depending affine groups $T(r)$ and $D(s)$ are defined by

$$T(r)\;:\;\; f(t) \;\mapsto\; f(t-r)\,,\; r \in \mathbb{R} \quad \text{and} \quad D(s)\;:\;\; f(t) \;\to\; \sqrt{s} f(st)\,,\; s > 0 \tag{2.1}$$

With this notations $\varphi_{l,j} = D(2^{-l})\, T(j)\, \varphi$ and corresponding formulas are valid. This paper is researched into connection coefficients for operators with the following properties.

Definition 2.1. Here will be written $\mathbf{K} \in \mathbb{H}_\lambda(\mathbf{V}_1, \mathbf{V}_2)$ or shorter $\mathbf{K} \in \mathbb{H}_\lambda$ with some $\lambda \in \mathbb{R}$, if $\mathbf{K} : \mathbf{V}_1 \mapsto \mathbf{V}_2$ is a linear operator with $\mathbf{V}_1$ as a subspace of $L_0^2(\mathbb{R})$ and $\mathbf{V}_2$ as a subspace of $L_{loc}^2(\mathbb{R})$, whereas

$$T(r)\, \mathbf{V}_i \subset \mathbf{V}_i \quad \text{and} \quad D(s)\, \mathbf{V}_i \subset \mathbf{V}_i, \tag{2.2}$$

$$\mathbf{K}\, T(r) = T(r)\, \mathbf{K} \qquad \text{and} \qquad \mathbf{K}\, D(s) = s^\lambda\, D(s)\, \mathbf{K} \tag{2.3}$$

are valid. Operators with the right property in (2.3) will called D-homogeneous of degree λ.

Example. Let $\mathbf{V}_1$ be the space of functions f with compact support and $f \in \mathrm{H}^n(\mathbb{R})$ (Sobolev space of order n). For $\mathcal{D} = \frac{d}{dt}$ the operator $\mathcal{D}^n$ with $n \in \mathbb{N}$ satisfies then $\mathcal{D}^n \in \mathbb{H}_n$. $\mathbf{V}_2$ can be taken as the space of all functions $g \in L^2(\mathbb{R})$ with compact support.

Example. With $f^{(-1)}(t) = \mathcal{I}(f)(t) := \int_{-\infty}^{t} f(\tau)\, d\tau$, $\mathbf{V}_1 = L_0^2(\mathbb{R})$ and $\mathbf{V}_2 = L_{loc}^2(\mathbb{R})$ results $\mathcal{I}^n \in \mathbb{H}_{-n}$ for $n \in \mathbb{N}$. Obviously the identity operator $\mathrm{I} = \mathcal{I}^{\,0} = \mathcal{D}^{\,0}$ satisfies $\mathrm{I} \in \mathbb{H}_0$.

Example. With suitable spaces $\mathbf{V}_1$, $\mathbf{V}_2$, the convolution operator

$$(\mathbf{K}f)(t) = \int_{-\infty}^{\infty} k(t-\tau) f(\tau)\, d\tau\,, \tag{2.4}$$

and the conventions $v_+(t) = \max(v(t), 0)$, $v_-(t) = \min(v(t), 0)$ the following special cases for definition 2.1 result:

1. $k(t)$ is one of the functions $t^{\alpha-1}$, $t_+^{\alpha-1}$, $t_-^{\alpha-1}$ with arbitrary positive α. The spaces are given by $\mathbf{V}_1 = \mathcal{C}_0$, $\mathbf{V}_2 = \mathcal{C}$. Now you get $\mathbf{K} \in \mathbb{H}_{-\alpha}$.
2. The same as above, but with $\alpha > 0.5$ and the changed space $\mathbf{V}_1 = L_0^2$. $\alpha \in \mathbb{N}$ provides the integrals of the previous example.

3. With $k(t) = \pi^{-1}\, t^{-1}$ and (2.4) in the sense of Cauchy principal value you get the Hilbert-Transformation. Now let $\mathbf{V}_1$ be a space of Hoelder continuous functions with compact support, $\mathbf{V}_1 \subset \mathcal{C}^\alpha,\ \alpha > 0$ and $\mathbf{V}_2 = \mathcal{C}$.

The discrete embedding of an operator $\mathbf{K} \in \mathbb{H}_\lambda$ over the projection $\tilde{\mathbf{P}}_0$ is given by

$$(\mathbf{K}\,\tilde{\mathbf{P}}_0 f)(t) = \sum_\nu S_{0\nu}\,\mathbf{K}\,\tilde{\varphi}_{0,\nu}(t) \xrightarrow{\tilde{\mathbf{P}}_0} \sum_\nu S^K_{0\nu}\,\tilde{\varphi}_{0,\nu}(t) = (\tilde{\mathbf{P}}_0 \mathbf{K}\,\tilde{\mathbf{P}}_0 f)(t) \tag{2.5}$$

with

$$S^K_{0l} = \sum_\nu S_{0\nu}\,\langle \mathbf{K}\,\tilde{\varphi}_{0,\nu}\ ,\ \varphi_{0,l}\rangle \qquad \text{or} \qquad S^K_0 = S_0\,K^{(0)}\ . \tag{2.6}$$

Here $K^{(0)}$ is the matrix induced by the corresponding system of scalar products. It's elements are special connection coefficients, the basic coefficients. Coming from $\varphi_{l,j} = D(2^{-l})\,T(j)\,\varphi, \cdots, \cdots$ the connection coefficients will defined by

$$\Gamma^{mk}_{lj}(\tilde{f}, f) = \langle \mathbf{K}\,\tilde{f}_{l,j}\ ,\ f_{m,k}\rangle\,. \tag{2.7}$$

Some shorter forms for the basic coefficients are used

$$\Gamma^k_j := \Gamma^{0k}_{0j}\,(\tilde{\varphi}, \varphi) \quad \text{and} \quad \Gamma^k_j(\tilde{f}, g) := \Gamma^{0k}_{0j}(\tilde{f}, g)\,. \tag{2.8}$$

The following theorems are proofed in [5].

Theorem 2.2. *The connection coefficients of* $\mathbf{K} \in \mathbb{H}_\lambda$ *satisfy*

$$2^{l\cdot\lambda}\,\Gamma^{mk}_{lj} = \Gamma^{m-l,k-2^{l-m}j}_{00}\,, \qquad 2^{l\cdot\lambda}\,\Gamma^{lk}_{lj} = \Gamma^{0,k-j}_{00} = \Gamma^{k-j}_0\,, \tag{2.9}$$

$$\Gamma^{l,k+n}_{l,j+n} = \Gamma^{l,k}_{l,j}\,, \quad \Gamma^{k+n}_{j+n} = \Gamma^k_j\,, \quad \Gamma^{l,k}_{l,j} = \Gamma^{l,k-j}_{l,0}\,, \quad \Gamma^k_j = \Gamma^{k-j}_0 \tag{2.10}$$

$$\Gamma^{mk}_{lj} = 2^{n\lambda}\,\Gamma^{m+n,k}_{l+n,j}\,, \tag{2.11}$$

if $\tilde{f}, f \in \mathbf{V}_1$.

Theorem 2.3. *Both for* $\tilde{f} = \tilde{\varphi},\ \tilde{f} = \tilde{\psi}$ *and* $f = \varphi,\ f = \psi$ *follows with* $\mathbf{K} \in \mathbb{H}_\lambda$

$$\sum_{\nu=s}^{u} h_\nu\,\Gamma^{m-1,\nu+2k}_{lj}(\tilde{f}, \varphi) = \Gamma^{mk}_{lj}(\tilde{f}, \varphi) = 2^\lambda \sum_{\nu=s}^{u} h_\nu\,\Gamma^{m,\nu+2k}_{l+1,j}(\tilde{f}, \varphi) \tag{2.12}$$

$$\sum_{\nu=s}^{u} g_\nu\,\Gamma^{m-1,\nu+2k}_{lj}(\tilde{f}, \varphi) = \Gamma^{mk}_{lj}(\tilde{f}, \psi) = 2^\lambda \sum_{\nu=s}^{u} g_\nu\,\Gamma^{m,\nu+2k}_{l+1,j}(\tilde{f}, \varphi) \tag{2.13}$$

$$\sum_{\nu=s}^{u} \tilde{h}_\nu\,\Gamma^{mk}_{l-1,\nu+2j}\,(\tilde{\varphi}, f) = \Gamma^{mk}_{lj}\,(\tilde{\varphi}, f) = 2^\lambda \sum_{\nu=s}^{u} \tilde{h}_\nu\,\Gamma^{m+1,k}_{l,\nu+2j}\,(\tilde{\varphi}, f) \tag{2.14}$$

$$\sum_{\nu=s}^{u} \tilde{f}_\nu \Gamma^{m,k}_{l-1,\nu+2j}(\tilde{\varphi}, f) = \Gamma^{mk}_{lj}(\tilde{\psi}, f) = 2^\lambda \sum_{\nu=s}^{u} \tilde{f}_\nu \Gamma^{m+1,k}_{l,\nu+2j}(\tilde{\varphi}, f) \tag{2.15}$$

(For the equations on the left sides only linearity is necessary.) If the basic coefficients are known, than step by step all other connection coefficients can be verified.

3. Calculation of Basic Coefficients

The proofs of the following theorems you find in [5] for the general case and in [7] for the special orthogonal case. They generalize some results in [1] and [12].

Theorem 3.1. *For* $\mathbf{K} \in \mathbb{H}_\lambda$ *and* $\mathcal{N} = u - s$, *cp.*(1.1), *the basic coefficients satisfy the system of equations*

$$\Gamma_0^k = 2^\lambda \sum_\nu \alpha_{2k-\nu}\, \Gamma_0^\nu\,, \quad 2k - \mathcal{N} \le \nu \le 2k + \mathcal{N}, \quad \forall k \in \mathbb{Z} \tag{3.1}$$

with $\alpha_\nu = \sum_\mu h_\mu \tilde{h}_{\nu+\mu}$. *The relations* $\alpha_0 = 1$, $\sum_\nu \alpha_{2\nu-1} = 1$, $\alpha_{2\nu} = 0$ *for* $\nu \neq 0$ *and* $\alpha_\nu = 0$ *for* $|\nu| > \mathcal{N}$ *are valid.*

The following definitions are basic for researching the system (3.1).

A submatrix $L = L(h, \tilde{h})$ of (3.1) is given by

$$L_{ij} = \alpha_{2i-j} \quad \text{with} \quad i, j = 1 - \mathcal{N}, \cdots, \mathcal{N} - 1 \tag{3.2}$$

and called here **Lawton matrix** of 2. kind.

An operator $\mathbf{K}$ will called **causal**, if

$$f(t) = 0 \quad \text{for} \quad t < T \quad \text{results ever} \quad (Kf)(t) = 0 \quad \text{for} \quad t < T. \tag{3.3}$$

For $\mathbf{K} \in \mathbb{H}_\lambda$ the case $T = 0$ in (3.3) is sufficient.

Theorem 3.2. *If* $\mathbf{K} \in \mathbb{H}_\lambda$ *is causal, then*

$$\Gamma_0^k(\tilde{\varphi}, \varphi) = 0 \quad \textit{for} \quad k < 1 - \mathcal{N} \tag{3.4}$$

is valid. If furthermore for $\nu > \mathcal{N} - 1$ *the basic coefficients* $G_\nu := \Gamma_0^\nu$ *are kwown then with the Lawton matrix* L *in* (3.2) *follows*

$$\sum_{\nu=1-\mathcal{N}}^{\mathcal{N}-1} (L_{k\nu} - 2^{-\lambda}\delta_{k\nu})\, \Gamma_0^\nu(\tilde{\varphi}, \varphi) = -\sum_{\nu=\mathcal{N}}^{3\mathcal{N}-2} \tilde{\alpha}_{2k-\nu} G_\nu, \quad k = 1-\mathcal{N}, \cdots, \mathcal{N}-1 \tag{3.5}$$

This system has then an unique solution if $\mu = 2^{-\lambda}$ *is no eigenvalue of the Lawton matrix* L. *If the right side of* (3.5) *vanishes and the eigenvalue* $\mu = 2^{-\lambda}$ *has order* 1, *then the solution becomes unique if an additional inhomogeneous linear equation can be found for the unknowns* Γ_0^ν.

Remark 3.3. Making stronger the condition (1.5) regarding $\{\tilde{h}_k\}$ by

$$\sum_k (-1)^k\, k^\nu\, \tilde{h}_k = 0 \quad \text{for} \quad \nu = 0, 1, ..., n\,, \tag{3.6}$$

(1.13) changes for better approximation properties with increasing n. In particular the moments of the dual wavelets vanish up to order n.

$$M_\nu(\psi) = \int_{-\infty}^{\infty} t^\nu \psi(t)\, dt = 0 \quad \text{for all} \quad \nu = 0, 1, ..., n\,, \tag{3.7}$$

Theorem 3.4. *Let be the scaling coefficients* $\tilde{h}_k$ *satisfied additionally* (3.6) *and* $\tilde{\varphi} \in H^n(\mathbb{R})$. *Then the basic coefficients of the differentiation operator* $\mathcal{D}^n$ $\Gamma_0^\nu(n) = \left\langle \tilde{\varphi}^{(n)} \, , \, \varphi_{0,\nu} \right\rangle$ *fulfill the homogeneous equations*

$$\sum_{\nu=1-\mathcal{N}}^{\mathcal{N}-1} (L_{k\nu} - 2^{-n}\delta_{k\nu})\, \Gamma_0^\nu(n) = 0, \qquad k = 1-\mathcal{N}, \cdots, 0, \cdots, \mathcal{N}-1 \tag{3.8}$$

and the inhomogeneous equation

$$\sum_{\nu=1-\mathcal{N}}^{\mathcal{N}-1} \nu^n\, \Gamma_0^\nu(n) = (-1)^n\, n! \tag{3.9}$$

Remark 3.5. Corresponding to the integration operator $\mathcal{I}^n$, which is causal, you have

$$\Gamma_0^\nu(-n) = \langle \mathcal{I}^n \tilde{\varphi} \, , \, \varphi_{0\nu} \rangle = 0 \quad \text{for} \quad \nu \le -\mathcal{N}, \quad \forall n \in \mathbb{N}, .$$

First you must calculate

$$G_\nu(-n) = \Gamma_0^\nu(-n) \quad \text{with} \;\; n \in \mathbb{N}, \quad \text{for} \quad \nu \ge \mathcal{N}.$$

on the right side of (3.5). In [5] recurrence formulas are developed for calculating the $G_\nu(-n)$, which at last only use discrete moments m_n of the scaling filters $h, \; \tilde{h}$

$$m_n(h) = \sum_{\nu=s}^{u} \nu^n\, h_\nu \, .$$

This formulas provide the $G_\nu(-n)$ as polynomials in ν of order $(n-1)$. Note that in [5] has been worked with different normed filters $a = \sqrt{2}\, h, \cdots$. The first three $G_\nu(-n)$ are given by

$$G_\nu(-1) = \Gamma_0^\nu(-1) = 1 \quad \text{for} \quad \nu \ge \mathcal{N},$$

$$G_\nu(-2) = \Gamma_0^\nu(-2) = \nu + \frac{\sqrt{2}}{2}\left[m_1(h) - m_1(\tilde{h})\right] \quad \text{for} \quad \nu \ge \mathcal{N},$$

$$G_\nu(-3) = \Gamma_0^\nu(-3) = \frac{1}{2}\nu^2 + \frac{\sqrt{2}}{2}\left[m_1(h) - m_1(\tilde{h})\right]\nu + C(3,\mathcal{I}) \quad \text{for} \quad \nu \ge \mathcal{N}$$

the last with

$$C(3,\mathcal{I}) = \frac{\sqrt{2}}{12}\left[m_2(h) + m_2(\tilde{h})\right] + \frac{1}{6}\left[(m_1(h))^2 - 3m_1(h)m_1(\tilde{h}) + \left(m_1(\tilde{h})\right)^2\right].$$

The remaining Γ_0^ν are found now by (3.5) after controlling that $\mu = 2^n$ for $n = 1, 2, 3$ is no eigenvalue of the Lawton matrix L. In the orthogonal case you obtain $\tilde{h} = h, \; \varphi = \tilde{\varphi}, \;\; \psi = \tilde{\psi}$ and you get the original Lawton matrix in [4]. The greatest eigenvalue becomes 1 if the wavelets build an orthogonal system, such that theorem 3.2 can be applied. Applying formulas given in [7] this special case would used for an identification algorithm in the engineering work [11].

In [5] is shown that the wavelet based quadrature filter $\{\Gamma_0^\nu(-1)\}$ can be decomposed, such that it's application is no more extensive then that of a good

quadrature formula. We think that this wavelet adapted filter gives better results in identification procedures.

Theorem 3.2 is also applicable in the case of different biorthogonal B-spline produced wavelets (cp.[2] and [3]), such that identification algorithms can also be realized with the help of this systems, cp. [10].

Remark 3.6. Corresponding to the differentiaton operator $\mathcal{D}^n$ theorems 3.2 and 3.4 are applicable for customary orthogonal or biorthogonal wavelets, like Daubechies wavelets, Symlets, Coiflets and B-Spline produced wavelets. If the order of these wavelets becomes sufficiently high then 2^{-n} becomes an eigenvalue of order 1. Practically this can be used in the cases $n = 1$ and $n = 2$. This extends the possibilities given in [1] and [12] on the biorthogonal case.

4. Applications and Outlook

Here an extract of [5] (generalization of [7]) is given. This works were written to give engineers some special background in parametric system identification. But sure they are useful also in other fields of applied mathematics, for instance in solving operator equations. In [11] such basics were used to work out a wavelet-based method that allows the direct identification of system parameters from data generated in dynamic tests of a structure. Of specific interest was an algorithm that requires the response data solely in the form of accelerations. The method was successful applied to multi-degree-of-freedom systems and to existing structural elements and structures in civil engineering. The parameters of linear time-invariant systems could be identified with a relatively high accuracy, even if the simulated data were contaminated by noise. The identified stiffness terms agreed better with the original values than the viscous damping parameters. Intended is the improvement of this applications by the use of biorthogonal wavelets and wavelet packets, cp. [10] and [9].

References

[1] G. Beylkin & B. Torresani, *Implementation of Operators via Filter Banks.* Applied and Computational Harmonic Analysis 3, 1996, 164–185.

[2] A. Cohen, I. Daubechies & J.C. Feauveau, *Biorthogonal bases of compactly supported wavelets.* Communications on Pure and Applied Mathematics, Vol.XLV, 485–560, 1992.

[3] A. Cohen, *Biorthogonal Wavelets.* Wavelets in Analysis and Applications II, 123–152, Academic Press 1992.

[4] W.M. Lawton, *Necessary and sufficient conditions for constructing orthonormal wavelet bases.* J. Math. Phys.32(1), 1440–1443, 1991.

[5] K. Markwardt, *Die schnelle Wavelet-Transformation als Grundlage für Verfahren zur System- und Parameteridentifikation.*Manuscript, pages 1–122 (2005), not published yet.

[6] K. Markwardt, *Biorthogonale Wavelet-Systeme in der Parameteridentifikation.* Proceedings of the 16th IKM 2003, Gürlebeck, Hempel & Könke (eds.), Weimar, Germany, June 10-12, 2003.

[7] K. Markwardt, *Systemanalyse und Parameteridentifikation mit Hilfe der schnellen Wavelet-Transformation.* Forschungbericht, 1–76, 2002, ISM, BUW, Weimar.

[8] K. Markwardt, *Betrachtungen zur Anwendung der Wavelet-Transformation in der Systemidentifikation.* 6. Institutskolloquium, Bericht 1/00, 2000, 107–126, ISM, Bucher, Burkhardt & Vormwald (eds.).

[9] M. Brehm, K. Markwardt and V. Zabel, *Applications of Wavelet Packets in System Identification.* Jahrestagung GAMM, 2005, Universit du Luxembourg.

[10] M. Brehm, K. Markwardt and V. Zabel, *Applications of Biorthogonal Wavelets in System Identification.* ECCOMAS 2004. Jyväskyla, Neittaanmäki, Rossi, K. Majava & O. Pironneau (eds.).

[11] V. Zabel, *Applications of Wavelet Analysis in System Identification.* Dissertation, 2003, Institute Structural Mechanics, Faculty of Civil Engeneering, Bauhaus-University Weimar

[12] Resnikoff, *Wavelet Analysis.* Springer, 1998

Klaus Markwardt
Coudraystr. 13 B
Bauhaus-University Weimar
Institute for Mathematics/Physics
99421 Weimar
Federal Republic of Germany
e-mail: `klaus.markwardt@bauing.uni-weimar.de`

Wavelet Analysis and Applications
Tao Qian, Mang I. Vai and Xu Yuesheng, Eds.
Applied and Numerical Harmonic Analysis, 255–261

Image Denoising by a Novel Digital Curvelet Reconstruction Algorithm

Jian Bai and Xiang-Chu Feng

Abstract. For an anisotropic image, wavelets lose their effects on singularity detection because discontinuities across edges are spatially distributed. Based on the idea of curvelet, a new digital curvelet reconstruction algorithm is proposed. Our algorithm provides sparser representations and keeps low computational complexity. When applying it to the image denoising, much better results than the original algorithm are obtained.

Keywords. Curvelet, ridgelet, digital curvelet, Radon transform, fast Slant Stack.

1. Introduction

Many image processing tasks take advantage of sparse representations of image data where most information is packed into a small number of samples. The wavelet transform is the most popular choices for this purpose. The success of wavelets is mainly due to the good performance for piecewise smooth functions in one dimension. Unfortunately, such is not the case in two dimensions. To overcome the weakness of wavelets in higher dimensions, E.J.Candes and D.L.Donoho introduced the concepts of ridgelet transform and curvelet transform[1,2]. Ridgelet system is very good at representing the smooth functions with line singularities. Essentially, Radon transform was used to the original image, and then the wavelet analysis in the Radon domain was applied. Curvelets are derived from theory of ridgelet. They are based on multiscale ridgelets combined with a spatial bandpass filtering operation to isolate different scales. Curvelet transform filters image into subbands, so there are many subband images with different frequencies. For the lowpass image, apply wavelet analysis to it. For the bandpass images, apply multiscale ridgelets to them. The length and width of curvelets at fine scales are related by a scaling law: $width \approx lenth^2$. Compare with the traditional isotropic relation in wavelet transform, they have anisotropic relation. This makes they are very good at representing the smooth functions with curve singularities. Thus curvelets have

great potentialities in the image denoising, enhancement and other application cases.

The digital realization of curvelet was proposed in [3,4]. J.L. Starck applied it to the image denoising and the very good results were obtained. He used the generalized Radon inverse transform to implement ridgelet reconstruction. Our algorithm computes the orthogonal projection of the original block image into the space spanned by the thresholded ridgelet bases. When the thresholded ridgelet bases span $n \times n$ (where n is the size of block image) space, the block image can be completely reconstructed. The orthogonal projection is the best approximation of the origin block image, so the new algorithm provides sparser representations. The new algorithm still keeps low computational complexity. It can be computed in order $O(N \log N)$, where $N = n^2$. In this paper we use it to digital curvelet reconstruction. The very high quality and signal-to-noise ratios are illustrated by denoising the noisy Lenna and barbara images.

2. Digital Curvelet Transform

Curvelet bases $r_\mu = r_\mu(x_1, x_2)$ are defined as tight frame of $L^2\left(R^2\right)$ in [1,3]. It is the sequence of the following steps: a. subband decomposition b. smooth partitioning c. renormalization d. ridgelet analysis. Curvelet transform uses ridgelet transform as a component step, so we firstly describe a digital ridgelet transform.

2.1. Digital Ridgelet

There are a number of methods that can implement discrete ridgelet transform. We use the method in [5]. Essentially, use fast Slant Stack algorithm to implement Radon transform, and then apply Meyer wavelet transform in t. The digital ridgelet analysis operator R applied to an $n \times n$ image $\left(I(u,v) : -\frac{n}{2} \le u, v \le \frac{n}{2}\right)$ is the $4n^2$ ridgelet coefficients:

$$RI = \left(\langle I, \rho_\lambda \rangle ; \lambda \in \mu, \mu = (j,k,s,l)\right) \tag{2.1}$$

The following theorem shows the relation between the digital ridgelet transform R and discrete Slant Stack S followed by the Meyer wavelet transform W.

Theorem 1 [5] The digital ridgelet transform is the 1-dimensional Meyer-wavelet transform in t, of the Slant Stack Radon transform:

$$(RI)(j,k,s,l) = << SI(\cdot, s, l), \psi_{j,k}(\cdot) >> \tag{2.2}$$

Let R^* be the adjoint of R, then $R^* = S^* \cdot W^{-1}$, where W^{-1} is the Meyer wavelet reconstruction operator, S^* is the adjont of S. R and R^* can be computed in the order $O(N \log N)$.

2.2. Digital Curvelet Transform

Now we describe a strategy for realizing a digital implementation of the curvelet transform.

Subband Decomposition: Image size is 256×256. We use Daubechies 4 wavelet to divide it into 8 subbands, at levels $j = 0, 1 \cdots 7$. The curvelet subband $s = 1$ corresponds to wavelet subbands $j = 0, 1, 2, 3$. Curvelet subband $s = 2$ corresponds to wavelet subbands $j = 4, 5, 6$. Curvelet subband $s = 3$ corresponds to wavelet subband $j = 7$. Hence, for image f, we get lowpass image f_1 and bandpass images f_2, f_3.

Partitioning: For f_2, partition it by 32×32 blocks $f_{2,i,j}$. There are 64 blocks $f_{2,i,j}\,(1 \le i \le 8, 1 \le j \le 8)$.
For f_3, partition it by 16×16 blocks $f_{3,m,n}$. There are 256 blocks $f_{3,m,n}\,(1 \le m \le 16, 1 \le n \le 16)$.

Ridgelet Analysis: For f_2, use 64×64 overlay blocks $g_{2,p,q}$ to cover it, where $(1 \le p \le 7, 1 \le q \le 7)$.

$$g_{2,p,q} = f_2\left([(p-1) \times 32 + 1, (p+1) \times 32] \times [(q-1) \times 32 + 1, (q+1) \times 32]\right).$$

For f_3, use 32×32 overlay blocks $g_{3,x,y}$ to cover it, where $(1 \le x \le 15, 1 \le y \le 15)$,

$$g_{3,x,y} = f_3\left([(x-1) \times 16 + 1, (x+1) \times 16] \times [(y-1) \times 16 + 1, (y+1) \times 16]\right).$$

Apply ridgelet transform to $g_{2,p,q}$ and $g_{3,x,y}$, getting the ridgelet coefficients $\alpha_{2,p,q,\lambda}$ and $\alpha_{3,x,y,\lambda}$, where λ is ridgelet index.

2.3. Reconstruction Algorithm

The above steps enjoy exact reconstruction, so the reconstruction algorithm is divided into the following steps:

Ridgelet Reconstruction: For ridgelet coefficients of each block image α_η, we apply the inverse transform in [5], where $R^{-1} = S^{-1}W^{-1}$ and S^{-1} is the generalized Radon inverse transform operator in [6].

Smooth Partition: We calculate a pixel value, $f_{2,i,j}$ from its four corresponding block values, namely, 64×64 blocks B_1, B_2, B_3 and B_4, in the following way:

$$h_1 = w\left(i_2/l\right) B_1\left(i_1, j_1\right) + w\left(1 - i_2/l\right) B_2\left(i_2, j_1\right)$$

$$h_2 = w\left(i_2/l\right) B_3\left(i_1, j_2\right) + w\left(1 - i_2/l\right) B_4\left(i_2, j_2\right)$$

$$\Delta f_{2,i,j} = w\left(j_2/l\right) h_1 + w\left(1 - j_2/l\right) h_2$$

where $w(x) = \cos^2(\pi x/2)$ is the smooth function. l =32 is the size of block, $i_2 = i_1 - l$, $j_2 = j_1 - l$, $i_1, j_1 > l$. Similarly, for $f_{3,m,n}$, we have $\Delta f_{3,m,n}$.

Subband Reconstruction: For each subband we get the reconstructed subband images Δf_1, Δf_2, Δf_3 and undo the bank of subband filters, using the reproducing formula: $\tilde{f} = \Delta_1(\Delta f_1) + \Delta_2(\Delta f_2) + \Delta_3(\Delta f_3)$.

3. New Reconstruction Algorithm

We use the following algorithm to implement ridgelet reconstruction.

Apply the ridgelet transform to the original block image I, threshold the ridgelet coefficents, getting the space V spanned by the thresholded ridgelets, index set T and the ridgelet coefficient matrix $M = \begin{cases} \langle I, \rho_\lambda \rangle & \lambda \in T \\ 0 & \lambda \notin T \end{cases}$.

The new algorithm computes the orthogonal projection of the original block image I into the space V. It can be divided into three steps:
Step1: Apply the adjoint ridgelet transform to M, getting $b = R^*M$. In fact, the Mallat algorithm is used to obtain $W^{-1}M$; the adjoint Slant Stack in [6] is used to compute $b = S^*\left(W^{-1}M\right)$.
Step 2: Solve f from equation:

$$L_v f = b \tag{3.1}$$

where $L_v f = R^*\left(\overline{Rf}\right)$, $\overline{Rf} = \begin{cases} Rf & \lambda \in T \\ 0 & \lambda \notin T \end{cases}$.

We use conjugate gradient to solve Eq3.1. Details are in [7]. The whole procedure takes $O(N \log N)$ which is the same as the cost of the original algorithm. For the block reconstructed image f, we have the following results:
Theorem 2 The block reconstructed image by the new algorithm is $f = \sum_{\lambda \in T} \langle I, \rho_\lambda \rangle \tilde{\rho}_\lambda$, where $\{\tilde{\rho}_\lambda\}_{\lambda \in T}$ is the dual frame of $\{\rho_\lambda\}_{\lambda \in T}$ which is the frame of V. f is the orthogonal projection of I into the subspace V.

Proof. According to $R^*(1_\lambda) = \rho_\lambda$, where 1_λ is characteristic matrix,
$1_\lambda(\mu) = \begin{cases} 1 & \mu = \lambda \\ 0 & \mu \neq \lambda \end{cases}$, so $M = \sum_{\lambda \in T} \langle I, \rho_\lambda \rangle 1_\lambda$,
we have $R^*M = \sum_{\lambda \in T} \langle I, \rho_\lambda \rangle \rho_\lambda$, $L_V f = \sum_{\lambda \in T} \langle f, \rho_\lambda \rangle \rho_\lambda$, where L_V is the frame operator of space V. It is invertible. $\{\tilde{\rho}_\lambda\}_{\lambda \in T}$ which is the dual frame of $\{\rho_\lambda\}_{\lambda \in T}$ can be defined by the inverse operator L_V^{-1} : $\tilde{\rho}_\lambda = L_V^{-1}\rho_\lambda$, so $f = L_V^{-1}R^*M = \sum_{\lambda \in T} \langle I, \rho_\lambda \rangle \tilde{\rho}_\lambda$.

To prove that f is the orthogonal projection of I into V, it is enough to test for the arbitrary $p \in T$ that $\langle I - f, \rho_p \rangle = 0$. In fact, $\langle I - f, \rho_p \rangle = \langle I, \rho_p \rangle - \sum_{\lambda \in T} \langle I, \rho_\lambda \rangle \langle \tilde{\rho}_\lambda, \rho_p \rangle$.
We know the dual frame in V has property:

$$\sum_{\lambda \in T} \langle \tilde{\rho}_\lambda, \rho_p \rangle \rho_\lambda = \rho_p$$

Therefore $\langle I - f, \rho_p \rangle = 0$. That ends the proof. □

For each block image with size $n \times n$, we use the new algorithm to implement ridgelet reconstruction, so a new digital curvelet reconstruction algorithm is obtained. Our algorithm introduces an extra redundancy factor of $16J + 1$. The article [4] used the generalized Radon inverse transform. In order to completely reconstruct the block image, $4n^2$ coefficients must be used. The new algorithm can completely reconstruct the block image when n^2 linearly independent bases are used.

4. Numerical Experiments

In this paper we add Gaussion white noise to Lenna and Barbara images with size 256×256. Similar to reference [4], we apply the hard-thresholding to it and use Monte-Carlo simulations to get the threshold. Let y_λ be the noisy coefficients, σ is noise standard deviation, $\overline{\sigma_\lambda}$ are estimated by evaluating curvelet transform of a few standard white noise images.

$$\overline{y_\lambda} = \begin{cases} y_\lambda & if |y_\lambda|/\sigma \geq k\overline{\sigma_\lambda} \\ 0 & if |y_\lambda|/\sigma < k\overline{\sigma_\lambda} \end{cases}.$$

In our experiments, we choose a subband-dependent value for k; we have $k = 3$ for the second subband ($s = 2$) while $k = 4$ for the third subband ($s = 3$).

The following figures show the results, where the signal-to-noise ratios unit is dB.The new algorithm outperforms original algorithm by 0.72db for Lenna and 0.78db for Barbara images. We can see that the edges and textures are much clearer by the new algorithm and the visual effect is greatly improved.

5. Conclusion

A new digital curvelet reconstruction algorithm is proposed. Instead of applying the generalized Radon inverse transform in [3,4], we compute the orthogonal projection of the original block image into the space spanned by the thresholded ridgelet bases. Because the orthogonal projection is the best approximation of the origin image, so the new algorithm provides sparser representations when applying it to the nonlinear approximation. The experiments of the image denoising show that the new algorithm exhibits much higher quality and SNR than the original algorithm and the visual effect is surprisingly good.

Figure 1: (Top left) Original image and (top right) noisy image 13.95db, (bottom left) denoising by the new algorithm 20.08db and (bottom right) denoising by the original algorithm 19.36db

Figure 2: (Top left) Original image and (top right) noisy image 13.95db, (bottom left) denoising by the new algorithm 18.81db and (bottom right) denoising by the original algorithm 18.03db

References

[1] E. J. Candes and D. L. Donoho, Curvelets—A Surprising Effective Nonadaptive Representation For Objects With Edges. Curve and Surface Fitting: Saint-Malo 1999, A. Cohen, C. Rabut, and L. Schumaker, eds., Vanderbilt University Press, (Nashville, TN), 1999.

[2] D. L. Donoho, Orthonormal Ridgelet and Linear Singularities. SIAM J. Math Anal., 31(5), 1062-1099, 2000.

[3] D. L. Donoho and M.R. Duncan, Digital curvelet Transform: Strategy, Implementation and Experiments. Proc. SPIE, 4056, 12-29, 2000.

[4] J. L. Starck, E. J. Candes, D. L. Donoho, The Curvelet Transform for Image Denoising. IEEE Trans. Image Processing, 11(6), 670-684, 2002.

[5] D. L. Donoho and Ana Georgina Flesia, Digital Ridgelet Transform based on True Ridge Functions. http://www.stat.Stanford.edu/donoho/Report.

[6] A.Averbuch, R. R. Coifman, D.L. Donoho, M. Israeli, J. Walden, Fast Slant Stack: A notion of Radon Transform for Data in a Cartesian Grid which is Rapidly Computible, Algebraically Exact, Geometrically Faithful and Invertible. http://www-stat.stanford.edu/ beamlab

[7] K. Grochenig, Acceleration of Frame Algorithm. IEEE Trans. Signal Processing, 41(12), 3331-3340, 1993.

Jian Bai
Department of Applied Mathematics
Xidian University
Xi'an
710071
China
e-mail: keywhite26@126.com

Xiang-Chu Feng
Department of Applied Mathematics
Xidian University
Xi'an
710071
China

Wavelet Analysis and Applications
Tao Qian, Mang I. Vai and Xu Yuesheng, Eds.
Applied and Numerical Harmonic Analysis, 263–271

Condition Number for Under-Determined Toeplitz Systems

Huaian Diao and Yimin Wei

Abstract. In this note, we prove that the structured condition number for Toeplitz under-determined systems with full row rank is not better than unstructured condition number in probability sense.

Mathematics Subject Classification (2000). Primary 15A09; Secondary 65F15, 65F10.

Keywords. Moore-Penrose inverse, Structured condition number, Under-determined Toeplitz systems.

1. Introduction

In signal and image processing, by using wavelet [1, 2, 3], the resulting system sometimes is singular. There are few papers concerning the singular linear system. In this note, we show that the structured condition number for Toeplitz under-determined systems with full row rank is not better than unstructured condition number in probability sense.

Structured matrices, for example, Toeplitz, Hankel, Vandermonde and Cauchy matrices, are very important in applied mathematics, computer science and engineering [4], such as in system theory, signal processing, network theory and linear prediction etc.

The problem for structured matrices, such as structured low rank approximation [5], is difficult because the matrix structure should be considered. Recent developments in structured matrices can be founded in [6, 7, 8, 9, 10, 11, 12, 13, 14, 15].

This work was completed with the support of the National Natural Science Foundation of China under grant No. 10471027 and Shanghai Education Committee.
Correspondence to: Yimin Wei, E-mail: ymwei@fudan.edu.cn.

Jin and Yuan [10] studied the first kind integral equation

$$\int_0^{+\infty} k(x-y)\sigma(y)dy = g(x)$$

by the wavelet method. The integral equation is discretized with respect to two different wavelet bases, one of them is a Toeplitz system, and the other one is a system with condition number $\kappa = \mathbf{O}(1)$ after a diagonal scaling.

Condition numbers measure the sensitivity of the output of a problem with respect to small perturbations of the input data. Now let us consider the following nonsingular linear system

$$Ax = b,$$

where $A \in \mathbf{R}^{n\times n}$ and $b \in \mathbf{R}^n$.

As we know the linear system has unique solution $x = A^{-1}b$. When there are small perturbations caused by algorithm on both A and b, how does x change? This has been studied intensively. Suppose that the perturbations on A and b are ΔA and Δb respectively, satisfying $\|\Delta A\|_2 \le \epsilon\|A\|_2$, and $\|\Delta b\|_2 \le \epsilon\|b\|_2$, and $A + \Delta A$ remains nonsingular. Let $x + \Delta x$ be the solution of the perturbed system

$$(A + \Delta A)(x + \Delta x) = b + \Delta b,$$

then we have [16, 17],

$$\frac{\|\Delta x\|_2}{\|x\|_2} \le \kappa_{A,b}(A,b)\frac{\epsilon}{1-\epsilon\kappa(A)},$$

where

$$\kappa(A) = \|A\|_2\|A^{-1}\|_2, \qquad \kappa_{A,b}(A,b) = \|A\|_2\|A^{-1}\|_2 + \frac{\|A^{-1}\|_2\|b\|_2}{\|x\|_2}$$

which is proved to be the condition number in [18]. Here $\|A\|_2 = \max\limits_{\|x\|_2=1} = \|Ax\|_2$, where $\|x\|_2$ is the spectral norm of x.

A condition number plays an important role in numerical analysis [19]. The condition number describes the sensitivity of the linear system solution x with respect to the perturbations on A and b. It is also important for the rectangular linear systems.

First, let us introduce the definition of Moore-Penrose inverse for rectangular matrices. For any $A \in \mathbf{R}^{m\times n}$, there exists a unique $n\times m$ complex matrix $A^\dagger$, called *Moore-Penrose inverse* of A, satisfying the following four matrix equations [20, 21, 22]

$$AXA = A, \quad XAX = X, \quad (AX)^H = AX, \quad (XA)^H = XA.$$

Here, for a complex matrix M, M^H denotes its conjugate transpose matrix.

It follows from the singular value decomposition [23] that we can write A as

$$A = U\begin{bmatrix} D & 0 \end{bmatrix} V^H, \tag{1.1}$$

where $U \in \mathbf{R}^{m\times m}$ and $V \in \mathbf{R}^{n\times n}$ are unitary matrices, and $D = diag(\sigma_1, \sigma_2, \cdots, \sigma_m)$ where $m = rank(A)$ and $\sigma_1 \geq \sigma_2 \geq \cdots \geq \sigma_m > 0$ are the singular values of A. It is easy to check that $A^\dagger$ can be expressed by:

$$A^\dagger = V \begin{bmatrix} D^{-1} \\ 0 \end{bmatrix} U^H. \tag{1.2}$$

If the coefficient matrix of linear system is rectangular with full row rank, then the problem becomes *under-determined system* [24]. This consists of, given $A \in \mathbf{R}^{m\times n}$ and $b \in \mathbf{R}^m$, finding $x \in \mathbf{R}^n$ to solve the following under-determined system [24]

$$Ax = b, \tag{1.3}$$

with the minimum spectral norm solution. It is well known that

$$x = A^\dagger b, \tag{1.4}$$

where $A^\dagger$ is the Moore-Penrose inverse of A.

Denote $x + \Delta x$ the minimum spectral norm solution to

$$(A + \Delta A)(x + \Delta x) = b + \Delta b. \tag{1.5}$$

with $\|\Delta A\|_2 \leq \epsilon\|A\|_2$, $\|\Delta b\|_2 \leq \epsilon\|b\|_2$ and ϵ small enough. And

$$x + \Delta x = (A + \Delta A)^\dagger (b + \Delta b).$$

The unstructured condition number of (1.3) with respect to a weight matrix $E \in \mathbf{R}^{m\times n}$ and a weight vector $f \in \mathbf{R}^n$ is defined by

$$\kappa_{E,f}(A, b) = \lim_{\varepsilon\to 0} \sup\Big\{ \frac{\|\Delta x\|_2}{\varepsilon\|x\|_2} : \quad (A + \Delta A)(x + \Delta x) = b + \Delta b, \quad \Delta A \in \mathbf{R}^{m\times n}, \Delta b \in \mathbf{R}^n, \ \|\Delta A\|_2 \leq \varepsilon\|E\|_2, \|\Delta b\|_2 \leq \varepsilon\|f\|_2 \Big\}. \tag{1.6}$$

When A is a structured matrix, such as Toeplitz matrix, which is constant along its diagonals, for examples, 3×4 Toeplitz matrix is given by

$$A = \begin{bmatrix} a_0 & a_1 & a_2 & a_3 \\ a_{-1} & a_0 & a_1 & a_2 \\ a_{-2} & a_{-1} & a_0 & a_1 \end{bmatrix},$$

where $a_i \in \mathbf{C}$, $i = -2, -1, \cdots, 3$. We expect that the small perturbation matrix ΔA on A keeping the same structures as A. The condition number for structured nonsingular matrices has been studied in [25, 26]. Rump obtained the explicit formula of *structured condition number* and got the ratio between structured condition number and unstructured condition number. Structured condition number can also be defined similar to (1.6):

$$\kappa_{E,f}^{struct}(A,b) = \limsup_{\varepsilon\to 0}\Big\{ \frac{\|\Delta x\|_2}{\varepsilon\|x\|_2} : \quad (A+\Delta A)(x+\Delta x) = b+\Delta b, \quad (1.7)$$
$$\Delta A \in \mathbf{R}_{struct}^{m\times n}, \Delta b \in \mathbf{R}^n,$$
$$\|\Delta A\|_2 \le \varepsilon\|E\|_2, \|\Delta b\|_2 \le \varepsilon\|f\|_2\Big\},$$

where $\mathbf{R}_{struct}^{m\times n}$ denotes $m\times n$ structured matrices.

In practice, we hope that the structured condition number is smaller than the unstructured one. But from many numerical experiments, this does not seem to be true. In this note, we will show that the structured condition number is rarely better than unstructured condition number for full row rank under-determined Toeplitz system from the probability viewpoint.

2. Main Result

In the following, we first seek the upper bound for unstructured condition number. It is well known that Golub and Van Loan [16, Theorem 5.7.1] presented the following results.

Lemma 2.1. *Let $A \in \mathbf{R}^{m\times n}$ and $0 \neq b \in \mathbf{R}^m$. Suppose that $rank(A) = m < n$ and $\Delta A \in \mathbf{R}^{m\times n}$ and $\Delta b \in \mathbf{R}^m$ satisfy*

$$\epsilon = \max\{\|\Delta A\|_2/\|A\|_2, \|\Delta b\|_2/\|b\|_2\} < \sigma_m(A).$$

Then

$$\frac{\|\Delta x\|_2}{\|x\|_2} \le 3\kappa_2(A)\epsilon + \mathbf{O}(\epsilon^{\mathbf{2}}), \quad (2.1)$$

where $\kappa_2(A) = \|A\|_2\|A^\dagger\|_2$.

From Lemma 2.1 the upper bound for the unstructured condition number of the under-determined system (1.3) can be obtained easily.

Theorem 2.2. *For the under-determined system* (1.3)*, when the weighted matrix $E = A$ and weighted vector $f = b$, the unstructured condition number for* (1.3) *has an upper bound*

$$\kappa_{A,b}(A,b) \le 3\kappa_2(A).$$

Proof. From (2.1) and the definition of unstructured condition nubmer (1.6), let $\epsilon \to 0$, then we draw the conclusion.

In this paper we only focus on the case that the structure is Toeplitz matrix. For nonsingular Toeplitz matrices, Böttcher and Grudsky [25] showed that the structured condition number is rarely better than usual condition number. Now how about the structured condition number for structured under-determined system? Is it always smaller than unstructured case? We will answer this question in the following context.

The following theorem gives a new lower bound of $\kappa_{A,b}^{\mathrm{Toep}}(A,b)/\kappa_{A,b}(A,b)$. Using the similar method in [25], we can prove the following lemma for rectangular matrices.

Lemma 2.3. *Let* $0 \neq x = (x_0, x_1, \cdots, x_{n-1})^T \in \mathbf{R}^n$ *and suppose that the polynomial* $x(t) = x_0 + x_1 t + \cdots + x_{n-1} t^{n-1}$ *has exactly* ℓ *zeros (counted with multiplicities) on* $\mathbf{T}$*, here* $\mathbf{T}$ *is the unite circle. Thus,*

$$x(t) = \Pi_{j=1}^{\ell}(t - u_j) z(t), \quad u_j \in \mathbf{T}, \quad \mathbf{z(t)} \neq \mathbf{0} \quad \textit{for } t \in \mathbf{T},$$

where $z(t)$ *is a polynomial of degree* $n - \ell - 1$*. Put* $\min|z| = \min\limits_{t \in \mathbf{T}} |z(t)|$*. Then there exits a Toeplitz matrix* T_0 *such that*

$$T_0 x = u_m, \quad \|T_0\|_2 \leq 2^{\ell/2} m^{\ell+1/2} \frac{1}{\min\limits_{t \in \mathbf{T}} |z(t)|} := M,$$

where u_m *is the* $m-$*th column of unitary matrix* U *in* (1.1)*.*

Now let us investigate the lower bound for the structured condition number for under-determined system (1.3).

Theorem 2.4. *As the notation above, we have*

$$\frac{\kappa_{A,b}^{\mathrm{Toep}}(A, b)}{\kappa_{A,b}(A, b)} \geq \frac{\min|z|}{2^{\ell/2} m^{\ell+1/2}} \frac{1}{3\|x\|_2}.$$

Proof. Since $x = A^{\dagger} b = A^T (AA^T)^{-1} b$, from (1.5) we have

$$x + \Delta x = (A + \Delta A)^T [(A + \Delta A)(A + \Delta A)^T]^{-1} (b + \Delta b).$$

Then we obtain that

$$\Delta x \quad = \quad (I - A^{\dagger} A)(\Delta A)^T (AA^T)^{-1} b + A^{\dagger}(\Delta b - \Delta A x) + \mathbf{O}(\epsilon^2). \tag{2.2}$$

Taking spectral norm and noting that $\mathbf{Im}(A^{\dagger}) \perp \mathbf{Im}(I - A^{\dagger} A)$, we have

$$\begin{aligned} \|\Delta x\|_2 &= \|(I - A^{\dagger} A)(\Delta A)^T (AA^T)^{-1} b\|_2 + \|A^{\dagger}(\Delta b - \Delta A x)\|_2 + \mathbf{O}(\epsilon^2) \\ &\geq \|A^{\dagger}(\Delta b - \Delta A x)\|_2 + \mathbf{O}(\epsilon^2). \end{aligned} \tag{2.3}$$

From Lemma 2.3, choosing $\Delta A_0 = \epsilon\|A\|_2 \frac{1}{M} T_0 \in \mathbf{R}^{m\times n}_{struct}$ and $\Delta b_0 = 0$, where $M = 2^{\ell/2} m^{\ell+1/2} \frac{1}{\min_{t\in\mathbf{T}} |z(t)|}$, we know $\|\Delta A_0\|_2 \le \|A\|_2$, and from (2.3), we have

$$\begin{aligned}
\kappa^{\text{Toep}}_{A,b}(A,b) &= \lim_{\epsilon\to 0} \sup_{\substack{\|\Delta A\|_2 \le \epsilon\|A\|_2 \\ \|\Delta b\|_2 \le \epsilon\|b\|_2}} \frac{\|\Delta x\|_2}{\epsilon\|x\|_2} \\
&\ge \lim_{\epsilon\to 0} \left(\frac{\|A^\dagger \Delta A_0 x\|_2}{\epsilon\|x\|_2} + \mathbf{O}(\epsilon) \right) \\
&= \left\| A^\dagger \frac{\|A\|_2 T_0}{M} x \right\|_2 \frac{1}{\|x\|_2} \\
&= \frac{1}{M} \|A^\dagger T_0 x\|_2 \|A\|_2 \frac{1}{\|x\|_2} \\
&= \frac{1}{M} \|A^\dagger u_n\|_2 \|A\|_2 \frac{1}{\|x\|_2} \\
&= \frac{1}{M} \|A^\dagger\|_2 \|A\|_2 \frac{1}{\|x\|_2} \\
&= \frac{\kappa_2(A)}{M\|x\|_2}.
\end{aligned}$$

Thus we have estimated the lower bound for structured condition number

$$\kappa^{\text{Toep}}_{A,b}(A,b) \ge \frac{\kappa_2(A)}{2^{\ell/2} m^{\ell+1/2} \frac{1}{\min\limits_{t\in\mathbf{T}} |z(t)|} \|x\|_2}.$$

From Theorem 2.2, we get the ratio lower bound between structured condition number and unstructured condition number

$$\frac{\kappa^{\text{Toep}}_{A,b}(A,b)}{\kappa_{A,b}(A,b)} \ge \frac{\min|z|}{2^{\ell/2} m^{\ell+1/2}} \frac{1}{3\|x\|_2}.$$

Now we can get the probability analysis of the structured condition number in the next theorem.

Theorem 2.5. *Let $x_0, x_1, \cdots, x_{n-1} \in \mathbf{C}$ be independent standard normal variables and put $x = (x_0, x_1, \cdots, x_{n-1})^H$. There exists universal positive constant ϵ and n_0 such that*

$$Prob\left(\frac{\kappa^{\text{Toep}}_{A,b}(A,b)}{\kappa_{A,b}(A,b)} \ge \frac{\epsilon}{n^{3/2}} \right) > \frac{99}{100},$$

for $n \ge n_0$.

Proof. Let $u_0, v_0, \cdots, u_{n-1}, v_{n-1}$ be independent standard normal. Then $x_0 = u_0 + \mathbf{i}v_0, \cdots, x_{n-1} = u_{n-1} + \mathbf{i}v_{n-1}$ and let

$$u(t) = u_0 + u_1 t + \cdots + u_{n-1} t^{n-1}, \quad v(t) = v_0 + v_1 + \cdots + v_{n-1} t^{n-1}, \quad x(t) = u(t) + \mathbf{i}v(t),$$

where $\mathbf{i} = \sqrt{-1}$.

In [27], Konyagin and Schlag proved that there is a universal constant $D \in (0, \infty)$ such that

$$\limsup_{m\to\infty} Prob\left(\min_{t\in\mathbf{T}} |u(t)| \le \frac{\delta}{\sqrt{n}}\right) \le D\delta,$$

where δ is an arbitrary positive real number. Then we can choose small δ such that $D\delta < 0.004$. Then there exists an n_0 such that

$$Prob\left(\min_{t\in\mathbf{T}} |x(t)| < \frac{\delta}{\sqrt{n}}\right) \le Prob\left(\min_{t\in\mathbf{T}} |u(t)| < \frac{\delta}{\sqrt{n}}\right) < 0.005, \quad for\ any\ n \ge n_0. \tag{2.4}$$

It follows from Theorem 2.4 that we have

$$\frac{\kappa^{\mathrm{Toep}}_{A,b}(A,b)}{\kappa_{A,b}(A,b)} \ge \frac{1}{\|x\|_2} \min_{t\in\mathbf{T}} |x(t)| \frac{1}{3\sqrt{m}} \ge \frac{1}{\|x\|_2} \min_{t\in\mathbf{T}} |x(t)| \frac{1}{3\sqrt{n}}.$$

Since u_i, v_j are independent standard normal variables, we know ${\|x\|_2}^2 = {\|u\|_2}^2 + {\|v\|_2}^2$ is χ^2_{2n}-distributed. From this the expected value $\mathbf{E}(\|\mathbf{x}\|^{\mathbf{2}})$ is $2n$, and from Chebychev's inequality we arrive at

$$Prob\left(\frac{1}{\|x\|_2} \le \frac{1}{20\sqrt{n}}\right) = Prob\left({\|x\|_2}^2 \ge 400n\right) \le \frac{2n}{400n} = 0.005. \tag{2.5}$$

Thus we have

$$Prob\left(\frac{1}{\|x\|_2} \le \frac{1}{20\sqrt{n}}\right) \le 0.005.$$

Then from (2.4) and (2.5), we obtain

$$Prob\left(\min_{t\in\mathbf{T}} |x(t)| < \frac{\delta}{\sqrt{n}} \quad \text{or} \quad \frac{1}{\|x\|_2} \le \frac{1}{20\sqrt{n}}\right) < 0.005 + 0.005 = 0.01.$$

And so

$$Prob\left(\min_{t\in\mathbf{T}} |x(t)| \ge \frac{\delta}{\sqrt{n}} \quad \text{and} \quad \frac{1}{\|x\|_2} > \frac{1}{20\sqrt{n}}\right) > 0.99.$$

Therefore we know that

$$\begin{aligned} Prob\left(\frac{\kappa^{\mathrm{Toep}}_{A,b}(A,b)}{\kappa_{A,b}(A,b)} \ge \frac{\delta}{60n^{3/2}}\right) &\ge Prob\left(\frac{1}{\|x\|_2} \min_{t\in\mathbf{T}} |x(t)| \frac{1}{3\sqrt{n}} \ge \frac{\delta}{60n^{3/2}}\right) \\ &> 0.99. \end{aligned}$$

If we choose $\epsilon = \frac{\delta}{60}$, then we complete the proof.

3. Concluding Remarks

In this note, we show that the structured condition numbers for Toeplitz under-determined systems with full row rank are rarely better than unstructured one in probability sense. In [28, 29], Diao and Wei investigated the structured condition number for the Drazin and group inverse solution of singular square linear systems [30] and got the expressions for the structured condition number. Xu, Wei

and Qiao [31] considered the condition numbers for rank-deficient structured least squares problem. We will compare the structured condition numbers with the unstructured one for the singular case in a forthcoming paper.

Acknowledgements. The authors would like to thank Prof. Tao QIAN and the referee for their valuable comments on our manuscript.

References

[1] I. Daubechies, *Ten Lectures on Wavelets,* SIAM Press 1992.

[2] Y. Meyer, *Wavelets - Algorithms and Applications*, SIAM Press, 1993.

[3] Ke Chen, *Matrix Preconditioning Techniques and Applications*, Cambridge University Press, 2005.

[4] R. Chan and M. Ng, *Conjugate gradient methods for Toeplitz systems*, SIAM Review, **38**(1996), 427–482.

[5] M. Chu, R. Funderlic and R. Plemmons, *Structured low rank approximation*, Linear Algebra Appl., **366**(2003), 157–172.

[6] R.H. Chan, J.G. Nagy and R.J. Plemmons, *Circulant preconditioned for Toeplitz least squares iterations*, SIAM J. Matrix Anal., **15**(1994), 80–97.

[7] G. Heinig, *Fast algorithms for Toeplitz least squares problems*, Current Trends in Operator Theory and its Applications, pp.167-197, Oper. Theory Adv. Appl., 149, Birkhauser, Basel, 2004.

[8] X. Jin, *Developments and Applications of Block Toeplitz Iterative Solvers*, Kluwer Academic Publishers and Science Press, Beijing, 2002.

[9] X. Jin and Y. Wei, *Numerical Linear Algebra and its Applications*, Science Press, Beijing, 2004.

[10] X. Jin and J. Yuan, *A wavelet method for the first kind integral equations with kernel* $k(x-y)$, Taiwanese Journal of Mathematics, **2**(1998), 427-434.

[11] M. Ng, *Iterative Methods for Toeplitz Systems*, Oxford University Press, New York, 2004.

[12] V. Olshevsky (Editor), *Structured Matrices in Mathematics, Computer Science, and Engineering I and II*, Contemporary Mathematics, Vol. 280 and 281, AMS Publications, 2001.

[13] V. Olshevsky (Editor), *Fast Algorithms for Structured Matrices: Theory and Applications*, Contemporary Mathematics, Vol. 323, AMS Publications, 2003.

[14] H. Park and L. Elden, *Schur-type methods for solving least squares problems with Toeplitz structure*, SIAM J. Sci. Comput., **22**(2000), 406–430.

[15] Y. Wei, J. Cai and M. Ng, *Computing Moore-Penrose inverses of Toeplitz matrix by Newton's iteration*, Math. Comput. Modelling, **40**(2004), 181–191.

[16] G.H. Golub and C.F. Van Loan, *Matrix Computations*, 3rd Edition, Johns Hopkins University Press, 1996.

[17] S.M. Rump, *Structured perturbations Part I: Normwise distances*, SIAM J. Matrix Anal. Appl., **25**(2003), 1–30.

[18] N. J. Higham, *Accuracy and Stability of Numerical Algorithms*, 2nd Edition, SIAM, Philadelphia, 2002.

[19] F. Cucker, H. Diao and Y. Wei, *Smoothed analysis of some condition numbers,* Numer. Linear Algebra Appl., **13**(2006), 71–84.

[20] A. Ben-Israel, and T.N.E. Greville, *Generalized Inverses: Theory and Applications*, 2nd Edition, Springer-Verlag, New York, 2003.

[21] S.L. Campbell and C.D. Meyer, *Generalized Inverse of Linear Transformations*, Pitman, London, 1979; Dover, New York, 1991.

[22] G. Wang, Y. Wei, and S. Qiao, *Generalized Inverses: Theory and Computations*, Science Press, Beijing, 2004.

[23] G.W. Stewart and J. Sun, *Matrix Perturbation Analysis*, Academic Press, New York, 1990.

[24] J. Demmel and N. Higham, *Improved error bounds for underdetermined system solvers,* SIAM J. Matrix Anal. Appl., **14** (1993), 1–14.

[25] A. Böttcher, S.M. Grudsky, *Structured condition numbers of large Toeplitz matrices are rarely better than usual condition numbers* Numer. Linear Algebra Appl., **12**(2005), 95–102.

[26] S.M. Rump, *Structured perturbation Part II: Componentwise distances*, SIAM J. Matrix Anal. Appl., **25**(2003), 31–56.

[27] S.V. Konyagin and W. Schlag, *Lower bounds for the absolute value of random polynomials on a neighborhood or the unit circle*, Trans. Amer. Math. Soc., **351**(1999), 4963-4980.

[28] H. Diao, *Structured perturbations of Drazin inverse*, Appl. Math. Comput., **158** (2004), 419–432.

[29] H. Diao and Y. Wei, *Structured perturbations of group inverse and singular linear system with index one*, J. Comput. Appl. Math., **173**(2005), 93–113.

[30] Y. Wei and H. Wu, *Convergence properties of Krylov subspace methods for singular linear systems with arbitrary index,* J. Comput. Appl. Math., **114** (2004), 305–318.

[31] W. Xu, Y. Wei and S. Qiao, *Condition numbers for structured least squares*, BIT, 46 (2006), 203–225.

Huaian Diao
City University of Hong Kong
83 Tat Chee Avenue, Kowloon Tong
Hong Kong, P.R. of China
e-mail: 50007445@student.cityu.edu.hk

Yimin Wei
School of Mathematical Sciences
Fudan University
Shanghai, 200433, P.R. of China
& Key Laboratory of Mathematics for Nonlinear Sciences
(Fudan University), Ministry of Education.
e-mail: ymwei@fudan.edu.cn

Wavelet Analysis and Applications
Tao Qian, Mang I. Vai and Xu Yuesheng, Eds.
Applied and Numerical Harmonic Analysis, 273–283

Powell–Sabin Spline Prewavelets on the Hexagonal Lattice

Jan Maes and Adhemar Bultheel

Abstract. In this paper we give an explicit construction of compactly supported prewavelets on differentiable, twodimensional, piecewise polynomial quadratic finite element spaces of $L_2(\mathbb{R}^2)$, sampled on the hexagonal grid. The obtained prewavelet basis is stable in the Sobolev spaces $\mathcal{H}^s$ for $|s| < \frac{5}{2}$. In particular, the prewavelet basis is generated by one single function vector $\boldsymbol{\psi}$ consisting of three generating functions ψ_1,ψ_2,ψ_3 that are globally invariant by a rotation of $2\pi/3$.

Mathematics Subject Classification (2000). Primary 65T60; Secondary 65D07.

Keywords. Powell–Sabin splines, prewavelets, local support.

1. Introduction

Spline multiresolution analysis has become a standard mathematical tool in a large number of areas including signal processing and image compression, computer graphics, and numerical solutions of differential and integral equations. The construction of multivariate wavelets on arbitrary triangulations is very challenging. In fact, even the case of continuous piecewise linear wavelets construction is unexpectedly complicated, see [6, 7, 8, 9, 10, 11, 17]. In this paper, we present an explicit construction of C^1 continuous piecewise quadratic prewavelets with compact support on the hexagonal lattice in $\mathbb{R}^2$. Our main motivation comes from the numerical treatment of elliptic variational problems.

Let $\mathcal{H}^s$, $s \in \mathbb{R}$ denote the usual Sobolev space with inner product $\langle \cdot, \cdot \rangle_{\mathcal{H}^s}$, and let $a(\cdot, \cdot)$ be a symmetric bilinear form such that $a(v, v) \sim \|v\|^2_{\mathcal{H}^s}$. We always

This work is partially supported by the Flemish Fund for Scientific Research (FWO Vlaanderen) project MISS (G.0211.02), and by the Belgian Programme on Interuniversity Attraction Poles, initiated by the Belgian Federal Science Policy Office. The scientific responsibility rests with the authors.

mean by $A \sim B$ that A can be bounded above and below by constant multiples of B. Let $\mathcal{H}^{-s}$ denote the dual of $\mathcal{H}^s$. Consider the elliptic variational problem:

$$\text{Given } f \in \mathcal{H}^{-s}, \text{ find } u \in \mathcal{H}^s \text{ such that } a(u,v) = f(v), \quad \forall v \in \mathcal{H}^s. \tag{1.1}$$

Suppose V is a finite dimensional subspace of $\mathcal{H}^s$ with basis $\{B_j : j = 1, \ldots, N\}$. The Galerkin approximate solution $u_V = \sum_{j=1}^N c_j B_j$ is the unique solution of (1.1) with $\mathcal{H}^s$ replaced by V and it can be found by solving the linear system

$$(a(B_i, B_j))_{i,j=1}^N (c_j)_{j=1}^N = (f(B_i))_{i=1}^N. \tag{1.2}$$

The stiffness matrix $A = (a(B_i, B_j))_{i,j=1}^N$ for a typical nodal basis is ill-conditioned. Suppose that there exist constants $0 < \underline{\alpha}, \overline{\alpha} < \infty$ (Riesz bounds) such that

$$\underline{\alpha} \sum_{j=1}^N |c_j|^2 \le \| \sum_{j=1}^N c_j B_j \|_{\mathcal{H}^s}^2 \le \overline{\alpha} \sum_{j=1}^N |c_j|^2, \tag{1.3}$$

then it is well-known that $\kappa(A) = \mathcal{O}(\overline{\alpha}/\underline{\alpha})$, [2]. So let $\{B'_j : j = 1, \ldots, N\}$ be another basis for V. Then we can solve the linear system (1.2) with the basis functions B_j replaced by B'_j. The new system can be considered to arise from (1.2) by preconditioning. Hence, we are interested in basis functions B'_j for which $\kappa((a(B'_i, B'_j))_{i,j=1}^N) = \mathcal{O}(1)$.

Several (pre-)wavelet constructions on polygonal domains generate Riesz bases on $\mathcal{H}^s$ for s in a range around zero, see e.g. [4, 18]. However, for most constructions at least a subset of the wavelets is only continuous, so that the range of stability is restricted to $s < \frac{3}{2}$. The only available wavelet Riesz basis on general polygons for $s \ge \frac{3}{2}$ is the basis constructed in [3], but, from a practical point of view, this basis is very hard to construct. The wavelet basis that we present in this paper is easy to construct, and it forms a Riesz basis for $\mathcal{H}^s$, $|s| < \frac{5}{2}$, which makes it a useful basis for preconditioning fourth order elliptic problems. It is however restricted to uniform triangulations of the hexagonal grid. Another construction that provides a Riesz basis for $\mathcal{H}^s$, $|s| < \frac{5}{2}$, is the cubic spline prewavelet basis on the uniform four-directional mesh [1]. The dimension of the cubic spline space in [1] is larger than the Powell–Sabin spline space that we use here, which gives more degrees of freedom in constructing prewavelets with certain properties, but at the cost of the construction complexity. The extra degrees of freedom are used to obtain symmetry properties. In comparison, the Powell–Sabin spline prewavelets have hexagonal symmetry for free.

Section 2 gives a short overview of Powell–Sabin splines on the hexagonal lattice and introduces a stable basis. In Section 3 we construct Powell–Sabin spline prewavelets using the two-step construction method from [17]. Finally we visualize the prewavelets in Section 4.

2. Preliminaries

Consider the hexagonal lattice Δ in $\mathbb{R}^2$ which is defined as the image of $\mathbb{Z}^2$ by a linear transformation corresponding to the matrix

$$\Gamma = \begin{bmatrix} 1 & -1/2 \\ 0 & \sqrt{3}/2 \end{bmatrix},$$

and let Δ^* be its refinement by drawing in the additional grid lines $y = l$, $y = \frac{\sqrt{3}}{3}(x+m)$, and $y = -\frac{\sqrt{3}}{3}(x+n)$, $l, m, n \in \mathbb{Z}$. In fact, Δ^* is the Powell–Sabin 6-split of Δ, see Figure 1. Define $S_2^1(\Delta^*)$ as the space of real-valued functions in $C^1(\mathbb{R}^2)$ whose restrictions on each triangle of the triangulation Δ^* are bivariate quadratic polynomials. Then each function $\phi \in S_2^1(\Delta^*)$ is called a uniform Powell–Sabin (PS) spline.

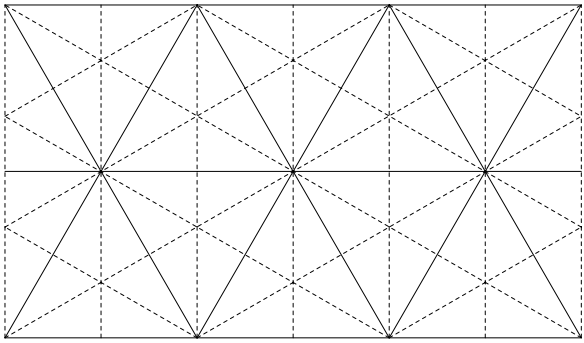

FIGURE 1. Hexagonal lattice Δ (black lines) with Powell–Sabin 6-split Δ^* (black and dotted lines)

Let $k \in \Delta$, then the interpolation problem

$$\left[\phi(l), \frac{\partial}{\partial x}\phi(l), \frac{\partial}{\partial y}\phi(l)\right] = \delta_{k,l}\left[\alpha, \beta, \gamma\right], \qquad l \in \Delta, \tag{2.1}$$

has a unique solution $\phi \in S_2^1(\Delta^*)$, see [16]. This allows to define a function vector $\boldsymbol{\phi} = [\phi_1, \phi_2, \phi_3]^T$ that generates a multiresolution analysis (MRA). Let each ϕ_i, $i = 1, 2, 3$, be the unique solution of (2.1) with

$$\alpha = \frac{1}{3},\ \beta = \frac{2}{3} - \delta_{i1}\frac{6}{3},\ \gamma = \left((-1)^{i-1} - \delta_{i1}\right)\frac{2\sqrt{3}}{3},$$

then the integer translates under Γ of the basis functions ϕ_i form a basis for $S_2^1(\Delta^*)$. Furthermore they form a partition of unity, see [5]. It can be checked that the three basis functions ϕ_1, ϕ_2, ϕ_3 are invariant by a rotation of $2\pi/3$.

Define the 2×2 dilation matrix D given by

$$D = \begin{bmatrix} 2 & 0 \\ 0 & 2 \end{bmatrix},$$

then we consider the refinement $\Delta_j := D^{-j}\Delta$, which can be obtained by midedge subdivision, and the corresponding PS 6-split $\Delta_j^* := D^{-j}\Delta^*$. This yields nested subspaces $V_j = S_2^1(\Delta_j^*) \subset L_2(\mathbb{R}^2)$, $j \in \mathbb{Z}$, such that

$$V_j \subset V_{j+1}, \quad j \in \mathbb{Z}, \tag{2.2}$$

the closure of their union is $L_2(\mathbb{R}^2)$, and their intersection contains only the zero function. In general, the basis functions on all standard refinements Δ_j of Δ can be written as

$$\boldsymbol{\phi}_{j,k}(u) = \boldsymbol{\phi}(D^j(u-k)), \qquad k \in \Delta_j, \quad u \in \mathbb{R}^2,$$

and the set $\{2^j\boldsymbol{\phi}_{j,k} \mid k \in \Delta_j\}$ forms a Riesz basis of V_j, i.e., for $\mathbf{c} = \{\mathbf{c}_k\}_{k\in\Delta_j} \in l_2^{3\times 1}(\Delta_j)$, $\mathbf{c}_k := (c_{1,k}, c_{2,k}, c_{3,k})^T$,

$$\left\| \sum_{k\in\Delta_j} \mathbf{c}_k^T 2^j \boldsymbol{\phi}_{j,k} \right\|_{L_2(\mathbb{R}^2)} \sim \|\mathbf{c}\|_{l_2^{3\times 1}(\Delta_j)}, \tag{2.3}$$

see [13, 14]. With $l_2^{3\times 1}(\Delta_j)$ we denote the Banach space of all sequences of 3×1 vectors $\mathbf{c}_k$ for which $\sqrt{\sum_{k\in\Delta_j} \|\mathbf{c}_k\|_2^2} < \infty$.

Because of the properties listed above we say that the sequence of closed subspaces $\{V_j\}_{j\in\mathbb{Z}}$ of $L^2(\mathbb{R}^2)$ forms a MRA of multiplicity 3, and the function vector $\boldsymbol{\phi}$ is called scaling vector. The nestedness (2.2) of the MRA implies that $\boldsymbol{\phi}$ needs to satisfy a matrix refinement equation of the form

$$\boldsymbol{\phi}(u) = \sum_{k\in\mathbb{Z}^2} \mathbf{A}_k \boldsymbol{\phi}(Du - \Gamma k), \quad u \in \mathbb{R}^2, \tag{2.4}$$

where $\mathbf{A}_k$ are 3×3 mask coefficient matrices. Moreover, $\mathbf{A}_{(-1,-1)}$ and $\mathbf{A}_{(0,-1)}$ are given by

$$\frac{1}{4}\begin{bmatrix} 1 & 0 & 2 \\ 0 & 1 & 2 \\ 0 & 0 & 0 \end{bmatrix}, \quad \frac{1}{4}\begin{bmatrix} 1 & 0 & 0 \\ 2 & 0 & 2 \\ 0 & 0 & 1 \end{bmatrix},$$

$\mathbf{A}_{(-1,0)}$, $\mathbf{A}_{(0,0)}$ and $\mathbf{A}_{(0,1)}$ are given by

$$\frac{1}{4}\begin{bmatrix} 0 & 2 & 2 \\ 0 & 1 & 0 \\ 0 & 0 & 1 \end{bmatrix}, \quad \frac{1}{6}\begin{bmatrix} 4 & 1 & 1 \\ 1 & 4 & 1 \\ 1 & 1 & 4 \end{bmatrix}, \quad \frac{1}{4}\begin{bmatrix} 0 & 0 & 0 \\ 2 & 1 & 0 \\ 2 & 0 & 1 \end{bmatrix},$$

and $\mathbf{A}_{(0,1)}$ and $\mathbf{A}_{(1,1)}$ are given by

$$\frac{1}{4}\begin{bmatrix} 1 & 2 & 0 \\ 0 & 0 & 0 \\ 0 & 2 & 1 \end{bmatrix}, \quad \frac{1}{4}\begin{bmatrix} 1 & 0 & 0 \\ 0 & 1 & 0 \\ 2 & 2 & 0 \end{bmatrix},$$

see e.g. [21].

3. Prewavelets

We are interested in complement spaces W_j of V_j such that

$$V_{j+1} = V_j \oplus^{\perp_{L_2}} W_j,$$

hence

$$L_2(\mathbb{R}^2) = \bigoplus_{j\in\mathbb{Z}}^{\perp_{L_2}} W_j.$$

We will refer to the basis functions of W_j as prewavelets. Note that the prewavelets have three vanishing moments since constant, linear and quadratic polynomials are contained in the space V_j.

The construction of PS prewavelets consists of two steps, cfr. [17]. First we construct a dual basis

$$\{\widetilde{\boldsymbol{\phi}}_{j,k} \mid k \in \Delta_j\} \subset V_{j+1} \tag{3.1}$$

for the basis $\left\{\boldsymbol{\phi}_{j,k}\ \left(\|\boldsymbol{\phi}_{j,k}\|_{L_2}^2\right)^{-1} \mid k \in \Delta_j\right\}$ of V_j, i.e.

$$\left\langle \widetilde{\boldsymbol{\phi}}_{j,k}, \boldsymbol{\phi}_{j,l}^T \right\rangle_{L_2} = \begin{cases} \|\boldsymbol{\phi}_{j,k}\|_{L_2}^2 & k = l, \\ 0 & k \neq l, \end{cases} \tag{3.2}$$

with $\|\boldsymbol{\phi}_{j,k}\|_{L_2}^2 := \operatorname{diag}(\langle \boldsymbol{\phi}_{j,k}, \boldsymbol{\phi}_{j,k}^T \rangle_{L_2})$. Since we search for a dual basis in the space V_{j+1} which is much larger than V_j, this basis is not unique. We will use this freedom to select a dual basis that is locally supported. Then, as the second step, for $l \in \Delta_{j+1} \setminus \Delta_j$ we define

$$\boldsymbol{\psi}_{j,l} := \boldsymbol{\phi}_{j+1,l} - \sum_{k\in\Delta_j} \left\langle \boldsymbol{\phi}_{j+1,l}, \boldsymbol{\phi}_{j,k}^T \right\rangle_{L_2} \left(\|\boldsymbol{\phi}_{j,k}\|_{L_2}^2\right)^{-1} \widetilde{\boldsymbol{\phi}}_{j,k}. \tag{3.3}$$

Note that, because of (3.1) and (3.2), $\boldsymbol{\psi}_{j,l} \in V_{j+1} \bigcap V_j^{\perp_{L_2}}$.

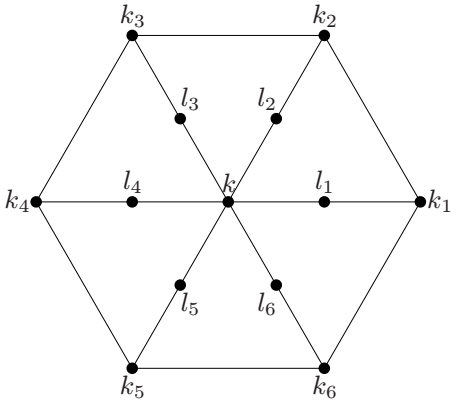

FIGURE 2. Grid around k

Let $k \in \Delta_j$ and define $k_1, \ldots, k_6 \in \Delta_j$ and $l_1, \ldots, l_6 \in \Delta_{j+1}$ as in Figure 2. We look for a dual function vector $\widetilde{\boldsymbol{\phi}}_{j,k}$ of the form

$$\widetilde{\boldsymbol{\phi}}_{j,k} := \widetilde{\mathbf{A}}_0 \boldsymbol{\phi}_{j+1,k} + \sum_{i=1}^{6} \widetilde{\mathbf{A}}_i \boldsymbol{\phi}_{j+1,l_i}$$

that satisfies (3.2), where the $\widetilde{\mathbf{A}}_i$ are 3×3 mask coefficient matrices. By construction we know that the support of each scaling vector $\boldsymbol{\phi}_{j,k}$ is the set of all triangles in Δ_j that have $k \in \Delta_j$ as a common vertex. Note that, by construction, the support of $\widetilde{\boldsymbol{\phi}}_{j,k}$ equals the support of $\boldsymbol{\phi}_{j,k}$, see Figure 2. Therefore it is sufficient to solve the system

$$\begin{cases} \langle \widetilde{\boldsymbol{\phi}}_{j,k}, \boldsymbol{\phi}_{j,k}^T \rangle_{L_2} = \|\boldsymbol{\phi}_{j,k}\|_{L_2}^2 & , \\ \langle \widetilde{\boldsymbol{\phi}}_{j,k}, \boldsymbol{\phi}_{j,k_i}^T \rangle_{L_2} = 0 & , \quad i = 1, \ldots, 6, \end{cases} \tag{3.4}$$

to obtain a dual basis. We have 63 equations and 63 unknown matrix entries. Since the system (3.4) is non-singular we find a unique solution,

$$\widetilde{\mathbf{A}}_0 = \begin{bmatrix} \frac{382603}{41310} & -\frac{318649}{82620} & -\frac{318649}{82620} \\ -\frac{318649}{82620} & \frac{382603}{41310} & -\frac{318649}{82620} \\ -\frac{318649}{82620} & -\frac{318649}{82620} & \frac{382603}{41310} \end{bmatrix},$$

$$\widetilde{\mathbf{A}}_1 = \begin{bmatrix} \frac{1691}{2754} & -\frac{551}{18360} & -\frac{551}{18360} \\ -\frac{779}{1836} & -\frac{608}{20655} & \frac{11761}{165240} \\ -\frac{779}{1836} & \frac{11761}{165240} & -\frac{608}{20655} \end{bmatrix},$$

$$\widetilde{\mathbf{A}}_2 = \begin{bmatrix} \frac{10241}{82620} & \frac{4123}{18360} & -\frac{2204}{20655} \\ \frac{4123}{18360} & \frac{10241}{82620} & -\frac{2204}{20655} \\ -\frac{82783}{165240} & -\frac{82783}{165240} & \frac{6346}{20655} \end{bmatrix},$$

$$\widetilde{\mathbf{A}}_3 = \begin{bmatrix} -\frac{608}{20655} & -\frac{779}{1836} & \frac{11761}{165240} \\ -\frac{551}{18360} & \frac{1691}{2754} & -\frac{551}{18360} \\ \frac{11761}{165240} & -\frac{779}{1836} & -\frac{608}{20655} \end{bmatrix},$$

$$\widetilde{\mathbf{A}}_4 = \begin{bmatrix} \frac{6346}{20655} & -\frac{82783}{165240} & -\frac{82783}{165240} \\ -\frac{2204}{20655} & \frac{10241}{82620} & \frac{4123}{18360} \\ -\frac{2204}{20655} & \frac{4123}{18360} & \frac{10241}{82620} \end{bmatrix},$$

$$\widetilde{\mathbf{A}}_5 = \begin{bmatrix} -\frac{608}{20655} & \frac{11761}{165240} & -\frac{779}{1836} \\ \frac{11761}{165240} & -\frac{608}{20655} & -\frac{779}{1836} \\ -\frac{551}{18360} & -\frac{551}{18360} & \frac{1691}{2754} \end{bmatrix},$$

$$\widetilde{\mathbf{A}}_6 = \begin{bmatrix} \frac{10241}{82620} & -\frac{2204}{20655} & \frac{4123}{18360} \\ -\frac{82783}{165240} & \frac{6346}{20655} & -\frac{82783}{165240} \\ \frac{4123}{18360} & -\frac{2204}{20655} & \frac{10241}{82620} \end{bmatrix}.$$

Theorem 3.1. *The set*

$$\{2^{j+1} \widetilde{\boldsymbol{\phi}}_{j,k} \mid k \in \Delta_j\} \cup \{2^{j+1} \boldsymbol{\phi}_{j+1,l} \mid l \in \Delta_{j+1} \setminus \Delta_j\} \tag{3.5}$$

is a Riesz basis for the space V_{j+1}.

Proof. We know that $\{2^{j+1}\boldsymbol{\phi}_{j+1,k} \mid k \in \Delta_{j+1}\}$ is a Riesz basis for V_{j+1}, see (2.3). Furthermore we have that the basis $\{2^{j+1}\boldsymbol{\phi}_{j+1,k} \mid k \in \Delta_{j+1}\}$ can be transformed into the set (3.5) by a matrix operation of the form

$$\mathbf{M} = \begin{bmatrix} \mathbf{K} & \mathbf{L} \\ \mathbf{0} & \mathbf{I}_n \end{bmatrix}, \tag{3.6}$$

where $\mathbf{I}_n$ denotes the $n \times n$ identity matrix with $n = \#\{l \in \Delta_{j+1} \setminus \Delta_j\}$ and $\mathbf{0}$ is a zero matrix. The matrix $\mathbf{K}$ has a block-structure of the form

$$\mathbf{K} = \begin{bmatrix} \widetilde{\mathbf{A}}_0 & \mathbf{0} & \mathbf{0} & \cdots \\ \mathbf{0} & \widetilde{\mathbf{A}}_0 & \mathbf{0} & \cdots \\ \mathbf{0} & \mathbf{0} & \widetilde{\mathbf{A}}_0 & \\ \vdots & \vdots & & \ddots \end{bmatrix},$$

and the matrix $\mathbf{L}$ is a sparse block-structured matrix with blocks $\widetilde{\mathbf{A}}_i$, $i = 1, \ldots, 6$. Note that

$$\mathbf{M}^{-1} = \begin{bmatrix} \mathbf{K}^{-1} & -\mathbf{K}^{-1}\mathbf{L} \\ \mathbf{0} & \mathbf{I}_n \end{bmatrix}.$$

Clearly $\mathbf{M}$ is uniformly bounded and has full rank which proves our claim. □

For all j, for all $l \in \Delta_{j+1} \setminus \Delta_j$, we define the prewavelets $\boldsymbol{\psi}_{j,l}$ as in (3.3). Note that these prewavelets are compactly supported. It is easily checked that $W_j = \operatorname{span}\{\boldsymbol{\psi}_{j,l} \mid l \in \Delta_{j+1} \setminus \Delta_j\}$. Indeed, suppose $w \in W_j$. Then by Theorem 3.1 we have

$$w = \sum_{l \in \Delta_{j+1} \setminus \Delta_j} \mathbf{c}_l^T \boldsymbol{\phi}_{j+1,l} + \sum_{k \in \Delta_j} \mathbf{c}_k^T \widetilde{\boldsymbol{\phi}}_{j,k},$$

or

$$[0 \quad 0 \quad 0] = \langle w, \boldsymbol{\phi}_{j,k}^T \rangle_{L_2} = \sum_{l \in \Delta_{j+1} \setminus \Delta_j} \mathbf{c}_l^T \langle \boldsymbol{\phi}_{j+1,l}, \boldsymbol{\phi}_{j,k}^T \rangle_{L_2} + \mathbf{c}_k^T \|\boldsymbol{\phi}_{j,k}\|_{L_2}^2,$$

which yields

$$\mathbf{c}_k^T = - \sum_{l \in \Delta_{j+1} \setminus \Delta_j} \mathbf{c}_l^T \langle \boldsymbol{\phi}_{j+1,l}, \boldsymbol{\phi}_{j,k}^T \rangle_{L_2} \left(\|\boldsymbol{\phi}_{j,k}\|_{L_2}^2 \right)^{-1}$$

and we get

$$w = \sum_{l \in \Delta_{j+1} \setminus \Delta_j} \mathbf{c}_l^T \boldsymbol{\psi}_{j,l}.$$

Theorem 3.2. *The set*

$$\{2^{j+1}\boldsymbol{\psi}_{j,l} \mid l \in \Delta_{j+1} \setminus \Delta_j\} \tag{3.7}$$

is a Riesz basis for the space W_j.

Proof. It is sufficient to show that

$$\left\| \sum_{l \in \Delta_{j+1} \setminus \Delta_j} \mathbf{c}_l^T 2^{j+1} \boldsymbol{\psi}_{j,l} \right\|_{L_2} \sim \|\mathbf{c}\|_{l_2(\Delta_{j+1} \setminus \Delta_j)}^{3 \times 1}.$$

By Theorem 3.1 and (3.3) it holds that

$$\left\| \sum_{l \in \Delta_{j+1} \setminus \Delta_j} \mathbf{c}_l^T 2^{j+1} \boldsymbol{\psi}_{j,l} \right\|_{L_2}^2 \sim \sum_{l \in \Delta_{j+1} \setminus \Delta_j} \mathbf{c}_l^T \mathbf{c}_l$$
$$+ \sum_{k \in \Delta_l} \left(\sum_{l \in \Delta_{j+1} \setminus \Delta_j} \mathbf{c}_l^T \langle \boldsymbol{\phi}_{j+1,l}, \boldsymbol{\phi}_{j,k}^T \rangle_{L_2} \left(\|\boldsymbol{\phi}_{j,k}\|_{L_2}^2 \right)^{-1} \right)^T$$
$$\cdot \left(\sum_{l \in \Delta_{j+1} \setminus \Delta_j} \mathbf{c}_l^T \langle \boldsymbol{\phi}_{j+1,l}, \boldsymbol{\phi}_{j,k}^T \rangle_{L_2} \left(\|\boldsymbol{\phi}_{j,k}\|_{L_2}^2 \right)^{-1} \right).$$

Both for fixed $k \in \Delta_j$ or for fixed $l \in \Delta_{j+1} \setminus \Delta_j$ the number of nonzero inner products $\langle \boldsymbol{\phi}_{j+1,l}, \boldsymbol{\phi}_{j,k}^T \rangle_{L_2}$ is bounded above by an absolute constant. Furthermore it is straightforward to check that

$$0 \leq \langle \boldsymbol{\phi}_{j+1,l}, \boldsymbol{\phi}_{j,k}^T \rangle_{L_2} \left(\|\boldsymbol{\phi}_{j,k}\|_{L_2}^2 \right)^{-1} \leq C$$

with C an absolute constant. This concludes the proof. □

Remark 3.3. Note that the prewavelets $\boldsymbol{\psi}_{j,l}$ and the dual functions $\widetilde{\boldsymbol{\phi}}_{j,k}$ can be obtained as scaled translates of a finite subset of them. Indeed, we have that

$$\begin{aligned} \boldsymbol{\psi}_{j,l}(u) &= \boldsymbol{\psi}(D^j(u-l)), \quad l \in \Delta_{j+1} \setminus \Delta_j,\ u \in \mathbb{R}^2, \\ \widetilde{\boldsymbol{\phi}}_{j,k}(u) &= \widetilde{\boldsymbol{\phi}}(D^j(u-k)), \quad k \in \Delta_j,\ u \in \mathbb{R}^2, \end{aligned}$$

with $\boldsymbol{\psi}$ and $\widetilde{\boldsymbol{\phi}}$ a generating wavelet vector resp. a generating dual scaling vector. Therefore the inner products appearing in the construction above have to be computed only once. As a consequence of the hexagonal symmetry of $\boldsymbol{\phi}$, both $\widetilde{\boldsymbol{\phi}}$ and $\boldsymbol{\psi}$ have also hexagonal symmetry, i.e. the corresponding generating functions are invariant by a rotation of $2\pi/3$.

Remark 3.4. We are interested in determining the exact range of Sobolev exponents s for which the prewavelet basis forms a Riesz basis for $\mathcal{H}^s$. It turns out that the range of such s is determined by the Sobolev regularity $s(\boldsymbol{\phi})$ of the scaling vector $\boldsymbol{\phi}$, i.e. the wavelet system is a Riesz basis for $\mathcal{H}^s$ for all s with $-s(\boldsymbol{\phi}) < s < s(\boldsymbol{\phi})$ and that this interval is sharp, cfr. [15]. It is well-known that PS splines are in the Sobolev spaces $\mathcal{H}^s$ for any $s < 5/2$, see [13] for a detailed proof.

Remark 3.5. The above construction can be used to construct prewavelets on bounded domains in $\mathbb{R}^2$ due to the explicit construction that we use.

Remark 3.6. It is also possible to extend this construction to arbitrary polygonal domains in $\mathbb{R}^2$. In that case, one should use a triadic refinement scheme instead of the dyadic scheme that we use here, see [20]. Unfortunately it remains an open problem whether the system (3.4) is non singular for arbitrary settings. However, using perturbation arguments, one can argue that a non-trivial solution to (3.4) should always exist in some sense.

Remark 3.7. A PS spline wavelet basis on arbitrary polygonal domains in $\mathbb{R}^2$ does exist, see [19]. In [12] it is shown that this wavelet basis is not a Riesz basis for L_2. Fortunately it does form a Riesz basis for $\mathcal{H}^s$ with s in a range around 2 which makes it suitable for preconditioning fourth order elliptic equations.

4. Visualization of the Functions

Finally we visualize a scaling function, a dual scaling function and a prewavelet, see Figures 3, 4, and 5.

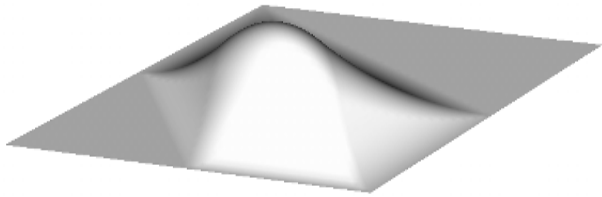

FIGURE 3. Scaling function

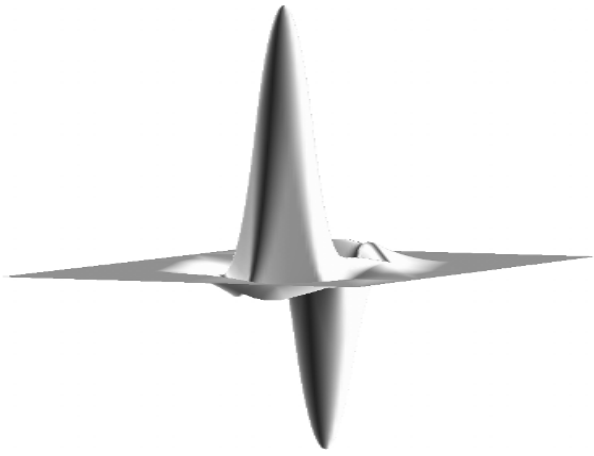

FIGURE 4. Dual scaling function

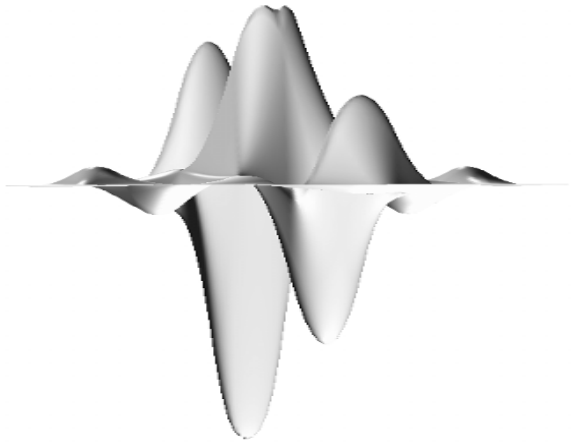

FIGURE 5. Prewavelet

References

[1] M. D. Buhmann, O. Davydov, and T. N. T. Goodman. Cubic spline prewavelets on the four-directional mesh. *Foundations of Computational Mathematics*, 3:113–133, 2003.

[2] W. Dahmen and A. Kunoth. Multilevel preconditioning. *Numer. Math.*, 63:315–344, 1992.

[3] W. Dahmen and R. Schneider. Wavelets on manifolds I: Construction and domain decomposition. *SIAM J. Math. Anal.*, 31:184–230, 1999.

[4] W. Dahmen and R. Stevenson. Element-by-element construction of wavelets satisfying stability and moment conditions. *SIAM J. Numer. Anal.*, 37(1):319–352, 2000.

[5] P. Dierckx. On calculating normalized Powell–Sabin B-splines. *Comput. Aided Geom. Design*, 15(3):61–78, 1997.

[6] G.C. Donovan, J. S. Geronimo, and D. P. Hardin. Intertwining multiresolution analysis and the construction of piecewise polynomial wavelets. *SIAM J. Math. Anal.*, 27:1791–1815, 1996.

[7] G.C. Donovan, J. S. Geronimo, and D. P. Hardin. Compactly supported, piecewise affine scaling functions over triangulations. *Constr. Approx.*, 16:201–219, 2000.

[8] M. S. Floater and E. G. Quak. Piecewise linear prewavelets on arbitrary triangulations. *Numer. Math.*, 82:221–252, 1999.

[9] M. S. Floater and E. G. Quak. Piecewise linear prewavelets over Type-2 triangulations. *Comput. Supplement*, 14:89–103, 2001.

[10] D. P. Hardin and D. Hong. Construction of wavelets and prewavelets over triangulations. *J. Comput. Appl. Math.*, 155:91–109, 2003.

[11] U. Kotyczka and P. Oswald. Piecewise linear prewavelets of small support. In C. K. Chui and L. L. Schumaker, editors, *Approximation Theory VIII, Vol 2*, pages 235–242. World Scientific, Singapore, 1995.

[12] J. Maes and A. Bultheel. Stable lifting construction of non-uniform biorthogonal spline wavelets with compact support. TW Report 437, Department of Computer Science, Katholieke Universiteit Leuven, Belgium, October 2005.

[13] J. Maes and A. Bultheel. Stable multiresolution analysis on triangles for surface compression. 2005. Submitted.

[14] J. Maes, E. Vanraes, P. Dierckx, and A. Bultheel. On the stability of normalized Powell–Sabin B-splines. *J. Comput. Appl. Math.*, 170(1):181–196, 2004.

[15] P. Oswald. *Multilevel finite element approximation: Theory and applications.* B.G. Teubner, Stuttgart, 1994.

[16] M. J. D. Powell and M. A. Sabin. Piecewise quadratic approximations on triangles. *ACM Trans. on Math. Software*, 3:316–325, 1977.

[17] R. Stevenson. Piecewise linear (pre-)wavelets on non-uniform meshes. In W. Hackbusch and G. Wittum, editors, *Multigrid Methods V*, pages 306–319. Springer-Verlag, Heidelberg, 1996.

[18] R. Stevenson. Locally supported, piecewise polynomial biorthogonal wavelets on non-uniform meshes. *Constr. Approx.*, 19(4):477–508, 2003.

[19] E. Vanraes, J. Maes, and A. Bultheel. Powell–Sabin spline wavelets. *Intl. Journal of Wavelets, Multiresolution and Information Processing*, 2(1):23–42, 2004.

[20] E. Vanraes, J. Windmolders, A. Bultheel, and P. Dierckx. Automatic construction of control triangles for subdivided Powell–Sabin splines. *Comput. Aided Geom. Design*, 21(7):671–682, 2004.

[21] J. Windmolders, E. Vanraes, P. Dierckx, and A. Bultheel. Uniform Powell–Sabin spline wavelets. *J. Comput. Appl. Math.*, 154(1):125–142, 2003.

Jan Maes
Department of Computer Science
Katholieke Universiteit Leuven
Celestijnenlaan 200A
B-3001 Heverlee
Belgium
e-mail: `jan.maes@cs.kuleuven.be`

Adhemar Bultheel
Department of Computer Science
Katholieke Universiteit Leuven
Celestijnenlaan 200A
B-3001 Heverlee
Belgium
e-mail: `adhemar.bultheel@cs.kuleuven.be`

Chapter 4: Time-Frequency Analysis, Adaptive Representation of Nonlinear and Non-stationary Signals

Wavelet Analysis and Applications
Tao Qian, Mang I. Vai and Xu Yuesheng, Eds.
Applied and Numerical Harmonic Analysis, 287–297

Time-Frequency Aspects of Nonlinear Fourier Atoms

Qiuhui Chen, Luoqing Li and Tao Qian

Abstract. In the standard Fourier analysis one uses the linear Fourier atoms $\{e^{int} : n \in \mathbb{Z}\}$. With only the linear phases nt Fourier analysis can not expose the essence of time-varying frequencies of nonlinear and non-stationary signals. In this note we study time-frequency properties of a new family of atoms $\{e^{in\theta_a(t)} : n \in \mathbb{Z}\}$, non-linear Fourier atoms, where a is any but fixed complex number with $|a| < 1$, and $d\theta_a(t)$ a harmonic measure on the unit circle parameterized by t. The nonlinear Fourier atoms $\{e^{in\theta_a(t)} : n \in \mathbb{Z}\}$ were first noted in [12] with some examples and theoretically studied in [8]. In this note we show that the real parts $\cos\theta_a(t), |a| < 1$, form a family of intrinsic mode functions introduced in the HHT theory [5]. We prove that for a fixed a the set $\{e^{in\theta_a(t)} : n \in \mathbb{Z}\}$, constitutes a Riesz basis in the space $L^2([0, 2\pi])$. Some miscellaneous results including Shannon type sampling theorems are obtained.

Mathematics Subject Classification (2000). Primary 94A12; Secondary 42C15.

Keywords. Nonlinear Fourier atom; Hilbert-Huang transform; time-frequency analysis; sampling theorem.

1. Introduction

The frequency of non-stationary signals varies with time. The traditional Fourier analysis, however, can not expose the time-varying property of frequency of non-stationary signals. This is due to the basic fact that in Fourier analysis a general signal is superposition of harmonic waves of which each has a constant frequency.

Recently Norden E. Huang [5] presented a new time-frequency method for nonlinear and non-stationary signal analysis: Hilbert-Huang Transform (HHT).

Qiuhui Chen is supported in part by NSFC under grant 10201034 and the Project-sponsored by SRF for ROCS, SEM. Luoqing Li is supported in part by NSFC under grant 10371033. Tao Qian is supported by University of Macau under research grant RG065/03-04S/QT/FST and Macao Science and Technology Development Fund (FDCT) 051/2005/A.

By using the algorithm of Empirical Mode Decomposition(EMD), any multi-component can be decomposed into a finite sum of *intrinsic mode functions* (IMFs), which are essentially of mono-component. Based on the EMD decomposition, further treatments can be done under the framework of the ideal time-frequency analysis. The notion of IMF defined by Huang plays a crucial role in the HHT theory. The original definition of IMFs is an engineering description: The occurrences of local maximums and minimums take turn, and between a pair of adjacent local extremes, the signal is monotone and passes through the zero once, and is of the local symmetry, i.e. the mean of a upper and an adjacent lower envelope based on the local extremes, respectively, is of the zero value. Experiments show that IMFs behave nicely with Hilbert transformation and offer meaningful instantaneous frequencies. IMFs are considered to be essentially of mono-component discussed in the notion of instantaneous frequency [2]. Based on the Bedrosian [1] and Nuttall [6] theorems a natural question occurs: For an amplitude - frequency modulation (AM and FM) signal $f = a(t)\cos\theta(t)$, under what conditions on a and θ the associated quadrature signal $a(t)e^{i\theta(t)}$ becomes analytic?

In [8], Qian proves that a strictly increasing function $\theta(t), t \in [0, 2\pi]$ with $m(\theta([0, 2\pi])) = 2\pi$ gives rise to an analytic signal $e^{i\theta(t)}$ if and only if $d\theta(t)$ is a harmonic measure on the circle, and this result has a counterpart for strictly increasing functions $\Theta(s)$ with $m(\Theta(\mathbb{R})) = 2\pi$ on the whole real line. In this note, we explore some time-frequency aspects of the family of the new nonlinear Fourier atoms $\{e^{in\theta_a(t)} : n \in \mathbb{Z}\}, |a| < 1$, where $d\theta_a(t)$ is a harmonic measure, that is, the derivative of $\theta_a(t)$ is the Poisson kernel (see §2). For further development of the theme the reader is recommended to [10] and [11].

In section 2, we show that $\cos\theta_a(t)$ is of mono-component. That essentially means that $\theta_a'(t) > 0$, the Hilbert transform of $\cos\theta_a(t)$ is $\sin\theta_a(t)$, and $\theta_a(t)$ can be decomposed into a sum of a linear part and a nonlinear but periodic part. In section 3, we prove that $\{e^{in\theta_a(t)} : n \in \mathbb{Z}\}$ forms a Riesz basis of $L^2([0, 2\pi])$, with the Riesz bounds $\frac{1-|a|}{1+|a|}$ and $\frac{1+|a|}{1-|a|}$. Section 4 mainly concerns sampling theorems in relation to this new family of atoms.

Before we start there is one point to note. Functions studied in below sometimes are defined on the unit circle, or equivalently on intervals with length 2π with equal function values at the two ends of each of such intervals; and sometimes are defined on the whole real line but 2π-periodic. These two cases should be clearly distinguished, especially when dealing with certain operators acting on function spaces. For instance, images of Fourier transformation operator on the first type of functions are Fourier series, and the involved integral regions in that case are intervals of length 2π. Correspondingly, when we deal with the first type of functions, then the Hilbert transformation is $\widetilde{\mathcal{H}}$ (see §2); and for the second type, the Hilbert transformation is $\mathcal{H}$. In order to avoid the ambiguity we shall clearly note which case we are working with, but we do not assign special notations for the two types of functions.

2. Nonlinear Fourier Atoms and Behavior with Hilbert Transform

We start our discussion with the Möbius transformation

$$\tau_a(z) = \frac{z-a}{1-\overline{a}z}$$

that is a conformal mapping one to one and onto from the unit disc to itself with the condition $\tau(a) = 0$. Define $\theta_a(t)$ by

$$e^{i\theta_a(t)} = \tau_a\left(e^{it}\right) = \frac{e^{it}-a}{1-\overline{a}e^{it}}.$$

Note that θ_a is defined on the unit circle and its derivative is the Poisson kernel (see [4] or [8])

$$\theta_a'(t) = p_a(t) = \frac{1-|a|^2}{1-2|a|\cos(t-t_a)+|a|^2}.$$

The function θ_a may be continuously extended to the whole real line with the property $\theta_a(t+2\pi) = \theta_a(t) + 2\pi$ whose derivative $p_a(t)$ is continuous and 2π-periodic. In this section, unless otherwise stated, we shall treat θ_a as defined in the whole real line. The corresponding period functions $e^{i\xi\theta_a(t)}$, $\xi > 0$, except for the trivial case $a = 0$ corresponding to $e^{i\xi t}$ of the linear phase ξt, are not included in the general form of Picinbono [7]. Indeed, the derivatives of the phases of the signals in [7] are sums of the Poisson kernels on the real line and therefore not periodic. The atomic case of Picinbono was studied in [8].

Let $a = |a|e^{it_a}$. Then

$$e^{i\theta_a(t)} = \frac{e^{it}-a}{1-\overline{a}e^{it}} = \frac{e^{it}-|a|e^{it_a}}{1-|a|e^{-it_a}e^{it}} = \frac{1-|a|e^{i(t_a-t)}}{1-|a|e^{i(t-t_a)}}\,e^{it} = \frac{A(t)}{\overline{A(t)}}\,e^{it},$$

where $A(t) = 1-|a|e^{i(t_a-t)}$. By noting that

$$\mathrm{Arg}A(t) = \arctan\frac{|a|\sin(t-t_a)}{1-|a|\cos(t-t_a)},$$

we get the explicit expression

$$\theta_a(t) = t + 2\arctan\frac{|a|\sin(t-t_a)}{1-|a|\cos(t-t_a)}. \tag{2.1}$$

Note that the first part is linear and the second part is periodic, and such a decomposition is unique.

It is interesting that the signal $\cos\theta_a(t)$ is a mono-component with frequency modulation. To see this, we need to show that its Hilbert transform is the corresponding sine function $\sin\theta_a(t)$.

The circular Hilbert transform ([4]) of a function $f = \sum_{k\in\mathbb{Z}} c_k e^{ikt} \in L^2([0,2\pi])$ is defined by

$$\widetilde{\mathcal{H}}f(t) = -i\sum_{k\in\mathbb{Z}}\mathrm{sgn}(k)c_k e^{ikt}.$$

It has a singular integral expression

$$\widetilde{\mathcal{H}}f(t) = \text{v.p.}\frac{1}{2\pi}\int_{-\pi}^{\pi} \cot\left(\frac{t-s}{2}\right) f(s)ds, \quad \text{a. e.}$$

On the other hand, the Hilbert transform for a function f on the real line is formally defined by

$$\mathcal{H}f(t) = \text{v.p.}\frac{1}{\pi}\int_{-\infty}^{\infty} \frac{f(s)}{t-s}ds.$$

The Bedrosian Theorem says that if f is a real-valued signal of low frequencies and g is real-valued of high frequencies, then $\mathcal{H}(fg) = f\mathcal{H}g$. In accordance with the Bedrosian Theorem, it has been well accepted that if $\mathcal{H}\left(a(t)\cos\phi(t)\right) = a(t)\sin\phi(t)$ and $\phi'(t) \geq 0$, then meaningful instantaneous amplitudes and frequencies may be defined through the amplitude-frequency modulation signal $s(t) = a(t)\cos\phi(t)$. In the case we regard $s(t)$ as of mono-component [2]. The following theorem states that $\cos\theta(t)$ is a mono-component with constant amplitude.

Theorem 2.1. *(i) Treating* $\cos\theta_a(t)$ *as a function defined on the unit circle, we have*

$$\widetilde{\mathcal{H}}\cos\theta_a(t) = \sin\theta_a(t);$$

and (ii) Treating $\cos\theta_a(t)$ *as a* 2π*-periodic function on the whole real line, we have*

$$\mathcal{H}\cos\theta_a(t) = \sin\theta_a(t).$$

Proof. The proof of (i) is contained in [8] and [12]. To make the current paper self-contain we present an outline of the proof. Note that $\tau_a(z)$ is an analytic function and $e^{i\theta_a(t)}$ its boundary value. We therefore have

$$e^{i\theta_a(t)} = \sum_{k=0}^{+\infty} c_k e^{ikt}$$

for a fast decay sequence $\{c_k : k \in \mathbb{Z}\}$. By the definition of the circular Hilbert transform, we have

$$\widetilde{\mathcal{H}}\left(e^{i\theta_a(t)}\right) = -i\left(\sum_{k=1}^{+\infty} c_k e^{ikt}\right) = -i\left(e^{i\theta_a(t)} - c_0\right).$$

This concludes $\widetilde{\mathcal{H}}\cos\theta_a(t) = \sin\theta_a(t)$.

Now we prove (ii). First note that in the Riemann improper integral and principal value sense the Hilbert transformation is well defined for the oscillatory function $\cos\theta_a(t)$. By the definition of the Hilbert transform, we have

$$\begin{aligned}\text{p.v.}\ \frac{1}{\pi}\int_{-\infty}^{\infty}\frac{1}{x-t}\cos\theta_a(t)dt &= \text{p.v.}\ \frac{1}{\pi}\int_0^{2\pi}\sum_{k=-\infty}^{\infty}\frac{1}{x-t+2k\pi}\cos\theta_a(t)dt \\ &= \text{p.v.}\ \frac{1}{2\pi}\int_0^{2\pi}\cot\left(\frac{x-t}{2}\right)\cos\theta_a(t)dt,\end{aligned}$$

where we used the identity $\lim_{N\to\infty}\sum_{k=-N}^{N}\frac{1}{x-t+2k\pi}=\frac{1}{2}\cot\left(\frac{x-t}{2}\right)$ which may be found, for instance, from [9]. Then the conclusion of (i) implies that of (ii). The proof of Theorem 2.1 is complete. □

We offer an explicit representation for the function $\cos\theta_a(t)$. First, by (2.1), we get that

$$\begin{aligned}\cos\theta_a(t) &= \cos\left(t+2\arctan\frac{|a|\sin(t-t_a)}{1-|a|\cos(t-t_a)}\right)\\ &= \cos\left(2\arctan\frac{|a|\sin(t-t_a)}{1-|a|\cos(t-t_a)}\right)\cos t\\ &\quad -\sin\left(2\arctan\frac{|a|\sin(t-t_a)}{1-|a|\cos(t-t_a)}\right)\sin t.\end{aligned}$$

Second, using the formulas $\cos 2t=\frac{1-\tan^2 t}{1+\tan^2 t}$ and $\sin 2t=\frac{2\tan t}{1+\tan^2 t}$, we have

$$\begin{aligned}\cos\theta_a(t) &= \frac{1-\left(\frac{|a|\sin(t-t_a)}{1-|a|\cos(t-t_a)}\right)^2}{1+\left(\frac{|a|\sin(t-t_a)}{1-|a|\cos(t-t_a)}\right)^2}\cos t-\frac{2\frac{|a|\sin(t-t_a)}{1-|a|\cos(t-t_a)}}{1+\left(\frac{|a|\sin(t-t_a)}{1-|a|\cos(t-t_a)}\right)^2}\sin t\\ &= \frac{(1-|a|\cos(t-t_a))^2-(|a|\sin(t-t_a))^2}{(1-|a|\cos(t-t_a))^2+(|a|\sin(t-t_a))^2}\cos t\\ &\quad -\frac{2|a|\sin(t-t_a)\,(1-|a|\cos(t-t_a))}{(1-|a|\cos(t-t_a))^2+(|a|\sin(t-t_a))^2}\sin t.\end{aligned}$$

Finally, through a direct computation, we have

$$\begin{aligned}\cos\theta_a(t) &= \frac{\cos t\,(1-|a|\cos(t-t_a))^2-\cos t\,(|a|\sin(t-t_a))^2}{(|a|\sin(t-t_a))^2+(1-|a|\cos(t-t_a))^2}\\ &\quad -\frac{2|a|\sin t\sin(t-t_a)\,(1-|a|\cos(t-t_a))}{(|a|\sin(t-t_a))^2+(1-|a|\cos(t-t_a))^2}\\ &= \frac{\cos t\left(1-2|a|\cos(t-t_a)+|a|^2\cos 2(t-t_a)\right)}{1+|a|^2-2|a|\cos(t-t_a)}\\ &\quad -\frac{2|a|\sin t\sin(t-t_a)+|a|^2\sin t\sin 2(t-t_a)}{1+|a|^2-2|a|\cos(t-t_a)}\\ &= \frac{\cos t-2|a|\,(\cos t\cos(t-t_a)+\sin t\sin(t-t_a))}{1+|a|^2-2|a|\cos(t-t_a)}\end{aligned}$$

$$+\frac{|a|^2\left(\cos t\cos 2(t-t_a)+\sin t\sin 2(t-t_a)\right)}{1+|a|^2-2|a|\cos(t-t_a)}$$
$$=\frac{\cos t-2|a|\cos t_a+|a|^2\cos(t-2t_a)}{1+|a|^2-2|a|\cos(t-t_a)}.$$

In particular, when a is a real number less than 1, $\cos\theta_a(t)$ can be simplified into

$$\cos\theta_a(t)=\frac{\left(1+|a|^2\right)\cos t-2|a|}{1+|a|^2-2|a|\cos t}.$$

3. Nonlinear Fourier Atoms as Riesz Basis

With the notation $\theta_a'=p_a$, $p_a(t)$ being the Poisson kernel, we have $p_0=1$. There hold the estimates for p_a :

$$\frac{1-|a|}{1+|a|}\le p_a(t)\le\frac{1+|a|}{1-|a|}.$$

Define

$$L^2_{p_a}([0,2\pi])=\left\{f:[0,2\pi]\to\mathbb{C}\ :\ \int_0^{2\pi}|f(t)|^2p_a(t)dt<\infty\right\}.$$

It is a Hilbert space equipped with the inner product

$$\langle f,g\rangle_{p_a}=\int_0^{2\pi}f(t)\overline{g(t)}p_a(t)dt$$

and the norm

$$\|f\|_{p_a}=\left(\int_0^{2\pi}|f(t)|^2p_a(t)dt\right)^{\frac{1}{2}}.$$

Note that for $a=0$ the space $L^2_{p_a}([0,2\pi])$ reduces to the classic case $L^2([0,2\pi])$ with the norm $\|f\|=\left(\int_0^{2\pi}|f(t)|^2dt\right)^{\frac{1}{2}}$. We have the equivalence between the two norms

$$\sqrt{\frac{1-|a|}{1+|a|}}\ \|\cdot\|\le\|\cdot\|_{p_a}\le\sqrt{\frac{1+|a|}{1-|a|}}\ \|\cdot\|. \tag{3.1}$$

Note that all the function sets $L^2_{p_a}([0,2\pi]),|a|<1$, are identical with different but equivalent norms. Through change of variable the classical Carleson's Theorem reduces to the assertion (also see [8]) that for any $f\in L^2_{p_a}([0,2\pi])$,

$$f(t)=\sum_{n\in\mathbb{Z}}c_n^a(f)e^{in\theta_a(t)},\quad a.e.$$

The identity of the function sets then implies that the last equality also holds for functions in $f\in L^2([0,2\pi])$. That is, the standard square integrable functions can be approximated by the nonlinear Fourier atoms with the weighted Fourier coefficients $c_n^a(f)$.

Theorem 3.1. *For any fixed a the system* $\{e^{in\theta_a(t)} : n \in \mathbb{Z}\}$ *forms a Riesz basis of* $L^2([0, 2\pi])$ *with the upper bound* $\frac{1+|a|}{1-|a|}$ *and the lower bound* $\frac{1-|a|}{1+|a|}$, *i.e.*

$$\frac{1-|a|}{1+|a|}\| \{c_j\} \|^2 \ \leq \ \left\| \sum_{j\in\mathbb{Z}} c_j e^{ij\theta_a(t)} \right\|^2 \ \leq \ \frac{1+|a|}{1-|a|}\| \{c_j\} \|^2 \tag{3.2}$$

for any ℓ^2*- sequence* $\{c_j : j \in \mathbb{Z}\}$.

Proof. Note that $\{\frac{1}{\sqrt{2\pi}} e^{in\theta_a(t)} : n \in \mathbb{Z}\}$ is a weighted orthonormal system with the weight p_a. This implies the Plancherel identity:

$$\|f\|_{p_a}^2 = \sum_{j\in\mathbb{Z}} \left|c_j^a(f)\right|^2,$$

where $f \in L^2_{p_a}([0, 2\pi])$ and the Fourier coefficients $c_j^a(f) = \left\langle f, \frac{1}{\sqrt{2\pi}} e^{ij\theta_a(t)} \right\rangle_{p_a}$. The Plancherel identity then implies that for any sequence $\{c_j : j \in \mathbb{Z}\} \in \ell^2$ the function

$$f(t) := \sum_{j\in\mathbb{Z}} c_j e^{ij\theta_a(t)}, \quad t \in [0, 2\pi],$$

is well defined and belongs to $L^2_{p_a}([0, 2\pi])$, and, further for $j \in \mathbb{Z}$, $c_j^a(f) = c_j$. Since f also belongs to $L^2([0, 2\pi])$, the equivalence (3.1) of the two norms of f together with the Plancherel identity in $L^2_{p_a}([0, 2\pi])$ then gives the relation (3.2). □

4. Shannon Type Sampling Theorem

For any function $f \in L^2(\mathbb{R})$, the generalized Fourier transform is defined by

$$\widehat{f}^a(\xi) = \frac{1}{\sqrt{2\pi}} \int_{-\infty}^{\infty} f(t) e^{-i\xi\theta_a(t)} p_a(t) dt, \tag{4.1}$$

where both θ_a and p_a are 2π-periodic extensions of the corresponding functions on the unit circle. Note that when $a = 0$, it is the classic Fourier transform

$$\widehat{f}(\xi) = \frac{1}{\sqrt{2\pi}} \int_{-\infty}^{\infty} f(t) e^{-i\xi t} dt.$$

In the distribution sense, we can check that the generalized Fourier transform of $\cos\theta_a(t)$ is $\frac{1}{2}(\delta(\xi - 1) + \delta(\xi + 1))$. The inverse formula of (4.1) is

$$f(t) = \frac{1}{\sqrt{2\pi}} \int_{-\infty}^{\infty} \widehat{f}^a(\xi) e^{i\xi\theta_a(t)} d\xi. \tag{4.2}$$

Theorem 4.1. *Suppose that* $\operatorname{supp}\widehat{f}^a \subset [-\Omega, \Omega]$. *Then*

$$f(t) = \sum_{n\in\mathbb{Z}} f\left(\theta_a^{-1}(n\frac{\pi}{\Omega})\right) \frac{\sin(\Omega\theta_a(t) - n\pi)}{(\Omega\theta_a(t) - n\pi)}. \tag{4.3}$$

Proof. Since $\widehat{f^a}$ has compact support in $[-\Omega, \Omega]$, we can represent $\widehat{f^a}$ by its standard Fourier series

$$\widehat{f^a}(\xi) = \sum_{n\in\mathbb{Z}} c_n e^{-in\xi\frac{\pi}{\Omega}},$$

where

$$c_n = \frac{1}{2\Omega}\int_{-\Omega}^{\Omega} \widehat{f^a}(\xi) e^{in\xi\frac{\pi}{\Omega}} d\xi = \frac{1}{2\Omega}\int_{-\infty}^{\infty} \widehat{f^a}(\xi) e^{in\xi\frac{\pi}{\Omega}} d\xi.$$

By invoking the inverse formula (4.2), we have

$$\begin{aligned} c_n &= \frac{\sqrt{2\pi}}{2\Omega}\frac{1}{\sqrt{2\pi}}\int_{-\infty}^{\infty} \widehat{f^a}(\xi) e^{i\xi\theta_a\left(\theta_a^{-1}(n\frac{\pi}{\Omega})\right)} d\xi \\ &= \frac{\sqrt{2\pi}}{2\Omega} f\left(\theta^{-1}(n\frac{\pi}{\Omega})\right). \end{aligned}$$

It then follows that

$$\begin{aligned} f(t) &= \frac{1}{\sqrt{2\pi}}\int_{-\infty}^{\infty} \widehat{f^a}(\xi) e^{i\xi\theta_a(t)} d\xi \\ &= \frac{1}{\sqrt{2\pi}}\int_{-\Omega}^{\Omega} \sum_{n\in\mathbb{Z}} \frac{\sqrt{2\pi}}{2\Omega} f\left(\theta^{-1}(n\frac{\pi}{\Omega})\right) e^{i\xi\left(\theta_a(t)-n\frac{\pi}{\Omega}\right)} d\xi. \end{aligned}$$

Since the series for $\widehat{f^a}$ converges also in $L^1([0, 2\pi])$, interchanging the order of integration and summation leads to

$$\begin{aligned} f(t) &= \sum_{n\in\mathbb{Z}} f\left(\theta^{-1}(n\frac{\pi}{\Omega})\right)\int_{-\Omega}^{\Omega} \frac{1}{2\Omega} e^{i\xi\left(\theta_a(t)-n\frac{\pi}{\Omega}\right)} d\xi \\ &= \sum_{n\in\mathbb{Z}} f\left(\theta_a^{-1}(n\frac{\pi}{\Omega})\right)\frac{\sin\left(\Omega\theta_a(t)-n\pi\right)}{\Omega\theta_a(t)-n\pi}. \end{aligned}$$

□

The convergence speed of the new sampling theorem can also be improved through over-sampling. To this end, we choose an arbitrary function g such that $\operatorname{supp}\widehat{g} \subset [-\delta, \delta]$ with $\delta = l\Omega$ for some positive integer $l > 1$, and $\widehat{g} = 1$ on $[-\Omega, \Omega]$. Thus, $\widehat{f^a}\widehat{g} = \widehat{f^a}$. Note that $\widehat{f^a}$ has the Fourier series expansion $\widehat{f^a} = \sum_{n\in\mathbb{Z}} c_n e^{in\xi\frac{\pi}{\delta}}$ with $c_n = \frac{\sqrt{2\pi}}{2\delta} f\left(\theta_a^{-1}\left(n\frac{\pi}{\delta}\right)\right)$. Hence

$$\begin{aligned} f(t) &= \frac{1}{\sqrt{2\pi}}\int_{-\infty}^{\infty} \widehat{f^a}(\xi) e^{i\xi\theta_a(t)} d\xi \\ &= \frac{1}{\sqrt{2\pi}}\int_{-\delta}^{\delta} \widehat{f^a}(\xi)\widehat{g}(\xi) e^{i\xi\theta_a(t)} d\xi \end{aligned}$$

$$
\begin{aligned}
&= \frac{1}{\sqrt{2\pi}} \int_{-\delta}^{\delta} \sum_{n\in\mathbb{Z}} \frac{\sqrt{2\pi}}{2\delta} f\left(\theta_a^{-1}\left(n\frac{\pi}{\delta}\right)\right) e^{-in\xi\frac{\pi}{\delta}} \widehat{g}(\xi) e^{i\xi\theta_a(t)} d\xi \\
&= \sum_{n\in\mathbb{Z}} f\left(\theta_a^{-1}\left(n\frac{\pi}{\delta}\right)\right) \frac{1}{\sqrt{2\pi}} \int_{-\delta}^{\delta} \frac{\sqrt{2\pi}}{2\delta} \widehat{g}(\xi) e^{i\xi\left(\theta_a(t) - n\frac{\pi}{\delta}\right)} d\xi \\
&= \sum_{n\in\mathbb{Z}} f\left(\theta_a^{-1}\left(n\frac{\pi}{\delta}\right)\right) \frac{\sqrt{2\pi}}{2\delta} g\left(\theta_a(t) - n\frac{\pi}{\delta}\right).
\end{aligned}
$$

If, in particular, we choose $\delta = (1+\lambda)\Omega$ and g being

$$
\widehat{g}(\xi) = \begin{cases} 1, & |\xi| \le \Omega, \\ 1 - \frac{|\xi|-\Omega}{\lambda\Omega}, & \Omega \le |\xi| \le (1+\lambda)\Omega, \\ 0, & |\xi| \ge (1+\lambda)\Omega. \end{cases}
$$

Then

$$
g(t) = \frac{4}{\sqrt{2\pi}} \frac{\sin\left(t\Omega(1+\frac{\lambda}{2})\right)\sin\left(t\frac{\Omega\lambda}{2}\right)}{\lambda\Omega t^2},
$$

and we have

$$
f(t) = \sum_{n\in\mathbb{Z}} f\left(\theta_a^{-1}\left(\frac{n\pi}{(1+\lambda)\Omega}\right)\right) G_\lambda\left(\theta_a(t) - \frac{n\pi}{(1+\lambda)\Omega}\right), \tag{4.4}
$$

where

$$
G_\lambda(x) = \frac{2}{(1+\lambda)\Omega} \frac{\sin\left((\theta_a(t) - \frac{n\pi}{(1+\lambda)\Omega})\Omega(1+\frac{\lambda}{2})\right)\sin\left((\theta_a(t) - \frac{n\pi}{(1+\lambda)\Omega})\frac{\Omega\lambda}{2}\right)}{\lambda\Omega(\theta_a(t) - \frac{n\pi}{(1+\lambda)\Omega})^2}.
$$

Note that (4.3) may be obtained by letting $\lambda \to 0$ in (4.4).

To end this note we point out that the standard Poisson summation formula may be generalized to the nonlinear Fourier atoms.

Denote by $L^2_{p_a}(\mathbb{R})$ the Hilbert space of square integrable functions on $\mathbb{R}$ with respect to the periodic weight function $p_a(t)$. Let $f \in L^2_{p_a}(\mathbb{R})$ and set

$$
\widetilde{f}(t) = \sum_{k\in\mathbb{Z}} f(t + 2k\pi).
$$

Then $\widetilde{f} \in L^2_{p_a}([0, 2\pi])$, and

$$
\widetilde{f}(t) = \sum_{k\in\mathbb{Z}} c_k^a e^{ik\theta_a(t)}.
$$

We now show that

$$
\widehat{f^a}(k) = c_k^a, \qquad k \text{ is any integer.}
$$

In fact, as in the standard case, for $k \in \mathbb{Z}$

$$\begin{aligned}
\widehat{f^a}(k) &= \frac{1}{\sqrt{2\pi}} \int_{-\infty}^{\infty} e^{ik\theta_a(t)} f(t) p_a(t) dt \\
&= \frac{1}{\sqrt{2\pi}} \sum_{n\in\mathbb{Z}} \int_0^{2\pi} e^{ik\theta_a(t)} f(t+2n\pi) p_a(t) dt \\
&= \frac{1}{\sqrt{2\pi}} \int_0^{2\pi} e^{ik\theta_a(t)} \sum_{n\in\mathbb{Z}} f(t+2n\pi) p_a(t) dt \\
&= \frac{1}{\sqrt{2\pi}} \int_0^{2\pi} e^{ik\theta_a(t)} \widetilde{f}(t) p_a(t) dt \\
&= c_k^a.
\end{aligned}$$

We thus have $\widetilde{f}(t) = \sum_{k\in\mathbb{Z}} \widehat{f^a}(k) e^{ik\theta_a(t)}$. Let $t = t_0$, where $\theta_a(t_0) = 0$, this last relation becomes

$$\sum_{k\in\mathbb{Z}} f(t_0 + 2k\pi) = \sum_{k\in\mathbb{Z}} \widehat{f^a}(k),$$

the new Poisson formula.

References

[1] E. Bedrosian, *A product theorem for Hilbert transform*. Proc. IEEE **51** (1963), 868-869.

[2] B. Boashash *Estimating and interpreting the instantaneous frequency of a signal, I. Fundamentals*. Proc. IEEE **80** (1992), 417-430.

[3] I. Daubechies, *Ten Lectures on Wavelets*. CBMS **61** SIAM, Philadelphia, 1992.

[4] J. B. Garnett, *Bounded Analytic Functions*. Academic Press, 1987.

[5] N. E. Huang et al, *The empirical mode decomposition and the Hilbert spectrum for nonlinear and non-stationary time series analysis*. Proc. R. Soc. London, **454** A (1998), 903-995.

[6] A. H. Nuttall, *On the quadrature approximation to the Hilbert transform of modulated signals*. Proc. IEEE (Letters) (1966), 1458-1459.

[7] B. Picinbono, *On instantaneous amplitude and phase of signals*. IEEE Transaction on Signal Processing, **45** (1997), 552-560.

[8] T. Qian, *Unit analytic signals and harmonic measures*. J. Math. Anal Appl. **314** (2006), 526-536.

[9] T. Qian, *Singular integrals with holomorphic kernels and Fourier multipliers on star-shap Lipschitz curves*. Studia Mathematica, **123**(3) (1997), 195-216.

[10] T. Qian, *Characterization of Boundary Values of Functions in Hardy Spaces With Application in Signal Analysis*, Journal of Integral Equations and Applications, Volume **17** Issue 2 (Summer 2005), 159-198.

[11] T. Qian, *Mono-components for decomposition of signals*, Math. Meth. Appl. Sci. 2006; **29**:1187-1198.

[12] T. Qian, Q. H. Chen and L. Q. Li, *Unit analytic signals with nonlinear phase.* Physica D: Nonlinear Phenomena, **303** (1-2) (2005), 80-87.

Qiuhui Chen
Faculty of Mathematics and Computer Science
Hubei University
Wuhan, 430062, P. R. China
e-mail: sqh@hubu.edu.cn

Luoqing Li
Faculty of Mathematics and Computer Science
Hubei University
Wuhan, 430062, P. R. China
e-mail: lilq@hubu.edu.cn

Tao Qian
Department of Mathematics
Faculty of Science and Technology
University of Macau
Macao (via Hong Kong)
e-mail: fsttq@umac.mo

Wavelet Analysis and Applications
Tao Qian, Mang I. Vai and Xu Yuesheng, Eds.
Applied and Numerical Harmonic Analysis, 299–319

Mono-components for Signal Decomposition

Tao Qian

Abstract. In relation to the study of instantaneous frequency, HHT and the EMD algorithm in signal analysis people have been trying to find solutions of the eigenfunction problem: Find $f(t) = \rho(t)e^{i\theta(t)}$ such that $Hf = -if$, $\rho(t) \geq 0$ and $\theta'(t) \geq 0, a.e.$, where Hf is Hilbert transform of f. This article serves as a survey on some recent studies, and presents some new results as well. In the survey part we first review the systematic study on the unimodular case, and then give a detailed account on a fundamental class of non-unimodular solutions, called H-atoms, in terms of starlike functions in one complex variable. As new result we construct certain circular mono-components that do not fall into the category of H-atoms but of the form $\rho(t)e^{i\theta_a(t)}$, where $\rho(t) \geq 0$, and $e^{i\theta_a(t)}$ is some Fourier atom, as well as those of the form $\rho(s)e^{i\phi_a(s)}$, where $e^{i\phi_a(s)}$ is one on the line induced from some Fourier atom under Cayley transform.

Mathematics Subject Classification (2000). Primary: 30D55, 31A20, 31C05; Secondary: 42A50, 42B20.

Keywords. Analytic signal, instantaneous frequency, Hilbert transform, Möbius transform, mono-component, empirical mode decomposition, HHT (Hilbert-Huang transform), starlike functions.

1. Introduction

In signal analysis one has been trying to understand, for a given signal, what are its instantaneous amplitude, instantaneous phase, and instantaneous frequency. A signal, denoted by $f(t)$, is assumed to be a real-valued locally (Lebesgue) integrable function. A common approach to find the instantaneous objects is as follows. One first introduces the associated analytic signal, $Af(t) = f(t) + iHf(t)$, where Hf is

The work was supported by research grant of the University of Macau No. RG079/04-05S/QT/FST and Macao Science and Technology Development Fund 051/2005/A.

the Hilbert transform of f, being assumed to exist. Hilbert transform is formally defined by the principal value singular integral

$$Hf(t) = \text{p.v.}\frac{1}{\pi}\int_{-\infty}^{\infty}\frac{f(s)}{t-s}ds,$$

which has the Fourier multiplier form

$$Hf(t) = \frac{1}{2\pi}\int_{-\infty}^{\infty} e^{i\xi t}\,(-i\text{sgn}(\xi))\,\hat{f}(\xi)d\xi,$$

where Fourier transform is defined by

$$\hat{f}(\xi) = \int_{-\infty}^{\infty} e^{-i\xi t}f(t)dt,$$

and sgn is the signum function that takes value 1 if $\xi > 0$; and -1 if $\xi < 0$.

The function Af may be written in the form $Af(t) = \rho(t)e^{i\theta(t)}$, with $\rho(t) \geq 0$, a.e. Consequently,

$$f(t) = \rho(t)\cos\theta(t). \tag{1.1}$$

Due to the relation $H^2 = -I$, where I stands for the identity operator, Af satisfies the relation

$$H(Af) = -iAf, \tag{1.2}$$

which is equivalent to

$$H(\rho(\cdot)\cos\theta(\cdot))(t) = \rho(t)\sin\theta(t). \tag{1.3}$$

With the uniquely determined modulation (1.1), one calls $\rho(t)$ and $\theta(t)$ the *instantaneous amplitude* and *instantaneous phase*, respectively, provided $\theta'(t) \geq 0$, a.e. Should the requirement be met, the function $\theta'(t)$ is defined to be the *instantaneous frequency*. Unfortunately, the requirement $\theta' \geq 0$ can hardly be met, and the definitions of instantaneous amplitude, phase and frequency via the associated analytic signal Af can be erroneous.

In a related aspect, in [9], Huang proposed an algorithm, called Empirical Mode Decomposition, to decompose a signal into a sum

$$f(t) = \sum \rho_i(t)\cos\theta_i(t), \tag{1.4}$$

where each entry of the sum is expected to be a real-mono-component (see definition in §2). He also obtained numerically rapid convergence. As a new type of signal decomposition Huang's algorithm appears very effective in practice, and has attracted a wide attention. On the other hand, the algorithm suffers for it does not always result in the desired decomposition in terms of mono-components. A mathematical formulation providing precise concepts and a related approximation theory is desired.

In [13], [17], [14], [15], a systematic study on the unimodular case $\rho \equiv 1$ is carried out. In a recent paper [16] the study of the unimodular case is extend to the general non-unimodular case. We found that the well established theory of

starlike functions in one complex variable best fits our purpose. Boundary values of starlike functions provide easily accessible circular mono-components.

The writing plan of the paper is as follows. §2 contains notation and terminology related to the eigenfunction problem. It also contains a discussion on dual mono-components. In §3 we deal with unimodular solutions of the problem. We introduce Fourier atoms and finite Blaschke products. In §4 we exam the relations between the solutions and the boundary values of functions in Hardy H^p spaces. Based on the unimodular solutions in §3, through elementary conformal mappings, we construct a large class of unimodular solutions. In §5 we present an important and fundamental class of solutions, called H-atoms, that is identical with a class of starlike functions in one complex variable. This, in particular, gives rise to a large class of solutions with the non-unimodular case. In §6 we construct some new types of mono-components, that do not fall into the category of H-atoms, but of the form $\rho(t)e^{i\theta_a(t)}$, where $\rho \geq 0$ and $e^{i\theta_a(t)}$ is a Fourier atom, as well as those of the form $\rho(t)e^{i\phi_a(t)}$, where $e^{i\phi_a(t)}$ is a mono-component on the line induced from a Fourier atom under Cayley transform.

We note that, apart from §6, all the other section §2, §3 and §4 serve as a survey of the main results obtained in [17], [14], [15] and [16].

The author wishes to acknowledge his sincere thanks to Sheng Gong who kindly recommended comprehensive references in complex analysis, including starlike functions in one and several complex variables. The author wishes to thank Qiu-hui Chen and Luo-qing Li, for their collaborations in this subject, especially in [17], and in some related work in relation to wavelets ([2], [3]), and the inspiring discussions from time to time. Sincere thanks are due to Jing-xin Yin and Gui-fang Xie for their very kind and constant help in supplying the author the necessary references.

2. Notation and Terminology

Denote by $\mathbf{S}$ for $\mathbf{S} = \mathbb{D}$ or $\mathbf{S} = \mathbb{C}^+$, the earlier being the open unit disc and the latter being the upper-half complex plane. In this notation $H_{\mathbf{S}}$ stands for $H_{\mathbb{C}^+}$ or $H_{\mathbb{D}}$, where $H_{\mathbb{C}^+}$ is the standard Hilbert transformation, H, on the line, and $H_{\mathbb{D}}$ is the circular Hilbert transformation, often denoted by $\tilde{H}$, on the circle. The circular Hilbert transformation is defined through

$$\tilde{H}f(t) = \text{p.v.}\frac{1}{2\pi}\int_{-\pi}^{\pi} \cot(\frac{t-s}{2})f(s)ds$$

with the Fourier multiplier form based on the Fourier expansion of $f(t)$:

$$\tilde{H}f(t) = \sum_{k=-\infty}^{\infty}{}' -i\,\text{sgn}(k)c_k e^{ikt}, \quad f(t) = \sum_{k=-\infty}^{\infty} c_k e^{ikt}.$$

Let f be an eigenfunction of the circular or non-circular Hilbert transformation $H_{\mathbf{S}}$. Then $H_{\mathbf{S}}f = kf, k \in \mathbb{C}$. Since $H_{\mathbf{S}}^2 f = k^2 f = -f$, we obtain $k = \pm i$, where i is the complex imaginary unit.

Definition 2.1. A function f is said to be an $H_{\mathbf{S}}$-eigenfunction if $H_{\mathbf{S}}f = -if$; and a dual $H_{\mathbf{S}}$-eigenfunction if $H_{\mathbf{S}}f = if$. An $H_{\mathbf{S}}$-eigenfunction f is called an $\mathbf{S}$-mono-component if, with the form $f(t) = \rho(t)e^{i\theta(t)}$, it satisfies $\rho(t) \geq 0$ and $\theta'(t) \geq 0$, a.e.; and, a dual $H_{\mathbf{S}}$-eigenfunction f is called a dual $\mathbf{S}$-mono-component if, with the form $f(t) = \rho(t)e^{i\theta(t)}$, it satisfies $\rho(t) \geq 0$ and $\theta'(t) \leq 0$, a.e.

In the sequel, with $\mathbf{S} = \mathbb{C}^+$, with terminologies like $H_{\mathbb{C}^+}$-eigenfunctions and $\mathbb{C}^+$-mono-components, we suppress the subscript $\mathbb{C}^+$ and simply write *H-eigenfunctions* and *mono-components*, respectively; and, with $\mathbf{S} = \mathbb{D}$, we write *circular H-eigenfunctions* and *circular mono-components* for $H_{\mathbb{D}}$-eigenfunctions and $\mathbb{D}$-mono-components, etc.

Very often, we investigate $\mathrm{Re}f$ instead of f, and, with the form $f(t) = \rho(t)e^{i\theta(t)}$, we have $\mathrm{Re}f = \rho(t)\cos\theta(t)$. In the case, we have, $H_{\mathbf{S}}f = \mp if$ if and only if $H_{\mathbf{S}}(\rho(\cdot)\cos\theta(\cdot))(t) = \pm\rho(t)\sin\theta(t)$. In the case, we call $\rho(t)\cos\theta(t)$ *a real $H_{\mathbf{S}}$-eigenfunction*, or *a real dual $H_{\mathbf{S}}$-eigenfunction,* respectively. If there is no confusion, then we may omit the word "*real*", and still call it *a $H_{\mathbf{S}}$-eigenfunction*, or *a dual $H_{\mathbf{S}}$-eigenfunction*.

If a signal is not $\mathbf{S}$-mono-component or a dual $\mathbf{S}$-mono-component, then it is called a $\mathbf{S}$-*multi-component*, or simply *multi-component*. Signals are usually multi-components.

Based on this notion the task would be two-fold. The first is to establish a bank of mono- and dual mono-components. The second is to study adaptive decomposition of signals into linear combinations of mono- and dual mono-components. The present paper addresses the first. Along with the results previously obtained in [13], [17], [14], [15] and [16], in this article we construct certain solutions of the eigenfunction problem of the form $\rho(t)e^{i\theta_a(t)}$, where $\rho \geq 0$ is non-constant and $e^{i\theta_a(t)}$ is a so-called Fourier atom on the circle (see [17] and [14]), as well as certain solutions of the form $\rho(s)e^{i\phi_a(s)}$, where $e^{i\phi_a(s)}$ is induced from a Fourier atom under Cayley transform.

In below we give some remarks on dual mono-components.

When expending $f \in L^2([0, 2\pi])$ into its Fourier series

$$f(t) = a_0 + \sum_{k=1}^{\infty} a_k \cos kt + b_k \sin kt,$$

or its complex Fourier series

$$f(t) = \sum_{k=-\infty}^{\infty} c_k e^{ikt},$$

the entries $\sin kt = \cos(\pi/2 - kt)$ and $e^{-ikt}, k > 0$, are dual circular mono-components. These can be verified directly, or derived from Theorem 2.2 (see below). They are also dual mono-components on the line if they are considered as periodic functions (see §3). The following result allows us to merely concentrate to the non-dual case.

Theorem 2.2. *$\rho(t)e^{i\theta(t)}$ is a (circular) mono-component if and only if $\rho(t)e^{-i\theta(t)}$ is a dual (circular) mono-component.*

Proof. Assume that $f(t) = \rho(t)e^{i\theta(t)}$ is a mono-component. We have,

$$H(\rho(\cdot)\cos\theta(\cdot))(t) = \rho(t)\sin\theta(t),$$

and, since $H^2 = -I$,

$$H(\rho(\cdot)\sin\theta(\cdot))(t) = -\rho(t)\cos\theta(t).$$

They can be re-written as

$$H(\rho(\cdot)\cos(-\theta(\cdot)))(t) = -\rho(t)\sin(-\theta(t)), \quad H(\rho(\cdot)\sin(-\theta(\cdot)))(t) = \rho(t)\cos(-\theta(t)).$$

The last two relations are equivalent to

$$H(\rho(\cdot)e^{-i\theta(\cdot)})(t) = i\rho(t)e^{-i\theta(t)}.$$

Therefore, $\rho(t)e^{-i\theta(t)}$ is a dual H-eigenfunction. Since $\rho \geq 0, -\theta' \leq 0$, it is a dual mono-component. The argument is reversible. For the circular case we replace H by $\tilde{H}$. The proof is complete. □

We show that for $k > 0$, $\sin kt$ is a dual (circular) mono-component. In fact, Theorem 2.2 implies that ie^{-ikt} is a dual (circular) mono-component. Therefore $\sin kt = \mathrm{Re}(ie^{-ikt})$ is a dual (circular) mono-component. In general, $f = u + iv$ is a dual (circular) eigenfunction if and only if $H_{\mathbf{S}}u = -v$.

In the rest of the paper we are bound to find mono-components, that is to solve the following

Hilbert Transformation Eigenfunction Problem: Find $f(t) = \rho(t)e^{i\theta(t)}$ such that $Hf = -if$, $\rho(t) \geq 0$ and $\theta'(t) \geq 0, a.e.$, where H is Hilbert transformation.

On the circle we can ask the same question with H replaced by $\tilde{H}$. We adopt the approach that we first find solutions on the unit circle and then induce the corresponding solutions on the line.

3. Unimodular Solutions of the Eigenfunction Problem

This section deals with the unimodular case $f(t) = \rho(t)e^{i\theta(t)}$, with $\rho = 1$. We proved the following theorem ([17],[14]).

Theorem 3.1. *Assume that θ is a continuous and strictly increasing function on $[0, 2\pi]$ with $|\theta([0, 2\pi])| = 2\pi$. Then the following two conditions are equivalent.*

(i) *$d\theta(t)$ is a harmonic measure on the unit circle.*
(ii)

$$\tilde{H}\cos\theta(t) = \sin\theta(t) + \mathrm{Im}a, \quad \text{and} \quad \tilde{H}\sin\theta(t) = -\cos\theta(t) - \mathrm{Re}a \tag{3.1}$$

for some $a \in \mathbb{D}$.

We note that by definition $d\theta(t)$ is a harmonic measure on the circle if $\theta'(t)$ is a Poisson kernel on the circle. For any complex number $a \in \mathbb{D}$ denote by $e^{i\theta_a(t)}$ the unimodular circular mono-component established through Theorem 3.1, called a *Fourier atom*. The function $\theta_a(t)$ is defined through the boundary value of a typical Möbius transform sending a to zero:

$$\tau_a(z) = \frac{z-a}{1-\bar{a}z}, \quad e^{i\theta_a(t)} = \frac{e^{it}-a}{1-\overline{a}e^{it}}. \tag{3.2}$$

The theorem implies that $\theta_a'(t)$ is the Poisson kernel of the circle at the point a, and $\theta_a(t)$ is, in fact, an absolutely continuous function. Note that when $a = 0$, $e^{i\theta_a(t)} = e^{it}$. The finite product of k copies of e^{it} is e^{ikt}. A generalized Fourier series and weighted Fourier transform theory are studied in [14].

This simplest unimodular case is further extended to a product of finite many Möbius transforms corresponding to Blaschke product, as given in [15].

Theorem 3.2. *Assume that θ is an absolutely continuous function on $[0, 2\pi]$ strictly increasing with $m(\theta([0, 2\pi])) = 2\pi n$, where m stands for the Lebesgue measure. Then the following two conditions are equivalent.*

(i) *$d\theta(t)$ is a sum of a number of n harmonic measures on the unit circle.*

(ii)

$$\tilde{H}\cos\theta(t) = \sin\theta(t) - (-1)^n \mathrm{Im}(\prod_{k=1}^{n} a_k) \tag{3.3}$$

and

$$\tilde{H}\sin\theta(t) = -\cos\theta(t) + (-1)^n \mathrm{Re}(\prod_{k=1}^{n} a_k) \tag{3.4}$$

for some $a_k \in D, k = 1, ..., n$.

Based on finite Blaschke products on the circle one can introduce two types of mono- and dual mono-components on the line. One is periodic extensions of the Fourier atoms. We make the extension $\theta_a(t + 2\pi) = \theta_a + 2\pi, -\infty < t < \infty$. Based on this, the periodic function $e^{i\theta_a(t)}, -\infty < t < \infty$, is a unimodular periodic mono-component on the line.

The second type is images of those functions under Cayley transformation: $\kappa : \mathbb{C}^+ \to \mathbb{D}$,

$$z = \kappa(w) = \frac{i-w}{i+w} \tag{3.5}$$

and the corresponding boundary relation

$$e^{it} = \frac{i-s}{i+s}, \quad s = \tan\frac{t}{2}. \tag{3.6}$$

Let $\phi_a(s) = \theta_a(2\arctan s), -\infty < s < \infty$, we obtain that $e^{i\phi_a(s)}$ is a unimodular non-periodic mono-component on the line ([14], [15]).

The second type was previously studied in [13] based on a different approach.

We cite the following spectrum results for the two types of mono-components ([2]). They will be recalled in §6.

Viewing $e^{i\theta_a(t)}$ as a periodic function on the line, we have ([2])

$$\frac{1}{\sqrt{2\pi}}\int_{-\infty}^{\infty} e^{i\theta_a(t)}e^{-i\xi t}dt = -\sqrt{2\pi}a\delta(\xi) + \frac{\sqrt{2\pi}(1-|a|^2)}{\bar{a}}\sum_{k=1}^{\infty}\bar{a}^k\delta(\xi-k). \tag{3.7}$$

For the non-periodic type on the line we have ([2])

$$\frac{1}{\sqrt{2\pi}}\int_{-\infty}^{\infty} e^{i\phi_a(t)}e^{-i\xi t}dt = -\sqrt{2\pi}\delta(\xi) + \frac{2\sqrt{2\pi}(1-|a|)}{(1+|a|)}e^{-\frac{1-|a|}{1+|a|}\xi}H(\xi), \tag{3.8}$$

where $H(\xi)$ is the Heaviside function.

We note that in either of the cases the spectrum contains nontrivial impulse at the origin. This prevents from direct use of Bedrosian's Theorem ([1]) in deducing mono- or dual mono-components of the form $\rho(t)e^{i\theta_a(t)}$ or $\rho(t)e^{i\phi_a(t)}$ with non-constant $\rho \geq 0$. We will come back to this in §6.

We present an example here.

Example. Taking $a = 1/2$ in Theorem 3.1, we have

$$e^{i\theta_a(t)} = c(t) + is(t),$$

where

$$c(t) = \frac{5\cos t - 4}{5 - 4\cos t}, \quad s(t) = \frac{3\sin t}{5 - 4\cos t}.$$

The theorem asserts that the function $c + is$ is a unimodular circular mono-component. As verification, now we prove this through a direct computation.

We will show

(i) $c^2(t) + s^2(t) = 1$;
(ii) $s'(t) = h(t)c(t), \quad h(t) \geq 0$;
(iii) $\widetilde{\mathcal{H}}\,(c(t)) = s(t)$.

Under (i)-(iii), we may write

$$c(t) = \cos\theta(t), \quad s(t) = \sin\theta(t), \quad \theta(t) = \int_0^t h(u)du, \quad \widetilde{\mathcal{H}}\,(\cos\theta(t)) = \sin\theta(t).$$

Now,

$$\begin{aligned} c^2(t) + s^2(t) &= \frac{(5\cos t - 4)^2 + (3\sin t)^2}{(5 - 4\cos t)^2} \\ &= \frac{25\cos^2 t + 16 - 40\cos t + 9\sin^2 t}{25 + 16\cos^2 t - 40\cos t}. \end{aligned}$$

On replacing 16 by $16\sin^2 t + 16\cos^2 t$ in the numerator, we have $c^2(t) + s^2(t) = 1$. This proves (i).

Next, we have

$$s'(t) = \left(\frac{3\sin t}{5 - 4\cos t}\right)' = \frac{15\cos t - 12}{(5 - 4\cos t)^2}.$$

Therefore

$$\frac{s'(t)}{c(t)} = \frac{3}{5 - 4\cos t} > 0.$$

To show (iii), we point out that

$$c(t) = -\frac{1}{2} + \frac{3}{4}\cos t + \ldots + \frac{3}{2^{n+1}}\cos nt + \ldots,$$
$$s(t) = \frac{3}{4}\sin t + \ldots + \frac{3}{2^{n+1}}\sin nt + \ldots.$$

The circular Hilbert transform may be applied term by term to the series $c(t)$, and we then obtain (iii). The term by term operation is justified by the L^2-boundedness of the circular Hilbert transform (Riesz Theorem) and by the convergence in the L^2-sense of the series representing function c .

From (i)-(iii), we know that, the phase

$$\theta(t) = \arctan\frac{\widetilde{\mathcal{H}}c(t)}{c(t)} = \arctan\frac{3\sin t}{5\cos t - 4},$$

satisfies that

$$\theta'(t) = h(t), \quad \cos\theta(t) = c(t), \quad \widetilde{\mathcal{H}}\cos\theta(t) = \widetilde{\mathcal{H}}c(t) = s(t) = \sin\theta(t).$$

Therefore, $e^{i\theta(t)}$ is a circular mono-component.

4. Boundary Values of Functions in Hardy Spaces

We first give some observations on boundary values of holomorphic functions.

If f belongs to $L^p(\mathbb{R}), 1 < p < \infty$, then the Cauchy integral

$$F(z) = \frac{1}{2\pi}\int_{\mathbb{R}} \frac{f(t)}{t - z}dt \tag{4.1}$$

is a holomorphic function in the upper-half complex plane, and Plemelj's formula holds:

$$\lim_{y\to 0+} F(x + iy) = \frac{1}{2}f(x) + i\frac{1}{2}Hf(x), \quad a.e.$$

The so called analytic signal, up to a multiple constant, is actually the boundary value of the Cauchy integral of the associated real signal. Distributionally,

$$\left(\frac{1}{(\cdot) - (x + iy)}\right)\hat{}\,(\xi) = \chi_{(0,\infty)}(\xi)e^{ix\xi}e^{-y|\xi|} = \frac{1}{2}(1 + \mathrm{sgn}\xi)e^{ix\xi}e^{-y|\xi|},$$

where $\chi_{(0,\infty)}$ denotes the characteristic function of the set $(0, \infty)$. A generalized Paseval's formula with (4.1) gives

$$F(z) = \frac{1}{2}\left[\frac{1}{2\pi}\int_{\mathbb{R}} e^{ix\xi}e^{-y|\xi|}\hat{f}(\xi)d\xi + i\frac{1}{2\pi}\int_{\mathbb{R}} e^{ix\xi}e^{-y|\xi|}(-i\mathrm{sgn}\xi)\hat{f}(\xi)d\xi\right].$$

Together with Plemelj's formula, this last representation in inverse Fourier transform shows that the spectrum of the Cauchy integral lies on the right-half of the real axis, and the Fourier multiplier of Hilbert transformation is $-i\text{sgn}\xi$.

The boundary value of an arbitrary holomorphic function in the upper-half complex plane does not necessarily have such property. The Cauchy integrals of functions in L^p spaces are actually functions in the Hardy H^p spaces. H^p spaces are large enough to fit our purpose. We introduce them as follows,

For $0 < p < \infty$, define the Hardy spaces

$$H^p(\mathbb{D}) = \{f \ : \ f \in H(\mathbb{D}), \ \|f\|_p = \sup_{0<r<1} \{\frac{1}{2\pi} \int_{\partial\mathbb{D}} |f(re^{it})|^p dt\}^{1/p} < \infty\},$$

and

$$H^p(\mathbb{C}^+) = \{f \ : \ f \in H(\mathbb{C}^+), \ \|f\|_p = \sup_{0<y<\infty} \{\int_R |f(t+iy)|^p dt\}^{1/p} < \infty\}.$$

For $p = \infty$, define

$$H^\infty(\mathbb{D}) = \{f \ : \ f \in H(\mathbb{D}), \ \|f\|_\infty = \sup_{z\in\mathbb{D}} |f(z)| < \infty\},$$

and

$$H^\infty(\mathbb{C}^+) = \{f \ : \ f \in H(\mathbb{C}^+), \|f\|_\infty = \sup_{w\in\mathbb{C}^+} |f(w)| < \infty\}.$$

For $p \geq 1, H^p$ are Banach spaces. For $p < 1, H^p$ are complete metric spaces under the metric

$$d(f,g) = \|f-g\|_p^p.$$

Since we are to study Hilbert transforms in our function spaces, we restrict ourselves to merely study $H^p(\mathbf{S}), 1 \leq p \leq \infty$.

In [15] we explore connections between eigenfunctions of Hilbert transformation and functions in Hardy H^p spaces. The following result is proved (Th. 3.2 and 4.3., [15]).

Theorem 4.1. *The function $f(t) = \rho(t)(c(t)+is(t))$, with $\rho \geq 0$ and $\rho \in L^p(\mathbf{S}), 1 \leq p \leq \infty, c^2 + s^2 = 1$, is the boundary value of a function in $H^p(\mathbf{S})$ if and only if $H_{\mathbf{S}}(\rho c) = \rho s$ modulo constants.*

We remark that $H_{\mathbf{S}}(\rho c) = \rho s$ is equivalent to $Hf = -if$. Note that for the frequently used case $\mathbf{S} = \mathbb{C}^+$ and $p = \infty$ the Hilbert transformation takes the distribution sense. Its formulation is naturally related to boundary values of functions in $H^\infty(\mathbb{R})$.

Denote by $\mathbf{D}$ the space of infinitely differentiable functions with compact support on the line, and $\mathbf{D}'$ the space of continuous linear functionals on $\mathbf{D}$, viz. the space of distributions.

Definition 4.2. Let T be a distribution and u a harmonic function in the upper-half complex plane. If

$$< T, \phi >= \lim_{y \to 0+} \int_{-\infty}^{\infty} u(x, y)\phi(x)dx, \quad \phi \in \mathbf{D},$$

then u is said to be a *harmonic representation of* T.

Obviously, a distribution may have more than one harmonic representations. The following result is known (see, for instance, [10] or [11]).

Theorem 4.3. *Let T be a distribution and U one of its harmonic representations. Let V be any harmonic conjugate of U, then V is a harmonic representation of some distribution, S.*

Definition 4.4. Any distribution S in Theorem 4.3 is called a *Hilbert transform* of T.

For a chosen harmonic representation of T its harmonic conjugates are not unique. As consequence the above defined Hilbert transform is unique only up to an additive constant. The relation $H^2 = -I$ now is changed to $H^2 = -I + [c]$, where $[c]$ denotes the class of constants.

Theorem 4.1 allows to obtain a large variety of unimodular H- and circular H-eigenfunctions through elementary conformal mappings.

We will be based on the following conformal mappings.

(i) The Cayley transform $\mathbb{C}^+ \to \mathbb{D}$ defined by

$$z = \kappa(w) = \frac{i - w}{i + w}.$$

The mapping $\kappa : \mathbb{C}^+ \to \mathbb{D}$ is univalent and onto.

(ii) The mappings $\mathbb{C}^+ \to \mathbb{D}$

$$\epsilon_L(z) = e^{i\frac{\pi z}{L}}, \quad L > 0.$$

They are onto but not univalent. They are periodic, satisfying $\epsilon_L(z + 2L) = \epsilon_L(z)$. Denote by $[\epsilon]$ the class of such mappings.

(iii) The Möbius transforms $\mathbb{D} \to \mathbb{D}$

$$\tau_a(z) = \frac{-\overline{a}}{|a|}\frac{z - a}{1 - \overline{a}z}, \quad a \in \mathbb{D}.$$

The conformal mappings are univalent and onto. We denote by $[\tau]$ the class of Möbius transforms.

(iv) The mappings $\mathbb{C}^+ \to \mathbb{C}^+$

$$\mu_{a,b,c,d}(z) = \frac{az + b}{cz + d}, \quad a, b, c, d \text{ real numbers, and } ad - bc > 0.$$

The conformal mappings are univalent and onto. We denote the class of such mappings by $[\mu]$.

(v) The mappings $\mathbb{C}^+ \to \mathbb{D}$

$$\nu_a(z) = \frac{|a^2+1|}{a^2+1}\frac{w-a}{w-\overline{a}}, \quad a \in \mathbb{C}^+ \setminus \{i\}.$$

The conformal mappings are univalent and onto. We denote the class of the mappings by $[\nu]$. Clearly, $\kappa \in [\nu]$.

(vi) Denote by $[f]$ and $[F]$ the classes of inner functions in $\mathbb{D}$ and $\mathbb{C}^+$, respectively. Inner functions are H^∞ functions with constant modulus 1 on the boundary.

(vii) Denote by $[b]$ and $[B]$ the classes of Blaschke products in $\mathbb{D}$ and $\mathbb{C}^+$, respectively.

We can construct functions in $[F]$ from the above listed elementary ones. Some examples are given in the following theorem.

Theorem 4.5. *We have*

(i) $[\tau] \circ [\epsilon] \subset [b] \circ [\epsilon] \subset [f] \circ [\epsilon] \subset [F]$.
(ii) $[\nu] = \kappa \circ [\mu] = [\tau] \circ \kappa \subset [b] \circ \kappa = [B] \subset [f] \circ \kappa = [F]$.
(iii) $[\tau] \circ [\epsilon] \circ [\mu] \subset [b] \circ [\epsilon] \circ [\mu] \subset [f] \circ [\epsilon] \circ [\mu] \subset [F]$.
(iv) *Products of functions in the classes in (i)-(iii) are functions in* $[F]$.

We draw the following remarks to the theorem.

Remark 4.6. The class $[b] \circ [\epsilon]$ in the assertion (i) consists of the unimodular mono-components on $\mathbb{R}$ of the form

$$F_1(t) = e^{i\sum \theta_{a_k}(\frac{\pi t}{L_k})}, \quad a_k \in \mathbb{D},\ L_k > 0,$$

where we take the convention that $\theta_{a_k}(t+2\pi) = \theta_{a_k}(t) + 2\pi$. The smallest class in (i) is $[\tau] \circ \epsilon_\pi$ that is the periodic version of Theorem 3.1.

Remark 4.7. The functions in the class $[\nu]$ of the assertion (ii) is the Cayley transform version of Theorem 3.2. They are the atomic cases of the class $[B]$. The class $[B]$ together with a factor of linear phase is studied in Picinbono [13].

Remark 4.8. The unimodular mono-components of the form $e^{i\mu(s)} = e^{i\frac{as+b}{cs+d}}$ are not periodic but with infinitely many oscillations. They are not Blaschke products, but belong to the class of "chirp " signals.

Remark 4.9. We may construct complicated mono-components based on the product rule specified in the assertion (iv). For instance, by multiplying the basic mono-component signals in (i), (ii) and (iii) we obtain, as long as convergent, the unimodular mono-component

$$e^{i\theta_0}\prod_{k=1}^{\infty}\frac{z_k - z}{z - \overline{z}_k}\exp(i\sum_{k=1}^{\infty}\theta_{w_k}(\frac{a_k z + b_k}{c_k z + d_k})),$$

where θ_0 is a real constant, $z_k, k = 1, 2, ...$, are complex numbers in the upper-half complex plane, $w_k, k = 1, 2, ...$ are complex numbers in the unit disc, and for each k, the real numbersa_k, b_k, c_k, d_k satisfy $a_k d_k - b_k c_k > 0$.

Next we give some spectrum results with distributions. We first introduce

Definition 4.10. Let T be a distribution and $f(x+iy)$ an analytic function in $\mathbb{C}^+$ such that for any $\phi \in \mathbf{D}$

$$< T, \phi >= \lim_{y \to 0+} \int_{\mathbb{R}} f(x+iy)\phi(x)dx,$$

then we say that T is an *upper-Hardy distribution*, and $f(x+iy)$ is an analytic representation of T. In such a case we may write $T = T^+$.

Let T be the tempered distribution represented by the boundary value of a function in $H^p(\mathbb{C}^+)$. From Definition 4.10, $T = T^+$ is an upper-Hardy distribution. The following theorem asserts that $\hat{T^+}$, the Fourier transform of T^+, has positive spectrum in the sense specified in the following theorem.

Theorem 4.11. *T^+ is the tempered upper-Hardy distribution represented by the boundary value of a function in $H^p(\mathbb{C}^+), 1 \le p \le \infty$, if and only if $\hat{T^+} \subset [0, \infty)$, that is,*

$$< \hat{T^+}, \phi >= 0, \text{ for all } \phi \in \mathbf{D} \text{ such that } \text{supp}\phi \subset (-\infty, 0].$$

The proof of the "only if" part is contained in [15], and that of "if" part is contained in [18]. Based on this theorem we generalized Bedrosian's Theorem to the L^p cases ([18]), as given in

Theorem 4.12. *Suppose $f \in L^p(\mathbb{R})$, $g \in L^q(\mathbb{R})$, $1/p + 1/q = 1/r$, $1 \le p, q, r \le \infty$. If $\text{supp}\hat{f} \subset [-\sigma, \sigma]$, supp $\hat{g} \subset \mathbb{R} \setminus (-\sigma - \delta, \sigma + \delta)$, where $\sigma, \delta > 0$, then*

$$H(fg) = fHg.$$

5. Boundary Values of Starlike Functions

In below, a connected and open set in the complex plane $\mathbb{C}$ is called a *domain*. A function f is said to be *univalent* if it takes different values at different points. Our definition for starlike domains, and therefore that for starlike functions, takes the narrow sense, that is, starlike with respect to the pole $z = 0$.

Definition 5.1. A domain Ω is said to be starlike if $0 \in \Omega$, and $tz \in \Omega, 0 < t < 1$, whenever $z \in \Omega$. A univalent and holomorphic function $f : \mathbb{D} \to f(\mathbb{D})$ is said to be *starlike* if $f(\mathbb{D})$ is starlike and $f(0) = 0$.

Closely related are *convex domains* and *convex functions*.

Definition 5.2. A domain Ω is said to be convex, if $0 \in \Omega$, and $tz_1 + (1-t)z_2 \in \Omega, 0 < t < 1$, whenever $z_1, z_2 \in \Omega$. A univalent and holomorphic function $f : \mathbb{D} \to f(\mathbb{D})$ is said to be *convex*, if $f(\mathbb{D})$ is convex and $f(0) = 0$.

Clearly, a convex domain is a starlike domain, and a convex function is a starlike function.

The Taylor expansion of a starlike function is of the form

$$g(z) = a_1 z + a_2 z^2 + \cdots + a_n z^n + \cdots, \quad |z| < 1. \tag{5.1}$$

We denote by S the class of univalent and holomorphic functions in $\mathbb{D}$ having the Taylor expansion

$$g(z) = z + a_2 z^2 + \cdots + a_n z^n + \cdots, \quad |z| < 1. \tag{5.2}$$

The totality of starlike functions in S is denoted by S^*, and the totality of convex functions in S is denoted by C. It may be shown that C is a proper subclass of S^*, and S^* is a proper subclass of S. We call functions in S^* *normalized starlike functions*; and those in C *normalized convex functions*. There has been a deep study with fruitful results on the classes C, S^* and S. Among literature on starlike functions we refer to [8], [6], [12], [4] and [7]. The most striking feature of the subtle analysis on the classes C, S^* and S would be its connections with Bieberbach conjecture (1916) whose final and celebrated proof was given by de Branges in 1984 ([8]). In this note we will explore some relations between starlike functions with our H-eigenfunction problem. We first introduce some concepts.

Definition 5.3. Let $\rho(t)$ and $\theta(t), 0 \le t \le 2\pi$, be absolutely continuous, $\rho \ge 0$, and

$$\int_0^{2\pi} \rho(t) e^{i\theta(t)} dt = 0. \tag{5.3}$$

With these properties, a function $f(t) = \rho(t)e^{i\theta(t)}$ is called a circular H-atom, if f is a circular mono-component satisfying $\theta(2\pi) - \theta(0) = 2\pi$; and, a dual circular H-atom, if f is a dual circular mono-component satisfying $\theta(2\pi) - \theta(0) = -2\pi$.

As consequence of Theorem 2.2, the following result addresses the symmetry property between circular and dual circular H-atoms.

Theorem 5.4. *$\rho(t)e^{i\theta(t)}$ is a circular H-atom if and only if $\rho(t)e^{-i\theta(t)}$ is a dual circular H-atom.*

The following results are contained in [6] (§1, Ch.10). If $f(z)$ is holomorphic, and it univalently maps $\mathbb{D}$ into a simply connected region Q whose boundary is a bounded rectifiable closed Jordan curve, then f continuously extends to $\bar{\mathbb{D}}$ such that on $\partial\mathbb{D}$ it is absolutely continuous with

$$\frac{df(e^{it})}{dt} = ie^{it} f'(e^{it}), \ a.e.,$$

where $f'(e^{it})$ is the non-tangential boundary value of $f'(z)$ in $\mathbb{D}$. If, moreover, $f(t) = \rho(t)e^{i\theta(t)}$ is the boundary value of a starlike function, then both $\rho(t)$ and $\theta(t)$ are absolutely continuous.

For practical reasons we only concern such ideal starlike functions. The importance of starlike functions lies on the following Theorem.

Theorem 5.5. *$\rho(t)e^{i\theta(t)}, 0 \le t \le 2\pi$, is a circular H-atom if and only if it is the boundary value $f(e^{it})$ of a starlike function $f(z)$ whose boundary is a bounded rectifiable closed Jordan curve.*

The proof is based on Argument Principle of univalent functions and the result for boundary values of functions in the $H^\infty(\mathbb{D})$ space ([15]). For details see [16].

In complex analysis the normalized starlike functions with respect to the pole ∞ have the Taylor expansion

$$f(z) = z + b_0 + \frac{b_1}{z} + \frac{b_2}{z^2} + \cdots \tag{5.4}$$

The existence of the first two entries, namely z and b_0, is mainly for a geometrically symmetric theory for this case. In particular, with the form (5.4), when $z = e^{it}$ goes along the unit circle in the anticlockwise direction, then $f(e^{it})$ goes along the boundary of $f(\mathbb{D})$ anticlockwise as well. For the theory of dual mono-component we, however, adopt the following definition that is analytically symmetric, and works well with Hilbert transform.

Definition 5.6. A function $f(z)$ is said to be starlike with respect to the pole ∞ if $f(\frac{1}{z})$ is starlike (with respect to the pole zero).

With this definition we have the counterpart result for dual circular H-atoms.

Theorem 5.7. *$\rho(t)e^{i\theta(t)}, 0 \le t \le 2\pi$, is a dual circular H-atom if and only if $\rho(t)e^{i\theta(t)}, 0 \le t \le 2\pi$, is the boundary value $f(e^{it})$ of a starlike function $f(z)$ with respect to the pole ∞, whose boundary is a bounded rectifiable closed Jordan curve.*

Example. (The Circle Family) The simplest example would be the circle family. Any fractional-linear transformation

$$w = f(z) = \frac{az}{cz + d}$$

that maps $\mathbb{D}$ into a disc $f(\mathbb{D}) \ni 0$, $f(0) = 0$, with the positive orientation as t rotates from 0 to 2π under the parametrization $z = e^{it}$, will give rise to a circular H-atom. We now form this family in a systematic way using Möbius transform. The Möbius transform $\tau_a(z) = (z - a)/(1 - \bar{a}z)$ has the power series expansion

$$\tau_a(z) = -a + b_1 z + b_2 z + \cdots,$$

where $b_1 = 1 - |a|^2 > 0$. We construct

$$f_a(z) = \frac{1}{b_1}(\tau_a(z) + a) = \frac{z}{1 - \overline{a}z}. \tag{5.5}$$

This function is in the class C. It maps discs in $\mathbb{D}$ into discs. The images $f_a(\mathbb{D}_r)$, $\mathbb{D}_r = r\mathbb{D}, 0 < r < 1$, are discs not centered at $z = 0$. Indeed,

$$f_a(re^{it}) = \frac{r}{\sqrt{1 - 2r|a|\cos(t - t_a) + |a|^2 r^2}} e^{i(t - \arg(1 - r|a|e^{i(t - t_a)}))},$$

where $a = |a|e^{it_a}$. It follows from Theorem 5.5 that for every fixed $r : 0 < r < 1$, the function $f_a(re^{it})$ is a circular H-atom. The mapping can be extended to $r : 1 \le r < 1/|a|$, and the diameter of the disc $f(\mathbb{D})$ passing through 0 is divided by 0 into two parts with lengths, respectively, $\frac{r}{1-r|a|}$ and $\frac{r}{1+r|a|}$. So, the closer the number $r|a|$ to 1, the closer the pole zero to the boundary of the image circle.

One can similarly formulate the ellipse family and the Casimire curve family.

As consequence of the Argument Principle finite products of circular H-atoms are multi-valent functions. We have the following

Theorem 5.8. *Finite products of circular and dual circular H-atoms are respectively circular mono-components and dual circular mono-components.*

The established theory on the classes S, S^* and C provides a source of starlike functions with a great variety. The basic references are [8], [6], [12], [4] and [7]. The reference [7], in particular, provides many working examples. We briefly recall, without proof, some results in the literature that may have significant impacts to our study.

(i) It may be shown that if $f(D)$ is starlike, then $f(D_r)$ is starlike for all $r \in (0, 1)$. In Example 2.1 on the circle family we assert this fact from the property of fractional-linear transformations. It, however, holds in general. This implies that when $z = re^{it}$ traces out the circle $|z| = r$ anticlockwise, then the complex number $f(z) = \rho e^{i\theta}$ must also traces out a complete circle anticlockwise . It follows that

$$\frac{\partial}{\partial t} \arg\{f(z)\} = \frac{\partial \theta}{\partial t} \geq 0.$$

This latter condition implies

$$Re\{\frac{zf'(z)}{f(z)}\} \geq 0, \quad z \in \mathbb{D}.$$

This turns to be a sufficient condition for starlike domains as well.

(ii) It may be shown that a function is convex in $\mathbb{D}$ if and only if $1 + z\frac{f''(z)}{f(z)}$ has a positive real part in $\mathbb{D}$. As consequence, $f(\mathbb{D}_r), 0 < r < 1$, is also convex. Based on this it may be shown that $f(z)$ is convex if and only if $F(z) = zf'(z)$ is starlike. Therefore, a convex function $f(z)$ has the formula

$$f(z) = \int_0^z \frac{F(\zeta)}{\zeta} d\zeta,$$

where $F(z)$ is a starlike function. The last relation also gives rise to a representation formula for all convex functions (see (iv) below).

(iii) If f and g are in class S^*, then their weighted product $f^\alpha g^\beta, \alpha + \beta = 1, 0 \leq \alpha, \beta \leq 1$, is in S^*.

If f and g are in the class C with the expansions

$$f(z) = \sum_{n=1}^{\infty} a_n z^n, \quad g(z) = \sum_{n=1}^{\infty} b_n z^n,$$

then their Hadamard product (also called Hadamard convolution)

$$(f * g)(z) = \sum_{n=1}^{\infty} a_a b_n z^n$$

is in C.

If f and g are in the class S^*, then the modified Hadamard product

$$(f \otimes g)(z) = \sum_{n=1}^{\infty} \frac{a_a b_n}{n} z^n$$

is in S^*.

(iv) If $P(z)$ is holomorphic with positive real part then there holds Herglotz's formula:

$$P(z) = \int_0^{2\pi} \frac{e^{it} + z}{e^{it} - z} d\alpha(t),$$

where $\alpha(t)$ is a non-decreasing function satisfying

$$\int_0^{2\pi} d\alpha(t) = 1, \quad \textit{and} \quad \alpha(t) = \frac{1}{2}[\alpha(t+0) + \alpha(t-0)]. \tag{5.6}$$

There is a one to one relationship between the functions $P(z)$ and $\alpha(t)$.

Based on Herglotz's formula one has the representation formula for starlike functions: A function f is starlike in $\mathbb{ID}$ if and only if

$$f(z) = z \ \exp\left(2 \int_0^{2\pi} \log \frac{1}{1 - e^{-it} z} d\alpha(t)\right),$$

where α is a non-decreasing function satisfying (5.6). Theoretically the formula provides all starlike functions with the pole zero.

(v) It is an interesting fact that if $f(z)$ is in S, then for small enough $r > 0$ the image $f(r\mathbb{ID})$ is starlike, and therefore $f(rz)$ is in S^*. One can show that there exists a positive number, $R_{ST} = \frac{e^{\pi/2}-1}{e^{\pi/2}+1} \approx 0.65579$, called *radius of starlike-ness*, such that whenever $r \leq R_{ST}$ the image $f(r\mathbb{ID})$ is starlike for all $f \in S$. The number R_{ST} is sharp in the sense that if $r > R_{ST}$, then there exists a function $f \in S$ such that $f(r\mathbb{ID})$ is not starlike. For the class S there is also a sharp constant, $R_{CV} = 2 - \sqrt{3} \approx 0.26 \cdots$, called *radius of convexity*, such that whenever $r \leq R_{CV}$ the set $f(r\mathbb{ID})$ is convex for all $f \in S$.

It is the identical relationship between circular H-atoms and certain starlike functions that motivates the definition of circular H-atoms (Theorem 5.5). There is no counterpart concepts on the line. Next we will induce mono-components and dual mono-components on the line based on those obtained on the circle.

Theorem 5.9. *Assume that* $\tilde{f}(t) = \rho(t)e^{i\theta(t)}, 0 \leq t < 2\pi$, *where* $\rho \in L^p([0, 2\pi)), 1 \leq p \leq \infty$. *Then,*

(i) *for* $1 \leq p \leq \infty$, $\tilde{f}(t)$ *is a (dual) circular mono-component if and only if* $f(t) = \rho(t)e^{i\theta(t)}, -\infty < t < \infty$, *is a (dual) mono-component on the line, where* ρ *and* θ *are extended to satisfy* $\rho(t+2\pi) = \rho(t)$ *and* $\theta(t+2\pi) = \theta(t)+2\pi$.

(ii) *for* $1 \le p < \infty$, *the function*

$$\frac{1}{(s^2+1)^{1/p}}\rho(2\arctan s)$$

belongs to $L^p(\mathbb{R})$, *and, if* $\tilde{f}(t)$ *is a (dual) circular mono-component, then*

$$F(s)=\frac{1}{(s^2+1)^{1/p}}\rho(2\arctan s)e^{i\left(\theta(2\arctan s)+\frac{2}{p}\arccos(\frac{-s}{\sqrt{s^2+1}})-\frac{2\pi}{p}\right)}, \quad -\infty < s < \infty,$$

is a (dual) mono-component on the line.

(iii) *for* $p=\infty$, $\tilde{f}(t)$ *is a (dual) circular mono-component if and only if*

$$F(s) = \rho(2\arctan s)e^{i\theta(2\arctan s)}, \quad -\infty < s < \infty,$$

is a (dual) mono-component on the line.

The proof of (i) is based on the following Lemma.

Lemma 5.10. *Let* $\tilde{f} \in L^p([-\pi,\pi)), 1 \le p \le \infty$, *and* f *be the* 2π*-periodic extension of* $\tilde{f}$ *to the real line. Then* Hf *is* 2π*-periodic, and, restricted in* $[-\pi,\pi)$, $Hf = \tilde{H}\tilde{f}$, *where* Hf *is defined by*

$$Hf(t) = \lim_{\epsilon\to 0, N\to\infty} \frac{1}{\pi}\int_{\epsilon<|t-s|<(2N+1)\pi} \frac{f(s)}{t-s}ds.$$

Proof. It may be easily shown (also see [14], or [15], or [2])

$$\begin{aligned} Hf(t) &= \frac{1}{\pi}\lim_{\epsilon\to 0, N\to\infty}\int_{(-\pi,\pi)\cap\{|x-t|>\epsilon\}} \Big(\sum_{k=-N}^{N}\frac{1}{t-x-2k\pi}\Big)f(x)dx \\ &= \frac{1}{2\pi}\lim_{\epsilon\to 0}\int_{(-\pi,\pi)\cap\{|x-t|>\epsilon\}} \cot\left(\frac{t-x}{2}\right)f(x)dx \\ &= \tilde{H}\tilde{f}(t), \quad a.e. \end{aligned}$$

The proofs of (ii) and (iii) are based on Cayley transform and the relations between the two H^p spaces in the respective contexts. We suppress the easy proof. □

6. Solutions of the Eigenfunction Problem in Relation to Fourier Atoms

In this sections we deal with solutions of the eigenfunction problem of the forms $\rho(t)^{i\theta_a(t)}, 0 \le t \le 2\pi$, and $\rho(s)e^{i\phi_a(s)}, -\infty < s < \infty$. We construct some examples.

A signal f is said to be of λ-*low-frequency* , if $\hat{f}(\xi) = 0$ for $|\xi| > \lambda$; and of λ-*high-frequency*, if $\hat{f}(\xi) = 0$ for $|\xi| < \lambda$. Bedrosian's Theorem ([1], [17]) asserts that if f_l and f_h are in $L^2(\partial\mathbf{S})$, and f_l is of λ-low- and f_h of λ-high-frequency, then

$$H_{\mathbf{S}}(f_l f_h) = f_l H_{\mathbf{S}} f_h.$$

Note that in the above notion, when $\mathbf{S} = \mathbb{D}$, $\hat{f}(\xi)$ stands for the Fourier coefficients of f defined on integers. The discrete type Bedrosian's theorem is studied in [17]. A generalization of Bedrosian's Theorem to the L^p cases is given in [18].

Initially we wish to characterize $\rho(t)$ and $\theta(t)$ such that $\rho(t)e^{i\theta(t)}$ is a (circular) H-eigenfunction. In practice, the amplitude is expected to be of lower frequencies. In view of Bedrosian's theorem, we would expect

$$H_{\mathbf{S}}(\rho(t)\cos\theta(t)) = \rho(t)H_{\mathbf{S}}\cos\theta(t).$$

In such case, $\rho(t)e^{i\theta(t)}$ is a (circular) H-eigenfunction if and only if $e^{i\theta(t)}$ is a (circular) H-eigenfunction. This idea initiates the study of the unimodular case, that is $\rho \equiv 1$, of which a large class of unimodular (circular) mono-components is discovered ([17], [14], [15] and [2]). This, in particular, contains the Fourier atoms $e^{i\theta_a(t)}$ and their products. The question is: Having obtained the (circular) mono-components $e^{i\theta_a(t)}$, can we go back to identify functions ρ such that $\rho(t)e^{i\theta_a(t)}$ are (circular) mono-components, as already expected in view of Bedrosian's Theorem?

Bedrosian's Theorem may be used to construct non-unimodular mono-components of the form $\rho(t)e^{ikt}, k = \pm 1, \pm 2, ...$ The Fourier transform of e^{ikt} is the Dirac function $\delta(\cdot - k)$. Bedrosian's Theorem suggests that if ρ is non-negative and bandlimited, its Fourier transform has compact support contained in $[-|k|+\alpha, |k|-\alpha]$, where $|k| - \alpha > 0$, then $\rho(t)e^{ikt}$ may be a mono-component or dual mono-component, for $k > 0$ or $k < 0$, respectively.

Construction of such functions ρ is not entirely trivial. Without loss of generality, we can only deal with the case $k \geq 1$. First take any even and square-integrable function g_1 with compact support in $[-k + \alpha, k - \alpha]$, $1/2 > \alpha > 0$. Let g_0 be its inverse Fourier transform. Since g_1 is even, g_0 is real-valued. The Paley-Wiener Theorem (or a direct computation using inverse Fourier transform) implies that g_0 is the restriction of an entire function, $g_0(z)$, to the line. The entire function is in the Paley-Wiener $(k - \alpha)$-class satisfying the estimate

$$|g_0(z)| \leq Me^{(k-\alpha)|\mathrm{Im}z|}. \tag{6.1}$$

Note that $g_0(z)e^{i(k-\alpha)z}$ is a function in Hardy $H^2(\mathbb{C}^+)$ and $e^{i\alpha z}$ is in Hardy $H^\infty(\mathbb{C}^+)$, and hence their product is in $H^2(\mathbb{C}^+)$. Owing to the remark after the statement of Theorem 4.1 we have

$$\begin{aligned} H(g_0(t)e^{ikt}) &= H\left([g_0(t)e^{i(k-\alpha)t}][e^{i\alpha t}]\right) \\ &= -i[g_0(t)e^{i(k-\alpha)t}][e^{i\alpha t}] \\ &= -ig_0(t)e^{ikt}, \end{aligned}$$

showing that $g_0(t)e^{ikt}$ is an H-eigenfunction. For the constant M in (6.1) we also have

$$H(Me^{ikt}) = -iMe^{ikt}.$$

With $G(t) = g_0(t) + M > 0$ the signal $G(t)e^{ikt}$ is a mono-component.

Note that the above argument implies that $H(G(t)e^{ikt}) = G(t)H(e^{ikt})$ that is a Bedrosian type result but not under the standard conditions $f_l, f_h \in L^2(\mathbb{R})$.

Example. Let $k \geq 1$. Take $g_1 = \chi_{[-\delta,\delta]}, \delta < k - 1/2$, where $\chi_{[-\delta,\delta]}$ is the characteristic function of the interval $[-\delta, \delta]$. Then g_0, being inverse Fourier transform of g_1, is the sinc function $\frac{1}{\pi}\frac{\sin \delta t}{t}$ bounded by δ/π. Therefore,

$$\left(\frac{1}{\pi}\frac{\sin \delta t}{t} + \frac{\delta}{\pi}\right) e^{ikt}, \quad \delta < k - 1/2,$$

is a mono-component; and, owing to Theorem 2.2,

$$\left(\frac{1}{\pi}\frac{\sin \delta t}{t} + \frac{\delta}{\pi}\right) e^{-ikt}, \quad \delta < k - 1/2,$$

is a dual mono-component.

Bedrosian's Theorem, however, cannot be directly used to produce non-unimodular H-eigenfunctions of the form $\rho(t)e^{i\theta_a(t)}$. In fact, the results (3.7) and (3.8) show that for each of the two cases the spectrum contains nontrivial impulses at the origin. There, however, do exist non-unimodular functions $\rho \geq 0$ that make $\rho(t)e^{i\theta_a(t)}$ to be (circular) mono-components. This shows that the spectrum condition in the standard Bedrosian's Theorem is not a necessary one. We first deal with the circular case. Let τ_a be the Möbius transform defined in (3.2). Set

$$h_1(z) = \frac{1}{2}(\tau_a(z) + \overline{\tau_a(z^*)}),$$

where $z^* = 1/\overline{z}$ is the symmetric point of z with respect to the unit circle. Obviously, $h(z)$ is real-valued on the circle. Since $|\tau_a(z)|$ is dominated by 1, the function $h(z) = h_1(z) + 3$ has positive boundary values on the line, denoted by $\rho(t)$, between 1 and 5. The meromorphic function h has a sole pole of order one at a, so $G(z) = h(z)\tau_a(z)$ has no pole and is bounded and holomorphic in $\mathbb{D}$. We have $G(e^{it}) = \rho(t)e^{i\theta_a(t)}$. By invoking Theorem 4.1 for $H^\infty(\mathbb{D})$, we conclude that $\rho(t)e^{i\theta_a(t)}$ is a circular mono-component.

Simple computation gives

Example.

$$\begin{aligned} G(e^{it}) = \rho(t)e^{i\theta_a(t)} &= \left(2\frac{\cos t - 2|a|\cos t_a + |a|^2\cos(t - 2t_a)}{1 - 2|a|\cos(t - t_a) + |a|^2} + 3\right) e^{\pm i\theta_a(t)}, \\ & 0 \leq t \leq 2\pi, \end{aligned} \tag{6.2}$$

where $a = |a|e^{it_a}, t_a \in \mathbb{R}$, is a circular or dual circular mono-component for the sign $\pm$ taking $+$ or $-$, respectively.

Example. Using the general result of §5, (i), Theorem 5.9 (also see [14] and [2]), the 2π-periodic extension of the above function,with $\theta_a(t + 2\pi) = \theta_a(t) + 2\pi$,

$$\begin{aligned} G(e^{it}) = \rho(t)e^{i\theta_a(t)} &= \left(2\frac{\cos t - 2|a|\cos t_a + |a|^2\cos(t - 2t_a)}{1 - 2|a|\cos(t - t_a) + |a|^2} + 3\right) e^{\pm i\theta_a(t)}, \\ & -\infty \leq t \leq \infty, \end{aligned} \tag{6.3}$$

is a mono- or dual mono-component.

The non-periodic case on the real line may be deduced accordingly ((iii) Theorem 5.9)). The non-linear Fourier atoms $e^{i\theta_a(t)}$ on the circle under Cayley transform $\kappa : \mathbb{C}^+ \to \mathbb{D}$,

$$z = \kappa(w) = \frac{i-w}{i+w}, \quad e^{it} = \frac{i-s}{i+s} \tag{6.4}$$

is transformed to $e^{i\phi_a(s)}$ on the line, where

$$\phi_a(s) = \theta_a(2\arctan s).$$

Under the setting the function $e^{i\phi_a(s)}$ is the boundary value of the bounded and holomorphic function $\tau_a \circ \kappa$ that conformally and univalently maps the upper-half complex plane to the unit disc. Therefore $e^{i\phi_a(s)}$ is a mono-component. Similarly, take the function G defined right before Example (6.2), and set $\rho_1(s)e^{i\phi_a(s)} = (G \circ \kappa)(s)$. The obtained function is the boundary value of a bounded and holomorphic function in $\mathbb{C}^+$ and therefore

Example. In such a manner, with function ρ defined in (6.2), the function

$$\rho(2\arctan s)e^{\pm i\theta_a(2\arctan s)}, -\infty < s < \infty,$$

is a mono- or dual mono-component on the line.

Alternatively we can directly construct the same function with explicit representation using a similar method as in the circular case. Let $b \in \mathbb{C}^+$ such that $\kappa(b) = a$. Then $(\tau_a \circ \kappa)(b) = 0$. Apart from a unimodular multiple constant, the mapping $\tau_a \circ \kappa$, with boundary value $e^{i\phi_a(s)}$, is equal to $\kappa_b(z) = \frac{z-b}{z-\overline{b}}$. Set

$$h(z) = \frac{1}{2}(\kappa_b(z) + \overline{\kappa_b(\overline{z})})$$

which is meromorphic with a sole pole of order one at b, with bounded and real-valued boundary values on the real line. We define

$$G(z) = (h(z) + 3)\kappa_b(z).$$

It is a bounded and holomorphic function in $\mathbb{C}^+$.

Example. Apart from a unimodular multiple constant $G(z)$ has the boundary value

$$\left(2\frac{(s-s_b)^2 - h_b^2}{(s-s_b)^2 + h_b^2} + 3\right)e^{i\phi_a(s)},$$

where $b = s_b + ih_b$. The latter is a mono-component; and

$$\left(2\frac{(s-s_b)^2 - h_b^2}{(s-s_b)^2 + h_b^2} + 3\right)e^{-i\phi_a(s)}$$

is a dual mono-component.

References

[1] E. Bedrosian, *A product theorem for Hilbert transform,* Proc. IEEE **51**(1963), 868-869.

[2] Q-H. Chen, L-Q. Li and T. Qian, Two families of unit analytic signals with nonlinear phase, accepted to appear in Physica D.

[3] Q-H. Chen, L-Q. Li and T. Qian, *Stability of frames generalized by non-linear Fourier atoms*, International Journal of Waveletss, Multiresolution and Information Processing, Vol. **3**, No.4 (2005), 1-12.

[4] P.L. Duren, *Univalent Functions,* Sprnger-Verlag, 1983.

[5] J. B. Garnett, *Bounded Analytic Functions*, Academic Press, 1987.

[6] G. M. Goluzin, *Geometric Theorey of Functions of a Complex Variable,* 2nd ed., Izdat. "Nauka": Moscow, 1966; English transl. Amer. Math. Soc., 1969.

[7] A. W. Goodman, *Univalent Functions,* Vol I, II, Mariner Publishing Co.,Tampa Florida, 1983.

[8] S. Gong, *The Bieberbach Conjecture*, AMS/IP, Studies in Advanced Mathematics, Volume 12, 1999.

[9] N. E. Huang et al, *The empirical mode decomposition and the Hilbert spectrum for nonlinear and non-stationary time series analysis*, Proc. R. Soc. Lndon, A(1998)454, 903-995.

[10] B.H. Li, *On distributions with parameter and their analytic representations*, Chinese Math. Ann., 1981, 2(4), 399-405.

[11] B.H. Li and L.K. Guo, *Riesz transformations of distributions and a generalized Hardy space*, Approx. Theory and its Appl., 1988, 5(4), 1-17.

[12] Ch. Pommerrenke, *Univalent Functions,* Vanderhoeck and Puprecht; Göttingen, 1975.

[13] B. Picinbono, *On instantaneous amplitude and phase of signals*, IEEE Transactions on Signal Processing, vol, **45**, No. 3, March, 1997, 552-560.

[14] T. Qian, *Analytic Signals and Harmonic Measures*, J. Math. Anal. Appl., 314 (2006) 526-536.

[15] T. Qian, *Characterization of Boundary Values of Functions in Hardy Spaces With Application in Signal Analysis*, Journal of Integral Equations and Applications, Volume **17** Issue 2 (Summer 2005), 159-198.

[16] T. Qian, *Mono-components for decomposition of signals,* Math. Meth. Appl. Sci. 2006; **29**:1187-1198.

[17] T. Qian, Q-H. Chen, and L-Q. Li, *Analytic unit quadrature signals with nonlinear phase*, Physica D 203 (2005) 80-87.

[18] T. Qian, Y. Xu, D. Yan, L.-X. Yan and B. Yu, *Bedrosian theorem for L^p functions,* preprint.

Tao Qian
Faculty of Science and Technology
University of Macau,
Av. Padre Tomhs Pereira S.J.,
Taipa, Macau
e-mail: `fsttq@umac.mo`

Wavelet Analysis and Applications
Tao Qian, Mang I. Vai and Xu Yuesheng, Eds.
Applied and Numerical Harmonic Analysis, 321–362

Signal-Adaptive Aeroelastic Flight Data Analysis with HHT

Martin J. Brenner, Sunil L. Kukreja and Richard J. Prazenica

Abstract. This paper investigates the utility of the Hilbert-Huang transform for the analysis of aeroelastic flight data. The recently-developed Hilbert-Huang algorithm addresses the limitations of the classical Hilbert transform through a process known as empirical mode decomposition. Using this approach, the data is filtered into a series of intrinsic mode functions, each of which admits a well-behaved Hilbert transform. In this manner, the Hilbert-Huang algorithm affords time-frequency analysis of a large class of signals. The purpose of this paper is to demonstrate the potential applications of the Hilbert-Huang algorithm for the analysis of aeroelastic systems. Applications for correlations between system input and output, and amongst output sensors, are discussed to characterize the time-varying amplitude and frequency correlations present in the various components of multiple data channels. Examples are given using aeroelastic flight test data from the F/A-18 Active Aeroelastic Wing aircraft and Aerostructures Test Wing.

Mathematics Subject Classification (2000). Primary 93B15; Secondary 93B30.

Keywords. aeroelasticity, adaptive signal decomposition, Hilbert-Huang, empirical mode decomposition, time-frequency analysis.

1. Introduction

The Hilbert transform is a classical tool that has been used in the structural dynamics community as an indicator of nonlinearity. It has also been used to estimate nonlinear damping and stiffness functions for single degree-of-freedom systems.

The Hilbert transform expresses a signal as a harmonic with time-dependent frequency and amplitude. In this respect, it is an ideal tool for the analysis of nonstationary data. Unfortunately, the Hilbert transform has several shortcomings that limit its usefulness in practice. Most notably, the Hilbert transform computes a single instantaneous frequency for a signal at each instant in time. Therefore, when applied to a multi-component signal (i.e., a signal from a system with multiple modes), the Hilbert transform computes an instantaneous frequency that corresponds to a weighted average of the component frequencies. Such an instantaneous frequency does not provide any information as to the values of the individual component frequencies [4]. A further limitation is that the Hilbert transform yields grossly distorted estimates of the frequency when applied to signals with nonzero mean and signals which have more extrema than zero crossings.

In order to address these shortcomings, an Empirical Mode Decomposition (EMD) was developed by Huang et al. [8, 9] as a means of decomposing a signal into a series of components known as Intrinsic Mode Functions (IMFs). These IMFs are computed based on local characteristics of the signal and can be viewed as an adaptive, data-dependent basis. The IMFs form a complete, nearly orthogonal set of basis functions. Most importantly, each IMF contains only a single frequency component at any instant in time and therefore admits a well-behaved Hilbert transform. Taken collectively, the Hilbert spectra of the IMFs yield complete time-frequency information about the original signal. This approach, which has been termed the Hilbert-Huang Transform (HHT), makes it possible to apply the Hilbert transform to an extremely general class of functions and signals.

Although a relatively new tool, the Hilbert-Huang transform algorithm has received considerable attention in a number of engineering disciplines. This HHT algorithm has been applied in the analysis of scientific data [8, 9, 10], structural system identification [27, 28, 29], and mechanical system fault detection [11, 15, 26, 30]. A recent adoption into the image processing field [13, 14, 16, 31], the two-dimensional EMD is an adaptive image decomposition without the limitations from filter kernels or cost functions. The IMFs are interpreted as spatial frequency subbands with varying center frequency and bandwidth along the image. The EMD is a truly empirical method, not based on the Fourier frequency approach but related to the locations of extrema points and zero crossings. Based on this, the concept of "empiquency," used for time or space and short for "empirical mode frequency," was adopted to describe signal (image) oscillations based on the reciprocal distance between two consecutive extrema points. High concentrations of extrema points have high empiquency with sparse areas having low empiquency. Hence, applications for time-frequency-space signal processing are feasible.

A problem with the very versatile and most commonly used Morlet wavelet in dynamics data analysis is its leakage generated by the limited length of the basic wavelet function, which makes the quantitative definition of the energy-frequency-time distribution difficult. The interpretation of the wavelet can also be counterintuitive. For example, definition of a local event in any frequency range requires analysis in the high-frequency range, for the higher the frequency the

more localized the basic wavelet. A local event in the low-frequency range requires an extended period of time to discern it. Such interpretation can be difficult if possible at all. Another problem with wavelet analysis is its nonadaptive nature. Wavelet basis functions are predefined, whether of one type, or a multi-wavelet basis, or a dictionary of wavelets is selected. Data analysis is then constrained to these bases. Since the Morlet wavelet is Fourier based, it also suffers the many shortcomings of Fourier spectral analysis. A truly adaptive basis is a necessary requirement for nonstationary and nonlinear time series analysis and should be based on and derived from the data.

In this paper, results are obtained from the new approach. With the HHT, the intrinsic mode functions yield instantaneous frequencies as functions of time that give sharp identification of embedded structures. The main conceptual innovation in this approach is the introduction of the instantaneous frequencies for complicated data sets, which eliminate the need of spurious harmonics to represent nonlinear and nonstationary signals. This paper looks at the effect of enhancements like local/on-line versions of the algorithm [21]. To date, HHT analysis has only been performed on individual signals without regard to correlation with other data channels, or system inputs-to-outputs. Application for correlations between system signals are introduced to characterize the time-varying amplitude and frequency modulations present in the various components of multiple data channels including input and distributed sensors. In these respects, this paper attempts to elucidate the way EMD behaves in the analysis of F/A-18 Active Aeroelastic Wing (AAW) aircraft [18], aeroelastic and aeroservoelastic flight test data as well as Aerostructures Test Wing [12] and pitch-plunge simulation data.

2. Empirical Mode Decomposition

The classical Hilbert transform is, in principle, an effective tool for time-frequency analysis. Unfortunately, in practice, it can only be applied to an extremely restricted class of signals. In order to extend the utility of the Hilbert transform to more general signals, Huang et al. [8, 9] developed the empirical mode decomposition (EMD) as a means of preprocessing data before applying the Hilbert transform. The EMD procedure decomposes the original signal into a set of intrinsic mode functions (IMFs), each of which admits a well-behaved Hilbert transform. The Hilbert transform is then applied to each individual IMF, yielding an instantaneous frequency and amplitude for each IMF. Therefore, this procedure, termed the Hilbert-Huang transform (HHT), enables the Hilbert transform to be applied to multi-component signals.

There are two criteria that each IMF must satisy in order to be amenable to the Hilbert transform. Namely, each IMF must have zero mean and the number of local extrema and zero crossings in each IMF can differ by no more than one. The first step in the EMD procedure is to connect all the local maxima of the original signal using a cubic spline. Similarly, the local minima are also connected with a cubic spline. The two splines define the envelope, and the mean of this envelope

is then calculated and subtracted from the original signal. The resulting signal is then tested to see if it satisfies the criteria for an IMF. If it does not, the sifting process is repeated until a suitable first IMF, $c_1(t)$, is obtained. The sifting process is then applied to the residual signal $x(t) - c_1(t)$ to obtain the next IMF. This process is repeated until all that is left is a final residual, $r(t)$, which represents the trend in the data and is not an IMF. Therefore, as shown in Eq. 1, the EMD procedure yields a decomposition of the original signal in terms of n IMFs and the residual, $r(t)$.

$$x(t) = \sum_{j=1}^{n} c_j(t) + r(t) \tag{1}$$

The number of IMFs obtained is dependent on the original signal.

The EMD procedure serves to generate IMFs that are amenable to the Hilbert transform. In particular, the manner in which the EMD is performed guarantees that each IMF will only possess a single harmonic at any instant in time. Currently, the EMD procedure is ad hoc in the sense that there is no rigorous mathematical theory behind it. Recent attempts are being made to formalize EMD, most notably the work of those who explored the properties of B-splines and their use in the EMD process. Despite the lack of a firm theoretical foundation, several mathematical properties of the IMFs are well understood [20]. In particular, it is clear from Eq. 1 that the IMFs, along with the residual, form a complete basis for the original signal $x(t)$. In addition, Huang et al. [8] demonstrated that the IMFs are nearly orthogonal with an orthogonality index (OI_{mn} defined in Eq. 2) for the IMFs. This definition seems to be global but actually only applies locally. Adjacent IMFs could have data with the same frequency but at different times.

$$OI_{mn} = \sum_{t=0}^{t=T} \sum_{j=1}^{m} \sum_{k(\neq j)=1}^{n} \frac{c_j(t)c_k(t)}{x(t)^2} \tag{2}$$

The EMD does not yield a unique basis for the original signal since there are countless sets of suitable IMFs that can be generated from a given signal. However, the various IMF sets from the different sifting criteria are all equally valid representations of the data provided their orthogonality indices are sufficiently small [8, 10]. The IMFs depend on the stoppage criterion, maximum number of siftings, intermittance criteria, the end point boundary conditions, and use of curvature- or extrema-based sifting [8, 9, 10]. The uniqueness problem can only be meaningful if all these parameters are fixed a priori. The problem is how to optimize the sifting procedure to produce the "best" IMF set. These questions are difficult to answer theoretically. In Huang et. al. [10], a confidence limit is defined for the first time without invoking the ergodic assumption. This provides a stable range of stopping criteria for the EMD-sifting operation, thereby making the HHT method more definitive. Discussion later points out that the EMD sifting process also acts in such a manner as to obtain IMFs that correspond to approximate bandpass filtering of the original signal.

Once the EMD procedure has been used to generate a set of IMFs, the Hilbert transform can be applied to each individual IMF. In this manner, an instantaneous frequency and amplitude is computed for each function. A common method for displaying the Hilbert spectrum is to generate a two-dimensional plot with time and frequency axes. The amplitude is then plotted as a color spectrogram in the time-frequency plane. By plotting the Hilbert spectra of all the IMFs together one obtains complete time-frequency information about the original signal.

To demonstrate the importance of the EMD in obtaining meaningful Hilbert spectra for general signals, consider the following signals.

$$\begin{aligned} x_1(t) &= \sin(2\pi t) + \sin(8\pi t) + \sin(32\pi t) \\ x_2(t) &= \sin(4\pi t) + t \end{aligned}$$

The signal x_1 is a combination of harmonics with frequencies of $\{1, 4, 16\}$ Hz while the signal x_2 is composed of a ramp signal and a 2-Hz sine wave. First, consider the Hilbert spectra obtained by directly applying the Hilbert transform to each signal. Figure 1 displays the resulting Hilbert spectra for both signals. The Hilbert spectrum of x_1 yields a fluctuating frequency with most of the energy concentrated at 7 Hz. This corresponds to the average of the three frequencies present in x_1 (each of which has the same amplitude) and gives no useful information about the original signal. This averaging is due to the fact that the Hilbert transform computes a single instantaneous frequency for the signal. The Hilbert spectrum of x_2 illustrates the effect of a nonzero mean. In this case, the estimated frequency is distorted and the 2-Hz harmonic is not identified at all.

Figure 2 displays the signal x_1 and its decomposition into four IMFs (imf1=c_1, imf2=c_2, etc.) and a residual. Clearly, each IMF has captured a different frequency component of the original signal. The fourth IMF is extremely small and results from boundary effects in the EMD process. The Hilbert spectra of the individual IMFs are plotted together in Fig. 2. Now, an effective Hilbert spectrum, or Hilbert-Huang spectrum, of x_1 has been obtained, with all three frequency components clearly identified. Similarly, Fig. 3 depicts two IMFs and a residual generated from the signal x_2. The 2-Hz frequency component has been sifted into the first IMF and the ramp component has been identified as the second IMF. The mean of the signal is 2, which has been separated out as the residual. The Hilbert spectrum clearly shows the 2-Hz component and estimates a low frequency for the ramp component. This occurs because the ramp is treated as part of a low frequency wave. The IMFs and Hilbert spectra in Figs. 2 and 3 illustrate that there are some minor boundary effects associated with the EMD process. Most importantly, these examples demonstrate that EMD makes it possible to apply the Hilbert transform to signals that otherwise do not admit well-behaved Hilbert transforms.

Finally, two more examples [21] illustrate automatic and adaptive (signal-dependent) time-variant filtering of general mixtures of signals. A signal composed of three components which significantly overlap in time and frequency is successfully decomposed in Fig. 4 for the sum of two sinusoidal frequency modulations and one Gaussian wave packet. Another example, accenting the nonharmonic nature

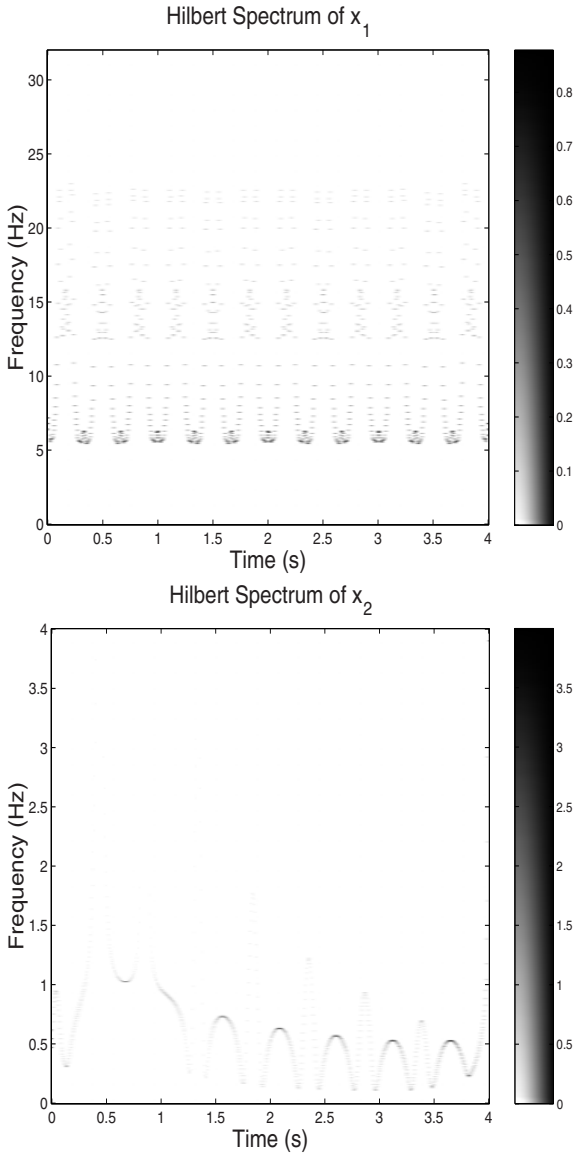

FIGURE 1. Time-frequency spectra from the Hilbert transforms of the signals x_1 and x_2.

of EMD, is given in Fig. 5. The analyzed signal (top) is the sum of three components, a sinusoid superimposed on two triangular waveforms with periods smaller and larger than the sinusoid. The decomposition performed by the EMD is given in

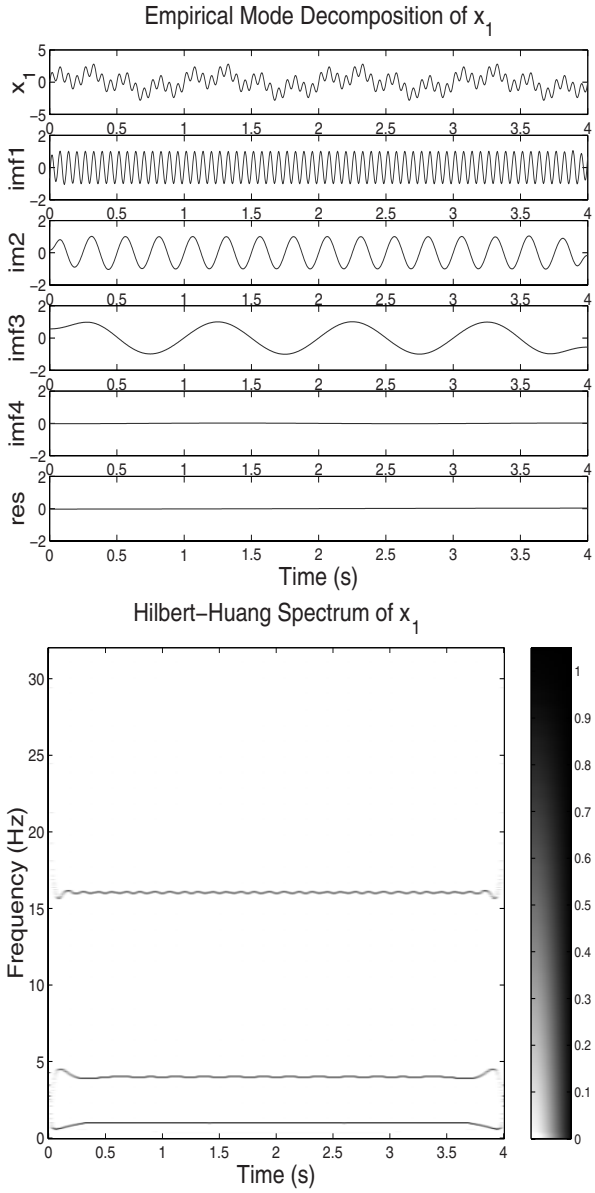

FIGURE 2. Empirical mode decomposition and the Hilbert-Huang spectrum of the signal x_1.

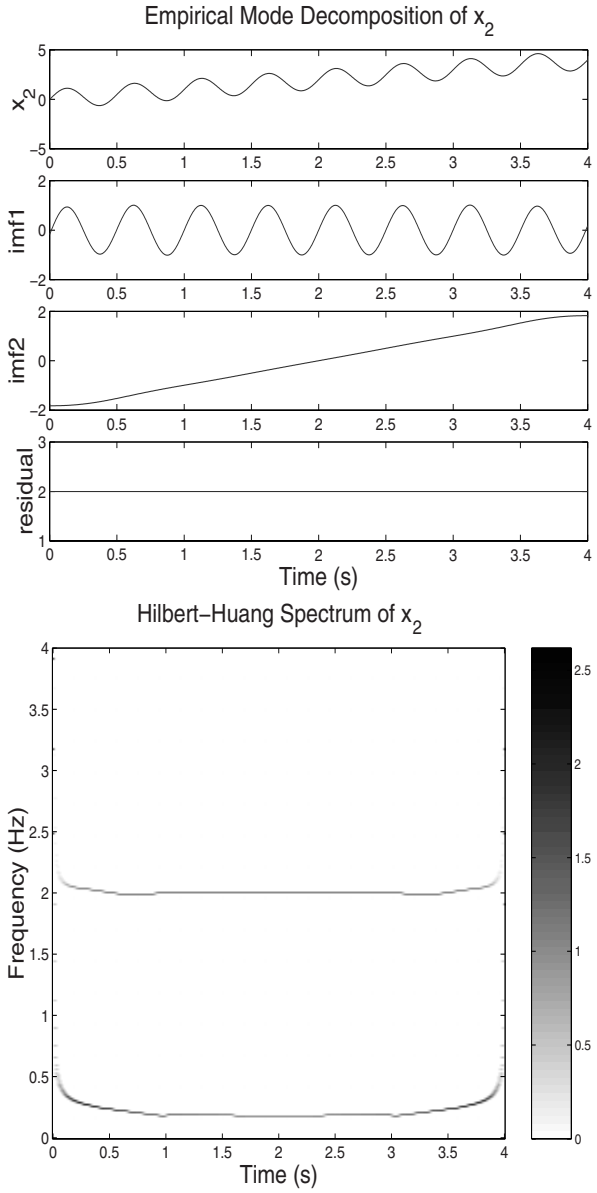

FIGURE 3. Empirical mode decomposition and the Hilbert-Huang spectrum of the signal x_2.

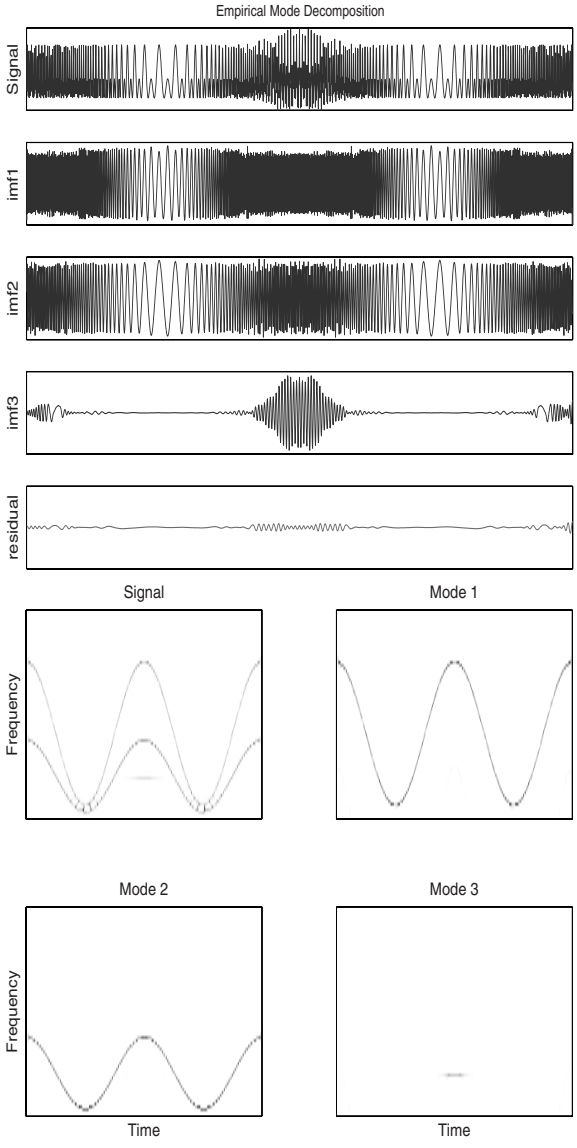

FIGURE 4. Empirical mode decomposition (EMD) and the Hilbert-Huang spectrum of the sum of two sinusoidal frequency modulations (FMs) and one Gaussian wave packet. Original signal (top), FM1, FM2, Gaussian wave packet, and residual.

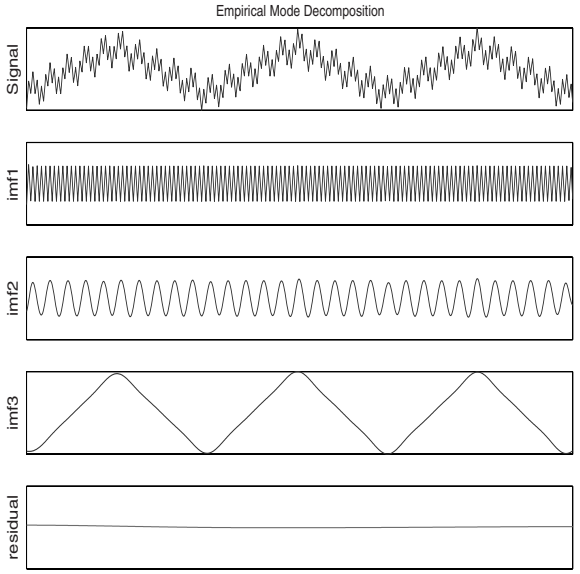

FIGURE 5. Empirical mode decomposition of the sum of one sinusoid with two triangular waveforms.
Original signal (top), high-frequency triangular, sinusoid, low-frequency triangular, and residual.

the three IMFs and the residual. In this case, both linear (sinusoid) and nonlinear (triangular) oscillations are effectively identified and separated. Harmonic analysis (Fourier, Morlet wavelets) would produce a less succinct and less descriptive decomposition.

2.1. Filtering Properties

The filtering properties of EMD have been studied in some detail [6, 7, 25]. The EMD process yields a data-dependent decomposition that focuses on local characteristics of the signal. In particular, EMD sifts out the highest-frequency component in the signal at any given time. Indeed, EMD has surprisingly been shown to behave as a dyadic bandpass filter when decomposing Gaussian white noise, much like a multiresolution wavelet decomposition. However, the EMD method as an equivalent dyadic filter bank is only in the sense of its global behavior over the entire time extent. In representing the time-frequency distribution, the Hilbert spectrum of each IMF is actually localized at any time. This is different from predetermined filtering such as with Morlet wavelet filtering.

2.2. Analytical Interpretation

The EMD is faced with the fundamental difficulty of not admitting an analytical definition, but of rather being defined by the algorithm itself, thus making

the analysis of its performance and limitations difficult. The need for rigorous mathematical foundation is imperative. This fundamental problem of the empirical mode decomposition has to be resolved since only with the intrinsic mode function can nonlinear distorted waveforms be resolved from nonlinear processes. There have been attempts to circumvent the mathematical difficulties in the EMD with some success by casting the IMFs in terms of B-splines [3], and applying them towards mechanical system fault-detection [15]. System identification of the IMFs as a multi-component system is suggestive in the light of multiresolution system identification procedures such as multiresolution singular value decompositions, Kalman filters, and subspace algorithms.

More significantly, characterization of IMFs as solutions to certain self-adjoint ordinary differential equations is demonstrated [22, 23]. Construction of envelopes which do not rely on the Hilbert transform is used directly to compute the coefficients of the differential equations. These equations are natural models for linear vibrational problems and provide further insight into both the EMD procedure and utilizing its IMF components to identify systems of differential equations naturally associated with the components. One of the uses of the EMD procedure is to study solutions to differential equations, and vibration analysis was a major motivation in the development of the Sturm-Liouville theory.

3. Hilbert Transform and Instantaneous Frequency

The Hilbert transform of a time-domain function or signal x is defined in Eq. 3,

$$y(t) = \mathrm{H}\{x(t)\} = \frac{1}{\pi}\ \mathrm{PV} \int_{-\infty}^{\infty} \frac{x(\tau)}{t-\tau} d\tau \tag{3}$$

where PV denotes the Cauchy principal value, needed because the integrand is singular at $\tau = t$. The Hilbert transform can be viewed as the convolution of the original signal with $1/t$, emphasizing temporal locality of $x(t)$. Note that, unlike Fourier analysis, the Hilbert transform of a time-domain signal is another time-domain signal. The Hilbert transform is sometimes applied to frequency-domain signals using a similar expression as Eq. 3, but this paper will focus on the time-domain case. In practice, the Hilbert transform is usually calculated using the Fourier transform. Therefore, the fast Fourier transform algorithm can be employed for the efficient calculation of the Hilbert transform.

A signal, x, and its Hilbert transform, y, can be used to define a complex analytical signal as in Eq. 4.

$$z(t) \quad = a(t)\mathrm{e}^{i\theta(t)} \quad = x(t) + iy(t) \tag{4}$$

Therefore, the Hilbert transform pair $\{x(t), y(t)\}$ can be expressed as a harmonic function with time-varying amplitude $a(t)$ and time-varying phase angle $\theta(t)$.

$$\begin{aligned} a(t) &= \sqrt{x(t)^2 + y(t)^2} \\ \theta(t) &= \tan^{-1}\left(\frac{y(t)}{x(t)}\right) \end{aligned}$$

Given the time-dependent phase angle, the instantaneous frequency of the signal can be defined as [5]

$$\omega(t) = \frac{d\theta(t)}{dt}.$$

In the context of Eq. 3 with instantaneous frequency, the Hilbert transform of an IMF can be interpreted as giving the best fit with a sinusoidal function to the data weighted by $1/t$. Instantaneous frequency can be computed using the derivative definition or centralized finite difference. [5] In general, there are an infinite number of ways to express a signal as in Eq. 4, so there can also be an infinite number of instantaneous frequencies. The Hilbert-transform pair was proposed to uniquely define the amplitude and phase by building the complex analytic signal from the given signal with the original signal, $x(t)$, as the real part and the orthogonal transformed signal, $y(t)$, the imaginary part, out of phase with $x(t)$ by $\frac{\pi}{2}$. Now given the set of Hilbert-transformed IMFs and associated instantaneous frequencies $\omega_j(t)$ for each IMF component, the Hilbert spectrum, $H(\omega, t)$, is defined as the time-frequency distribution of the IMF amplitudes.

$$H(\omega_j, t_i) = a_j(t_i), \forall\, \omega_j(t_i) \quad \Longleftrightarrow \quad x(t) = \sum_{j=1}^{n} a_j(t) \mathrm{e}^{i \int \omega_j(t) dt} \tag{5}$$

Note that Fourier analysis yields the decomposition

$$x(t) = \sum_{j=0}^{\infty} a_j e^{i\omega_j t}$$

which is similar to the form of the Hilbert transform in Eq. 5. A key difference, however, is that the Fourier decomposition is in terms of harmonics with constant amplitudes and frequencies. In contrast, the Hilbert transform yields instantaneous amplitudes and frequencies. Therefore, in principle, the Hilbert transform is an ideal tool for the time-frequency analysis of a general class of signals, including nonstationary signals.

Another important distinction between Fourier analysis and the Hilbert transform is that the Fourier decomposition is in terms of multiple harmonics of constant amplitude and frequency, thereby producing artificial harmonics to maintain energy conservation for nonstationary and nonlinear data. In contrast, the Hilbert transform of a signal yields an expression in terms of a single harmonic with a time-varying frequency and amplitude. For this reason, the Hilbert transform is only suitable for the analysis of mono-component signals, or signals that are composed of a single frequency component at any instant in time. This is a considerable limitation as it implies that the Hilbert transform cannot be directly applied to signals that are composed of multiple harmonics. As was shown, the Hilbert transform fails to identify the individual frequencies and instead computes a single instantaneous frequency that corresponds to a weighted average of the component frequencies. The resulting instantaneous frequency is both physically invalid and erroneous [4] since a multi-component signal has more than one instantaneous frequency. An additional limitation of the Hilbert transform is that

it yields extremely distorted estimates of the instantaneous frequencies of signals with nonzero mean and signals that have more local extrema than zero crossings.

The EMD responds to the dilemma surrounding the applicability of instantaneous frequency. It decomposes a multi-component signal into its associated mono-components while not obscuring or obliterating the physical essentials of the signal and allows the traditional definition of instantaneous frequency to be complete by being applicable to signals of both mono- and multi-component. To follow the true frequency evolution within a multi-component signal, it is necessary to break down the components into individual and physically meaningful intrinsic parts. The adaptive and nonarbitrary decomposition using EMD produces an orthogonal set of intrinsic components each retaining the true physical characteristics of the original signal. The mono-components or intrinsic modes satisfy the conditions for a well-defined notion of instantaneous frequency. These conditions include symmetry, no dependence on predefined time scales, revelation of the nature of simultaneous amplitude and phase variation, and near-orthogonality.

Finally, since instantaneous frequency displays frequency variation with time, changes of dynamic states indicative of nonlinearity can be identified. For example, if the instantaneous frequency of a new mode is about half of the frequency of the old mode in a bifurcation, period doubling occurs. If the instantaneous frequency of the new mode is disproportionate with the old mode, quasi-periodic bifurcation occurs. Similarly, intermittence and chaotic motion can be determined. A dynamic state can be diagnosed simultaneously by observing the changes in time of the instantaneous frequency components and their corresponding energy. In summary, the concept of mode defined in relation to instantaneous frequency as a periodic-modal structure in the instantaneous time-frequency plane is found to be more appropriate than artificial sinusoidal harmonics in characterizing nonlinear responses [26]. Instantaneous frequency is a quantity critical for understanding nonstationary and nonlinear processes.

4. Local On-Line Decompositions

In the original EMD formulation, sifting iterations are applied to the predefined full length signal as long as there exists a locality at which the mean of the upper and lower envelopes is not considered sufficiently small enough. Excessive iterations on the entire signal to achieve a better local approximation contaminates other parts of the signal by overcompressing the amplitude and overdecomposing it by spreading out its components over adjacent intrinsic modes; i.e., overiteration leads to overdecomposition. The various stoppage criteria (to fulfill that the number of extrema and the number of zero crossings must differ at most by one, and that the mean between the upper and lower envelopes must be close to zero) are attempts to avoid the rigor of the symmetry of the envelopes without a mathematically rigorous definition for an adaptive basis. The hierarchical and nonlinear nature of the EMD algorithm will not provide that the EMD of segmented signals will be the segmentation of individual EMDs. Therefore, a variation referred to as local

EMD [21] introduces an intermediate step in the sifting process. Localities at which the error remains large are identified and isolated, and extra iterations are applied only to them. This is achieved by introducing a weighting function such that maximum weighting is on those connected segments above a threshold amplitude, with a soft decay to zero outside those supports, much like soft-thresholding is done in wavelet denoising.

Another option is based on the idea that sifting relies on interpolations between extrema, and thus only requires a finite number of them (five minima and five maxima in the case of the recommended cubic splines [3, 8]) for local interpolation. Extraction of a mode could therefore be moving blockwise instead of globally over the entire time span. This led to the development of the on-line EMD [21]. A prerequisite for the sliding window extraction of a mode is to apply the same number of sifting steps to all blocks in order to prevent possible discontinuities. Since this would require the knowledge of the entire signal, the number of sifting operations is proposed to be fixed a priori to a number less than 10 for effective application of the on-line version of the EMD algorithm operating in coordination with the local EMD described above. The leading edge of the window progresses when new data become available, whereas the trailing edge progresses by blocks when the stopping criterion is met on a block. Therefore, an IMF and corresponding residual are computed sequentially, then again applied to this residual, thus extracting the next mode with some delay.

An aileron command multisine input used on the F/A-18 AAW for aeroservoelastic response and flutter clearance is shown in Fig. 6 (top plots) using the standard EMD (left) and local/on-line version (right). The bandpass nature of IMFs [6, 7, 25] is reflected in the three standard IMF mean frequencies, $\{23.9, 16.3, 7.7\}$ Hz for each of IMFs $\{\#1, \#2, \#3\}$, respectively, and on-line corresponding IMF mean frequencies $\{23.6, 13.0, 7.2\}$ Hz. Immediately noticeable is the more efficient extraction of the signal components by the local/on-line algorithm, most evident by the second and third IMFs (imf2 and imf3) being more sparse than the corresponding standard IMFs. Besides the obvious advantage of an on-line algorithm for decomposing data, it has been found to clearly surpass the standard global algorithm in terms of computational burden, especially with long original data records. An added bonus is that it generally has better orthogonality properties among the IMFs, witnessed by an order of magnitude improvement in the orthogonality index defined in Eq. 2.

5. Local Analytic Signal Correlation

Since the IMFs allow permissible, meaningful, physically sensible, and unique interpretations of instantaneous frequency of general signals of interest, they fit into the class of asymptotic signals such that the time variation of the IMF amplitude and frequency may directly be recovered from the time variation of the amplitude and of the phase derivative of the associated analytic signal. An IMF after performing the Hilbert transform can be written as in Eq. 4. These complex components

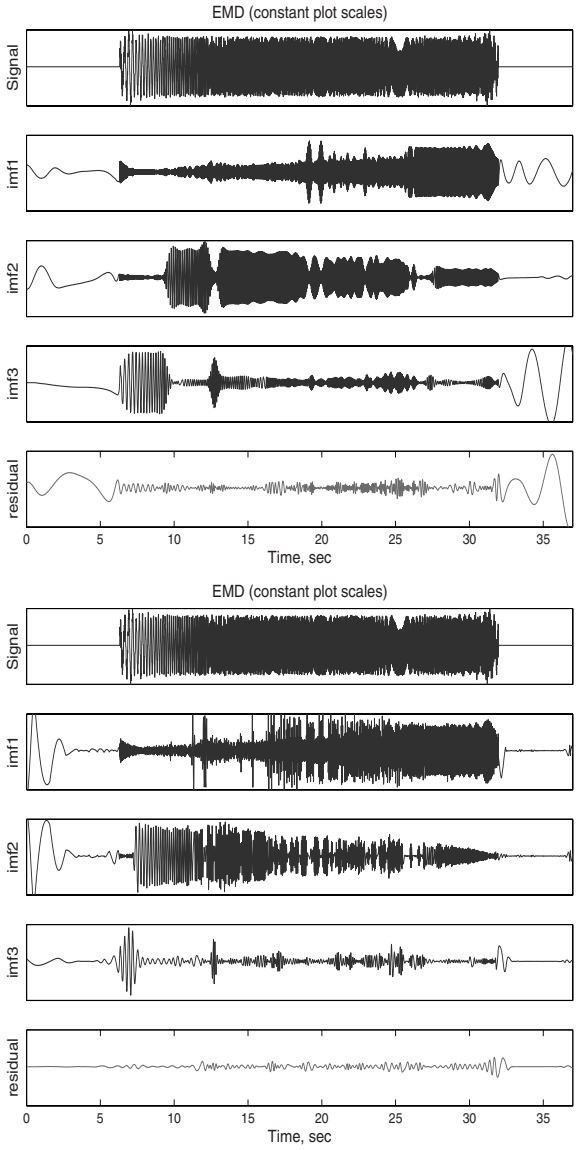

FIGURE 6. Standard (top) and local/on-line (bottom) empirical mode decomposition of an F/A-18 AAW multisine aileron command input, with original signal at top and residual at bottom.

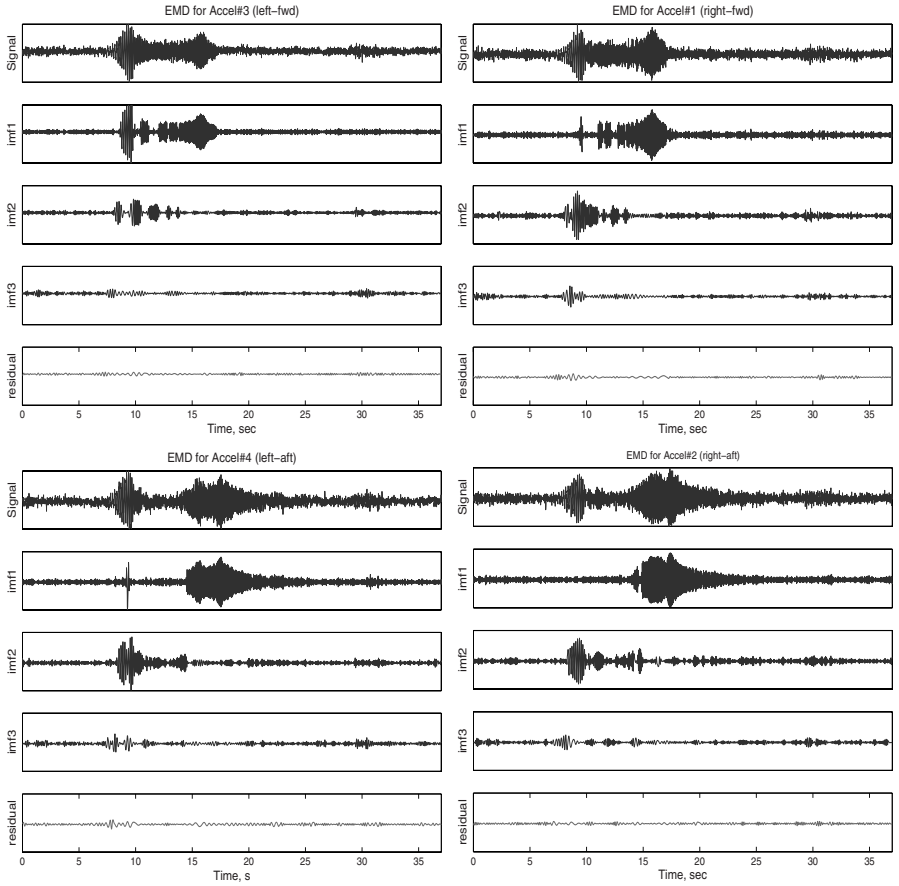

FIGURE 7. EMDs (constant vertical plot scales) of F/A-18-AAW aircraft left-fwd wingtip accel (top-left, Accel#3), right-fwd wingtip accel (top-right, Accel#1), left-aft wingtip accel (bottom-left, Accel#4), and right-aft wingtip accel (bottom-right, Accel#2), responses from the multisine symmetric aileron command shown in Fig. 6 (original signal at top and residual at bottom in each set).

are now used for analysis of analytic data correlations [1, 2] between input-output and amongst spatially distributed sensor outputs. Note that these analyses are all local in nature since there are no assumptions of stationarity, and differ from classical double-time expressions [1] by being instantaneous.

5.1. Local Correlation Coefficient

Correlations are made between transformed IMFs of various signals given the associated complex analytic signals

$$\begin{aligned} Z_x(t) = &\quad A_x(t)e^{i\phi_x(t)} &&= x(t) + ix_H(t) \\ Z_y(t) = &\quad A_y(t)e^{i\phi_y(t)} &&= y(t) + iy_H(t) \end{aligned}$$

by considering the *cross-analytic* signal defined in Eq. 6 by

$$\begin{aligned} Z_{xy}(t) &= Z_x^*(t)Z_y(t) = A_x(t)A_y(t)e^{i\phi_{xy}(t)} \\ &= A_x(t)A_y(t)e^{i[(\omega_y-\omega_x)t+(\phi_{0y}-\phi_{0x})]} \end{aligned} \tag{6}$$

which is not necessarily analytic but can be used to characterize the time variation of the phase difference between components *at similar frequencies* extracted from two simultaneously acquired signals. This Hilbert demodulation technique is only applicable for analytic components, in this case the transformed IMFs of the original signals. If the two components are mainly in-phase and a change occurs in the cross-analytic signal, the instantaneous frequencies of the two components may be drifting apart and this produces an instantaneous contribution to the phase difference from Eq. 6. A measure of the local correlation between components, in terms of simultaneous changes in instantaneous amplitude or frequency (phase) between analytic signals, is the Hilbert Local Correlation Coeffcient, $HLCC$.

$$HLCC(t) = \quad \frac{Re[Z_{xy}]}{|Z_{xy}|} \quad = \cos[\phi_{xy}(t)]$$

As a simple illustration of the utility of the $HLCC$, Fig. 7 shows the EMDs of wingtip accelerometer responses (accels) due to a symmetric aileron input, with the top plot in each set being the original signal, followed by EMDs 1-3 and the residual. The top two sets represent the forward (fwd) wingtip accels, and corresponding IMFs seem not to compare quite as well as the bottom two IMF sets of aft wingtip accels for the same input. The bottom IMF sets seem much more correlated with each other than the top two sets.

Table 1 lists the means, medians, and standard deviations of the $HLCC$ data over the time span of the maneuver. Note that $HLCC_{xy}^{mn}$ indicates correlation coefficients between Accel#m and Accel#n, using cross-analytic IMF function Z_{xy} correlating Accel#m's IMFx to Accel#n's IMFy. Results from the table indicate strongest Hilbert local correlation coefficients for Z_{xy} when $x = y$, as expected since this is a correlation between similar bandpass characteristics of IMFs from different responses due to the same input. For comparison, the standard statistical signal correlation coefficient between Accel#1 and #3 is $C^{13} = 0.8633$, and between Accel#2 and #4 is $C^{24} = 0.8332$ (correlating fwd-to-fwd accels and aft-to-aft accels, respectively, wingtip-to-wingtip). This is consistent with the top original signal plots in Fig. 7 in that the forward wingtip accels (top two, fwd) seem to correlate reasonably well with each other, as also between the bottom two (aft), but not top compared with the bottom. Evident in Table 1 is the common standard deviations (STD in all the correlations, near $STD = 0.7$). In the $HLCC$ values good commonality is found between the mean and medians comparing $HLCC^{13}$

and $HLCC^{24}$ in that the trend is similar amongst the cross-analytic IMF functions Z_{xy} where x and y correspond to respective IMF numbers in different accel EMDs. This is surprising, since in Fig. 7 the correlation in corresponding IMFs seems much worse between the two fwd accels (top plot IMFs) than between the two aft accels (bottom plot IMFs).

TABLE 1. $HLCC$ results from F/A-18 AAW wingtip accelerations.

Z_{xy}	Mean $HLCC^{13}$	Median $HLCC^{13}$	STD^{13}
Z_{11}	0.3283	0.5968	0.6801
Z_{12}	0.0917	0.1782	0.7171
Z_{13}	0.0098	0.0252	0.7113
Z_{21}	0.0953	0.1870	0.7148
Z_{22}	0.1844	0.3500	0.7048
Z_{23}	0.1187	0.2364	0.7136
Z_{31}	-0.0071	-0.0175	0.7075
Z_{32}	0.0845	0.1753	0.7097
Z_{33}	0.2403	0.4425	0.6866
Z_{11}	Mean $HLCC^{24}$	Median $HLCC^{24}$	STD^{24}
Z_{12}	0.0502	0.1080	0.7142
Z_{13}	0.0005	-0.0106	0.7057
Z_{21}	0.0492	0.0896	0.7095
Z_{22}	0.2197	0.4012	0.7023
Z_{23}	0.0692	0.1319	0.7052
Z_{31}	0.0032	0.0062	0.7056
Z_{32}	0.0996	0.2025	0.7183
Z_{33}	0.1553	0.2877	0.7027

Figure 8 shows the $HLCC$ functions between Accel#1 and Accel#3 ($HLCC^{13}_{xy}$) at 5-20 s. Decomposing and representing correlations like this allows a true time-localized instantaneous measure revealing subtle properties in the data and inconspicuous relations to other data sets using analytic components.

5.2. Instantaneous Transfer Function

In addition to investigating correlations between sensors, an instantaneous system transfer function is introduced with instantaneous magnitude and the $HLCC$ as a phase parameter between input-output analytic signals. This is viable in terms of the HHT inducing analytic properties to the IMFs to yield localized system input-output properties. Instantaneous transfer function (ITF), its instantaneous magnitude (IM), and its instantaneous phase (IP) are defined.

$$ITF(t) = \frac{Z_{xy}(t)}{Z_{xx}(t)}; \quad IM(t) = |ITF(t)|; \quad IP(t) = \cos^{-1}[HLCC(t)] = \phi_{xy}(t)$$

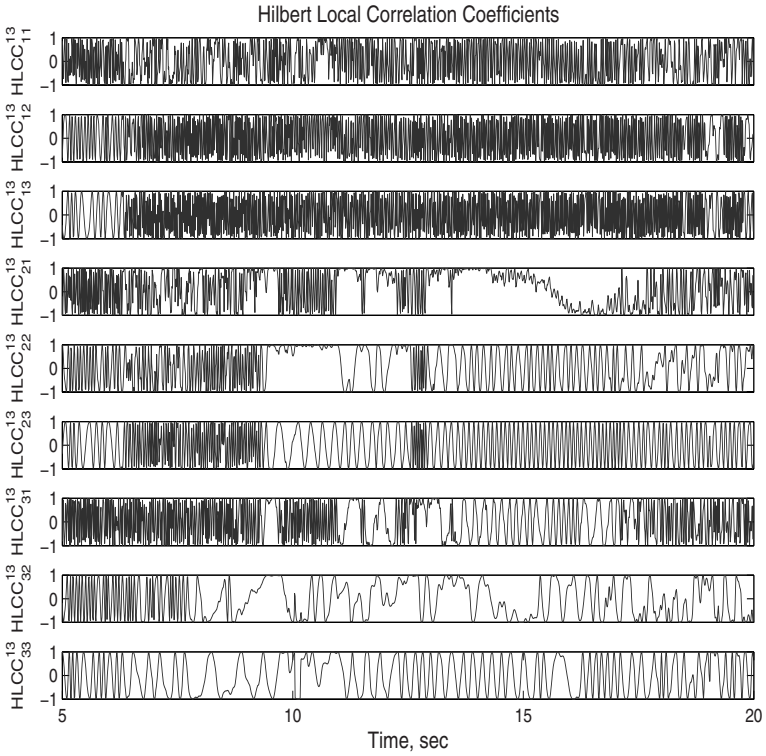

FIGURE 8. $HLCC^{13}_{xy}$ functions between IMFs of Accel#1 (top right, Fig. 7) and Accel#3 (top left, Fig. 7).

In Fig. 9 the top set of plots represent instantaneous magnitude (IM^{a1}_{xy}) and the bottom plots represent instantaneous phase (IP^{a1}_{xy}) from the instantaneous transfer function (ITF^{a1}_{xy}) of the aileron command input (Fig. 6) to Accel#1 (top right, Fig. 7) analytic IMFs (Hilbert-transformed i.e., $\{Z_x, Z_y\}$). Note that ITF^{mn}_{xy} indicates transfer functions between Input#m and Accel#n, using cross-analytic IMF function Z_{xy} correlating Input#m's IMFx to Accel#n's IMFy. In this sense, by interpreting the input-output Hilbert-transformed pairs of IMFs as a multicomponent system of input-output signals, local stability measures are deemed to be feasible by tracking gain, phase, and instantaneous frequencies between each IMF pair. How these local IMF properties correspond to global system properties, given the analytic transformed IMFs, and aeroelastic and aeroservoelatic applications in stability and health monitoring, are currently being researched.

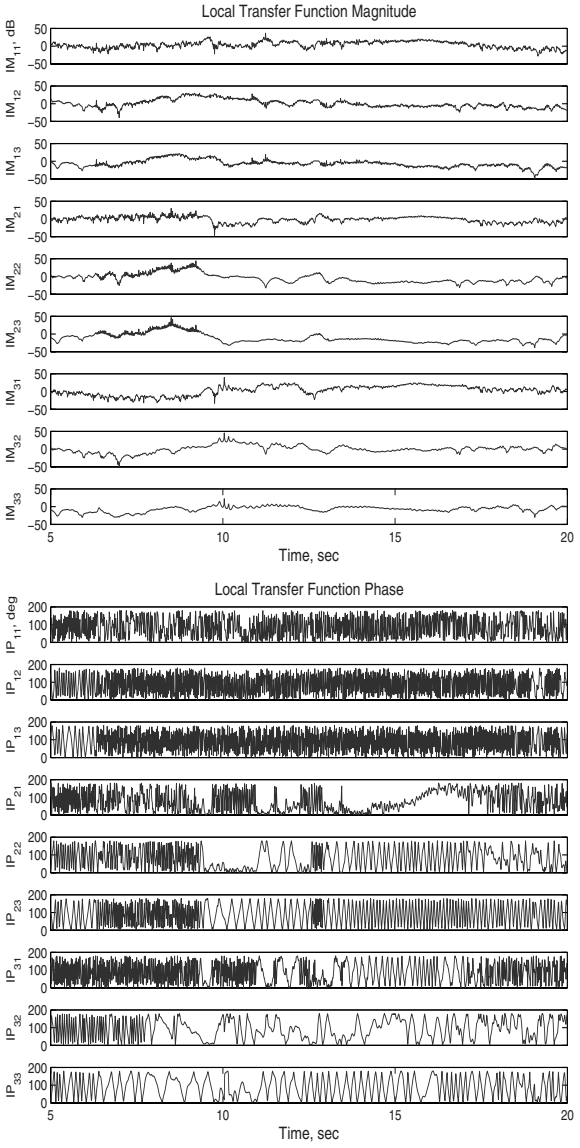

FIGURE 9. Instantaneous log-magnitude (IM_{xy}^{a1}, top plot set) and phase (IP_{xy}^{a1}, bottom plot set) of IMF transfer functions from F/A-18 AAW aileron input (Fig. 6) to Accel#1 (top right, Fig. 7).

5.3. Empirigrams and Empirical Local Correlation Coefficient

Given two EMDs from different signals, select a common number of IMFs to use for correlation (as three were selected in earlier examples for input and outputs). This is generally not difficult, especially for aeroelasticity data, since the higher-numbered IMFs approach a residual characteristic quickly. From the transformed IMFs, $\{Z_x(t), Z_y(t)\}$, define the corresponding set of two-dimensional Hilbert *empirigrams*, $\{H_x(\eta_x, t), H_y(\eta_y, t)\}$, where for each common $\eta = \eta_x = \eta_y$, the IMF number from the input EMD corresponds with the output EMD. Define in Eq. 7 the Hilbert *cross-empirigram*

$$H_{xy}(\eta, t) = H_x^*(\eta, t) H_y(\eta, t) \tag{7}$$

which correlates the respective IMFs from the two Hilbert empirigrams. Empirigrams relate to time-scale wavelet scalograms [5], which relate to time-frequency maps, since scales relate to frequencies in standard wavelet decompositions. Because of the bandpass nature of IMFs discussed previously, a similar construction emanates with the HHT. As with wavelet scalograms, the real part of the cross-empirigram (co-empirigram) gives the instantaneous contribution of each IMF to the correlation between two signals. An Empirical Local Correlation Coefficient, $ELCC(\eta, t)$, is then defined as

$$ELCC(\eta, t) = \frac{Re[H_{xy}(\eta,t)]}{|H_{xy}(\eta,t)|} = \frac{Re[H_{xy}(\eta, t)]}{|H_x(\eta, t)||H_y(\eta, t)|}$$

where $ELCC(\eta, t)$ (between ± 1, as the $HLCC$) gives the instantaneous contribution between corresponding IMFs from the two signals to the correlation coefficient. Figure 10 shows an imaged decomposition plot of the $ELCC$ between the input signal from Fig. 6 to Accel#1 in Fig. 7, but includes all nine IMFs from the EMDs of the input and output. The first row represents the contributions of the first input IMF to first output IMF, etc., up to the ninth IMF. In each IMF row there is much oscillation (higher frequency in the first and lower frequency to the ninth) of contributions from corresponding IMFs to the correlation. There are generally stronger correlations over longer time spans in the higher-numbered IMFs (lower frequencies), but the lower-numbered IMF correlations are less obvious due to the higher frequency content. There is a tendency to cycle from high-to-low-to-high [strong(positive)-to-none-to-strong(negative)] correlation very rapidly. A more detailed depiction in the zoomed-in bottom plot, between 10-11 s, demonstrates a rich interplay between correlation of mid-to-lower IMFs (higher frequencies) over the shorter time period. Yet another view is presented in Fig. 11, where the contours are split up discretely in three dimensions showing the heavy emphasis in the higher frequencies because the contours are more congested in each of the IMF levels. These representations highlight the areas of commonality and incongruity between corresponding input-output IMFs.

From the Hilbert spectrum $H(\omega, t)$ the energy spectrum $H^2(\omega, t)$ gives instantaneous energy,

$$IE(t) = \int_\omega H^2(\omega, t) d\omega$$

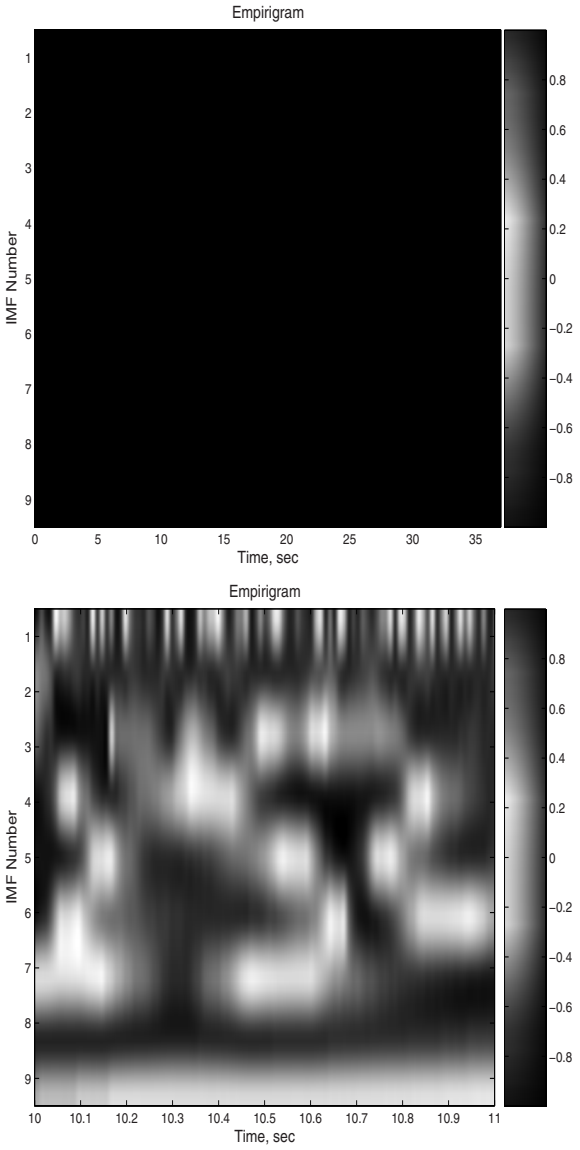

FIGURE 10. Empirical local correlation coefficient $ELCC$ plots using two different representations of the $ELCC$ between the input signal from Fig. 6 to Accel#1 in Fig. 7. Top plot is an intrinsic mode component-by-component depiction, starting from the first at the top to the ninth at the bottom, where individual intrinsic functions are clearly delineated. Bottom plot is zoomed-in portion between 10-11 s of the same $ELCC$.

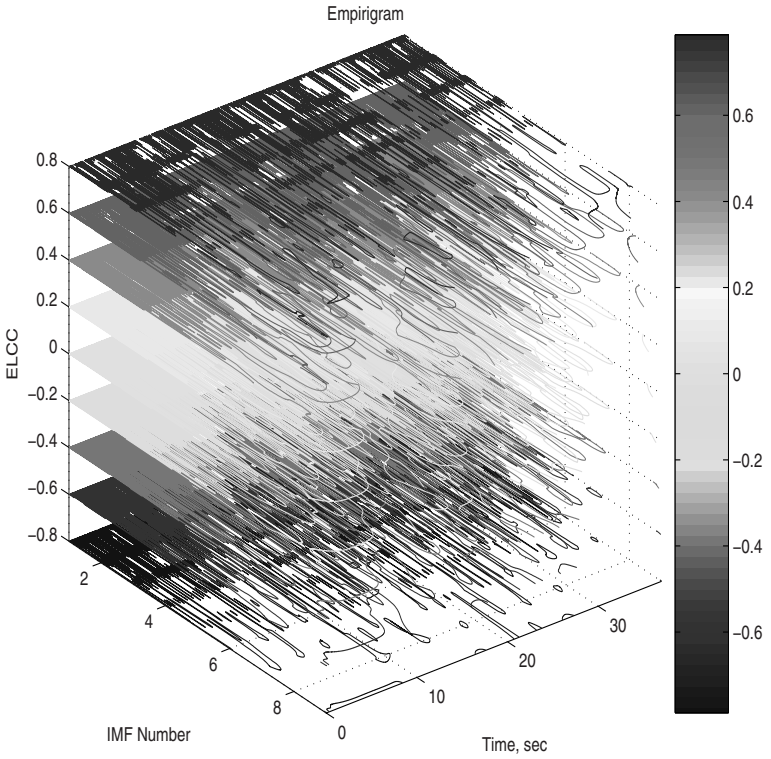

FIGURE 11. *ELCC* represented using a three-dimensional contour of the result in Fig. 10.

which is an indication of the energy fluctuations with time being weighted by the Hilbert spectrum localized energy over the entire set of IMFs. Corresponding to the signals in Fig. 7 are the instantaneous energy profiles of the output accelerometer responses in Fig. 12 (top set of four plots). The aft wingtip accels (bottom plots) are very similar (from the symmetric aileron input), indicating energy at $\{7-10, 13-20, 30\}$ s time locations. In this case, with the particular multisine input from Fig. 6 programmed over the $3-35$ Hz frequency range, these times correspond closely to the primary F/A-18 AAW modal frequencies in a corresponding frequency range, i.e., $\{6-9, 12-20, 30-35\}$ Hz, as will be shown with marginal Hilbert spectra. The forward accelerometer responses in the top plots are also very similar indicating modes near $\{6, 12-17, 25-32\}$ Hz. Instantaneous energy over a sensor suite is therefore a nonstationary indicator of time-varying energy distribution amongst the sensor array.

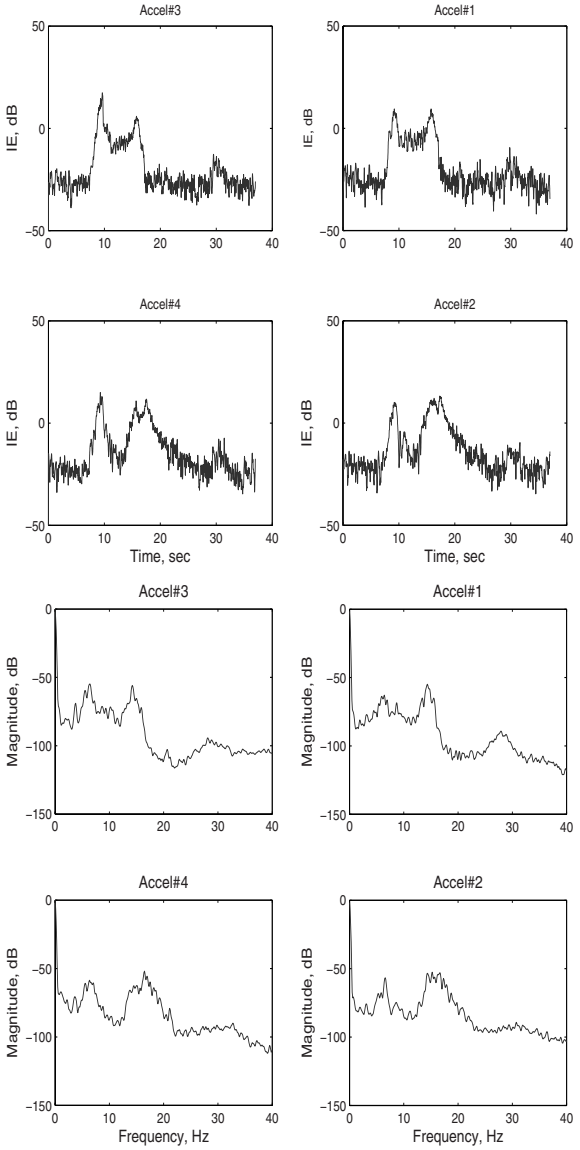

FIGURE 12. Instantaneous energy (top plot set) and marginal spectra (bottom plot set) of right-fwd wingtip accel (top right, Accel#1), right-aft wingtip accel (bottom right, Accel#2), left-fwd wingtip accel (top left, Accel#3), and left-aft wingtip accel (bottom left, Accel#4) responses, respectively in each set, from the multisine symmetric aileron command shown in Fig. 6.

6. Marginal Spectra

From the Hilbert spectrum $H(\omega, t)$, the marginal spectrum is also defined.

$$h(\omega) = \int_t H(\omega, t)dt$$

Corresponding to the signals in Fig. 7 are the marginal spectra of the output accelerometer responses in Fig. 12 (bottom set of four plots). The aft wingtip accels (bottom plots) are again similar showing modal response at $\{5-10, 12-20, 30-35\}$ Hz. The forward accelerometer responses in the top plots are also again very similar indicating modes near $\{6, 12-17, 25-32\}$ Hz.

The marginal spectrum measures total amplitude (or energy) contributions from each frequency value over the entire data record in a probabilistic sense. Frequency in either $H(\omega, t)$ or $h(\omega)$ is very different from Fourier spectral analysis. In the Fourier analysis the existence of energy at a frequency implies a wave component persisting through the data. Energy at the marginal Hilbert frequency, however, implies a higher likelihood (expected value over time) for such a wave to have appeared locally. As stated earlier, the Hilbert transform of an IMF gives the best fit with a sinusoidal function to the data weighted by $1/t$, which makes it instantaneous. In fact, the Hilbert spectrum is a weighted nonnormalized joint amplitude-frequency-time distribution in which the weight assigned to each time-frequency cell is the local amplitude. Consequently, frequency in the marginal spectrum indicates only the likelihood that an oscillation with such a frequency exists. Exact occurrence of frequency content is given in the full Hilbert spectrum. The Fourier spectrum is meaningless for nonstationary data, and there is little similarity between Hilbert and Fourier from previous studies [8, 9] for nonstationary data. Also, marginal cross-spectra between signals does not make sense since the time-dependence (causality) is lost and the frequencies are time-ignorant, so an input-output correlation at a certain frequency is meaningless.

The time-frequency Fourier spectrum, a spectrogram, suffers from the same restrictions over time due to windowing distortions. There is a lower bound on the local time-frequency resolution uncertainty product of the spectrogram due to the windowing operation. *This limitation is an inherent property of the spectrogram and is not a property of the signal or a fundamental limit* [17]. For many other time-frequency distributions, the local uncertainty product is less than that of the Fourier spectrogram and can be arbitrarily small. These results are contrary to the common notion that the uncertainty principle limits local quantities. Similar considerations apply to window-based filter bank (wavelet) methods. This limitation is due to the window and not to any inherent property of the signal.

This is a key point for application and understanding of HHT analysis, that windowing is not a factor, so standard time-frequency resolution limitations based on the uncertainty principle do not apply. As seen in the on-line analysis, an adaptive sliding window method has good performance simply requiring adequate data in the window to initiate a sifting process for satisfying the two IMF properties for analyticity.

7. Wing Dynamics Analysis

Dynamics between different sensors from the same input will now be investigated. This information will be used to guide the analysis of a group of wing accelerometer responses from a single input in terms of input-output correlation contribution for the F/A-18 AAW aircraft [18] and Aerostructures Test Wing (ATW) [12].

7.1. F/A-18 Active Aeroelastic Wing (AAW) Aircraft

Collective F/A-18 AAW aileron position, used as the multisine input, was obtained as the average of four position transducer measurements from the right and left ailerons. Outputs are twelve wing structural accelerometers located at the left (six accels) and correponding right (six accels) outer wings, all sampled at 400 sps, as designated in Table 2.

Table 2. F/A-18 AAW wing accelerometer nomenclature.

3. L-wt-fwd 3. L-wingtip forward	1. R-wt-fwd 1. R-wingtip forward
7. L-wof-fwd 7. L-wing outer-fold forward	5. R-wof-fwd 5. R-wing outer-fold forward
11. L-wif-fwd 11. L-wing inner-fold forward	9. R-wif-fwd 9. R-wing inner-fold forward
4. L-wt-aft 4. L-wingtip aft	2. R-wt-aft 2. R-wingtip aft
8. L-wof-aft 8. L-wing outer-fold aft	6. R-wof-aft 6. R-wing outer-fold aft
12. L-wif-aft 12. L-wing inner-fold aft	10. R-wif-aft 10. R-wing inner-fold aft

EMDs were calculated for the input and all outputs, with mean frequencies calculated for all the output IMFs compared to the single input IMFs. Table 3 is a summary of the results. Included are the first six IMFs averaged amongst the accels, percentage differences of these compared to the input IMFs, and standard deviations of output sensor IMFs (numbered 1-12). The accels correspond very well amongst each other in IMF frequencies (as frequency decreases, from left to right). The comparison to the input frequency is excellent even though input and output EMDs are performed independently. Orthogonality of the IMFs in each case was also very good. This shows that for this type of data, where responses are all from a common input (whether it is known or not), IMFs can be used for sensor-to-sensor correlation and input-output analysis.

Now the concept of the using the essentially-orthogonal analytic IMFs from the inputs and outputs is pursued to establish a multi-loop connotation of input IMFs to output IMFs for correlation and even stability properties. The input IMFs are interpreted as an orthogonal decomposition of the input(s), and the same for output IMFs for output(s). This can be generalized to multi-input-multi-output

TABLE 3. IMF frequencies from F/A-18 AAW input collective aileron position and outer wing response data.

Signal	IMF1	IMF2	IMF3	IMF4	IMF5	IMF6
0. Input	116.62	59.61	29.34	16.75	9.05	4.90
1.	99.05	56.94	27.90	12.56	6.96	3.62
2.	123.85	71.36	35.15	16.83	9.35	5.02
3.	114.47	66.05	33.78	15.06	7.95	5.32
4.	127.56	78.71	41.73	21.06	11.92	6.58
5.	105.83	58.52	32.06	17.17	9.34	5.47
6.	96.31	54.96	29.24	14.91	8.64	4.63
7.	115.93	58.77	30.88	16.59	8.66	4.32
8.	102.99	52.76	27.14	15.35	8.65	4.83
9.	112.19	60.61	31.99	17.78	9.90	5.17
10.	115.39	64.07	36.09	19.05	10.29	5.72
11.	124.91	66.06	32.99	18.32	10.53	5.19
12.	129.41	66.05	34.02	17.97	9.66	4.92
Average Output IMF Frequencies						
Mag	114.0	62.9	32.8	16.9	9.3	5.1
Wrt Inp	2.3%	5.2%	10.4%	0.8%	2.9%	3.2%
Output IMF Frequency STDs						
Mag	11.2	7.3	4.0	2.2	1.3	0.7
Wrt Avg	9.8%	11.7%	12.1%	13.2%	13.9%	14.4%

(MIMO) signal analysis where in reality each signal is represented by its EMD. Recall from the transformed input-output IMFs, $\{Z_x(t), Z_y(t)\}$, the corresponding set of empirigrams $\{H_x(\eta_x, t), H_y(\eta_y, t)\}$ were defined in Eq. 7 for each set of $\eta = \eta_x = \eta_y$ common IMFs from the input and output EMDs. For the analysis described here it is not necessary to use an identical number, η, of IMFs from input and output (but this restriction is maintained here for simplicity). Then the Hilbert cross-empirigram $H_{xy}(\eta, t) = H_x^*(\eta, t)H_y(\eta, t)$ correlates the respective analytic IMFs from the two Hilbert empirigrams. Now define

$$\sigma_{xy}(\eta) \quad = \quad \sigma[H_x^*(\eta, t)H_y^T(\eta, t)]$$

where σ_{xy} represents the η-vector of singular values from the singular value decomposition (SVD) of the product of the empirigrams. The singular values represent relative contributions from the principal cross-correlation analytic IMFs as a result of correlation of all input analytic IMFs to all output analytic IMFs over the entire time span. Therefore, higher σ-valued cross-analytic IMFs have more input-output significance in terms of operator norm from input to output. The maximum singular value, $\bar{\sigma}_{xy} = \max_\eta(\sigma_{xy}(\eta))$, of this input-output operator corresponds to the structured singular value with a full-complex uncertainty block structure. In this context, for $M^{\eta \mathbf{x} \eta} = H_x^*(\eta, t)H_y^T(\eta, t)$, a complex matrix operator of input analytic IMFs to output analytic IMFs, $\mu_\Delta(M)$ is a measure of the smallest uncertainty

$\Delta = \mathbf{C}^{\eta \mathbf{x} \eta}$ (note that if $\eta_x \neq \eta_y$, then $\Delta = \mathbf{C}^{\eta_\mathbf{y} \mathbf{x} \eta_\mathbf{x}}$ is not square) that causes instability if interpreted as a constant matrix feedback loop [32],

$$\mu_{\{\Delta = \mathbf{C}^{\eta \times \eta}\}}(M) \quad = \quad \bar{\sigma}[H_x^*(\eta, t) H_y^T(\eta, t)]$$

and for scalar uncertainty structure $\Delta = \{\delta I_\eta : \delta \in \mathbf{C}\}$ representing diagonal structure between input-output IMFs,

$$\mu_\Delta(M) \quad = \quad \rho[H_x^*(\eta, t) H_y^T(\eta, t)]$$

where ρ is the spectral radius (largest magnitude eigenvalue). This is distinctly different from the full-block structure in that uncertainty is only between corresponding input-output analytic IMFs (similar dominant frequencies), while ignoring uncertainty across different analytic IMFs (of different dominant frequencies) between input and output. This is obviously less conservative but generally less realistic as well, especially for nonlinear effects which cross frequencies. Larger μ_Δ values in either case represent effects of uncertainty between input and output such that higher correlated IMFs relate to more sensitivity to uncertainty at those dominant IMF frequencies.

For MIMO signal analysis, it would be most appropriate to combine complex blocks (either full or scalar) for each input-output into a multi-block structure, where each complex sub-block corresponds to an input-output analytic IMF complex uncertainty structure. In computation this is often expanded in a block-diagonal context with repeated scalar and full blocks [32], where in this case each of these blocks would correspond to a single input-output analytic IMF uncertainty structure.

TABLE 4. Normalized μ_Δ results from F/A-18 AAW left and right wing acceleration data.

Full Block	3. L-wt-fwd 4. L-wt-aft	7. L-wof-fwd 8. L-wof-aft	11. L-wif-fwd 12. L-wif-aft	9. R-wif-fwd 10. R-wif-aft	5. R-wof-fwd 6. R-wof-aft	1. R-wt-fwd 2. R-wt-aft
Fwd-wing	0.29	0.29	0.73	1.00	0.62	0.80
Aft-wing	0.65	0.67	0.56	0.19	0.31	0.72
Scalar Block	**3. L-wt-fwd 4. L-wt-aft**	**7. L-wof-fwd 8. L-wof-aft**	**11. L-wif-fwd 12. L-wif-aft**	**9. R-wif-fwd 10. R-wif-aft**	**5. R-wof-fwd 6. R-wof-aft**	**1. R-wt-fwd 2. R-wt-aft**
Fwd-wing	0.11	0.13	0.19	1.00	0.47	0.49
Aft-wing	0.23	0.42	0.27	0.11	0.06	0.34

To compare input-to-output correlations from aileron position to wing accels for different uncertainty structures, structured singular values were computed for the full-block and scalar-block structures between the collective aileron position and F/A-18 AAW wing accelerometer responses, then normalized with respect to the largest of the group. Table 4 lists the results for both types of uncertainty structures. Accelerometer#9 has the highest correlation (=1.00) with the input aileron position in either case. Interestingly, comparison between left and right wing accels is poor even from a symmetric aileron input, thereby indicating asymmetry and/or nonlinearity. Lower μ_Δ values indicate a degree of robustness to uncertainty in a feedback stability sense, and as pointed out previously, scalar uncertainty is prevalently less conservative (as evidenced from absolute values before normalizing since

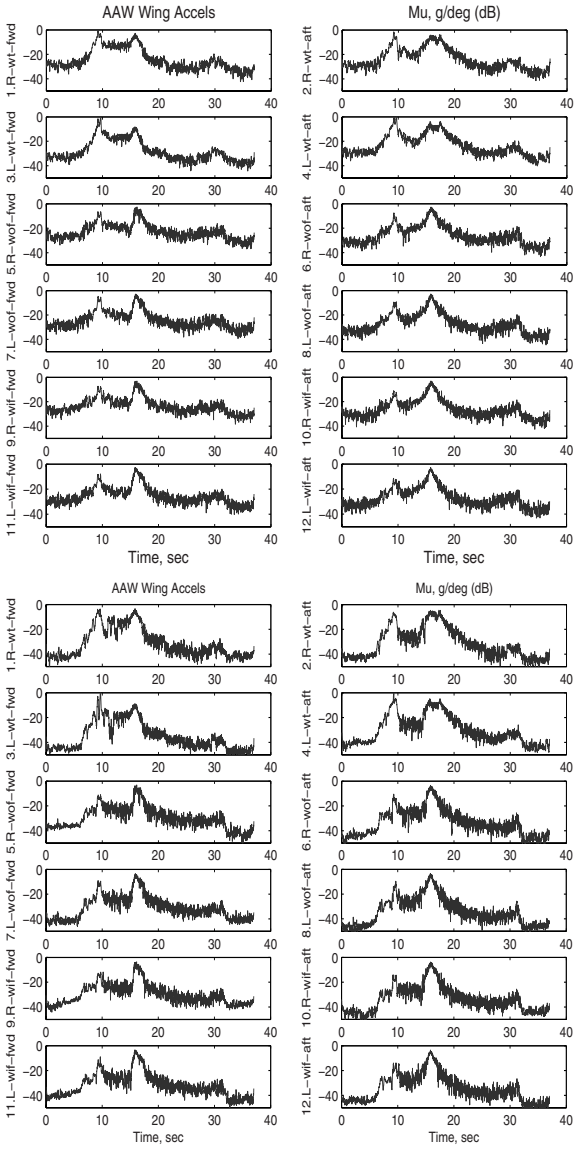

FIGURE 13. Time-varying $\mu_\Delta(M,t)$ (dB) for full-block (top plots) and scalar-block (bottom plots) uncertainty.

the normalization factor is almost equal between the uncertainty structures). If an a priori bound on gain levels (normalization) between input-output is defined such that $\| \Delta \|_\infty < 1$ is considered acceptable in some sense (stability, health diagnostic, safety margin), then μ_Δ has an absolute (scaled) interpretation such that $\mu_\Delta > 1$ indicates that an acceptable threshold has been exceeded, and this can be used as a health, stability, or safety monitor.

A time-dependent interpretation is also available by calculating $\mu_\Delta(M,t)$ at each time point.

$$\begin{aligned} \mu_\Delta(M,t) &= \rho[H_x^*(\eta,t_i)H_y^T(\eta,t_i)]\forall t_i \quad \text{(scalar-block)} \\ &= \bar{\sigma}[H_x^*(\eta,t_i)H_y^T(\eta,t_i)]\forall t_i \quad \text{(full-block)} \end{aligned}$$

In Fig. 13 are plots of $\mu_\Delta(M,t)$ for each input-to-output (aileron-to-accel) normalized analytic IMFs where it is evident that values close to one (0 dB) are near a unity operator norm limit. Again, this depends on the bound $\| \Delta \|_\infty < 1$ indicating an acceptable threshold, in this case maximum input-to-output gain normalized to one. Values close to one (0 dB) approach the acceptable limit. This uncertainty structure application has implications for model validation in the time domain [19].

7.2. Aerostructures Test Wing (ATW)

Another example which includes an actual instability is taken from Aerostructures Test Wing [12] (ATW) flight test data. The input is a sine sweep PZT voltage and outputs are three wingtip accelerometer responses. The EMDs of the PZT input and center wingtip accelerometer output near the flutter condition are displayed in Fig. 14. Flutter response EMDs of the center wingtip accelerometer and corresponding $\mu_\Delta(M,t)$ plots between input analytic IMFs and all three wingtip accelerometer output analytic IMFs are shown in Fig. 15. The input PZT was not activated during the flutter occurrence, so the input is essentially a small arbitrary oscillation about zero. It is evident that at the point of instability past 7.5 s, $\mu_\Delta(M,t)$ appropriately approaches a value of one (0 dB) since the input and output are normalized to unity, and assuming this limit corresponds to the limit of stability, and output response approaches its upper limit at flutter.

8. Parameter Estimation Using HHT

The Hilbert transform can used for estimating modal parameters such as natural frequencies and damping ratios. For a single-mode system, the damped natural frequency can be easily determined from the Hilbert transform of the impulse response function. In this case, the damped natural frequency ω_d is given by the slope of the instantaneous phase angle plotted as a function of time, and damping ratio ζ is estimated in a straightforward manner [24].

For a linear single-mode system characterized by a pair of complex conjugate eigenvalues, the eigenvalues are directly related to the modal parameters as $-\zeta\omega_n + \omega_d$ should be imaginary, where ω_n denotes the natural frequency. The impulse response function is

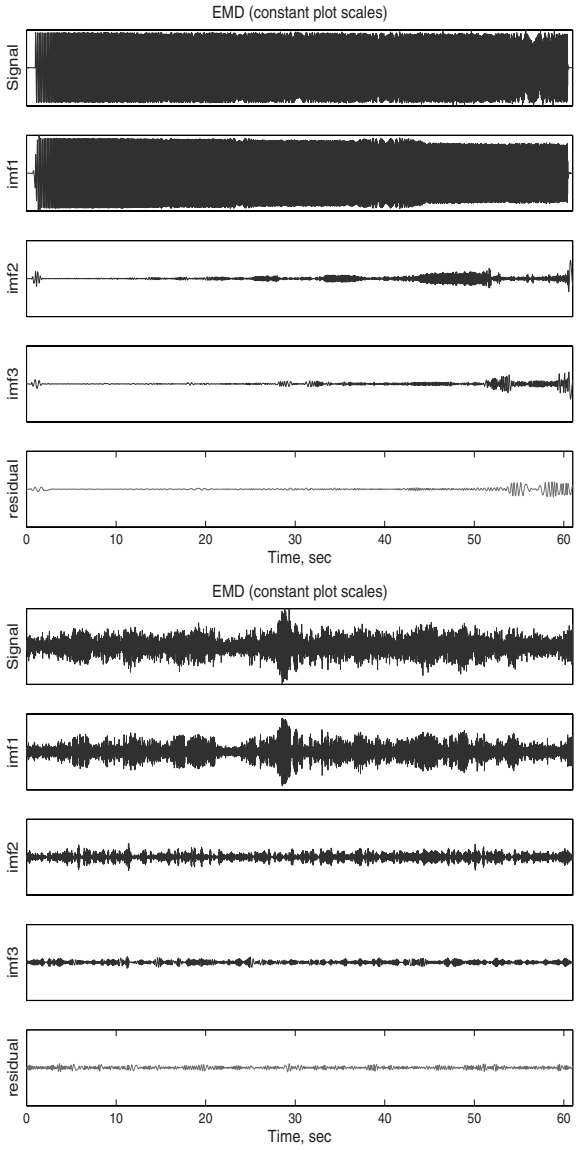

FIGURE 14. Empirical mode decomposition of the ATW input PZT (left plot) and center wingtip accelerometer (right plot) at Mach 0.82, 10,000 feet (3,048 m) altitude, just before flutter (original signal at top and residual at bottom in each set).

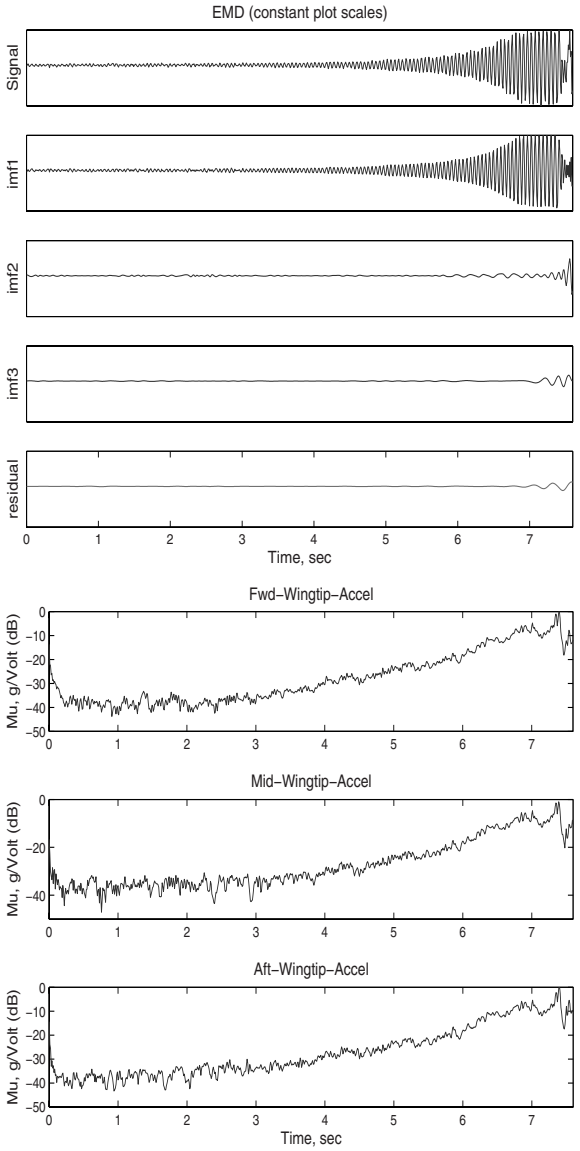

FIGURE 15. Empirical mode decomposition of the center wingtip accelerometer (left plot) near Mach 0.83, 10,000 feet (3,048 m) altitude, at flutter (original signal at top and residual at bottom), and time-varying $\mu_\Delta(M,t)$ for full-block uncertainty between input and output IMFs of the three wingtip accelerometer outputs (right plots).

$$h(t) = \frac{1}{m\omega_d} \mathrm{e}^{-\zeta\omega_n t} \sin(\omega_d t)$$

where m denotes the mass. Provided the damping ratio is small, the following relationships hold [24]

$$\begin{aligned} \mathrm{H}\left\{\mathrm{e}^{-\zeta\omega_n t}\sin(\omega_d t)\right\} &= \mathrm{e}^{-\zeta\omega_n t}\cos(\omega_d t) \\ \mathrm{H}\left\{\mathrm{e}^{-\zeta\omega_n t}\cos(\omega_d t)\right\} &= -\mathrm{e}^{-\zeta\omega_n t}\sin(\omega_d t) \end{aligned}$$

where again H denotes the Hilbert transform. Therefore, the Hilbert transform of the impulse response function can be written as

$$\mathrm{H}\{h(t)\} := \tilde{h}(t) = \frac{1}{m\omega_d} \mathrm{e}^{-\zeta\omega_n t}\cos(\omega_d t).$$

The impulse response function can then be viewed as the real part of the following analytic signal [24]

$$\begin{aligned} z(t) &= h(t) + \mathrm{i}\tilde{h}(t) \\ &= \frac{1}{m\omega_d} \mathrm{e}^{-\zeta\omega_n t}\sin(\omega_d t) + \mathrm{i}\frac{1}{m\omega_d} \mathrm{e}^{-\zeta\omega_n t}\cos(\omega_d t). \end{aligned}$$

The amplitude of this signal is given by

$$a(t) = \sqrt{h(t)^2 + \tilde{h}(t)^2} = \frac{1}{m\omega_d} \mathrm{e}^{-\zeta\omega_n t}$$

which represents the envelope of the impulse response. Taking the natural logarithm of the amplitude yields

$$\ln\left(a(t)\right) = -\zeta\omega_n t - \ln\left(m\omega_d\right).$$

The slope σ of the natural log of $a(t)$ plotted against time gives $\sigma = -\zeta\omega_n$. Given that ω_d can be obtained from the slope of the phase plotted against time, and using the definition of the damped natural frequency, there results ω_n,

$$\begin{aligned} \omega_d &= \sqrt{1-\zeta^2}\omega_n \\ \omega_d^2 &= (1-\zeta^2)\omega_n^2 = \omega_n^2 - \sigma^2 \\ \omega_n &= \sqrt{\omega_d^2 + \sigma^2} \end{aligned}$$

and the damping ratio can be calculated as $\zeta = \sigma/\omega_n$. This approach to damping estimation is in the same spirit as the logarithmic decrement technique commonly used in structural dynamics.

Most systems have multiple modes, however, which implies that the impulse response function will generally contain contributions from several modes. Therefore, because they are valid only for single-mode systems, logarithmic decrement or the approach based on the Hilbert transform cannot be used for estimating damping. As emphasized earlier, the Hilbert transform does not yield meaningful frequency information for multiple-mode systems since it attempts to identify a single instantaneous frequency at each time step. The Hilbert-Huang algorithm makes

it possible to apply the above technique for damping and frequency estimation because it can decompose a multi-component signal into a series of single-component signals through the EMD process. By performing EMD on the impulse response function of a multiple-mode system, the contributions of the different modes can be extracted and analyzed separately. This approach has been applied by Yang et al. [27, 28, 29] in a series of papers in which the Hilbert-Huang algorithm was used for parameter estimation of several multiple degree-of-freedom structures. A similar analysis is used here to estimate damping ratios and frequencies for aeroelastic systems.

As an example, consider a prototypical linear pitch-plunge aeroelastic system that has been studied extensively in the literature. The system consists of an airfoil with pitch and plunge degrees of freedom, and the input is the deflection of the trailing edge flap. In this study, the flow velocity U is varied until the linear flutter speed is reached at approximately $U = 11.8$ m/s.

Because this system has two outputs, pitch and plunge, there are two impulse response functions that can be measured. Each of these functions generally contains contributions from both modes of the system. As an example, Fig. 16 depicts the pitch and plunge impulse response functions for a flow velocity of $U = 8$ m/s. These were obtained by simulating the pitch and plunge responses to an impulse applied to the trailing edge flap. The plunge impulse responses are used over a range of flow velocities to measure frequencies and damping ratios using the Hilbert-Huang algorithm. These impulse response functions are obtained by way of simulation in this paper, but in practice they can be obtained by way of system identification techniques such as taking the inverse Fourier transform of the measured frequency response function or identifying first-order Volterra kernels from measured input-output data.

The plunge impulse response functions were used to estimate the damped natural frequencies, damping ratios, and natural frequencies over a range of flow velocities. The results are summarized in Table 5, which lists the actual and estimated damped natural frequencies and damping ratios for flow velocities ranging from $U = 1$ m/s to $U = 11.9$ m/s (just past the linear flutter speed). The actual frequencies and damping ratios were calculated by solving for the eigenvalues of the system. The estimation of the modal parameters for $U = 8$ m/s is demonstrated in Figs. 17 and 18. Figure 17 illustrates the EMD of the plunge impulse response function at $U = 8$ m/s. In this case, both modes of vibration are evident in the first intrinsic mode function. This is because the first, higher-frequency mode damps out quickly and the second mode persists for a longer period of time. Therefore, the frequencies and damping ratios of both modes were estimated by using different portions of the first IMF, as depicted in Fig. 18. The figure shows plots of the instantaneous phase and the natural log of the amplitude of the first IMF. Recall that the slopes of these lines are used to estimate the modal parameters. The initial portion of the amplitude plot is not a straight line because of initial transients in the IMF and possible boundary effects. Therefore, the portions of the plot that most resembled straight lines were used for the slope calculations

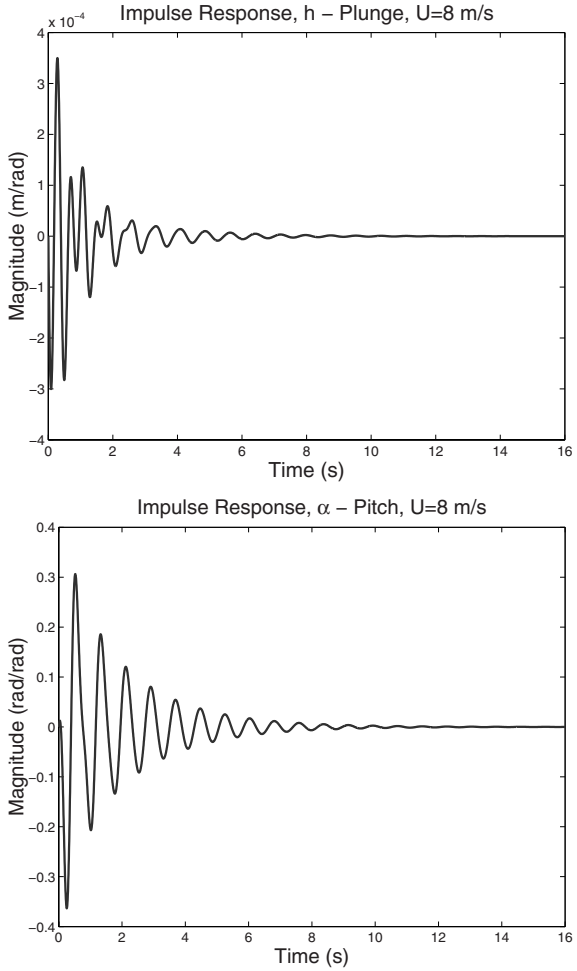

FIGURE 16. Plunge and pitch impulse response functions for $U = 8$ m/s

for each mode, as labeled in the figure. Because this analysis technique is only approximate depending on the magnitude of the damping ratio (increased error for larger damping), the amplitude curve tends to oscillate about an average slope. Therefore, the slope in each case was obtained using a linear least-squares curve-fit of the data [27, 28, 29].

The results presented in Table 5 show that the estimates of the damped natural frequencies and damping ratios are fairly accurate in most cases. As the linear flutter speed (approximately $U = 11.8$ m/s) is approached, the plunge mode is not discernible in the IMFs. In this regime, the system behaves essentially as a single-mode system and it was not possible to estimate the damping and frequency

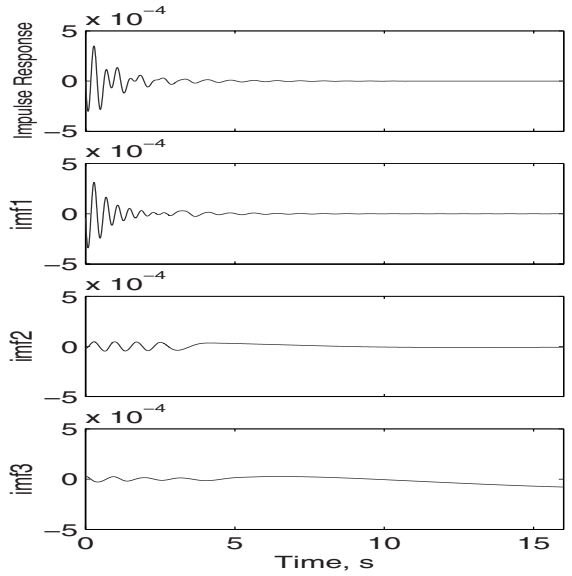

FIGURE 17. Empirical mode decomposition of the plunge impulse response function (m/rad) at $U = 8$ m/s.

of the plunge mode. The actual and estimated damping ratios for each mode are plotted as a function of flow velocity in Fig. 19.

A few observations are now presented. The first IMF was used to estimate the parameters of both modes. The analysis would be somewhat cleaner if each mode appeared in a different IMF. This is indeed the case in the work of Yang et al. [27, 28, 29] in which the frequency range of each IMF is controlled in the EMD process. Therefore, controlling the frequency range of each IMF is an option that could enhance the parameter estimation procedure. Also, even though parameters for both modes were estimated using a single IMF, the same results would generally not be obtained from an analysis of the impulse response function without the benefit of EMD. Although the IMF used in the analysis contains contributions from two modes, only one mode is present in the signal at any point in time. In contrast, the impulse response function may contain contributions from both modes over the same time period. This example demonstrates some potential benefits of the HHT for extracting modal parameters from aeroelastic data.

9. Conclusions

Application of the Hilbert-Huang algorithm for system signal decompositions, studying the effect of enhancements such as local/on-line behavior, understanding

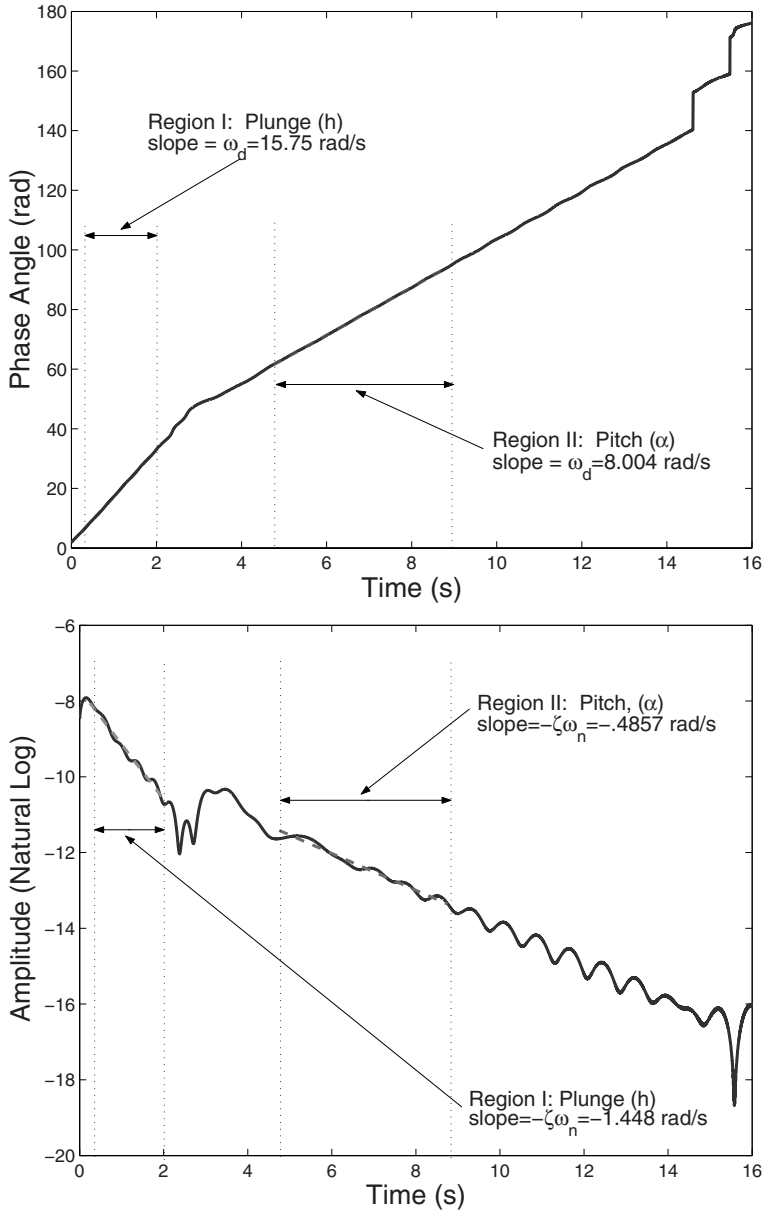

FIGURE 18. Instantaneous phase and amplitude plots used to estimate modal parameters from the first IMF of the plunge impulse response function at $U = 8$ m/s.

TABLE 5. Actual and estimated (Est) damped frequencies (Hz) and damping ratios.

Velocity (m/s)		ω_d	Est ω_d	ζ	Est ζ
1	Plunge	2.765	2.735	.0854	.0874
	Pitch	1.027	1.022	.0441	.0444
3	Plunge	2.739	2.709	.0855	.0881
	Pitch	1.057	1.050	.0503	.0490
5	Plunge	2.684	2.655	.0862	.0895
	Pitch	1.119	1.096	.0553	.0591
7	Plunge	2.595	2.567	.0877	.0926
	Pitch	1.217	1.214	.0590	.0579
9	Plunge	2.454	2.452	.0906	.0957
	Pitch	1.366	1.362	.0607	.0637
11	Plunge	2.198	–	.1012	–
	Pitch	1.628	1.619	.0544	.0544
11.5	Plunge	2.073	–	.1174	–
	Pitch	1.755	1.744	.0392	.0394
11.6	Plunge	2.040	–	.1262	–
	Pitch	1.788	1.775	.0305	.0305
11.7	Plunge	2.009	–	.1392	–
	Pitch	1.819	1.806	.0176	.0177
11.8	Plunge	1.984	–	.1552	–
	Pitch	1.844	1.831	.0016	.0017
11.9	Plunge	1.967	–	.1713	–
	Pitch	–	–	-.0145	-.0146

filtering properties, and especially for investigating correlations between input-output and between system sensors in terms of instantaneous properties, is revealed. System input-output signal analysis is introduced to characterize the time-varying amplitude and frequency components of multiple data channels, including input-to-output and distributed sensors, in terms of the intrinsic mode functions (IMFs) of the Hilbert-Huang transform (HHT). Significant departures from Fourier and other time-frequency or time-scale wavelet approaches are exposed. In these respects, this paper attempts to show how the HHT behaves in a sometimes non-intuitive and subtle manner in the analysis of F/A-18 Active Aeroelastic Wing (AAW) aircraft aeroelastic flight test data. Online stability analyses and modal identification are also presented. Examples are given using aeroelastic test data from the F/A-18 Active Aeroelastic Wing aircraft, an Aerostructures Test Wing, and pitch-plunge simulation.

An objective signal-adaptive basis function derivation, the Hilbert-Huang algorithm yields intrinsic mode functions giving instantaneous frequencies as functions of time that permit identification of embedded structures. There is a multiresolution quality in the empirical mode decomposition process which even deals

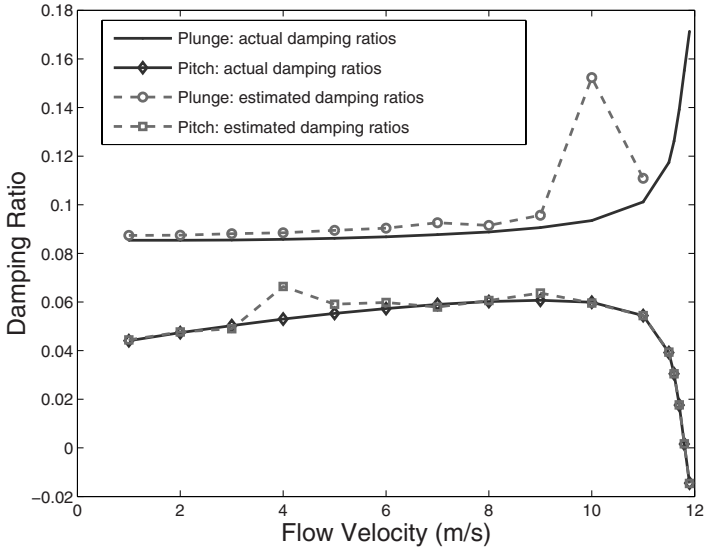

FIGURE 19. Actual and estimated damping ratios.

with intermittency by allowing multiple time-scales within an intrinsic mode function, but not allowing a similar time-scale simultaneously with other IMFs. System identification in the IMF sub-component environment is a practical endeavor in the domain of multiresolution system identification. It should be noted that the idea of exploiting local properties for signal analysis applies to spatial data as well as temporal data with frequency and scale (translation and duration) variations. From the idea of empiquency to describe oscillations in images based on extrema points there are potential applications for general time-space-frequency-scale signal processing.

Modern intelligent control and integrated aerostructures require control feedback signal processing cognizant of system stability and health. Time-varying linear or nonlinear modal characteristics derived from flight data are all within the realm of HHT. Further research will investigate these issues and HHT connections between localized instantaneous dynamics, health diagnostics, and global system stability and performance for monitoring and prediction.

References

[1] Bendat, J. S. and A.G. Piersol, *Random Data Analysis and Measurement Procedures*, John Wiley & Sons, Inc., Chap. 12-13, 2000.

[2] Buresti, G., G. Lombardi, and J. Bellazzini, "On the analysis of fluctuating velocity signals through methods based on the wavelet and Hilbert transforms," *Chaos, Solitons and Fractals*, **20**(2004), pp. 149-158.

[3] Chen, Q., N. Huang, S. Riemenschneider, and Y. Xu, "A B-spline approach for empirical mode decompositions," *Advances in Computational Mathematics*, 2004.

[4] Cohen, L., "Time-Frequency Distributions - A Review," *Proc. IEEE*, **77**(7), 1989, pp. 941-981.

[5] Flandrin, P., *Time-Frequency/Time-Scale Analysis*, Academic Press, 1999.

[6] Flandrin, P., G. Rilling, and P. Gonçalvès, "Empirical Mode Decomposition as a Filter Bank," *IEEE Signal Processing Letters*, **11**(2), Feb 2004, pp. 112-114.

[7] Flandrin, P. and P. Gonçalvès, "Empirical Mode Decompositions as Data-Driven Wavelet-Like Expansions," accepted for publication in *International Journal of Wavelets, Multiresolution and Information Processing*, 2005.

[8] Huang, N. E., Z. Shen, S.R. Long, M.C. Wu, H.H. Shih, Q. Zheng, N-C Yen, C.C. Tung, and H.H. Liu, "The empirical mode decomposition and the Hilbert spectrum for nonlinear and non-stationary time series analysis," *Proc. Royal Society London A*, **454**(1998), pp. 903-995.

[9] Huang, N. E., Z. Shen, and S.R. Long, "A New View of Nonlinear Water Waves: The Hilbert Spectrum," *Annual Review of Fluid Mechanics*, **31**(1999), pp. 417-457.

[10] Huang, N. E., M-L.C. Liu, S.R. Long, S.S.P. Shen, W. Qu, P. Gloersen, and K.L. Fan, "A confidence limit for the empirical mode decomposition and Hilbert spectral analysis," *Proc. Royal Society London A*, **459**(2003), pp. 2317-2345.

[11] Jha, R., F. Yan, and G. Ahmadi, "Energy-Frequency-Time Analysis of Structural Vibrations using Hibert-Huang Transform," AIAA-2004-1975.

[12] Lind, R., D.F. Voracek, R. Truax, T. Doyle, S. Potter, and M. Brenner, "A flight test to demonstrate flutter and evaluate the flutterometer," *The Aeronautical Journal*, Oct 2003.

[13] Linderhed, A., "2D empirical mode decompositions in the spirit of image compression," *Wavelet and Independent Component Analysis Apps IX, SPIE Proc.*, **4738**(2002), pp. 1-8.

[14] Linderhed, A., "Image compression based on empirical mode decomposition," *Proc. of SSAB 04 Symp. on Image Analysis*, Uppsala, Sweden, Mar 11-12, 2004, pp. 110-113.

[15] Liu, B., S. Riemenschneider, and Y. Xu, "Gearbox fault diagnosis using empirical mode decomposition and Hilbert spectrum," submitted for publication in *MSSP*, 2004.

[16] Liu, Z. and S. Peng, "Boundary Processing of Bidimensional EMD Using Texture Synthesis," *IEEE Signal Processing Letters*, **12**(1), Jan 2005, pp. 33-36.

[17] Loughlin, P. J. and L. Cohen, "The Uncertainty Principle: Global, Local, or Both?," *IEEE Transactions on Signal Processing*, **52**(5), May 2004, pp. 1218-1227.

[18] Pendleton, E., D. Bessette, P. Field, G. Miller, and K. Griffin, "Active Aeroelastic Wing Flight Research Program: Technical Program and Model Analytical Development," *AIAA Journal of Aircraft*, **37**(4), Jul-Aug 2000, pp. 554-561.

[19] Poolla, K., P. Khargonekar, A. Tikku, J. Krause, and K. Nagpal, "A Time-Domain Approach to Model Validation," *IEEE Transactions on Automatic Control*, **39**(5), May 1994, pp. 951-959.

[20] Qian, Tao, Q. Chen, and L. Li, "Analytic Unit Quadrature Signals with Nonlinear Phase", Physica D: Nonlinear Phenomena, Vol. 203, Issues 1-2, pp. 80-87 (2005).

[21] Rilling, G., P. Flandrin, and P. Gonçalvès, "On Empirical Mode Decomposition and its algorithms," *IEEE-EURASIP Workshop on Nonlinear Signal/Image Processing*, Grado, Italy, 2003.

[22] Sharpley, R. C. and V. Vatchev, "Analysis of the Intrinsic Mode Functions," submitted for publication in *Constructive Approximations*, 2005.

[23] Vatchev, V., *Intrinsic Mode Functions and the Hilbert Transform*, Ph.D thesis, Dept of Mathematics, U. of South Carolina, 2004.

[24] Worden, K. and G.R. Tomlinson, *Nonlinearity in Structural Dynamics: Detection, Identification, and Modeling*, Institute of Physics Publishing Ltd, Bristol and Philadelphia, 2001.

[25] Wu, Z., N.E. Huang, "A study of the characteristics of white noise using the empirical mode decomposition method," *Proc. Royal Society London A*, **460** (2004), pp. 1597-1611.

[26] Yang, B. and C.S. Suh, "Interpretation of crack-induced rotor non-linear response using instantaneous frequency," *Mechanical Systems and Signal Processing*, **18**(2004), pp. 491-513.

[27] Yang, J. N., Y. Lei, S. Pan, and N. Huang, "System identification of linear structures based on Hilbert-Huang spectral analysis. Part 1: Normal modes," *Earthquake Engineering and Structural Dynamics*, **32**(2003), pp. 1443-1467.

[28] Yang, J. N., Y. Lei, S. Pan, and N. Huang, "System identification of linear structures based on Hilbert-Huang spectral analysis. Part 2: Complex modes," *Earthquake Engineering and Structural Dynamics*, **32**(2003), pp. 1533-1554.

[29] Yang, J. N., Y. Lei, S. Pan, and N. Huang, "Identification of Natural Frequencies and Dampings of In Situ Tall Buildings Using Ambient Wind Vibration Data ," *Journal of Engineering Mechanics*, **130**(1), May 2004, pp. 1-8.

[30] Yang, J. N., Y. Lei, S. Pan, and N. Huang, "Hilbert-Huang Based Approach for Structural Damage Detection," *Journal of Engineering Mechanics*, **130**(1), 2004, pp. 85-95.

[31] Yang, Z., D. Qi and L. Yang, "Signal Period Analysis Based on Hilbert-Huang Transform and Its Application to Texture Analysis," *Third Intl Conf Image/Graphics, ICIG'04*, pp. 430-433.

[32] Zhou, K., with J. Doyle, *Essentials of Robust Control*, Prentice Hall, New Jersey, 1998.

Martin J. Brenner
Aerospace Engineer, Aerostructures Branch
NASA Dryden Flight Research Center
Edwards, CA 93523-0273, USA
e-mail: Martin.J.Brenner@nasa.gov

Sunil L. Kukreja
Aerospace Engineer, Aerostructures Branch
NASA Dryden Flight Research Center
Edwards, CA 93523-0273, USA
e-mail: Sunil.Kukreja@nasa.gov

Richard J. Prazenica
Visiting Assistant Professor
UF Research in Engineering Educational Facility (REEF)
University of Florida
Shalimar, FL 32579, USA
e-mail: prazenic@ufl.edu

Wavelet Analysis and Applications
Tao Qian, Mang I. Vai and Xu Yuesheng, Eds.
Applied and Numerical Harmonic Analysis, 363–376

An Adaptive Data Analysis Method for Nonlinear and Nonstationary Time Series: The Empirical Mode Decomposition and Hilbert Spectral Analysis

Norden E. Huang

Abstract. An adaptive data analysis method, the Empirical Mode Decomposition and Hilbert Spectral Analysis, is introduced and reviewed briefly. The salient properties of the method is emphasized in this review; namely, physical meaningful adaptive basis, instantaneous frequency, and using intra-wave frequency modulation to represent nonlinear waveform distortion. This method can perform and enhance most of the traditional data analysis task such as filtering, regression, and spectral analysis adaptively. Also presented are the mathematical problems associated with the new method. It is hope that this presentation will entice the interest of the mathematical community to examine this empirically based method and inject mathematical rigor into the new approach.

Mathematics Subject Classification (2000). Primary 99Z99; Secondary 00A00.

1. Introduction

Data analysis is necessary for science and engineering, for data is the only link we have with the reality. Consequently, data analysis serves two purposes: First, it provides validation of our theories or models. Second, it provides the guide of the underlying mechanisms as a base for discovery, creation or improvements of the theories and models. Either way, the data contains information we are seeking; the goal of data analysis is to find the information in the data. The common tasks involved in data analysis are finding the distributions, filtering, time-frequency, regressions and error analyses. Even on the limited scope of filtering to cleanse the data of unwanted noise, we still face with the daunting task of determining which part of the data is noise and which part is valid information. In the filtering process we should only eliminate the noise, but not degrade the information. As we do not

have a complete knowledge base of the underlying mechanisms for most of the physical problems we face today, we should inject as little subjective specifications as possible in the process of data analysis, so that we do not prejudice the results. A truly objective data analysis method should be adaptive to the data and let the data set speaks for itself.

Traditional time-frequency analysis methods, however, all follows the well established mathematical rules: the methods all start with a definition of basis, and convolve the signal with the basis to get amplitude and frequency either for distributions or for filtering. Such an approach has the great advantage of having a solid mathematical foundation. Once the algorithm is established, data analysis can go forward mechanically. Unfortunately, within the comfortable fold of solid mathematic foundation, the methods can not be adaptive at all. Furthermore, this well trodden path also restricts the methods developed under this paradigm to linear and stationary assumptions.

As data can come from all sources ranging from relatively well established physical sciences, to complicated biologic processes and social-economic phenomena., most of the driving mechanisms are so complicatedly intertwined and interacting that the data we obtained are also highly variable, not only from one case to another but also from time to time even limited to one single case. In other words, we have to face data from nonlinear and nonstationary processes. This requirement is known for a long time, but remedy is slow to come. To accommodate for data from nonstationary processes, we have met more success. Methods (see for example, Flandrin, 1999) such as spectrogram, Wigner-Ville distribution, Wavelet analysis are all examples. To accommodate for data from nonlinear processes, however, our progress has been very slow. The available methods (see, for example, Tong, 1990, Krantz and Schreiber, 1997 and Diks, 1998) are limited to handle data from deterministic low dimensional chaotic systems.

Even for data from nonstationary processes, the available methods are also limited to linear systems, for the methods were mostly based on the well established *a priori* basis approach, where all the analysis is based on convolution of the data with the established basis. This powerful mathematical tool, unfortunately, has drained all the physics out of the analyzed results, for any *a priori* basis could not possibly fit all the variety of data from drastically different underlying driving mechanisms. Any misfit will automatically be assigned to the various orders of harmonics with respect to the selected basis. Though results so obtained satisfy the mathematical requirements, they lack physical meaning. Furthermore, the convolution processes involve integration, which make the results suffering the limitation imposed by the uncertainty principle, and preventing us from examine the details of the data and their underlying mechanisms.

Let us take a simple example to examine the characteristics of data from a nonlinear system. Consider the Duffing equation without damping given as

$$\frac{d^2x}{dt^2} + x + \varepsilon x^3 = \gamma \cos \omega t \,, \tag{1.1}$$

where ε is a parameter, not necessarily small; γ is the magnitude of the driving force. We can easily rewrite this equation slightly as follows:

$$\frac{d^2x}{dt^2} \; + \; x \; (1 \; + \; \varepsilon x^2 \,) \; = \; \gamma \cos \omega t \; . \tag{1.2}$$

If we treat the quantity in the parenthesis as a single number designated as L:

$$L \; = \; 1 \; + \; \varepsilon \, x^2, \tag{1.3}$$

then the quantity L can be treated as the pendulum length or the spring constant. Either way, L changes with position; therefore, the frequency of the system should also change with position even within one oscillation period. Such intra-wave frequency modulation is the special characteristics of a nonlinear system; and it requires a detailed frequency representation that is unattainable form *a priori* basis approach. For example, following the classic perturbation analysis by imposing a linear structure on a nonlinear system, one would find the solution consisted of endless harmonics. The effect of the harmonics is to find enough sinusoidal components to fit the deformed final waveform, commonly known as harmonic distortions. It is well know that each term in this perturbation solution does not have physical meaning, only the totality of all the terms represents the physics. But using any *a priori* basis analysis, one would inevitably obtain a collection of the harmonics of one form or the other depending on the basis function selected; thus rendered the interpretation of spectral analysis problematical. The harmonics representation here is a poor substitute of the detailed instantaneous frequency description of the intra-wave frequency modulation. But such a detailed description will call for a drastic new approach. In fact to describe intra-wave frequency modulation, we cannot use *a priori* basis approach. An easy alternative is to use the Hilbert Transform, which is defined as

$$y(t) \; = \; \frac{1}{\pi} \; P \int_{-\infty}^{\infty} \frac{x(\tau)}{t - \tau} \; , \tag{1.4}$$

in which *x(t)* is the given function of *Lp* class, *y(t)* is the Hilbert transform, which is the complex conjugate of x(t), and *P* indicates the principal value of the singular integral. As y(t) is the complex conjugate, we have

$$z(t) \; = x \, (t) \; + \; j \; y(t) \; = \; a \, (t) \, e^{j \, \theta(t)} \; , \tag{1.5}$$

where

$$a(t) \; = \; \left(x^2 \; + \; y^2\right)^{1/2} \quad ; \quad \theta(t) \; = \; \tan^{-1} \frac{y}{x} \quad . \tag{1.6}$$

Here a is the instantaneous amplitude, and θ is the phase function; thus the instantaneous frequency, with the stationary phase approximation, is simply

$$\omega \;=\; \frac{d\theta}{dt}\;. \tag{1.7}$$

This definition also coincides with the classical wave theory. This definition of instantaneous frequency is indeed local, for it is defined through differentiation rather than integration. Therefore, the resulting instantaneous frequency should be able to describe the intra-wave frequency modulation. This approach has been recommended by Hahn (1996) for applications signal processing. Unfortunately, this straightforward and simple-minded approach does not work at all. Although the Hilbert transform is valid under a very general condition, for the instantaneous frequency derived from the above approach to make physical sense, the function has to be 'mono-component' as discussed by Cohen (1995) and Huang et al. (1998, 1999). This has been illustrated by Huang et al (1998) with a simple function as

$$x(t) \;=\; a \;+\; \cos\,\alpha t, \tag{1.8}$$

with a as an arbitrary constant. Its Hilbert transform is simply

$$y(t) \;=\; \sin\,\alpha t\,; \tag{1.9}$$

therefore, the instantaneous frequency according to Equation (7) is

$$\omega \;=\; \frac{\alpha\;(1\;+\;a\,\sin\,\alpha t)}{1+2a\,\cos\,\alpha t\;+\;a^2}\;. \tag{1.10}$$

Equation (10) can give any value for the instantaneous frequency, depending on the value of a. In order to recover the frequency of the input sinusoidal signal, the constant has to be zero. This simple example illustrates a crucial condition for the Hilbert Transform approach to work here: The function will have to be zero mean locally. This seemingly trivial condition has created great misunderstanding, which has prompted Cohen (1995) to list a number of 'paradoxes' concerning instantaneous frequency. Some of the paradoxes concerning negative frequency are direct consequence of this condition.

Another obvious consequence of this condition is the difficult experience by all previous attempts to use the Hilbert transform: how to reduce or decompose an arbitrary function to a 'mono-component' one with local zero mean? And more fundamentally, if the function is nonstationary, how can one find the local mean? These difficulties have forced the past applications of Hilbert transform to extract a narrow band component with a band-pass filter on the original data (Melville, 1983). As the band-pass filter is a linear operator, any signal passing through it will lost all its 'harmonics', and suffer deformation of the fundamental wave shape. Such approach certainly satisfies the condition demanded by the instantaneous frequency computation through Hilbert transform; it has unwittingly drained some interesting information form the data, the nonlinear characteristics associated with the signal.

With all these difficulties, the real applications of Hilbert transform will have to wait for the development of the Empirical Mode Decomposition (EMD) (Huang et al. 1998, 1999, 2003). Together with the Hilbert Spectral Analysis (HSA), the combination established a new adaptive time-frequency analysis method.

2. The Empirical Mode Decomposition and Hilbert Spectral Analysis

The details of both Empirical Mode Decomposition (EMD) and the Hilbert Spectral Analysis (HSA) are given in Huang et al. (1996, 1998 and 1999). The following summary is based on a simplified version given in Huang (2005). The EMD method is necessary to reduce any data from nonstationary and nonlinear processes into simple oscillatory function that will yield meaningful instantaneous frequency through the Hilbert transform. Contrary to almost all the previous decomposing methods, EMD is empirical, intuitive, direct, and adaptive, with the *a posteriori* defined basis based on and derived from the data. The decomposition is designed to seek the different simple intrinsic modes of oscillations in any data based on the principle of scale separation. The data, depending on it complexity, may have many different coexisting modes of oscillation at the same time. Each of these oscillatory modes is represented by an Intrinsic Mode Function (IMF) satisfying the following conditions:

(a) in the whole data set, the number of extrema and the number of zero-crossings must either equal or differ at most by one, and

(b) at any point, the mean value of the envelope defined by the local maxima and the envelope defined by the local minima is zero.

The IMF is a counter part to the simple harmonic function, but it is much more general: instead of constant amplitude and frequency, IMF can have both variable amplitude and frequency as functions of time. This definition is inspired by the simple example of constant plus sinusoidal function given above. The total number of the IMF components is limited to $ln_2 N$, where N is the total number of data points. It satisfies all the requirements for a meaningful instantaneous frequency through Hilbert transform.

Pursuant to the above definition for IMF, one can implement the needed decomposition of any function, known as sifting, as follows: Take the test data; identify all the local extrema; divide the extrema into two sets: the maxima and the minima. Then connect all the local maxima by a cubic spline line to form an upper envelope. Repeat the procedure for the local minima to form a lower envelope. The upper and lower envelopes should encompass all the data between them. Their mean is designated as m_1, and the difference between the data and m_1 is designated as, h_1, a proto-IMF:

$$X(t) - m_1 = h_1 . \tag{2.1}$$

Ideally, *h1* should satisfy the definition of an IMF by construction of *h1* described above, which should have made it symmetric and having all maxima positive and all minima negative. Yet, in changing the local zero from a rectangular to a curvilinear coordinate system some inflection points could become additional extrema. New extrema generated this way actually reveal the hidden modes missed in the initial treatment. The sifting process sometimes can recover signals representing low amplitude riding waves with repeated siftings.

The sifting process serves two purposes: to eliminate riding waves, and to make the wave profiles more symmetric. While the first condition is absolute necessary for Hilbert transform to give a meaningful instantaneous frequency, the second condition is also necessary in case the neighboring wave amplitudes having too large a disparity. As a result, the sifting process has to be repeated many times to reduce the extracted signal an IMF. In the subsequent sifting process, *h1* is treated as the data for the next round of sifting; therefore,

$$h_1 \; - \; m_{11} \; = \; h_{11} \; . \tag{2.2}$$

After repeated sifting, up to k times, h_{1k}:

$$h_{1\,(k-1)} \; - m_{1k} \; = \; h_{1k} \; . \tag{2.3}$$

If h_{1k} becomes an IMF, it is designated as c_1:

$$c_1 \; = \; h_{1k} \; , \tag{2.4}$$

the first IMF component from the data. Here we have a critical decision to make: when to stop. Too many rounds of sifting will reduce the IMF to FM page criterion; to few rounds of sifting will not have a valid IMF. In the past, two different criteria have been used: The first one was used in Huang et al. (1998), based on a Cauchy type of convergence test. Specifically, the test is to require the normalized squared difference between two successive sifting operations defined as

$$SD_k \; = \; \frac{\sum\limits_{t=0}^{T} |h_{k-1}(t) \; - \; h_k(t)|^2}{\sum\limits_{t=0}^{T} h_{k-1}^2(t)} \; , \tag{2.5}$$

to be small. If this squared difference, SD_k, is small than a predetermined value, the sifting process will be stopped. Though this criterion is rigorous, it is very difficult to implement, for this criterion does not depend on the definition of the IMFs. The squared difference might be small, but there is no guarantee that the function will have the same numbers of zero-crossings and extrema, a necessary for a meaningful instantaneous frequency through Hilbert transform. These shortcomings prompted Huang et al. (1999 and 2003) to propose an alternative based on the agreement

of the numbers of zero-crossings and extrema. Specifically, an S-number is pre-selected. The sifting process will stop only if S consecutive times the numbers of zero-crossings and extrema stay the same, and are equal or at most differ by one. This second choice is not without its difficulty: how to select the S number. Obviously, any selection is *ad hoc*, and a rigorous justification is needed. But in Huang et al. (2003), they found the optimal S number to be around 4 to 8 for a variety of data sets. Such a selection could be used as a guide. Even if one chooses to eschew such an arbitrary selection, and ensemble of S number could give an ensemble mean of the various selection as shown in Huang et al (2003), which is even more meaningful.

With either stoppage criterion, the, *c1*should contain the finest scale or the shortest period component of the signal. We can, then, remove *c1*from the rest of the data by

$$X(t) - c_1 = r_1 . \tag{2.6}$$

Since the residue, r_1, contains all longer period variations in the data, it is treated as the new data and subjected to the same sifting process as described above. This procedure can be repeated to all the subsequent r_j's, and the result is

$$\begin{aligned} r_1 - c_2 &= r_2 , \\ &\ldots \\ r_{n-1} - c_n &= r_n \end{aligned} \tag{2.7}$$

The sifting process should stop when the residue, r_n, becomes a constant, a monotonic function, or a function contains only a single extrema, from which no more IMF can be extracted. Even for data with zero mean, the final residue still could be different from zero. If the data have a trend, the final residue should be that trend. By summing up Equations (16) and (17), we finally obtain

$$X(t) = \sum_{j=1}^{n} c_j + r_n . \tag{2.8}$$

Thus, sifting process produces a decomposition of the data into n-intrinsic modes, and a residue, r_n. When apply the EMD method, a mean or zero reference is not required; EMD only needs only the locations of the local extrema. The sifting process generates the zero reference for each component. Without the need of the zero reference, EMD avoids the troublesome step of removing the mean values for the large non-zero mean.

Two special notes here deserve our attention. First, the sifting process offered a way to circumvent the difficulty of define the local mean in a nonstationary time series, where no length scale exists for one to implement the traditional mean operation. The envelope mean employed here does not involve time scale; however, it is local. Second, the sifting process is a Reynolds-type decomposition: separating variations from the mean, except that the mean is a local instantaneous

mean, so that the different modes are almost orthogonal to each other, except for the nonlinearity in the data.

Recent studies by Flandrin et al. (2004) and Wu and Huang (2004) established that the EMD is equivalent to a dyadic filter bank, and it is also equivalent to an adaptive wavelet. Being adaptive, we have avoided the shortcomings of using any *a priori*-defined wavelet basis, and also avoided the spurious harmonics that would have resulted. The components of the EMD are usually physically meaningful, for the characteristic scales are defined by the physical data.

Having established the decomposition, we can also identify a new use of the IMF components as filtering. Traditionally, filtering is carried out in frequency space only. But there is a great difficult in applying the frequency filtering when the data is either nonlinear or nonstationary or both, for both nonlinear and nonstationary data generate harmonics of all ranges. Therefore, any filtering will eliminate some of the harmonics, which will cause deformation of the data filtered. Using IMF, however, we can devise a time space filtering. For example, a low pass filtered results of a signal having n-IMF components can be simply expressed as

$$X_{lk}\ (t)\ =\ \sum_{k}^{n} c_j\ +\ r_n\ ; \tag{2.9}$$

a high pass results can be expressed as

$$X_{hk}\ (t)\ =\ \sum_{1}^{k} c_j\ ; \tag{2.10}$$

and a band pass result can be expressed as

$$X_{bk}\ (t)\ =\ \sum_{b}^{k} c_j\ . \tag{2.11}$$

The advantage of this time space filtering is that the results preserve the full nonlinearity and nonstationarity in the physical space.

Having obtained the Intrinsic Mode Function components, we can compute the instantaneous frequency for each IMF component as the derivative of the phase function. And we can also designate the instantaneous amplitude from the Hilbert transform to each IMF component. Finally, the original data can be expressed as the real part, RP, of the sum of the data in terms of time, frequency and energy as:

$$X(t)\ =\ RP\sum_{j=1}^{n} a_j(t)\ e^{i\ \int\ \omega_j(t)\ dt}\ . \tag{2.12}$$

Equation (22) gives both amplitude and frequency of each component as a function of time. The same data, if expanded in a Fourier representation, would

have a constant amplitude and frequency for each component. The contrast between EMD and Fourier decomposition is clear: The IMF represents a generalized Fourier expansion with a time varying function for amplitude and frequency. This frequency-time distribution of the amplitude is designated as the Hilbert Amplitude Spectrum, *H(s, t)*, or simply the Hilbert spectrum.

From the Hilbert spectrum, we can also define the marginal spectrum, *h(sn)*, as

$$h(\omega) = \int_0^T H(\omega, t)dt. \tag{2.13}$$

The marginal spectrum offers a measure of total amplitude (or energy) contribution from each frequency value. It represents the cumulated amplitude over the entire data span in a probabilistic sense.

The combination of the Empirical Mode Decomposition and the Hilbert Spectral Analysis is designated by NASA as the Hilbert-Huang Transform (HHT) for short. Recent studies by various investigators indicate that HHT is a super tool for time-frequency analysis of nonlinear and nonstationary data (Huang and Attoh-Okine, 2005, Huang and Shen, 2005). It is based on an adaptive basis, and the frequency is defined through the Hilbert transform. Consequently, there is no need for the spurious harmonics to represent nonlinear waveform deformations as in any of the *a priori* basis methods, and there is no uncertainty principle limitation on time or frequency resolution from the convolution pairs based also on *a priori* bases. A summary of the comparison between Fourier, Wavelet and HHT analyses is given in Table 1.

After this basic development of the HHT method, there are some recent developments, which have either added insight to the results or enhanced the statistical significance of the results. Some of the recent developments are summarized in the following section.

3. An Alternative View on Nonlinearity

Having presented the Hilbert spectral analysis, we will explore the alternative view of Hilbert analysis on nonlinearity effects in the data. When one decomposing any data with an *a priori* basis, an inevitable consequence is to have harmonics, which are mathematic artifacts rather than physical entities. Take the water surface waves as an example, which are certainly nonlinear. Therefore, in the traditional view, we have to employee harmonics of the fundamental to fit the nonlinearly distorted profile. Yet, all of the harmonics are not dispersive; they are all bounded waves and have to propagate at the same phase speed as the fundamental. As a result, the wave spectra of water waves based on Fourier analysis is an entangled and inseparable mixture of bounded and free waves. Thus it makes the interpretation of the spectrum extremely difficult for any range other than the energy containing part (see, Huang, et al., 1998, 1999). The intra-wave modulation through Hilbert spectral analysis offers a physically meaningful alternative. A simple example as given by Huang et al (1998) is the mathematic model,

TABLE 1. Comparisons between Fourier, Wavelet and Hilbert-Huang Transform in Data analysis.

	Fourier	Wavelet	Hilbert
Basis	*a priori*	*a priori*	Adaptive
Frequency	Convolution: Global, Uncertainty	Convolution: Global, Uncertainty	Differentiation: Local, Certainty
Presentation	Energy-frequency	Energy-time-frequency	Energy-time-frequency
Nonlinear	No	No	Yes
Non-stationary	No	Yes	Yes
Feature extraction	No	Discrete: no Continuous: yes	Yes
Theoretical base	Theory	Theory	Empirical

$$x(t) = \cos(\alpha t + \varepsilon \sin 2\alpha t), \tag{3.1}$$

which has an intra-wave modulated instantaneous frequency of

$$\omega(t) = \alpha\,(1 + 2\varepsilon \cos \alpha t\,). \tag{3.2}$$

This frequency truthfully depicts the behavior of the oscillator. Yet using Fourier representation the data would have to be decomposed into the fundamental and harmonics as

$$x(t) = \left(1 - \frac{\varepsilon}{2}\right) \cos \alpha t + \frac{\varepsilon}{2} \cos 3\alpha t + \ldots. \tag{3.3}$$

Although the two representations are equally valid mathematically, the intra-wave approach is obviously more physically meaning. For more complicated cases, examples can be found in Huang et al (1998, 1999).

4. The Recent Developments

After considering the basics of HHT analysis, some recent developments in the following areas will be discussed in some details:

4.1 The Normalized Hilbert Transform
4.2 Confidence Limit
4.3 Statistical Significance of IMFs

4.1. The Normalized Hilbert Transform

It is well known that, although the Hilbert transform exists for any function of Lp class, the phase function of the transformed function will not always yield physically meaningful instantaneous frequencies. The limitations have been summarized succinctly in two theorems:

First, in order to separate the contribution of the phase variation into the phase and amplitude parts, the function have to satisfy the limitation stipulated in the Bedrosian theorem (1963), which states that the Hilbert transform for the product of two functions, *f(t)* and *h(t)*, can be written as

$$H\,[f(t)\,h(t)\,]\;=\;f(t)\,H\,[\,h(t)\,]\,, \tag{4.1}$$

only if the Fourier spectra for *f(t)* and *h(t)* are totally disjoint in frequency space, and the frequency content of the spectrum for *h(t)* is higher than that of *f(t)*. This limitation is critical, for we need to have

$$H[\,a(t)\,\cos\,\theta(t)\,]\;=\;a(t)\;H\,[\cos\,\theta(t)\,]\,, \tag{4.2}$$

otherwise, we cannot use Equation (6) to define the phase function, for the amplitude variation would mix with the phase function. Bedrosian theorem requires that the amplitude is varying be so slowly that the frequency spectra of the envelope and the carrier waves are disjoint. This is possible only for trivial cases, for unless the amplitude is constant, any local deviation can be considered as a sum of delta-functions, which has a wide white spectrum. Therefore, the spectrum for varying amplitude would never be totally separate from that of the carrier. This limitation has made the application of the Hilbert transform even to IMFs problematic. To satisfy this requirement, Huang and Long (2003) have proposed the normalization of the IMFs in the following steps: Starting from an IMF, one first finds all the maxima of the IMFs, defining the envelope by spline through all the maxima, and designating the envelope as *E(t)*. Now, normalize the IMF by dividing the IMF by *E(t)*. Thus, we have the normalized function having amplitude always equal to unity. Thus we have circumvented the limitation of Bedrosian theorem.

Then, there is the new restriction given by the Nuttall theorem (1966), which stipulates that the Hilbert transform of cosine is not necessarily the sine with the same phase function for a cosine with an arbitrary phase function. Nuttall gave an energy based error bound, E, defined as the difference between *y(t)*, the Hilbert transform of the data, and *Q(t)*, the quadrature (with phase shift of exactly 90a) of the function as

$$\Delta E\;=\;\int\limits_{t=0}^{T}|y(t)\;-\;Q(t)\,|^{2}\;dt\;=\;\int\limits_{-\infty}^{0}S_{q}(\omega)\,d\omega\,, \tag{4.3}$$

in which S_q is Fourier spectrum of the quadrature function. Though the proof of this theorem is rigorous, the result is hardly useful, for it gives a constant error

bound over the whole data range. With the normalized IMF, Huang and Long (2003) have proposed a variable error bound based on a simple argument, which goes as follows: compute the difference between squared amplitude of the normalized IMF and unity. If the Hilbert transform is exactly the quadrature, the difference between it and unity should be zero; otherwise, the Hilbert transform cannot be exactly the quadrature. Consequently, the error can be measured simply by the difference between the squared normalized IMF and unity, which is a function of time. Huang and Long (2003) and Huang et al. (2005) have conducted detailed comparisons and found the result quite satisfactory.

Even with the error indicator, we can only know that the Hilbert transform is not exactly the quadrature; we still do not have the correct answer. This prompts a drastic alternative, eschewing the Hilbert transform totally. An exact quadrature has been found (Huang et al., 2005), and it would resolve the difficulties associated with the instantaneous frequency computation.

4.2. The Confidence Limit

The confidence limit for the Fourier spectral analysis is based on the ergodic theory, where the temporal average is treated as the ensemble average. This approach is only valid if the processes are stationary. Huang et al. (2003) has proposed a different approach by utilizing the fact that there are infinite many ways to decompose one given function into difference components. Using EMD, we can still obtain many different sets of IMFs by changing the stoppage criteria by changing the *S*-number. The confidence limit so derived does not depend on the ergodic theory.

From the confidence limit study, Huang et al. (2003) also found the optimal *S*-number, when the differences reach a local minimum. Based on their limited experience from different data sets, they concluded that an *S*-number in the range of 4 to 8 performed well. Logic also dictates that the *S*-number should not be too high (which would drain all the physical meaning out of the IMF), nor too low (which would leave some riding waves remaining in the resulting IMFs).

4.3. The Statistical Significance of IMFs

The EMD is a method to separate the data into different components by their scales. There is always the question: On what is the statistical significance of the IMFs based? In data containing noise, how can we separate the noise from information with confidence? This question was addressed by both Flandrin et al. (2004) and Wu and Huang (2004) through the study of signals consisting of noise only. Using white noise, Wu and Huang (2004) found the relationship between the mean period and RMS values of the IMFs. Furthermore, from the statistical properties of the scattering of the data, they found the bounds of the data distribution analytically. They concluded that when a data set is analyzed with EMD, if the mean period-RMS values exist within the noise bounds, the components most likely represent noise. On the other hand, if the mean period-RMS values exceed the noise bounds, then those IMFs must represent statistically significant information.

5. Mathematical Problem Associated with HHT

HHT is an empirically based method. This limitation is not severe when we consider it as a data analysis tool, for all the data are empirical values without analytic expressions anyway. We are at the stage of the wavelet analysis in the earlier 80s: producing useful results but waiting for mathematical foundation to rest our case. The outstanding mathematical problems, as listed by Huang (2005), are summarized here. We hope the mathematicians working in wavelet analysis will be interested in this new alternative and help as follows:

A. Adaptive data analysis methodology in general
B. Nonlinear system identification methods
C. Prediction problem for nonstationary processes (end effect)
D. Spline problem (best spline implement of HHT, convergence and 2-D)
E. Optimization problem (the best IMF selection and uniqueness)
F. Approximation problem (Hilbert transform and quadrature)
G. Miscellaneous questions concerning the HHT

6. Conclusions

The combination of EMD and HSA has provided an adaptive method to analyze nonstationary and nonlinear time series. It can perform and enhance most of the traditional data analysis tasks, such as filtering, regressions, and spectral analysis adaptively. Although adaptive signal analysis is long sought goal for the engineering community (Windrows and Stearns, 1985), the requirement here is much more stringent: we have to deal both nonlinearity and nonstationarity; therefore, the simple feedback method used for stationary processes would not be sufficient. This stringent requirement has put the new method on an empirical base at the present time. As far as data analysis is concerned, the lack of analytic expression would not be a problem, for none of the data came in analytical form anyway. Nevertheless, a purely empirical approach will certainly present a problem for a rigorous mathematical proof of the validity of the method. It is an earnest hope that the usefulness of the method will eventually interested the mathematicians to examine the method critically and constructively, so that the method will find its mathematical foundation established rigorously similar to what Daubechies (1992) had done for the Wavelet analysis.

References

[1] Bedrosian, E., 1963: *On the quadrature approximation to the Hilbert transform of modulated signals,* Proc. IEEE, 51, 868-869. Cohen, L., 1995: Time-frequency Analysis, Prentice Hall, Englewood Cliffs, NJ

[2] Diks, C., 1997: *Nonlinear Time Series Analysis,* World Scientific Press, Singapore.

[3] Daubechies, I., 1992: *Ten Lectures on Wavelets,* Philadelphia SIAM.

[4] Flandrin, P. 1999: *Time-Frequency / Time-Scale Analysis.* Academic Press, San Diego, CA.

[5] Flandrin, P., Rilling, G. and Gonçalvès, P., 2004: *Empirical mode decomposition as a filterbank.* IEEE Signal Proc Lett. 11 (2): 112-114.

[6] Hahn, S. L. 1996: *Hilbert Transforms in Signal Processing.* Artech House, Boston, MA

[7] Huang, N. E., 2005: *Introduction to Hilbert-Huang transform and its associated mathematical problems. 1-32, Hilbert-Huang Transform in Engineering,* Ed. N. E. Huang and N. Attoh-Okine, 2005, CRC Press, New York.

[8] Huang N. E., S. R. Long, and Z. Shen, 1996: *Frequency Downshift in Nonlinear Water Wave Evolution.* Advances in Appl. Mech. 32, 59-117.

[9] Huang, N. E., Shen, Z., Long, S. R., Wu, M. C., Shih, S. H., Zheng, Q., Tung, C. C. and Liu, H. H. 1998 *The empirical mode decomposition method and the Hilbert spectrum for non-stationary time series analysis,* Proc. Roy. Soc. London, A454, 903-995.

[10] Huang, N. E., Z. Shen, R. S. Long, 1999: *A New View of Nonlinear Water Waves - The Hilbert Spectrum,* Ann. Rev. Fluid Mech. 31, 417-457.

[11] Huang, N. E., Wu, M. L., Long, S. R., Shen, S. S. P., Qu, W. D., Gloersen, P. and Fan, K. L. 2003 *A confidence limit for the empirical mode decomposition and the Hilbert spectral analysis,* Proc. of Roy. Soc. London, A459, 2317-2345.

[12] Huang, N. E., Wu, Z., Long, S. R., Arnold, K. C., Blank, K., Liu, T. W. 2005 *On instantaneous frequency,* Proc. of Roy. Soc. London (Submitted)

[13] Huang, N. E. and Long, S. R. 2003 *A generalized zero-crossing for local frequency determination.* US Patent pending.

[14] Huang, N. E. and N. Attoh-Okine, Ed. 2005: *Hilbert-Huang Transform in Engineering,* CRC Press, New York.

[15] Huang, N. E. and Samuel S. S. Shen, Ed. 2005: *Introduction to Hilbert-Huang Transform and Applications.* 311 pp, World Scientific, Singapore.

[16] Kantz, H. and T. Schreiber, 1997: *Nonlinear Time Series Analysis,* Cambridge University Press, Cambridge.

[17] Melville, W. K., 1983: *Wave modulation and breakdown.* J. Fluid Mech. 128, 489-506.

[18] Nuttall, A. H., 1966: *On the quadrature approximation to the Hilbert Transform of modulated signals,* Proceedings of IEEE, 54, 1458-1459.

[19] Tong, H., 1990: *Nonlinear Time Series Analysis,* Oxford University Press, Oxford.

[20] Windrows, B and S. D. Stearns, 1985: *Adaptive Signal Processing,* Prentice Hall, Upper Saddle River, NJ

[21] Wu, Z. and Huang, N. E. 2004: *A study of the characteristics of white noise using the empirical mode decomposition method*, Proc. Roy. Soc. London, A460, 1597-1611.

Norden E. Huang
Research Center for Data Analysis
National Central University
Chungli, Taiwan 32001 ROC
e-mail: `Norden@ncu.edu.tw`

Part 2. Wavelet Applications

Wavelet Analysis and Applications
Tao Qian, Mang I. Vai and Xu Yuesheng, Eds.
Applied and Numerical Harmonic Analysis, 381–388

Transfer Colors from CVHD to MRI Based on Wavelets Transform

Xiaolin Tian, Xueke Li, Yankui Sun and Zesheng Tang

Abstract. A new algorithm based on wavelet transform to transfer colors from image of Chinese Virtual Human Data (CVHD) to Magnetic Resonance Images (MRI) has been proposed and implemented. The algorithm firstly extracts the primary components from both CVHD and MR images by wavelet-based multi-resolution analysis, then mapping colors from CVHD to MRI between these primary components with the similar characters. Finally these colors in MRI will be transferred to all pixels of the MRI according to their characters. Several experiment results have been reported, which have confirmed the effectiveness of this new color-transferring scheme.

Keywords. Medical Image Processing, CVHD, Color MRI, Wavelet Transform, Multi-resolution Analysis.

1. Introduction

Magnetic resonance imaging (MRI) is a imaging method primarily used to demonstrate alterations of tissues in living organisms. Current MRI technology displays images as gray tone images. Because human eyes are more sensitive to different colors than to different gray tones, many scientists are working hard to have color MRI. A color MRI would significantly improve both the visualization and the parcellation of structures visualized by MRI, which enable more effective diagnosis.

The most popular and simplest way to have a color MRI is to assign individual red(R), green(G), and blue(B) channels to each pixel to separately encode three co-registered images with different contrasts into a single composite pseudo-color image[2][3][4]. This basic idea has several varieties but all varieties belongs to either a pseudo-color methodology or a semi-natural color composite MRIs[5][6][7], shown below in figure 1.

The work was supported by both Science and Technology Development Fund of Macao SAR (No. 001/2005/A) and the National Natural Science Foundation of China (No. 30470487).

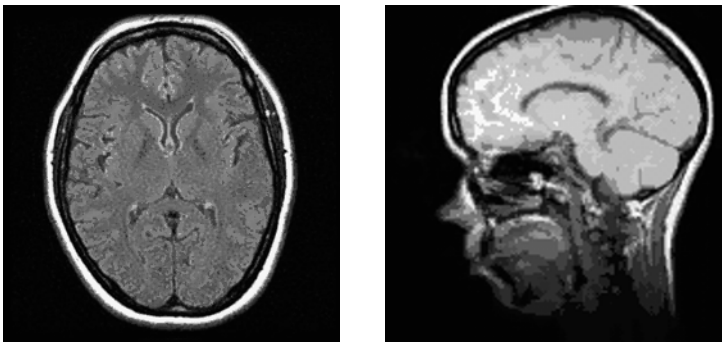

(a) (b)

FIGURE 1. Pseudo color images from [2](left) and [4](right).

Another way of creating a colored MRI is to calculate the natural colors using other digital images of the same object. An algorithm has been proposed and implemented to transfer colors from the full-color cross-sections of the visible human datasets to the MRIs[8][9].In this approach, the MRI are transformed to components by independent component analysis(ICA)[10], which enhances physical characteristics of the tissue. The mapping functions for generating color values from independent components are obtained using the radial basis function(RBF)[11] network by training the network with sample data chosen from a visible female data set. Two transferred color MR images from [8] have been showed in figure 2.

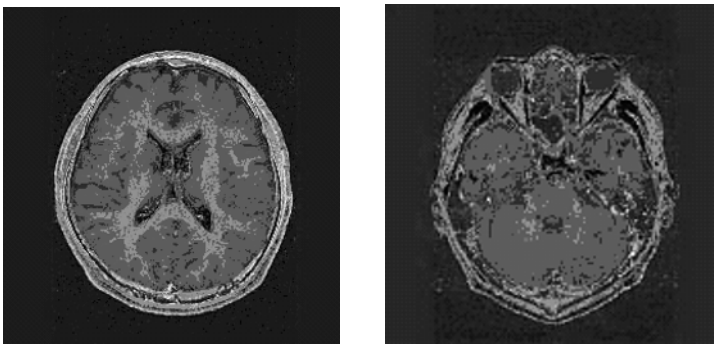

(a) (b)

FIGURE 2. Natural color MR images from [8].

In this paper, a new algorithm based on wavelet transform has been proposed to transfer natural colors from images from the Chinese Virtual Human Data(CVHD)[12] to MRI. Instead of using complex artificial neural networks(RBF),

this new approach uses wavelet transforms to obtain multi-resolution images for both CVHD and MR images. The primary components of both the CVHD and the MR images will be extracted by the clustering of the lower resolution images, and then the transferring of colors from an image of CVHD to several MR images whose primary components have similar characteristics. Finally these colors in the primary components of the MR images will be transferred to all pixels in the MR images based on their characters. Several experiment results have been reported in the paper, which have confirmed the effectiveness of this new color-transferring scheme.

2. Major Steps of the New Algorithm

There are three major parts of the new algorithm: pre-processing, kernel processing, and post-processing, as described step by step below:

I. Preprocessing:

1. Select two corresponding images of the same human body part from the CVHD and the MR image database. Remove the background color[1], and then convert the RGB image from CVHD to a HSV image.
2. Normalize both the CVHD and MR images from step 1 to the same size and similar gray level distribution using gray level histogram transformation.
3. Register the two images of CVHD and MR so that more accurate corresponding spatial locations can be achieved.

II. Kernel Processing:

4. Calculate a series of different resolution images for the results of step 3 through a multilevel 2-D wavelet decomposition and reconstruction.
5. Calculate the primary components from the lower resolution images by clustering.
6. Calculate the statistical features for each primary component obtained from step 5. Setup the corresponding pairs of the primary components between the lower resolution images of CVHD and MR according to their spatial locations.
7. Calculate the same statistical features for both the original(highest) resolution images of CVHD and MR. Copy colors from the original(highest) resolution image of CVHD to the original(highest) resolution MR image pixel by pixel if their features belong to the pair of corresponding primary components.
8. Assign a color to every pixel in the MR image by recursively extending a color to the closest neighbor distance-wise in the feature space.

III. Post-processing:

9. Increase the color contrast of the colored MR image from step 8 through histogram equalization.
10. Smooth/denoise the resulting colored MR image of step 9.

3. Algorithm Implemented

In our research, the algorithm was implemented using Matlab[13]. Symlets Wavelets, which are improved Daubechies Wavelets, have been used to construct multiresolution images. For the colored images of CVHD, wavelet transform was applied to three images–the H, S, and V components of the CVHD images. A total of six levels of different resolution images for each original image have been reconstructed from wavelet decomposition coefficients. Four different color groups have been decided for the representation of the eyes, skin, nervous gray, and nervous white, which means that at least four primary components are needed in both images. The real color of each group and its varieties are calculated from these four primary components. Primary components are obtained from, in our case, the lowest resolution image of the V component of the HSV CVHD image in two steps: first, apply the nearest neighbor clustering, and then pass the component attributes to the other components of the CVHD image. The four primary components of the MR image are also calculated from the lower resolution image, which will significantly reduce the clustering and feature calculation time. The features used in this algorithm are the color values and gray level values combined with the locational and spatial info. The relationships of the corresponding primary components between the CVHD and the MR images, which are color-transferring pairs, are set up according to the similarities of their spatial locations only. The color transferring work is done in two steps: First, the color is transferred from the original CVHD image to the original MR image if both pixels belong to the color transferring component pair; Secondly, colors in the MR image are transferred according to the neighboring color that has the most similar features as the one to be colored. The second step is implemented recursively until all pixels of the MR image have been assigned a color.

4. Experiment Results

The images of the head part of a body have been chosen since we only have corresponding head parts of both the CVHD and the MR images in our testing database. Figure 3 shows the original image of CVHD used in the test with their lower resolution images through the wavelet transform. The original CVHD image is the coloring source image, and the four primary components are obtained from the lowest resolution image. Figure 4 shows the original MR image used in our test with their lower resolution images by the same wavelet transform. The original MR image is the coloring target image and the four primary components are also obtained from its lowest resolution image.

Figure 5 shows several resulting colored MR images calculated using the new algorithm. The first row of figure 5 shows the original MRIs. The second row of figure 5 shows the color MRIs after the first coloring step of the new algorithm. The third row of figure 5 shows the color MRIs after the second coloring step. The fourth row of figure 5 shows the color MRIs after post-processing.

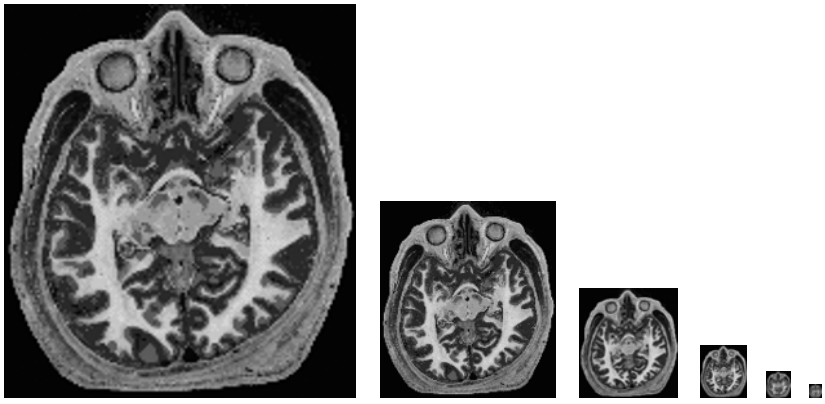

FIGURE 3. The original image of CVHD and its lower resolution images through the wavelet transform.

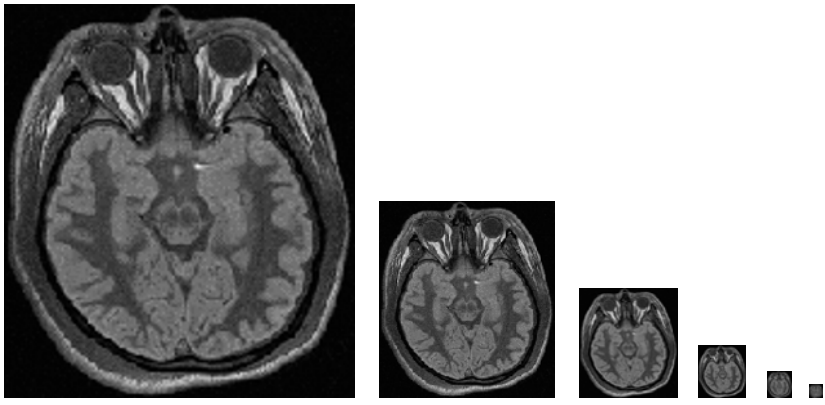

FIGURE 4. The original MR image and its lower resolution images through the wavelet transform

5. Discussions and Conclusions

In this paper, a new algorithm to obtain color MR Images has been proposed. The algorithm does not need the calculations of the independent components of the images and does not need the training mapping function by artificial neural network as proposed in [8]. This new algorithm simply calculates the primary components from the lower resolution images obtained through the wavelet transform, and the set up color mapping functions between corresponding primary components of the lower resolution images. The testing results have shown that color MR images can be obtained in this manner with more nature colors compared with the results

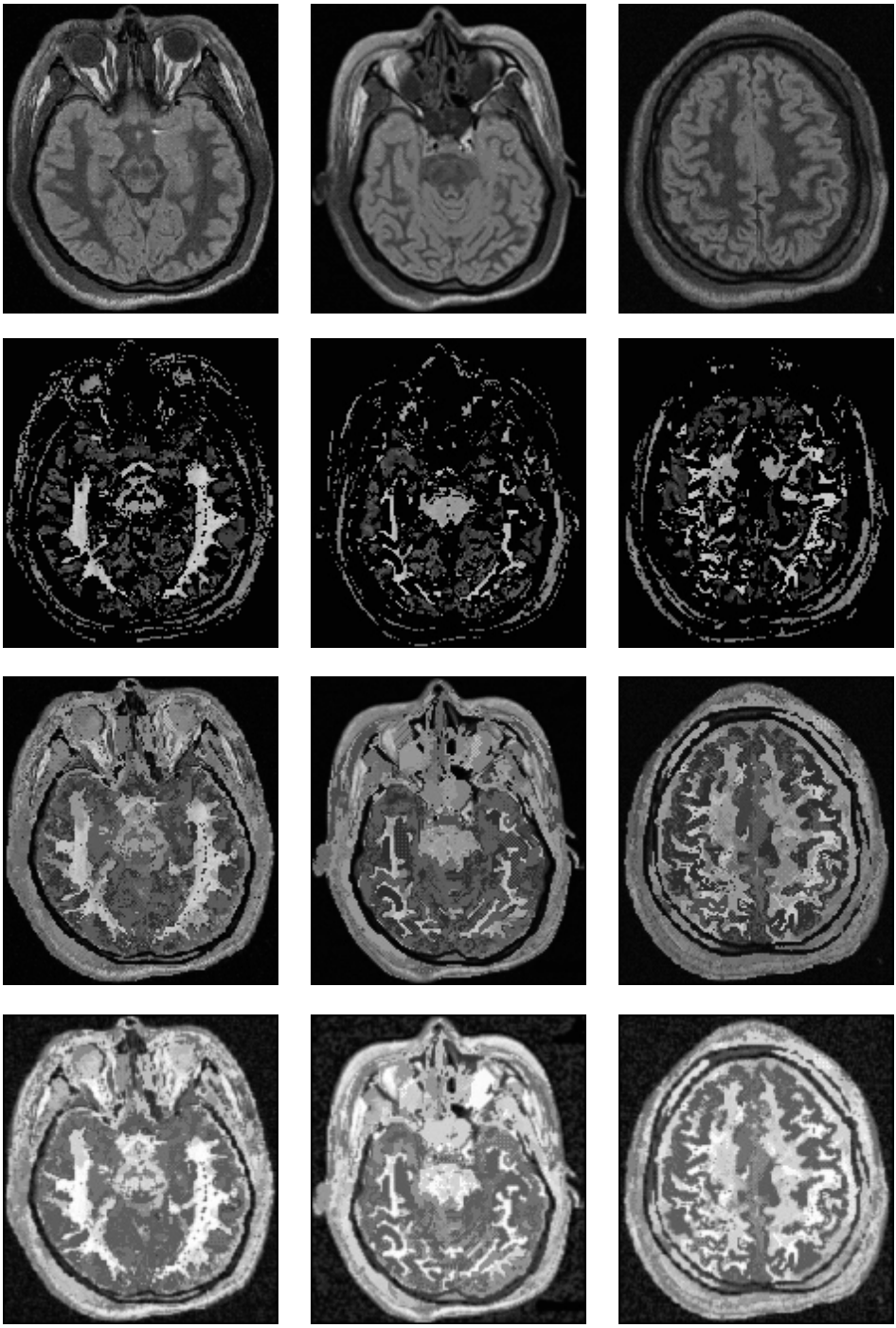

FIGURE 5. The original MR images with their coloring results at various steps

from [8], showed in the figure 2. In other words, this new algorithm can create color MRI more accurate.

All works reported in this paper are just beginning results. There are many issues that can be improved through further research to achieve better coloring results. For instance, instead of using one color source image, using different corresponding color CVHD images for a single MR images will achieve better results, but it also needs more time to calculate the different primary components and such. There is still a long way to go to have a real MRI coloring systems.

Acknowledgement

The MR images and the full color cross-section images of the Chinese Visible Human Project used in our research and shown in this paper are provided by Prof. Zhang Shaoxiang, who is the leader of the *Chinese Virtual Human* research team in the Third Military Medical University in Chongqing, China[12].

We would like to express our sincere appreciation for their help and support.

References

[1] Xiaolin Tian, Yan Zhao, Chengjun Tao, Zesheng Tang, *Background Removal for Color Images Based on Color Components Differences*, Proceedings of the Sixth IASTED International Conference on Signal and Image Processing, August 23-25, Hawaii, USA, 2004.

[2] Kenneth L. Weiss, Qian Dong, William J. Weadock, Robert C. Welsh, and Gaurang V. Shah, *Multiparametric Color-encoded Brain MR Imaging in Talairach Space*, Radiographics. 2002;22:e3-e3.

[3] K.L. Weiss, H. Pan, J. Storrs, W. Strub, J.L. Weiss, L. Jia, and O.P. Eldevik, *Clinical Brain MR Imaging Prescriptions in Talairach Space: Technologist- and Computer-Driven Methods*, AJNR Am. J. Neuroradiol., May 1, 2003; 24(5): 922 - 929.

[4] W.E. Phillips, H.K. Brown, J. Bouza, R.E. Figueroa, *Neuroradiologic MR applications with multiparametric color composite display*, Magn Reson Imaging. 1996;14(1):59-72.

[5] Michael D. Abràmoff, Ad P. G. Van Gils, Gerard H. Jansen and Maarten P. Mourits, *MRI Dynamic Color Mapping: A New Quantitative Technique for Imaging Soft Tissue Motion in the Orbit. Investigative Ophthalmology and Visual Science*, 2000; 41:3256-3260

[6] Bradley M. Hemminger, *Isoluminance: a color technique for visualizing multivariable medical image data*, Proceedings SPIE Vol 1896, pp.325-335.

[7] J. Ward, V. Magnotta, N.C. Andreasen, W. Ooteman, P. Nopoulos, and R. Pierson, *Color Enhancement of Multispectral MR Images: Improving the Visualization of Subcortical Structures*, Journal of Computer Assisted Tomography. 25(6):942-949, November/December 2001.

[8] Shigeru Muraki, Toshiharu Nakai and Yasuyo Kita, *Basic Research for Coloring Multichannel MRI Data*, Proceedings of the 11th IEEE Visualization 2000 Conference, p.33.

[9] Shigeru Muraki, Toshiharu Nakai and Yasuyo Kita, *An Attempt to Develop Color Magnetic Resonance Imaging (MRI) by using Visible Human Data*, The Third Visible Human Project Conference Proceedings 2000.

[10] S. Muraki and T. Nakai, *Independent Component Analysis of multichannel MRI Data*, Proc. ISMRM 2000, 582.

[11] C.M. Bishop, *Neural Networks for Pattern Recognition*, Clarendon Press, 1995.

[12] S.X. Zhang, P. A. Heng et. al., *Creation of the Chinese visible human data set*, The Anatomical Record (Part B: New Anatomist), Vol.275B, 2003, pp.190-195.

[13] Hu Chang Hua et. al., *System Analysis and design based on MATLAB—Wavelet Analysis*, Xidian University Press.

Xiaolin Tian
Faculty of Information Technology
Macau University of Science and Technology,
Taipa, Macao
e-mail: xltian@must.edu.mo

Xueke Li
Faculty of Information Technology
Macau University of Science and Technology,
Taipa, Macao
e-mail: kenry_lee@yahoo.com.cn

Yankui Sun
Department of Computer Science and Technology
Tsinghua University,
Beijing, China
e-mail: syk@tsinghua.edu.cn

Zesheng Tang
Faculty of Information Technology
Macau University of Science and Technology,
Taipa, Macao
e-mail: ztang@must.edu.mo

Wavelet Analysis and Applications
Tao Qian, Mang I. Vai and Xu Yuesheng, Eds.
Applied and Numerical Harmonic Analysis, 389–396

Medical Image Fusion by Multi-resolution Analysis of Wavelets Transform

Xueke Li, Xiaolin Tian, Yankui Sun and Zesheng Tang

Abstract. A novel algorithm for the multimodalities medical images fusion based on wavelet transform has been proposed and implemented. The auto-adaptive weighted coefficients have been calculated recursively to maximize the mutual information between the source image and the result image. Adopting multi-resolution analysis of wavelet transform, we achieved the MRI and CT image fusion. In addition, the new algorithm has been extended to MRI and color image fusion. The experiment results demonstrate that the new algorithm with wavelet transform have better fusion results compared with other mutual information fusion schemes without wavelet transform.

Keywords. Medical image fusion, Mutual information, Multi-resolution analysis, Wavelet transform.

1. Introduction

Medical image fusion is a process of combining the useful features from each of two or more different modalities medical images into a single medical image. In recent years, with the increase of clinic application demands, the research of multi-modality medical image fusion has attracted more and more attention. Just as the radiotherapy plan often benefits from the complementary information in images of different modalities, dose calculation is based on the computed tomography (CT) data, while tumor outlining is often better performed in the corresponding magnetic resonance (MR) scan. For medical diagnosis, CT provides the best information on denser tissue with less distortion, MRI provides better information on soft tissue with more distortion, PET provides better information on blood flow and flood activity with low space resolution, and color image data provides the best integrated information on natural body structure in general. With more available multimodality medical images in clinical applications, the idea of combining

The work was supported by both the Macao Science and Technology Development Fund (No. 001/2005/A) and the National Natural Science Foundation of China (No. 30470487).

images from different modalities has become highly important and medical image fusion has been marked as a new and promising research field.

Several image fusion approaches based on wavelet transforms have already been proposed [1][2][3][4]. Image fusion algorithms based on multi-scale wavelet transforms are also very popular in recent researches [5][6][7]. Existing algorithms for image data fusion are not quite satisfactory for object detection. In order to improve the resolution of the target image and to suppress the detection noise of each sensor, the images are decomposed with wavelet transform, and thus the wavelet coefficients and the approximation coefficients at different scales are obtained. We took the coefficients with large absolute values between the multi-resolution images as the important wavelet coefficients and computed the weighted mean value of the approximation coefficientsThe fusion image can then be obtained using the inverse wavelet transform for the wavelet coefficients and the weighted approximation coefficients.

However, the majority of fusion algorithms employing the wavelet transform have not attempted to acclimatize themselves to the wavelet coefficients based on the mutual information between the multimodality medical images. Specifically, no reports about the medical images fusion between MRI and color images have been found. In our research, the multi-resolution wavelet analysis were implemented for the multimodality medical images, and then in the wavelet transform region, the mutual information for the different weighted coefficient are compared. When the mutual information is maximal, we achieve the best fusion result by taking the corresponding wavelet coefficient through the inverse wavelet transform.

2. New Image Fusion Algorithm

2.1. The Scheme of Fusion

In this research, the image fusion scheme involves six steps recursively: Decompose the input images, which already have their backgrounds removed[8]; Select a fusion strategy; Fuse image F; Calculate the mutual information; Find the maximum of the mutual information; And output the fused image as shown in figure 2.1.

Step 1: Decompose the image A and the image B by forward wavelet transformation. In this case, each image is decomposed into the same level using a periodic discrete wavelet transform. The wavelet transform decomposes each image into low and high-frequency sub-layer images. At a given level, a series of parameter sets of the forward wavelet transformation can be obtained. When the input images are the CT and MRI, the MRI is described as image A and the CT image is described as image B. When the input images are the MRI and color image, the MRI is still described as image A and the color image is described as image B.

Step 2: Select both of the wavelet weighted approximation coefficient a and b. a and b are initialized to 0.5. In addition, a and b are kept so that $a+b=1, 0<a, b<1$.

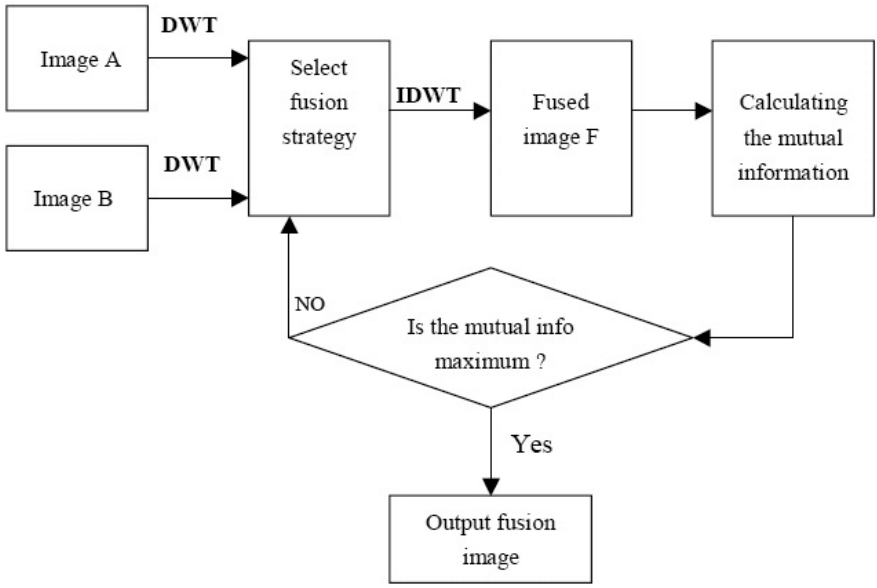

FIGURE 1. Image fusion scheme in this research

Step 3: Obtain the fusion image F by using the inverse wavelet transform incorporating with the selected coefficients as shown in expressions 2.1.

$$C_F(u,v) = aC_A(u,v) + bC_B(u,v) \tag{2.1}$$

In the above expressions, the parameter u is the decomposition vector and the parameter v is the corresponding bookkeeping matrix. $C_A(u,v), C_B(u,v)$ and $C_F(u,v)$ express respectively the wavelet transform coefficient of image A, image B and the fusion image F.

Step 4: Calculate the mutual information between the MRI image and the fusion image F.

Step 5: Compare the value of the latest mutual information with the value of the previous mutual information. Update the values of a and b for the new fused image F. Repeat steps 3 through 5 until a maximum for the mutual information is achieved.

Step 6: Output the fusion image F at the maximal mutual information as the experiment result.

2.2. Evaluation of the Fusion Result

In this research, we propose to use the mutual information(MI) to describe the fusion results. It is known that MI is a basic concept from information theory, measuring the statistical dependence between two random variables or the amount

of information that one variable contains about the other. The mutual information or entropy is widely used in image compression and a large MI of the two medical image pixel pairs shows that the images have been well fused[12][13].

We can calculate the MI according to the following equation[12]:

$$MI_{AB}(x,y) = \sum_{i=0}^{l-1}\sum_{j=0}^{l-1} P_{AB}(x,y)\log(P_{AB}(x,y)/P_A(x)P_B(y))$$

3. Experiment Results

In this section, we report the results of the experiments on fusing MRI and CT and fusing MRI and color images through the proposed image fusion scheme. Figure 2 shows the original CT and MRI images to be fused. Each image is resized to 146 pixels by 164 pixels with 256 gray levels.

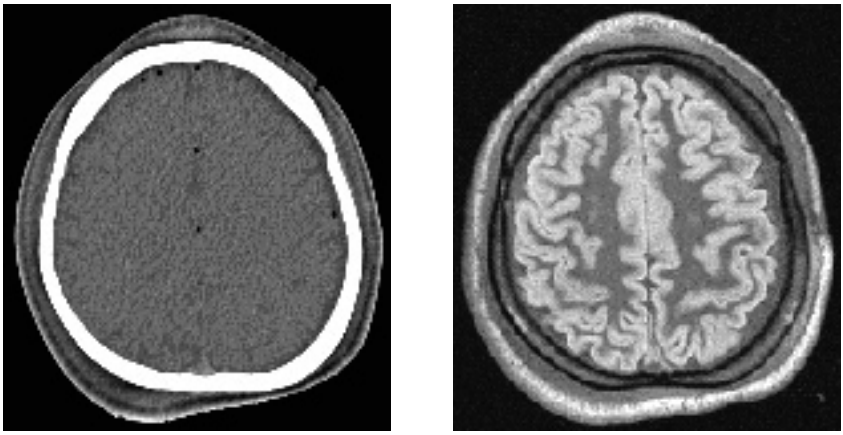

(a) CT image (b) MR image

FIGURE 2. The original CT and MR images

Figure 3(a) shows the fusion result by the mutual information maximum without wavelet transform [13], Figure 3(b) shows the fusion result by the proposed algorithm with the wavelet transform.

Figure 4 shows the original MRI and Color images to be fused. Each image is resized to 256 pixels by 256 pixels with 256 gray levels.

Figure 5(a) shows the fusion result by a MI algorithm without wavelet transform [13]. Figure 5(b) shows the fusion result by our method.

According to expression 2.1, the fusion performance results can are shown in Table 1. From the data in table 1, the advantage of the proposed fusion scheme has been confirmed.

(a) The fused image by original Max MI algorithm[12]

(b) The fused image by the algorithm of this paper

FIGURE 3. The fused image results of two different algorithms

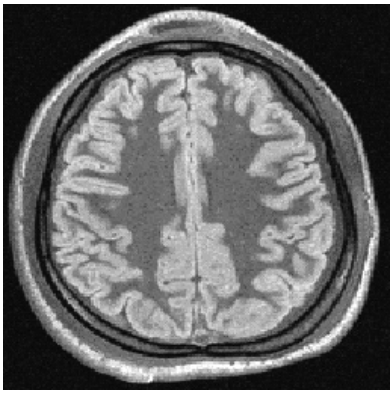

(a) MR image

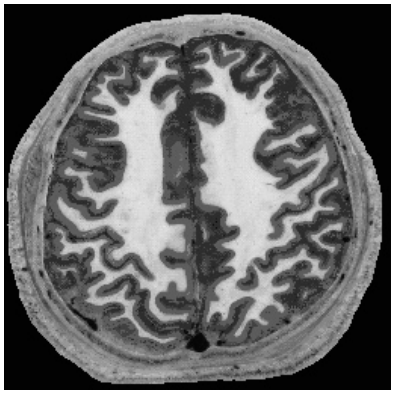

(b) Color image

FIGURE 4. The original multi-modalities medical images

TABLE 1. The fusion performance assessing results

MRI and Fusion result image	Fig2(b) and 3(a)	2(b) and 3(b)	4(a) and 5(a)	4(a) and 5(b)
Mutual information MI_{AB}(x, y)	3.2667	3.5746	4.3292	4.4067

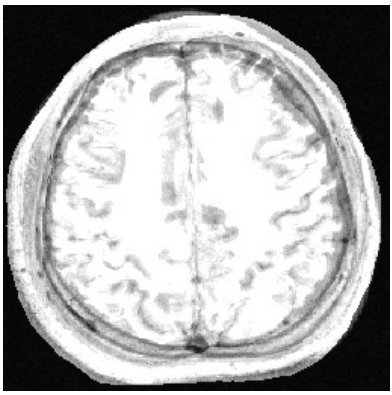

(a) The fused image by original algorithm of the Max. MI between the MRI and Color images

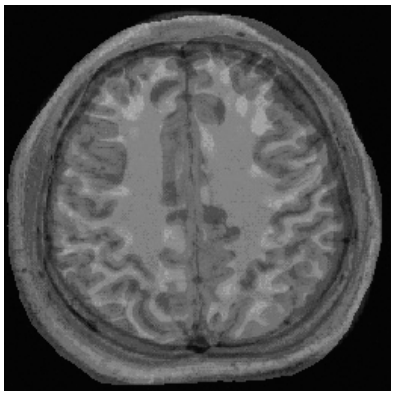

(b) The fused image by the algorithm of this paper

FIGURE 5. The fused image results of two different algorithms

4. Conclusions

A new image fusion algorithm based on wavelet transform to reach the maximum mutual information has been described and applied to the fusion of multimodality medical images. Our image fusion algorithm shows better results compared to the algorithm of maximal mutual information without wavelet transform [12],[13];

This algorithm can also be used for the fusion of MRI and color images.

Acknowledgement

The CT/MR images and the full color cross-section images of the Chinese Visible Human Project used in our research and shown in this paper are provided by Prof. Zhang Shaoxiang, who is the leader of the *Chinese Virtual Human* research team in the Third Military Medical University in Chongqing, China[11].

We would like to express our sincere appreciation for their help and support.

References

[1] Z. Zhang and R. S. Blum, *A categorization and study of multiscale-decomposition-based image fusion schemes*, Proceedings of the IEEE, vol. 87(8), pp. 1315–1328, August 1999.

[2] L. J. Chipman, T. M. Orr, and L. N. Graham, *Wavelets and image fusion*, in Proc. SPIE, vol. 2569, pp. 208–219, 1995.

[3] H. Li, B. S. Manjunath and S. K. Mitra, *Multisensor image fusion using the wavelet transform*, Graphical Models and Image Processing, vol. 57, pp. 235–245, May 1995.

[4] Paul Hill, Nishan Canagarajah and Dave Bull, *Image Fusion using complex wavelets*, BMVC, pp.478-496, 2002.

[5] Zhao Ruizhen, Xu Long and Song Guoxiang, *Muliscale image data fusion with wavelet transform*, Journal of computer-aided design & computer graphics, 361-364,vol 4(14), April 2002.

[6] Yan Hao, Hou Zengguang and Tan Min, *Multi-scale Image Data Fusion Based on Wavelet Transform*, computer engineering and applications, vol. 134, pp.131-134, 2003.

[7] Guihong Qu, Dali Zhang and Pingfan Yan, *Medical image fusion by wavelet transform modulus maxima*, OSA, pp.184-190, 2001.

[8] Xiaolin Tian, Yan Zhao, Chengjun Tao, Zesheng Tang, *Background Removal for Color Images Based on Color Components Differences*, Proceedings of the Sixth IASTED International Conference on Signal and Image Processing, August 23-25, Hawaii, USA, 2004.

[9] L. Rabiner, *A tutorial on hidden Markov models and selected applications in speech recognition*, Proceedings of the IEEE, vol. 77, pp.257–285, February 1989.

[10] Guixi Chang and Wanhai Yang,*A Wavelet-Decomposition-Based Image fusion Scheme and ITS Performance Evaluation*, ACTA Automatica Sinica, vol 6(28), November 2002

[11] S. X. Zhang, P. A. Heng and et al., *Creation of the Chinese visible human data set*, The Anatomical Record (Part B: New Anatomist), Vol.275B, 2003, pp.190-195.

[12] Josien P. W. Pluim, J. B. Antoine Maintz and Max A. Viergever, *Mutual information based registration of medical images: a survey*, IEEE TRANSACTIONS ON MEDICAL IMAGING, VOL. XX, NO. Y, MONTH 2003.

[13] Zhou yongxin and Luo Shuqian, *Medical Image Registration Based on Mutual Information of Feature Points*, Journal Of Computer-Aided Design & Computer Graphics, vol.14.July 2002.

Xueke Li
Faculty of Information Technology
Macao University of Science and Technology, Macao
Taipa, Macau
e-mail: kenry_lee@yahoo.com.cn

Xiaolin Tian
Faculty of Information Technology
Macao University of Science and Technology, Macao
Taipa, Macau
e-mail: xltian@must.edu.mo

Yankui Sun
Department of Computer Science and Technology
Tsinghua University,
Beijing, China
e-mail: syk@tsinghua.edu.cn

Zesheng Tang
Faculty of Information Technology
Macao University of Science and Technology, Macao
Taipa, Macau
e-mail: ztang@must.edu.mo

Wavelet Analysis and Applications
Tao Qian, Mang I. Vai and Xu Yuesheng, Eds.
Applied and Numerical Harmonic Analysis, 397–405

Salient Building Detection from a Single Nature Image via Wavelet Decomposition

Yanyun Qu, Cuihua Li, Nanning Zheng,
Zejian Yuan and Congying Ye

Abstract. We describes how wavelet decomposition can be used in detecting salient building from a single nature image. Firstly, we use Haar wavelet decomposition to obtain the enhanced image which is the sum of the square of LH sub-image and HL sub-image. Secondly, we separate the candidates of building from the background based on projection profile. Finally, we discriminate the building by Principle Component Analysis(PCA) in RGB color space. The proposed approach has been tested on many real-world images with promising results.

Mathematics Subject Classification (2000). Primary 99Z99; Secondary 00A00.
Keywords. Salient building detection, wavelet decomposition, PCA.

1. Introduction

Man-made structure detection is important in many applications such as automatic navigation, virtual reality, image understanding etc. But there are some difficulties in automatic detection of building. Firstly, there are lots of clutters in the natural scene image, and the edge detection is very noisy. This make it complicate to separate the building from background. Secondly, unlike the aerial views of buildings, the realistic view is unconstrained which makes it difficult to use predefined models or model-specific properties in detection. Finally, it is difficult to represent building. Building detection is an active research field recently, which can be classified as detection from aerial images and from ground view images. For structure detection of buildings from aerial images, the state-of-art approaches mainly use hypothesis of the roof presence, the low-level image information such as edges, lines, and junctions, and as well as use other information

The work is supported by the Chinese National Nature Science Foundation No.**60205001** and the Foundation of Creative Research Group Programming No.**60021302**.

such as illumination, shadow, height, and DEM[1][2][3][4][5][6][7] . There are also some works about building detection from a building facade image. In [8] a perception grouping based method is used to detect building for image retrieval, and in [9] a model of multiscale random field is proposed to detect building. The disadvantages of these methods are the computing complexity of either line detection or line classification.

We propose a novel approach to detect the salient building which is distinct because of its height and other features. Firstly Haar wavelet decomposition is used to obtain four sub-images: LL sub-image, LH sub-image, HL sub-image, HH sub-image. We use LH sub-image and HL sub-image to enhance the image. Secondly, we propose a projection profile based approach to extract building candidates. Finally, the salient building is discriminated by applying Principle Component Analysis(PCA) in RGB color space.

The organization of this paper is as follows. In section 2 we briefly review two dimension multi-resolution analysis. In section 3 we proposed the wavelet-based segmentation method. Principle component analysis(PCA) in RGB color space is used to discriminate the building in section 4, and conclusion is given in the last section.

2. Review of 2-D Multi-resolution Analysis

Wavelet transformation is popular in 1990s and is widely used in signal processing, image processing and analysis, image compression and coding etc. $L^2(R^2)$ can be constructed by the separable wavelet orthogonal basis which are the product of the 1-D scaling function and the 1-D wavelet function. Let $\{V_j\}_{j\in \mathrm{Z}}$ be the sequence scaling subspace in $L^2(R)$, and $\{V_j^2\}_{j\in \mathrm{Z}}$ which are in space $L^2(R^2)$ can be constructed by the tensor product space $V_j^2 = V_j \otimes V_j$. Let $\{W_j^2\}_{j\in \mathrm{Z}}$ be the wavelet sequence subspace, so $W_j^2 = (V_j^2)^{\perp}$ and $V_j^2 = V_{j+1}^2 \oplus W_{j+1}^2$. The following theorem gives the fundamental theory of constructing the orthonormal bases of $L^2(R^2)$.

Theorem 2.1. [10]*Let ϕ denote the scaling function, ψ denote the corresponding the wavelet function in $L^2(R)$. Define the following wavelet function:*

$$\psi^1(x) = \phi(x_1)\psi(x_2). \tag{2.1}$$

$$\psi^2(x) = \psi(x_1)\phi(x_2) \tag{2.2}$$

$$\psi^3(x) = \psi(x_1)\psi(x_2) \tag{2.3}$$

Let

$$\psi_{j,n}^k(x) = \frac{1}{2^j}\psi^k(\frac{x_1 - 2^j n_1}{2^j}, \frac{x_2 - 2^j n_2}{2^j})$$

where $1 \le k \le 3$. The function system $\{\psi_{j,n}^1, \psi_{j,n}^2, \psi_{j,n}^3\}_{n\in \mathrm{Z}^2}$ are the orthonormal basis in W_j^2, and $\{\psi_{j,n}^1, \psi_{j,n}^2, \psi_{j,n}^3\}_{(j,n)\in \mathrm{Z}^3}$ are the orthonormal basis in $L^2(R^2)$.

The three wavelet functions extract the image details at different scale and direction. From equ(2.1), (2.2), (2.3), we obtain that

$$\hat{\psi}^1(w_1, w_2) = \hat{\phi}(w_1)\hat{\psi}(w_2) \tag{2.4}$$

$$\hat{\psi}^2(w_1, w_2) = \hat{\psi}(w_1)\hat{\phi}(w_2) \tag{2.5}$$

$$\hat{\psi}^3(w_1, w_2) = \hat{\psi}(w_1)\hat{\psi}(w_2) \tag{2.6}$$

The magnitude $\hat{\psi}^1(w_1, w_2)$ emphasizes the details which has low frequency in horizontal direction and high frequency in vertical direction, the magnitude $\hat{\psi}^2(w_1, w_2)$ emphasizes the details which has high frequency in horizontal direction and low frequency in vertical direction, the magnitude $\hat{\psi}^3(w_1, w_2)$ emphasizes the details which has high frequency in both directions.

3. Extraction of Building Candidates via Wavelet Decomposition

There are many methods to segment regions of interest which can be classified as edge-based method and region-based method. However the performance is not generally because of the variance of image noise, illumination and building texture. To improve the performance of building detection, we propose a novel approach which is based on wavelet decomposition.

The wavelet decomposition can break down an image into four sub-images:

LL sub-image: Both horizontal and vertical directions have low frequency.

LH sub-image: The horizontal direction has low frequency, and the vertical one has high-frequency.

HL sub-image: The horizontal direction has high frequency, and the vertical one has low-frequency.

HH sub-image: Both horizontal and vertical directions have high frequency.

The building is detected from a ground view image. Since the wall and windows have regular shape in building facade, we separate building candidates by using an image projection profile based method. As mentioned in [11], LH-image is the result that the image is convolved by a lower-pass filter along the horizontal direction and by a higher-pass filter along the vertical direction. So the horizontal detail is enhanced while the vertical detail is smoothed. The result of the HL sub-image is opposite to that of the LH one. The vertical detail is enhanced while the horizontal detail is smoothed. This operation on the image is just like edge detection.By denoting the LH sub-image by $H_2(x, y)$ and the HL sub-image by $V_2(x, y)$, we construct an enhanced image as

$$B(x, y) = H_2(x, y)^2 + V_2(x, y)^2 \tag{3.1}$$

Although many orthogonal wavelets meet with our needs, we use the simplest orthogonal wavelet–Haar wavelet which is discontinuous and resemble the step function. It was defined as

$$h(t) = \begin{cases} 1, 0 \le t < \frac{1}{2} \\ -1, \frac{1}{2} \le t \le 1 \\ 0, others \end{cases} \tag{3.2}$$

and

$$h_{j,k}(t) = 2^{-\frac{1}{2}} h(2^{-j}t - k), j, k \in z \tag{3.3}$$

It is easy to obtain from equ(3.3)

$$h_{j,k}(t) = \begin{cases} 2^{-\frac{j}{2}} & 2^j k \le t < (2k+1)2^{j-1} \\ -2^{-\frac{j}{2}} & (2k+1)2^{j-1} \le t < (k+1)2^j \\ 0 & others \end{cases} \tag{3.4}$$

From equ(3.2) (3.3) (3.4), it's obvious that Haar wavelet functions act as the gradient-based edge detection, while the wavelets do not have the property. Furthermore Haar wavelet makes the computation easier. We compare the performance of Haar wavelet and other orthogonal wavelets on the synthesized image which contains a white rectangle in the black background. Due to the space limitation, we only show the result of **db4** wavelet and Haar wavelet in Figure 1. It is clear that the horizontals and verticals in the enhanced image are shifted when we use **db4** wavelete decomposition, while Haar wavelet does not cause the problem. Testing results demonstrate that Haar wavelet is more suitable to building detection. We use one level Haar wavelet decomposition, and select HL sub-image and LH sub-image to compute the enhanced image in order to improve the computational efficiency. An example using Haar wavelet decomposition for enhanced image is shown in Figure 2.

In the following, we explain the extraction of the building candidate based on projection profile. The image edges within the building of the same column or row are accumulated at the same location of the projection profile histograms. There exist high frequency peaks in the horizontal and vertical histograms where the building located. The building candidates can be separated based on the vertical projection profile and horizontal projection profile. Because there exist image textures other than buildings in the image, we should choose appropriate threshold values to select those peaks that corresponds to the horizontal and vertical positions of buildings in the image. The projection profile based approach is as follows.

Step 1. Denoise the image B(x,y) to make the background flatter.

Step 2. Compute the amplitude projections of $B(x, y) \in R^{m \times n}$ along its row, that is

$$X_r(x) = \sum_{y=1}^{m} B(x, y), 1 \le x \le n$$

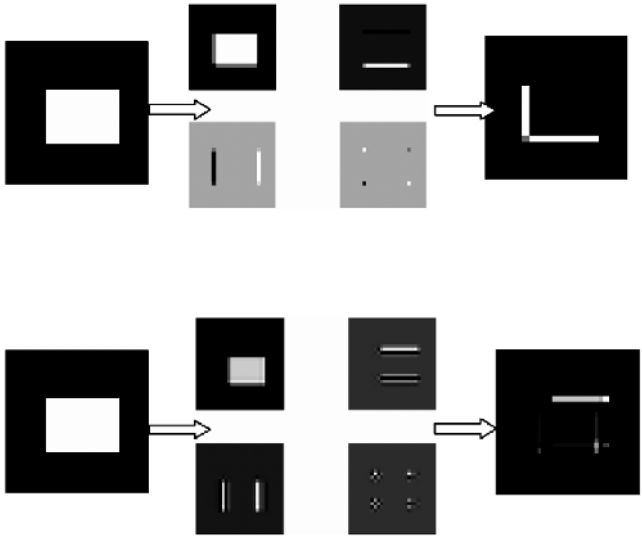

FIGURE 1. The comparison between Haar wavelet decomposition and **db4** wavelet decomposition. The first row is the result after Haar wavelet decomposition and the second row is the result after **db4** wavelet decomposition. In each row, the left is original image, the middle is the sub-images, and the right is the enhanced image.

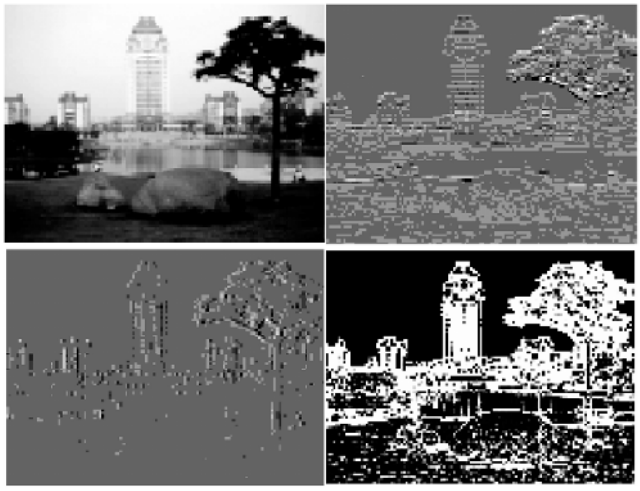

FIGURE 2. The sub-images and enhanced image of a building image. From left to right and up to down, they are the LL sub-image, LH sub-image, HL sub-image, and the enhanced image.

Step 3. Find the first non-zero value in the array $X_r(x)$, and obtain the corresponding index which is the upper bound of buildings, that is

$$upper = \min_x\{x\,|X_r(x) > 0\,\}$$

Delete the part above the upper bound, and obtain the image $Bcut(x, y)$.

Step 4. Find the non-zero value in every column from top to down in $Bcut(x, y)$, and obtain the corresponding index array, that is

$$S(y) = \min_x\{x\,|Bcut(x, j) > 0\ , j = y\}, 1 \le y \le m.$$

Step 5. Find the maximum and minimum in array $S(y)$, and compute the mean as the lower bound, that is

$$lower = (\max\{S(y)\} + \min\{S(y)\})/2.$$

Delete the part below the lower, and denote the image as $Btop(x, y)$

Step 6. Compute the amplitude projections of $Btop(x, y)$along its column, that is

$$X_c(y) = \sum_{x=1}^{n-upper-lower} Btop(x, y), 1 \le y \le m,$$

and cluster the indices whose corresponding values are non-zero, to obtain the left bound $Bleft(i)$ and the right bound $Bright(i)$, the length of the array $Bleft(i)$ is the number of building candidates.

Step 7. Find the region $region(i)$in the original image corresponding region in image B(x,y).

Remark: From step 1 to step 5, the operation is to separate the high buildings from the sky and the low building group. From step 6 to step 7, the operation is to separate salient building candidates from each other. Figure 3 illustrates the result of the approach.

4. Building Discrimination by PCA in RGB Color Space

From section 3, we obtain building candidates which may be building or not.We need to discriminate buildings in the next step. A hypothesis is generated that the desired region can be classified into two classes one of which is building, the other of which is tree, because we believe that the hypothesis can cover a significant fraction of the building image. In order to make the discrimination problem simple, we consider the negative sample, i.e. trees. We compute the principle color of the tree color samples and compare the color of building candidates with it. Let $\{A_i\}, 1 \le i \le m$, be the color vector generated from the desired region, where m is the number of the points which correspond to separated region, and the mean vector is denoted by μ . The new vectors are given by

$$\bar{A}_i = A_i - \mu, i = 1, 2 \cdots m \tag{4.1}$$

FIGURE 3. The segmentation result. The building candidates are indicated by rectangle.

The covariance matrix is given by

$$Cov = A^T A$$

where $A = [\bar{A}_1^T, \bar{A}_2^T, \cdots \bar{A}_m^T]^T$.

Compute the eigenvector corresponding to the largest eigenvalue of the matrix Cov, denoting it by the principle color in desired region, i.e.,

$$Cov * V = \lambda_{\max} V \tag{4.2}$$

The principle color of tree sample was denoted by V_{mod}. The color similarity between the model and the desired region is measured by the city block distance, and the desired region is classified as the building if the distance is larger than a threshold σ i.e.,

$$flag(i) = \begin{cases} 0 & \| V - V_{\text{mod}} \| < \sigma \\ 1 & others \end{cases}$$

where $flag(i)$ denote the class label of the desired region.

Experiments are performed on real-world images using matlab 6.5 on Intel P4 2.4G platform. The average time taken in processing an 372×496 image is no more than 2s, which is faster than that in [9]. Figure 4 shows some examples of building detection from a few of real ground view images.

5. Conclusion

This paper focuses on detecting salient building from a ground view building image. Wavelet decomposition and projection profile based approach are proposed to separate the building from the background. PCA is implemented in the RGB color space in order to discriminate the building. Real-world images are used to

FIGURE 4. Building detection example. The detected building is indicated by red rectangle

evaluate the proposed method, and the experimental results demonstrate that the proposed method is feasible and effect.

References

[1] D.M. McKeown, *Toward Automatic Cartographic Feature Extraction, Mapping and Spatial Modelling for Navigation.* L.F. Pau, ed., NATO ASI series **65** (1990), 149-180.

[2] R.B.Irvin and D.M. McKeown, *Methods for Exploiting the Relationship Between Buildings and Their Shadows in Aerial Imagery.* IEEE Trans. Systems, Man, and Cybernetics**19** (1989), 1564-1575.

[3] J.C. McGlone and J.A. Shufelt, *Projective and Object Space Geometry for Monocular Building Extraction.* Proc. IEEE Conf. Computer Vision and Pattern Recognition, 2000, 54-61.

[4] J.A. Shufelt, *Exploiting Photogrammetric Methods for Building Extraction in Aerial Images.* Int'l Archives of Photogrammetry and Remote Sensing**XXXI, B6/S** (1996), 74-79.

[5] J.A. Shufelt, *Projective Geometry and Photometry for Object Detection and Delineation.* PhD thesis, Computer Science Dept., Carnegie Mellon Univ., available as Technical Report CMU-CS-96-164, 29 July 1996.

[6] C. Lin, R. Nevatia, *Building Detection and Description from a Single Intensity Image.* Computer Vision and Image Understanding **72** (1998),101-121.

[7] H. Kauppinen, T. Seppanen, M. Pietikainen, *An experimental comparison of autoregressive and Fourier-based descriptors in 2D shape classi1cation.* IEEE Trans. Pattern Anal. Mach. Intell **17(2)** (1995), 201-207.

[8] A. Iqbal and J.K.Aggarwal, *Applying perceptual grouping to content-based image retrieval:Builing images.* In Proc. IEEE Int. Conf. CVPR **1** (1999), 42-48.

[9] S. Kumar and M. Hebert, *Man-made Structure Detection in Natural Images using a Causal Multiscale Random Field.* In Proc. IEEE Int. Conf. on CVPR**1** (1999), 119-126.

[10] S.Mallat, *A Wavelet Tour of Signal Processing.* 2rd Edition, Acadamic Press, 1999.

[11] Y.Y.Tang, H.Ma,J.Liu,B. Li, and D. Xi, *Multiresolution Analysis in Extraction of Refoerence Lines from Documents with Gray Level Background.* IEEE Trans. Pattern Anal. Mach. Intell **19(8)** (1997), 921-926.

Yanyun Qu
Institute of Artificial Intelligence and Robotics, Xi'an Jiaotong University
Xi'an,710049
Department of Computer Science, Xiamen University
P.R.China
e-mail: yyqu@xmu.edu.cn

Cuihua Li
Department of Computer Science, Xiamen University
P.R.China
e-mail: chli@xmu.edu.cn

Nanning Zheng
Institute of Artificial Intelligence and Robotics, Xi'an Jiaotong University
P.R.China
e-mail: nnzheng@mail.xjtu.edu.cn

Zejian Yuan
Institute of Artificial Intelligence and Robotics, Xi'an Jiaotong University
P.R.China
e-mail: zjyuan@aiar.xjtu.edu.cn

Congying Ye
Department of Computer Science, Xiamen University
P.R.China

Wavelet Analysis and Applications
Tao Qian, Mang I. Vai and Xu Yuesheng, Eds.
Applied and Numerical Harmonic Analysis, 407–417

SAR Images Despeckling via Bayesian Fuzzy Shrinkage Based on Stationary Wavelet Transform

Yan Wu, Xia Wang and Guisheng Liao

Abstract. An efficient despeckling method is proposed based on stationary wavelet transform (SWT) for synthetic aperture radar (SAR) images. The statistical model of wavelet coefficients is analyzed and its performance is modeled with a mixture density of two zero-mean Gaussian distributions. A fuzzy shrinkage factor is derived based on the minimum mean error (MMSE) criteria with bayesian estimation. In this case, the ideas of region division and fuzzy shrinkage are adopted according to the interscale dependencies among wavelet coefficients. The noise-free wavelet coefficients are estimated accurately. Experimental results show that our method outperforms the refined Lee filterwavelet soft thresholding shrinkage and SWT shrinkage algorithms in terms of smoothing effects and edges preservation.

Keywords. SAR image despeckling, fuzzy shrinkage factor, MMSE, regions division, Bayesian estimation, SWT.

1. Introduction

The synthetic aperture radar (SAR) generates images that are severely degraded by speckle, a type of multiplicative noise. Due to its granularity in an image, speckle noise makes it very difficult to visually and automatically interpret SAR data. Therefore, reduction of the speckle noise is important in most detection and recognition systems where speckle is present.
In the past ten years, many algorithms have been developed to suppress speckle noise in order to facilitate postprocessing tasks. The earliest method is multilook

This work was supported by the National Defence Foundation (51431020204DZ0101) and the Postdoctoral Science Foundation of China (J63104020156).

processing, but this method sacrifices the spatial resolution. Later, the spatial filters which are based on the minimum mean square error (MMSE) criteria are traditionally used, such as the Lee-filter[1], the Kuan-filter[2,3] and the Frost-filter[4], but an insufficient existing in these techniques is that the region with edges or strong textures are blurred after filtering. Then some statistical adaptive filters for speckle reduction appeared, they are capable of adapting the size or the shape of the local window according to the underlying structural features. Examples of such filters are the refined-Lee filter[5] and Epos filter[6], etc. They outperform the former filters. Recently, there has been considerable interest in using the wavelet transform as a powerful tool for recovering noisy data. As an outcome of the wavelet theory, despeckling in the domain where SAR images are defined by detail coefficients of the noisy image, either hard or soft, are firstly proposed by Donoho[7]. These methods involve a preprocessing step consisting of a logarithmic transform to convert the multiplicative noise into the additive noise. The key point in these thresholding techniques is the selection of an appropriate threshlold. If its value is too small, the recovery image will remain noisy. On the other hand, if its value is too large, artifacts like pseudo-Gibbs oscillations may appear near discontinuities in the reconstructed signal. Another approach involves the stationary wavelet transform (SWT). F.Argenti et al. applies a local linear MMSE estimator in the stationary wavelet transform domain[8]. The method avoids using the logarithmic transform, but it does not utilize statistical assumptions about the wavelet coefficients. This is a drawback in cases where good statistical models exist. Furthermore, the filter performs the same in wavelet domain.

In this paper, we propose an efficient SWT despeckling method based on bayesian estimation using MMSE criteria. We avoid using the log-transform. Firstly, we analyze the statistical properties of the wavelet coefficients, and model the coefficients with a mixture density of two zero-mean Gaussian distributions. Then we derive a bayesian wavelet shrinkage factor based on MMSE criteria. Finally, according to the interscale dependencies of the wavelet coefficients, we adopt fuzzy shrinkage to the factor and divide different regions among the coefficients. Different methods are used for different regions. The algorithm achieves good performance.

2. The Statistical Model in SWT Domain

2.1. SWT

SWT[9] is a special version of the DWT that has preserved translation invariance. This means that a translation of the original signal does not cause a translation of the corresponding wavelet coefficients. Instead of subsampling, the SWT utilizes recursively dilated filters in order to halve the bandwidth from one level to another. At scale 2^j the filters are dilated by inserting 2^{j-1} zeros between the filter coefficients of the prototype filters. This is performed in order to reduce the bandwidth by a factor of two from one level to another.

$$h_k^j = \begin{cases} h_{k/2^j} & \text{if } m \in Z \\ 0 & \text{else} \end{cases} \tag{2.1}$$

$$g_k^j = \begin{cases} g_{k/2^j} & \text{if } m \in Z \\ 0 & \text{else} \end{cases} \tag{2.2}$$

where $\{h_k\}$ and $\{g_k\}$ are low-pass and high-pass filters, respectively.
For images, image rows and columns are then filtered separately. Filtering equations to obtain the level $j+1$ from the level j are the following (where (a,b) is for the pixel position):

$$A_{X,j+1}(a,b) = \sum_{k,m} h_k^j h_m^j A_{X,j}(a+k, b+m) \tag{2.3}$$

$$W_{X,j+1}^h(a,b) = \sum_{k,m} g_k^j h_m^j A_{X,j}(a+k, b+m) \tag{2.4}$$

$$W_{X,j+1}^v(a,b) = \sum_{k,m} h_k^j g_m^j A_{X,j}(a+k, b+m) \tag{2.5}$$

$$W_{X,j+1}^d(a,b) = \sum_{k,m} g_k^j g_m^j A_{X,j}(a+k, b+m) \tag{2.6}$$

where $A_{X,j}$ is the approximation of the original image at the scale 2^j, giving the low-frequency content. Images details are contained in three high-frequency images $W_{X,j}^h$, $W_{X,j}^v$, $W_{X,j}^d$ corresponding to horizontal, vertical and diagonal detail orientations, respectively. Since SWT does not include downsampling operations, it is a redundant transform.

2.2. The Statistical Model in SWT Domains

Wavelet coefficients of SAR images typically exhibit strong non-Gaussian statistics. The correct choice of priors for wavelet coefficients is certainly a very important factor. Several different priors have been considered for the wavelet coefficients. In [10], wavelet coefficients are modeled as a generalized Gaussian distribution (GGD), which matches well the histograms of typical SAR images. However, in the bayesian estimation process, there usually does not exist a closed-form solution for the estimate of noise-free wavelet coefficients when the signal prior is described by the GGD. Among alternative methods, a mixture density of two zero-mean Gaussian distributions has been proposed due to its relatively simple form and high accuracy in modeling the distribution of wavelet coefficients[11]. One mixture component is corresponding to significant coefficients (representing "homogeneity"), and the other is corresponding to significant coefficients (representing "heterogeneity").
For SAR imagery, we have a multiplicative speckle model: $X = YF$, where X is the noisy observation, Y is the noise-free signal and F is normalized speckle random variable with unit mean. Assuming that W_X represents the noisy wavelet coefficients, its mixture probability density function (pdf) is given by

$$p_{W_X}(w_x) = \sum_{k=0,1} p(s=k) p(w_x | s=k) \tag{2.7}$$

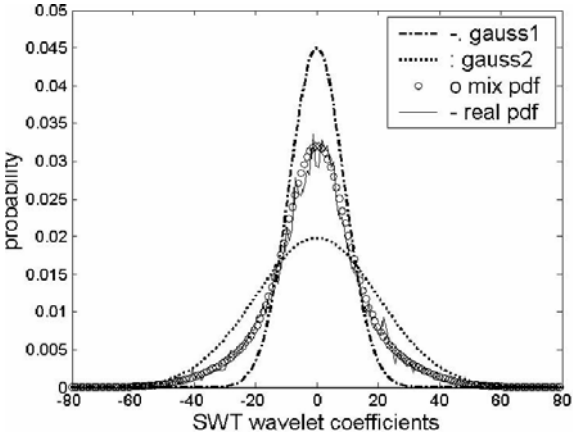

FIGURE 1. Histogram of SWT wavelet coefficients and the Mixture-Gaussian model.

where $p(w_x|s = k)$ is a zero-mean Gaussian distribution and $S = 0$ or 1 represents each Gaussian component in the mixture distribution.
We demonstrate one typical example in Figs. 1 to show the performance of the mixture-Gaussian model in matching the distribution of SWT wavelet coefficients of a real SAR image. In the figure, the mixture Gaussian distribution is labeled as "mix pdf" and two pure Gaussian components are labeled as "gauss1" and "gauss2", respectively. As the figure shows, the mixture-Gaussian model provides a fairly accurate approximation to the distribution of wavelet coefficients of real SAR image.

3. Bayesian Fuzzy Wavelet Estimate

3.1. Bayesian Wavelet Estimation

The wavelet decomposition operation can be written as

$$W_X = W[X] = W[YF] = W[Y] + W[Y(F-1)] = W_Y + W_N \tag{3.1}$$

where W_N is an additive signal-dependent noise. Shrinkage estimate of the noise-free wavelet coefficient is $\hat{W}_Y = \eta W_X$, where η is the shrinkage factor. Based on the MMSE criteria, the optimal shrinkage factor η' is obtained by minimizing the mean square error between $\hat{W}_Y$ and W_Y

$$\eta' = \arg\min_{\eta} E[(\hat{W}_Y - W_Y)^2] \tag{3.2}$$

which has the MMSE solution in the form of

$$\eta' = \frac{E[W_X^2] - E[W_X W_N]}{E[W_X^2]} \tag{3.3}$$

To calculate the η, it is necessary to estimate all unknown parameters in Eq.(10). Based on a mixture-Gaussian model of wavelet coefficients, the MMSE estimate of noise-free wavelet coefficients $\hat{W}_Y$ is

$$\hat{W}_Y = \sum_{k=0,1} p(s=k|w_x)\frac{\sigma^2_{W_X} - \sigma^2_{W_N}}{\sigma^2_{W_X}} W_X \tag{3.4}$$

where $\sigma^2_{W_X}$ is the variance of the noisy wavelet coefficients W_X in the corresponding state S and $p(s=k|w_x)$ is calculated based on the Bayes rule

$$p(s=k|w_x) = \frac{p(w_x|s=k)p(s=k)}{p(W_X)} \tag{3.5}$$

The unknown probabilities in Eq.(12) are calculated with the expectation-maximization(EM) algorithm[11].

Proof. Since the speckle-noise random variable F is usually normalized as: $E[F] = 1$, $E[F-1] = 0$. Thus, due to the high-pass nature of wavelet functions, we have $E[W_N] = 0$. Furthermore, because of the zero-mean mixture-Gaussian distribution model of W_X, thus $E[W_X] = 0$. Therefore, we obtain

$$E[W_N^2] = \sigma^2_{W_N}; \quad E[W_X^2] = \sigma^2_{W_X} \tag{3.6}$$

Since W_Y and W_N are statistically independent, thus

$$E[W_X W_N] = E[(W_Y + W_N)W_N] = E[W_Y W_N] + E[W_N^2] = \sigma^2_{W_N}; \tag{3.7}$$

Combining Eq.s(10), (13), (14) with Eq.(7), we can obtain Eq.(11).

□

The variance of noise in wavelet domain $\sigma^2_{W_N}$ equals[12]

$$\sigma^2_{W_N} = \frac{\Psi_j \mu_X^2 + \sigma^2_{W_X}}{1 + C_F^2} C_F^2 \tag{3.8}$$

where $\mu_X = E[X]$, the normalized standard deviation of noise C_F equals $\sqrt{(4/\pi - 1)/L}$ for amplitude images and $\sqrt{1/L}$ for intensity images ($L \geq 1$), and parameter Ψ_j is defined as $\Psi_j = \left(\sum_k (h_k)^2\right)^2 \sum_m \left(g_m\right)^2\Big)^{2(j-1)}$, where h and g are the high-pass and low-pass filters at the decomposition level j, respectively.

3.2. Fuzzy Shrinkage Factor

Since the shrinkage factor based on the MMSE criteria is the minimum mean value and this factor from each wavelet coefficient obtained by SWT is invariable, we adopt fuzzy transform to modify it according to the variety of the wavelet coefficients. This factor is redefined by

$$\eta_{f,j} = \frac{\eta'}{1 + exp(\alpha(c - \sigma_j^2))} \tag{3.9}$$

where $c = |W_{X,j}||\hat{W}_{Y,j+1}|$; For each image detail $W_{X,j} = W_{Y,j} + W_{N,j}$, $\sigma_j = Median(|W_{X,j} - Median(W_X, j)|)/0.6745$, σ_j^2 is its threshold value[13], and σ_j

is the noise standard deviation at scale 2^j. Since noise mostly exists in subimage HH, σ_j is calculated by the standard deviation of the wavelet coefficients in HH; $\alpha < 0$ and $\eta_{f,j} = \eta'$ when α =-∞. α determines the convergence speed of the function. To suppress the noise, we hope that the absolute value of α is smaller when noise variance is bigger, i.e., the convergence speed is slower. Thus we define the expression of α by

$$\eta = (\frac{W_X - W_{X,min}}{W_{X,max} - W_{X,min}} - 1) \times 1000\,. \tag{3.10}$$

Since we use the intensity image, we set the scope of α as [0,−1000]. $W_{X,min}$ is the minimization of W_X in the corresponding decomposition level and $W_{X,max}$ is the maximization. Thus,

$$\hat{W}_Y = \sum_{k=0,1} p(s = k|W_X)\eta_{f,j}W_X\,. \tag{3.11}$$

3.3. Regions Division

As the wavelet transform deepened its application in image coding and denoising, researchers proposed some more complicated and more accurate models that exploit interscale dependencies and intrascale dependencies among wavelet coefficients. Hidden markov random field tree model[14] can capture the interscale dependencies, but it costs too much time to calculate the parameters in the model. To take spatial dependence into account, we adopt the ideas of region division and fuzzy transform. The method is easy and feasible, furthermore, it costs little in computation.

As the scale increases, the large wavelet coefficients of the signal almost keep invariable, but the wavelet coefficients of the noise tend to decrease greatly. In [14], for the necessity to distinguish signal from noise ahead, the author indicated that the pixel was considered as noise if $c < \sigma_j^2$ and the pixel was considered as signal if $c > \sigma_j^2$. As this dividing method is a little coarse, we further redefine the criteria of region division. We choose proper n_1 and n_2 $(0 < n_1 < 1 < n_2 < \infty)$ so that we can obtain the following cases: the probability which denote that the pixel is in homogenous neighborhood (i.e. the point is noise) is close to 1 when $c < n_1\sigma_j^2$; the probability which denote that the pixel is an edge point (i.e. the point is signal) is close to 1 when $c > n_2\sigma_j^2$; and the pixel is considered to be in the regions between homogenous neighborhood or edge point when $n_1\sigma_j^2 \le c \le n_2\sigma_j^2$. Finally, choosing $n_1 = 1/2$ and $n_2 = 5/3$ in the paper according to our many experiments. For each image detail $W_{X,j}(a,b) = W_{Y,j}(a,b) + W_{N,j}(a,b)$, the estimate of noise-free $\hat{W}_Y$ is

$$\hat{W}_{Y,j} = \begin{cases} 0 & c < n_1\sigma_j^2 \\ \sum_{k=0,1} p(s = k|W_X)\eta_{f,j}W_{X,j} & n_1\sigma_j^2 \le c \le n_2\sigma_j^2 \\ W_{X,j} & c > n_2\sigma_j^2 \end{cases} \tag{3.12}$$

The steps of the proposed algorithm are as follows:

1. Decompose the original SAR image by SWT and the number of decomposition level is 3.
2. Estimate parameters of the mixture-Gaussian model with EM algorithm, and then calculate the value of $\sigma^2_{W_N}$.
3. Shrink three detail subimages at the decomposition level 3 according to Eq.(11), and obtain the estimate of $\hat{W}_{Y,3}$.
4. At decomposition level 2 and 1, the despeckling algorithm is applied separately to detail subimages according to Eq.(19).
5. Apply an inverse SWT to the despeckled detail images.

4. Experimental Results and Discussion

In our experiments, we are quantifying the algorithm performance in terms of smoothing effects and edge preservation. We use equivalent number of looks (ENL) to measure the smoothing effects of despeckling methods. It is defined as $ENL = \mu^2/\sigma^2$, where μ and σ are the mean and the variance of intensity value over a homogenous region. Furthermore, as a measure of edge preservation, we adopt the Pratt's figure of merit [16], which is defined by

$$FOM = \frac{1}{max(N_A, N_I)} \sum_{i=1}^{N_A} \frac{1}{1 + d_i^2 \alpha} \tag{4.1}$$

where N_A and N_I are the numbers of original and filtered edge pixels, respectively, d_i is the Euclidean distance between the original edge pixel and the nearest filtered edge pixel, and α is a constant, which is typically set to 1/9. FOM ranges between 0 and 1, with unity for ideal edge detection.

The proposed algorithm is tested on two 256×256 real SAR images. We find that the refined Lee filter possesses the best standard spatial trade off between noise reduction and feature preservation. Therefore we also include the refined Lee filter in the comparison. The other methods include the following: wavelet soft thresholding shrinkage algorithm and SWT shrinkage algorithm[8]. The original SAR images are shown in Fig. 2 (a) and Fig. 3 (a), respectively. The filtered images by the refined Lee filter are shown in Fig. 2 (b) and Fig. 3 (b), respectively. The filtered images by the wavelet soft thresholding algorithm are shown in Fig. 2(c) and Fig. 3 (c), respectively. The filtered images by SWT shrinkage algorithm[8] are shown in Fig. 2 (d) and Fig. 3 (d), respectively. The filtered images by the proposed algorithm are shown in Fig. 2(e) and Fig. 3 (e), respectively. These results are obtained by using bior2.2 mother wave-let. We observe that oscillations appear near the edges in Fig. 2 (c), and it illuminates that DWT may cause Gibbs effects. Fig. 2 (d) is over-smoothed and thus many features are blurred, the reason is that the algorithm does not model the wavelet coefficients or divided regions. However, it is observed that Gibbs effects presented in Fig. 2 (c) disappear from Fig. 2 (d). Thus it still outperforms soft thresholding algorithm. As it appears, the refined Lee filter outperforms two algorithms above in terms of smoothing effects and edge preservation. From Fig. 2 (e), it is observed that the proposed algorithm

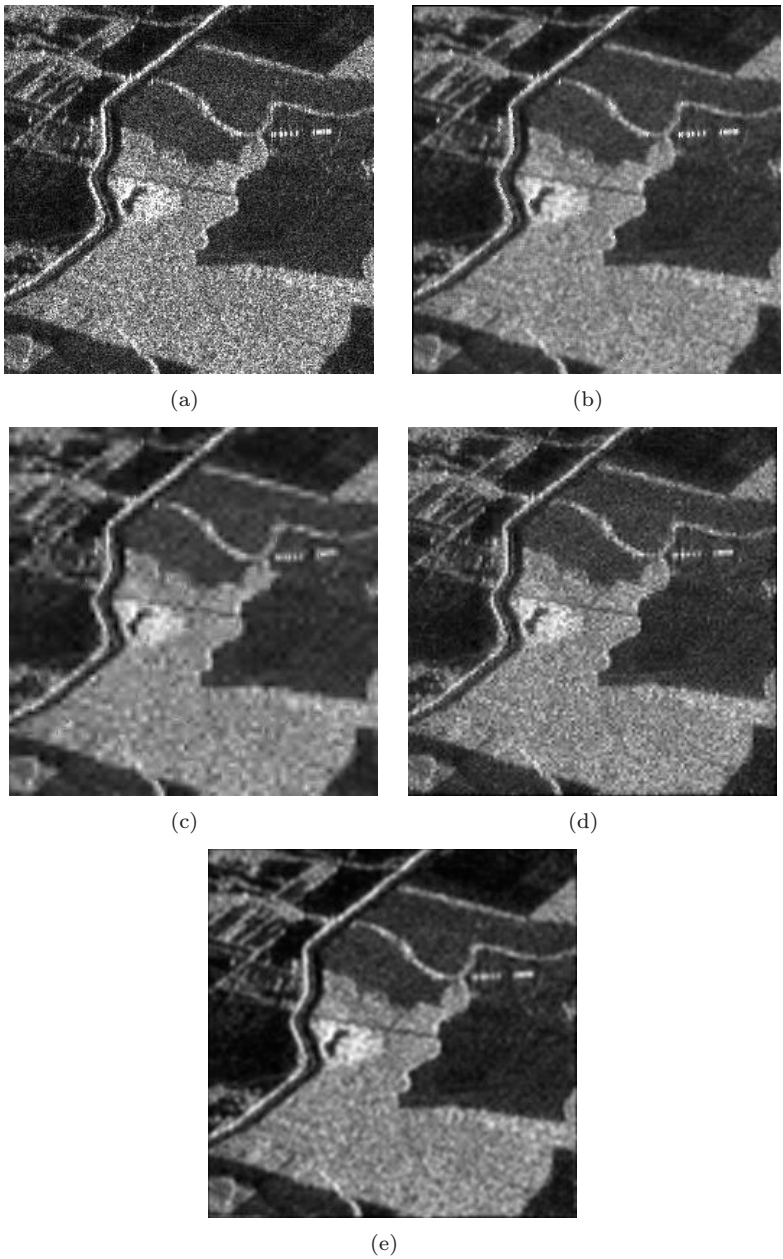

FIGURE 2. Comparison of different despeckling methods (a)The original SAR image (b) The refined Lee filter (c) Soft thresholding shrinkage algorithm (d)SWT shrinkage algorithm (e)The proposed algorithm

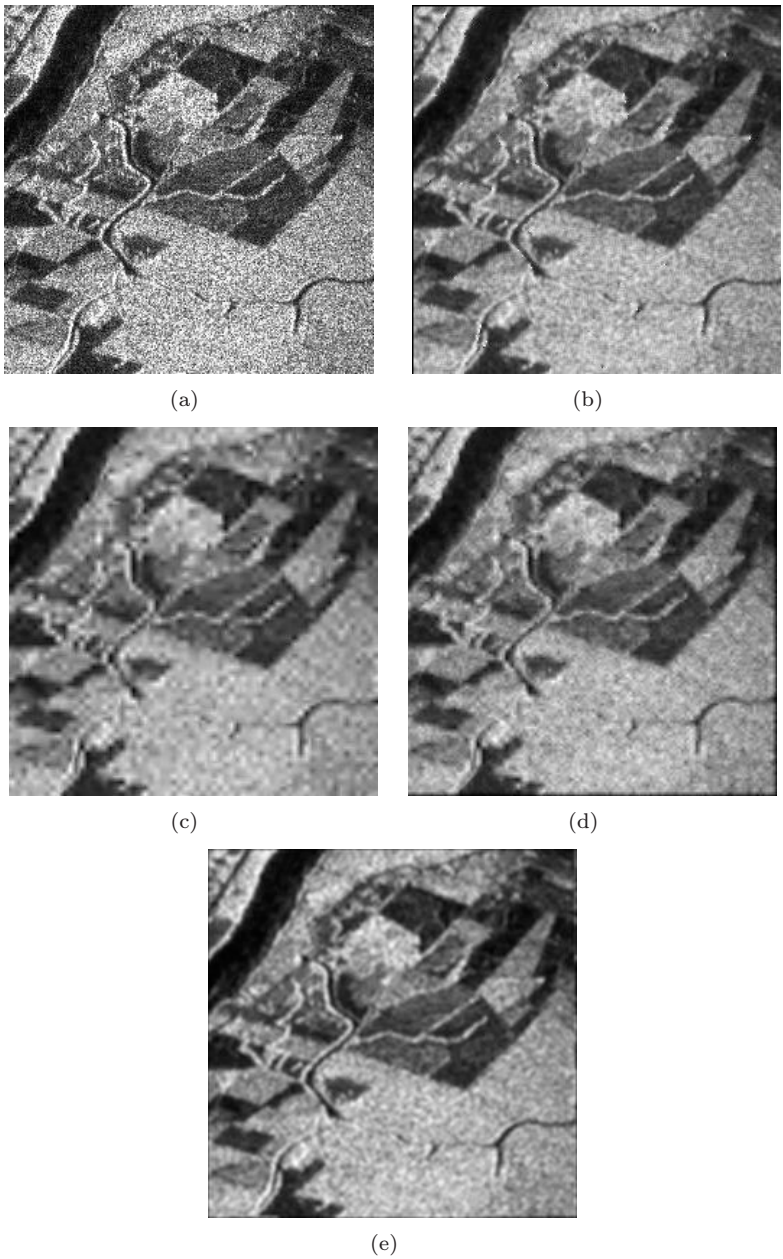

(a) (b) (c) (d) (e)

FIGURE 3. Comparison of different despeckling methods (a)The original SAR image (b) The refined Lee filter (c) Soft thresholding shrinkage algorithm (d)SWT shrinkage algorithm (e)The proposed algorithm

TABLE 1. Comparisons of different despeckling methods in terms of ENL and FOM

	SAR image1		SAR image2	
	ENL	FOM	ENL	FOM
The original image	8.579		11.993	
Soft thresholding	36.195	0.6877	64.990	0.6587
The refined Lee	44.363	0.7761	71.928	0.7419
SWT shrinkage algorithm	39.037	0.6973	67.884	0.6858
The proposed algorithm	58.881	0.7943	85.493	0.7518

has a good despeckling performance and typically preserves minor edges, at the same time, it sharpens edges. It is because that the proposed algorithm adopts the ideas of region division and fuzzy shrinkage. The ENL and FOM values of applying these four despeckling algorithms to the two real SAR images are listed in Table 1, from which we note the following observations: (1) under all conditions, the proposed algorithm achieves remarkable improvement over the other three methods; (2) the SWT shrinkage algorithm [8] outperforms the wavelet soft thresholding algorithm. The evaluation fits the visual analysis above. The visual effect analysis in Fig. 3 and its evaluation consist with the cases above.

5. Conclusions

The proposed algorithm combines image multiscale analysis with bayesian shrinkage. The multiplicative model introduced in high-frequency images, permits to retain coefficients produced by significant structures presented in the image and suppress those produced by the speckle noise. We modeled wavelet coefficients with a mixture density of two zero-mean Gaussian distributions. Then a fuzzy shrinkage factor is derived based on the MMSE criteria with bayesian estimation. The ideas of region division and fuzzy shrinkage are adopted according to the interscale dependencies among wavelet coefficients. Finally the noise-free wavelet coefficients are estimated accurately. Experimental results show that our method outperforms the other three despeckling methods in terms of speckle reduction and edges preservation.

References

[1] J.S.Lee, *Digital image enhancement and noise filtering by use of local statistics.* IEEE Trans on Pattern Anal. Machine Intell, vol.2, no.2, pp.156–163,1980.

[2] D.T.Kuan, AA.Sawchuk, TC.Strand, *Adaptive noise smoothingfilter for images with signal-dependent noise.* IEEE Trans on Pattern Anal. Machine Intell, vol.7, no.2,pp.165–177, 1985.

[3] D.T.Kuan, AA.Sawchuk, TC.Strand, *Adaptive restoration of images with speckle.* IEEE Trans on Acoust.,Speech,Signal Processing,vol.35 no.3, pp. 373–383,1987.

[4] V.S.Frost, JA.Stiles, KS.Shanmugan, JC.Holtaman, *A model for radar images and its application to adaptive digital filtering of multiplicative noise.* IEEE Trans on Pattern Analysis and Machine Intelligence, vol.4, No.2, pp. 157–166,1982.

[5] Lopes.A, Touzi.R, Nezry.E, *Adaptive speckle filters and scene heterogeneity.* IEEE Trans Geosci. Remote Sensing, vol. 28, pp.992–1000, Nov. 1990.

[6] Hagg W. Sites M., *Efficient speckle filtering of SAR images.* Processing of the International Geoscience and Remote Sensing ymposium (IGARSS5),1994

[7] D.L.Donoho, *De-Noising by soft-thresholding.* IEEE Trans. Information Theory.vol.41,pp.613–627, 1995

[8] F.Argenti, *Speckle removal from SAR images in the undecimated wavelet domain.* IEEE Trans Geosci. Remote Sensing, vol.40, no.11, pp.2363–2374, 2002.

[9] G.P.Nason,BW.Silverman, *The stationary wavelet transform and some statistical applications.* Dept. Math., Univ.Bristol, U.K., Tech. Rep.,BS8 1TW, 1995

[10] H.Chipman,E.Kolaczyk,R.McCulloch, *Adaptive bayesian wavelet shrinkage.* J.Amer. Statist.Assoc., vol.92, pp. 1413–1421,1997.

[11] R.A.Redner,HF.Walker, *Mixture densities, maximum likelihood and the EM algorithm.* SIAM Rev., vol, 26, no.2,pp.195-239,1984.

[12] F.Samuel, *Multiscale MAP filtering of SAR images.* IEEE Trans Image processing,vol 10, no.1, pp.49–60,Jan, 2001.

[13] P.Thitima, *A simple SAR speckle reduction by wavelet thresholding.* http://www.gisdevelopment.net/aars/acrs/1998/ps1/ps1014pf.htm.

[14] Matthew S. Crouse. Robert D. Nowak. *Wavelet-Based Statistical Signal Processing Using Hidden Markov Models.*IEEE Trans Image processing, vol 46, no.4, pp. 886–902,April, 1998.

[15] Yongjian Yu.,Scott TA. *Speckle reducing anisotropic diffusion.* IEEE Trans Image processing.vol 11,no.11,pp.927–935,Nov,2002.

Yan Wu
National key lab. of radar signal processing, Xidian Univ.,
Xi'an, 710071, China
School of electronics engineering, Xidian Univ.
Xi'an, 710071, China
e-mail: ywu@mail.xidian.edu.cn

Xia Wang
School of electronics engineering, Xidian Univ.,
Xi'an, 710071, China

Guisheng Liao
National key lab. of radar signal processing, Xidian Univ.,
Xi'an, 710071, China

Wavelet Analysis and Applications
Tao Qian, Mang I. Vai and Xu Yuesheng, Eds.
Applied and Numerical Harmonic Analysis, 419–430

Super-Resolution Reconstruction Using Haar Wavelet Estimation

C.S. Tong and K.T. Leung

Abstract. High resolution image reconstruction refers to the reconstruction of a high resolution image from a set of shifted, blurred low resolution images. Many methods have been developed, and most of them are iterative methods. In this paper, we present a direct method to obtain the reconstruction. Our method takes advantages of the properties of Haar wavelet transform of the high resolution image and its relationship with the low resolution images. Thus the coefficients of the Haar wavelet transform of the high resolution image can be estimated from the low resolution images. Our method is very simple to implement and is very efficient. Experiments show that it is robust to boundary conditions and superior to the least - squares method especially in the low - noise case.

Keywords. High resolution image reconstruction, Haar wavelet transform.

1. Introduction

Nowadays, more and more people prefer to take photos using a digital camera instead of the traditional camera. They seek a high resolution digital camera, but there are not many people can afford to buy this kind of camera. Therefore, high resolution image reconstruction (HRIR) can help these people to get a high resolution image from a set of low resolution images. These low resolution images are under-sampled with subpixel displacement from the high resolution image. More importantly, such a technique enables us to make the best use of the existing limits of digital photography and have important applications in remote sensing.

From Zhang *et al.*[16], we know that there are many HRIR algorithms such as frequency domain method [15, 9, 8], the projection onto convex sets method [11, 12], the maximum a posteriori (MAP) method [13, 5, 6, 10, 4, 14], and inversion problem with regularization [7, 6]. Recently, researchers proposed using wavelet technique or preconditioned conjugate gradient (PCG) method to restore the high resolution image [3, 2]. These techniques are very powerful but they seem

to be sensitive to boundary conditions. Chan *et al.*[1, 2] discussed the importance of the boundary condition in the regularization problem. They mention that ringing effect will appear at the boundary of the image using zero boundary condition. Reflective boundary condition (Neumann boundary condition) gives about 1.0dB PSNR better result than zero boundary condition and periodic boundary condition for test images. If the assumption is not suitable for the image, the error propagates in each iteration and gives a poor result. In the mathematical model, the matrix representation for the shift, blur and down-sampling operator have to be changed for different types of boundary condition. There is a parameter that controls the model regularity. If this parameter is overestimated, the solution is still blurred. Moreover, the solution is ill - conditioned. This means that choosing an appropriate parameter directly affects the quality of solution. All the problems mentioned above thus make regularization a difficult but key issue in super-resolution reconstruction. In section 2, we will propose a simple and effective method for solving HRIR problem that avoid the regularization problem and the boundary condition problem.

2. High Resolution Image Reconstruction

In HRIR, we assume the low resolution images have subpixel displacements between each other. This special relationship provides enough information for restoring the high resolution image. Suppose we have q^2 $M \times M$ $I_{l_1 l_2}$ low resolution images where q is the magnification factor, l_1 and l_2 are positive integers smaller than and equal to $q-1$ and they represent the low resolution image I which has a l_1 vertical downward and l_2 horizontal rightward shift. For $q=2$, the 4 low resolution images are $I_{00}, I_{01}, I_{10}, I_{11}$. The pixels in the low resolution image are the average of $h_{l_1 l_2} \times w_{l_1 l_2}$ pixels in the high resolution image. $h_{l_1 l_2}$, $w_{l_1 l_2}$ and q can be different values for different low resolution images. For simplicity, they are set to a certain value. We will propose a general mathematical model which is suitable for different values of $h_{l_1 l_2}$, $w_{l_1 l_2}$ and q in future. The $qM \times qM$ high resolution image defined as f. Figure 1 illustrates the pixel relationship between low resolution image I_{00}, I_{11} and high resolution image f with $h_{00} = w_{00} = h_{11} = w_{11} = 2$. The relationship of the pixel between the low resolution image and high resolution image is given by

$$(I_{l_1 l_2})ij = \sum_{\substack{x \in X_{l_1} \\ y \in Y_{l_2}}} f(x,y)/(h_{l_1 l_2} w_{l_1 l_2}), \tag{2.1}$$

where i and j are integers with $1 \le i, j \le M$, $X_{l_1} = \{2i - 1 + k + l_1 | k = 0, \ldots, h_{l_1 l_2} - 1\}$ and $Y_{l_2} = \{2j - 1 + k + l_2 | k = 0, \ldots, w_{l_1 l_2} - 1\}$. In our experiment, we set the magnification factor q equal to 2. Thus, we assume all the low resolution images have the same magnification factor and the pixels in the low resolution image are the average of 2×2 pixels in the high resolution image.

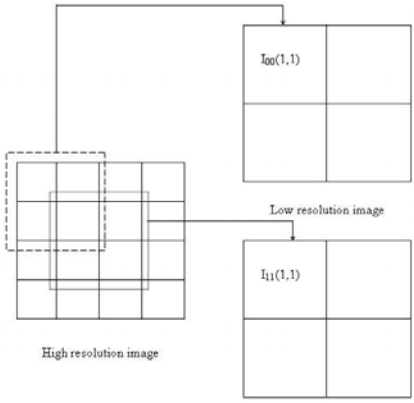

FIGURE 1. The relationship between the high resolution image and low resolution images

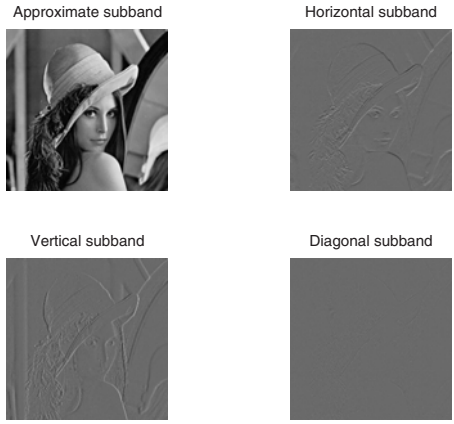

FIGURE 2. The Haar wavelet transform of Lena image

Haar wavelet is the well-known and simple example of an orthonormal wavelet. For simplicity, we use the 1 level wavelet decomposition. The $qM \times qM$ high resolution image after applying the Haar wavelet transform consists of 4 subbands: approximate subband (LL), horizontal subband (H), vertical subband (V) and diagonal subband (D). These subbands are the half size of the high resolution image. Approximate subband is down-sampling of the high resolution image. The pixel relationship between the approximate subband and the high resolution image is given by

$$(LL)ij = \sum_{\substack{x \in X_{LL} \\ y \in Y_{LL}}} f(x,y)/2, \tag{2.2}$$

where $X_{LL} = \{2i - 1 + k | k = 0, 1\}$ and $Y_{LL} = \{2j - 1 + k | k = 0, 1\}$. Horizontal subband contains the horizontal edges and details of the high resolution image. The horizontal detail coefficients are defined as:

$$(H)ij = \frac{1}{2}\left(\sum_{\substack{x \in X_{Ha} \\ y \in Y_{Ha}}} f(x,y) - \sum_{\substack{x \in X_{Hb} \\ y \in Y_{Hb}}} f(x,y) \right), \tag{2.3}$$

where $X_{Ha} = \{2i - 1\}$, $Y_{Ha} = \{2j - 1 + k | k = 0, 1\}$, $X_{Hb} = \{2i\}$ and $Y_{Hb} = \{2j - 1 + k | k = 0, 1\}$. The vertical and diagonal detail coefficients are defined similarly. Each subband have $M \times M$ coefficients. Figure 2 shows the image Lena after applying the Haar wavelet transformation. The top left image is the approximate subband which is the low resolution image of the original image. The top right image displays the horizontal edges, the bottom left image shows the vertical edges. The last image illustrates the diagonal edge. We found that there are connections between the set of low resolution images and these subbands. We use the pixel relationship between the low resolution images with the help of Taylor series to approximate those subbands. Since the coefficients of the horizontal, vertical and diagonal subbands are the pixels difference in the high resolution image and the pixels in the low resolution images are the averages of the pixels in the high resolution image, we take advantages of this dependence to interpolate those subbands. A good approximation of the subbands means that we can reconstruct the high resolution image well.

2.1. First Order Approximation

In last section we mentioned that we use the Taylor series to interpolate the wavelet coefficient subbands. Now we give more details on this algorithm. Recall equations (2.1) and (2.2), we can formulate the following relationship:

$$(I_{l_1 l_2})ij = \sum_{\substack{x \in X_{l_1} \\ y \in Y_{l_2}}} f(x,y)/(h_{l_1 l_2} w_{l_1 l_2}).$$

Putting $l_1 = l_2 = 0$ and $h_{00} = w_{00} = 2$. We obtain

$$(I_{00})ij = \sum_{\substack{x \in X_0 \\ y \in Y_0}} f(x,y)/4,$$

where $X_0 = \{2i - 1 + k | k = 0, 1\}$ and $Y_0 = \{2j - 1 + k | k = 0, 1\}$. Then the relationship between I_{00} and LL is

$$2(I_{00})ij = (LL)ij.$$

The approximate subband can be interpolated by low resolution image I_{00} exactly. To approximate the horizontal subband, we apply first order Taylor series expansion for the high resolution image:

$$f(x+\triangle x, y+\triangle y) \approx f(x,y) + \triangle x f_x(x,y) + \triangle y f_y(x,y), \tag{2.4}$$

where $f_x(x,y)$ and $f_y(x,y)$ are the first order derivatives. As an example, consider the coefficient of the horizontal subband $(H)ij$. From (2.3) we have

$$(H)ij = \frac{f(2i-1,2j-1)-f(2i,2j-1)}{2} + \frac{f(2i-1,2j)-f(2i,2j)}{2}. \tag{2.5}$$

Let $x = 2i-1$ and $y = 2j-1$, the coefficient of the horizontal subband become

$$(H)ij = \frac{f(x,y)-f(x+1,y)}{2} + \frac{f(x,y+1)-f(x+1,y+1)}{2}.$$

Using (2.4), we have

$$\begin{aligned} f(x,y)-f(x+1,y) &\approx f(x,y)-(f(x,y)+f_x(x,y)) \\ &= -f_x(x,y), \end{aligned}$$

and similarly when $\triangle x = 2$ we obtain

$$f(x,y)-f(x+2,y) \approx -2f_x(x,y)$$

which implies

$$f(x,y)-f(x+1,y) \approx \frac{f(x,y)-f(x+2,y)}{2}$$

or equivalently

$$f(2i-1,2j-1)-f(2i,2j-1) \approx \frac{f(2i-1,2j-1)-f(2i+1,2j-1)}{2}. \tag{2.6}$$

In the same way,

$$f(2i-1,2j)-f(2i,2j) \approx \frac{f(2i-1,2j)-f(2i+1,2j)}{2}. \tag{2.7}$$

Substituting (2.6) and (2.7) into (2.5), we have

$$\begin{aligned} (H)ij &\approx \frac{1}{2}\left(\frac{f(2i-1,2j-1)-f(2i+1,2j-1)}{2}+\frac{f(2i-1,2j)-f(2i+1,2j)}{2}\right) \\ &= \frac{f(2i-1,2j-1)-f(2i+1,2j-1)}{4}+\frac{f(2i-1,2j)-f(2i+1,2j)}{4} \\ &= (I_{00})ij-(I_{10})ij. \end{aligned}$$

We can obtain a similar relationship between the vertical subband and the low resolution images I_{00}, I_{01}. For the diagonal subband,

$$(D)ij = \frac{f(2i-1,2j-1)+f(2i,2j)-(f(2i,2j-1)+f(2i-1,2j))}{2}.$$

Putting $x = 2i-1$, $y = 2j-1$ and applying equation (2.4), we have

$$\begin{aligned} f(x,y)+f(x+1,y+1) &\approx f(x,y)+(f(x,y)+f_x(x,y)+f_y(x,y)), \\ f(x+1,y)+f(x,y+1) &\approx f(x,y)+(f(x,y)+f_x(x,y)+f_y(x,y)), \end{aligned}$$

which implies

$$f(2i-1,2j-1)+f(2i,2j-1)=f(2i,2j-1)+f(2i,2j),$$

and

$$(D)ij \approx 0.$$

Therefore, the first order approximation of the Haar wavelet subbands are given by:

$$\begin{aligned}(LL)ij &= 2(I_{00})ij,\\ (H)ij &\approx (I_{00})ij-(I_{10})ij,\\ (V)ij &\approx (I_{00})ij-(I_{01})ij,\\ (D)ij &\approx 0.\end{aligned}$$

The high resolution image can be obtained by taking inverse Haar wavelet transform on these subbands. This result shows our method no need to use I_{11}, hence we only need to use 3 low resolution images for reconstruction. The low resolution image I_{11} is difficult to obtain, since the camera hard to has a precise subpixel shift in both horizontal and vertical direction. The other low resolution images can be taken precisely. Therefore, our method need less data and easy to implement. Also, the first order approximation does not need boundary condition to provide extra information. This implies our method in first order approximation does not suffered any boundary condition problems.

2.2. Second Order Approximation

In section 2.1, we propose the first order approximation for high resolution image wavelet subbands. If the pixels in the high resolution image change linearly, the first order approximation gives a good reconstruction. But most of the changes are not linear; they may be occurred in quadratic or cubic form. When the changes are not linear, we use second or higher order Taylor series expansion to approximate the subbands. We are concentrate on interpolate the subbands except the approximate subband as the approximate subband can be interpolated by the low resolution image I_{00} exactly. The second order Taylor series is

$$\begin{aligned}f(x+\triangle x,y+\triangle y) \approx\ & f(x,y)+\triangle x f_x(x,y)+\triangle y f_y(x,y)+\frac{1}{2}((\triangle x)^2 f_{xx}(x,y)\\ & +2(\triangle x)(\triangle y)f_{xy}(x,y)+(\triangle y)^2 f_{yy}(x,y)).\end{aligned} \tag{2.8}$$

Recall the equation (2.5), we have

$$(H)ij=\frac{f(2i-1,2j-1)-f(2i,2j-1)}{2}+\frac{f(2i-1,2j)-f(2i,2j)}{2}.$$

Using the similar technique in section 2.1 we can show that

$$\begin{aligned}(H)ij &\approx \frac{f(2i-1,2j-1)-f(2i+1,2j-1)}{4}+\frac{f(2i-1,2j)-f(2i+1,2j)}{4}\\ &\quad +\frac{1}{4}(f_{xx}(2i-1,2j-1)+f_{xx}(2i-1,2j))\\ &= \frac{3}{2}((I_{00})ij-(I_{10})ij)-((I_{10})ij-(I_{00})i+1,j).\end{aligned}$$

The vertical subband can be interpolated alike. To interpolate the diagonal subband we define the $P_s(x,y)$ as,

$$P_s(x,y) = f(x,y)+f(x+s,y+s)-f(x+s,y)-f(x,y+s).$$

Then,

$$(D)ij = \frac{P_1(2i-1,2j-1)}{2}.$$

By using equation (2.8)

$$\begin{aligned}(D)ij &\approx \frac{P_2(2i-1,2j-1)}{8}\\ &= \frac{(I_{00})ij+(I_{11})ij-(I_{10})ij-(I_{01})ij}{2}.\end{aligned}$$

Then the second order approximation are:

$$\begin{aligned}(LL)ij &= 2(I_{00})ij,\\ (H)ij &\approx \frac{3}{2}((I_{00})ij-(I_{10})ij)-\frac{1}{2}((I_{10})ij-(I_{00})i+1,j),\\ (V)ij &\approx \frac{3}{2}((I_{00})ij-(I_{01})ij)-\frac{1}{2}((I_{01})ij-(I_{00})i,j+1),\\ (D)ij &\approx \frac{(I_{00})ij+(I_{11})ij-(I_{10})ij-(I_{01})ij}{2}.\end{aligned}$$

In general, the higher order approximation can give a better performance than the lower order approximation for low-noise image. But if the low resolution images are noisy, there could be noise amplification effects. Since the interpolation of the diagonal subband involved all the low resolution images, we believe that the second order approximation of the diagonal subband is more susceptible noise amplification with noisy low resolution images than first order approximation. Suppose all the images contain same amount of noise, the diagonal subband has the largest noise amplification. The other subbands would not have such large noise amplification, as they are only approximated by two noisy low resolution images. The noisy low resolution images enlarge the error of approximation, the reconstructed image also suffer from noise and gives a poor quality. Thus, we propose to use the first order approximation to interpolate the diagonal subband for higher order approximation. This idea provides two advantages. First, we use the first order approximation for the diagonal subband that means we only need 3 low resolution

images to obtain our reconstruction. Compare with other reconstruction methods, our method needs less data to reconstruct a high resolution image. Second, we reduce the noise amplification during the reconstruction. Since the first order approximation of the diagonal subband does not include any images, which is independent of noise. In the second order approximation, the approximated coefficients in horizontal and vertical subbands require boundary condition to provide extra information during reconstruction especially on the last row or column of the wavelet subband. Thus, we use 3 different boundary conditions (Periodic boundary condition, Reflective boundary condition and Zero boundary condition) in experiments which show our method in second order approximation is robust to the boundary condition. Also, numerical results show our method gives a better performance than the traditional Least-squares method.

3. Numerical Results

In this section, we illustrate the performance of the first order and second order approximation for high resolution image reconstruction. Our method is not a iterative method, it is direct and fast. All the results can be generated in about 1 to 2 seconds in matlab with Pentium-4 CPU 3.2GHz computer. To study the performance of the reconstruction method, we use the peak signal - to - noise ratio (PSNR) to compare the reconstructed image $\hat{f}$ with the original image f. The PSNR is defined as

$$\text{PSNR} = 10 \log_{10} \frac{255^2 NM}{\|f - \hat{f}\|_2^2}$$

where the size of image f is $N \times M$.

We use the Lena image of size 512×512 as the original image in our experiments. To obtain the set of low resolution images. We first add Gaussian white noise to the original image. The four 254×254 low resolution images can be obtained by down-sampling with factor of 2 with original boundary. Then we compare our method with Least-squares model (Tikhonov method) [2]: Sec:2. The results of the Least - squares model quote from Chan *et al.* [2]. Note that our imaging model is slightly different from Chan *et al.*'s, our reconstructed image differs from their reconstructed image by a half pixel shift in both horizontal and vertical direction so a direct comparison is not technically fair. However, the difference is small and we believe that the qualitative conclusions that we will draw from the results are still meaningful. In practice, the set of the low resolution images which have the precise subpixel shift in horizontal and vertical direction are difficult to obtain especially the low resolution image I_{11}. In our method, only the approximation of diagonal subband requires low resolution image I_{11}. Therefore, the second order approximation of the diagonal subband is replaced by the first order approximation. Now we only need 3 low resolution images for the reconstruction.

Table 1 shows the results of reconstructed Lena image with different noise level and boundary conditions. The second and third row shows the results of Lena

TABLE 1. The results for the first order approximation by using 3 low resolution images

SNR	Boundary Condition	Least-Squares model		1st Order Approximation
		PSNR	β^*	
40	Periodic	33.89	0.0197	35.82
	Reflective	35.89	0.0134	
	Zero	N/A	N/A	
30	Periodic	33.16	0.0216	34.54
	Reflective	34.51	0.0175	
	Zero	N/A	N/A	

image with noise level at SNR = 40dB and 30dB respectively. The results of zero boundary condition are not available, because Chan *et al.* claim that the reconstructed image would be suffered ringing effect when the zero boundary condition are used, and the reconstruction result is worst. In second row and third column, we compare the results of Least - square method among the boundary conditions. We can see that the results of periodic boundary condition has about 2.0dB lower than that of reflective boundary condition. For the first order approximation, the reconstruction do not require any boundary conditions. Thus the result has the unique value 35.82dB which is better than the Least - square method in periodic and zero boundary condition. The first order approximation's result is close to the Least - square method in reflective boundary condition. We only use 3 low resolution images then the result is comparable to the Least - square method by using 4 low resolution images with optimum parameter. For SNR = 30dB, our method works better than Least - square method among all boundary conditions and Least - square method still sensitive to the boundary conditions. There are about 1.5dB difference between periodic and reflective boundary condition. Therefore, first order approximation by using 3 low resolution image is comparable to the Least - square method by using 4 low resolution image with optimum parameter and it is robust to the boundary condition.

TABLE 2. The results for the second order approximation by using 3 low resolution images

SNR	Boundary Condition	Least-Squares model		2nd Order Approximation
		PSNR	β^*	
40	Periodic	33.89	0.0197	37.29
	Reflective	35.89	0.0134	37.27
	Zero	N/A	N/A	37.29
30	Periodic	33.16	0.0216	34.94
	Reflective	34.51	0.0175	34.93
	Zero	N/A	N/A	34.95

Table 2 illustrate the second order approximation results with different boundary conditions. The results of Least - square method are same as table 1. Compare table 1 and 2, we can find that there are about 1.4dB and 0.5dB improvement from second order to first order approximation at SNR = 40dB and 30dB respectively. In the column 4, we can see that the second order approximation obtain very close results among the boundary conditions in SNR = 40dB and 30dB. The difference between the boundary conditions are only 0.02dB. This shows our method is robust to boundary condition. Also, table 2 also shows the second order approximation is superior to Least - square method.

4. Conclusion and Further Work

From the experiment results, our method only uses three low resolution images which give a better performance than the traditional Least-square method by using 4 low resolution images with optimum parameter. One of the most important observation is that our method can work well with zero boundary condition thus avoiding the justify which boundary condition to use. Our method works extremely well in the low-noise case. In the noisy image case, it is only slightly better than the Least-squares model. However, we only need 3 low resolution images. We shall integrate wavelet denoising technique into our method to improve the results for noisy images. To sum up, our method can work with just 3 low resolution images and is robust to the boundary condition. Since the I_{11} image is very difficult to obtain accurately, our method do not need this image also give a good result. It is a direct, fast and easy to implement method. Our method can work with wider class of images as it can work with zero boundary condition. Also, our method has a far superior results in noise case. In the future, we will concentrate on remove noise with the reconstructed image and attempt other interpolate method to approximate the wavelet subbands.

Acknowledgment

This research was partially funded by RGC research grant HKBU2021/04P and a Faculty Research Grant from the Hong Kong Baptist University. The authors would also like to thank Prof. Tony Chan for his distinguished lecture series talk on ENO - Haar wavelet in HKBU on 15 April 2005 which inspired our approach, and to Prof. Michael Ng for his valuable comments and discussion.

References

[1] R. Chan, T. Chan, M. Ng, W. Tang, and C. Wong. Preconditioned iterative methods for high-resolution image reconstruction from multisensors. In Franklin Luk, editor, *Proceedings to the SPIE Symposium on Advanced Signal Processing: Algorithms, Architectures, and Implementations*, volume 3461, pages 348–357, 1998.

[2] R. H. Chan, T. F. Chan, L. Shen, and Z. Shen. Wavelet algorithms for high-resolution image reconstruction. *SIAM Journal on Scientific Computing*, 24:1408–1432, 2003.

[3] R. H. Chan and M. K. Ng. Conjugate gradient methods for toeplitz systems. *SIAM Review*, 38(3):427–482, 1996.

[4] T. J. Connolly and R. G. Lane. Gradient methods for superresolution. In *Proceedings of the International Conference on Image Processing*, volume 1, pages 917–920, 26-29 Oct. 1997.

[5] R. C. Hardie, K. J. Barnard, and E. E. Armstrong. Joint map registration and high-resolution image estimation using a sequence of undersampled images. *IEEE Trans. on Image Processing*, 6(12):1621–1633, 1997.

[6] R. C. Hardie, K. J. Barnard, J. G. Bognar, E. E. Armstrong, and E. A. Watson. High resolution image reconstruction from a sequence of rotated and translated frames and its application to an infrared imaging system. *Optical Engineering*, 37:247–260, 1998.

[7] M. C. Hong, M. G. Kang, and A. K. Katsaggelos. An iterative weighted regularized algorithm for improving the resolution of video sequences. *Proc. 1997 Int. Conf. Image Processing*, 2:474–477, 1997.

[8] E. Kaltenbacher and R. C. Hardie. High resolution infrared image reconstruction using multiple, low resolution, aliased frames. In OH Dayton, editor, *Proceedings of the IEEE National Aerospace Electronics Conference (NAECON)*, volume 2, pages 702–709, 1996.

[9] S. P. Kim, N. K. Bose, and H. M. Valenzuela. Recursive reconstruction of high resolution image from noisy undersampled multiframes. *IEEE Transactions on Acoustics, Speech and Signal Processing*, 38:1013–1027, 1990.

[10] N. Nguyen, P. Milanfar, and G. Golub. A computationally efficient superresolution image reconstruction algorithm. *IEEE Trans. on Image Processing*, 10(4):573–583, 2001.

[11] P. Oskoui-Fard and H. Stark. Tomographic image reconstruction using the theory of convex projections. *IEEE Transactions on Medical Imaging*, 7(1): 45–58, 1988.

[12] A. J. Patti and Y. Altunbasak. Artifact reduction for set theoretic super resolution image reconstruction with edge adaptive constraints and higher-order interpolants. *IEEE Trans. Image Processing*, 10(1):179–186, 2001.

[13] R. R. Schultz and R. L. Stevenson. Extraction of high-resolution frames from video sequences. *IEEE Transactions on Image Processing*, 6:996–1011, 1996.

[14] J. H. Shin, J. S. Yoon, J. K. Paik, and M. Abidi. Fast superresolution for image sequence using motion adaptive relaxation parameters. In *Proceedings of the 1999 International Conference on Image Processing*, volume 3, pages 676–680, 1999.

[15] R. Y. Tsai and T. S. Huang. Multiframe image restoration and registration. *Advances in Computer Vision and Image Processing*, 1:317–339, 1984.

[16] D. Zhang, H. Li, and M. Du. Fast map-based multiframe super-resolution image reconstruction. *Image and Vision Computing*, 23:671–679, 2005.

C.S. Tong
Centre for Mathematical Imaging and Vision
Hong Kong Baptist University
Department of Mathematics
Kowloon Tong, HK
e-mail: cstong@hkbu.edu.hk

K.T. Leung
Centre for Mathematical Imaging and Vision
Hong Kong Baptist University
Department of Mathematics
Kowloon Tong, HK
e-mail: ktleung@math.hkbu.edu.hk

Wavelet Analysis and Applications
Tao Qian, Mang I. Vai and Xu Yuesheng, Eds.
Applied and Numerical Harmonic Analysis, 431–441

The Design of Hilbert Transform Pairs in Dual-Tree Complex Wavelet Transform

Fengxia Yan, Lizhi Cheng and Hongxia Wang

Abstract. An approach for designing biorthogonal dual-tree complex wavelet transform filters is proposed, where the two related wavelets form an approximate Hilbert transform pair. Different from the existing design techniques, the two wavelet filter banks obtained here are both of linear phase. By adjusting the parameters, wavelet filters with rational coefficients may be achieved. The designed examples show that the lengths of wavelet filters may be effectively shorted while efficient approximation to Hilbert transform pairs is still kept. The validity of the proposed design scheme is exhibited through an application to dual-tree complex wavelet for iris image enhancement.

Keywords. Hilbert transform pairs, biorthogonal wavelet, linear phase, dual-tree complex wavelet, iris image enhancement.

1. Introduction

The real Discrete Wavelet Transform (DWT) is a powerful tool for signal and image processing. It, however, has some disadvantages, including, (1) It is shift-sensitive because the input signal shift generates unpredictable changes in DWT coefficients; (2) It suffers from poor directionality because DWT coefficients reveal merely three spatial orientations; (3) It lacks of the phase information that accurately describes non-stationary signal behavior; that undermine its usage in many applications. Many researchers have proposed different techniques to overcome simultaneously some or all of these drawbacks [1-5]. In recent years, some researchers proposed to design two wavelet bases to work together in order to gain some specific effects.

In particular, Kingsbury has demonstrated that dramatic improvements can be achieved in wavelet-based signal processing by utilizing a pair of wavelet transforms where the wavelets form a Hilbert transform pair. Kingsbury calls a wavelet

This work was supported by the National Science Foundation of China (NSFC) under Grant 60573027.

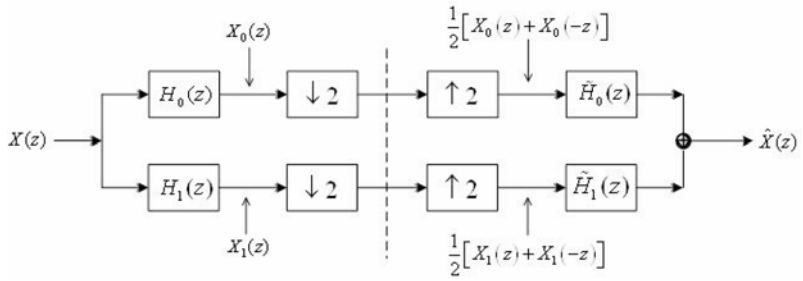

FIGURE 1. Biorthogonal wavelet filter banks

transform of this type a dual-tree complex wavelet transform (DT-CWT) [5-6], which is a form of discrete wavelet transform which generates complex coefficients by using a dual tree of wavelet filters to obtain their real and imaginary parts. The DT-CWT, which is based on (approximate) Hilbert pairs of wavelets, has many advantages such as shift-invariance, directional selectivity, perfect reconstruction, limited redundancy and offering phase information. The obtained phase information is associated with quasi-analytic wavelet decomposition and has been exploited for various image-processing applications [7-8]. Selesnick formulated the design problem in [9] for the minimal length scaling filters such that 1) the wavelets each has a specified number of vanishing moments, and 2) the half-sample delay approximation is flat at $\omega = 0$ with specified degree. However, his formulation leads to nonlinear design equations, and the filters would have to be obtained using Gröbner bases. In [10-11], he describes the other two design procedures based on spectral factorization. But the wavelet filters designed by these methods are of long length and nonlinear phase.

In this paper, we present a new algorithm for designing two biorthogonal wavelets forming a Hilbert transform pair approximately. Wavelet filter banks obtained here are all of linear phase, i.e., their coefficients are all symmetric. Results of the designed examples show that our algorithm can shorten the length of the filters efficiently while still keep the satisfied approximation to Hilbert transform pairs. Furthermore, we use the designed filter banks in dual-tree complex wavelet transform for iris image enhancement. Results of experiments show that our design method is effective for reducing computational complexity and improving performance.

2. The Design of Linear Phase Biorthogonal Wavelet Filters

2.1. Biorthogonal Wavelet Filter Banks

Fig. 1 is the filter scheme of one level biorthogonal wavelet decomposition and reconstruction. Multirate filter analysis shows that

$$\begin{aligned}\hat{X}(z) &= \frac{1}{2}[X_0(z)+X_0(-z)]\tilde{H}_0(z)+\frac{1}{2}[X_1(z)+X_1(-z)]\tilde{H}_1(z)\\ &= \frac{1}{2}[H_0(z)\tilde{H}_0(z)+H_1(z)\tilde{H}_1(z)]X(z)\\ &+ \frac{1}{2}[H_0(-z)\tilde{H}_0(z)+H_1(-z)\tilde{H}_1(z)]X(-z).\end{aligned} \tag{2.1}$$

The first perfect reconstruction (PR) condition requires aliasing cancellation and forces the above term in $X(-z)$ to be zero. Hence $H_0(-z)\tilde{H}_0(z)+H_1(-z)\tilde{H}_1(z)=0$, this can be achieved if

$$H_1(z)=z^{-k}\tilde{H}_0(-z),\tilde{H}_1(z)=z^k H_0(-z) \tag{2.2}$$

where k must be odd (usually $k=\pm 1$). The second PR condition is that the transfer function from $X(z)$ to $\hat{X}(z)$ should be unity; i.e. $H_0(z)\tilde{H}_0(z)+H_1(z)\tilde{H}_1(z)=2$. If we define a product filter $P(z)=H_0(z)\tilde{H}_0(z)$, then the PR condition becomes

$$P(z)+P(-z)=2. \tag{2.3}$$

Equivalently,

$$\sum_n h_0(n)\tilde{h}_0(n+2k)=\delta(k). \tag{2.4}$$

Besides, the low pass filers should satisfy the following normalization conditions

$$\sum_n h_0(n)=\sqrt{2}\,,\quad \sum_n \tilde{h}_0(n)=\sqrt{2}. \tag{2.5}$$

Considering the filter banks (FB) in Fig. 1 are not only PR FB but also wavelet systems, let N and $\tilde{N}$ denote the number of vanishing moments of the wavelet and its dual, respectively, we have the following equations

$$\begin{aligned}\sum_n (-1)^n n^k h_0(n) &= 0,\quad k=0,1,...,N-1\\ \sum_n (-1)^n n^k \tilde{h}_0(n) &= 0,\quad k=0,1,...,\tilde{N}-1.\end{aligned} \tag{2.6}$$

2.2. The Design of Linear Phase Biorthogonal Wavelet Filters with a Parameter

Assuming the biorthogonal wavelet filter banks are linear phase, and let L and $\tilde{L}$ be the length of $H_0(z)$ and $\tilde{H}_0(z)$, and N, $\tilde{N}$ be the vanishing moments. Then, one can represent $H_0(z)$ and $\tilde{H}_0(z)$ in the form of

$$H_0(z)=Q(z)(1+z^{-1})^N,\tilde{H}_0(z)=\tilde{Q}(z)(1+z^{-1})^{\tilde{N}}. \tag{2.7}$$

When felicitously select the length of the scale filters and the vanishing moments, we can obtain a group of biorthogonal PR filters with a parameter by solving the equations (2.4)-(2.6). As the technique in [12], in order to achieve biorthogonal wavelet filters, using equation (2.7), we employ Daubechies's Theorem [13, 14] to determine the interval which the parameter can be included. The following examples give the coefficient lists with a parameter and the intervals which the corresponding parameters can be included.

Example 1: with $L = 7,\ \tilde{L} = 9$ and $N = 2,\ \tilde{N} = 4$

$$\begin{aligned} h_0 &= \{-\frac{t}{16}, \frac{1-2t}{16}, \frac{t+4}{16}, \frac{3+2t}{8}, \frac{t+4}{16}, \frac{1-2t}{16}, -\frac{t}{16}\} \\ \tilde{h}_0 &= \{\frac{8t^3-6t^2+3t}{32(1+2t)}, \frac{-16t^3+20t^2-12t+3}{32(1+2t)}, \frac{-8t^3+6t^2+5t+20}{16(1+2t)}, \\ &\quad \frac{2t-3}{8(1+2t)}, \frac{16t^3-20t^2+28t+5}{32(1+2t)}, \frac{2t-3}{8(1+2t)}, \cdots\} \end{aligned}$$

The parameter $t \in [0.186, 1.129]$.

Example 2: with $L = 6,\ \tilde{L} = 10$ and $N = 3,\ \tilde{N} = 3$

$$\begin{aligned} g_0 &= \{s, \frac{1}{8}(1+8s), \frac{1}{8}(3-16s), \frac{1}{8}(3-16s), \frac{1}{8}(1+8s), s\} \\ \tilde{g}_0 &= \{\frac{s(3+48s+512s^2)}{8(-1+16s)}, \frac{(1+8s)(3+48s+512s^2)}{64(1-16s)}, \\ &\quad \frac{-1}{64}(9+112s+512s^2), \frac{7+288s+1280s^2+8192s^3)}{64(-1+16s)}, \\ &\quad \frac{45-304s-512s^2}{64(1-16s)}, \frac{7+288s+1280s^2+8192s^3)}{64(-1+16s)}, \cdots\} \end{aligned}$$

The parameter $s \in [-0.186, 0.31]$.

Example 3: with $L = 8,\ \tilde{L} = 8$ and $N = 5,\ \tilde{N} = 1$

$$\begin{aligned} g_0 &= \{s, \frac{96s+1}{32}, \frac{32s+5}{32}, \frac{5(16s-1)}{16}, \frac{5(16s-1)}{16}, \frac{32s+5}{32}, \frac{96s+1}{32}, s\} \\ \tilde{g}_0 &= \{\frac{2s(3+192s+8192s^2)}{64s-1}, \frac{(1+96s)(3+192s+8192s^2)}{16(1-64s)}, \\ &\quad \frac{15+736s+26624s^2+786432s^3}{16(1-64s)}, \\ &\quad \frac{5-40s+1536s+65536s^3}{4(1-64s)}, \frac{5-40s+1536s+65536s^3}{4(1-64s)}, \cdots\} \end{aligned}$$

The parameter $s \in [-0.336, 0.368]$.

Using this technique, we can obtain many other linear phase biorthogonal wavelet filters which include a parameter, such as biorthogonal wavelets filters with $L = 7,\ \tilde{L} = 13$ and $N = 4,\ \tilde{N} = 4$; $L = 11,\ \tilde{L} = 5$ and $N = 4,\ \tilde{N} = 2$; $L = 8,\ \tilde{L} = 4$ and $N = 3,\ \tilde{N} = 1$; etc.

3. The Hilbert Transform Pairs of Biorthogonal Wavelet Bases

3.1. The Hilbert Transform Pairs

Recall the definition of Hilbert transform, $\psi_g(t)$ is the Hilbert transform of $\psi_h(t)$, if

$$\hat{\psi}_g(\omega) = \begin{cases} -j\hat{\psi}_h(\omega), \omega > 0 \\ j\hat{\psi}_h(\omega), \omega < 0 \end{cases} \qquad i.e. \qquad \psi_g(t) = \mathcal{H}\{\psi_h(t)\}. \tag{3.1}$$

Let $\{H_0(z), H_1(z); \tilde{H}_0(z), \tilde{H}_1(z)\}$ and $\{G_0(z), G_1(z); \tilde{G}_0(z), \tilde{G}_1(z)\}$ are two biorthogonal wavelet filter banks. They both satisfy the above conditions (2.1)-(2.6), and the corresponding wavelets functions are $\{\psi_h(t), \tilde{\psi}_h(t)\}$ and $\{\psi_g(t), \tilde{\psi}_g(t)\}$ respectively. If $\psi_g(t) = \mathcal{H}\{\psi_h(t)\}$ and $\tilde{\psi}_g(t) = -\mathcal{H}\{\tilde{\psi}_h(t)\}$, then $\{\psi_h(t), \tilde{\psi}_h(t)\}$ and $\{\psi_g(t), \tilde{\psi}_g(t)\}$ are called as Hilbert transform pairs [15]. Furthermore, if both the scale filters $H_0(z)$ and $G_0(z)$ of the two biorthogonal wavelet filter banks are linear phase, and the corresponding wavelet functions $\psi_g(t)$ is the Hilbert transform of $\psi_h(t)$, then the lengths of $H_0(z)$ and $G_0(z)$ need to be odd and even separately. It fitly accords with the dual-tree complex wavelet transform introduced by Kingsbury. Since the wavelet bases form a Hilbert transform pair, the frequency response of the function $\psi_h(t) + j\psi_g(t)$ must have high attenuation in the region $-\infty < \omega < 0$, i.e. $\psi_h(\omega) + j\psi_g(\omega)$ approximates zero as $\omega < 0$. We consider finding suitable filters by maximizing

$$\frac{\max |O(\omega)|^2}{\int_{-\infty}^{0} |O(\omega)|^2 \, d\omega}, \tag{3.2}$$

where $O(\omega) \triangleq \psi_h(\omega) + j\psi_g(\omega)$.

3.2. The Design of Hilbert Transform Pairs of Biorthogonal Wavelet

In section 2.2, we have obtained many groups of biorthogonal linear phase wavelet filters with a parameter. To form Hilbert transform pairs, we let the lengths of $H_0(z)$ and $G_0(z)$, which corresponding to the analysis filters of the two trees of the dual-tree complex wavelet, to be odd and even separately. The optimal parameter set $\alpha^* = (t^*, s^*)$ can be obtained from

$$\alpha^* = \arg\max_{\alpha} \frac{\max |O(\omega)|^2}{\int_{-\infty}^{0} |O(\omega)|^2 \, d\omega}, \tag{3.3}$$

where $\alpha = (t, s)$ denote the parameter set of the biorthogonal wavelet filters to be designed. Once the parameters t and s are known, the scale and wavelet functions $H_0(z)$, $\tilde{H}_0(z)$, $G_0(z)$ and $\tilde{G}_0(z)$ can be easily computed. The wavelet functions are generated by the following equations ($z = e^{j\omega}$ and $\hat{H}(\omega) \hat{=} H(e^{j\omega})$):

$$\begin{cases} \hat{\varphi}_h(\omega) = \frac{1}{\sqrt{2}} \hat{H}_0\left(\frac{\omega}{2}\right) \hat{\varphi}_h\left(\frac{\omega}{2}\right) \\ \hat{\psi}_h(\omega) = \frac{1}{\sqrt{2}} \hat{H}_1\left(\frac{\omega}{2}\right) \hat{\varphi}_h\left(\frac{\omega}{2}\right) \end{cases}, \begin{cases} \hat{\tilde{\varphi}}_h(\omega) = \frac{1}{\sqrt{2}} \hat{\tilde{H}}_0\left(\frac{\omega}{2}\right) \hat{\tilde{\varphi}}_h\left(\frac{\omega}{2}\right) \\ \hat{\tilde{\psi}}_h(\omega) = \frac{1}{\sqrt{2}} \hat{\tilde{H}}_1\left(\frac{\omega}{2}\right) \hat{\tilde{\varphi}}_h\left(\frac{\omega}{2}\right) \end{cases}. \tag{3.4}$$

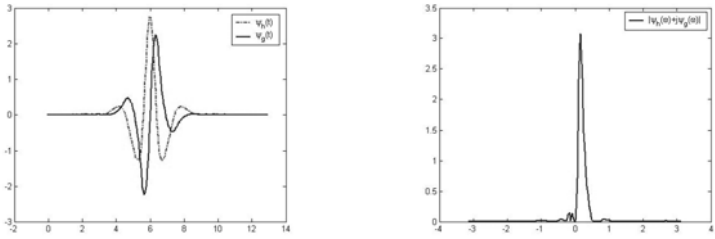

(a) (b)

FIGURE 2. (a) 13-7 and 10-6 biorthogonal wavelet functions (b)$|\psi_h(\omega) + j\psi_g(\omega)|$

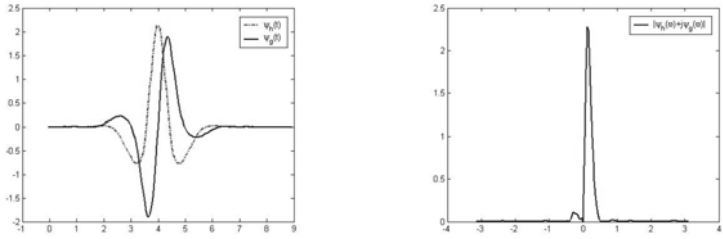

(a) (b)

FIGURE 3. (a) 9-7 and 8-8 biorthogonal wavelet functions (b)$|\psi_h(\omega) + j\psi_g(\omega)|$

According to the above design procedure, we construct three groups of Hilbert transform pairs. The corresponding optimal parameters are obtained by solving (3.3). The values of the optimal parameters (t^*, s^*) and the figures of the corresponding wavelet functions and $|\psi_h(\omega) + j\psi_g(\omega)|$ are given below.

Example 1: 13-7 tap and 10-6 tap linear phase biorthogonal wavelet filters which the corresponding wavelet functions constitute approximate Hilbert transform pairs. $t^* = -0.016$, $s^* = -0.008$ *Example 2:* 9-7 tap and 8-8 tap linear phase biorthogonal wavelet filters which the corresponding wavelet functions constitute approximate Hilbert transform pairs. $t^* = 0.244$, $s^* = -0.020$ *Example 3:* 13-7 tap and 8-8 tap linear phase biorthogonal wavelet filters which the corresponding wavelet functions constitute approximate Hilbert transform pairs. $t^* = -0.025$, $s^* = -0.025$ Especially, the parameters t^* and s^* can be approximated properly by some rational $t^*_{rational}$ and $s^*_{rational}$, so that the coefficients of the two filter banks are all rational numbers. For example, as to *Example 1* , we can choose $t^*_{rational} = -1/64$, $s^*_{rational} = -1/128$. Then the corresponding symmetric rational coefficients of the scaling filters are as follows:

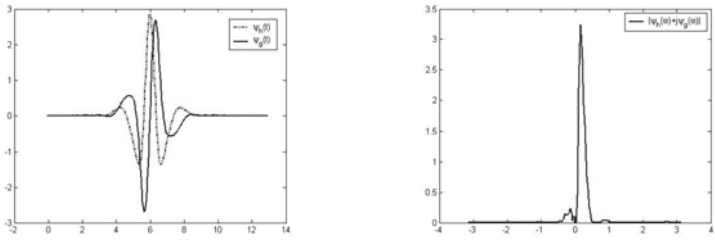

(a) (b)

FIGURE 4. (a) 13-7 and 8-8 biorthogonal wavelet functions (b)$|\psi_h(\omega) + j\psi_g(\omega)|$

$$
\begin{aligned}
h_0(n) &= \{-\frac{1}{64}\ \frac{1}{32}\ \frac{17}{64}\ \frac{7}{16}\ \frac{17}{64}\ \frac{1}{32}\ -\frac{1}{64}\} \\
3\times\tilde{h}_0(n) &= \{-\frac{1}{64}\ -\frac{1}{32}\ \frac{149}{1024}\ -\frac{105}{1024}\ -\frac{1267}{2048}\ \frac{443}{512}\ \frac{1259}{512}\ \frac{443}{512}\ \cdots\} \\
g_0(n) &= \{-\frac{1}{128}\ \frac{15}{128}\ \frac{25}{64}\ \frac{25}{64}\ \frac{15}{128}\ -\frac{1}{128}\} \\
9\times\tilde{g}_0(n) &= \{\frac{85}{4096}\ \frac{1275}{4096}\ -\frac{2349}{2048}\ -\frac{1235}{2048}\ \frac{1515}{256}\ \frac{1515}{256}\ -\frac{1235}{2048}\ \cdots\}. \qquad (3.5)
\end{aligned}
$$

As to *Example 2* , we choose $t^*_{rational} = 1/8$, $s^*_{rational} = -1/64$, then the corresponding symmetric rational coefficients of the scaling filters are:

$$
\begin{aligned}
h_0(n) &= \{0\ -\frac{1}{128}\ \frac{3}{64}\ \frac{33}{128}\ \frac{13}{32}\ \frac{33}{128}\ \frac{3}{64}\ -\frac{1}{128}\ 0\} \\
10\times\tilde{h}_0(n) &= \{\frac{19}{256}\ \frac{57}{128}\ -\frac{11}{4}\ \frac{263}{128}\ \frac{1325}{128}\ \frac{263}{128}\ \cdots\} \\
g_0(n) &= \{0\ -\frac{1}{64}\ -\frac{1}{64}\ \frac{9}{64}\ \frac{25}{64}\ \frac{9}{64}\ -\frac{1}{64}\ -\frac{1}{64}\} \\
\tilde{g}_0(n) &= \{\frac{1}{32}\ -\frac{1}{32}\ -\frac{7}{32}\ \frac{23}{32}\ \frac{23}{32}\ -\frac{7}{32}\ -\frac{1}{32}\ \frac{1}{32}\ 0\}. \qquad (3.6)
\end{aligned}
$$

Since all the denominators of the coefficients have the form of 2^k, $k \in Z$, the operations needed for the wavelet transform using these two groups of filters are only additions and shifts. Hence the complex wavelet transform can be computed very quickly. The figures (Fig.2-Fig.4) show that the wavelet functions designed in these examples are quite smooth and short supported, and $|\psi_h(\omega) + j\psi_g(\omega)|$ approximate zero for $\omega < 0$ as expected in each example. Comparing these figures with the designed results in [11], we find that they perform as well as the Example 3 of [11] in approximating a Hilbert transform pair. But the lengths of filters in our examples are much shorter (the filters of Example 3 in [11] are of length 13 and 11) and the corresponding wavelet functions are smoother, furthermore, the coefficients are symmetric, while in [11] are all asymmetric. Since we focus on designing linear phase biorthogonal FIR wavelet filters to form approximate

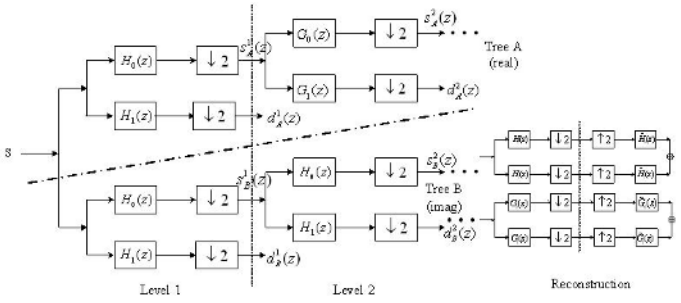

FIGURE 5. 1D dual-tree complex wavelet transform

Hilbert transform pairs, the corresponding complex wavelet transform provides a fast algorithm and a rapid, multiscale decomposition.

4. Application in Dual-Tree Complex Wavelet Transform for Iris Image Enhancement

Reliable automatic recognition of persons based on biometrics has been receiving extensive attention over the past decade. Recently, iris recognition is becoming an active topic in biometric due to its high reliability for personal identification [16-19]. In [19], the iris image preprocessing includes three steps: i) localization; ii) normalization; iii) enhancement. The iris image enhancement is an important step in the iris recognition system for the reasons in [19].

As far as image-processing applications are concerned, the main advantage as compared to the DWT is that the complex wavelet transform can give shift invariance and better directionality. As mentioned in section 3, the wavelet filter banks designed in this paper are of symmetric coefficients, shorter length and can generate smoother wavelets. These properties are quite advantageous to their application in complex wavelet transform for image processing, such as image enhancement. Fig.5 is the scheme of 1D dual-tree complex wavelet transform introduced by Kingsbury in [6], where $\{H_0(z), H_1(z); \tilde{H}_0(z), \tilde{H}_1(z)\}$ and $\{G_0(z), G_1(z); \tilde{G}_0(z), \tilde{G}_1(z)\}$ are two biorthogonal wavelet filter banks. When the two wavelets form a Hilbert transform pair, and two trees are sub-sampled differently, the whole transform is not only PR but also approximately shift invariant.

Using dual-tree complex wavelet transform of the linear phase biorthogonal wavelet pairs of *Example 2* (9-7 and 8-8 biorthogonal wavelet filters in equation (3.6)) in section 3.2, we consider enhancing the iris image by the enhancement algorithm introduced in [15]. Fig.6 represents the preprocessing procedures of the iris image. The methods of localization, normalization and estimation of local average intensity are as in [19]. Fig.6 (d) is subtracted from the normalized image to

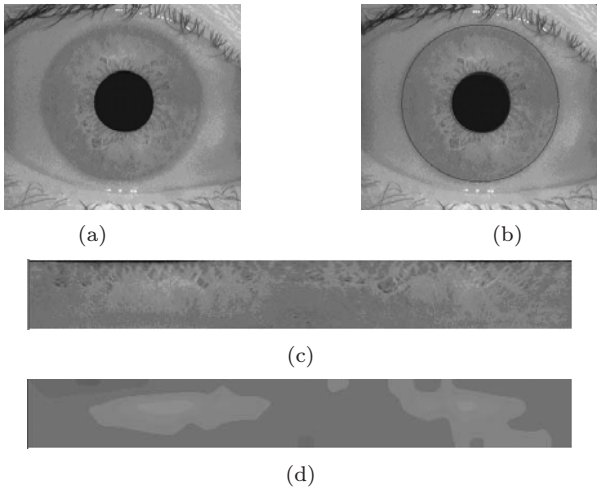

FIGURE 6. Iris image preprocessing: (a) original image; (b) localized image; (c) normalized image; (d) estimated local average intensity

compensate for a variety of lighting conditions. Fig.7 lists the enhanced results of the lighting corrected iris image: (a) is the enhanced image by the local histogram equalization [19]; (b) is the enhance image by DWT [20]; (c) is the enhanced image by our DT-CWT method. We can see that in the iris texture region, the enhanced iris image based on the dual-tree complex wavelet transform shows more clearly details of the randomly distributed and irregular small blocks, which constitute the most distinguishing characteristics of the iris; while in the non-texture region, it is smoother and introduces less distortional information. The improvement of the performance mainly due to the good properties of shift invariance and better directionality of the DT-CWT. Because the coefficients of all filters are symmetric and rational, the computational complexity is remarkably reduced. All these properties will benefit the subsequent processing in feature extraction and matching.

5. Conclusion

This paper presents the design of Hilbert transform pairs formed by two biorthogonal wavelet bases and their applications in DT-CWT for iris image enhancement. In terms of our new designing scheme, we can obtain wavelet filters which are all of linear phases and quite short lengths. Furthermore, the corresponding wavelet functions would be smoother than those designed by the existing algorithms. Especially, wavelet filters with rational coefficients have been obtained by adjusting the parameters, which can effectively reduce the computational complexity in the com-

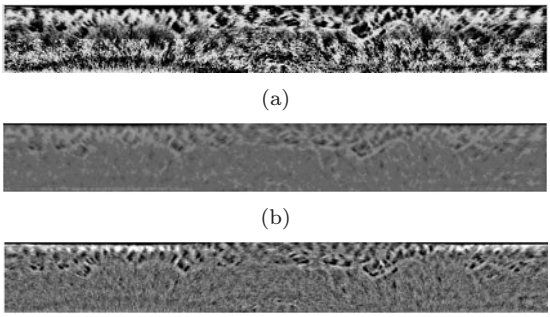

(a)

(b)

(c)

FIGURE 7. (a) Enhanced image by local histogram equalization; (b) Enhanced image by DWT; (c) Enhanced image by our DT-CWT method

plex wavelet transform. The new designed Hilbert transform pairs of biorthogonal wavelet filters have been used in dual-tree complex wavelet transform to enhance the iris image. Experiment results show that the algorithm based on dual-tree complex wavelet do perform better than those based on real wavelet transform and local histogram equalization.

Acknowledgment

The authors are very grateful to professor Tao Qian and the anonymous reviewers who give us many valuable comments and advice.

References

[1] J. Liang and T. W. Parks, *A translation invariant wavelet representation algorithm with applications.* IEEE Trans. on SP, vol. 44, no. 2, pp. 225-232, Feb. 1996.

[2] E. J. Candes, *Ridglets: theory and applications.* PhD thesis, Stanford University, 1998.

[3] I. W. Selesnick and L. Sendur, *Iterated oversampled filter banks and wavelet frames.* In Wavelet Apllications VII, Proceedings of SPIE, 2000.

[4] M. Do and M. Vetterli, *Pyramidal directional filter banks and curvelets.* In IEEE Proc. Int. Conf. Image Processing, 2001.

[5] N. G. Kingsbury, *The dual-tree complex wavelet transform: a new technique for shift invariance and directional filters.* In Proceedings of the Eighth IEEE DSP Workshop, Utah, August, 1998.

[6] N. G. Kingsbury, *Complex wavelets for shift invariant analysis and filtering of signals.* Applied and Computational Harmonic Analysis, vol. 10, no. 3, pp. 234-253, May 2001.

[7] J. K. Romberg, H. Choi, R. G. Baraniuk and N.G. Kingsbury, *Hidden Markov tree model for complex wavelet transform.* IEEE Transactions on Singal Processing, 2001.

[8] P. de Rivaz and N.G. Kingsbury, *Complex wavelet features for fast texture image retrieval.* In IEEE Proc. Int. Conf. Image Processing, 1999.

[9] I. W. Selesnick, *Hilbert transform pairs of wavelet bases.* IEEE Signal Processing Letters, vol. 8, no. 6, June 2001.

[10] I. W. Selesnick, *The design of Hilbert transform pairs of wavelet bases via the flat delay filter.* In Proc. IEEE Int. Conf. Acoust., Speech, Signal Processing (ICASSP), May 2001.

[11] I. W. Selesnick, *The design of approximate Hilbert transform pairs of wavelet bases.* IEEE Signal Processing, vol. 50, pp. 1144-1152, May 2002.

[12] L. Z. Cheng and D.L. Liang, *General construction of 9/7 wavelet filter and its application in image compression.* Optical Engineering, vol. 42, no.8, 2003.

[13] I. Daubechies, *Orthonormal bases of compactly supported wavelets.* Commun. Pure and Applied Maths., vol. 41, no. 2, pp. 909-980, 1988.

[14] A. Cohen, I. Daubechies and J.C. Feauveau, *Biorthogonal bases of compactly supported wavelets.* Commun. Pure and Applied Math, vol. 45, no. 1, pp. 485-560, 1992.

[15] H. X. Wang, *The research of new types of wavelets based on filter banks and their applications.* PhD thesis, National University of Defense Technology, 2004.

[16] J. Daugman, *High confidence visual recognition of persons by a test of statistical independence.* IEEE Trans. Pattern Aanly. Machine Intell., vol. 15, pp. 1148-1161, Nov. 1993.

[17] J. Daugman, *Demoulation by complex-valued wavelets for stochastic pattern recognition.* Int. J. Wavelets, Multi-Res. And Info. Processing, vol. 1, no. 1, pp. 1-17, 2003.

[18] J. Daugman, *How Iris Recognition Works.* IEEE Transactions on Circuits and Systems for Video Technology, vol. 14, no. 1, Jan. 2004.

[19] Li Ma, Tieniu Tan, Yunhong Wang and Dexin Zhang, *Efficient iris recognition by characterizing key local variations.* IEEE Transactions on Image Processing, vol. 13, no. 6, pp. 739-749, June 2004.

[20] P. Sakellaropoulos, L. Costaridou and G. Panayiotakis, *A wavelet-based spatially adaptive method for mammographic contrast enhancement.* Physics in Medicine Biology, vol. 48, no. 6, pp. 783-803, 2003.

Fengxia Yan
Department of Mathematics & System, School of Science, National University of Defense Technology, Changsha, 410073, Hunan, P.R. China
e-mail: xialang3@163.com

Lizhi Cheng
Department of Mathematics & System, School of Science, National University of Defense Technology, Changsha, 410073, Hunan, P.R. China
e-mail: lzcheng@hotmail.com

Hongxia Wang
Department of Mathematics & System, School of Science, National University of Defense Technology, Changsha, 410073, Hunan, P.R. China
e-mail: whx8292@hotmail.com

Wavelet Analysis and Applications
Tao Qian, Mang I. Vai and Xu Yuesheng, Eds.
Applied and Numerical Harmonic Analysis, 443–452

Supervised Learning Using Characteristic Generalized Gaussian Density and Its Application to Chinese Materia Medica Identification

S.K. Choy and C.S. Tong

Abstract. This paper presents the estimation of the characteristic generalized Gaussian density (CGGD) given a set of known GGD distributions based on some optimization techniques, and its application to the Chinese Materia Medica identification. The CGGD parameters are estimated by minimizing the distance between the CGGD distribution and known GGD distributions. Our experimental results show that the proposed signature based on the CGGD together with the use of Kullback-Leibler distance outperforms the traditional wavelet-based energy signature. The recognition rate for the proposed method is higher than the energy signature by at least 10% to around 60% - 70%. Nevertheless, the extraction of CGGD estimators still retains comparable level of computational complexity. In general, our proposed method is very competitive compared with many other existing Chinese Materia Medica classification methods.

Mathematics Subject Classification (2000). Primary 68T10; Secondary 65T60.

Keywords. supervised learning, generalized Gaussian density, Kullback-Leibler distance, similarity measurement, wavelets.

1. Introduction

Wavelets have recently emerged as an effective tool to analyze texture information as they provide a multi-resolution and orientation representation of an image by efficient transform. Thus, several well-known texture signatures such as generalized Gaussian density [1-2] signature, energy [3] signature, co-occurrence [4] signature, high order moments and wavelet-domain Hidden Markov Tree models [5-6] based on wavelet subbands are widely used in texture image retrieval.

For the image classification problem, a wide variety of texture feature extraction methods have been proposed based on different techniques. Some features are extracted directly from the gray-scale image and make use of its co-occurrence properties [7], whereas some are extracted by wavelet transform followed by applying statistical measure on the transformed coefficients [3-6].

For the GGD signature, it has been shown that the image retrieval performance is superior to many other existing techniques. However, the GGD signature is seldom used for supervised learning (image classification). The main reason is that a slight change in GGD parameters may lead to a substantial variation in its distribution and hence it is difficult to characterize a benchmark distribution from known GGD distributions. In this paper, we will show how to estimate the characteristic GGD given a series of known GGD distributions based on some optimization techniques. We will also study and compare the recognition performance of the CGGD with the energy signature on Chinese drugs identification.

The outline of this paper is as follows. In the next section, we review several wavelet-based features including the energy signature and the generalized Gaussian density signature. In section 3, we measure the discrepancy between GGD distributions based on Kullback-Leibler distance and define the CGGD as the distribution that minimizes the mean discrepancy to known GGD distributions. In section 4, we conduct an experiment and summarize the classification results of a feasibility study on 10 Chinese Materia Medica. Then, we conclude with some discussions in section 5.

2. Review of Wavelet Signatures

For N levels' discrete wavelet transform, the image is decomposed into $3N$ high-pass subbands and one low-pass subband. Note that all wavelet signatures discussed in this paper are derived from high-pass subbands and thus the low-pass subband will be neglected. The standard order of the $3N$ subbands (hereafter high-pass subband is referred to as subband) is labeled as follows

$$\{S_1, S_2, \ldots, S_{3N}\} = \{NHL, NLH, NHH, \ldots, 1HL, 1LH, 1HH\}, \tag{1}$$

where NHL, NLH and NHH are subbands with horizontal, vertical and diagonal detail coefficients at level N respectively. In this section, we shall only report the wavelet-based energy signature and the GGD signature to characterize each subband.

2.1. Energy Signature

Let S_k be the k^{th} subband of size $X \times Y$ and $h_{i,j}$ be its $(i,j)^{th}$ coefficient, then the root-mean-square (RMS) energy of S_k is defined as

$$E_{S_k} = \left(\frac{1}{XY} \sum_{j=1}^{Y} \sum_{i=1}^{X} h_{i,j}^2 \right)^{1/2}. \tag{2}$$

The RMS energy signature $\{E_{S_k}\}_{k=1,2,...,3N}$ represents the distribution of the energy of the subbands. An alternative measure of the energy signature is the mean of the absolute value of the subband and is given by

$$AE_{S_k} = \frac{1}{XY}\sum_{j=1}^{Y}\sum_{i=1}^{X}|h_{i,j}|. \tag{3}$$

In practice, the combination of E_{S_k} and AE_{S_k} are often used to enhance the retrieval rate or as a feature vector for classification. Here, we refer to $\{E_{S_k}\}_{k=1,2,...,3N} \cup \{AE_{S_k}\}_{k=1,2,...,3N}$ as the Extended Energy (EE) signature.

2.2. Modelling of Wavelet Coefficients by Generalized Gaussian Density

Experiments show that for a variety of images, the distribution of the wavelet coefficients of all subbands can be modeled by the GGD, which is defined as

$$p(h;\alpha,\beta) = \frac{\beta}{2\alpha\Gamma(1/\beta)}e^{-(|h|/\alpha)^{\beta}}, \tag{4}$$

where $\Gamma(z) = \int_0^{\infty} e^{-t}t^{z-1}dt$, $z > 0$ is the Gamma function. Here, α models the width of the *pdf* (standard deviation) whereas β corresponds to the shape of the GGD. Note that $\beta = 2$ yields the Gaussian density function and $\beta = 1$ yields the Laplacian density function. The GGD parameters α and β can be estimated by Maximum Likelihood Estimation (MLE) [1] or Moment Estimation (ME) [2]. The GGD signature of an image is then referred to as $\{\alpha_{S_k}, \beta_{S_k}\}_{k=1,2,...,3N}$.

3. Similarity Measurement

In pattern recognition, classification of images can be treated as measuring the discrepancy between feature vectors (i.e. input test feature vector and characteristic feature vector). For the EE signature, the simplest measure is to use norm-based metric. For the GGD signature, it is noted that a slight change in GGD parameters may lead to a substantial deviation in its distribution. Thus, it is more reasonable to measure the similarity (or equivalently, discrepancy) between the actual GGD distributions rather than their parameters. Here, we shall adopt the use of Kullback-Leibler distance (KLD) to measure the discrepancy of two distributions p and q and it is given by

$$KLD(p,q) = \sum_i p_i log\frac{p_i}{q_i}, \tag{5}$$

where $log(p_i/q_i)$ is defined to be zero for $p_i = 0$ or $q_i = 0$. Substitute Eq. (4) into Eq. (5) and after some manipulations. We have the following form for the Kullback-Leibler distance between two GGD distributions [1]

$$D\{p_1(\bullet,\alpha_1,\beta_1),p_2(\bullet,\alpha_2,\beta_2)\}=log\left(\frac{\beta_1\alpha_2\Gamma(1/\beta_2)}{\beta_2\alpha_1\Gamma(1/\beta_1)}\right)+\left(\frac{\alpha_1}{\alpha_2}\right)^{\beta_2}\frac{\Gamma((\beta_2+1)/\beta_1)}{\Gamma(1/\beta_1)}-\frac{1}{\beta_2}. \tag{6}$$

Hence, two GGDs are close to each other when $D(p_1,p_2)$ is small and vice versa and the discrepancy between two wavelet subbands can be calculated accurately using only the GGD parameters.

3.1. Estimation of Characteristic GGD

In addition to computing the discrepancy between two GGDs, it is also desirable to estimate the characteristic GGD distribution $p(\bullet,\hat{\alpha},\hat{\beta})$ given L known GGD distributions $\{p(\bullet,\alpha_i,\beta_i)\}_{i=1,2,\ldots,L}$ in which the CGGD best fits the known GGD distributions. Let $\theta_i=(\alpha_i,\beta_i)$ and $J(\theta_i,\theta)=\sum_{i=1}^{L}D\{p(\bullet,\theta_i),p(\bullet,\theta)\}$. Mathematically, it computes

$$\hat{\theta}=arg\min_{\theta}J(\theta_i,\theta), \tag{7}$$

which yields

$$\hat{\alpha}=\left(\frac{\hat{\beta}}{L}\sum_{i=1}^{L}w_i\right)^{1/\hat{\beta}}, \tag{8}$$

$$1+\frac{1}{\hat{\beta}}\left[log\left(\frac{\hat{\beta}\sum_{i=1}^{L}w_i}{L}\right)+\Psi(\frac{1}{\hat{\beta}})\right]-\frac{\sum_{i=1}^{L}\left[w_i log\alpha_i+\frac{w_i}{\beta_i}\Psi(\frac{\hat{\beta}+1}{\beta_i})\right]}{\sum_{i=1}^{L}w_i}=0, \tag{9}$$

where $w_i=\frac{\alpha_i^{\hat{\beta}}\Gamma((\hat{\beta}+1)/\beta_i)}{\Gamma(1/\beta_i)}$, and $\Psi(z)=\frac{\Gamma'(z)}{\Gamma(z)}$ is a di-gamma function. The transcendental equation (9) can be solved numerically using Newton-Raphson or Brent's iterative algorithm. The solution $p(\bullet,\hat{\alpha},\hat{\beta})$ (see Fig. 1) is then the CGGD distribution generated by $\{p(\bullet,\alpha_i,\beta_i)\}_{i=1,2,\ldots,L}$. By Eq. (6), the total distance (TD) between a test image $Q_1=\{\alpha_1^{(k)},\beta_1^{(k)}\}_{k=1,2,\ldots,3N}$ and the CGGD $Q_2=\{\hat{\alpha}_2^{(k)},\hat{\beta}_2^{(k)}\}_{k=1,2,\ldots,3N}$ obtained from the training images is the sum of all the distance D between two corresponding subbands in the same level. i.e.

$$TD\{Q_1,Q_2\}=\sum_{k=1}^{3N}D(p_{Q_1}^{(k)},p_{Q_2}^{(k)}). \tag{10}$$

The CGGD provides an effective characterization of GGD distributions and thus the supervised learning based on CGGD parameters can be implemented very efficiently. In addition, the computational complexity in the similarity measurement and the storage of the signature is vastly reduced compared with using the whole set of wavelet coefficients, which may contain hundreds of parameters.

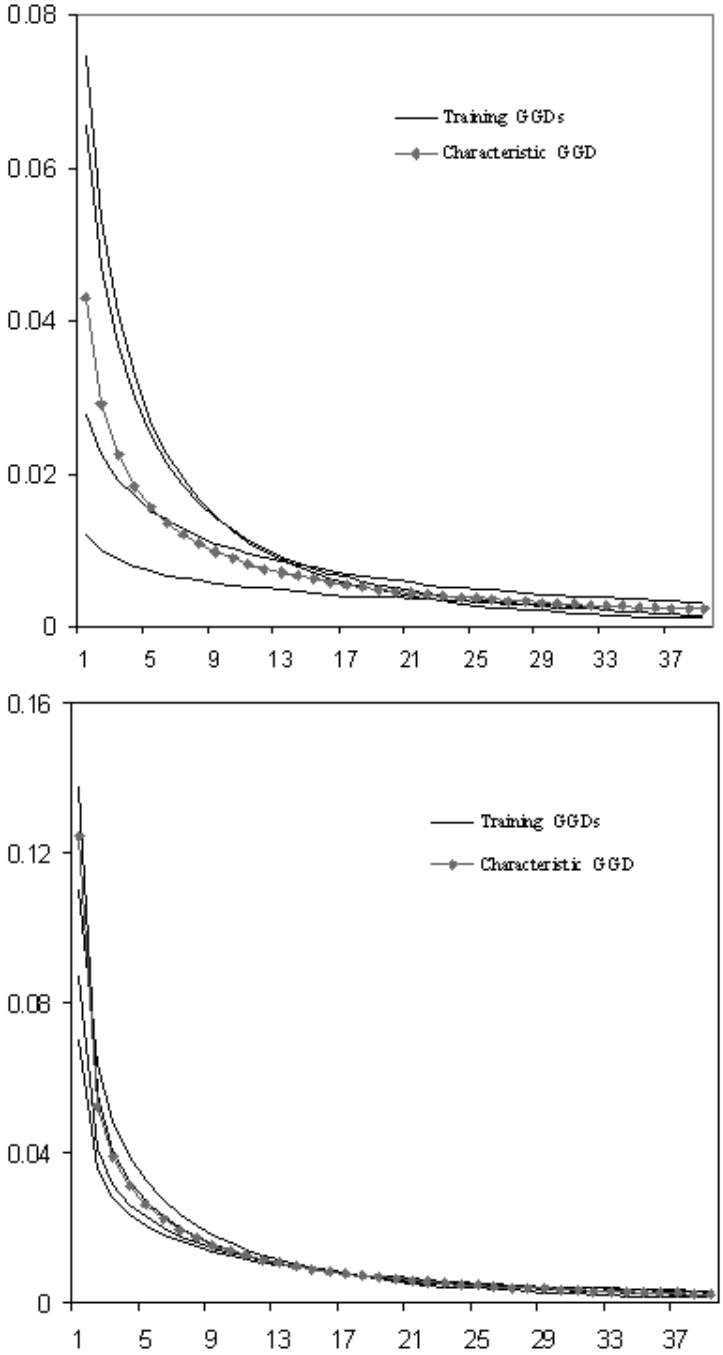

FIGURE 1. Two typical examples of training GGDs and CGGD with L=4.

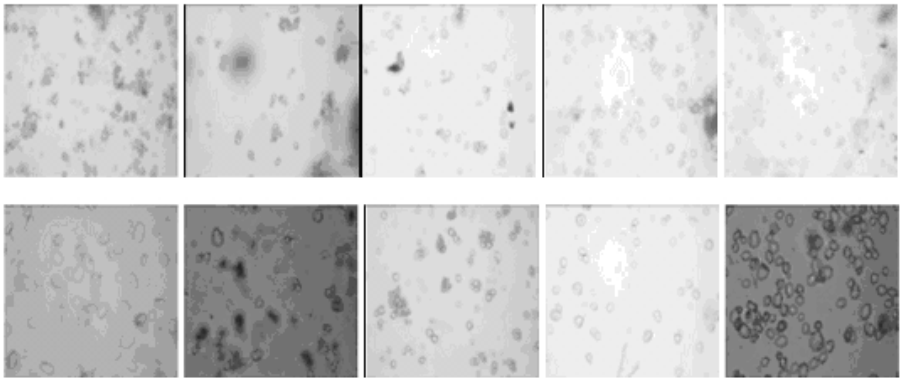

FIGURE 2. Ten different types of gray-scale starch grains images; from left to right, and top to bottom: BaiZhi, BanLanGen, ChuanWu, FenFangJi, GuangFangJi, ShanYao, TianHuaFen, TianNanXing, TuFuLing, ZheBeiMu.

4. Experimental Results and Discussion

4.1. Background of Chinese Materia Medica Identification

Chinese Materia Medica (CMM) is becoming very popular worldwide. But in order to secure its worldwide adoption, efficient yet effective methods for classification of the ingredients of CMM is of paramount importance. The traditional method relies on human senses and is quite subjective. It also requires very long training times and can only be taught in interactive environment. Since misclassification can have serious consequences, more accurate and objective technique is sought.

More recently, a number of research papers and reports in CMM identification using image processing techniques have already been published, and the methods of extracting information for herbs classification had been investigated. One of the classification techniques [8] was based on a powder-form starch grains image (see Fig. 2). A segmented sample of grains in the binarized image is chosen manually and randomly and each sample is further processed to obtain basic features such as area and perimeter for classification. This process, however, is time-consuming and subjective and therefore it is undesirable for herbs classification in real time application.

One of our motivations in this paper is to apply the CGGD signature with a suitable discrepancy measure on the starch grains image for classification and then to build an efficient, objective, and accurate classification system, thus rendering the drug identification process objective and automated, serving as a benchmark standard for CMM identification.

TABLE 1. Recognition rates of wavelet signatures using different measures

Signature+Discrepancy Measure	Recognition rate
EE+L_1	40.00%
CGGD+KLD	64.00%

4.2. Supervised Learning and Recognition Performance

Ten images have been taken for each of 10 different Chinese drugs (see Fig. 2): 5 sample images for each drug are used for training and the other 5 reserved for testing. Note that all signatures in this paper are derived by 2-levels' wavelet decomposition with coiflet 5 as a wavelet function. In the training phase, 10 characteristic EE signatures via Eq. (2) and Eq. (3) are obtained by considering the mean of the training feature vectors and the 10 sets of CGGD signatures $\{\hat{\alpha}_i^j, \hat{\beta}_i^j\}_{i=1,2,\ldots,10;j=1,2,\ldots,6}$ are also obtained via Eq. (8) and Eq. (9).

In the testing phase, we compare the EE signature of an input test sample with each of the 10 characteristic EE signatures using $L_p - norm$. For the GGD signature, we compare the test GGD signature with each of the 10 CGGD signatures by using Eq. (10). That is, if we denote Ω_i as a characteristic image signature of the i^{th} drug and Ω_t as a signature of the input test sample. Then the input test sample is assigned to the i^{th} drug if

$$\overline{d}[\Omega_i, \Omega_t] < \overline{d}[\Omega_j, \Omega_t], \ for\ i \neq j; j = 1, 2, \ldots, 10, \tag{11}$$

where $\overline{d}[\bullet]$ is some distance measures. In this paper, we shall only report the results based on two measures of discrepancy, namely, $L_1 - norm$ for the EE signature and the KLD distance for the CGGD. Table 1 shows the summary of the recognition rates for the two signatures using two measures of discrepancy. Note that using the GGD parameters obtained by optimization method leads to recognition rate of 64%. For the EE signature with $L_1 - norm$, the recognition rate is 40% which is considered unsatisfactory. This indicates that our proposed CGGD is more robust than the EE signature.

Instead of using 5 training samples, it is of interest to know the recognition rate using different number of training samples. Figure 3 plots the recognition rates vs. number of samples used in the training phase. Note that the classification performance for the CGGD+KLD is always better than the EE+L_1 and we can achieve 70% recognition using 7 training samples. In particular, it is observed that the classification rate for the CGGD+KLD increases monotonically with the number of training samples, while there is an unstable sharp change for the EE+L_1 (when no. of training samples = 5). This implies again our proposed CGGD is a robust feature and has a better recognition performance. The only drawback for the CGGD is that the computational complexity is higher than the EE signature as the transcendental Eq. (9) is a highly non-linear equation which needs to be solved numerically.

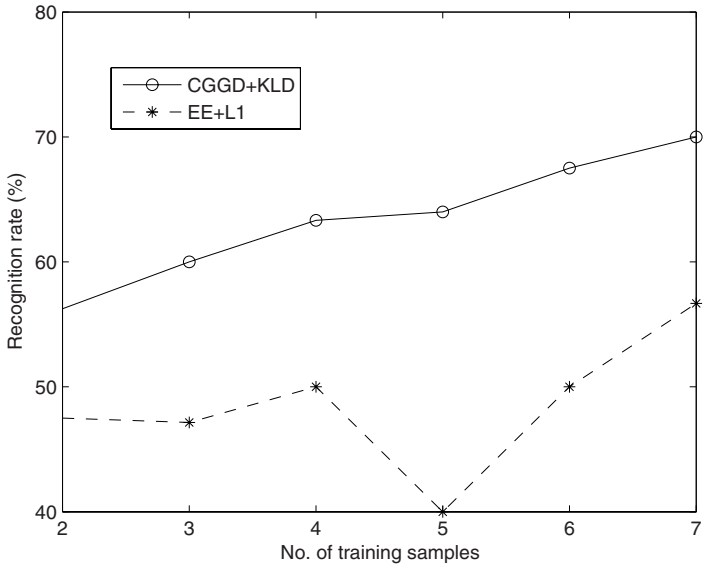

FIGURE 3. Recognition rates vs. no. of training samples

In addition to the top 1 recognition, it is often desirable to ensure that the correct drug should be the top M "closest" to the input test sample. This can be referred to as the cumulative percentage of the input test sample belonging to one of the top M best matches. In the 5-training samples case, we can achieve 80% top M recognition rate at $M = 2$ for the CGGD+KLD, which is considered satisfactory. If we use 7 training samples, the top M recognition rate is over 90% at $M = 2$. This suggests that we can apply the proposed feature in conjunction with other features (e.g. high order moments) to carry out a multi-stage recognition to further improve the classification performance.

5. Conclusions

We have introduced the estimation of the characteristic generalized Gaussian density and made use of it with the Kullback-Leibler distance to identify Chinese Materia Medica. The CGGD parameters are estimated by minimizing a mean distance between a CGGD distribution and a set of known GGD distributions. These CGGD parameters provide an effective characterization of GGD distributions and thus are suitable for supervised learning.

Our experiments show that the CGGD and KLD seem to be an effective signature and discrepancy measure in this small scale study. The recognition performance for the CGGD+KLD outperforms the EE+L_1 by at least 10% which is

considered satisfactory. Moreover, our proposed method is efficient and objective compared with many other existing CMM classification methods in which manual segmentation is necessary.

For a large scale study, we are currently extracting more independent features to further improve the recognition performance such as exploiting the feature from spatial statistics. We are also investigating the use of more sophisticated statistical techniques (e.g. using clustering analysis) and design a statistical multi-stage recognition system for classification.

Acknowledgment

This work is partially supported by Faculty Research Grant from the Hong Kong Baptist University.

References

[1] M. N. Do, M. Vetterli, Wavelet-Based Texture Retrieval Using Generalized Gaussian Density and Kullback-Leibler Distance, *IEEE Trans. Image Processing*, **11**(2), pp. 146-158, 2002.

[2] K. Sharifi and A. Leon-Garcia, Estimation of Shape Parameter for Generalized Gaussian Distribution in Subband Decomposition of Video, *IEEE Trans. Circuits and Systems, Video Tech.*, **5**(1), pp. 52-56, 1995.

[3] M. Unser, Texture Classification and Segmentation Using Wavelet Frames, *IEEE Trans. Image Processing*, **4**(2), pp. 1549-1560, 1995.

[4] A. L. Amet, A. Ertuzun, A. Erqil, Texture Defect Detection Using Subband Domain Co-occurrence Matrices, *Proceedings of IEEE Southeast Symp. for Image Analysis and Interpretation*, pp. 976-979, April 6-7, 1998.

[5] G. L. Fan and X. G. Xia, On Context-Based Bayesian Image Segmentation: Joint Multi-context and Multiscale Approach and Wavelet-Domain Hidden Markov Models, *Proceedings of the* 35^{th} *Asilomar Conference on Signals, Systems and Computers*, Pacific Grove, CA, Nov 4-7, 2001.

[6] G. L. Fan and X. G. Xia, Maximum Likelihood Texture Analysis and Classification Using Wavelet-Domain Hidden Markov Models, *Proceedings of the* 34^{th} *Asilomar Conference on Signals, Systems and Computers*, Pacific Grove, CA, Oct 29-Nov 1, 2000.

[7] R. F. Walker, P. Jackway, and I. D. Longstaff, Improving Cross-Cooccurrence Matrix Feature Discrimination, *Proceedings of the* 3^{rd} *Conference on Digital Image Computing: Techniques and Application*, pp. 643-648, Dec 6-8, 1995.

[8] W. J. Zhang, Pharmacognostic study of Arctium Tomentosum Mill. and Microscopic Study of Chinese Materia Medica, Master of Medicine Thesis, Liaoning College of Traditional Chinese Medicine, 2001.

S.K. Choy
Centre for Mathematical Imaging and version
Department of Mathematics
Hong Kong Baptist Univeristy
Kowloong Tong
Hong Kong
e-mail: skchoy@math.hkbu.edu.hk

C.S. Tong
Centre for Mathematical Imaging and version
Department of Mathematics
Hong Kong Baptist Univeristy
Kowloong Tong
Hong Kong
e-mail: cstong@hkbu.edu.hk

Wavelet Analysis and Applications
Tao Qian, Mang I. Vai and Xu Yuesheng, Eds.
Applied and Numerical Harmonic Analysis, 453–462

A Novel Algorithm of Singular Points Detection for Fingerprint Images

Taizhe Tan and Jiwu Huang

Abstract. It is very important to effectively detect singularities (core and delta)for fingerprint matching, fingerprint classification and orientation flow modeling. In this paper, based on multilevel partitions in a fingerprint image, we present a new method of singularity detection to improve the accuracy and reliability of the singularities. Firstly, based on the information of the orientation field, with the Poincaré index method, we detect singularities which are estimated by different block sizes and various methods of orientation field estimation (smoothing or no smoothing). Secondly, based on the corresponding relationship between the singularities detected by multilevel block sizes and by different methods of orientation field estimation, we extract the singularities precisely and reliably. Finally, an experiment is done in the NJU-2000 fingerprint database that has 2500 fingerprints. The result shows that the method performs well and it is robust to poor quality images.

Keywords. fingerprint, singularity, multilevel partitions, orientation field smoothing.

1. Introduction

In recent years, the automatic fingerprint authentication technology has received more attention since fingerprint recognition based on distinctive personal traits has the potential to become an irreplaceable part of many identification systems [1, 2]. In a general way, in a fingerprint authentication system, it mainly includes fingerprint collection, fingerprint feature extraction, fingerprint matching and fingerprint classification and so on. Moreover, the fingerprint classification[3, 4, 5, 6, 7, 8] can be directly determined by the number, type and positions of the singular points. The singular points also represent the intrinsic points of reference within the fingerprint image and can therefore be used to register or approximately align two

This work was completed with the support of the Foundation for Doctor Start-up of Guangdong University of Technology(053017).

different images during matching. Thus, it is of great significance that the singularities are detected accurately and reliably.

Global patterns of ridges and furrows form special configurations in the central region of fingerprint, which is called pattern area. The pattern areas of loop or whorl types of fingerprints contain two types of singular points (delta and core). The delta provides the starting point for ridge tracing and ridge counting. The core can be used as reference point during fingerprint matching. The singular points are shown in Fig. 1.

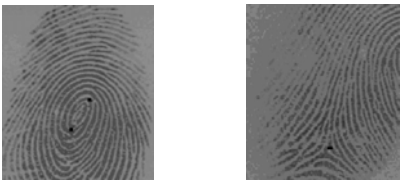

FIGURE 1. Examples of core point and delta point

There are some papers which have touched directly upon singularity detection of fingerprint images. Herny[9]defines the core as the upper point of the innermost ridge of the fingerprint. Srinivasan and Murthy[10]proposed an approach based on the examination of the local characteristics of the orientation image. They examined the dominant direction of the orientation in four quadrants around each point and used several rules to detect and classify the singular points. This method is very heuristic in its approach. An interesting implementation of the Poincaré method for locating singular points was proposed by Bazen and Gerez[11]. In this method, according to Green's theorem, a closed line integral over a vector field can be calculated as a surface integral over the rotation of this vector field; in practice, instead of summing angle differences along a closed path, the authors compute the "rotation" of the orientation image (through a further differentiation) and then perform a local integration (sum) in a small neighborhood of each element. Zhang et al.[12] suggested the corner detection method to find the region of singularities and gray level of ridges was tracked to get the position of singularities. However, estimating the location of the singular point itself is a difficult problem. Existing methods are based on computing the Poincaré index of the orientation image at each pixel position. These methods are sensitive to noise and generate many false singularities in noisy images. An elegant and practical method based on the Poincaré index being the main method for singularity detection was proposed by Kawagoe and Tojo[4]. Most of the approaches addressed in the literature for singularity detection operate on the fingerprint orientation image.

For images of better quality, the focus is how to fix the precise locations of singular points. For different partition sizes, the larger the partition size is, the more the position windage is. But the robust of the arithmetic is bad when the partition size is comparatively small. Whereas low quality images have serious noise pollution, the reliable orientation field estimation becomes difficult intrinsically, so

the precise locations of singular points are difficult to identify, meanwhile, there are many fake singularities detected in the mistaken directions. Thereby it is a very arduous task to effectively detect singularities from the fingerprint images. In this paper, in order to improve the precision and reliability of the detected singularities, we detect the singularities by partitioning the fingerprint image with multilevel sizes and using the relationship characters of locations of the estimated singularities based on the different methods for estimating the fingerprint orientation field, where the singularities detection is based on the Poincaré index.

This paper is organized as follows. The traditional Poincaré index theory and our method are introduced in section 2. Section 3 describes our detailed arithmetic. Experiments and discussions are given in the last section.

2. Singularity Detection Based on Poincaré Index

Poincaré index suggested by Kawagoe and Tojo[4] is used to detect singularities. Let o' be the orientation field of fingerprint image, the Poincaré index at pixel (i, j) of image which is enclosed by the digital curve can be computed as formula 2.1–2.4.

$$Poincaré(i,j) = \frac{1}{2\pi}\sum_{k=0}^{N_\Psi}\Delta(k) \tag{2.1}$$

$$\Delta(k) = \begin{cases} \delta(k), & \text{if } \mid \delta(k) \mid < \frac{\pi}{2}; \\ \pi + \delta(k), & \text{if } \delta(k) \leq -\frac{\pi}{2}; \\ \pi - \delta(k), & \text{otherwise.} \end{cases} \tag{2.2}$$

$$\delta(k) = o'(\Psi_x(i'), \Psi_y(i')) - o'(\Psi_x(i), \Psi_y(i)) \tag{2.3}$$

$$i' = (i+1) \mod N_\Psi \tag{2.4}$$

Where $\Psi_x(i)$ and$\Psi_y(i)$ are the x and y coordinates of the ith point of a closed digital curve with N_Ψ pixels respectively. The point(i, j) will be core point if the value of Poincaré index is 1/2, and delta point if the value of Poincaré index is -1/2.

K. Karu et al.[5] and J. G Chen et al.[8] both present the methods of singular points based on Poincaré index. In both methods, the measures of eliminating the noise pollution are taken. Although the method of smoothing time after time and iterative computing by K. Karu et al.[5] eliminates the noises partially, the model area information tends to be changed, besides the precision of the position of singularities is debased and /or the true singularities are lost, and the computation complexity is also increased. Moreover, using the different templates to check singularities, J. G Chen et al.[8] address the method of eliminating the noises in a way. But the singular points near fingerprint image margin are difficult to be detected since the sizes of the blocks and the template for Poincaré index computation are larger.

Both the methods above have their own merits and demerits respectively. In this paper, we present a method as follows: Firstly, fingerprint images are partitioned with multilevel block sizes and ridge directions of each block image are

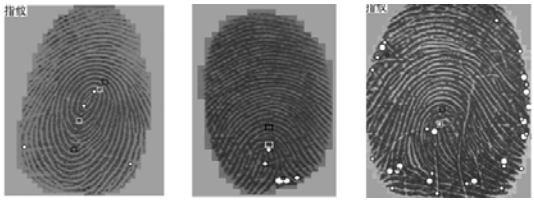

FIGURE 2. Singularities detected with our method, and corresponding relationship between these singularities' positions

estimated by smoothing and no smoothing processing respectively. By using the information of the estimated block directions, the Poincaré index of the centre point of each block is computed, and the types and locations of the singular points for different partitions are determined with the Poincaré index computed. Secondly, in order to ensure the locations of singularities are relatively precise, the centroid of the convergence area of the singularities detected in same way (block size) is regarded as the location of singular point of this partition way. There is a corresponding position relationship among the singularities detected by multilevel partitions and by the above-mentioned methods (shown in Fig. 2). For the sake of getting the precise locations of singularities, the locations of the singularities detected by the way of the small block size and no smoothing directions are regarded as the true locations of the final singularities. Finally, based on the corresponding relationship between the singularities detected by multilevel partitions and by different methods of orientation field estimation, we eliminate the false singularities, and retain the true, thereby the precision and reliability of the singularities are taken into account. The examples of singularities detected with our method and corresponding relationship between these singularities' positions are shown in Fig. 2. In the Figure, the large black square blocks denote the core points detected with 16×16 block image and smoothing the orientation field, the small black square blocks denote the delta points detected with 16×16 block image and no smoothing the orientation field, the large white square blocks denote the core points detected with 8×8 block image and smoothing the orientation field, the largest white ellipses denote the delta points detected with 8×8 block image and no smoothing the orientation field, the larger white ellipses denote the delta points detected with 8×8 block image and smoothing the orientation field, and the small white ellipses denote the core points detected with 8×8 block image and no smoothing the orientation field, where the central point of each plot corresponds with the location of the singular point detected in different ways.

3. Arithmetic Describing

Our arithmetic includes the following steps: (1) Image segmentation, (2) singularity detection based on multilevel partitions and different methods for direction

estimation, and (3) locating singularity's ultimate precise position based on the corresponding relationship between the singularities detected above.

3.1. Fingerprint Image Segmentation

Image area is segmented for the sake of getting the valid fingerprint area. In our method, the block-wise average grayscale and standard deviation are used to segment the image. The block is considered as the foreground if its grayscale mean and standard deviation satisfy some predefined standard, otherwise, the background.

3.2. Singularity Detection Based on Multilevel Partitions and Different Methods of Direction Estimation

3.2.1. Fingerprint Image Multilevel Partitions. The partition sizes are set with m levels, the size of each level block is $W_0 \times W_0, W_1 \times W_1, \ldots, W_{m-1} \times W_{m-1}, (W_i = W_0 \times (i+1), i = 0, 1, \ldots, m-1, where, W_0 = 8, m = 2)$.

3.2.2. Multilevel Partitions Based Singularity Detection. 1. **Fingerprint Image Orientation Estimation.** After each partition, a set of block images is gained. We use the method presented by Jain, Hong and Bolle[13] to estimate the orientation of each block image (u, v). But, here the orientation field is not processed with smoothing. 2. **Singularity Detection.** For a certain block size, a set of singularities is gotten by the Poincaré index. Assume that the sets of core and delta detected by the different block sizes are $\{CP_{i,j}\}$ and $\{DP_{i,j}\}$ respectively, where let i be the partition level and j be the jth point. To be more concrete, singularity detection includes the steps as follows:

Step 1. The Poincaré index of each block (u, v) is computed according to the orientation field, and based on the value of Poincaré index of each block, the core point and delta point are determined with the interested point within the template. Because the smaller the size of template is, the easier it is for the singularities on the image edge to be detected and the less the computation complexity is, the template size for computing the Poincaré index of core is 2×2, and for delta is 3×3. The interested points are all adopted as the center point of the template. It needs noting that only the delta points are detected in the second level of partition (16×16).

Step 2. Once the centroid coordinate of the convergence area of the singularities detected by Poincaré index in same block size is computed, hereby, CP_i and DP_i, the sets of the singularities which have the comparatively precise locations will be gained, where i denotes the partition level. The method for computing the centroid coordinate is k-means arithmeticz[14].

Step 3. The orientation of each block is smoothed with 2 dimension low-pass filter, and the size of filter is 5×5. Again, the value of Poincaré index of each block is computed by the smoothed orientation field and the new core and delta points are determined. The method is the same as before, but only the core points are detected in the second level of partition (16×16). Lastly, new sets of singularities CP'_0, DP'_0 and CP'_1 are gained.

3.3. Locating Singularity's Ultimate Precise Position

In this section, the singularity's ultimate location will be decided. Once the location of the singularity detected by the smallest block size and no smoothing orientation field is taken as the true location of the final singularity, and at the same time the character of corresponding relationship between the positions of singularities detected in our method in the same fingerprint image is considered, the fake singularity will be eliminated and the true be gotten. The approaches and rules of determining singularities are described as follows:

3.3.1. Locating Core Point.

1. Let each core point $CP'_{0,r}$ (r denotes the rth core) detected by the block size $W_0 \times W_0$ and smoothing the orientation field be the norm core point, and the cores of the set CP_0 are searched out within a certain distance according to the formula 3.1:

$$(CP_{0,j} \cdot x - CP'_{0,r} \cdot x)^2 + (CP_{0,j} \cdot y - CP'_{0,r} \cdot y)^2 < Threshold_0 \tag{3.1}$$

   If there is only one core $CP_{0,j}$, then the core $CP_{0,j}$ is determined as the true core point and is marked. And if there are cores CP'_1 which meet the formula 3.2 condition, then the core $CP_{0,j}$ is marked as the highest score and the core $CP'_{1,min}$ which is the nearest to the norm core $CP'_{0,r}$ is marked.

$$(CP'_{1,j} \cdot x - CP'_{0,r} \cdot x)^2 + (CP'_{1,j} \cdot y - CP'_{0,r} \cdot y)^2 < Threshold_1 \tag{3.2}$$

   Otherwise, the core $CP_{0,j}$ is marked as the second grade score.
2. If the conditions above are not met, then another judgment depends on whether there is a set of the core $CP_{0,j}$ in which the core $CP_{0,j}$ is very near to the norm core $CP'_{0,r}$ within a certain distance of the threshold value, where the distance threshold value is smaller. (1) If there is only one core $CP_{0,j}$ in the set, then $CP_{0,j}$ is determined as the true core point and is marked as the highest score. (2) If there is no $CP_{0,j}$ at all but there are some core points CP'_1 which meet with the formula 3.2, then the core $CP'_{1,min}$ which is the nearest to the norm core $CP'_{0,r}$ is marked, and the core $CP_{0,min}$ that is the nearest to the norm core $CP'_{0,r}$ and that is located between the core $CP'_{1,min}$ and the norm core $CP'_{0,r}$ is determined as the true core and is marked as the second grade score. (3) In cases other than the above two, the next step is performed.
3. First of all, It is important to tell whether there is a set of the core CP_0 that meet the condition that the form is the same as the formula 3.1, where the $Threshold_0$ in the formula 3.1 is changed to $Threshold_2 (Threshold_2 > Threshold_0)$. If there is no set of the core CP_0 that meet the condition above, then step 6 is performed. If there is this set, then the core CP_0 is marked as TCP_0, and whether there are the core CP'_1 which meet the condition has to be judged further according to formula 3.2. If it is valid, then the next step is performed. Otherwise, step 6 is carried out.
4. The core $CP'_{1,min}$ that is the nearest to the norm core $CP'_{0,r}$ is determined and marked from within the core CP'_1 which meet the formula 3.2. For every

core $TCP_{0,j}$, if it is located between the core $CP'_{1,min}$ and the norm core $CP'_{0,r}$, then let $TCP_{0,j}$ be $TCP'_{0,s}$ and again judge whether the distances between $TCP'_{0,s}$, $CP'_{0,r}$ and $CP'_{1,min}$ are nearer and whether the core $TCP'_{0,s}$ is located between the core $CP'_{1,min}$ and the norm core $CP'_{0,r}$. (1) If there is only one core $TCP'_{0,s}$ which meets the condition, then it is the true core point and marked as the highest score. (2) If there is more than one, then the true core points are determined by the same method as in the condition **(2)** of step **2**. (3) Otherwise, step 6 is carried out.

5. In the precondition of step **4**, if the core $TCP'_{0,s}$, $CP'_{0,r}$ and $CP'_{1,min}$ are largely in line, then the linearity measure between $TCP'_{0,s}$ and the line formed by $CP'_{0,r}$ and $CP'_{1,min}$ is computed according to the formulas 3.3 and 3.4, the minimum is found.

$$LineLevel = (a'^2 + b'^2 - c'^2)/2a'b' \tag{3.3}$$

$$Min_{LL} = \min\{Linelevel_0, LineLevel_1, LineLevel_2 \cdots\} \tag{3.4}$$

Where a', b' and c' denote the distance of $TCP'_{0,s}$ and $CP'_{0,r}$, the distance of $CP'_{0,r}$ and $CP'_{1,min}$ and the distance of $TCP'_{0,s}$ and $CP'_{1,min}$ respectively. (1) If Min_{LL} is smaller than a predefined threshold value, then the corresponding core $TCP'_{0,s}$ is regarded as the true core point and marked as the highest score. (2) If the condition above is not met, then judge once again whether there is a set of $TCP'_{0,s}$ that is within the predefined distance of the norm core $CP'_{0,r}$. If there is only one core $TCP'_{0,s}$ which meet the condition, then it is the true core point and marked as the highest score, or else, the core $TCP'_{0,s}$ nearest to the norm core $CP'_{0,r}$ is regarded as the true core and marked as the second grade score. (3) Otherwise, step **6** is carried out.

6. In other cases, the norm core $CP'_{0,r}$ is regarded as the true core point. And if there is a core $CP'_{1,min}$ that is within the predefined distance of the norm core and is the core nearest to the norm core, then the core $CP'_{1,min}$ is marked and the norm core $CP'_{0,r}$ is marked as the second grade score. Otherwise, as the third grade score.

3.3.2. Locating Delta Point. Step 1. Let each delta point $DP'_{0,r}$ (r denotes the rth core) detected by the block size $W_0 \times W_0$ and smoothing the orientation field be the norm delta point, and the delta set DP_0 are searched out within the predefined distance of the norm delta point. If there is only one delta $DP_{0,j}$, then the delta $DP_{0,j}$ is determined as the true delta point and is marked. And if there are some deltas DP'_1 which are within the predefined distance of the norm delta point, then the delta $DP_{0,j}$ is marked as the highest score and the delta $DP'_{1,min}$ which is the nearest to the norm delta $DP'_{0,r}$ is marked. Otherwise, the delta $DP_{0,j}$ is marked as the second grade score.

Step 2. If there is more than one delta like $DP_{0,j}$ which meets the conditions above, then the delta $DP_{0,min}$ that is nearest to the norm delta $DP'_{0,r}$ is marked as the true delta. And if there are deltas like DP_1 which are within the predefined

distance of the norm delta $DP'_{0,r}$, then the corresponding delta $DP_{0,min}$ is given the highest score, otherwise, given the second grade score.

Step 3. If there are only the delta DP_1 and no delta $DP_{0,j}$, which meet the conditions above, then the norm delta $DP'_{0,r}$ is marked as the delta and given the second grade score.

In all the steps above, the true deltas that have been detected are marked so as to avoid being involved in other delta detections.

3.3.3. Core Point Checking. Several cores detected above may be fake. So the detected cores ought to be checked according to the inherent structural characteristic of the fingerprint model area. The principles include: 1. the core with the highest score serves as the new norm and the core which is not reliable is checked; 2. If there are two or more than two cores detected, then they are checked by the concavo-convex characteristics of the model area which is defined by two cores; and 3. the distance between the two cores detected is smaller than that of the corresponding two norm cores CP'_0 and than that of the corresponding two cores CP'_1 which are detected on the large block size (16×16), and the directions of the vector radius of the curvature circle formed on the two true cores respectively are opposite generally. Last, the checked cores are sorted by their scores and placed in array of cores.

4. Experimental Results and Conclusions

A fingerprint singularity detection experiment based on the proposed algorithm is carried out on 500 typical fingerprint samples of NJU fingerprint database which contains 2500 images taken from 250 different fingers, 10 images per finger, and

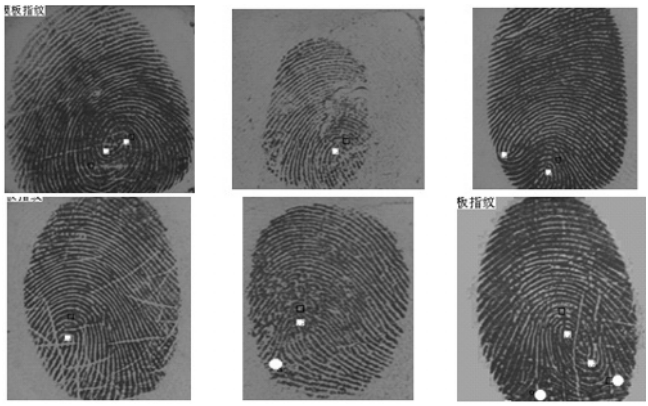

FIGURE 3. Examples of singularities detected Note: Results of the proposed method are denoted with the center of white ellipses, results of Poincaré index method based on are denoted with the center of black blocks

these fingerprint images are of varying quality in order to provide a realistic situation. In order to evaluate the performance of our algorithm, there is a comparison between the method based on the Poincaré index direct computation and our proposed method. In the method based on the Poincaré index direct computation, to improve the reliability of singularity detection, we adopt the larger block size (16×16) and smooth the orientation field. Fig. 3 shows some examples of singularity detection for typical fingerprints based on the two methods above. According to the experimental results, compared with the method of the Poincaré index direct computation, our method of singularities detection is more reliable and precise. For fingerprint images of poorer quality, our algorithm can still be used to get accurate and reliable singularities.

In this paper, a robust singularity detection algorithm is presented, which is based on the new idea of multilevel partition as well as the conformity of the singularities detected by multilevel partition and by the different methods of the orientation field estimation. Utilizing the characteristic of the corresponding relationship between the singularities detected by different approaches and measures of checking singularities, our method can improve the precision and reliability of singularity detection effectively and is robust to the low quality fingerprint images.

Although there are demerits in the singularity detection of images of quite low quality, it can meet fingerprint classification and fingerprint matching because the detected singularities are sorted by the reliability of singularity and some measures are adopted to restrict the position error to a very small degree.

References

[1] Yin YL, Ning XB, Zhang XM, *Development and application of automatic fingerprint identification technology.* Journal of Nanjing University (Natural Sciences) **38(1)** (2002), 29–35.

[2] Maltoni D., Maio D., Jain A. K. and Prabhakar S, *Handbook of Fingerprint Verification.* Springer Verlag, 2003.

[3] A. K. Jain, S. Prabhakar, and L. Hong, A Multichannel Approach to Fingerprint Classification, *Proc. of Indian Conference on Computer Vision, Graphics, and Images Processing (ICVGIP'98).* New Delhi, India, December 21–23,1998.

[4] M. Kawagoe and A. Tojo, *Fingerprint pattern classification.* Pattern Recognition **17(3)** (1984), 295–303.

[5] K. Karu and A. K. Jain, *Fingerprint Classification.* Pattern Recognition **29(3)** (1996), 389–404.

[6] A. K. Jain, S. Prabhakar and S. Pankanti,*Mathing and Classification:A Case Study in Fingerprint Domain.* Pro. INSA-A (Indian National Science Academy) **67(2)** (2001), 67–85.

[7] Lumini A., Maio D., Maltoni D., *Continuous vs Exclusive Classification for Fingerprint Retrieval.* Pattern Recognition **18(10)** (1997), 1027–1034.

[8] Cheng JG, Tian J, Ren Q, Zhang TH,Singular Point-based Fingerprint Classification, *Second Workshop on Biometrics in conjunction with the 6^{th} International Conference for Young Computer Scientists.* Hangzhou,China,S4-27–S4-34,2001.

[9] E. R. Herny, *Classification and use of Fingerprints.* George Routledge and Sons, London, 1900.

[10] V. S. Srinivasan and N. N. Murthy, *Detection of Singular Points in Fingerprint Images.* Pattern Recognition **25(2)** (1992), 139–153.

[11] Bazen A. M. and Gerez S. H., *Systematic Methods for the Computation of Directional Fields and Singular Points of Fingerprints.* IEEE Transactions on PAMI **24(7)** (2002), 905–919.

[12] Zhang WW, Wang S, Wang YS,Corner Detection Based Singularity Detection of Fingerprint Image, *Second Workshop on Biometrics in conjunction with the 6^{th} International Conference for Young Computer Scientists.* Hangzhou,China,S4-51–S4-56,2001.

[13] A. K. Jain, L. Hong and R. Bolle, *On-line Fingerprint Verification.* IEEE Trans. Pattern Anal. and Machine Intell **19(4)** (1997), 302–314.

[14] J.B. MacQueen, Some methods for classification and analysis of multivariate observations,*Pro. Symp. Math. Statistics and Probablity.* University of California Press, Berkeley 1967.

Taizhe Tan
School of Information Science & Technology at Sun Yat-sen (Zhongshan) University
510275 Guangzhou,China;
Faculty of Computer, Guangdong University of Technology
510090 Guangzhou,China
e-mail: `tantaizhe@263.net`

Jiwu Huang
School of Information Science & Technology at Sun Yat-sen (Zhongshan) University
510275 Guangzhou,China

Wavelet Analysis and Applications
Tao Qian, Mang I. Vai and Xu Yuesheng, Eds.
Applied and Numerical Harmonic Analysis, 463–475

Wavelet Receiver: A New Receiver Scheme for Doubly-Selective Channels

Guangjian Shi and Silong Peng

Abstract. We present a new receiver scheme, termed as *wavelet receiver*, for doubly-selective channels to combat the annoying Doppler effect. The key point is to convert the Doppler effect to Doppler diversity, taking advantage of the diversity technique to improve system performance. To this end, a new framework based on multiresolution analysis (MRA) is established. In this framework, we find that RAKE receiver which can only combat the multipath fading, is a special case of *wavelet receiver* which can exploit joint multipath and Doppler fading. Theoretical analysis and experimental simulation show that *wavelet receiver* can greatly enhance system performance.

Mathematics Subject Classification (2000). Primary 42C40; Secondary 60G35.

Keywords. Doubly-selective channel, Doppler diversity, multiresolution analysis (MRA), wavelet receiver.

1. Introduction

Time selectivity and frequency selectivity characterize the fading channel and they exhibit somewhat of similarity in terms of scattering function of channel [1]. Inspired by the success of RAKE receiver in the scenario of frequency selective channel, which resolves the received signal to multipath diversity, we seek for the possible receiver scheme for doubly-selective channels.

The idea originated by Sayeed [2] may be the first attempt of converting the Doppler effect to Doppler diversity. This idea has been extended to various systems. Its application to OFDM system can be found in [3, 4] and to space-time diversity can be found in [5]. But the method of Sayeed, which is referred as time-frequency representation (TFR) method, suffers from a drawback: the basis functions of TFR method are not orthogonal.

This work was supported by National Natural Science Foundation of China with No.60272042.

In this paper, we follow Sayeed's idea but exploit the Doppler diversity in another way. It based on the fact that usually used shaping pulses are the scaling functions of wavelet. For example, the square root raised cosine (SRRC) pulses with excess bandwidth in [0,1/3] is the scaling function of Meyer wavelet [6], [7] and the rectangle pulse is the scaling function of Harr wavelet. It stimulates us to study the Doppler diversity in multiresolution analysis (MRA) framework. In the MRA framework, we find that the RAKE receiver is a special case of *wavelet receiver*. The superiority of *wavelet receiver* over RAKE receiver is in that *wavelet receiver* can exploit orthogonality of wavelet space in addition to that of scaling space. On the other hand, *wavelet receiver* can be implemented by a series of parallel RAKE receivers, which will be detailed in section 4.

The paper is organized as follows. System model and preliminary knowledge of MRA are introduced in the next section. In Section 3, the diversity concept is reviewed and the sufficient and necessary conditions for the existence of Doppler diversity are also established. Our proposed *wavelet receiver* is the focus of Section 4. In Section 5, Numerical experiments are provided. At last conclusion is drawn in Section 6.

1.1. Notation

Let us introduce some notational conventions used in this paper. Z denotes the integer field, Z^- the nonpositive integer set and $L^2 = \{x(t) : \int_{-\infty}^{\infty} |x(t)|^2 dt < \infty\}$ square integrable space. $Q(x) = 1/\sqrt{2\pi}\int_x^{-\infty} e^{-x^2/2}dx$ denotes the Q-function, $\Gamma(\cdot)$ denotes Γ-function and $\delta_{i,j}$ is Kronecker delta function. $card\{\cdot\}$ is reserved for cardinality of set, $(\cdot)^{\perp}$ for orthogonal complement. We denote the inner product as $< \cdot, \cdot >$, L^2 norm as $\| \cdot \|$, projection operator of space X as $P_X(\cdot)$. $E(\cdot)$ is expectation of random variable.

2. Preliminaries

2.1. System Model and RAKE Receiver

Consider a typical wireless system and channel is assumed to be doubly-selective. The equivalent low pass model can be expressed as

$$r(t) = s(t) + z(t), \tag{2.1}$$

where

$$s(t) = \int_{-\infty}^{\infty} h(t, t-\tau)x(\tau)d\tau \tag{2.2}$$

and $z(t)$ is the additive white Gaussian noise (AWGN) with power spectrum density (PSD) $\sigma^2/2$ per dimension, $x(t)$ is pulse shaping function and $h(t,\tau)$ denotes the time-varying impulse response of the channel. $h(t,\tau)$ is assumed to be wide-sense stationary with uncorrelated scatter (WSSUS) complex Gaussian stochastic process. In a system equipped with bandwidth W, $s(t)$ can be expressed as [1]

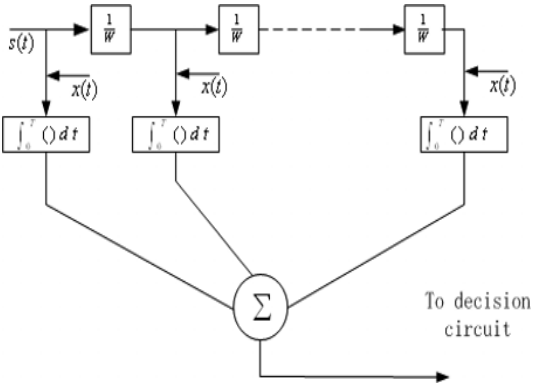

FIGURE 1. The structure of RAKE receiver

$$s(t) = \sum_{n=-\infty}^{\infty} h_n(t)x(t - n/W). \tag{2.3}$$

If fading is slow, we can get the following signal model

$$s(t) = \sum_{n=-\infty}^{\infty} h_n x(t - n/W). \tag{2.4}$$

In such case, there exists a kind of optimum receiver originated by Price and Green. Its structure is shown in Fig.1, which is somewhat analogous to the ordinary garden rake, so it's often referred to as RAKE receiver [1].

2.2. Multiresolution Analysis(MRA)

This paper is established on the basis of multiresolution analysis, so in this subsection we will introduce some fundamental knowledge of MRA although it is presented in the most compact form.

Theorem 2.1 (Mallat). [8, p.129] *If a sequence of successive approximation spaces V_j satisfies the following*

1. $\cdots V_2 \subset V_1 \subset V_0 \subset V_{-1} \subset V_{-2} \subset \cdots$
2. $\overline{\bigcup_{j\in Z} V_j} = L^2(R)$
3. $\bigcap_{j\in Z} V_j = \{0\}$
4. $f \in V_0 \Rightarrow f(\cdot - n) \in V_0$ *for all* $n \in Z$
5. $f \in V_j \Leftrightarrow f(2^j \cdot) \in V_0$
6. *there exists* $\phi(x)$ *so that* $\{\phi_{0,n} : n \in Z\}$ *is an orthonormal basis in* V_0

Then conclusions *can be drawn that there exist wavelet* $\psi(x)$*, whose translations and scaled versions* $\psi_{j,k}(x) = 2^{-j/2}\psi(2^{-j}x - k)$ *satisfy:*

$$\begin{aligned} \textit{Let} \quad W_j &= \textit{span}\{\psi_{j,k}(x)\ k \in Z\},\ \textit{then} \\ V_{j-1} &= V_j \bigoplus W_j\ \textit{for}\ j \in Z \\ L_2 &= \textit{span}\{\psi_{j,k}(x)\ j,k \in Z\}. \end{aligned}$$

In the next subsection, we will see that the scaling space V_0 is just the space spanned by the shaping pulses. For further reference convenience, we introduce a corollary as below

Corollary 2.2. $L_2 = V_0 + \bigoplus_{j=-\infty}^{0} W_j$ *and* $V_0^{\perp} = \bigoplus_{j=-\infty}^{0} W_j$.

This corollary gives the exact structure of the orthogonal complement of V_0. Now we arrive at the following signal representation

$$s(t) = \sum_{n=-\infty}^{\infty} a_n \phi_{0,n}(t) + \sum_{j=-\infty}^{0} \sum_{k=-\infty}^{\infty} b_{j,k}\psi_{j,k}(t). \tag{2.5}$$

2.3. Nyquist Pulse and Wavelet

William [7] has noted that Square Root Raised Cosine (SRRC) pulse with excess bandwidth in [0,1/3] is the scaling function of Meyer wavelet. In fact, scaling function of any wavelet can be used as Nyquist pulse. Nyquist pulse $x(t)$ satisfies $\sum_{m=-\infty}^{\infty} X(f + m/T) = T$, which is just the equivalent counterpart of theorem 2.1's condition 6 in frequency domain [1, p. 558] and [8, p. 132]. It implies scaling function of any wavelet satisfies Nyquist pulse condition. On the other hand, the generally used shaping pulse is exact scaling function of wavelet. For example, the Square Root Raised Cosine (SRRC) pulse with excess bandwidth ranged at [0,1/3] is the scaling function of Meyer wavelet function [6], [7] and the rectangle pulse is that of Haar wavelet.

3. Multipath and Doppler Diversity

In this section, diversity concepts are reviewed from a new perspective and at the same time the necessary and sufficient condition for the existence of the Doppler diversity is presented.

Diversity with order L traditionally is viewed as independent transmission of the same information L times with a specified but the same waveform

$$r_i(t) = \alpha_i \exp(-j\theta_i)s(t)\ i = 1 \cdots L. \tag{3.1}$$

In fact, the same information can be transmitted by different waveforms as long as the receivers have the knowledge about them. So we can extend the concept of diversity to more general form

$$r_{i_k}(t) = \alpha_{i_k} \exp(-j\theta_{i_k}) s_k(t) \; i_k = 1, \cdots, L_k \; k = 1, \cdots K, \tag{3.2}$$

with order

$$L = \sum_{k=1}^{K} L_k.$$

With such extension, we now can define multipath and Doppler diversity in the doubly-selective channels.

Definition 3.1. Multipath diversity is defined as $m(t) = P_{V_0} s(t)$, Doppler diversity as $d(t) = P_{V_0^{\perp}} s(t)$.

Definition 3.2 (Multipath Diversity Order (MDO)). According to the expression

$$m(t) = \sum_{n=-\infty}^{\infty} a_n \phi_{0,n}(x), \tag{3.3}$$

define MDO as the number: $card\{n : a_n \neq 0, \; n \in Z\}$.

Definition 3.3 (Doppler Diversity Order (DDO)). According to the expression

$$d(t) = \sum_{j=-\infty}^{0} \sum_{k=-\infty}^{\infty} b_{j,k} \psi_{j,k}(x), \tag{3.4}$$

define DDO as the number: $card\{(j,k) : b_{j,k} \neq 0, \; j \in Z^-, \; k \in Z\}$.

3.1. Existence Theorem for Doppler Diversity

Theorem 3.4 (Existence Theorem for Doppler Diversity). *The Doppler Diversity exists if and only if* $card\{(j,k) : b_{j,k} \geq \sigma^2, \; j \in Z^-, \; k \in Z\}$ *is nonzero, where* $b_{j,k} = E(| < r(t), \psi_{j,k}(t) > |^2)$

Proof. The proof is presented in Appendix 7.1 □

4. Wavelet Receiver

Besides the multipath diversity, the Doppler diversity now is well structured. In this section, we take advantage of this structure to maximize the joint multipath and Doppler diversity. This comes to our proposed *wavelet receiver*.

The structure of *wavelet receiver* is shown in Fig. 2, which is composed of a series of parallel RAKE receivers. Each RAKE receiver is characterized by three parameters: the matched filter, the interval of translation and the order of the diversity. *Wavelet receiver* can be viewed as a kind of 2D-RAKE receiver.

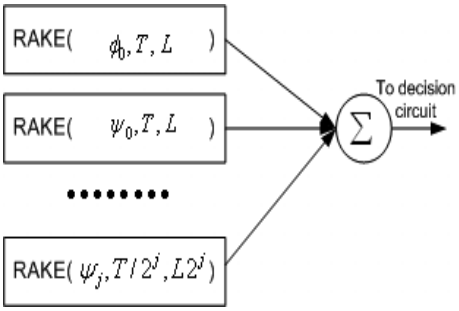

FIGURE 2. The structure of wavelet receiver

The decision variable for coherent detection of *wavelet receiver* with maximal ratio combiner can be expressed as

$$\begin{aligned} D &= Re[\int_0^T r(t)s^*(t)dt] \\ &= Re[\sum_{n=-\infty}^{\infty} \int_0^T r(t)h_n^*(t)x^*(t-n/W)dt] \\ &= Re[\sum_{n=-\infty}^{\infty} a_n \int_0^T r(t)x^*(t-n/W)dt \\ &+ \sum_{j=-\infty}^{0} \sum_{k=-\infty}^{\infty} b_{j,k} \int_0^T r(t)\psi_{j,k}^*(t)dt] \\ &= Re[2\varepsilon \sum_{n=-\infty}^{\infty} |a_n|^2 + 2\varepsilon \sum_{j=-\infty}^{0} \sum_{k=-\infty}^{\infty} |b_{j,k}|^2 \\ &+ \int_0^T z(t)s^*(t)dt], \end{aligned} \tag{4.1}$$

where ε denotes the energy of the shaping pulse. It is clear that the diversity of a system combines multipath diversity item $E_{mul} = 2\varepsilon \sum_{n=-\infty}^{\infty} |a_n|^2$ and Doppler diversity item $E_{dop} = 2\varepsilon \sum_{j=-\infty}^{0} \sum_{k=-\infty}^{\infty} |b_{j,k}|^2$. If the channel is slow fading, all $b_{j,k}$ tend to be zeros, the *wavelet receiver* reduces to the RAKE receiver. The additional performance gain E_{dop} enhances the signal-to-noise-ratio (SNR) from

$$SNR_r = \frac{E_{mul}}{\sigma^2}$$

to

$$SNR_w = \frac{E_{mul} + E_{dop}}{\sigma^2},$$

where SNR_r and SNR_w denote the SNR of the RAKE receiver and *wavelet receiver* respectively. We term this phenomenon as SNR enhancement effect of *wavelet receiver*.

4.1. Independence Analysis

Independence is crucial to diversity technique. The statistical characteristics of the noise components determine the optimal combining algorithm. If the maximum ratio combiner is used, the independence of noise components is expected. In this subsection, we present noise independence analysis. The independence can be obtained by the orthogonality of the basis function. For notation simplicity, we stack the scaling function in V_0 and wavelets in $\{W_j,\ j \in\ Z^-\}$ into the B_i with uniform index i. The noise component projected to B_i is obtained as

$$N_i =< z(t), B_i(t) >, \tag{4.2}$$

so

$$\begin{aligned} E(N_i N_j^*) &= E\int_{-\infty}^{\infty}\int_{-\infty}^{\infty} z(t)z^*(\tau)B_i^*(t)B_j(\tau)dtd\tau \\ &= \sigma^2\int_{-\infty}^{\infty} B_i^*(t)B_j(t)dt \\ &= \sigma^2\delta_{i,j}. \end{aligned} \tag{4.3}$$

4.2. Performance Analysis

In this subsection, the performance analysis of *wavelet receiver* is presented. For performance comparison, we give the BER [1] analysis of the BPSK modulated signaling using the *wavelet receiver* and RAKE receiver, although the result for other modulated signaling is also available. For *wavelet receiver*, the BER is

$$p_w = Q(\sqrt{SNR_w}), \tag{4.4}$$

and

$$p_r = Q(\sqrt{SNR_r}) \tag{4.5}$$

for the RAKE receiver.

In case of statistical fading channel, system performance P not only depends on the SNR, but also the statistical distribution of the E_{mul} and E_{dop}. That is

$$P = \int_0^{\infty} P(\gamma)p(\gamma)d\gamma, \tag{4.6}$$

where

$$\gamma = 2\varepsilon\sum_{n=-\infty}^{\infty}|a_n|^2/\sigma^2 + 2\varepsilon\sum_{j=-\infty}^{0}\sum_{k=-\infty}^{\infty}|b_{j,k}|^2/\sigma^2. \tag{4.7}$$

[1]The probability that a bit-error will occur in a given time is referred to as the bit-error rate (BER).

Following the derivation of the [1, p.846-847], we get the error probability P in the Rayleigh fading channel can be approximated by

$$P \approx \left(\begin{array}{c} 2T-1 \\ T \end{array} \right) (\frac{1}{4\gamma_1})^L (\frac{1}{4\gamma_2})^{T-L}, \tag{4.8}$$

where T, L denote the total and multipath diversity order respectively and $\gamma_1 = \varepsilon/\sigma^2 E(a_n)$, $\gamma_2 = \varepsilon/\sigma^2 E(b_{j,k})$ are average SNR per channel for multipath and Doppler diversity gain. And the corresponding performance P_r of RAKE receiver is

$$P_r \approx \left(\begin{array}{c} 2L-1 \\ L \end{array} \right) (\frac{1}{4\gamma_1})^L. \tag{4.9}$$

4.3. Channel Estimation

The *wavelet receiver* challenges new channel estimation algorithms. In coherent detection, not only the multipath diversity gains, but also the Doppler diversity gains are needed to be estimated. It obviously complicates the channel estimation algorithm. The variable to be estimated, in fact, is exponentially grown as the scale parameter limits to infinity ($j \to \infty$). Let the multipath diversity order (MDO) be L, the number of variables to be estimated for Doppler diversity gain is $(2^{J+1}-1)L$ if the maximal scale is 2^J.

To avoid the channel gain estimation for the Doppler diversity branches, we can use the noncoherent detection for Doppler diversity. This come to our *wavelet receiver Form 2*, we termed it as *half coherent wavelet receiver*. To distinguish with each other, we termed above *wavelet receiver* as *wavelet receiver Form 1* or *coherent wavelet receiver*. In this paper, *half coherent wavelet receiver* is realized simply by square-law combiner for all Doppler diversity branches. Of course if more prior knowledge is available, weighted square-law combiner can be applied to optimize the performance.

5. Experiments

In experiments, the time variation of channel is model as Jake's model. The Doppler power spectrum of mobile radio channel is

$$\zeta(\Delta t) = 1/2E[(h_n(t)h_n^*(t+\Delta t))] = J_0(2\pi f_m \Delta t),$$

where $J_0(t)$ is the zero-order Bessel function of the first kind and f_m is the maximum Doppler frequency [1, p.809]. The maximal value of Δt is T. We usually use the normalized maximum Doppler spread $f_m T$ as the parameter of the Jake's model

$$\zeta(t) = J_0(2\pi f_m T t), \tag{5.1}$$

where t ranges [0,1]. In this paper, Jake's model is simulated by IFFT method [9]. The shaping pulse is SRRC with excess bandwidth 1/3 and the maximal scale parameter J is set to 5.

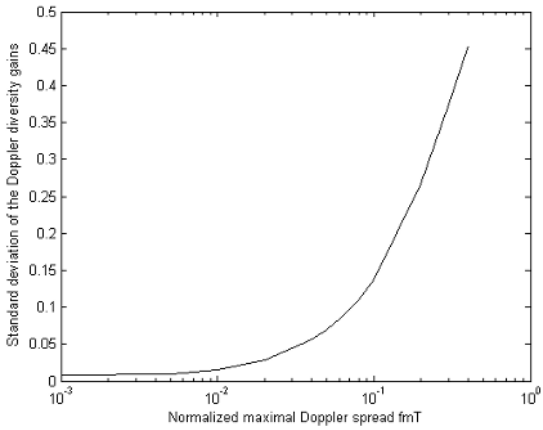

FIGURE 3. Plot of the standard deviation of Doppler diversity gains over normalized maximum Doppler spread f_mT.

5.1. Simulation Result 1

The variance of Doppler diversity gain $b_{j,k}$ depends on the normalized maximum Doppler spread f_mT. In this experiment, we will present the numerical result. The result is tabulated in Table 1, where $S(a)$,$S(b)$ denotes standard deviation of gain in multipath diversity branch and Doppler diversity branch respectively, and $m(b)$ is the mean of Doppler diversity gain. The normalized maximum Doppler spread is set as $0.001, 0.005, 0.01, 0.02, 0.04, 0.05, 0.06, 0.08, 0.1, 0.2, 0.3$ and 0.4 respectively. At any specified value, 1000 Monte Carlo simulation is run. Fig. 3 illustrates the standard deviation of the Doppler diversity gain increases monotonously with f_mT, which verifies the intuition that more Doppler diversity is obtained when the channel statistics varies faster. Although the value in Table 1 is obtained at $\varepsilon = 8$, the ratio between the $S(a)$ and $S(b)$ has no dependence on ε.

5.2. Simulation Result 2

Fig. 4 shows the performances of RAKE receiver and corresponding *wavelet receiver* in different normalized maximum Doppler spread f_mT. Coherent detection with maximum ratio combiner is assumed. In the Fig. 4, SNR per bit is evaluated as $\varepsilon/\sigma^2 E(a_n)$, which is identical to the case of RAKE receiver. *Wavelet receiver* has significant performance improvement compared with RAKE receiver. These improvement is obviously contributed to the SNR enhancement effect of *wavelet receiver*. The performance of *half coherent wavelet receiver* with square-law combiner for Doppler diversity gains is also presented in Fig. 5. We can see if lower BER is desired, *half coherent wavelet receiver* is also a better choice.

TABLE 1. Relation between normalized maximum Doppler spread f_mT and standard deviation of multipath diversity gain $S(a)$, mean and standard deviation of Doppler diversity gain $m(b)$, $S(b)$

f_mT	0.001	0.005	0.01	0.02	0.04	0.05	0.06	0.08	0.1	0.2	0.3	0.4
$S(a)$	5.5714	4.418	4.5605	4.417	4.6089	4.5446	4.5336	4.4874	4.499	4.8212	5.1648	5.4374
$m(b)$	6.459	-16.91	-24.24	-6.763	18.54	17.48	-3.323	-1.061	23.56	41.91	58.19	11.92
$S(b)$	0.007573	0.01001	0.01575	0.02872	0.05590	0.06951	0.08349	0.1106	0.1381	0.2665	0.3750	0.4544

$*10^{-5}$

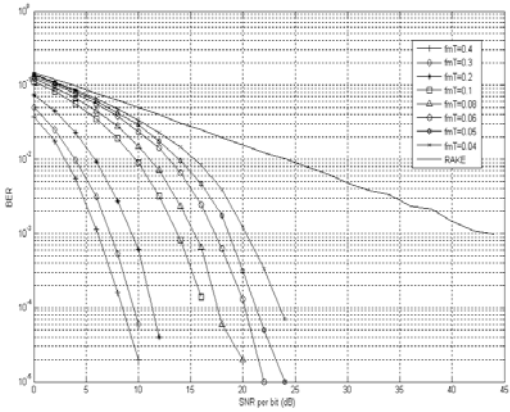

FIGURE 4. Performance comparison between RAKE receiver and *coherent wavelet receiver* with different normalized maximum Doppler spread $f_m T$.

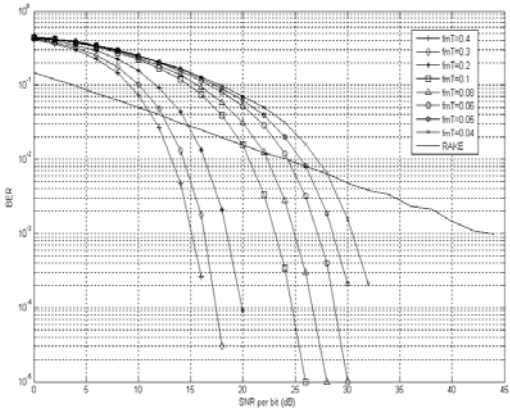

FIGURE 5. Performance comparison between RAKE receiver and *half coherent wavelet receiver* with different normalized maximum Doppler spread $f_m T$.

6. Conclusion

We have proposed a novel framework to exploit the Doppler diversity, which provides a new way to investigate mobile communication systems with fast fading channel. Based on the well-established wavelet theory, we have derived the structure of Doppler diversity. Two forms of *wavelet receiver* are established. It shows

that the time variations can be totally captured by *wavelet receiver*. And the quantitive relations between Doppler diversity and normalized maximum Doppler spread furthers the understanding of the fast fading communications systems.

Multiresolution analysis framework unites the signal processing of the fast and slow fading channel. In this united framework, we can exploit the achievements of the slow fading channel to benefit the fast fading channel processing. This promises great application scenarios of the *wavelet receiver*, such as its application to CDMA or OFDM systems etc., which will be our future work.

7. Appendices

7.1. Proof of the Theorem 3.4

Proof. According to (2.5)

$$\begin{aligned} B_{j,k} &= < r(t), \psi_{j,k} > = < s(t), \psi_{j,k} > + < z(t), \psi_{j,k} > \\ &= b_{j,k} + b_{j,k}^{noise}, \end{aligned}$$

we can get

$$E(|B_{j,k}|^2) = E(|b_{j,k} + b_{j,k}^{noise}|^2) = b_{j,k}^2 + \sigma^2, \tag{7.1}$$

due to the fact that $z(t)$ is AWGN with PSD σ^2. Now using the conclusion of Definition 3.3, we arrive at conclusion of this theorem. □

7.2. The Derivation of the SNR of the Wavelet Receiver

The output of maximum ratio combiner of *wavelet receiver* can be expressed as a decision variable formed in (4.1)

$$D = E_{mul} + E_{dop} + \int_0^T z(t)s^*(t)dt. \tag{7.2}$$

The noise power is

$$E(|\int_0^T z(t)s^*(t)dt|^2) = \|s(t)\|^2\sigma^2, \tag{7.3}$$

and $\|s(t)\|^2 = E_{mul} + E_{dop}$, so the SNR of the *wavelet receiver* is

$$SNR_w = \frac{(E_{mul} + E_{dop})^2}{(E_{mul} + E_{dop}) * \sigma^2} = \frac{E_{mul} + E_{dop}}{\sigma^2} \tag{7.4}$$

References

[1] J. G. Proakis *Digital Communications,* 4th ed. New York: MaGraw-Hill, 2001.

[2] A. M. Sayeed and B. Aazhang "Joint multipath-Doppler diverity in Mobile wireless comunications," *IEEE Trans. Commun.*, vol. 49, pp. 123-132, Jan. 1999.

[3] B. C. Kim and I. T. Lu "Doppler diversity for OFDM wireless mobile communications Part I: frequency domain approach," in *proc. 2003 IEEE Vehicular Technology Conf.(VTC 57th)*, 22-25 Apr. 2003 vol. 4, pp. 2677-2681.

[4] B. C. Kim and I. T. Lu "Doppler diversity for OFDM wireless mobile communications. Part II: time-frequency processing," in *proc. 2003 IEEE Vehicular Technology Conf.(VTC 57th)*, 22-25 Apr. 2003, vol. 4, pp. 2682-2685.

[5] A. G. Feng, Q. Yin, J. G. Zhang and Z. Zhao "Joint space-multipath-Doppler RAKE receiving in DS-CDMA systems over time-selective fading channels," in *proc. IEEE Int. Symp. on Circuits Syst.* vol.1, pp. 601-604, May 2002.

[6] W. Chen, Q. Yang, W. J. Jiang, and S. L. Peng "On bandlimited scaling function," *Journal of Computionational Mathematics*, vol. 20, pp. 373-380, Apr. 2002.

[7] W. J. Willime and C. D. Jeffrey "The square root raised cosine wavelet and tts relation to the Meyer functions," *IEEE Trans. Singal Processing*, vol. 49, pp. 248-251, Jan. 2001.

[8] I. Daubechies, *Ten Lectures on Wavelets,* Philadelphia, SIAM, 1992.

[9] C. Komninakis and J. F. Kirshman "Fast Rayleigh fading simulation with an IIR filter and polyphase interpolation," available at http://rfdesign.com/ar/407rfdf2x.pdf

Guangjian Shi
National ASIC Design center
Institute of Automation, Chinese Academy of Sciences, Beijing, China
e-mail: `guangjianshi@yahoo.com.cn`

Silong Peng
National ASIC Design center
Institute of Automation, Chinese Academy of Sciences, Beijing, China
e-mail: `silong.peng@ia.ac.cn`

Wavelet Analysis and Applications
Tao Qian, Mang I. Vai and Xu Yuesheng, Eds.
Applied and Numerical Harmonic Analysis, 477–487

Face Retrieval with Relevance Feedback Using Lifting Wavelets Features

Chon Fong Wong, Jianke Zhu, Mang I Vai,
Peng Un Mak and Weikou Ye

Abstract. By using support vector machine (SVM), this paper presents a novel face retrieval scheme in face database based on lifting wavelets features. The relevance feedback mechanism is also performed. The scheme can be described in three stages as follows. First, lifting wavelets decomposition technique is employed because it not only can extract the optimal intrinsic features for representing a face image, but also can accelerate the speed of the wavelets transform. Second, Linear Discriminant Analysis (LDA) is adopted to reduce the feature dimensionality and enhance the class discriminability. Third, relevance feedback using SVM is applied to learn on user's feedback to refine the retrieval performance. The experimental evaluation has been conducted on ORL dataset in which the results show that our proposed approach is effective and promising.

Keywords. face retrieval, face recognition, Content-based image retrieval (CBIR), Lifting Wavelets Transform (LFWT), Principal Component Analysis (PCA), Linear Discriminant Analysis (LDA), Support Vector Machine (SVM), relevance feedback.

1. Introduction

Face retrieval can be considered as a problem of similar face searching in the feature space by integrating content-based image retrieval (CBIR) [1] and face recognition [2] techniques. Among many approaches for facial representations, wavelets decomposition technique [3, 4] is a powerful method that is used to extract the intrinsic features for face recognition and image retrieval. However, due to the semantic gap existing between low-level features and high-level concepts [5], it is often difficult to achieve satisfactory retrieval performance by using rigid similarity measure on low-level features in a larger face database. One of the feasible ways to bridge the gap is to utilize relevance feedback to refine the retrieval results [5].

In this paper, we study the problem of face retrieval with SVM-based relevance feedback. We propose to use lifting wavelets features extraction algorithm because it can find the optimal bases for the representation of a face image [13]. Moreover, lifting scheme provides wavelets transform to be performed in spatial space and maps integers to integers, which accelerates the speed of the wavelets transform [6]. As the dimension of the feature vectors extracted by LFWT is still high, this is not proper for the retrieval task. To tackle this problem, Linear Discriminant Analysis (LDA) [8] is utilized to further reduce the feature dimesionality and enhance the class discriminability. Because LDA directly applied to feature vectors may cause the singularity problem at the within-class scatter matrix, Principal Component Analysis (PCA) [7] is commonly pre-performed for dimension reduction [8]. While the discriminant and lower-dimensional feature vectors are extracted, the remaining key element of face retrieval is to design a robust classifier. Previously, the face classifier based on the nearest feature line (NFL) [10] and nearest feature space (NFS) was exploited [3]. However, in the case of small training samples in databases, the ability of these classifiers for making confident decisions under different class boundaries is still needed to be explored. It is well-known that SVM [9] classifier has a good generalization performance in tacking small sample size in pattern recognition. When incorporated with relevance feedback, SVM classifier can be learned from training data of relevance face images and irrelevance face images marked by the users. Then the model can be used to find more relevance face images in the whole database [11, 12].

The rest of the paper is organized as follows. In Section 2, detailed description of lifting wavelets transform is presented. Subspace analysis methods, such as PCA and LDA, will be studied in Section 3. Section 4 briefly introduces relevance feedback technique. SVM classification method is reviewed in Section 5. Section 6 discusses the experimental results. Conclusions are drawn in Section 7.

2. Lifting Wavelets Transform

Any discrete wavelets transform (DWT) or two subband filtering with finite filters can be decomposed into a finite sequence of simple filtering steps, which are called the lifting steps. This decomposition corresponding to a factorization of the polyphase matrix of wavelet or subband filters into elementary matrices is described as follows.

The polyphase representation of a discrete-time filter $h(z)$ is defined as

$$h(z) = h_e(z^2) + z^{-1}h_o(z^2) \tag{2.1}$$

where h_e denotes the even coefficients, and h_o denotes the odd coefficients:

$$h_e(z) = \sum_k h_{2k} z^{-k}, \text{ and } h_o(z) = \sum_k h_{2k+1} z^{-k} \tag{2.2}$$

The synthesis filters $h(z)$ and $g(z)$ (low-pass and high-pass filters respectively) can thus be represented by their polyphase matrix $P(z) = \begin{bmatrix} h_e(z) & g_e(z) \\ h_o(z) & g_o(z) \end{bmatrix}$ and $\tilde{P}(z)$ can be also defined for the analysis filters analogously. The filters $h_e(z)$,$h_o(z)$,$g_e(z)$ and $g_o(z)$, along with their analysis counterparts, are Laurent polynomials. As the set of all Laurent polynomials exhibits a commutative ring structure, within which polynomial division with remainder is possible, long division between Laurent polynomials is not a unique operation [6].

The Euclidean algorithm [6] can be used to decompose $P(z)$and $\tilde{P}(z)$as

$$P(z) = \prod_{i=1}^{m} \begin{bmatrix} 1 & s_i(z) \\ 0 & 1 \end{bmatrix} \begin{bmatrix} 1 & 0 \\ t_i(z) & 1 \end{bmatrix} \begin{bmatrix} K & 0 \\ 0 & 1/K \end{bmatrix} \tag{2.3}$$

$$\tilde{P}(z) = \prod_{i=1}^{m} \begin{bmatrix} 1 & 0 \\ -s_i(z^{-1}) & 1 \end{bmatrix} \begin{bmatrix} 1 & -t_i(z^{-1}) \\ 0 & 1 \end{bmatrix} \begin{bmatrix} 1/K & 0 \\ 0 & K \end{bmatrix} \tag{2.4}$$

As this factorization is not unique, several pairs of $\{s_i(z)\}$ and $\{t_i(z)\}$ filters are admissible; however, in case of DWT implementation, all possible choices are equivalent.

Due to the computational complexity, it has been shown in [6] that using the lifting scheme instead of the standard filter bank algorithm, can asymptotically lead to a relative speed-up to 64% for Daubechies 9/7 filter which is implemented by the scheme shown in Figure 1.

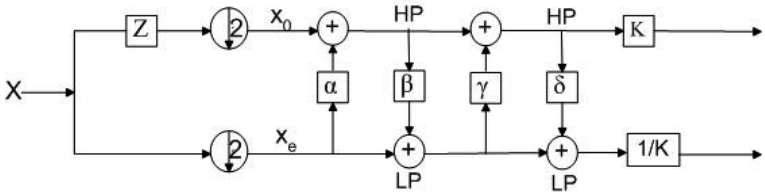

FIGURE 1. Block diagram of the forward wavelet transform using lifting scheme: the implementation of Daubechies 9/7 filter α=-1.586134342; β=-0.05298011854; γ=0.8829110762; δ=0.4435068522; K=1.149604398)

The best selection of wavelet filter and transform basis has been proposed for face recognition [13]. Similar to [13], we always select the low frequency subimage for further decomposition as it is less sensitive to vary images. The two-level wavelet lowest frequency subimage is used for PCA training in this paper. For example, an original image resolution of 128x128, size of the sub-image is reduced by 16 times. Figure 2 shows that a two-level decomposition using Daubechies 9/7 filter, the length of feature vector is $128 \times 128/2^{2\times 2} = 1024$.

FIGURE 2. An original image with resolution 128×128, and the two-level wavelet decomposition

3. Subspace Analysis

3.1. Principle Component Analysis (PCA)

The Principle Component Analysis (PCA) is a popular and powerful tool to reduce the dimensionality of the given data under unsupervised settings [7]. Consider a set of L feature vectors $\{\vec{g}_1, \vec{g}_2, \cdots, \vec{g}_L\}$ taking values in an n dimensional feature space. $\Sigma_{\vec{g}} \in R^{nxn}$ is defined as the covariance matrix of the feature vector $\vec{g}$: $\Sigma_g = \{[\vec{g} - \varepsilon(\vec{g})][\vec{g} - \varepsilon(\vec{g})]^T\}$, where ε is the expectation operator. Then PCA of a random vector $\vec{g}$ factorizes its covariance matrix $\Sigma_{\vec{g}}$ into the following form:

$$\Sigma_{\vec{g}} = \Phi\Lambda\Phi \text{ with } \Phi = [\vec{\varphi}_1, \vec{\varphi}_2, \cdots, \vec{\varphi}_n] \tag{3.1}$$

$$\Lambda = diag\{\lambda_1, \lambda_2, \cdots, \lambda_n\} \tag{3.2}$$

where $\Phi \in R^{nxn}$ is an orthogonal eigenvector matrix and $\Lambda \in R^{nxn}$ is a diagonal eigenvalues matrix with diagonal elements in decreasing order ($\lambda_1 \geq \lambda_2 \geq \cdots \lambda_n$). The projection can be obtained via $\vec{y} = T_{pca}^T[\vec{g} - \varepsilon(\vec{g})]$, where eigenvectors $T_{pca} = [\vec{\varphi}_1, \vec{\varphi}_2, \cdots, \vec{\varphi}_p]$, $p < n$ and $T \in R^{nxp}$. The lower dimensional vector captures the most expressive features of the original data.

3.2. Linear Discriminant Analysis (LDA)

Different from the unsupervised learning of PCA, LDA seeks to find a linear transformation that maximizes the between-class scatter and minimizes the within-class scatter on the given data and class labels. Empirically, LDA has shown better performance than PCA for dimension reduction [14].

LDA training is carried out via scatter matrix analysis. Assume each face image belongs to c-class, the within-and between-class scatter matrices $\Sigma_\omega \in R^{pxp}, \Sigma_b \in R^{pxp}$ are computed as follows:

$$\Sigma_\omega = \sum_{i=1}^{c} P_r(\omega_i)\varepsilon\{(\vec{y} - \vec{m}_i)(\vec{y} - \vec{m}_i)^T | \omega = \omega_i\} \tag{3.3}$$

$$\Sigma_b = \sum_{i=1}^{c} P_r(\omega_i)(\vec{m}_i - \vec{m}_0)(\vec{m}_i - \vec{m}_0)^T \tag{3.4}$$

where $P_r(\omega_i)$ is the priori class probability and usually is replaced by $1/c$, and $\vec{m}_i$ is mean vector, $\vec{m}_0$ overall mean vector. Various measures are available for quantifying the discriminatory power. One commonly used is:

$$J(A) = \arg\max_A \frac{A\Sigma_b A^T}{A\Sigma_\omega A^T} \tag{3.5}$$

where A is an $m \times n$ matrix with $(m \leq n)$. The advantage of using this ratio is that it has been proven that if Σ_ω is a non-singular matrix then this ratio is maximized when $\Sigma_b A^* = \Sigma_\omega A^* \Lambda_A$ and A^* is the eigenvector matrix of $\Sigma_\omega^{-1}\Sigma_b$, Λ_A is a diagonal matrix. There are at most $c-1$ nonzero generalized eigenvectors. Let T_{fld} denote the reduction matrix of A^*, the reduced feature vectors for classification can then be derived as $\vec{u} = T_{fld}^T \vec{y}$.

4. Relevance Feedback

Relevance feedback [5] is a technique that takes advantage of human-computer interaction to refine high level queries represented by low level features. It is used to incorporate user's concept with the learning process [15, 16] for CBIR.

In our face retrieval system, after a user submits a query by a given sample, the system will return a set of similar images to the user. The returned images may be relevant (positive) or irrelevant (negative) to the user's target. Thus, relevance feedback is engaged as a query refinement technique for helping the retrieval task. The relevance feedback mechanism solicits the user to mark the relevance on the retrieved images and then refines the results by learning the feedbacks by the user.

In order to learn the user's feedback effectively, we employ a popular yet powerful machine learning technique, i.e., Support Vector Machine, to attack the problem. SVM is a state-of-the-art classification technique with excellent generalization performance. It has been shown with successful applications in relevance feedback [11, 17, 18].

5. Support Vector Machine

Support Vector Machine (SVM) [9] is a popular technique for classification. The basic idea of SVM is to look for the optimal separating hyperplane (OSH) which best separates the data points into two classes with a maximum margin in a projected feature space based on the Structure Risk Minimization principle.

Consider the problem of separating the set of training vectors into two separated classes, $(\vec{x}_1, y_1), ...(\vec{x}_N, y_N)$, where $\vec{x}_i \in R^d$,$y_i \in \{-1, +1\}$ with a hyperplane $\vec{w} \cdot \vec{x} + b = 0$. The set of vectors is said to be optimally separated by the hyper-

plane if it is separated without error and the margin is maximal. For all $\vec{x}_i$, if the following constraints are satisfied,

$$y_i(\vec{w} \cdot \vec{x}_i + b) \geq 1, \quad i = 1, \cdots, N \tag{5.1}$$

the distance from the closest point to the hyperplane is $1/\|\vec{w}\|$. Hence, the hyperplane that optimally separates the data is the one that minimizes the objective function:

$$\Phi(\vec{w}) = \frac{1}{2}\|\vec{w}\|^2 = \frac{1}{2}(\vec{w} \cdot \vec{w}) \tag{5.2}$$

The solution to the optimization problem of (5.2) under the constraints of (5.1) is given by the saddle point of the Lagrange functional:

$$L(\vec{w}, b, \alpha) = \frac{1}{2}\|\vec{w}\|^2 - \sum_{i=1}^{N} \alpha_i \{y_i [(\vec{w} \cdot \vec{x}_i) + b] - 1\} \tag{5.3}$$

where α_i are the Lagrange multipliers. The parameters can be found by solving the following quadratic programming problem:

$$\max L(\alpha) = \sum_{i-1}^{N} \alpha_i - \frac{1}{2} \sum_{i=1}^{N} \sum_{j=1}^{N} \alpha_i \alpha_j y_i y_j \vec{x}_i \cdot \vec{x}_j \tag{5.4}$$

subject to:

$$\sum_{i=1}^{N} \alpha_i y_i = 0 \text{ and } \alpha_i \geq 0 \tag{5.5}$$

The solution to $\vec{w}$ can be expressed $\vec{w} = \sum_i \alpha_i y_i \vec{x}_i$ in terms of a subset of training patterns, called support vectors, which lie on the margin. The decision function can thus be written as

$$f(\vec{x}) = sign(\sum\nolimits_i \alpha_i y_i \vec{x}_i \cdot \vec{x} + b) \tag{5.6}$$

So far the discussion has been restricted to the case where the training data is linearly separable. To generalize the OSH to the non-separable case, SVM introduces slack variables and a penalty factor such that the objective function can be modified as

$$\Phi(\vec{w}, \xi) = \frac{1}{2}(\vec{w} \cdot \vec{w}) + C(\sum_{i=1}^{N} \xi_i) \tag{5.7}$$

The input data can also be mapped through some nonlinear mapping into a high-dimensional feature space in which the OSH is constructed. Thus the dot production can be represented by $k(\vec{x}_i, \vec{x})$ when the kernel k satisfy Mercer's condition [19]. Table 1 shows three typical kernel functions [20]. Finally, we obtain the decision function

TABLE 1. Types of kernel functions

Kernel function	$k(\vec{x}_i, \vec{x}), i = 1, 2, \cdots N$
Polynomial	$\left(\gamma \vec{x}_i^T \vec{x} + r\right)^d, \gamma > 0$
Radial basis function (RBF)	$\exp\left(-\gamma \left\|\vec{x}_i - \vec{x}\right\|^2\right), \gamma > 0$
Sigmoid	$\tanh\left(\gamma \vec{x}_i^T \vec{x} + r\right)$

γ, d and r are kernel parameters.

$$f(\vec{x}) = sign(\left(\sum\nolimits_i \alpha_i y_i \cdot k(\vec{x}_i \cdot \vec{x}) + b\right) \tag{5.8}$$

Because SVM enjoys solid theoretical foundations from the perspective of statistical learning theory, it has shown many advantages when applied to problems with limited training samples. Consequently, it can achieve excellent empirical performance when applied to real-world problems.

6. Experimental Result

6.1. Experimental Setup

To evaluate the performance of our face retrieval system, we perform experiment using face dataset from ORL [21]. The ORL dataset consists of 400 frontal face images corresponding to 40 subjects, each subject with 10 different images. The size of each image is 92x112 pixels, with 256 grey levels per pixel, as shown in Figure 3.

FIGURE 3. Example of face images used for retrieval

6.2. Implementation Details

In our experiments, we use 20 classes each with 5 images as the training set, all images are decomposed by LFWT, the lowest subband forms facial feature vectors (Dimension=644). Afterwards, we process these facial feature vectors with PCA and LDA to further reduce the dimension to 19 for retrieval task. To present face retrieval approach, the metric of evaluation is taking average retrieval accuracy which is defined as the average ratio of the number of relevant face images in top N returns over the total number of relevant face images in the face dataset.

In the retrieval process, each face image is assumed as user's query. The system will measure it with all the remaining face images in the dataset, the returned face images are ranked by their distances from the boundary of SVM classifier. If the result is non-satisfactory, user is suggested to mark the returned images as relevant face images (+1) or irrelevant face images (-1) in top N, then perform further rounds of feedback. SVM uses both relevant (+1) and irrelevant (-1) face images as the training data to construct a more informative classifier, thus to predict more relevant face images from the dataset.

To implement the relevance feedback algorithm with SVM, we modify the codes of public *libsvm* library [22].

6.3. Average Retrieval Accuracy

The whole process is repeated for 400 times to generate the average retrieval accuracy. The Euclidean distance method is viewed as the baseline in this experiment. From Figure 4, it can be seen that our proposed LFWT+LDA+SVM (kernel is Radial basis function) method outperforms LFWT+LDA+Euclidean distance method. Moreover, with only one round feedback, the accuracy can reach to 99.6%.

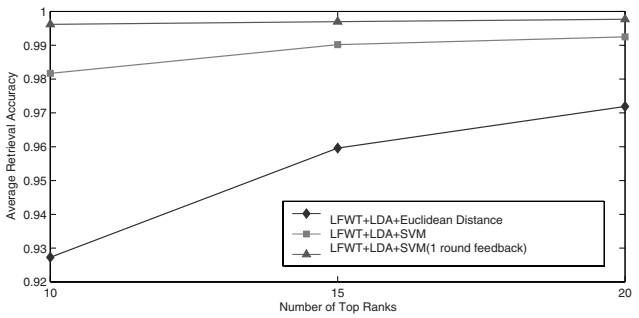

FIGURE 4. Retrieval performance of different methods on ORL dataset

In order to demonstrate our proposed scheme is effective and robust, we make a comparison with recent face recognition methods which use ORL dataset for performance evaluation, as shown in Table 2.

TABLE 2. Performance of different methods on ORL dataset

Methods	**Eigenvectors**	**Recognition Rate**
LFWT+LDA+NN	19	92.7%
PCA+NFL [10]	40	96.9%
LFWT+LDA+NFS [3]	60	96.1%
LFWT+LDA+SVM	**19**	**98.2%**

We observe that our proposed method has a lower-dimensional feature vectors and better recognition rate. In fact, average retrieval accuracy in top 10 on ORL dataset can be viewed as recognition rate. Furthermore, with relevance feedback involved, the system can achieve 100% accuracy. Therefore, we can summarize that our proposed scheme is promising for the challenging face retrieval task in a larger face database. Our experiment is implemented in a personal computer with Pentium 4 1.6GHz CPU with 256MB RAM.

7. Conclusions

This paper proposed a novel scheme for face retrieval using the lifting wavelets features and presented an effective relevance feedback algorithm using support vector machine for improving the retrieval performance. The LFWT is used to extract facial features because it increases the discriminability meanwhile decreases the dimensionality of the features. Moreover, it is faster than other wavelets transform approaches as it computes the wavelets transform in real domain and others in complex domain. In our experiment, we observed that the dimension of the feature vectors and the numbers of training samples used for SVM learning are two important factors to impact the overall performance of our face retrieval system. Further, we noted that the retrieval accuracy can be significantly improved through learning user's interaction with relevance feedback. This makes our scheme more effective for the applications with larger face databases. Experimental results have shown that our proposed scheme enjoys advantages in speed and retrieval performance, which makes it promising for practical face retrieval applications.

References

[1] Smeulders, A.W., Worring, M., Santini, S., Gupta, A., Jain, R, "Content-based image retrieval at the end of the year," *IEEE Trans. Pattern Analysis and Machine Intelligence* vol. 22, pp. 1349-1380, 2000

[2] R. W. Chellappa, C.L. and Sirohey, S. "Human and machine recognition of faces: a survey," *Proc. of IEEE* 83 (1995) 705-741

[3] J.-T. Chien and C.-C. Wu, "Discriminant waveletfaces and nearest feature classifiers for face recognition," *IEEE Trans. Pattern Analysis and Machine Intelligence,* vol. 24, pp. 1644-1649, 2002

[4] R. Foltyniewicz, "Automatic face recognition via wavelets and mathematical morphology," *Proc. Int'l Conf. Pattern Recognition*, pp. 13-17,1996.

[5] Y.Rui, T.S.Huang, et al., "Relevance feedback: A power tool for interactive content-based image retrieval", *IEEE trans. Circuits and video technolog.*, 8(5):644-655, Sep.1998

[6] Daubechies, I. and W. Sweldens. "Factoring wavelet transforms into lifting steps," *J. Fourier Anal. Appl.,* Vol. 4, Nr. 3, 1998.

[7] M.A. Turk and A.P. Pentland, "Face recognition using eigenfaces," presented at *Computer Vision and pattern Recognition*, Proceedings CVPR'91, pp. 586-591, 1991

[8] P.N. Belhumeur, J.P. Hespanha, and D.J. Kriegman, "Eigenfaces vs. Fisherfaces: recognition using class specific linear projection," *IEEE Trans. PAMI*, vol. 19, pp. 711-720, 1997.

[9] V. Vapnik, The Nature of Statistical Learning Theory, *Springer-Verlag*, New York, 1995

[10] S. Z. Li and J. Lu, "Face recognition using the nearest feature line method," Neural Networks, IEEE Transactions on, vol. 10, pp. 439-443, 1999.

[11] P.Hong, Q.Tian, and T.S.Huang, "Incorporate support vector machines to content-based image retrieval with relevant feedback," *IEEE Proc. Int'l Conf. Image Processing (ICIP'00),* pp.750-753, 2000

[12] Simon Tong and Edward Chang, "Support vector machine active learning for image retrieval," *Proc. ACM Multimedia (MM'01),* pp.107-118, 2001

[13] A.Z.Kouzani, F.He, and K.Sammut, "Wavelet packet face representation and recognition," *Proc. IEEE Conf.* Systems, Man, and Cybernetics, pp.1614-1619,1997

[14] A.M. Martinez and A.C. Kak, "PCA versus LDA," PAMI, *IEEE Trans. on*, vol. 23, pp. 228-233, 2001

[15] Z. Su, H.J. Zhang, S. Li, and S.P. Ma, "Relevance Feedback in content-based Image Retrieval: Bayesian Framework, Feature Subspaces, and Progressing Learning," *IEEE Trans. Image Processing,* Vol. 12, No. 8, pp. 924-937, 2003.

[16] Y. Rui, T.S. Huang, and S. Mehrotra, "Content-based Image Retrieval with Relevance Feedback in MARS," Proc. of the International Conf. on Image Processing, pp. 815-818, 1997.

[17] C.-H. Hoi and M.R. Lyu., "Group-based relevance feedback with support vector machine ensembles", *Proc. Int'l Conf. Pattern Recognition*, (ICPR'04), Cambridge, UK, pp. 874-877, 2004

[18] C.-H. Hoi and M.R. Lyu., "A novel log-based relevance feedback technique in content-based image retrieval", *Proc. ACM Multimedia (MM'04)*, pp. 24-31, 2004

[19] C.J.C. Burges, "A Tutorial on Support Vector Machines for Pattern Recognition", *Data Mining and Knowledge Discovery*, 2(2) pp. 1-47, 1998.

[20] M.O.Stitson, J.A.E.Weston, et al., "Theory of Support Vector Machine", Technical report, CSD-TR-96-17, Univ. of London

[21] Olivetti Oracle Research Lab (ORL), "ORL website: http://mambo.ucsc.edu/psl/olivetti.html."

[22] C.-C. Chang and C.-J. Lin, LIBSVM : a library for support vector machine, 2001. Software available at http://www.csie.ntu.edu.tw/∼cjlin/libsvm/

Chon Fong Wong
Department of Electrical and Electronics Engineering
Faculty of Science and Technology
University of Macau
Macau SAR, PR. China
e-mail: planks@macau.ctm.net

Jianke Zhu
Room 101, Floor 1, Ho Sin-Hang Engineering Building
Compupter Science and Engineering Department
C.U.H.K.,Shatin,
Hong Kong PR. China
e-mail: jkzhu@cse.cuhk.edu.hk

Mang I Vai
Department of Electrical and Electronics Engineering
Faculty of Science and Technology
University of Macau
Macau SAR, PR. China
e-mail: fstmiv@umac.mo

Peng Un Mak
Department of Electrical and Electronics Engineering
Faculty of Science and Technology
University of Macau
Macau SAR, PR. China
e-mail: fstpum@umac.mo

Weikou Ye
Department of Physics
Shaoxing University
Shaoxing, PR. China
e-mail: wlywg@mail.sxptt.zj.cn

Wavelet Analysis and Applications
Tao Qian, Mang I. Vai and Xu Yuesheng, Eds.
Applied and Numerical Harmonic Analysis, 489–502

High-Resolution Image Reconstruction Using Wavelet Lifting Scheme

Shengwei Pei, Haiyan Feng and Minghui Du

Abstract. High-resolution image reconstruction refers to reconstruction of high-resolution images from multiple low-resolution, shifted, blurred samples of a true image. By expressing the true image as a square integrable function, Point Spread Function (PSF) can be used to construct biorthogonal wavelet filters directly and some algorithms for high-resolution image reconstruction were proposed based on the filters. However, the filters are the piecewise linear spline and corresponding primal and dual wavelet functions are all one vanishing moments. In order to improve the quality of reconstructed high-resolution images, we propose a method in this paper which can increase the numbers of vanishing moments of the wavelet functions so as to improve the performance of the biorthogonal filters using wavelet lifting scheme. Experiment results show that the method can improve the quality of reconstructed high-resolution images effectively. Also, we derive a fast algorithm that can reconstruct high-resolution images efficiently when blurring matrix is block-circulant-circulant-block (BCCB) matrix or Toeplitze-plus-Hankel system with Toeplitze-plus-Hankel block (THTH) matrix.

Mathematics Subject Classification (2000). Primary 65T60; Secondary 68U10.

Keywords. high-resolution reconstruction, super-resolution reconstruction, wavelet, lifting scheme, image processing.

1. Introduction

In some special scenes, for example, satellite imaging and some military infrared imaging, high-resolution digital images are necessary. Due to the limitations of digital camera, such as integrated circuit technology, cost, etc., usually desired high-resolution images are not available. In order to increase the resolution of

This research is supported by Ministry of Education, Government of Guangdong Province (Research Grant No.8303069).

images, the information from low-resolution images is collected and used to reconstruct the desired high-resolution images. This process is called high-resolution image reconstruction. Recently, high-resolution and super-resolution image reconstruction have been one of the most active research fields. Several methods for high-resolution image or super-resolution image reconstruction were proposed [1, 2, 3, 4, 5, 6]. Tsai and Huang [1] gave an approach with Fourier Transform to reconstruct super-resolution images. Nguyen and Milanfar [2] proposed an efficient method that considered sampling lattice and employed wavelet interpolation to reconstruct high-resolution images. A regularized method based on multi-channel sampling was proposed by Hong [3]. ML (Maximum Likelihood) method was proposed by Tom in [4]. At present, the MAP (Maximum a-Posteriori) method [5, 6] is researched widely and has good performance in the quality of reconstructed images, but the method is very complicated. Projection Onto Convex Set (POCS) method was proposed by H. Stark in [7], which described an iterative approach to incorporate prior knowledge into the reconstruction process.

Here we follow the research work in Bose and Boo [8] and Chan [9] and consider reconstructing high-resolution images from the low-resolution images of the same scene by wavelet lifting scheme. By expressing a true image as a square integrable function [9], Point Spread Function (PSF) can be used to construct biorthogonal filters directly. Some algorithms for high-resolution image reconstruction [9, 10] were proposed based on the filters. However, the filters are the piecewise linear spline and the corresponding primal and dual wavelet functions are all one vanishing moments [11, 15]. The quality of reconstructed images is related tightly with the numbers of vanishing moment of wavelet functions. Thus, in order to get better quality of reconstructed images, wavelet lifting scheme can be employed to increase the numbers of vanishing moment of wavelet functions so as to improve the performance of the biorthogonal wavelet filters. In this paper, we analyze the high-resolution reconstruction approach from the wavelet and multiresolution point of view [9], then, based on wavelet lifting scheme, we propose a method for high-resolution image reconstruction. Also, a fast algorithm for solving $Lf = g$ is derived when L is BCCB or THTH matrix.

This paper is arranged as follows: In section 2, a mathematical model of high-resolution image reconstruction is given. In section 3, we give the algorithm proposed by Chan [9] and then derive our algorithm based on the wavelet lifting scheme. Numerical experiment results are given in section 4 to illustrate the effectiveness of the method. The conclusion about the algorithm will be shown in section 5.

2. Mathematical Model

Here we give a brief introduction to the mathematical model of the high-resolution image reconstruction problem. Details about the model can be found in [8]. Suppose that the imaging sensor array has $N_1 \times N_2$ pixels. Let the actual length

and width of each pixel be T_1 and T_2 respectively. These sensors are called low-resolution sensors. Our aim is to construct a high-resolution image of the same scene by using an array of $K_1 \times K_2$ low-resolution sensors. More precisely, we want to reconstruct an image with $M_1 \times M_2$ pixels, where $M_1 = K_1 N_1$ and $M_2 = K_2 N_2$. So, the length and width of each of these high-resolution pixels will be T_1/K_1 and T_2/K_2, respectively. Here, Let $K_1 = K_2 = K$ and $f(x_1, x_2)$ be the intensity of the scene at any point. By reconstructing the high-resolution image, we mean to find or approximate the values:

$$\frac{K^2}{T_1 T_2} \int_{iT_1/K}^{(i+1)T_1/K} \int_{jT_2/K}^{(j+1)T_2/K} f(x_1, x_2) dx_1 dx_2; \quad 0 \le i \le M_1, 0 \le j \le M_2.$$

In order to get enough information to resolve the high-resolution image, there must be subpixel displacements between the sensors in the sensor arrays. Ideally, for sensor $(k_1, k_2), 0 \le k_1, k_2 \le K$, its horizontal and vertical displacements $d^x_{k_1,k_2}$ and $d^y_{k_1,k_2}$ with respect to the point (0, 0) are given by:

$$d^x_{k_1,k_2} = (k_1 + \frac{1-K}{2})\frac{T_1}{K}; \quad d^y_{k_1,k_2} = (k_2 + \frac{1-K}{2})\frac{T_2}{K}.$$

For this low-resolution sensor, the average intensity registered at its (n_1, n_2)th pixel is modeled by:

$$g_{k_1,k_2}[n_1, n_2] = \frac{1}{T_1 T_2} \int_{T_1 n_1 + d^x_{k_1,k_2}}^{T_1(n_1+1)+d^x_{k_1,k_2}} \int_{T_2 n_2 + d^y_{k_1,k_2}}^{T_2(n_2+1)+d^y_{k_1,k_2}} f(x_1, x_2) dx_1 dx_2 + \eta_{k_1,k_2}[n_1, n_2]. \quad (2.1)$$

According to (2.1), if we intersperse all the low-resolution images g_{k_1,k_2} to form an $M_1 \times M_2$ image g by assigning:

$$g[Kn_1 + k_1, Kn_2 + k_2] = g_{k_1,k_2}[n_1, n_2].$$

then g is the approximate of the f. Here, g can be called observed high-resolution image. In order to get an image that is better than the observed high-resolution image, we have to get f.

In (2.1), we can see that $g_{0,0}[0, 0]$ involves the points outside the region of image we have known, so the system is underdetermined. To compensate for this, one imposes the boundary conditions on f for x_i outside the domain. Usually, periodic boundary condition is a common one, but the symmetric boundary condition and zero boundary condition can also be imposed. The symmetric boundary condition is a new one and has good performance in boundary artifacts. In the following text, we will give algorithms for periodic and symmetric boundary conditions respectively.

Using any above boundary condition and ordering the discretized values of f and g in a row-by-row fashion, we obtain an $M_1 M_2 \times M_1 M_2$ linear system as:

$$Lf = g. \quad (2.2)$$

where L is the convolution operator (blurring matrix), g is a vector formed from the low-resolution images and f is the desired high-resolution image.

According to the separable property of Point Spread function (PSF), we can get the following equation:

$$L = L^x \otimes L^y. \tag{2.3}$$

where $\otimes$ is the Kronecker tensor product. For periodic and symmetric boundary conditions, the system (2.2) is ill-conditioned and susceptible to noise.

3. Reconstruction

3.1. The Basic Principle

For (2.1), we can consider the process as a lowpass filter imposed on image f. So $L_2^p, L_4^p, L_2^s, L_4^s$ can also be considered as lowpass filters. L_2^p, L_4^p, L_2^s and L_4^s denote the L in (2.2) under the condition of periodic and symmetric boundary conditions for 2×2 sensor arrays and 4×4 sensor arrays respectively. Here, we recall the scaling function $f(x_1, x_2) \in L_2(R^2)$ in wavelet transform:

$$\phi = 4 \sum_{\alpha \in Z} a(\alpha)\phi(2 \cdot -\alpha).$$

where sequence $a(\alpha)$ is a refinable mask (also known as a scaling coefficient or a lowpass filter).

According to the blurring matrix L given in (2.3), we can obtain the refinable mask for 2×2 sensor arrays from PSF directly [9]. It is listed as follows: $m_2(\alpha) = 1/4, 1/2, 1/4; \alpha = -1, 0, 1$. For 4×4 sensor arrays, the refinable mask is the stable refinable function ϕ with dilation 4. It is listed as follows: $m_4(\alpha) = 1/8, 1/4, 1/4, 1/4, 1/8; \alpha = -2, \cdots, 2$. We can see that the masks (filters) are all piecewise linear splines and Deslauriers-Dubuc filters [11] and their corresponding scaling functions are Deslauriers-Dubuc interpolating scaling functions [15, 16].

The refinable masks, wavelet masks and their duals can be found in [8]. The tensor product dual pairs of the refinement symbols are given by $\hat{a}(\omega) = \hat{m}(\omega_1)\hat{m}(\omega_2)$ and $\hat{a}^d(\omega) = \hat{m}^d(\omega_1)\hat{m}^d(\omega_2)$. The corresponding wavelet symbols b_v and b_v^d can also be gotten (See [9]).

Let $f \in S^1(\phi^d)$, then:

$$\begin{aligned} f &= \sum_{\alpha \in Z^2} \langle f, 2\phi(2 \cdot -\alpha)\rangle 2\phi^d(2 \cdot -\alpha) \\ &= 2 \sum_{\alpha \in Z^2} v(\alpha)\phi^d(2 \cdot -\alpha). \end{aligned} \tag{3.1}$$

where $v(\alpha), \alpha \in Z^2$ are the pixel values of the high-resolution image we are seeking, and they form the discrete representation of f under the basis $2\phi^d(2 \cdot -\alpha), \alpha \in Z^2$. Then $(a * v)(\alpha)$ is the observed high-resolution image. According to biorthogonal

wavelet theory, we know that refinement masks and wavelet masks satisfy the following equation [9, 12]:

$$\bar{\hat{a}}^d\hat{a} + \sum_{v\in Z^2\setminus\{(0,0)\}} \bar{\hat{b}}_v^d\hat{b}_v = 1.$$

So, according to the above equation, an iterative algorithm for high-resolution image reconstruction is obtained as follows:

$$\hat{v}_{n+1} = \bar{\hat{a}}^d\hat{a}\hat{v} + (1-\beta)(\sum_{v\in Z_2^2\setminus\{(0,0)\}} \bar{\hat{b}}_v^d\hat{b}_v)\hat{v}_n. \tag{3.2}$$

where factor $(1-\beta)$ is used to denoise in each iterative cycle. The equation (3.2) can be written as follows using matrices:

$$(L^dL + \beta/(1-\beta)I)f = 1/(1-\beta)L^dg. \tag{3.3}$$

where L, L^d are the matrices generated by $\hat{a}, \bar{\hat{a}}^d$ respectively.

3.2. Wavelet Lifting

According to the descriptions above, we can get analysis and synthesis filters m, m^d, r and r^d directly from PSF [9]. After simple computation, we know that the vanishing moment of the wavelet functions corresponding to the filters are all ones. Since the quality of recovered images is related tightly with the numbers of vanishing moment, larger numbers of vanishing moment of the wavelet functions are desirable [13]. Lifting is an elementary modification of perfect reconstruction filters, which is used to improve the wavelet properties such as vanishing moment. In order to improve the quality of reconstructed images, we can use lifting scheme to increase the numbers of vanishing moments of wavelet functions corresponding to r, r^d. Here, we use primal lifting and dual lifting to modify m, r, m^d and r^d in turn. For 2×2 sensor arrays, according to the lifting theory [14], we have:

$$\begin{aligned} \hat{m}^l(\omega) &= \hat{m}(\omega) + \hat{r}(\omega)\hat{l}_l^*(2\omega); \\ \hat{r}^{dl}(\omega) &= \hat{r}^d(\omega) - \hat{m}^d(\omega)\hat{l}_l(2\omega); \end{aligned} \tag{3.4}$$

$$\begin{aligned} \hat{m}^{dl}(\omega) &= \hat{m}^d(\omega) - \hat{r}^d(\omega)\hat{l}_d(2\omega); \\ \hat{r}^l(\omega) &= \hat{r}(\omega) + \hat{m}(\omega)\hat{l}_d^*(2\omega); \end{aligned} \tag{3.5}$$

where $\hat{m}^l(\omega), \hat{r}^{dl}(\omega), \hat{m}^{dl}(\omega)$ and $\hat{r}^l(\omega)$ are the Fourier transforms of lifted m, r^d, m^d, r respectively; $\hat{m}^d(\omega), \hat{r}^d(\omega), \hat{r}(\omega), \hat{m}(\omega)$ are the Fourier transforms of m^d, r^d, r, m respectively; $\hat{l}_l(\omega), \hat{l}_d(\omega)$ are Fourier transforms of two FIR filters corresponding to primal lifting and dual lifting respectively, and $\hat{l}_l^*(\omega), \hat{l}_d^*(\omega)$ are their complex conjugates. Here we want to create two vanishing moments wavelet functions corresponding to r^d and r. After computation, the shortest filters l_l and l_d have Fourier transforms:

$$\hat{l}_l(2\omega) = \frac{1}{8}e^{iw}(\cos(\omega) - 1). \tag{3.6}$$

$$\hat{l}_d(2\omega) = -\frac{3}{8}e^{iw}(\cos(\omega) - 1). \tag{3.7}$$

Inserting (3.6) and (3.7) into (3.4) and (3.5) respectively, gives:

$$m_2^l(\alpha) = \frac{1}{128}, 0, \frac{23}{128}, \frac{5}{8}, \frac{23}{128}, 0, \frac{1}{128}; \quad \alpha = -3, -2, \cdots, 3.$$

$$m_2^{dl}(\alpha) = -\frac{5}{64}, \frac{1}{16}, \frac{33}{32}, \frac{1}{16}, -\frac{5}{64}; \quad \alpha = -2, -1, \cdots, 2.$$

For 4×4 sensor arrays, the PSF can be considered as a refinable function with dilation 4. For filters m_4, m_4^l, their lifted filters m_4^l, m_4^{dl} are all symmetric and can be written as follows [16, 17, 18]:

$$m_4^l(\alpha) = -\frac{1}{3072}, -\frac{1}{3072}, \frac{7}{3072}, \frac{47}{384}, \frac{389}{1536}, \frac{377}{1536}, \frac{389}{1536}, \frac{47}{384}, \frac{7}{3072}, -\frac{1}{3072}, -\frac{1}{3072};$$

$$m_4^{dl}(\alpha) = -\frac{1}{512}, -\frac{29}{512}, \frac{15}{128}, \frac{165}{512}, \frac{61}{256}, \frac{165}{512}, \frac{15}{128}, -\frac{29}{512}, -\frac{1}{512}.$$

Now, we obtain the lifted filters.

3.3. Reconstruction Computation

We assume that the PSF is symmetric and the size of high-resolution images is $M \times M$. For L and L^d in (3.3), $L = L^x \otimes L^y, L^d = L^{d,x} \otimes L^{d,y}$. For 2×2 sensor arrays with periodic boundary condition, $L^x, L^y, L^{d,x}$ and $L^{d,y}$ can be expressed as $L_2^{p,x}, L_2^{p,y}, L_2^{p,d,x}, L_2^{p,d,y}$. Since PSF is symmetric and all the images are square, we have $L_2^{p,x} = L_2^{p,y}$ and $L_2^{p,d,x} = L_2^{p,d,y}$. For 2×2 sensor arrays with symmetric boundary condition, we can also get $L_2^{s,x}, L_2^{s,y}, L_2^{s,d,x}$ and $L_2^{s,d,y}$. Similarly, we have $L_2^{s,x} = L_2^{s,y}, L_2^{s,d,x} = L_2^{s,d,y}$. For 4×4 sensor arrays, similarly, $L_4^{p,x}, L_4^{p,y}, L_4^{p,d,x}, L_4^{p,d,y}$ and $L_4^{s,x}, L_4^{s,y}, L_4^{s,d,x}, L_4^{s,d,y}$ can also be gotten for periodic boundary condition and symmetric boundary condition respectively. So, according to equation (2.3), the following equations hold:

$$\begin{aligned}
L_2^p &= L_2^{p,x} \otimes L_2^{p,y}; \qquad L_2^{p,d} = L_2^{p,d,x} \otimes L_2^{p,d,y};\\
L_4^p &= L_4^{p,x} \otimes L_4^{p,y}; \qquad L_4^{p,d} = L_4^{p,d,x} \otimes L_4^{p,d,y};\\
L_2^s &= L_2^{s,x} \otimes L_2^{s,y}; \qquad L_2^{s,d} = L_2^{s,d,x} \otimes L_2^{s,d,y};\\
L_4^s &= L_4^{s,x} \otimes L_4^{s,y}; \qquad L_4^{s,d} = L_4^{s,d,x} \otimes L_4^{s,d,y}.
\end{aligned} \tag{3.8}$$

According to the assumptions above, $L_2^{p,x}, L_2^{p,d,x}, L_2^{s,x}, L_2^{s,d,x}, L_4^{p,x}, L_4^{p,d,x}, L_4^{s,x}$ and $L_4^{s,d,x}$ are all $M \times M$ matrices. We now give $L_2^{p,x}$ and $L_2^{s,x}$ as follows for an example:

$$L_2^{p,x} = \begin{bmatrix} \frac{5}{8} & \frac{23}{128} & 0 & \frac{1}{128} & & & & \frac{1}{128} & 0 & \frac{23}{128} \\ \frac{23}{128} & \frac{5}{8} & \frac{23}{128} & 0 & \frac{1}{128} & & & & \frac{1}{128} & 0 \\ 0 & \frac{23}{128} & \frac{5}{8} & \frac{23}{128} & 0 & \frac{1}{128} & & & & \frac{1}{128} \\ \frac{1}{128} & 0 & \frac{23}{128} & \frac{5}{8} & \frac{23}{128} & 0 & \frac{1}{128} & & & \\ & \frac{1}{128} & 0 & \frac{23}{128} & \frac{5}{8} & \frac{23}{128} & 0 & \frac{1}{128} & & \\ & & \ddots & \ddots & \ddots & \ddots & \ddots & \ddots & \ddots & \\ & & & \frac{1}{128} & 0 & \frac{23}{128} & \frac{5}{8} & \frac{23}{128} & 0 & \frac{1}{128} \\ \frac{1}{128} & & & & \frac{1}{128} & 0 & \frac{23}{128} & \frac{5}{8} & \frac{23}{128} & 0 \\ 0 & \frac{1}{128} & & & & \frac{1}{128} & 0 & \frac{23}{128} & \frac{5}{8} & \frac{23}{128} \\ \frac{23}{128} & 0 & \frac{1}{128} & & & & \frac{1}{128} & 0 & \frac{23}{128} & \frac{5}{8} \end{bmatrix};$$

$$L_2^{s,x} = \begin{bmatrix} \frac{103}{128} & \frac{23}{128} & \frac{1}{128} & \frac{1}{128} & & & & \\ \frac{23}{128} & \frac{81}{128} & \frac{23}{128} & 0 & \frac{1}{128} & & & \\ \frac{1}{128} & \frac{23}{128} & \frac{5}{8} & \frac{23}{128} & 0 & \ddots & & \\ \frac{1}{128} & 0 & \frac{23}{128} & \frac{5}{8} & \ddots & \ddots & \frac{1}{128} & \\ & \frac{1}{128} & 0 & \ddots & \ddots & \frac{23}{128} & 0 & \frac{1}{128} \\ & & \ddots & \ddots & \ddots & \frac{5}{8} & \frac{23}{128} & \frac{1}{128} \\ & & & \frac{1}{128} & 0 & \frac{23}{128} & \frac{81}{128} & \frac{23}{128} \\ & & & & \frac{1}{128} & \frac{1}{128} & \frac{23}{128} & \frac{103}{128} \end{bmatrix}. \tag{3.9}$$

If the boundary condition is chosen to be periodic, then L and L^d in (3.3) are all block-circulant-circulant-block (BCCB) matrices and (3.3) can be solved by three FFTs in $O(M^2 \log(M^2))$ operations [19, section 5.1.3]. If the boundary condition is symmetric, then L and L^d in (3.3) are all block Toeplitze-plus-Hankel system with Toeplitze-plus-Hankel blocks (THTH) matrix and (3.3) can be solved by three 2D fast cosine transforms (FCTs) in $O(M^2 \log(M^2))$ operations [17].

3.4. Fast Algorithm for Solving $Lf = g$

In this subsection, we give a fast algorithm which can decrease computation complexity and speed up computation efficiently in solving (3.3). During computation, $L_2^{p,x}, L_2^{p,d,x}, L_4^{p,x}, L_4^{p,d,x}, L_2^{s,x}, L_2^{s,d,x}, L_4^{s,x}$ and $L_4^{s,d,x}$ can be stored in the memory of a computer in the manner of sparse matrices, but it will be complex and difficult to store L, L^d and $L \otimes L^d$ as sparse matrices. So, we derive a method from (3.3) for reducing memory occupancy and thus speeding up the computation. According to [19, 20], we know that $L_2^{p,x}, L_2^{p,d,x}, L_4^{p,x}, L_4^{p,d,x}, L_2^{s,x}, L_2^{s,d,x}, L_4^{s,x}$ and $L_4^{s,d,x}$ can be diagonalized by matrix A (Fourier transform or Cosine transform matrix) and its inverse matrix A^{-1}. Here, we take $L_2^{p,x}, L_2^{p,y}$ as an example. Assume that the diagonal matrix of $L_2^{p,x}$ is $D_2^{p,x}$ and the diagonal matrix of $L_2^{p,y}$ is $D_2^{p,y}$, then:

$$L_2^{p,x} = A D_2^{p,x} A^{-1}. \tag{3.10}$$

$$L_2^{p,y} = A D_2^{p,y} A^{-1}. \tag{3.11}$$

Assume that $A \otimes A = A_{2n}$, $A^{-1} \otimes A^{-1} = A_{2n}^{-1}$ and $D_2^p = D_2^{p,x} \otimes D_2^{p,y}$. According to (3.10) and (3.11) and assumptions above, L_2^p can be written:

$$\begin{aligned} L_2^p &= L_2^{p,x} \otimes L_2^{p,y} = AD_2^{p,x}A^{-1} \otimes AD_2^{p,y}A^{-1} \\ &= (A \otimes A)(D_2^{p,x}A^{-1} \otimes D_2^{p,y}A^{-1}) \\ &= (A \otimes A)(D_2^{p,x} \otimes D_2^{p,y})(A^{-1} \otimes A^{-1}) \\ &= A_{2n}D_2^pA_{2n}^{-1}. \end{aligned} \tag{3.12}$$

Similarly, following equation also holds:

$$L_2^{p,d} = A_{2n}D_2^{p,d}A_{2n}^{-1}. \tag{3.13}$$

According to (3.12), we know that the diagonal matrix of L_2^p is D_2^p. Similarly, the diagonal matrix of $L_2^{p,d}$ is $D_2^{p,d}$ and $D_2^{p,d} = D_2^{p,d,x} \otimes D_2^{p,d,y}$. So, (3.3) can be rewritten as follows:

$$f = (L_2^{p,d}L_2^p + \frac{\beta}{1-\beta}I)^{-1}(\frac{1}{1-\beta})L_2^{p,d}g. \tag{3.14}$$

As we know, $\beta/(1-\beta)I$ is a diagonal matrix, so following equation holds:

$$A_{2n}((\frac{\beta}{1-\beta})I)A_{2n}^{-1} = (\frac{\beta}{1-\beta})I$$

According to the descriptions above, we can get:

$$(L_2^{p,d}L_2^p + \frac{\beta}{1-\beta}I)^{-1} = A_{2n}((D_2^{p,d,x} \otimes D_2^{p,d,y})(D_2^{p,x} \otimes D_2^{p,y}) + (\frac{\beta}{1-\beta})I)^{-1}A_{2n}^{-1}. \tag{3.15}$$

Inserting (3.15), (3.13) into (3.14), gives:

$$f = A_{2n}(D_2^{p,d}D_2^p + \frac{\beta}{1-\beta}I)^{-1}(\frac{1}{1-\beta})D_2^{p,d}A_{2n}^{-1}g. \tag{3.16}$$

For any $MM \times 1$ matrix L, $M \times M$ matrix A, B and $P = A \otimes B$, following equation holds (See appendix for mathematical proof):

$$PL = S^{-1}(BS(L)A^T). \tag{3.17}$$

where S is an operator to order L into an $M \times M$ matrix in a row-by-row fashion, and S^{-1} is an operator to order $BS(L)A^T$ into an $MM \times 1$ matrix in a row-by-row fashion. So (3.16) can be rewritten as follows:

$$\begin{aligned} f &= S^{-1}(AS((D_2^{-p,d}D_2^{-p} + \\ &\quad (\frac{\beta}{1-\beta})^{-1}I)(\frac{1}{1-\beta})\ D_2^{p,d}S^{-1}(A^{-1}S(g)(A^{-1})^T))A^T). \end{aligned} \tag{3.18}$$

where $D_2^{-p}, D_2^{-p,d}$ are inverse matrices of D_2^p and $D_2^{p,d}$. From (3.18), we can see that it need not to construct $L_2^{p,d}$ and this will reduce memory occupancy and thus speed up computation greatly. According to the definition of FFT, IFFT, FCT and IFCT, (3.18) can be solved by two FFTs and two IFFTs in $O(M^2 \log(M^2))$

operations when boundary condition is periodic or by two FCTs and two IFCTs when boundary condition is symmetric, but not three 2D FFTs or FCTs given in [9, 20]. Due to the decrease in memory occupancy, the computation can also be speeded up, especially when the size of images is large.

4. Numerical Experiments

Numerical experiments were conducted to test the algorithm proposed in this paper. We will illustrate effectiveness of the algorithm by the experiment results. In these experiments, high-resolution images are all size 256×256. For 2×2 sensor arrays, we use four low-resolution images of size 128×128 to conduct experiments. For 4×4 sensor arrays, sixteen low-resolution images of size 64×64 are used in test experiments. The peak signal-to-noise ratio (PSNR), which compares the reconstructed image $\mathbf{f}_c$ with the original image $\mathbf{f}$, is defined by:

$$\mathrm{PSNR} = 10 \log_{10} \frac{255^2 NM}{\|\mathbf{f} - \mathbf{f}_c\|_2^2}.$$

We give the experiment results in Table 1-Table 4. In these tables, β^* means the optimal values of β; "biorthogonal" means the biorthogonal method proposed in [9]; "dual" means to only apply dual lifting to the reconstruction process, and "primal and dual" means to apply primal lifting and dual lifting to the reconstruction process at the same time. Table 1 is the experiment results for 2×2 sensor arrays when boundary conditions is periodic. Table 2 is the results for 2×2 sensor arrays with symmetric boundary condition. We can see that the "dual" and "primal and dual" methods improve the quality of reconstructed images significantly. Especially, the "primal and dual" is more efficient than "dual". We can also see that the method we proposed is more efficient for the images with greater SNR. Table 3 and Table 4 are the experiment results for 4×4 sensor arrays with periodic boundary condition and symmetric boundary condition respectively. From the two tables, we can see the same effect as it shown in Table 1 and Table 2. In comparison with 2×2 sensor arrays, the efficiency of the method for 4×4 sensor arrays is slightly reduced. From the Table 1 and the Table 2, we can also see that the method is susceptible to noise, namely, the method is more effective on the low-resolution images with greater SNR value. Visual experiment results are shown in Figure 1 and Figure 2.

5. Conclusion

In this paper, we proposed an algorithm for high-resolution image reconstruction based on wavelet lifting scheme. By the method, we improved the work of chan [9] greatly. The method can also be easily extended to super-resolution image reconstruction. Using the experiment results, we have shown that our method is effective in high-resolution image reconstruction. However, for 4×4 sensor arrays, performance of the method is worse than it for 2×2 sensor arrays. The experiment

TABLE 1. 2×2 sensor arrays with periodic boundary condition

		biorthogonal		dual		primal and dual	
image	SNR	PSNR	β^*	PSNR	β^*	PSNR	β^*
Boat	30db	34.89	0.013	34.991	0.016	35.11	0.021
	40db	41.40	0.017	41.43	0.018	41.516	0.019
Lena	30db	35.92	0.027	35.969	0.029	35.992	0.031
	40db	42.70	0.025	42.737	0.034	42.779	0.035

TABLE 2. 2×2 sensor arrays with symmetric boundary condition

		biorthogonal		dual		primal and dual	
image	SNR	PSNR	β^*	PSNR	β^*	PSNR	β^*
Boat	30db	36.048	0.012	36.44	0.039	36.598	0.22
	40db	44.874	0.0013	44.981	0.00027	45.265	0.031
Lena	30db	37.403	0.027	37.592	0.075	37.699	0.31
	40db	45.612	0.0001	45.75	0.00043	46.13	0.035

TABLE 3. 4×4 sensor arrays with periodic boundary condition

		biorthogonal		dual		primal and dual	
image	SNR	PSNR	β^*	PSNR	β^*	PSNR	β^*
Boat	30db	34.89	0.013	34.991	0.016	35.11	0.021
	40db	41.40	0.017	41.43	0.018	41.516	0.019
Lena	30db	35.92	0.027	35.969	0.029	35.992	0.031
	40db	42.70	0.025	42.737	0.034	42.779	0.035

TABLE 4. 4×4 sensor arrays with symmetric boundary condition

		biorthogonal		dual		primal and dual	
image	SNR	PSNR	β^*	PSNR	β^*	PSNR	β^*
Boat	30db	34.910	0.011	34.939	0.018	34.957	0.018
	40db	43.00	0.015	43.14	0.0145	45.21	0.02
Lena	30db	36.127	0.027	36.17	0.026	36.35	0.029
	40db	44.00	0.031	44.18	0.033	44.37	0.035

results also show that the method is susceptible to noise. At the same time, a fast algorithm was derived in this paper for solving $Lf = g$ under the periodic and symmetric boundary conditions.

(a) Original high-resolution "boat" image (256×256)

(b) Low-resolution image with 30db white noise is added (128×128)

(c) Reconstructed HR image by the method by "Chan" with periodic boundary condition

(d) Reconstructed HR image by "primal and dual lifting" method with periodic boundary condition

(e) Reconstructed HR image by the method by "Chan" with symmetric boundary condition

(f) Reconstructed HR image by "primal and dual lifting" method with symmetric boundary condition

FIGURE 1. Experiment results for 2×2 sensor arrays

Appendix

Assume that A, B are all $M \times M$ matrices and $P = A \otimes B$. Let g be an $MM \times 1$ arbitrary matrix, then following equation holds:

$$P \cdot g = S^{-1}(B \cdot S(g) \cdot A^T). \tag{A.1}$$

where S is an operator to order g to an $M \times M$ matrix in a row-by-row fashion, and S^{-1} is an operator to order an $M \times M$ matrix to an $MM \times 1$ matrix in a row-by-row fashion.

Proof. Assume that the (k, i)th element of A is $A(k, i)$. According to the property of Kronecker tensor product, P can be represented as an $M \times M$ block matrix, and its (m, n)th element can be represented as $A(m, n) \cdot B$. So we can write $Pg = f$

(a) Original high-resolution "boat" image (256×256)

(b) Low-resolution image with 30db white noise is added (64×64)

(c) Reconstructed HR image by the method by "Chan" with periodic boundary condition

(d) Reconstructed HR image by "primal and dual lifting" method with periodic boundary condition

(e) Reconstructed HR image by the method by "Chan" with symmetric boundary condition

(f) Reconstructed HR image by "primal and dual lifting" method with symmetric boundary condition

FIGURE 2. Experiment results for 4×4 sensor arrays

as:

$$\begin{bmatrix} A(1,1)\cdot B & A(1,2)\cdot B & \cdots & A(1,M)\cdot B \\ A(2,1)\cdot B & A(2,2)\cdot B & \cdots & A(2,M)\cdot B \\ \vdots & \vdots & \cdots & \vdots \\ A(M,1)\cdot B & A(M,2)\cdot B & \cdots & A(M,M)\cdot B \end{bmatrix} \begin{bmatrix} g_{1,1} \\ \vdots \\ g_{M,1} \\ g_{1,2} \\ \vdots \\ g_{M,M} \end{bmatrix} = \begin{bmatrix} f_{1,1} \\ \vdots \\ f_{M,1} \\ f_{1,2} \\ \vdots \\ f_{M,M} \end{bmatrix}$$

According to (A.1), the (m,j)th element of f can be represented by:

$$f_{m,j} = \sum_{k=1}^{M} A(j,k) \sum_{p=1}^{M} B(m,p) \cdot g_{p,k}. \tag{A.2}$$

Let $y = BGA^T$, where

$$G = \begin{bmatrix} g_{1,1} & g_{1,2} & \cdots & g_{1,M} \\ g_{2,1} & g_{2,2} & \cdots & g_{2,M} \\ \vdots & \vdots & \cdots & \vdots \\ g_{M,1} & g_{M,2} & \cdots & g_{M,M} \end{bmatrix}.$$

According to the definition of y, the (m, j)th element of y is

$$y_{m,j} = \sum_{k=1}^{M} A(j,k) \sum_{p=1}^{M} B(m,p) \cdot g_{p,k}. \tag{A.3}$$

we can see that (A.3) has the same representation as (A.2), so $y_{m,j} = f_{m,j}$ and $P \cdot g = S^{-1}(B \cdot S(g) \cdot A^T)$.

□

Acknowledgment

Many thanks to Education Ministry of Guangdong Province, P.R. China.

References

[1] R.Y. Tsai and T.S. Huang, *Multipleframe image restoration and registration*, Advances in Computer Vision and Image Processing. **1**(1984),317-339.

[2] N. Nguyen and P. Milanfer, *An efficient wavelet-based algorithm for image super-resolution*, Proc. International Conference of Image Processing. 2000, 351-354.

[3] M.C. Hong, M.G. Kang, and A.K. Katsaggelos, *A regularized multi-channel restoration approach for globally optimal high-resolution video sequence*, SPIE VCIP, **3024** (1997), 1306-1317.

[4] B.C. Tom etc., *Reconstruction of a high-resolution image by simultaneous registration, restoration, and interpolation of low-resolution images*, Proc. 1995 IEEE Int. Conf. Image Processing, 1995, 539-542.

[5] R.R. Schulz and R.L. Stevenson, *Extraction of high-resolution frames from video sequence*, IEEE Trans. Image Processing, **5** (1996), 996-1011.

[6] Di zhang and Minghui Du, *Fast hybrid approach to large-magnification super-resolution image reconstruction*, Optical Engineering, SPIE, **44** (2003), 037005-1-9.

[7] H. Stark and P. Oskoui, *High resolution image recovery from image plane arrays, using convex projections*, J. Optical. Soc. AM. A, **6** (1989), 1715-1726.

[8] N. Bose and K. Boo, *High-resolution image reconstruction with multisensors*, International J. Imaging System and Technology, **9** (1998), 294-304.

[9] Raymond H. Chan and Tony F. Chan, etc., *Wavelet Algorithms for High-resolution Image Reconstruction*, SIAM, J. Sci. Comput., **24** (2003), 1408-1432.

[10] Raymond H. Chan, and Tony F. Chan, Lixin Shen and Zhouwei Shen, *Wavelet Deblurring Algorithm for Spatially Varying Blur from High-resolution Image Reconstruction*, Research report, CUHK-2000-20, Department of Mathematics, The Chinese University of HongKong, 2000.

[11] G.Deslauriers and S. Dubuc, *Interpolation dyadique, in "Fractals, dimensions non enti" res et applications*, Masson, Paris, 1987.

[12] I. Daubechies, *Ten lectures on wavelets*, CBMS-NSF Regional Conf. Ser. In Appl. Math., Vol.61. SIAM, 1992.

[13] David S. Taubman and Michael W. Marcelin, *JPEG 2000 Image Compression Fundamentals, Standards and Practice*, Kluwer Academic Publishers, 2001.

[14] Stephane Mallat, *A Wavelet Tour of Signal Processing*, Elsevier Academic Press, 1999.

[15] G.Deslauriers and S. Dubuc, *Symmetric iterative interpolation processes*, Constr. Approx. **5** (1998),49-68.

[16] Wim Sweldens, *The Lifting Scheme: A Custom-Design Construction of Biorthogonal Wavelets*, Applied and Computational Harnonic Analysis, **3** (1996), 186-200.

[17] W. Lawton and S. L. Lee, and Z. Shen, *Stability and orthonormality of multivariate refinable functions*, SIAM J. Math. Anal., **28** (1997), 999-1014.

[18] Z. Shen, *Extension of matrices with Laurent polynomial entries*, proceedings of the 15th IMACS World Congress 1997 on Scientific Computation, Modeling and Applied Mathematics, A. Syclow, 1997, 57-61.

[19] R. Gonzalez and R. Woods, *Digital Image Processing*, Addison-Wesley, Reading, MA, 1993.

[20] Michael K. Ng, Raymond H. Chan and Wun-Cheung Tang, *A Fast Algorithm for Deblurring Models with Neumann Boundary Conditions*, SIAM J. Sci. Comput., **21** (1999), 851-866.

Shengwei Pei
Research & Development Center,
China Academy of Space Technology,
Beijing,
P.R. China
e-mail: `eeswpei@yahoo.com.cn, eeswpei@scut.edu.cn`

Haiyan Feng
Division of Science and Technology.
South China University of Technology
Guangzhou, Guangdong Province, 510640
P.R. China
e-mail: `adhyfeng@scut.edu.cn`

Minghui Du
School of Electronic and Information Engineering.
South China University of Technology
Guangzhou, Guangdong Province, 510640
P.R. China
e-mail: `ecmhdu@scut.edu.cn`

Wavelet Analysis and Applications
Tao Qian, Mang I. Vai and Xu Yuesheng, Eds.
Applied and Numerical Harmonic Analysis, 503–513

Mulitiresolution Spatial Data Compression Using Lifting Scheme

B. Pradhan, K. Sandeep, Shattri Mansor,
Abdul Rahman Ramli and Abdul Rashid B. Mohamed Sharif

Abstract. In many applications referring to terrain visualization, there is need to visualize terrains at different levels of detail. The terrain should be visualized at different levels for different parts; for example, a region of high interest should be in a higher resolution than a region of low or no interest. The lifting scheme has been found to be a flexible method for constructing scalar wavelets with desirable properties. In this paper, it is extended to the GIS data compression. A newly developed data compression approach to approximate the land surface with a series of non-overlapping triangles has been presented. Over the years the TIN data representation has become a case in point for many researchers due its large data size. Compression of TIN is needed for efficient management of large data and good surface visualization. This approach covers following steps: First, by using a Delaunay triangulation, an efficient algorithm is developed to generate TIN, which forms the terrain from an arbitrary set of data. A new interpolation wavelet filter for TIN has been applied in two steps, namely splitting and elevation. In the splitting step, a triangle has been divided into several sub-triangles and the elevation step has been used to 'modify' the point values (point coordinates for geometry) after the splitting. Then, this data set is compressed at the desired locations by using second generation wavelets. The quality of geographical surface representation after using proposed technique is compared with the original terrain. The results show that this method can be used for significant reduction of data set.

Keywords. Delaunay triangulation, Triangulated irregular network (TIN), Geographical Information System, Lifting scheme, Second generation wavelet, Image compression, Multiresolution Analysis

1. Introduction

Recently, most of the methods for image compression are based on wavelets and related techniques. Wavelet approaches for image compression tend to outperform Fourier approaches because of its ability to represent both spatially localized features and smooth regions in an image. The superior compression capability of wavelets combined with their natural multiresolution structure makes them a good representation for storing images. While working with dyadic wavelet decomposition digital images are represented by wavelet coefficients. These types of representation in dyadic wavelet decomposition are known as linear decomposition over a fixed orthogonal basis. The non-linearity in the approximation of images by wavelets is introduced by the thresholding of the wavelet coefficients. This type of approximation can be viewed as *mildly* nonlinear. Recently, several *highly* nonlinear methods for capturing the geometry of images were developed, such as wedgelets [1] as well as edge-adapted nonlinear multiresolution and geometric spline approximation [2]. This paper presents a new approach for non-linear image compression method using second generation wavelets. A random set of points has been approximated to represent a surface by Delaunay triangulation. The theory, computations, and applications of Delaunay triangulations and Voronoi diagrams have been described in detail n the literature [3, 4, 5, 6, 7, 8, 9, 10, 11, 12]. The present work describes a fast algorithm based on Tsai's Convex Hull Insertion algorithm [10] and [11] for the construction of Delaunay triangulations and Voronoi diagrams of arbitrary collections of points on the Euclidean plane. The original algorithm has been improved further for a faster computation of geometric structures. The source code has been written in FORTRAN compiler. Once the triangulated irregular network has been created from the random set of points was further subjected to compression by using second generation wavelets. Results were shown in a comparative study basis for the TIN data compression at different level of resolution

2. Delaunay Triangulation

Many researchers [13] and [14] have suggested different ways to construct triangulations with the local equilateral property. A well known construction called the Delaunay Triangulation simultaneously optimizes several of the quality measures such as max-min angle, min-max circumcircle, and min-max min-containment circle. The Delaunay triangulation "DT" of a point set is the planar dual of the famous Voronoi diagram. The Voronoi diagram is a partition of the plane into polygonal cells one for each input point so that the cell for input point $'a'$ consists of the region of the plane closer to $'a'$ than to any other input point. So long as no four points lie on a common circle then each vertex of the Voronoi diagram has degree three and the DT which has a bounded face for each Voronoi vertex and vice versa will indeed is a triangulation. If four or more points do lie on a common circle then these points will be the vertices of a larger face that may then be triangulated to give a triangulation containing the DT Voronoi diagrams and Delaunay

triangulations have been generalized in numerous directions. For more information on Delaunay triangulations and Voronoi diagrams see the surveys by [15] and [16]. There is a nice relationship between Delaunay triangulation and three dimensional convex hulls. Lift each point of the input to a paraboloid in three-space by mapping the point with coordinates (x, y) to the point $(x, y, x^2 + y^2)$. The convex hull of the lifted points can be divided into lower and upper parts: a face belongs to the lower convex hull if it is supported by a plane that separates the point set from $(0, 0, -\infty)$. It can be shown that the DT of the input points is the projection of the lower convex hull onto the xy-plane as depicted in Figure 1. Finally a direct characterization: if a and b are input points the DT contains the edge $\{a, b\}$ if and only if there is a circle through a and b that intersects no other input points and contains no input points in its interior Moreover each circumscribing circle (circumcircle) of a DT triangle contains no input points in its interior.

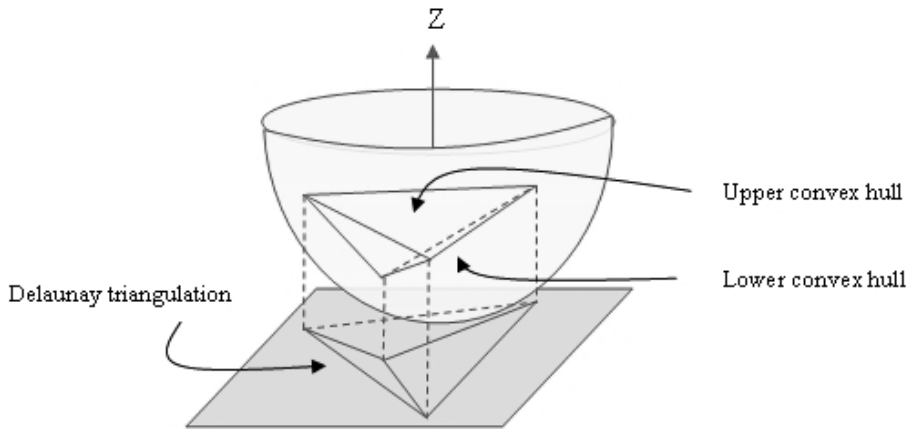

FIGURE 1. The lifting transformation maps the DT to the lower convex hull.

Some properties of Delaunay triangulations have been discussed as follows. Let Y denote a finite planar point set.

- A Delaunay triangulations $D(Y)$ of Y is one, such that for any triangle in $D(Y)$, the interior of its circumcircle does not contain any point from Y. This specific property is termed as Delaunay property.
- The Delaunay triangulation $D(Y)$ of Y is unique, provided that no four points in Y are co-circular. Since neither the set X of pixels nor its subsets satisfy this condition, we initially perturb the pixel positions in order to guarantee unicity of the Delaunay triangulations of X and of its subsets. Each perturbed pixel corresponds to one unique unperturbed pixel. From now on, we denote the set of perturbed pixels by X, and the set of unperturbed pixels by $\tilde{}X$.
- For any $y \epsilon Y$, $D(Y \setminus y)$ can be computed from $D(Y)$ by a *local* update. This follows from the Delaunay property, which implies that only the cell $C(y)$ of

y in $D(Y)$ needs to be retriangulated. Recall that the cell $C(y)$ of y is the domain consisting of all triangles in $D(Y)$ which contain y as a vertex. Figure 1 shows a vertex $y \epsilon D(Y)$ and the Delaunay triangulation of its cell $C(y)$.

- $D(Y)$ provides a partitioning of the convex hull $[Y]$ of Y.

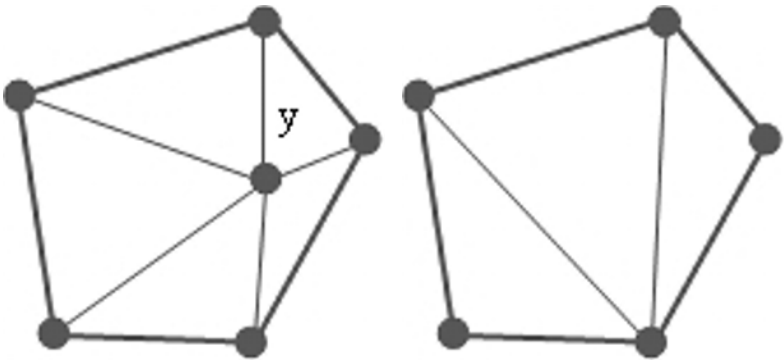

(a) (b)

FIGURE 2. Removal of the vertex $y \epsilon D(Y)$, and the Delaunay triangulation of its cell $C(y)$. The five triangles of the cell $C(y)$ in (a) are replaced by the three triangles in (b)

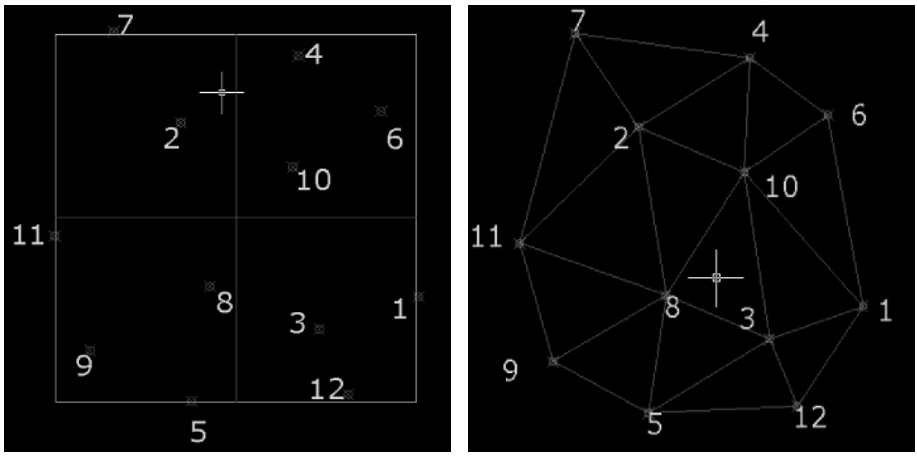

(a) (b)

FIGURE 3. Figure 3(a) shows irregular set of points and Figure 3(b) shows the TIN data structure using Delaunay triangulation

3. Interpolation Wavelet Filters for TIN

An interpolation wavelet filter for TIN lies in subdivision process which has two steps [17]. One is a splitting step; the other one is an elevation step. In the splitting step, a triangle is divided into several sub-triangles. The elevation step is to calculate the point values (point coordinates for geometry) after the splitting. Let us discuss this partition step mathematically. Consider a data set to be partitioned into two groups, called S and e. Using P to express the point coordinates, one can construct an estimation of P_s based on P_e.

$$\tilde{P}_s = E(P_e) \tag{1}$$

The estimation function (filter) (E) can be a local estimation or global estimation. A global estimation is generally computationally expensive; therefore, a local estimation using only neighboring points is preferred. After the estimation step, a wavelet term, W_s and an approximation term, A_s for the original data can be constructed as:

$$\begin{aligned} W_s &= P_s - \tilde{P}_s \\ A_e &= P_e + C(W_s) \end{aligned} \tag{2}$$

The correction function C is a customizable function based on different optimization requirements. An inverse transform can be constructed as:

$$\begin{aligned} P_e &= A_e - C(W_s) \\ P_s &= W_s + E(P_e) \end{aligned} \tag{3}$$

If the original point set can be partitioned into a nested group, then the above process can be iteratively applied to different sets in this group. A nested group has the flowing structure:

$$\begin{aligned} &e^0 \subset e^1 \subset e^2 \subset \cdots\cdots \subset e^N \\ &e^i \bigcup s^i = e^{i+1}, i = 0, \ldots, N-1 \end{aligned} \tag{4}$$

e^N denotes the finest representation of the geometry. e^N can be partitioned into e^{N-1} and s^{N-1}; then e^{N-1} can be partitioned into e^{N-1} and s^{N-1}, and so on, until e^1 is partitioned into e^0 and s^0. Note that the superscripts are used to represent different resolutions (larger numbers represent finer resolution). Based on this nested (or hierarchical) structure of the partition, one can construct wavelets and approximations of the data as:

$$\begin{aligned} A_{e^N} &= P_{e^N} \\ e^i = e^{i-1} \bigcup s^{i-1}, B_{e^{i-1}} &= A_{e^i}(e^{i-1}), B_{s^{i-1}} = A_{e^i}(s^{i-1}) \\ W_{e^{i-1}} &= B_{e^{i-1}} - E(B_{e^{i-1}}), i = N, N-1, \ldots, 1 \\ A_{e^{i-1}} &= B_{e^{i-1}} + C(W_{s^{i-1}}) \end{aligned} \tag{5}$$

Here, B is an intermediate symbol to represent the partitioning result. A_{e^i} is partitioned into two components: $A_{e^i}{}^{(e^{i-1})}$ and $A_{e^i}{}^{(s^{i-1})}$, which belong to e^{i-1} and s^{i-1} respectively. Based on equation (5), the original data P_{e^N} is decomposed into A_{e^0}, W_{s^0}, W_{s^1}, ..., $W_{s^{N-1}}$. Equation (5) is the analysis transform, which decomposes the finer representation into a coarser representation plus details. The synthesis transforms in the inverse transform and is shown in equation (6). The reconstructed A_{e^0}, A_{e^1}, ..., $A_{e^N}(= P_{e^N})$ yield a multiresolution representation of the original data.

$$\begin{gathered} B_{e^i} = A_{e^i} - C(W_{s^i}) \\ B_{s^i} = W_{s^i} + E(B_{e^i}), i = 0, 1, \ldots, N-1 \\ e^{i+1} = e^i \bigcup s^i, A_{e^{i+1}}(e^i) = B_{e^i}, A_{e^{i+1}}(s^i) = B_{s^i} \\ P_{e^N} = A_{e^N} \end{gathered} \tag{6}$$

In the above derivation of a wavelet representation [18, 19, 20, 21] the process does not depend on a regular setting for the data; therefore, it can be used in both the regular and irregular setting cases. This is an important advantage of the lifting scheme [22] and [23]. If the filters E and C and are the same for every point at a given level, the scheme is a uniform scheme. If they also do not change with the resolution, i, the scheme is a stationary scheme as well. However, equations (5) and (6) are general formulas. Non-stationary and non-uniform schemes can be written in this form with indices on E and C. Nevertheless, those schemes could cost more computing resources and may be less effective for data compression in GIS applications.

4. An Example

Figure 4 shows an example that illustrates the basic idea of the above construction process. Here E and C depend on e0 and s0; therefore, it is a non-stationary and non-uniform transform. Given irregular data on points $e^1 = \{t_0, t_1, t_2, t_3, t_4, \}$, the one step partition and wavelet transform are:

$$\begin{gathered} A_{e^1} = P_{e^1}, e^0 = \{t_0, t_2, t_4\}, s^0 = \{t_1, t_3\} \\ e^1 = e^0 \bigcup s^0, B_{e^0} = A_{e^1}(e^0), B_{s^0} = A_{e^1}(s^0), \lambda_1 = \tfrac{t_1 - t_0}{t_2 - t_0}, \lambda_1 = \tfrac{t_3 - t_2}{t_4 - t_2} \\ W_{s^0} = B_{s^0} - (B_{e^0}) = \begin{bmatrix} P_{t_1} \\ P_{t_3} \end{bmatrix} - \begin{bmatrix} 1-\lambda_1 & \lambda_1 & 0 \\ 0 & 1-\lambda_2 & \lambda_2 \end{bmatrix} \begin{bmatrix} P_{t_0} \\ P_{t_2} \\ P_{t_4} \end{bmatrix} \\ A_{e^0} = B_{e^0} + C(W_{s^0}) = \begin{bmatrix} P_{t_0} \\ P_{t_2} \\ P_{t_4} \end{bmatrix} + \begin{bmatrix} 1-\lambda_1 & 0 \\ \lambda_1 & 1-\lambda_2 \\ 0 & \lambda_2 \end{bmatrix} \begin{bmatrix} W_{t_1} \\ W_{t_3} \end{bmatrix} \end{gathered} \tag{7}$$

In this example, a linear estimator and corrector are used for E and C. If λ_1 and λ_2 are 0.5, the correction step makes the norm defined in equation (8) take a similar value than the uncorrected value. (Note that in equation (8), A_{e^0} (t_j) for $t_j \notin e^0$ refers to the estimation value $E(A_{e^0})$ at t_j. This is an example of the

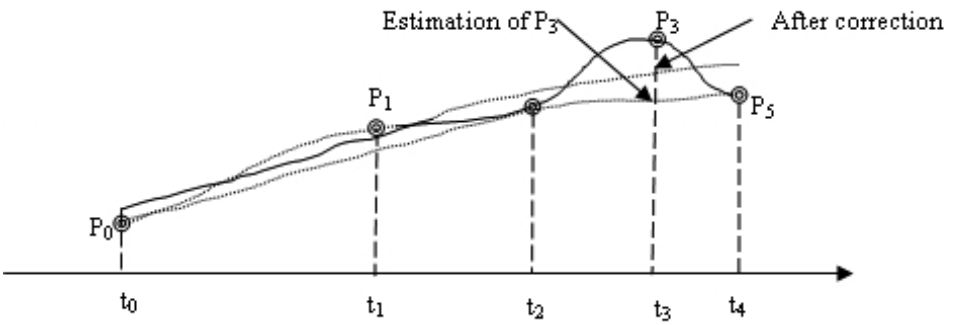

FIGURE 4. Example that illustrates the basic idea of construction of lifting scheme process.

optimization in the correction step. Equation (7) is the analysis transform for the first step. The synthesis transform can be derived by replacing the estimator and the corrector in equation (6).

$$norm = \sum_{t_j \in e_1} (A_{e^1}(t_j) - A_{e^0}(t_j))^2 \tag{8}$$

The above scheme is one type of filter based on the lifting scheme. This is called an approximation filter, in which every point value will change after each iteration. The other type of filter based on the lifting scheme is an interpolation filter, in which a point value reaches its final position once it is calculated. If the correction term is omitted in equation (5), the filter becomes an interpolation filter. An approximation filter may be optimal in a defined global norm. However, interpolation filters have the advantage of interpolating point values, which may be useful in some GIS applications. Therefore, choosing the type of filter depends on the application. For example, approximation filters are generally used in processing image because the whole scene of an image is more important to the viewer than any individual pixel. For GIS terrain data, however, interpolation is generally preferred because point values are often more useful than a general shape. Therefore, interpolation wavelet filters will be used in this research for processing three-dimensional terrain data.

5. Results and Discussion

Results for irregular triangulated network data for three-dimensional GIS terrain have been presented. The original data was in an irregular fashion. Delaunay triangulation method for the creation of the TIN has been applied to the original data. A new algorithm has been developed for the creation of the TIN. Further, TIN

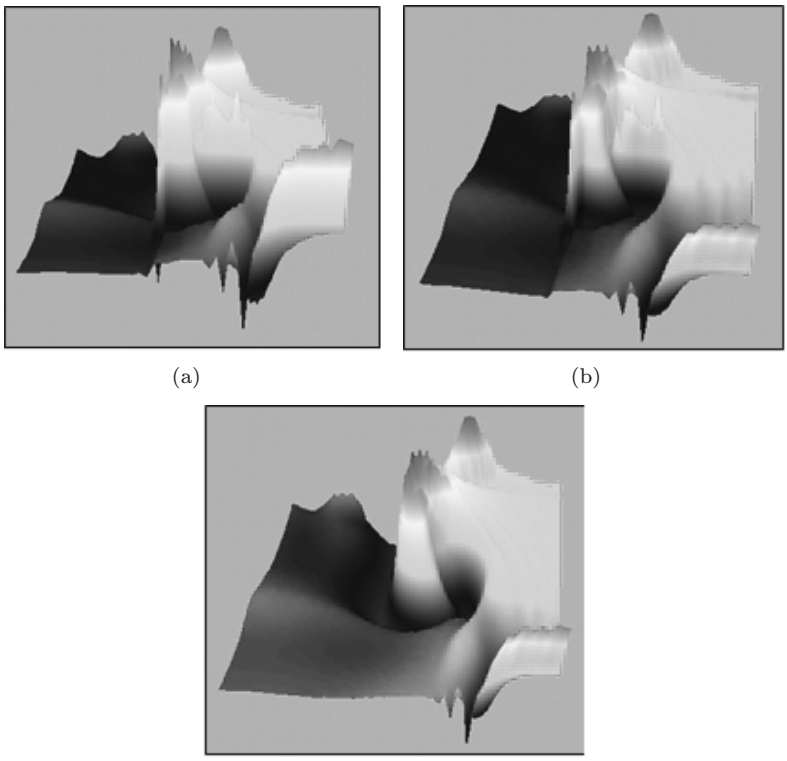

(a) (b)

(c)

FIGURE 5. Figure (a): shows the original TIN data; Figure (b): shows the wavelet compression at the level of 12% and Figure (c): shows the wavelet compression at level of 23%

was compressed using the second generation wavelets. A new algorithm for second generation wavelet compression is proposed. Based on the initial configuration of the original TIN, different resolutions are constructed during wavelet analysis. Figures 7 and 8 above show the results computed using the wavelet based lifting scheme algorithm. Figure 6 shows the original data. Figure 7 shows the results after 12% compression and figure 8 shows after 23% compression. Different compression schemes, such as Huffman coding can be applied to these wavelet coefficients to further reduce the storage size. This work also provides current implementation of wavelet coefficients during the compression operation. The proposed algorithm has the multiresolution capability and easy to compress due to large number of wavelet coefficients with small magnitudes which is suitable for distributed GIS applications such as web displaying. The research is ongoing. The future work

includes the wavelet compression analysis for different sets of terrain at different level of resolution to verify the results with existing compression techniques.

Conclusion

The construction of Triangulated Irregular Network using Delaunay triangulation has been shown. This approach uses fast and efficient second generation wavelets algorithm for multiresolution analysis of GIS data compression. This algorithm is easy to perform the mathematical and computational operation with minimal time, irrespective of the large data. Our algorithm scheme preserves high-gradient regions that might exist in a given data set. We have tested our method with various data sets. The computational cost of our algorithm depends on the different approaches used. The initial triangulation can be done in $O(n \log n)$, the gradient approximation can be done in $O(n \log n)$. The individual refinement step has to check all the original data points lying in the involved triangles, so the complexity of each step is $O(n)$. How often the iteration step is executed depends on the error value given in the input. As a general rule, the authors have assumed that no more iteration should be done than they are original data sites. So the overall complexity is $O(n^2)$. We are currently investigating the detailed error analysis for the different sets of data sets at different scales.

Acknowledgement

Authors would like to thank Addin Osman and Lawal Billa for their useful support concerning the manuscript putting in current Latex format.

References

[1] Donoho, D., 1999, "Wedgelets: nearly-minimax estimation of edges", *Annals of Stat.*, vol. 27, pp. 859-897

[2] Demaret, L., Dyn, N., Floater, M. S. and Iske, A., 2004, "Adaptive thinning for terrain modelling and image compression", in *Advances in Multiresolution for Geometric Modelling*, N. A. Dodgson, M. S. Floater, and M. A. Sabin (eds.), Springer-Verlag, Heidelberg, pp. 321-340

[3] Kao, T., Mount, D. M., and Saalfeld, A., 1991, "Dynamic maintenance of Delaunay triangulations": *Proc. Auto-Carto I0*, Baltimore, Maryland, p. 219-233

[4] Lawson, C. L., 1972, "Generation of a triangular grid with application to contour plotting", California Institute of Technology, Jet Pollution Laboratory, Technical Memorandum No. 299

[5] Lee, D. T., and Schachter, B. J., 1980, "Two algorithms for constructing a Delaunay triangulation", *Intern. Jour. Computer and Information Sciences*, v. 9, no. 3, p. 219-242

[6] Macedonio, G. and Pareschi, M. T., 1991, "An algorithm for the triangulation of arbitrary distributed points: applications to volume estimate and terrain fitting", *Computers & Geosciences*, v. 17, no. 7, p. 859-874

[7] Mirante, A. and Weingarten, N., 1982, "The radial sweep algorithm for constructing triangulated irregular networks", *IEEE Computer Graphics and Applications*, v. 2, no. 3, p. 11-21

[8] Puppo, E., Davis, L., DeMenthon, D. and Teng, Y. A., 1992, "Parallel terrain triangulation", *Proc. 5th Intern. Symposium on Spatial Data Handling*, v. 2, Charleston, South Carolina, p. 632–641

[9] Sibson, R., 1978, "Locally equiangular triangulations", *Computer Jour.*, v. 21, no. 3, p. 243-245

[10] Tsai, V. J. D., and Vonderohe, A. P., 1991, "A generalized algorithm for the construction of Delaunay triangulations in Euclidean n-space", *Proc. GIS/LIS '91*, v. 2, Atlanta, Georgia, p. 562-571

[11] Tsai,V. J. D., 1993, "Fast topological construction of Delaunay triangulations and Voronoi diagrams", *Computer & Geosciences*, Vol. 19, No. 10, pp. 1463- 1474

[12] Watson, D. F., 1981, "Computing the n-dimensional Delaunay tessellation with application to Voronoi polytopes", *Computer Jour.*, v. 24, no. 2, p. 167-172

[13] Evans, W., Kirkpatrick, D. and Townsend, G., 2001, "Right-Tringulated Irregular Networks. Algorithmica", *Special Issue on Algorithms for Geographical Information Systems*, 30, 2, pp. 264-286

[14] Absolo, M. J., Blat, J., and De Giusti, A., 2000, "A Hierarchial Tringulation for Multiresolution Terrain Models." *The Journal of Computer Science & Technology (JCS&T)*, 1, 3

[15] Fortune, S., 1991, "Voronoi diagrams and Delaunay triangulations", *In Computing in Euclidean Geometry*, ed. F. K. Hwang and D. Z. Du, World Scientific

[16] Aurenhammer, F., 1991, "Voronoi diagrams–a survey of a fundamental geometric data structure", *ACM Computing Surveys*, v. 23, no. 3, p. 345-405

[17] Kiema, J. B.K., and Bhr, H.-P., 2001, "Wavelet compression and the automatic classification of urban environments using high resolution multispectral imagery and laser scanning data", *Geoinformatics*, 5, 165-179

[18] Cohen, A., 2001, "Applied and computational aspects of nonlinear wavelet approximation", *Multivariate Approximation and Applications*, N. Dyn, D. Leviatan, D. Levin, and A. Pinkus (eds.), Cambridge University Press, Cambridge, pp. 188-212

[19] Dyn, N., Levin, D. and Gregory, J. A., 1990, "A butterfly subdivision scheme for surface interpolation with tension control", *ACM Transaction on Graphics*, 9, 160-169

[20] Mallat, S., 1989, A theory of multiresolution signal decomposition: The wavelet representation. *IEEE Trans. On Pattern Analysis and Machine Intelligence*, 11, 674-693

[21] Wu, J. and Amaratunga, K., 2003, "Wavelet triangulated irregular networks", *International Journal of Geographical Science*, vol. 17, no. 3, pp. 273- 289

[22] Sweldens, W., 1994, "Construction and Applications of wavelets in Numerical Analysis", Unpublished PhD thesis, Dept. of Computer Science, Katholieke Universiteit Leuven, Belgium

[23] Sweldens, W., 1996, "The lifting scheme: A custom-design construction of biorthogonal wavelets", *Appl. Comput. Harmon. Anal.*, 3(2):186- 200

B. Pradhan
Faculty of Engineering, University Putra Malaysia, 43400, UPM, Serdang
Selangor Darul Ehsan, Malaysia
Tel. +603-89467543, Fax. +603-86566061
Contact Author:
e-mail: biswajeet@mailcity.com

K. Sandeep
Department of Mechanical Engineering
Institute of Technology
Banaras Hindu University (BHU)
Tel. +91-542-2368427, Fax.+91-542-2368428

Shattri Mansor
Faculty of Engineering, University Putra Malaysia, 43400, UPM, Serdang
Selangor Darul Ehsan, Malaysia
Tel. +603-89467543, Fax. +603-86566061
Contact Author:
e-mail: biswajeet@mailcity.com

Abdul Rahman Ramli
Faculty of Engineering, University Putra Malaysia, 43400, UPM, Serdang
Selangor Darul Ehsan, Malaysia
Tel. +603-89467543, Fax. +603-86566061
Contact Author:
e-mail: biswajeet@mailcity.com

Abdul Rashid B. Mohamed Sharif
Faculty of Engineering, University Putra Malaysia, 43400, UPM, Serdang
Selangor Darul Ehsan, Malaysia
Tel. +603-89467543, Fax. +603-86566061
Contact Author
e-mail: biswajeet@mailcity.com

Wavelet Analysis and Applications
Tao Qian, Mang I. Vai and Xu Yuesheng, Eds.
Applied and Numerical Harmonic Analysis, 515–523

Ridgelet Transform as a Feature Extraction Method in Remote Sensing Image Recognition

Yuanyuan Ren, Shuang Wang, Shuyuan Yang and Licheng Jiao

Abstract. Using ridgelet transform to do the feature extraction, and RBFNN to do the recognition and classification, a remote sensing image recognition method is put forward in this paper. We do mathematical implementation and experimental investigation of ridgelet transform to analyze its characteristic and show its performance. Since ridgelet transform outperforms wavelet transform in extracting the linear features of objects, the proposed method has higher efficiency than that of wavelets. The simulation in remote sensing image shows its feasibility..

Keywords. Ridgelet transform,Radon transform,Dyadic wavelet,Image recognition and classification.

1. Introduction

Feature extraction is a necessary process in image classification and recognition. The aim of it is to reduce the complexity of the original problem by means of projecting the input patterns to a lower-dimensional space, i.e. to represent the target with fewer items without loss in another space. This calls for a sparser representation of the objective. Indeed, it is one of the main objectives of computational harmonic analysis (CHA) [1]. Wavelets, with its good time-frequency characteristic and its sparseness in representing the 0-dimensional (0-D) singularities of signals (i.e. the point-like targets), is an efficient tool for feature extraction, and has been widely used in the detection and recognition of various digital images. However, it is not the optimal basis to represent higher dimensional singularities such as linear singularities in 2-dimensional (2-D) space, and hyperplane singularities in higher dimensional spaces [2]. An obvious example of linear singularities in 2-D are edges, which usually contain abundant information, especially in textual

This work was supported by the National Science Foundation under grant no. 60133010.

images and SAR images. Ridgelets are superpositions of ridge functions or simple elements that are in some way related to ridge functions. With its orientation, ridgelets can represent objects with linear singularity in 2-D sparsely, and result in fewer features to represent more information and consequently improve accuracy of classification. Throughout the development of ridgelets, monoscale ridgelets [3], orthonormal ridgelets [4], finite ridgelets [5], and ridgelets frame [6] have been proposed sequentially. In remote sensing signal processing, recognition of 2-D radar targets is an important task. Radar images, such as planes and ships, often have stronger linear features. It can make contribution to the subsequent disposals of recognition and classification when a proper feature extraction tool is used. In this paper finite ridgelets are adopted for feature extraction. We firstly apply ridgelet transform to the pretreated images and then recognize and classify the targets with a simple RBFNN. Feature extractions based on the wavelet transform are also discussed for comparison. Experimental results illustrate the superiority of ridgelets to wavelets in extracting the linear features.

This paper is arranged as follows: the next section briefly explains the concept of the ridgelet transform and sparseness conception. In section 3 the detailed implementation of the referred algorithm is presented. Experimental results are shown in section 4 and the conclusion in section 5.

2. Implementation of Ridgelet Transform

The concept of ridgelets was firstly proposed by Cands [7] in 1998. Compared with wavelets, ridgelets have orientation and thus can sparsely represent linear singularities in 2-D, plane-like singularities in 3-D.

2.1. 2-D Ridgelet Transform in Image Processing

2-D ridgelet transform[2, 7] is defined as follows:

Let $\psi : \Re \to \Re$ satisfy $\int \psi(t)dt = 0$, for all $a > 0, b \in \Re, \theta \in [0, 2\pi)$, define bivariant function $\psi_{a,b,\theta} : \Re^2 \to \Re^2$:

$$\psi_{a,b,\theta}(x) = a^{-1/2} \cdot \psi((\cos(\theta)x_1 + \sin(\theta)x_2 - b)/a) \tag{1}$$

Where ψ is a 1-D wavelet function. Function $\psi_{a,b,\theta}$ is constant along "ridges", while a wavelet form transverse to these ridges, hence the name ridgelets.

For a bivariant function, its ridgelet coefficients are defined as:

$$R_f(a, b, \theta) = \int \bar{\psi}_{a,b,\theta}(x) f(x) dx =< \psi_{a,b,\theta}, f > \tag{2}$$

Suppose the Radon coefficients $Rf(u, t) = \int f(x)\delta(u'x - t)dx$ of $f(x)$ be the integral of f along $u'x = t$, and then we get:

$$R_f(a, b, u) =< \psi_{a,b}, Rf(u, \cdot) > \tag{3}$$

where $\psi_{a,b}(t) = \psi((t - b)/a)/\sqrt{a}$ is 1-D wavelets.

It can be inferred from above that the ridgelet transform is precisely the application of 1-D wavelet transform to the slices of the Radon transform where u is constant and is varying [2]. And its coefficients of a function are equal to the

orthogonal multiplication of its Radon transform with 1-D wavelets. Linear singularities in images are translated into point-like singularities by Radon transform, and these singularities can be best represented by wavelet transform. Through such transform, the ability of ridgelets to represent linear targets in higher dimensional space can be performed.

2.2. Dyadic Wavelet Transform

Dyadic wavelets [8, 9] lie between continuous wavelets and discrete wavelets. In dyadic wavelets, the scales are discretized while the shifts are continuous, which is different from discrete wavelets whose scales and shifts are both discretized, and the continuous wavelets whose scales and shifts are both continuous. Dyadic wavelets have the time translation invariance and are important in singularity detection. In this paper, 1-D dyadic wavelet transform is adopted. It is defined as follows:

$$\mathrm{W}_{2^j} f(t) = f * \psi_{2^j}(t) = \frac{1}{2^j} \int_R f(x) \psi(\frac{t-x}{2^j}) dx \tag{4}$$

Suppose $\psi(t)$ is a wavelet satisfying the permission condition. Let its scale varies along the dyadic sequence in time domain, hence the name dyadic wavelet. Since dyadic wavelet transform does not allow sub-sampling, it can better preserve the whole properties as well as its completeness, stability and redundancy. The singularity of a signal with its magnification can be confirmed by the variation of dyadic wavelet transform coefficients with scale parameter in one place. Since the local maxima are corresponding to the singularity points, the magnification and location of singularities can be detected by the dyadic wavelet transform [9].

2.3. The Analysis of Sparseness Conception

The conception about the "sparseness" can be traced back to a thesis written by Olshausen and Field [10]. They proposed that images can be presented by superstitions of base functions in different sampling blocks and searched for a sparse representation for the sampling block to reconstruct the original images. For a sampling block X^p, its sparse representation through transform is as below:

$$X^{\mathrm{p}} \approx \sum_{\mu} \theta_{\mu}^{p} \phi_{\mu} \tag{5}$$

where ϕ_μ are the base functions and θ_μ^p the corresponding coefficients. The higher the degrees of approximation of the coefficients are, the sparser the expression is. Ridgelet transform has the higher degrees of approximation than wavelet in 2-D, and thus can get sparser representation for linear singularities.

It can also be seen from the distribution graph below (Fig.1 (a) (b)) that after Radon transform, though there are many low values around the several distinct higher peeks, the number of peaks corresponding to the linear features in the original image which containing information are few. In contrast, though the distribution of wavelet transform coefficients (Fig.1 (c) (d)) is compact, the number of its peeks is more than the above graph. And in such a case, we propose the "coefficients convergence" method. Points around the peeks are converged.

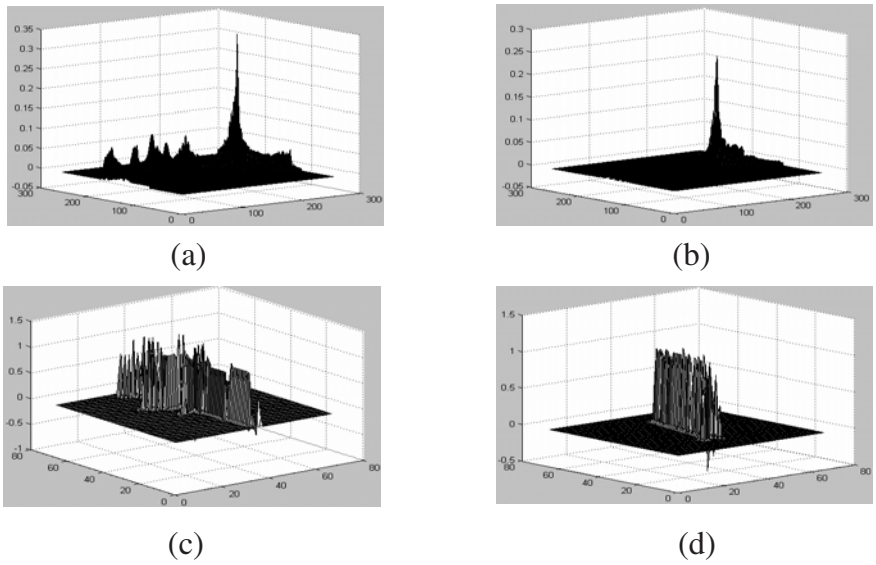

FIGURE 1. Distribution of coefficients (3-D) (a) Radon coefficients of planes, (b) Radon coefficients of ships; (c) wavelet coefficients of planes; (d) wavelet coefficients of ships

3. Recognition of Remote Sensing Image Based on Ridgelet Transform

For the remote sensing targets, the screening process is inevitably affected by the screening condition and weather, thus appear distortion, blurring, dithering. So these have to be pretreated first. After pretreatment, they have been changed into binary images.

3.1. Analysis of Algorithm

Before transform, samples are thinned to extrude their linear features. The skeletons of ships and planes are shown in Fig.2. After thinning, the redundancies of images are slashed while primary information is retained. We then transform images with ridgelet transform, by the way of dyadic wavelet transform implemented by $\tilde{A}Trous$ algorithm after Radon transform implemented by FSS (Fast-Slant-Stark) [11]. It can be seen from the explanatory drawing that the skeletons of the same type of targets (Fig.2 (a) (b) (c) (d)) resemble each other, while skeletons of different objects differ. Since the number of basic skeletons after thinning is no more than 6, we converge the transformed coefficients to 6 points at most as features. Choose the approximation coefficients as wanted information and use these information to converge, thus produce the feature matrix of the images.

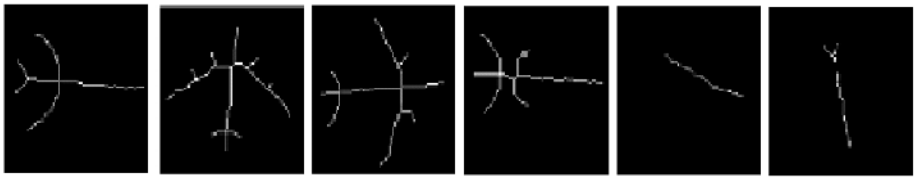

(a) (b) (c) (d) (e) (f)

FIGURE 2. (a)-(d): Skeletons of different type of planes (e) (f): skeletons of ships

3.2. Detailed Algorithm

Based on the analysis mentioned above, we adopt the following scheme to extract features with ridgelet transform:

1. Pretreatment of images with mathematical morphology: for the binary input image $f(m,n), 1 \leq m \leq 128, 1 \leq n \leq 128$ of 128×128, dilation is first used, and then thinning, thus get the treated image f_1;
2. Radon transform: Radon transform is taken for with the Fast-Slant-Stark method, and the transformed image is denoted by f_2 is 256×256;
3. Dyadic wavelet transform: dyadic wavelet transform is done to each slice of f_2, with $\tilde{A}Trous$ algorithm, thus each column in the radon transformed matrix is changed into $2^i - 1$ columns according to the preset scale i, each of which stores the corresponding frequency component coefficients at corresponded scale and the first stores the approximating component, select the low frequency coefficients as features. The size of the transformed matrix is 256×256, denoted by R_i;
4. Feature extraction and selection:
   (a). For the discrimination: converge the ridgelet transform coefficients R_i of each image into several representing points, pick-up the first 6 largest values as features and form the feature matrix;
   (b). For the classification: singular value decomposition is applied on the ridgelet transform coefficients matrix R_i of each image, Select the first 25 values to compose the feature vector;
5. An RBFNN is adopted as a classifier to implement the classification. Samples obtained through the above steps are sent into the network for training and testing.

4. Experimental Results

Experiments of target recognition and classification based on the ridgelet transform for extracting the features combined with RBFNN are put into practice: First are the experiments on recognition. The samples are shown in Fig. 3.

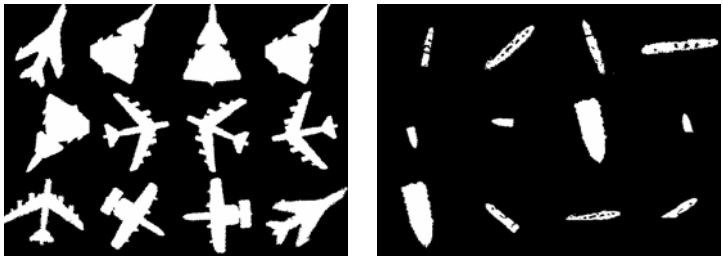

FIGURE 3. Samples 1:Planes and ships

TABLE 1. Comparison of wavelet and the referred method for recognition

	Level[1]	Wavelet transform		The referred method	
		SMR[2]	RPR[3]	SMR	RPR
Experiment 1:	L=1	86	90.49 percent	23	97.46 percent
Training samples: 160	L=2	100	88.94 percent	27	97.01 percent
Testing samples: 904	L=3	73	91.92 percent	43	95.24 percent
Experiment 2:	L=1	36	91.82 percent	13	97.05 percent
Training samples: 160	L=2	49	88.86 percent	14	96.82 percent
Testing samples: 440	L=3	40	90.91 percent	30	93.18 percent
Experiment 3:	L=1	35	90.28 percent	11	96.94 percent
Training samples: 240	L=2	37	89.72 percent	14	96.11 percent
Testing samples: 360	L=3	35	90.28 percent	28	92.22 percent

Experiment 1 is carried out under the following condition: there are totally 1064 2-D pictures, 80 from which about planes and ships respectively are randomly selected for training, while 904 are for detection. Experiment 2 is under the same condition with reference [12]: 280 ships and 320 planes composing totally 600 samples are included. 80 respectively are randomly selected for training, while 440 for detection. Experiment 3 is under the same condition with the reference [13]: 280 ships and 320 planes composing totally 600 samples are included, 40 percent of which are for training, while 60 percent for detection([1] Level: decomposition level;[2] SMR: Samples of Miss Recognized; [3] RPR: Rate of Proper Recognized).

The experimental results show the higher rate of ridgelet transform than wavelet through the identical procedure in recognition. And the results in experiment 2 are better than the rate of 94.5 percent listed in reference [12]; the results in experiment 3 are better than that listed in reference [13].

The RPR of the referred method decreases with the increasing decomposition level. The reason for this phenomenon is that, as the decomposition level increasing, scale becomes coarser, and information contained in the obtained image decreased, lead to the lower recognition rate. Therefore the following experiments will carried out only in the level 1. Then are the experiments on classification of planes, samples are shown in Fig. 4.

TABLE 2. Results of classification of 4 different kinds of planes

Experiment 4:		SMR	RPR
Training samples: 81	Wavelets	24	79.13 percent
Testing samples: 115	The referred method	3	97.39 percent

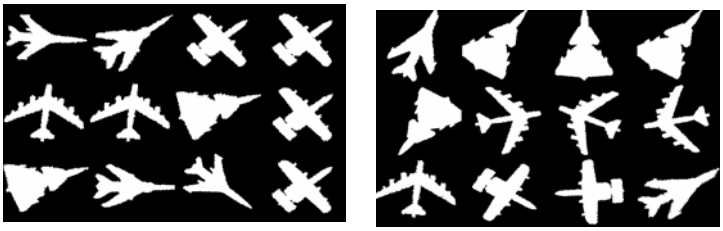

FIGURE 4. Samples 2:4 different kinds of planes

Experiment 4 is done under the following condition: there are totally 196 2-D pictures about 4 kinds of planes, in which 81 are randomly selected for training and 115 for detection. Adjust the parameters and get the experimental results in Table 2:

Finally are the experiments on the bridges in SAR images of Washington.D.C from Sandia National Laboratory, which includes 12 bridges.SAR images, for their complicated background and speckle noise, are difficult to distinguish between different bridges. So the standard deviations of each frequency component as well as mean values are extracted in the features selection process. Fig.5 shows the bridges used in the experiments. To make up the deficiency of the samples, images are rotated at intervals of 6 degrees with the bicubic interpolation method, and this produces 780 images in all, 260 of which are taken for training and 520 for testing. The experimental results are shown in table 3.

TABLE 3. Results of classification of 12 bridges

Experiment 5:		SMR	RPR
Training samples: 260	Reference [14]	-	85.76 and 93.65 percent
Testing samples: 520	The referred method	32	93.85 percent

The results in reference [14] are listed as comparison. In the above chart, the data 85.76 percent in reference [14] is got by the Radon transform with RBFNN as classifier while 93.65 percent is got by the Radon transform with SVM as classifier.

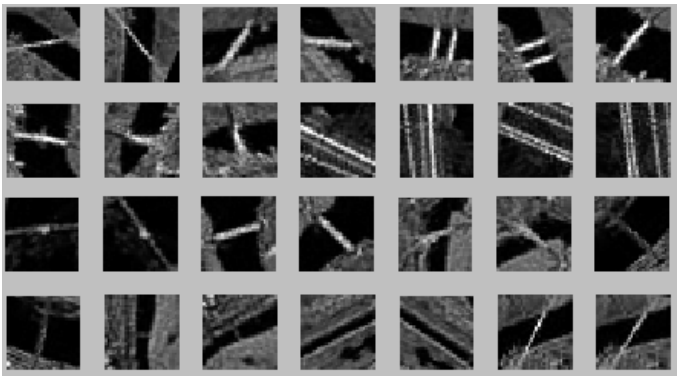

FIGURE 5. Samples 3:12 bridges in SAR image (where the two adjacent images are of the same kind. And the 25th and 26th bridges are fake targets seen from top to down and from left to right).

5. Conclusion and Discussions

Ridgelet transform used in feature extraction is introduced in this paper. Feature extractions are implemented based on the ridgelet transform, and then neural network is used for the subsequent recognition and classification. The experimental results show the ridgelet transform is more efficient than wavelet transform in recognizing and classifying the remote sensing images for its fewer decomposition coefficients, as well as its better application prospect. The drawback of it is that it requires longer calculation time in feature extraction than wavelet transform. This is caused by the concrete way of implementation of ridgelet transform, i.e. the radon transform combined with dyadic wavelet transform. The further research is to increase the implementation efficiency of the ridgelet transform. When a fast and efficient method of ridgelet transform is obtained, this problem can be solved.

References

[1] E.J. Cands, *Ridgelets and Their Derivatives: Representation of Image with Edges,* Department of Statistics, Stanford University 1999.

[2] E.J. Cands, and D.L. Donoho, Ridgelets: the Key to Higher-dimensional Intermittency?, Phil.Trans. R.Soc. Lond. A. (1999). 357:2495.

[3] E.J. Cands, *Monoscale Ridgelets for the Representation of Images with Edges*, Department of Statistics, Stanford University 1999.

[4] D.L Donoho, *Orthonormal Ridgelets and Linear Singularities,* SIAMJ. Math. Anal, 2000, 31 (5): 1062.

[5] M.N.Do and M.Vetterli, *The Finite Ridgelet Transform for Image Representation*, Image Processing. IEEE Transactions on 12.(2003) :16-28.

[6] T.Shan,L.C. Jiao and X.C.Feng,*Ridgelets Frame,* In: Aurlio, C.C, Mohamed, S.K. (Eds.): Proceedings of Image Analysis and Recognition. Lecture Notes in Computer Science, Vol. 3211. Springer-Verlag, Berlin Heidelberg New York (2004) 479-486.

[7] E.Cands, *Ridgelets: theory and applications,* Ph.D. thesis, Department of Statistics, Stanford University, 1998.

[8] S.Mallat, *A Wavelet Tour of Signal Processing*, Academic Press.1999.

[9] B.Hou, F.Liu and L.C. Jiao, *Linear detection based on ridgelet transform*, China science, Vol.46 No.2, April. 2003: 73 105.

[10] B.A.Olshausen and D.J. Field, *Emergence of simple-cell receptive field properties by learning a sparse code for natural images*, Nature, 381 607-609, 1996.

[11] A.Averbuch, R.R.Coif man,D.L. Donoho, M.Israeli and J.Walden, *Fast Slant Stack: A Notion of Radon Transform for Data in a Cartesian Grid which is Rapidly Computable, Algebraically Exact, Geometrically Faithful an Invertible*, Department of Statistics, Stanford University (2001).

[12] Y.N.Zhang, J.b. Hong, X.h.Wang and R.c Zhao, *An efficient image target recognition method for remote sensing,* Signal Processing,Vol.18. No.1 Feb.2002

[13] Y.N.Zhang, J.b. Hong,Y. Liao and R.c Zhao,, *Remote sensing image recognition based on SVM*, Journal of Northwestern Polytechnical University, Nov.2002. Vol.20 No.4.

[14] L.C.Jiao, *AIntelligence signal and image processing*, Journal of xidian university, 2003.9,144-150.

Yuanyuan Ren
National Key Lab for Radar Signal Processing and Institute of Intelligent Information Processing
Xidian University, 710071, Xi'an, China
e-mail: snowyraining@sohu.com

Shuang Wang
National Key Lab for Radar Signal Processing and Institute of Intelligent Information Processing
Xidian University, 710071, Xi'an, China

Shuyuan Yang
National Key Lab for Radar Signal Processing and Institute of Intelligent Information Processing
Xidian University, 710071, Xi'an, China

Licheng Jiao
National Key Lab for Radar Signal Processing and Institute of Intelligent Information Processing
Xidian University, 710071, Xi'an, China

Wavelet Analysis and Applications
Tao Qian, Mang I. Vai and Xu Yuesheng, Eds.
Applied and Numerical Harmonic Analysis, 525–542

Analysis of Frequency Spectrum for Geometric Modeling in Digital Geometry

Zhanchuan Cai, Hui Ma, Wei Sun and Dongxu Qi

Abstract. In order to explore the properties of frequency spectrum for geometric modeling, a complete orthogonal piecewise k-degree polynomials in $L^2[0,1]$, so-called U-system, is introduced. The expansion in U-series has advantageous properties for approximations in both quadratic norm and uniform. Using U-system with finite items, it can be realized to exactly represent geometric modeling. This paper analyzes the properties of frequency spectrum for geometric modeling in theory and gives some interesting results in geometric transform.By comparing U-system with Fourier system,experiments indicate that U-system is more suitable for analyzing frequency spectrum for geometric modeling than Fourier system is.

Mathematics Subject Classification (2000). Primary 99Z99; Secondary 00A00.

Keywords. U-system, geometric modeling, energy, frequency spectrum, normalization.

1. Introduction

With the increasing use of geometric modeling in industry, algorithms processing geometric signals become more and more important[1] . In the field of digital geometric processing, it is vital that the different geometric graphs can be represented by some basic graphical elements. In many cases of CAGD, objects are always described as one/ several group of graphs, such as machine parts and components, cartoons, surfaces of buildings and so on [2][3]. It is remarkable that there is close relation between geometric problems and image processing. For example, in pattern recognition, people need to match the graph based on its characters after

This project is supported by "Mathematics mechanization method and its application on Information Technology" (the National Grand Fundamental Research 973 Program of China under Grant No.2004CB3180000), the National Natural Science Foundation of China (No. 60133020), Guangdong Provincial Science and Technology Foundation (No. 2004A10302005, No. 051Z205005) and The China Scholarship Council. Corresponding author:Wei Sun(Email:lwhite@263.com).

getting the geometric graph of a certain object by edge detection. So, it is necessary to discuss the effective methods on how to make frequency spectrum analysis with the data coming from these geometric graphs. In the domain of CAGD [4] [5], discussion of frequency spectrum will help to classify graphs [15] [16].

Firstly, in the theories and applications of communication and signal processing, the class of complete orthogonal functions in $L^2[0,1]$ is the basic and important mathematical tool. Secondly, if there is a felicitous class of complete orthogonal functions system, which can exactly express a widely kind of groups of parametric geometric modeling by finite functions, we can take them as the most basic graphical elements. Thus we can get a new expression of the group of geometric graphs based on those functions. Moreover, we may use some theories on the class of orthogonal complete functions to do further analysis and synthesis of geometric information and other relative important research.

Currently, despite the recent promising progress of digital geometric processing, it still lacks analysis of frequency spectrum like digital image. The research of digital geometry has been rarely conjoint with the analysis of frequency spectrum, mainly because of the choice of orthogonal complete functions. In fact, not all class of orthogonal complete functions is suitable for the analysis and synthesis of geometric information. It is well known that Fourier system, Legendre system and Chebyshev system are the class of orthogonal functions system [6][7]. However, they cannot exactly express commonly geometric information (curves, surfaces) by using finite items, such as the phenomena of Gibbs (See FIGURE 9). So they are not suitable for analysis of frequency spectrum for geometric modeling of digital Geometry [15][17]. Moreover, because of the strong discontinuity of Walsh and Harr systems, they cannot be used as a tool for those applications, which need the finite items to approximate continuous function [6].

Twenty years ago, Qi and Feng proposed the U-system and gave the relatively completed theories [8]. While in [19], they study a similar idea on the triangle. Using these theories, in [9], motivated by in the work in [8], Micchelli and Xu constructed orthogonal multiwavelets for any invariant sets in R^n and later they used the wavelet to develop Galerkin methods and collocation methods to solve integral equations with weakly singular kernels. This indicates the application foreground of U-system [9-13].

The $k-$degree U-system consists of a series of piecewise $k-$degree polynomials. It includes not only differentiable functions but also piecewise ones, which include all kinds of discontinuous points on [0, 1]. It means that discontinuous points in different levels are conducive to express geometric information.

In this paper we investigate a special class of complete orthogonal functions in $L^2[0,1]$, so-called U-system, U-system can exactly express common geometric information (curves, surfaces) by using finite items .So U-system are suitable for analysis of frequency spectrum for geometric modeling in digital geometry [15][16][17]. Moreover, we analyze frequency and normalized frequency properties of geometric modeling in theory and experiment. We find that normalized frequency and normalized energy for the same geometric modeling are invariant in

geometric transform, such as translation, scale and rotation. In the end, some experimental results are given.

2. Piecewise Linear Complete Orthogonal U-system

As preparing, this part firstly introduce the definition of piecewise linear U-system.

The piecewise linear complete orthogonal function system on the interval [0, 1], so called U-system,is constructed as following:

Consider the linear function space on the interval [0, 1], denoted by S10, and then the following two function:

$$U_0(x) = 1, \quad 0 \le x < \frac{1}{2} \qquad (1)$$

$$U_1(x) = \sqrt{3}(1-2x), \quad \frac{1}{2} < x \le 1 \quad (2)$$

Structure the standard orthogonal base of S10. Further consider the piecewise linear function space divided by the point $x = \frac{1}{2}$ on the interval [0,1], denoted by S11. Obviously, the dimension of S11 is 4. Besides the two functions showed in (1) $\sim$ (2), we need two piecewise linear functions:

$$U_2(x) = \begin{cases} \sqrt{3}(1-4x), & 0 \le x < \frac{1}{2} \\ \sqrt{3}(4x-3), & \frac{1}{2} < x \le 1 \end{cases} \qquad (3)$$

$$U_3(x) = \begin{cases} 1-6x, & 0 \le x < \frac{1}{2} \\ 5-6x, & \frac{1}{2} < x \le 1 \end{cases} \qquad (4)$$

Where the first three function in (1) $\sim$ (3) is orthogonal each other. The fourth function in (4) can be easily obtained based on the piecewise linear condition and the orthogonality with the second function. Note that the fourth function is odd symmetric on the point $x = \frac{1}{2}$, but it is not symmetric on the interval [0, $\frac{1}{2}$] and [$\frac{1}{2}$, 1]. Summarily, the four functions in (1) $\sim$ (4) constitute a group of standard orthogonal base.

Next, consider the piecewise liner function space S12 on the interval [0,1], divided by the point $x = \frac{1}{4}$,$x = \frac{1}{2}$,$x = \frac{3}{4}$. Because the dimension of S12 is 8, there must be 8 orthogonal piecewise linear functions. That is to say that, four piecewise linear function divided by the point $x = \frac{1}{4}$,$x = \frac{1}{2}$,$x = \frac{3}{4}$ must be constructed besides the four function above. Therefore, using "compressing and copying" generates the other four functions.

So-called "compressing and copying" can be divided into two parts. First, compress the third and the fourth function on the half of the interval, [0, $\frac{1}{2}$]; Next, direct-copy and opposite-copy it on [$\frac{1}{2}$, 1]. Then, every function generates two new function on S12, which are contrary parity on the point $x = \frac{1}{2}$. "Compressing and copying" is showed in the following figure:

"Compress and copy" the third and the fourth function, and then the four new functions can be expressed as following:

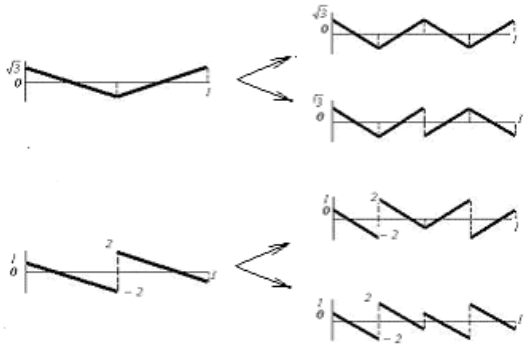

$$U_4(x) = \begin{cases} U_2(2x), & 0 \le x < \frac{1}{2} \\ U_2(2-2x), & \frac{1}{2} < x \le 1 \end{cases} \quad (5)$$

$$U_5(x) = \begin{cases} U_2(2x), & 0 \le x < \frac{1}{2} \\ -U_2(2-2x), & \frac{1}{2} < x \le 1 \end{cases} \quad (6)$$

$$U_6(x) = \begin{cases} U_3(2x), & 0 \le x < \frac{1}{2} \\ U_3(2-2x), & \frac{1}{2} < x \le 1 \end{cases} \quad (7)$$

$$U_7(x) = \begin{cases} U_3(2x), & 0 \le x < \frac{1}{2} \\ -U_3(2-2x), & \frac{1}{2} < x \le 1 \end{cases} \quad (8)$$

It is easy to be verify that the eight piecewise linear functions in (1)∼(8) constitute a group of standard orthogonal base on S12. It is stressed that, the "compressing and copying" mentioned above which generates the new function have the generality. That is to say that, when consider eight equal sub-interval on [0, 1] and the dimension of piecewise linear function space S13, 16, more 8 new function need to be added. These functions can be generated by "compressing and copying" mentioned above.

Generally, construct the $2n+1$ orthogonal base function on S1n, "compress and copy" the latter 2n function of these functions to obtain 2n+1 functions, and add them to constitute the standard orthogonal base on space S1 (n+1). $n = 0, 1, 2, 3, ...$ It can be proved that, when $n \to \infty$, the obtained infinite piecewise linear function group have the standard orthogonality and completeness.

Piecewise linear standard orthogonal complete system in $L^2[0,1]$ can be expressed by:

$$U_0(x) = 1, U_1(x) = \sqrt{3}(1-2x), 0 \le x \le 1$$

$$U_2^{(1)}(x) = \begin{cases} \sqrt{3}(1-4x), & 0 \le x < \frac{1}{2} \\ \sqrt{3}(4x-3), & \frac{1}{2} < x \le 1 \end{cases}$$

$$U_2^{(1)}(x) = \begin{cases} 1-6x, & 0 \le x < \frac{1}{2} \\ 5-6x, & \frac{1}{2} < x \le 1 \end{cases}$$

.....

$$U_{n+1}^{2k-1}(x) = \begin{cases} U_n^k(2x), & 0 \le x < \frac{1}{2} \\ U_n^k(2-2x), & \frac{1}{2} < x \le 1 \end{cases}$$

$$U_{n+1}^{2k}(x) = \begin{cases} U_3(2x), & 0 \le x < \frac{1}{2} \\ -U_3(2-2x), & \frac{1}{2} < x \le 1 \end{cases}$$

$$k = 1, 2, 3, ..., 2^{n-1}, n = 2, 3, ...$$

The value of the function takes average limited value on two sides on the divided point. Such 16 defined function on piecewise linear U system is showed in FIGURE 1. (b)

3. The k-degree U-system

In this section, the k-degree U-system is introduced [8].

3.1. Construction of k-degree U-system

Step 1: Taking first k+1 polynomials in Legendre orthogonal system, and denote them as,$U_0(x), U_1(x), ..., U_i(x), x \in [0, 1]$

Step 2: Construct k+1 new functions $f_i(x), i = 1, 2, ..., k+1, x \in [0, 1]$,and let them satisfy conditions:

(i) $f_i(x)$ is a k-degree piecewise polynomial divided by the point $x = \frac{1}{2}$;
(ii) $< f_i(x), f_j(x) >= \delta_{ij}, i, j \in \{1, 2, ..., k+1\}$;
(iii) $< f_i(x), x^j >= 0, i \in \{1, 2, ..., k+1\}, i \in \{0, 1, 2, ..., k+1\}$.

Where$< \bullet, \bullet >$ denotes the inner product in L^2[0,1]. Thus, we get the series of functions: $U_0(x), U_1(x), ..., U_k(x), f_1(x), f_2(x), ..., f_{k+1}(x)$;

Step 3: Using "squish-repeat", or "direct-copy and opposite-copy" [14] constructs the other $2 \cdot (k+1)$ functions.

Beginning from $f_1(x)$, each function generates two new ones as follows,

$$f_{i,1}(x) = \begin{cases} f_i(2x), & 0 \le x < \frac{1}{2} \\ f_i(2-2x), & \frac{1}{2} < x \le 1 \end{cases}$$

$$f_{i,2}(x) = \begin{cases} f_i(2x), & 0 \le x < \frac{1}{2} \\ -f_i(2-2x), & \frac{1}{2} < x \le 1 \end{cases}$$

The rest may be deduced by analogy, and we can obtain the class of k-degree U-system.

Obviously, when $k = 0$, the 0-degree U-system is just the series of Walsh functions. That means Walsh functions are the special case of U-system.

When $k = 0, 1, 2, 3$, the relative functions are shown in FIGURE 1 (a), (b), (c), (d). It is noticeable that, in FIGURE 1, functions of U-system are denoted as $U_l^{(j)}$, where l denotes the number of fragments and j does the j^{th} function[8].

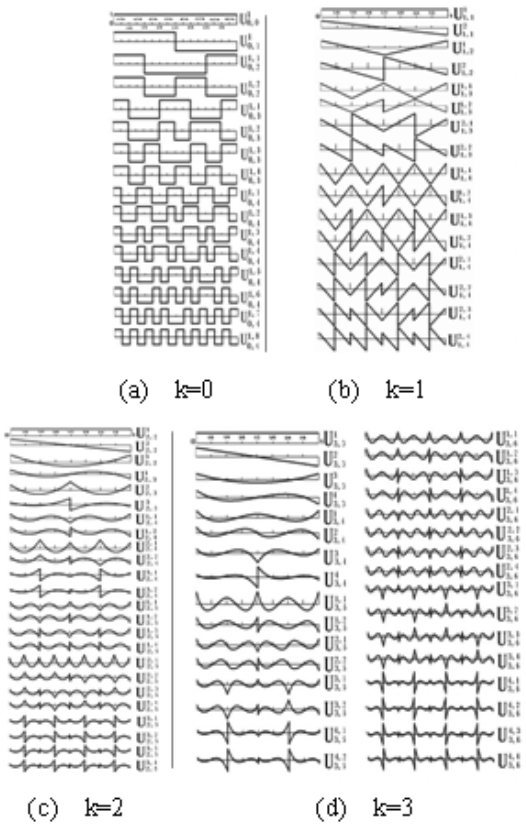

FIGURE 1. $k-$degree U-system (when k=0,1,2,3)

3.2. Properties of k-degree U-system

K-degree U-System has some properties [8]:

(i) Orthonormality $< f_i(x), f_j(x) >= \delta_{ij}, i, j = 0, 1, 2, ...$

(ii) Convergence of Fourier-U Series by Group

For a given function F, let

$$P_{n+1}F = \sum_{i=0}^{n} a_i U_{k,i}$$

Then let $P_{n+1}F$ is the best L_2-approximation to F from the space $span(U_{k,j})_0^n$..
Thus we have

$$\lim_{n \longrightarrow \infty} ||F - P_n F||_2 = 0, F \in L_2[0, 1]$$

$$\lim_{n\longrightarrow\infty} ||F - P_n F||_\infty = 0, F \in C[0,1]$$

These denote that Fourier-U series have the properties of L_2-convergence, completeness and convergence uniform by group.

(*iii*) Fourier-U Series Reproduction

If F is a piecewise k-degree polynomial, which has some discontinuous points on $x = \frac{q}{2^r}$ (q and r are integers), it can be exactly express with finite items of Fourier-U series. The k-degree U-system has much abundant discontinuity information. Especially using convergence uniform by group and Fourier-U series reproduction, we can analyse frequency spectrum of geometric modeling.

4. Orthogonal Representation of Parametric Curves and Surfaces [21] [22] of Geometric Modeling

Let $s, t \in [0,1]$, for simplicity, we take one degree U-system as an example. Assuming that the interval $[0,1]$ is divided into eight sub-intervals. Then, approximation function is expressed:

$$F_f(s,t) = f_i(s,t)$$

where $s \in [\frac{m}{8}, \frac{m+1}{8}), t \in [\frac{n}{8}, \frac{n+1}{8}), m, n = 0, 1, ..., 7$

Let

$$P(s,t) = \begin{pmatrix} x(s,t) \\ y(s,t) \\ z(s,t) \end{pmatrix} = \sum_{i=0}^{15}\sum_{j=0}^{15} \lambda_{i,j} U_{1,i} U_{1,j}(t)$$

The curves or surfaces in the given geometric modeling are expressed parametric polynomials:

$$\begin{cases} x(s,t) = F_x(s,t) \\ y(s,t) = F_y(s,t) \\ z(s,t) = F_z(s,t) \end{cases}$$

Where $\lambda_{i,j} = \int_0^1 P(s,t) U_{1,i} U_{1,j} dsdt, i, j = 0, 1, 2, ..., 15. P(s,t)$ can be exactly expressed by the given $F_{i,j}(s,t)$ with finite items. So we call $\lambda_{i,j}$ as frequency spectrum of $P(s,t)$.

The "energy" of $P(s,t)$ is defined as following:

$$E = (\sum_{i=0}^{15}\sum_{j=0}^{15} \lambda_{i,j}^2)^{\frac{1}{2}}$$

5. Frequency Spectrum Theorem

According to the above defined $\lambda_{i,j}$, we can obtain these frequency spectrum theorems in below. These theorems are very helpful and strongly mathematic tools for analyzing frequency spectrum for geometric modeling.

Theorem 5.1 (Superposed Theorem). *If frequency spectrum of function $F_1(s,t)$ is $\lambda_{i,j}^{(1)}, i,j = 0,1,2,...,n$, and frequency spectrum of function $F_2(s,t)$ is $\lambda_{i,j}^{(2)}, i,j = 0,1,2,...,n$, then frequency spectrum of function $F(s,t) = F_1(s,t) + F_2(s,t)$ should be $\lambda_{i,j}^{(1)} + \lambda_{i,j}^{(2)}$.*

Proof.

Frequency spectrum of function $F(s,t)$ is

$$\begin{aligned}\lambda_{i,j} &= \int_0^1 \int_0^1 P(s,t)U_{1,i}U_{1,j}dsdt \\ &= \int_0^1 \int_0^1 (P_1(s,t)U_{1,i}U_{1,j}dsdt + \int_0^1 \int_0^1 P_2(s,t)U_{1,i}U_{1,j}dsdt \\ &= \lambda_{i,j}^{(1)} + \lambda_{i,j}^{(2)}\end{aligned}$$

□

Corollary 5.2. *If frequency spectrum of function $F_m(s,t)$ is $\lambda_{i,j}^{(m)}, i,j=0,1,2,...,n$; $m = 0,1,2,...$; where $\lambda_{i,j}^{(m)} = ((\lambda_{i,j}^{(m)})_x, (\lambda_{i,j}^{(m)})_y, (\lambda_{i,j}^{(m)})_z)$,then frequency spectrum of function*

$$F(s,t) = \sum_{j=1}^{n} F_j(x,y)$$

should be

$$\sum_{m=1}^{n} \lambda_{i,j}^{(m)}$$

Theorem 5.3 (Retarded Theorem). *If frequency spectrum of function $F(x,y)$ is $\lambda_{i,j}, i,j = 0,1,2,...,n$, then frequency spectrum of function $F(x \pm a, y \pm b) \pm c$ should be $\lambda_{i,j} + (\mp a\delta(k), \mp b\delta(k), \pm c\delta(k))$, where $\delta_{i,j} = \begin{cases} 0, & i \neq 0 \quad or \quad j \neq 0 \\ 1, & i = 0 \quad and \quad j = 0 \end{cases}$ a,b,c is random constant.*

Proof.

Supposed that $F(x,y)$are expressed parametric polynomials:

$$P(s,t) = \begin{pmatrix} x(s,t) \\ y(s,t) \\ z(s,t) \end{pmatrix}$$

then frequency spectrum of function $F(x,y)$ is $\lambda_{i,j} = \int_0^1 \int_0^1 P(s,t)U_{1,i}U_{1,j}dsdt$

$F(x \pm a, y \pm b) \pm c$ are expressed parametric polynomials:

$$P^{'}(s,t) = \begin{pmatrix} x^{'}(s,t) \\ y^{'}(s,t) \\ z^{'}(s,t) \end{pmatrix} = \begin{pmatrix} x(s,t) \pm a \\ y(s,t) \pm b \\ z(s,t) \mp c) \end{pmatrix}$$

So $\lambda^{'}_{i,j} = \int_0^1 \int_0^1 P^{'}(s,t) U_{1,i} U_{1,j} dsdt = \lambda_{i,j} + (\mp a\delta_{i,j}, \mp b\delta_{i,j}, \mp c\delta_{i,j})$,

where $\delta_{i,j} = \begin{cases} 0, & i \neq 0 \quad \text{or} \quad j \neq 0 \\ 1, & i = 0 \quad \text{and} \quad j = 0 \end{cases}$ a,b,c is random constant.

□

Corollary 5.4. *If frequency spectrum of function $F(x,y)$ is $\lambda_{i,j}, i,j = 0,1,2,...,n$, then frequency spectrum of function $F(x-a, y-a)+a$ should be $\lambda_{i,j}+(a\delta(k), b\delta(k), c\delta(k))$, where $\delta_{i,j} = \begin{cases} 0, & i \neq 0 \quad or \quad j \neq 0 \\ 1, & i = 0 \quad and \quad j = 0 \end{cases}$ a is random constant. That is to say, frequency spectrum of function $F(x-a, y-a)+a$ is $\lambda_{i,j}+a(i = 0 \quad and \quad j = 0)$ or $i \neq 0 \quad or \quad j \neq 0)$.*

Theorem 5.5 (Inverse Ratio Theorem). *If frequency spectrum of function $F(x,y)$ is $\lambda_{i,j}, i,j = 0,1,2,...,n$, then frequency spectrum of function $K_1 F(K_2 x, K_3 y)$ should be $(\frac{1}{K_2}(\lambda_i)_x, \frac{1}{K_3}(\lambda_i)_y, K_1(\lambda_i)_z)$. where K_1, K_2, K_3 is random constant.*

Proof.

Supposed that $F(x,y)$are expressed parametric polynomials:

$$P(s,t) = \begin{pmatrix} x(s,t) \\ y(s,t) \\ z(s,t) \end{pmatrix}$$

then frequency spectrum of function $F(x,y)$ is $\lambda_{i,j} = \int_0^1 \int_0^1 P(s,t) U_{1,i} U_{1,j} dsdt$

$K_1 F(K_2 x, K_3 x)$ are expressed parametric polynomials:

$$P^{'}(s,t) = \begin{pmatrix} x^{'}(s,t) \\ y^{'}(s,t) \\ z^{'}(s,t) \end{pmatrix} = \begin{pmatrix} \frac{1}{K_2} x(s,t) \\ \frac{1}{K_3} y(s,t) \\ K_1 z(s,t) \end{pmatrix}$$

So $\lambda^{'}_{i,j} = \int_0^1 \int_0^1 P^{'}(s,t) U_{1,i} U_{1,j} dsdt = (\frac{1}{K_2}(\lambda_i)_x, \frac{1}{K_3}(\lambda_i)_y, K_1(\lambda_i)_z)$, where K_1, K_2, K_3 is random constant.

□

Corollary 5.6. *If frequency spectrum of function $F(x,y)$ is $\lambda_{i,j}, i,j = 0,1,2,...,n$, then frequency spectrum of function $\frac{1}{K}(Kx, Ky)$ should be $\frac{1}{K}\lambda_{i,j}$, where K is random constant.*

6. The Properties of Frequency Spectrum

According to the above defined

$$\lambda_{i,j} = \int_0^1 \int_0^1 P(s,t)U_{1,i}U_{1,j}dsdt, \quad i,j = 0,1,2,...,15.$$

have the following properties. (See FIGURE 8).

Here, we only give the proof of translation transform. The others are similar.

Theorem 6.1. *if* $P^{'}(s,t) = P(s,t) + P_0$ *then* $\lambda^{'}_{i,j} = \lambda_{i,j} + P_0\delta_{i,j}$, *where*

$$\delta_{i,j} = \begin{cases} 0, & i \neq 0 \quad or \quad j \neq 0 \\ 1, & i = 0 \quad and \quad j = 0 \end{cases}$$

Proof.

if $P^{'}(s,t) = P(s,t) + P_0$ then

$$\begin{aligned} \lambda^{'}_{i,j} &= \int_0^1 \int_0^1 (P(s,t) + P_0)U_{1,i}U_{1,j}dsdt \\ &= \int_0^1 \int_0^1 (P(s,t)U_{1,i}U_{1,j}dsdt + \int_0^1 \int_0^1 P_0U_{1,i}U_{1,j}dsdt \\ &= \lambda_{i,j} + P_0\delta_{i,j} \end{aligned}$$

where $\delta_{i,j} = \begin{cases} 0, & i \neq 0 \quad \text{or} \quad j \neq 0 \\ 1, & i = 0 \quad \text{and} \quad j = 0 \end{cases}$ □

Theorem 6.2. *Energy is invariant in rotation for the same geometric modeling.*

Proof.

Supposed geometric modeling rotated by θ circled coordinates axes z, then $x^{'} = x\cos\theta - y\sin\theta, y^{'} = y\cos\theta + x\sin\theta, z^{'} = z$,

So $(\lambda^{'}_{i,j})_x = \int_0^1 \int_0^1 (x(s,t)\cos\theta - y(s,t)\sin\theta)U_{1,i}U_{1,j}dsdt$

$= \cos\theta \int_0^1 \int_0^1 x(s,t)U_{1,i}U_{1,j}dsdt - \sin\theta \int_0^1 \int_0^1 y(s,t)U_{1,i}U_{1,j}dsdt$

$= (\cos\theta)(\lambda_{i,j})_x - (\sin\theta)(\lambda_{i,j})_y$.

The same as, $(\lambda^{'}_{i,j})_y = (\cos\theta)(\lambda_{i,j})_y - (\sin\theta)(\lambda_{i,j})_x$.

So $((\lambda^{'}_{i,j})_x)^2 + ((\lambda^{'}_{i,j})_y)^2 = ((\lambda_{i,j})_x)^2 + ((\lambda_{i,j})_y)^2$.

That is, $E^{'} = E$.

Experimental results see FIGURE 5. □

In order to make the frequency satisfy the invariance in rotation, translation, scale transforms, it can be defined normalized frequency as following:

$NF_{i,j} = \frac{||\lambda_{i,j}||}{||\lambda_{1,1}||}, i \neq 0$ or $j \neq 0$. Especially, when $i = 0, j = 0$, we call $\lambda_{0,0}$ as "DC" term.

Next, we prove the invariance in rotation, translation, scale transform.

Theorem 6.3. *Normalized frequency is invariant in rotation, translation, scale transforms for the same geometric modeling.*

Proof.

Let $\lambda_{i,j}^{'}$ be obtained from$\lambda_{i,j}$, $\lambda_{i,j}$translated byP_0 and scaled by γ. The corresponding $\lambda_{i,j}^{'}$ is

$$\begin{aligned}\lambda_{i,j}^{'} &= \int_0^1 \int_0^1 \gamma(P(s,t)+P_0)U_{1,i}U_{1,j}dsdt \\ &= \gamma[\int_0^1 \int_0^1 (P(s,t)U_{1,i}U_{1,j}dsdt + \int_0^1 \int_0^1 P_0U_{1,i}U_{1,j}dsdt] \\ &= \gamma(\lambda_{i,j}+P_0\delta_{i,j}), \text{ where } \delta_{i,j} = \begin{cases} 0, & i \neq 0 \quad \text{or} \quad j \neq 0 \\ 1, & i = 0 \quad \text{and} \quad j = 0 \end{cases}\end{aligned}$$

So $NF_{i,j}^{'} = \frac{||\lambda_{i,j}^{'}||}{||\lambda_{1,1}^{'}||} = \frac{||\lambda_{i,j}||}{||\lambda_{1,1}||} = NF_{i,j}$.

that is, normalized frequency is invariant in translation, scale transform.

Similarly, it is easily proved that normalized frequency is invariant in rotation transform. □

Accordingly, the "normalized energy" of $P(s,t)$ is defined as following:

$$NE = (\sum_{i=0}^{15}\sum_{j=0}^{15}(NF_{i,j}^2))^{\frac{1}{2}}, i \neq 0 \quad \text{or} \quad j \neq 0.$$

It is obvious that normalized energy satisfies the invariance in rotation, translation, scale transforms. So we obtain the theorem as following:

Theorem 6.4. *Normalized energy is invariant in rotation, translation, scale transforms for the same geometric modeling.*

7. Experimental Examples

For analysis and theorem the above, we have done lots of experiments to verify them. The experiment indicates that U-system is a new method for signal analyzing

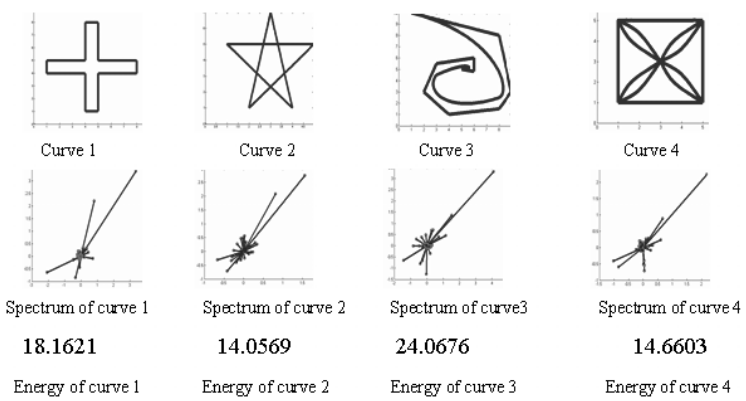

FIGURE 2. Spectral Analysis of Curves

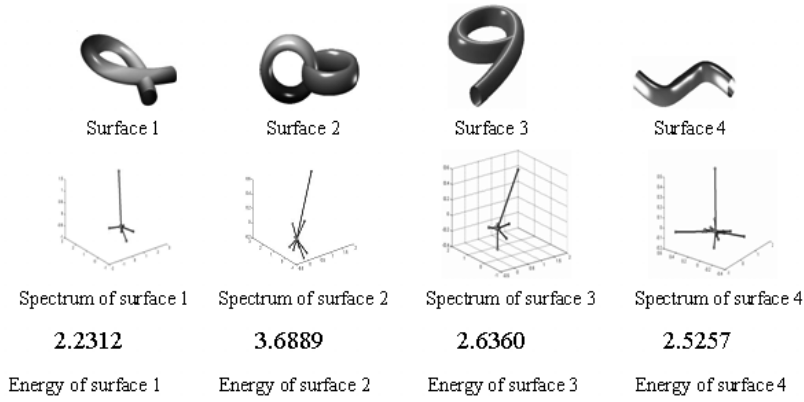

FIGURE 3. Spectral Analysis of Surfaces

and interesting exploring for analyzing frequency spectrum for geometric modeling. In this section, we will give some experimental results.

Experiment 1: In this experiment, frequencies spectrum of curves are denoted as vectors (λ_x, λ_y). We give the results of frequency and energy analysis of some curves by using three-degree U-system (See FIGURE 2). Using these spectrums,

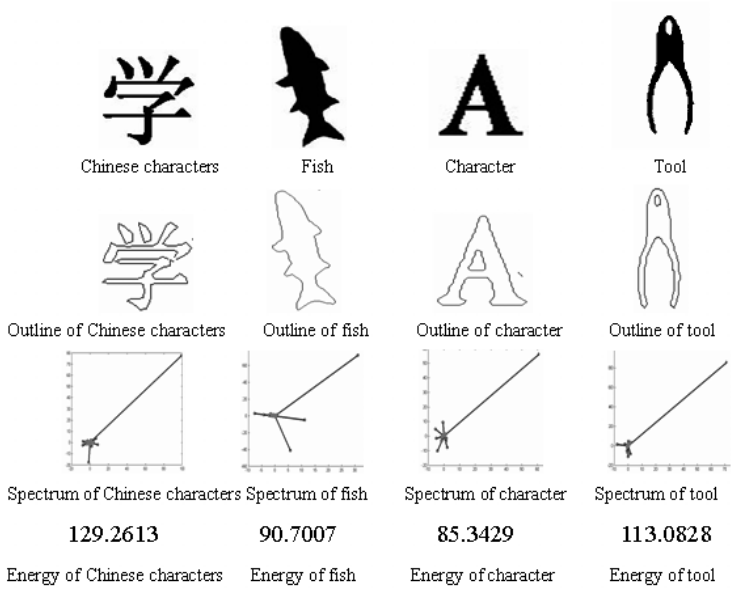

FIGURE 4. Spectral Analysis of Modeling

	Initial	Translation $P_0(9,7)$	Translation $P_0(-10,-12)$	Scale $(\alpha = 3)$	Scale $(\alpha = 0.09)$	Scale $(\alpha = 0.2)$
Curves		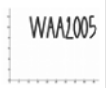				
Frequency	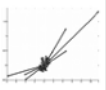	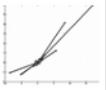	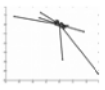	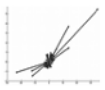	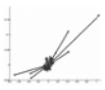	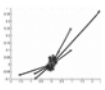
Energy	76.3464	101.0656	59.5451	229.0393	6.8712	15.2693
Normalized Frequency	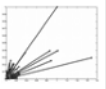	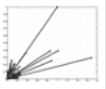	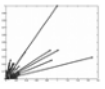	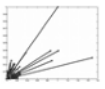	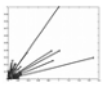	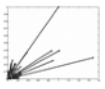
Normalized Energy	3.1222	3.1222	3.1222	3.1222	3.1222	3.1222

	Initial	Rotation $(\theta = \pi/4)$	Rotation $(\theta = \pi/2)$	Rotation $(\theta = -\pi/4)$	Rotation $(\theta = -\pi/2)$	Reflection $(\theta = \pi)$
Curves		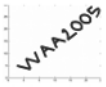	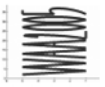	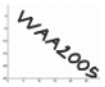	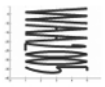	
Frequency	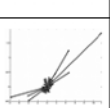		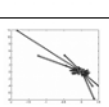		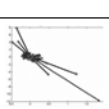	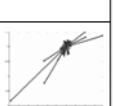
Energy	76.3464	76.3464	76.3464	76.3464	76.3464	76.3464
Normalized Frequency	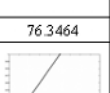	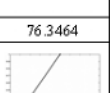	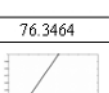	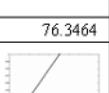	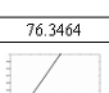	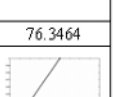
Normalized Energy	3.1222	3.1222	3.1222	3.1222	3.1222	3.1222

FIGURE 5. Normalized Frequency Analysis of Curves in U-system

we can exactly reconstruct these curves. However, the other orthogonal functions system, such as Fourier system, Legendre system and Chebyshev system, cannot completely reconstruct these curves by using finite items.

Experiment 2: In this experiment, frequencies spectrum of surfaces are denoted as vectors $(\lambda_x, \lambda_y, \lambda_z)$. We give the results of frequency and energy analysis of some surfaces by using three-degree U-system (See FIGURE 3). Using these

spectrums, we can exactly reconstruct these surfaces. However, the other orthogonal functions system, such as Fourier system, Legendre system and Chebyshev system, cannot completely reconstruct these surfaces by using finite items.

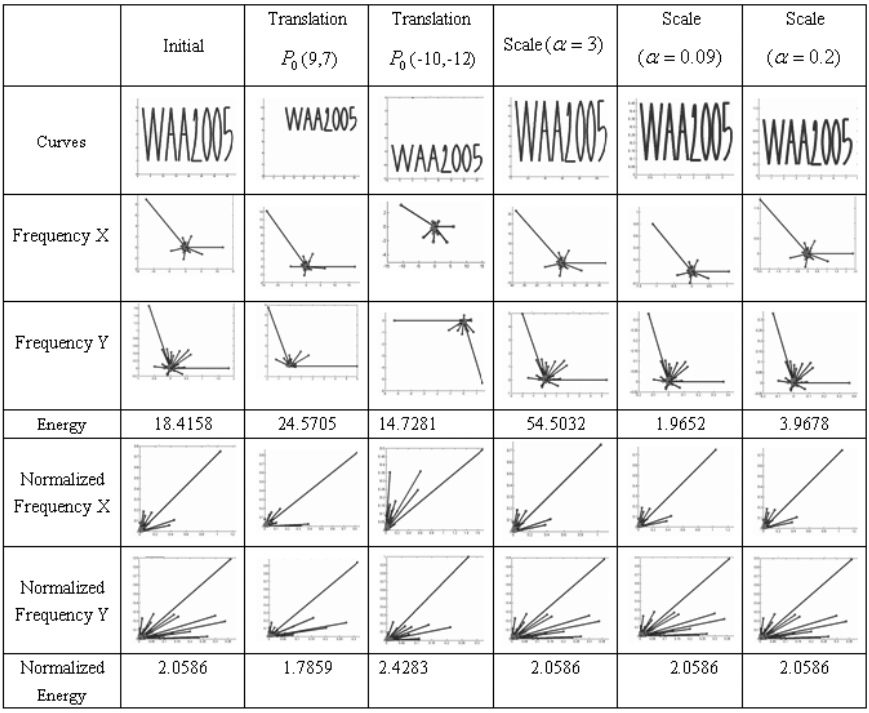

FIGURE 6. Normalized Frequency Analysis of Curves in Fourier System

Experiment 3: In this experiment, frequencies spectrum of geometric modeling are denoted as vectors (λ_x, λ_y). We give the results of frequency and energy analysis of geometric modeling by using one-degree U-system (See FIGURE 4). Using these spectrums, we can exactly reconstruct these outlines of geometric modeling.However, the other orthogonal functions system, such as Fourier system, Legendre system and Chebyshev system, cannot completely reconstruct these outlines by using finite items.

Experiment 4: FIGURE 5. lists the results of normalized frequency analysis of curves by using three-degree U-system. In FIGURE 5, curves are denoted as vectors (λ_x, λ_y). Some results about "frequency and normalized frequency" and "energy and normalized energy" of group of geometric graphics are shown in FIGURE 5. FIGURE 5 indicates normalized frequency and normalized energy for the same geometric modeling are invariant in geometric transform, such as translation, scale and rotation.

	Initial	Translation $P_0(9,7)$	Translation $P_0(-10,-12)$	Scale ($\alpha = 3$)	Scale ($\alpha = 0.09$)	Scale ($\alpha = 0.2$)
Curves						
Frequency X	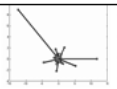	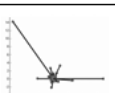	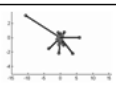	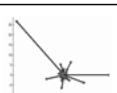	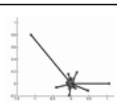	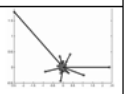
Frequency Y	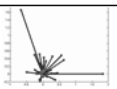	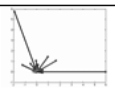	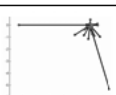	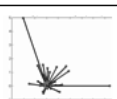	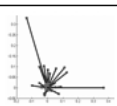	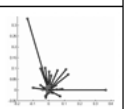
Energy	18.4158	24.5705	14.7281	54.5032	1.9652	3.9678
Normalized Frequency X	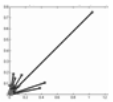	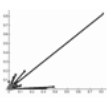	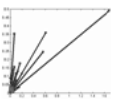	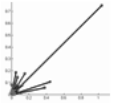	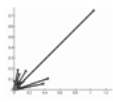	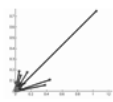
Normalized Frequency Y	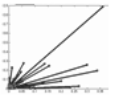	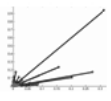	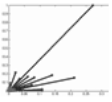	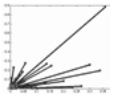	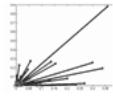	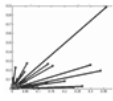
Normalized Energy	2.0586	1.7859	2.4283	2.0586	2.0586	2.0586

FIGURE 7. Normalized Frequency Analysis of Curves in Fourier System

Geometric Transform	The curves or surfaces	Frequency
Identical Transform	$P(s,t)$	$\lambda_{i,j} = \int_0^1 \int_0^1 P(s,t) U_{1,i}(s) U_{1,j}(t) dsdt$
Translation	$P'(s,t) = P(s,t) + P_0$	$\lambda'_{i,j} = \lambda_{i,j} + P_0 \delta_{i,j}, where \quad \delta_{i,j} = \begin{cases} 0, i \neq 0, or, j \neq 0 \\ 1, i = 0, and, j = 0 \end{cases}$
Scale	$P'(s,t) = \alpha P(s,t)$	$\lambda'_{i,j} = \alpha \lambda_{i,j}$
Rotation	$[P'(s,t)^T, I] = [P(s,t)^T, I]T$	$[\lambda'_{i,j}, 1] = T[\lambda_{i,j}, 1]$

FIGURE 8. Frequency Spectrum Properties of Curves and Surfaces in the U-system

Experiment 5: FIGURE 6,7. lists the results of normalized frequency analysis of curves by using Fourier system. FIGURE 6,7, curves are denoted as vectors (λ_x, λ_y) . Some results about "frequency and normalized frequency" and "energy

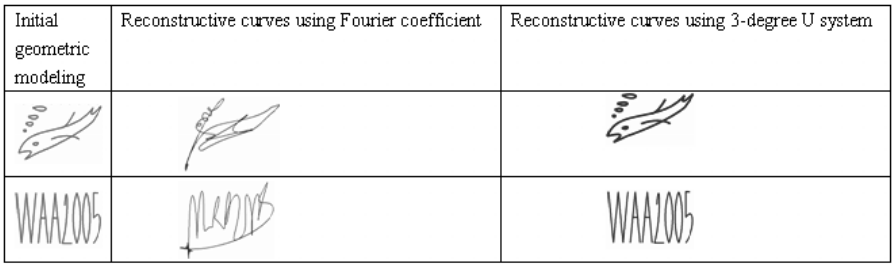

FIGURE 9. Comparing Fourier Transform with U system

and normalized energy" of geometric modeling in the Fourier system are shown in FIGURE 6,7. FIGURE 6,7 indicates normalized frequency and normalized energy for the same geometric modeling in the Fourier system are not all invariant in geometric transform, such as translation, scale and rotation.

FIGURE 5,6,7 indicate that using U-system with finite items, we can obtain an exact expression of geometric modeling. So it is more suitable for analysis of frequency spectrum for geometric modeling than Fourier system.

FIGURE 8. Frequency spectrum properties of curves and surfaces in the U-system.

FIGURE 9. Comparing Fourier transform with U system.

8. Conclusions and Future Work

From analysis the above, it can be concluded that, because of the strong continuity of Fourier system and Legendre system and Chebyshev system, they cannot exactly express common geometric modeling by using finite items, such as the phenomena of Gibbs (See FIGURE 9). So they are not suitable for analysis of frequency spectrum for geometric modeling of digital geometry [15][16]. Moreover, because of the strong discontinuity of Walsh and Harr systems, they cannot be used as a tool for those applications. However, using U-system with finite items, it can be realized exact expression of geometric modeling. According to the expression, we use frequency spectrum to calculate their "energy". So U-system is suitable for analysis of frequency spectrum for geometric modeling .In theory, we have proved that normalized frequency and normalized energy for the same geometric modeling are invariant in geometric transforms, such as rotation, translation, scale transforms. We also give some experimental results to support our conclusion.

In the theories and applications of communication and signal processing, U-system is the basic and important math tool. So, In future, we will further explore the properties of frequency spectrum of geometric modeling and applications in the field such as pattern recognition and digital signal processing.

Acknowledgment

This project is supported by "Mathematics mechanization method and its application on Information Technology" (the National Grand Fundamental Research 973 Program of China under Grant No.2004CB3180000), the National Natural Science Foundation of China (No. 60133020), Guangdong Provincial Science and Technology Foundation (No. 2004A10302005, No. 051Z205005), The China Scholarship Council and the Research Foundation of Sun Yat-sen University.

References

[1] Zhou Kun, Bao Hujun, Shi Jiaoying, *A Unified Framework for Digital Geometric Processing.* J. of Chinese Computers. **25** (2002), 904–909.

[2] Donald Hearm, M.Pauline Baker, *Computer Graphics with OpenGL.* 3rd Edition, Pearson Press, 2000.

[3] James D. Foley etc, *Computer Graphics, Principles and Practice.* Second Edition, Beijing, Engineering Industry Press, 2002.

[4] Wang Guojin, etc, *Computer Aided Geometric Design.* Higher Education Press and Springer Press, 2001. 1-17 (in Chinese).

[5] Shi Fazhong, *Computer Aided Geometric Design and Non-Uniform Rational B-Spline.* Higher Education Press, 2001(in Chinese)

[6] Chong Zhongkan,*Orthogonal functions and its applications.*1982.

[7] Henning F. Harmuth, *Sequency Theory Foundations and Applications.*1977.

[8] Yuyu Feng, Dongxu Qi, *A Sequence of Piecewise Orthogonal Polynomials.* J. of SIAM J. Math. Anal. **15(4)** (1984), 834–844.

[9] Charles A. Micchelli and Yuesheng Xu, *Using the Matrix Refinement Equation for the Construction of Wavelets on Invariant Sets.* Applied and Computational Harmonic Analysis. **1** (1994), 391–401.

[10] G. Battle, *Wavelets of Federbush-Lemarie type.* preprint, 1993

[11] P. Federbush, *A mass zero cluster expansion.* Part 1, The expansion, Comm. Math. Phys. **81** (1981), 327–340.

[12] Qi Dongxu, Feng Yuyu, *On the Convergence of Fourier-U Series.* J. of University of Science and Technology of China,Issue of Math.... **5** (1983), 7–17.

[13] Qi Dongxu, Feng Yuyu, *On the Orthogonal Complete system U.* Acta.Scientiarum Naturalium Universitatis Jilinensis **2** (1984), 21–31.

[14] Zhang Qishan, Zhang Youguang, *The Theory of Bridge Function and Its Application.*Beijing: National Defence Industry Press, 1992 (in Chinese).

[15] Dongxu Qi, *Frequency Spectrum Analysis in Digital Geometry (Special report).*Hefei City,2005.

[16] Dongxu Qi, Chenjun Tao,Ruixia Song, Hui Ma, Wei Sun, Zhanchuan Cai, *Representation for a Group of Parametric Cures Based on the Orthogomal Complete U-system.*J. of Computer,2005 (accepted).

[17] Hui Ma, Ruixia Song, Chenjun Tao, Dongxu Qi, *Orthogonal Complete U-system and Its Application in CAGD.*the first Korea-Chin Joint Conference on Geometric and Visual Computing,2005(accepted).

[18] Ruixia Song, Hui Ma, Dongxu Qi, *A New Class of Complete Orthogonal Functions and Its Applications Based on U-system.*The 4th International Conference on Wavelet Analysis and Its Applications 2005 (accepted).

[19] Y.Y.Feng and D.X.Qi, *On the Harr and Walsh Systems on a Triangle.*MRC Technical Summary Report No.2235, University of Wisconsin-Madison, 1981.

[20] Knut Morken, *Computer Aided Geometric Design.*Computer Aided Geometric Design. **22(9)** (2005), 838–848.

[21] Dinesh Manocha and John F. Canny, *Algorithm for implicitizing rational parametric surfaces.*Computer Aided Geometric Design. **9(1)** (1992), 25–50.

Zhanchuan Cai
School of Information Science and Technology,
Sun Yat-sen University Guangzhou,
510275 P.R. China

Hui Ma
Faculty of Information Technology,
Macao University of Science and Technology,
Macao

Wei Sun
School of Information Science and Technology,
Sun Yat-sen University Guangzhou,
510275 P.R. China

Dongxu Qi
School of Information Science and Technology,
Sun Yat-sen University Guangzhou,
510275 P.R. China;
Faculty of Information Technology,
Macao University of Science and Technology,
Macao

Wavelet Analysis and Applications
Tao Qian, Mang I. Vai and Xu Yuesheng, Eds.
Applied and Numerical Harmonic Analysis, 543–559

Detection of Spindles in Sleep EEGs Using a Novel Algorithm Based on the Hilbert-Huang Transform

Zhihua Yang, Lihua Yang and Dongxu Qi

Abstract. A novel approach for detecting spindles from sleep EEGs (electroencephalograph) automatically is presented in this paper. Empirical mode decomposition (EMD) is employed to decompose a sleep EEG, which are usually typical nonlinear and non-stationary data, into a finite number of intrinsic mode functions (IMF). Based on these IMFs, the Hilbert spectrum of the EEG can be calculated easily and provides a high resolution time-frequency presentation. An algorithm is developed to detect spindles from a sleep EEG accurately, experiments of which show encouraging detection results.

Mathematics Subject Classification (2000). Primary 94A13; Secondary 42A16.

Keywords. Empirical mode decomposition, Hilbert-Huang transform, signal detection.

1. Introduction

Sleep is a complicated physiological process. Research on sleep is very important to both clinical diagnosis and curative effect evaluation in nervous psychiatry. Generally, sleep consists of two phases: no-rapid eye movement (NREM) and rapid eye movement(REM). The NREM phase can be decomposed into 4 stages according to sleep depths [6]. A crucial clue for the sleep depth to be at the second or the third stages is that the sleep-spindles, whose frequencies are between 12 and 20Hz, take place in the EEG (electroencephalo-graph) [7].

Traditionally, sleep-spindles are detected visually by neurologists or sleep experts. Research on automated sleep analysis can be traced back to as early as the 1970s [12, 13, 9, 11, 2, 8, 10, 5]. In recent years, two novel algorithms for automated

This work was supported by NSFC (Nos. 60475042, 60133020), the National Key Basic Research Project of China (No.2004CB318000) and the Scientific and Technological Planning Project of Guangzhou city.

detection of spindles in sleep EEG were developed by using classical time-frequency analysis [7, 3]. Since EEGs are typically nonlinear and non-stationary signals and the duration of a sleep-spindle is usually very short, it is usually difficult to obtain satisfactory results in automated detection of sleep-spindles by using traditional time-frequency analysis.

Recently, a novel analysis method for nonlinear and non-stationary data, which is called *Hilbert-Huang Transform (HHT)*, was developed [4]. Its key part is the so-called *empirical mode decomposition (EMD)*, with which any complicated data set can be decomposed into a finite and often small number of *intrinsic mode function(IMF)* that admit well-behaved Hilbert transforms. EMD is adaptive, and therefore, highly efficient. It is based on the local characteristic time scale of the data and is applicable to nonlinear and non-stationary processes. With the Hilbert transform, the IMFs yield instantaneous frequencies as functions of time that give sharp identifications of embeded structures. The final presentation of the results is a time-frequency-energy distribution, designated as the Hilbert spectrum, which has high time-frequency localization.

Because of these properties, in this paper, HHT is employed to analyze sleep EEGs and an algorithm to detect spindles from sleep EEGs automatically is developed. Experiments show an encouraging detection rate which is higher than those developed in [7, 3].

This paper is organized as follows: Section 2 is a brief summary on the Hilbert-Huang Transform; Analysis of EEG data based on HHT is given in Section 3; In Section 4, a novel algorithm for automated detection of sleep-spindles is proposed. Experiments to support the algorithm are conducted and the anti-noise ability is discussed in Section 5; Finally, Section 6 is the conclusion of this paper.

2. Hilbert-Huang Transform

The Hilbert-Huang Transform (HHT) was proposed by Huang et al [4]. It consists of two parts: (1) *Empirical Mode Decomposition (EMD)*, and (2) *Hilbert Spectral Analysis*. With EMD, any complicated data set can be decomposed into a finite and often small number of *intrinsic mode functions (IMF)*. An IMF is defined as a function satisfying the following conditions:

(a) The number of extrema and the number of zero-crossings must either be equal or differ at most by one;
(b) At any point, the mean value of the envelope defined by the local maxima and the envelope defined by the local minima is zero.

An IMF defined as above admits well-behaved Hilbert transforms. EMD decomposes signals adaptively and is applicable to nonlinear and non-stationary data (Fundamental theory on nonlinear time series can be found in [1]). In this section, a brief introduction is given to make this paper somewhat self-contained. The readers are referred to [4] for details.

For an arbitrary function $X(t)$ in L_p-class [14], its Hilbert transform $Y(t)$ is defined as

$$Y(t) = \frac{1}{\pi} P \int_{-\infty}^{\infty} \frac{X(t')}{t - t'} \mathrm{d}t', \tag{2.1}$$

where P indicates the Cauchy principal value. Consequently an analytic signal $Z(t)$ can be produced by

$$Z(t) = X(t) + iY(t) = a(t)e^{i\theta(t)}, \tag{2.2}$$

where

$$a(t) = [X^2(t) + Y^2(t)]^{\frac{1}{2}}, \ \theta(t) = \arctan(\frac{Y(t)}{X(t)}) \tag{2.3}$$

are the instantaneous amplitude and the phase of $X(t)$. Since the Hilbert transform $Y(t)$ is defined as the convolution of $X(t)$ and $1/t$ by Eq. (2.1), it emphasizes the local properties of $X(t)$ even though the transform is global. In Eq. (2.2), the polar coordinate expression further clarifies the local nature of this representation. With Eq. (2.2), the instantaneous frequency of $X(t)$ is defined as

$$\omega(t) = \frac{d\theta(t)}{dt}. \tag{2.4}$$

However, there is still considerable controversy on this definition. A detailed discussion and justification can be found in [4].

EMD is a necessary pre-processing of the data before the Hilbert transform is applied. It reduces the data into a collection of IMFs and each of them represents a simple oscillatory mode that is a counterpart of a simple harmonic function, but is much more general. With this definition, one can decompose any function according to the following algorithm.

Algorithm 2.1. Let $X(t)$ be a signal.

Step 1 Initialize: $r_0(t) = X(t), \ i = 1$;

Step 2 Extract the i-th IMF as follows:

- **(a)** Initialize: $h_0(t) = r_{i-1}(t), \ j = 1$;
- **(b)** Extract the local minima and maxima of $h_{j-1}(t)$;
- **(c)** Interpolate the local maxima and the local minima by cubic splines to form $u_{j-1}(t)$ and $l_{j-1}(t)$ as the upper and lower envelops of $h_{j-1}(t)$ respectively;
- **(d)** Calculate $m_{j-1}(t) = \frac{u_{j-1}(t)+l_{j-1}(t)}{2}$ as an approximation of the local mean of $h_{j-1}(t)$ at t;
- **(e)** Let $h_j(t) = h_{j-1}(t) - m_{j-1}(t)$;
- **(f)** If the stopping criterion is satisfied, i.e., $h_j(t)$ is an IMF, set $\mathrm{imf}_i(t) = h_j(t)$; Else go to (b) with $j = j + 1$.

Step 3 Let $r_i(t) = r_{i-1}(t) - \mathrm{imf}_i(t)$;

Step 4 If $r_i(t)$ still has at least 2 extrema, go to Step 2 with $i = i + 1$; otherwise the decomposition is finished and $r_i(t)$ is the residue.

By Algorithm 2.1, any signal $X(t)$ can be decomposed into finite IMFs, $\mathrm{imf}_j(t)$ $(j = 1, \cdots, n)$, and a residue $r(t)$, where n is nonnegative integer depending on $X(t)$, i.e.,

$$X(t) = \sum_{j=1}^{n} \mathrm{imf}_j(t) + r(t). \tag{2.5}$$

For each $\mathrm{imf}_j(t)$, let $X_j(t) = \mathrm{imf}_j(t)$. Its corresponding instantaneous amplitude $a_j(t)$ and instantaneous frequency $\omega_j(t)$ can be computed with Eqs. (2.3) and (2.4). By Eqs. (2.2) and (2.4), $\mathrm{imf}_j(t)$ can be expressed as the real part, Re, in the following form:

$$\mathrm{imf}_j(t) = \mathrm{Re}\left[a_j(t) \exp\left(i \int \omega_j(t) dt\right)\right]. \tag{2.6}$$

Therefore, by Eqs. (2.5) and (2.6), $X(t)$ can be expressed as the IMF:

$$X(t) = \mathrm{Re} \sum_{j=1}^{n} a_j(t) \exp\left(i \int \omega_j(t) dt\right) + r(t). \tag{2.7}$$

It is interesting to compare the representation above with the following classical Fourier expansion:

$$X(t) = \sum_{j=1}^{\infty} a_j e^{i\omega_j t}, \tag{2.8}$$

where both a_j and ω_j are constants. Contrasting Eq. (2.7) with Eq. (2.8), it is apparent that the IMF expansion provides a generalized Fourier expansion. It relieves the restriction of the constant amplitude and fixed frequency of Fourier expansion, and arrives at a variable amplitude and frequency representation. With the IMF expansion, the amplitude and frequency modulations are clearly separated. Its main advantage over Fourier expansion is that it accommodates nonlinear and non-stationary data perfectly.

Equation (2.7) enables us to represent the amplitude and the instantaneous frequency as functions of time in a three-dimensional plot, in which the amplitude is contoured on the time-frequency plane. The time-frequency distribution of amplitude is designated as the Hilbert amplitude spectrum or simply Hilbert spectrum, denoted by $H(\omega, t)$. It can also be defined equivalently in mathematics as follows: Let $X(t)$ be decomposed into finite IMFs $\mathrm{imf}_j(t)$ $(j = 1, \cdots, n)$ and a residue $r(t)$ by Algorithm 2.1, then,

$$H(\omega, t) = \begin{cases} 0 & \text{if } J_{\omega,t} \text{ is an empty set,} \\ \sum_{j \in J_{\omega,t}} a_j(t), & \text{otherwise,} \end{cases} \tag{2.9}$$

where $J_{\omega,t} = \{j | 0 \le j \le n \text{ satisfying } \omega_j(t) = \omega\}$.

$H(\omega, t)$ gives a time-frequency-amplitude distribution of a signal $X(t)$. If amplitude squared is more desirable commonly to represent energy density, then the squared values of amplitude can be substituted to produce the Hilbert energy spectrum.

3. HHT for EEG Data

To observe the performance of the HHT for EEG data, a 6 second segment, denoted by $X(t)$, is selected from a sleep EEG which is sampled when the sleep is at the 2nd stage of a NREM phase. It contains two sleep-spindles, marked by 'A' and 'B' respectively, as shown in Fig.1. With Algorithm 2.1, it is decomposed into seven IMFs and a residue, which are shown in Fig. 2(c1) $\sim$ (c8) respectively from top to bottom. From Fig.2(c2), it is easy to see that there are two sub-segments of high amplitude in the periods from about 20 to 160 and from about 750 to 1050 respectively, whose frequencies are around 13Hz (the first consists of about 9 waves within 0.7s(140 points) and the second consists of 18 waves within 1.5s(300 points)). Such a sub-segment whose amplitude is high and frequency is between 12 $\sim$ 20Hz is a possible spindle wave we want to detect, which is called a *PSW* for simplicity. Based on the analysis of this example, it seems possible to detect sleep-spindles based on features in some of the IMFs, such as the second one shown in Fig.2(c2). To examine the observation, let us consider another example as shown in Fig.3. It is also a sleep EEG segment of 6 seconds, in which only one sleep-spindle, marked by 'A', is included. Similarly, with Algorithm 2.1, it is decomposed into seven IMFs and a residue, which are shown in Fig. 4(c1) $\sim$ (c8) respectively from top to bottom. It is observed that the second IMF does not contain PSWs. However, in the third IMF as shown in Fig.4(c3), there is a PSW starting at about the 800 and ending at the 1000 (corresponding the part marked by 'A' in Fig.3). By conducting more experiments like Fig.2 and Fig.4, we conclude that, for a sleep EEG segment which contains spindles, in general, one cannot determine in which IMF the interesting sub-segments may appear. In fact, a spindle consists of a number of oscillatory modes which are the same or similar in local characteristic time scale (an oscillatory mode is a wave between a pair of successive maxima or a pair of successive minima [4]), when a EEG segment is decomposed by EMD, these oscillatory modes may be dispersed to different IMFs. Therefore, the PSWs cannot be detected based on some IMFs and consequently

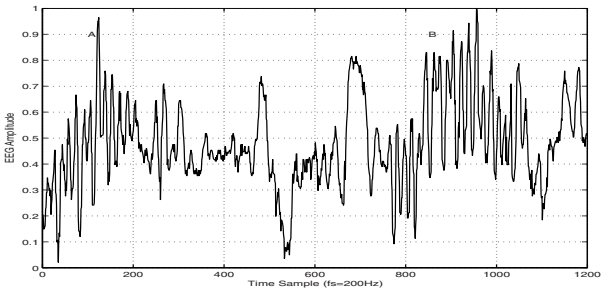

FIGURE 1. A sleep EEG segment of 6 seconds at the second sleep stage, in which two sleep-spindles are included as marked by 'A' and 'B' respectively.

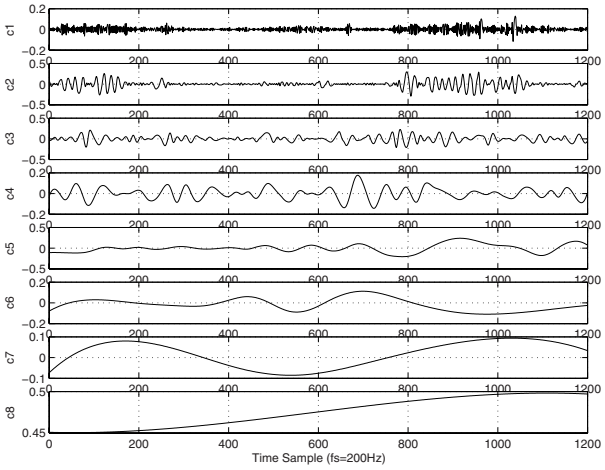

FIGURE 2. The resulting EMD components from the EEG data of Fig. 1. The last component, c8, is not an IMF, it is the residue.

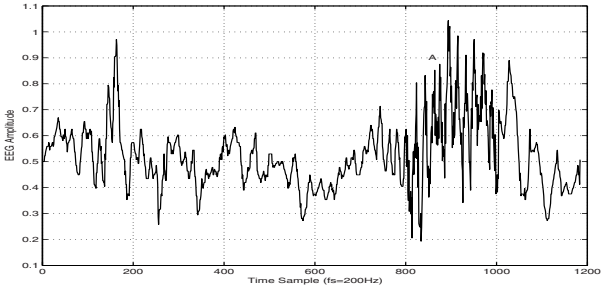

FIGURE 3. A sleep EEG segment of 6 seconds long at the second sleep stage, in which a sleep-spindle is included as marked by 'A'.

the Hilbert spectrum, which is the global time-frequency-energy distribution, is considered as a natural substitution for the detection of sleep-spindles from EEGs.

Since IMFs have good time-frequency resolution as described in Section 2 (see [4]), one can predict that, in the Hilbert spectrum of a sleep EEG segment, high energies will take place within its PSWs. This prediction is verified by the graphs of the Hilbert spectrum of the sleep EEG segments: Fig. 5 and Fig. 6 are respectively the contour maps of the Hilbert spectrums of the sleep EEG segments shown in Fig. 1 and Fig. 3. In Fig. 5, one can find two high energy bands whose frequencies are $8 \sim 20$Hz or so: one starts at about 0 and ends at 200, the other starts at about 750 and ends at 1050, as highlighted by the two rectangles in the figure. Similarly, in Fig. 6, there is a high energy band whose frequencies are $8 \sim 20$Hz or so, starting at about 730 and ending at 1000, as highlighted by the

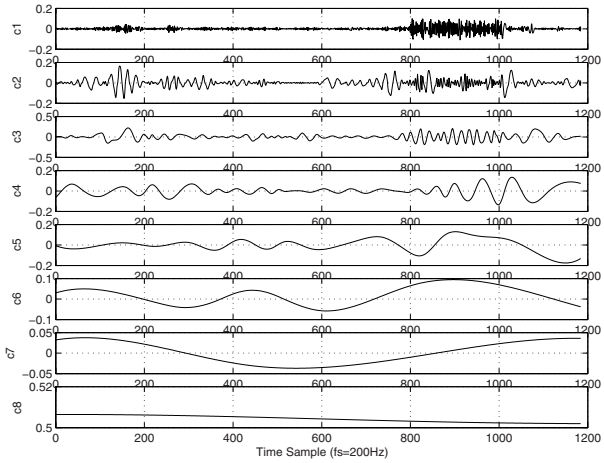

FIGURE 4. The resulting EMD components from the EEG data of Fig. 3. The last component, c8, is not an IMF, it is the residue.

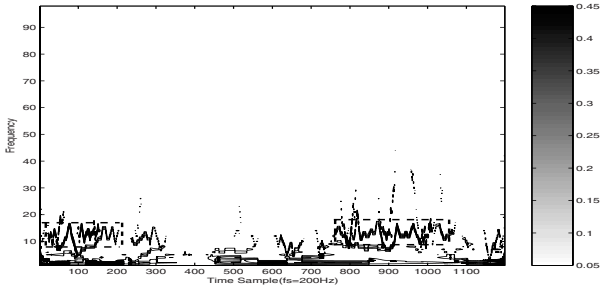

FIGURE 5. The contour map of Hilbert spectrum for the EEG data of Fig. 1.

rectangle in Fig. 6. Therefore, the locations and durations of the sleep-spindles can be detected from the Hilbert spectrum of sleep EEGs successfully.

4. A Novel Algorithm for Automated Detection of Sleep-Spindles

In this section, an auto-detection algorithm for sleep-spindle detection is developed and, consequently, experiments are conducted to support the algorithm.

Based on the discussion above and the fact that the duration of a sleep-spindle is usually longer than 0.5s in practice, a novel method for automated detection of spindles from a EEG is developed in this section.

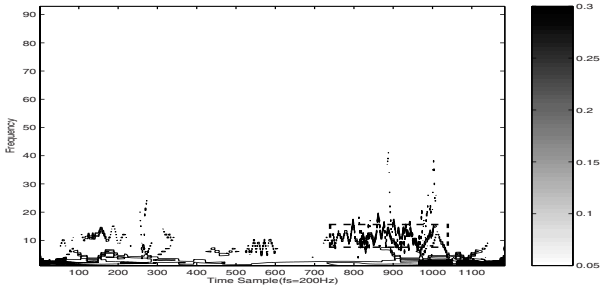

FIGURE 6. The contour map of Hilbert spectrum for the EEG data of Fig. 3.

In practice, a sleep EEG contains a large amount of data. It is terribly time-consuming to calculate the Hilbert spectrum of a global sleep EEG signal. Experiments show that the time needed for calculating the Hilbert spectrum, which is called the CPU time hereafter for simplicity, does not depend linearly on the data length of the signal. When the length of data is longer than 1500 or so, the CPU time needed increases rapidly. The five dotted curves in Fig. 7 illustrates how the CPU times depend on the datum lengths for five signals of 2000 random data ranging from 0 to 1, when a PC of Pentium IV-1.7GHz is used. It should be pointed out that the graph changes somewhat if the signals is replaced by another signal.

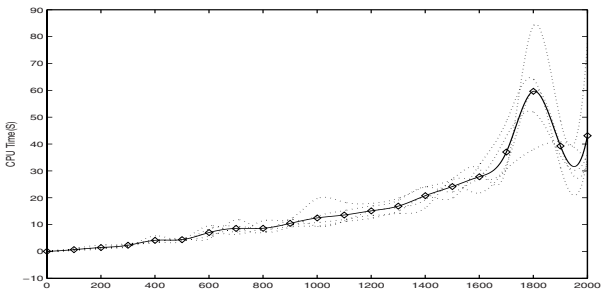

FIGURE 7. CPU time as a function of the length of the data set

The solid curve in Fig. 7 is the average of the five dotted curves, which illustrates how the CPU time depends on the datum length in the rough. Thus, to save CPU time, a global EEG signal should be divided into many short segments. The length of the short segments should be as long as possible to keep enough integrality of data if the CPU time is acceptable. According to Fig. 7, it is a reasonable tradeoff to divide the global EEG signal into segments of $1200 \sim 1600$ data (about $6 \sim 8$ seconds for frequency of sampling = 200Hz). In our experiments, the global sleep EEG is divided into segments of 1200 data points. The corresponding time for each segment is about 6 seconds.

After a sleep EEG is divided as before, we decompose each segement with EMD into IMFs. Since the first IMF usually consists of the highest frequency components of the segment, such as noise (see Fig. 2(c1) and Fig. 4(c1)), it is discarded in our algorithm. For each segment, the sleep-spindles are detected by the following algorithm.

Algorithm 4.1. Let $x(t)$ be a segment of data of length 1200. The sleep-spindles are detected as follows:

Step 1 Decompose $x(t)$ with EMD into IMFs, then remove the first IMF. For each other IMF, calculate its instantaneous frequency and instantaneous amplitude by Eqs. (2.4) and (2.3). Quantify the instantaneous frequency into integers between 1 and 100Hz.

Step 2 Compute the Hilbert spectrum $H(\omega, t)$; here it is a matrix of 100 rows and 1200 columns. Then normalize the amplitude of $H(\omega, t)$ linearly such that the values of $H(\omega, t)$ range from 0 to 255.

Step 3 Extract the 8th to 20th rows of $H(\omega, t)$ to form a sub-matrix, denoted by M, of 13 rows and 1200 columns.

Step 4 Calculate the maximum of each column of M to generate an array, $C = (C[1], \cdots, C[1200])$. It is an energy measure of the data on frequencies ranging from $8 \sim 20$Hz at each local time. Then, define a smoothed version of C as:

$$C_1[k] = \frac{1}{L} \sum_{i=k-L/2}^{k+L/2} C[i],$$

where L, an even integer, is the width of the smoothing window ($L = 50$ in the experiments of this paper) and the boundary extension is conducted as: $C[i] = C[1]$ for $i \leq 0$ and $C[i] = C[1200]$ for $i > 1200$.

Step 5 Let T be a threshold. Then, we search $1 \leq k \leq 1100$ and $I \geq 100$ such that

$$C_1[k + i - 1] \geq T \text{ for } i = 1, 2, \cdots, I,$$

and

$$C_1[k + I] < T \text{ or } k + I = 1200.$$

Then a sleep-spindle that starts at k and has duration I is detected. We set $T = 50$ in the experiments of this paper.

5. Experiments

In this section, experiments are conducted to support our algorithm on sleep-spindle detection.

For the segment of a sleep EEG shown in Fig. 1, according to Steps 1 and 2 of Algorithm 4.1, its IMFs and Hilbert spectrum $H(\omega, t)$ are calculated as shown in Figs. 2 and 5 respectively. By Step 3 of Algorithm 4.1, the sub-matrix M of the 8th to 20th rows of $H(\omega, t)$ is generated as shown in Fig. 8. Then the energy array

C of M and the smoothed version, C_1, are calculated in accordance with Step 4 of Algorithm 4.1, which are shown in Fig. 9: the top is C and the bottom is C_1. Finally, by Step 5, two spindles of a sleep EEG are detected in this segment as shown in Fig. 10, in which the starting points, the durations, and the end points are marked by the dotted lines. The first starts at about the 20th datum (namely: the 0.1th second) with a duration of about 0.8s and the second starts at about the 750th datum (namely: the 3.75th second) with a duration of about 1.5s.

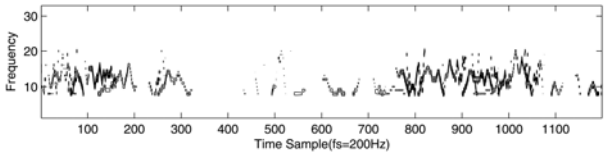

FIGURE 8. The sub-matrix M generated by the 8th – 20th rows of the Hilbert spectrum $H(\omega, t)$ shown in Fig. 5

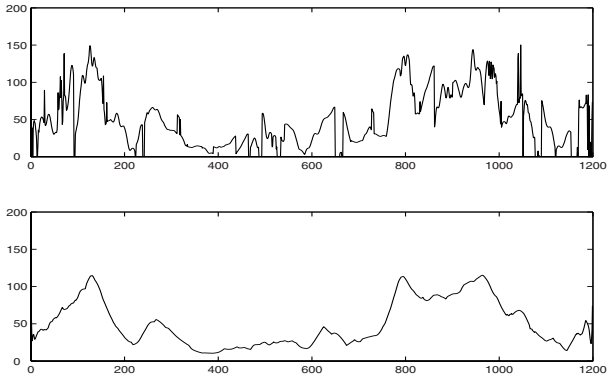

FIGURE 9. The top: The energy array of M shown in Fig. 8, C, each of whose component is the maximum of the elements in the corresponding column of M. The bottom: The smoothed version C_1 of C calculated according to Step 4 of Algorithm 4.1.

Similarly, Figs. 4 and 6 are the IMFs and the contour map of the Hilbert spectrum $H(\omega, t)$ of the segment shown in Fig. 3 in accordance with Steps 1 and 2 of Algorithm 4.1. The corresponding sub-matrix M calculated by Step 3 are shown in Fig. 11. Then, the energy array C of M and the smoothed version, C_1, calculated by Step 4, are displayed graphically in Fig. 12: the top is C and the bottom is C_1. Fig. 13 is the detection result by Step 5, in which a sleep-spindle is detected and marked with dotted lines. It starts at about the 750th datum (namely: the 3.75th second) with a duration of about 1.25s.

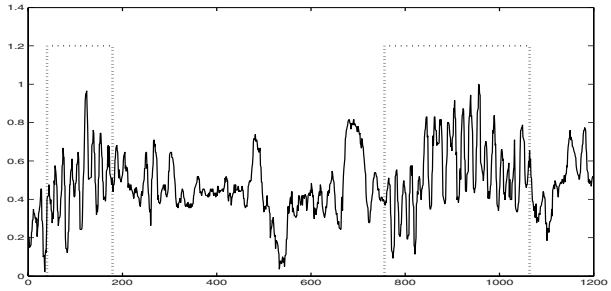

FIGURE 10. The detection result for the segment in Fig. 1. Two sleep-spindles are detected and marked with dotted lines. The first starts at about the 20th datum (namely: the 0.1th second) with a duration of about 0.8s and the second starts at about the 750th datum (namely: the 3.75th second) with a duration of about 1.5s.

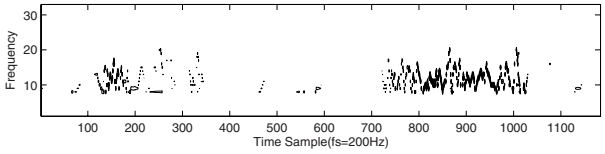

FIGURE 11. The sub-matrix M generated by the 8th – 20th rows of the Hilbert spectrum $H(\omega, t)$ shown in Fig. 6

To test our detection algorithm, 100 segments, each of which consists of 1200 data (about 6 seconds with frequency of sampling 200Hz) and all of which contain 183 spindles, are selected from a sleep EEG database. The locations and durations of these sleep-spindles have been determined visually by experts. For an automated detection algorithm, its detection accuracy depends on two aspects: (1) the accuracy of the location detected and (2) the accuracy of the duration detected. To estimate them quantitatively, a mis-detection degree is introduced as follows.

Definition 5.1. Let X(t) be a sleep EEG segment which contains a sleep-spindle starting at t_b and ending at t_e. For an automated detection method for sleep-spindles, the mis-detection degree, simply denoted by MD, is defined as follows:

1. if one sleep spindle is detected from X(t), with starting point t'_b and end point t'_e, then
$$MD = \frac{L_\vee - L_\wedge}{L}, \tag{5.1}$$
where, $L_\vee = \max(t_e, t_e^{'}) - \min(t_b, t_b^{'})$, $L_\wedge = \min(t_e, t_e^{'}) - \max(t_b, t_b^{'})$ and $L = t_e - t_b$ as shown in Fig. 14.
2. if no spindle or more than one spindle is/are detected, then $MD = \infty$.

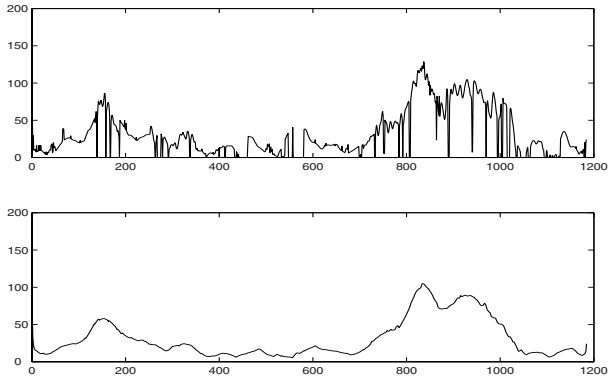

FIGURE 12. The top: The energy array of M, shown at the bottom of Fig. 11, denoted by C, each of whose component is the maximum of the elements in the corresponding column of M. The bottom: The smoothed version C_1 of C calculated according to Step 4 of Algorithm 4.1.

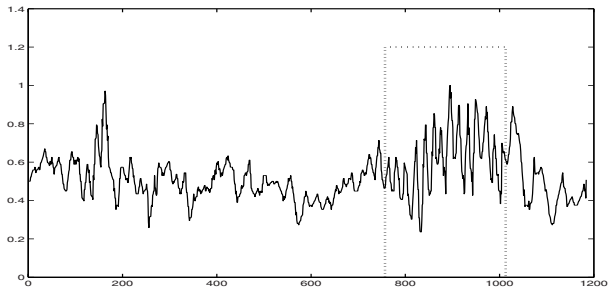

FIGURE 13. The detection result for the segment in Fig. 3. A sleep-spindle is detected and marked with dotted lines, which starts at about the 750th datum (namely: the 3.75th second) with a duration of about 1.25s.

It is easy to see that MD is a nonnegative number and MD=0 if and only if the sleep-spindle is detected accurately, and the smaller MD is, the more accurately the detection does. Table 1 lists the distribution of the MDs produced by Algorithm 4.1 for all the 183 samples and the corresponding histogram is displayed in Fig. 15, in which all the MDs greater than 1 is included into that of MD=1.1. It is encouraging to see that most of the MDs are between 0 and 0.2, which shows that our algorithm arrives at satisfying detection results in both locations and durations.

Let us compare our technique with those in [3, 7]. The same dataset is employed to conduct the experiments. The distributions of the corresponding MDs

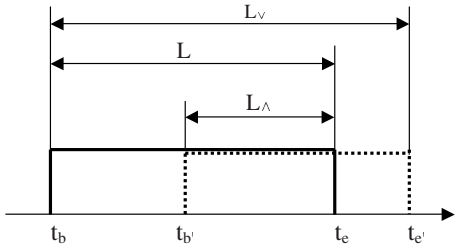

FIGURE 14. $L_\vee, L_\wedge$ and L in Definition 2

TABLE 1. The distribution of the MDs produced by Algorithm 4.1, NS is the number of spindles whose MDs are within the given interval.

MD	0 ∼0.1	0.1 ∼0.2	0.2 ∼0.3	0.3 ∼0.4	0.4 ∼0.5	0.5 ∼0.6	0.6 ∼0.7	0.7 ∼0.8	0.8 ∼0.9	0.9 ∼1	> 1
NS	1101	443	86	51	43	25	17	7	3	3	51

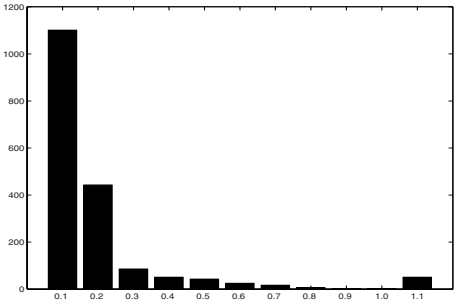

FIGURE 15. The histogram of the MDs corresponding to Table 1

calculated according to the algorithms in [7] and [3] are listed in the 3th and 4th rows of Table 2 respectively. To compare more conveniently, the distribution of the MDs by our algorithm is also listed in the 2nd row of Table 2. The corresponding histogram is shown in Fig. 16, in which all the MDs greater than 1 is included into that of MD=1.1. It is noticed that the MDs produced by our algorithm concentrate much closer to 0 than those by [3] and [7], which implies that our detection does better than theirs. To describe the detection result quantitatively, we define the detection rate as the ratio of the number of MDs which are less than some given threshold, T, to the total number of spindles. With this definition and $T = 0.2, 0.5$ and 1 respectively, the detection rates according to Algorithm 4.1, the algorithms in [7] and [3] are listed in Table 3.

Before the end of this section, let us discuss the detection of spindles from noisy sleep EEGs by Algorithm 4.1. It is easy to understand that Algorithm 4.1

TABLE 2. The distributions of the MDs calculated according to Algorithm 4.1, the algorithms in [7] and [3]. NS_j are the numbers of spindles whose MDs are within the given intervals, with j=1, 2, and 3 corresponding to Algorithm 4.1, the algorithms in [7] and in [3] respectively.

MD	0 ∼0.1	0.1 ∼0.2	0.2 ∼0.3	0.3 ∼0.4	0.4 ∼0.5	0.5 ∼0.6	0.6 ∼0.7	0.7 ∼0.8	0.8 ∼0.9	0.9 ∼1	> 1
NS_1	1101	443	86	51	43	25	17	7	3	3	51
NS_2	893	466	164	88	42	23	12	9	11	9	113
NS_3	752	367	231	97	44	48	26	12	10	13	230

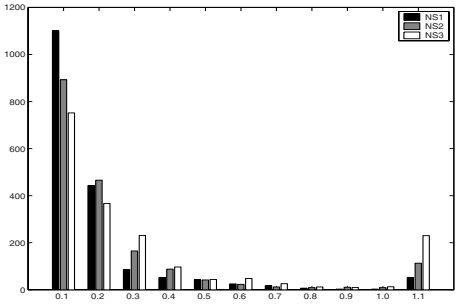

FIGURE 16. The histogram of the MDs corresponding to Table 2

TABLE 3. The detection rates corresponding to Algorithm 4.1, the algorithms in [7] and [3] for $T = 0.2, 0.5$ and 1

Detection rate	$T = 0.2$	$T = 0.5$	$T = 1$
Algorithm 4.1	84.4%	94.2%	97.2%
Algorithm in [7]	74.3%	90.3%	93.8%
Algorithm in [3]	61.1%	81.5%	87.4%

can do well for noisy sleep EEG signals since the frequencies of sleep spindles, about 13Hz, are usually much lower than those of noise. Another reason for this anti-noise ability is that the first IMF has no contribution to the Hilbert spectrum. To demonstrate our view, a great number of experiments have been conducted and excellent results are obtained. Fig. 17 are three noisy versions of Fig. 3 by adding Gaussian white noises with SNR (Signal Noise Ratio, which is defined as the ratio of signal variance to noise variance in dB.) 20dB, 25dB and 30dB respectively from top to bottom. The detection results are shown in Fig. 18, corresponding to those in Fig. 17 from top to bottom. It is easy to see that, spindles can be detected successfully with a minor change in the locations and durations even though the SNRs are very low.

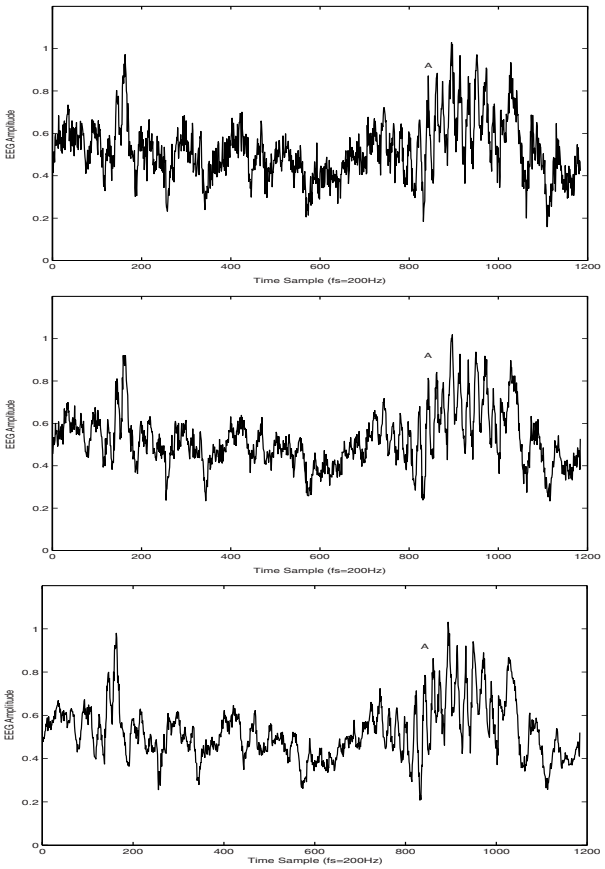

FIGURE 17. Three noisy versions of Fig. 3 by adding Gaussian white noises with SNR 20, 25 and 30 respectively from top to bottom.

6. Conclusion

In this paper, a novel approach for detecting spindles automatically from a sleep EEG based on the Hilbert-Huang transform is developed. Empirical mode decomposition is employed to decompose sleep EEGs into a finite and often small number of intrinsic mode functions. Then the Hilbert spectrum $H(\omega, t)$ is used to give a high resolution time-frequency presentation and extract features of EEGs. Consequently, an algorithm is proposed to detect spindles automatically from a sleep EEG. Experiments show more accurate detection results than those in [7, 3]. Finally, the anti-noise ability of the algorithm is demonstrated theoretically and experimentally.

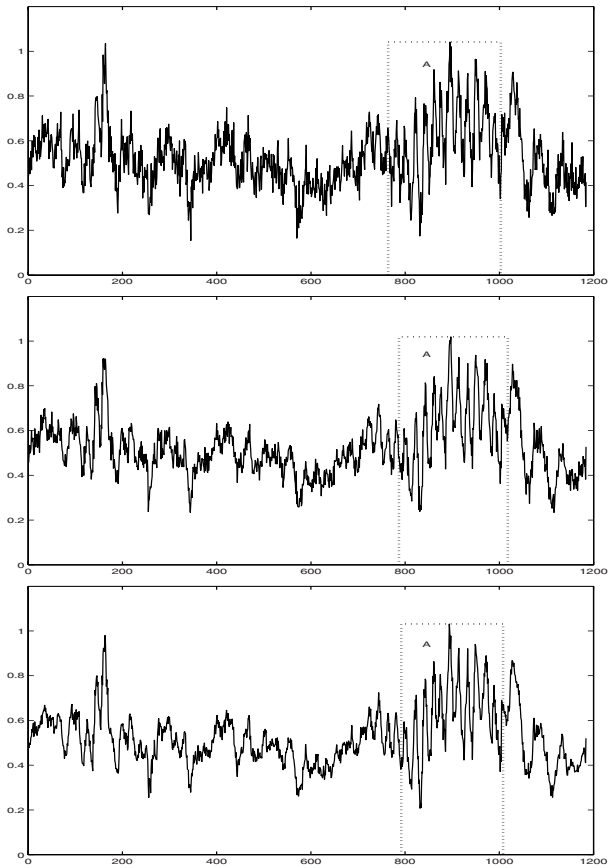

FIGURE 18. The detection results of Fig. 17 correspondingly from top to bottom by Algorithm 4.1

References

[1] Hongzhi An and Min Chen. *Non-linear Time series Analysis*. Shanghai Science & Technology Press, China, 1998.

[2] J. Doman, C. Detka, and T. Hoffman et al. Automating the sleep laboratory: Implementation and validation of digital recording and analysis. *International Journal of Biomedical Computing*, 38(3):277–290, 1995.

[3] Fei Huang and Chongxun Zheng. Automated recognition of spindles in sleep electroencephalogram base on time-frequency analysis. *Journal of Xi'An Jiao Tong University*, 36(2):218–220, 2002.

[4] N. E. Huang, Z. Shen, and S. R. Long et al. The empirical mode decomposition and the Hilbert spectrum for nonlinear and non-stationary time series analysis. *Proceedings of the Royal Society of London*, A(454):903–995, 1998.

[5] M. J. Korenberg. A robust orthogonal algorithm for system identification and time-series analysis. *Biological Cybernetics*, 60:267–276, 1989.

[6] Leukel. *Essential of Physiological Psychology*. The CV Company, USA, 1978.

[7] Jianping Liu, Shiyong Yang, and Chongxun Zheng. High resolution time-frequency analysis method for extracting the sleep spindles. *Journal of Biomedical Engineering*, 17(1):50–55, 2000.

[8] N. Pradhan and P. K. Sadasivan. The nature of dominant lyapunov exponent and attractor dimension curve of eeg in sleep. *Computers in Biology and Medicine*, 26(5):419–428, 1996.

[9] J. Pricipe, S. K. Gala, and T. G. Chang. Sleep staging automation base on the theory of evidence. *IEEE Transactions on Biomedical Engineering*, 36(5):503–509, 1987.

[10] Shannahoff-Khalsa David S., Gillin J. Christian, and etc. Ultradian rhythms of alternating cerebral hemispheric eeg dominance are coupled to rapid eye movement and non-rapid eye movement stage 4 sleep in humans. *Sleep Medicine*, 2(4):333–346, 2001.

[11] N. Schaltenbrand, R. Lengelle, and J. P. Macher. Neural network model: Application to automatic analysis of human sleep. *Computer and Biomedical Research*, 26(2):157–171, 1993.

[12] J. R. Smith, I. Karacan, and M. C. K. Yang. Automated analysis of the human sleep EEG. *Waking and Sleeping*, 2:229–237, 1978.

[13] E. Stanus, B. Lacroix, and M. Kerkhofs et al. Automated sleep coring: A comparative reliability study of two algorithms. *Electroencephalography and Clinical Neurophysiology*, 66(4):448–454, 1987.

[14] E. C. Titchmarsh. *Introduction to the Theory of Fourier Integrals*. Oxford University Press, 1948.

Zhihua Yang
Information Science School
GuangDong University of Business Studies,
Guangzhou 510320, P. R. China
e-mail: yangyangzh@tom.com

Lihua Yang
School of Mathematics and Computing Science
Sun Yat-sen University, Guangzhou 510275, P. R. China
e-mail: mcsylh@mail.sysu.edu.cn

Dongxu Qi
Faculty of Information Technology
Macao University of Science and Technology, Macao

School of Information Science and Technology
Sun Yat-sen University, Guangzhou 510275, P. R. China
e-mail: dxqi@must.edu.mo

Wavelet Analysis and Applications
Tao Qian, Mang I. Vai and Xu Yuesheng, Eds.
Applied and Numerical Harmonic Analysis, 561–574

A Wavelet-Domain Hidden Markov Tree Model with Localized Parameters for Image Denoising

Minghui Yang, Zhiyun Xiao and Silong Peng

Abstract. Wavelet-domain hidden Markov tree models have been popularly used in many fields. The hidden Markov Tree (HMT) model provides a natural framework for exploiting the statistics of the wavelet coefficients. However, the training process of the model parameters is computationally expensive. In this paper, we propose a HMT model with localized parameters which has a fast parameter estimation algorithm with no complex training process. Firstly, Wold decomposition is used to reduce the influence on the estimation of image noise variance due to texture. Secondly, coefficients in each subband are classified into two classes based on spatially adaptive thresholds. Thirdly, parameters of different class are estimated using the local statistics. Finally, the posterior state probability is estimated with an up-down step like the traditional HMT model. We apply this model to image denoising and compare it with other models for several test images to demonstrate its competitive performance.

Mathematics Subject Classification (2000). Primary 42C40; Secondary 94A08.

Keywords. Hidden Markov tree, wavelet transform, wold decomposition.

1. Introduction

In recent years, wavelet transform has become a popular tool for statistical signal processing, since it has many attractive properties, such as locality, multiresolution and compression. In many algorithms, wavelet coefficients have been modeled either as jointly Gaussian, or as non-Gaussian but independent. Jointly Gaussian models can capture the correlations between wavelet coefficients, but they are in conflict with the compression characteristic of wavelet transform. Non-Gaussian models assume the coefficients are statistical independent. However, the wavelet transform cannot completely decorrelate real-world signals, so that the assumption that the coefficients are independent is unrealistic.

This work was supported by National Natural Science Fund of China with No.60272042.

Sendur et al. [1] considered the dependencies between the wavelet coefficients and their parents. For this purpose, some non-Gaussian bivariate distributions were proposed and corresponding nonlinear shrinkage functions were derived from the models using Bayesian estimation theory. The performance can also be improved by estimating simple bivariate model in a local neighborhood [2].

Crouse et al. [3] proposed a hidden Markov tree as a statistical model for such properties of wavelet coefficients. This model first introduced the hidden state variables to match wavelet coefficients, then used Markovian dependencies between the hidden state variables to characterize the dependencies between the wavelet coefficients. For estimating the model parameters, an iterative Expectation Maximization (EM) approach was used which assumed that all wavelet coefficients and state variables within a common scale be identically distributed. Nevertheless, the training process was still computationally expensive.

Romberg et al. [4] introduced a simplified HMT model which specified the HMT parameters with just nine parameters (independent on the size of the image and the number of wavelet scales). A class of universal parameters was obtained by training a class of images, then these parameters were fixed and modeled a wide range of images. This universal HMT (uHMT) model can be very simple, because it requires no training. But the fixed parameters may be not exact for another kind of images.

Xiao et al. [5] tried to find a fast estimation technique for the HMT model parameters. They used adaptive thresholds to classify the wavelet coefficients into two classes, and estimated the model parameters by computing local statistics. This method gave better results with less run time.

We propose an image denoising algorithm for natural images. This new method not only introduces Wold decomposition into the estimation of the noise variance, but also improves Xiao's method.

The paper is organized as follows: Section 2 presents the estimation of the noise variance. In section 3, we details the improved HMT model with localized parameters. Section 4 shows the experimental results and compares with other algorithms. Finally, we conclude in section 5.

2. Estimation of the Noise Variance

2.1. Pervious Work

Image denoising is just to estimate the original signal f from a corrupted image g by removing noise n . Generally, the noise is assumed to be additive white Gaussian noise,

$$g = f + n \tag{2.1}$$

The compression property indicates that wavelet coefficients are energy compacted. Because of the orthogonal property of the wavelet transform, the noise in wavelet-domain is identical independent distributed with small magnitude. Thus,

small coefficients are more likely due to noise and large coefficients due to important signal features. Therefore, by setting small wavelet coefficients to zero, one effectively removes noise without degrading the signal.

Many wavelet thresholding methods have been discussed before. Donoho et al. [6] described a principle for spatially adaptive method which worked by shrinkage of the wavelet coefficients. They gave an asymptotic optimal threshold as the universal $\sigma_n\sqrt{2\log(N)}$, where σ_n was the standard deviation of the additive noise. These thresholds depended on the sample size N. As described in [7], deviding the threshold by 2 yields a soft threshold estimator that is close to the true value. Chang et al. [8] proposed a spatially adaptive wavelet thresholding method based on context modeling. Each wavelet coefficients was modeled as a random variable of a generalized Gaussian distrtibution with an unknown parameter estimated by its context. A good approximation to the optimal threshold which minimized the mean squared error of the soft-thresholding estimator was given as below:

$$T_B = \sigma_n^2/\sigma_x \tag{2.2}$$

where σ_n^2 was the additive noise variance and σ_x was the localized standard deviation of the signal.

The noise variance used in the threshold estimation methods is usually unknown. People often estimate it by using the robust median estimator in the highest subband $HH1$ of the wavelet transform

$$\hat{\sigma_n} = median(|Y[i,j]|)/0.6745 \tag{2.3}$$

where $Y[i,j] \in$ subband $HH1$.

2.2. Wold Decomposition Used in Estimation

To estimate the variance σ_n^2 of the noise n from the corrupted image g, we need to suppress the influence of the original image f . In the previous methods for noise variance estimation, the original figure is supposed to be a piecewise smooth signal. In the highest subband, the influence of f can be ignored and the coefficients are approximately Gaussian random variables of the noise variance σ_n^2 .

However, the assumption is not suitable for natural scene. Many real images are composed of both smooth and textured regions. So the influence of the signal f cannot be ignored in the highest subband of the wavelet transform. One can first segment the noisy image into two parts: texture region and piecewise smooth region. Then the noise variance can be estimated in the piecewise smooth region. But the segmentation is computationally expensive, and is always disturbed by the additive noise.

In the texture analysis, Francos et al. [9] had presented a unified texture model which was applicable to a wide variety of texture types found in natural images. On the basis of the two-dimensional Wold decomposition for homogeneous random fields, the texture field was decomposed into a sum of two mutually orthogonal components: a purely indeterministic component and a deterministic component.

Now we introduce the Wold decomposition into noisy natural images analysis. The noisy natural images can be decomposed into two components: a indeterministic component and a deterministic component. The indeterministic component includes the additive noise and the stochastic part in texture model. The deterministic component includes the piecewise smooth region and the deterministic part in texture model. Then the noise variance is estimated based on the indeterministic component.

The first step of the estimation algorithm is to compute the spectrum of the noisy image. The image is first zero-meaned, then the magnitude of the signal discrete Fourier transform is computed. Assumed the size of the image is N by N, the magnitude image is translated by $(N/2, N/2)$ so that the zero frequency is at the center of the frequency plane.

As the spectral measure associated with the deterministic field is singular, we need to locate the singularities in the magnitude image. The second step is to find the local maxima of the magnitude by searching a 5 by 5 neighborhood of each frequency sample.

Thirdly, the local maxima are examined for their harmonic peaks if their values are above 10% of the magnitude range. As the magnitudes of the additive noise may also act as local maxima, the threshold should be set larger than 5% which is often used in texture analysis in order to save the harmonic peaks.

Fourthly, starting from each harmonic peak, a region is grown outwards continuously until the value of the magnitude is lower than a small portion of this peak value (10% in our experiments). This region is regarded as the support region of the local peak in question. However, there still have many noise in the local peaks and their support regions. Two morphological transformations, namely closing and opening, can be used to construct a mask, which can wipe off the isolated points. The resulting support regions are obtained by selecting in the mask.

Fifthly, after the spectral support of the deterministic component is determined, the component frequencies are separated from the rest, which comprises the indeterministic component.

Finally, the noise variance is estimated from the indeterministic component.

Figure 1 shows an example of Wold decomposition using in a noisy image. The deterministic component and the indeterministic component after inverse discrete fourier transform are displayed as Figure 1 (g) and Figure 1 (h). The results of noise variance estimation compared with traditional estimation results are listed in table 1.

3. The Localized HMT Model

3.1. Wavelet-Domain HMT Model

The wavelet-domain HMT model was first proposed for statistical signal processing and analysis in [3]. The wavelet decomposition transforms the image into a multiscale representation with a quad-tree structure. The HMT model was developed by

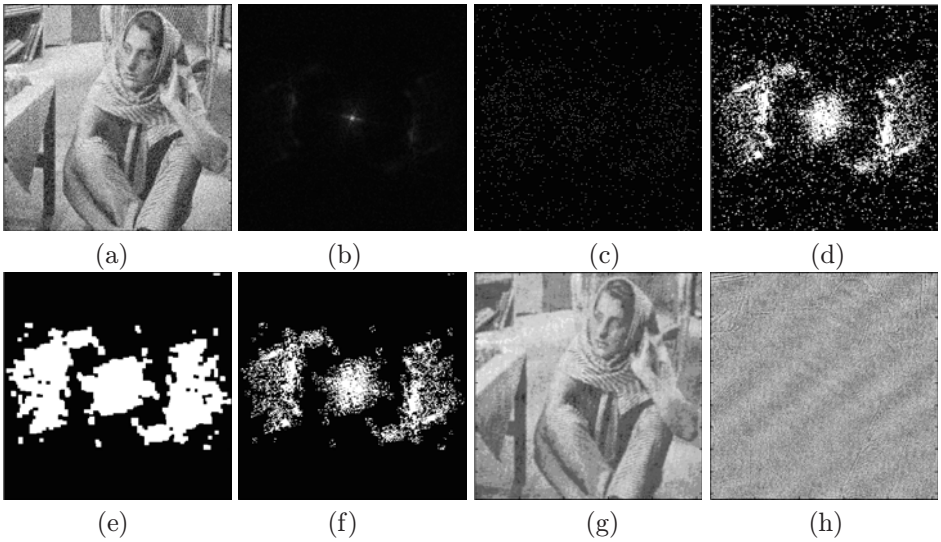

FIGURE 1. Example of Wold decomposition using in noisy image. (a) original image corrupted by noise ($\sigma_n = 0.1$), (b) the Fourier magnitude image, (c) the local maxima, (d) the support region of the local maxima, (e) the mask to wipe off the isolated points, (f) the support region in the mask, (g) the deterministic component, (h) the indeterministic component.

connecting hidden state variables vertically across scales to capture the statistical inter-scale dependencies between the wavelet coefficients of signals and images.

In the tree structure, we denote the node index as i . The scale covering the node i is denoted as j . The node i has a parent node denoted as $\rho(i)$ at the scale $j+1$, and four children nodes denoted as $c(i)$ at the scale $j-1$. Smaller j corresponds to higher resolution analysis. The set of descendants of a node i, including itself, is denoted as $T(i)$. The root node index is 1, then $T(1)$ denote the whole tree.

The wavelet coefficient and the hidden state variable of the node i are denoted as w_i and S_i respectively. In the HMT model, the wavelet coefficient w_i is conditionally independent of all other random variables given its state S_i .

To capture the non-Gaussian nature of the wavelet coefficients, we model the marginal probability $f(w_i)$ of each coefficient as a two-state, zero-mean Gaussian mixture model in this paper as

$$f_W(w_i) = \sum_{m=S,L} P_{S_i}(m) * f_{W|S}(w_i|S_i = m) \tag{3.1}$$

where $P_{S_i}(m) = p(S_i = m|w, \theta)$ denotes the conditional probability mass function (pmf) of the node i given the model parameters θ . $m = S, L$ means the state m of coefficient is small or large. The parameters for the HMT model include:

1. $P_{S_1}(m)$, the pmf for the root node S_1 .
2. $\varepsilon_{i,\rho(i)}^{m,n} = P_{S_i|S_{\rho(i)}}(m|S_{\rho(i)} = n)$, the state transition probability from the parent state variable $S_{\rho(i)}$ to its child's states S_i, where $S_i = m$ and $S_{\rho(i)} = n$.
3. $\mu_{i,m}$,$\sigma_{i,m}^2$, the mean and variance of the wavelet coefficient w_i given $S_i = m$. Generally $\mu_{i,m} = 0$.

These parameters can be grouped into a model parameter vector θ as:

$$\theta = \{P_{S_1}(m), \varepsilon_{i,\rho(i)}^{m,n}, \sigma_{i,m}^2\} \tag{3.2}$$

In image denoising, the estimation problem can be expressed in the wavelet domain as :

$$w_i = y_i + n_i \tag{3.3}$$

where w_i, y_i, and n_i denote the wavelet coefficients of the observed data, the signal and the noise, respectively.

If the HMT model $\theta = \{P_{S_1}(m), \varepsilon_{i,\rho(i)}^{m,n}, \gamma_{i,m}^2\}$ for the noise signal is estimated, $\gamma_{i,m}^2$ is the variance of the noisy wavelet coefficient w_i, then the conditional mean estimate of y_i given w_i is

$$\hat{y_i} = E[y_i|w_i, \theta] = \sum_{m=S,L} P_{S_i(m)} \frac{\sigma_{i,m}^2}{\sigma_{i,m}^2 + \sigma_n^2} w_i \tag{3.4}$$

where $\sigma_{i,m}^2 = max(0, \gamma_{i,m}^2 - \sigma_n^2)$. The final signal estimate is computed as the inverse wavelet transform of these estimates of the signal wavelet coefficients.

3.2. The Localized HMT Model

In the HMT model, the basic problem is parameter estimation. As the state of the wavelet coefficients is unobserved, direct maximum likelihood estimation is intractable. Therefore, the iterative EM approach was used in the parameters estimation.

For an n-pixel image, generally, the HMT model has approximately $4n$ parameters. These parameters need a lot of signal samples in the training step. Crouse et al. [3] used an robustly estimation by assuming that the model parameters are the same in each scale. This approach reduced the total number of the HMT model parameters from $4n$ to $4J$, where J presents the number of wavelet scales. Romberg et al. [4] reduced the number of parameters to nine, by exploiting the inherent self-similiarity of real-world images. Fan et al. [10] developed an initialization scheme for the EM algorithm to achieve more efficient HMT model training. These methods all assumed that the HMT model are identically distributed in each scale. However, the assumption are not reliable for natural images. For example, the pmf of wavelet coefficients' state in the piecewise smooth region should not equal the pmf in the texture region. Xiao et al. [5] proposed a fast parameter estimation

technique for the HMT model. The parameters in this model are localized. We improved this algorithm and incorporate it with the noise variance estimation.

3.2.1. Wavelet Coefficients Classification. As described in the previous section, Chang et al.[8] proposed a spatially adaptive wavelet thresholding method based on context modeling. These thresholds can be used in shrinkage of wavelet coefficients. Considering the compression property of wavelet transform, we can classify the wavelet coefficients into two states, large and small, by introducing the adaptive thresholds computed by equation 2.3. The estimation of noise variance has been discussed in section 2.

The needed localized standard deviation σ_x is computed as:

$$\sigma_x^2[i,j] = max(0, \frac{1}{< N[i,j] >} \sum_{[k,j]\in N[i,j]} w^2[k,j] - \sigma_n^2) \tag{3.5}$$

where $N[i,j]$ denotes the neighborhood of the location i in scale j, and $< N[i,j] >$ denotes the number of coefficients including in $N[i,j]$.

We use a binary mask $B[i,j]$ to denote the state of the wavelet coefficients, with '1' denotes 'large' state and '0' denotes 'small' state.

$$B[i,j] = \begin{cases} 0, & w[i,j] < T_B[i,j] \\ 1, & w[i,j] \geq T_B[i,j] \end{cases} \tag{3.6}$$

Because large values of wavelet coefficients tend to propagate across scales, $B[i,j]$ is modified by its parent state.

$$B[i,j] = B[i,j] * B[\rho(i), j+1] \tag{3.7}$$

3.2.2. Localized Parameters Estimation. When we have classified the wavelet coefficients into two states, we can estimate the localized parameters $\theta = \{P_{S_1}(m), \varepsilon_{i,\rho(i)}^{m,n}, \gamma_{i,m}^2\}$.

1. The pmf for the root rode S_1 in the coarsest scale J

$$P_{S_1}(m) = \frac{1}{< N[i,J] >} \sum_{[k,J]\in N[i,J]} B_m[k,J], \qquad m = 0,1 \tag{3.8}$$

   where $B_m[k,J]$ denotes the pixel whose state value is m in $B[k,J]$.

2. The state transition probability

$$\varepsilon_{i,\rho(i)}^{m,n} = \frac{\sum_{[k,j]\in N[i,j]} B_m[k,j] * B_n[\rho(k), j+1]}{\sum_{[k,j]\in N[i,j]} B_n[\rho(k), j+1]} \tag{3.9}$$

   We use the relation of two binary masks of two scales to simulate the true state transition probability.

3. The state variance of the noisy signal

$$\gamma_{i,m}^2 = \frac{\sum_{[k,j]\in N[i,j]} w^2[k,j] * B_m[k,j]}{\sum_{[k,j]\in N[i,j]} B_m[k,j]} \tag{3.10}$$

   The variance of each state is calculated in the state mask.

The estimation of state variance $\gamma^2_{i,m}$ are not consistent with Xiao's method, since the denominator is the sum of $B_m[k,j]$ instead of the whole number of $N[i,j]$.

3.2.3. Posterior State Probability Estimation. Given initial localized parameters θ, we can calculate the posterior state probability $P_{S_i}(m) = p(S_i = m|w,\theta)$ with an upward-downward step described in [3]. The state variance $\gamma^2_{i,m}$ can also be updated at the same time. Then the signal state variance $\sigma^2_{i,m}$ is computed given $\gamma^2_{i,m}$.

3.2.4. Posterior State Probability Estimation. Using equation 3.4, the signal wavelet coefficients are estimated, then the final signal estimate is computed by the inverse wavelet transform.

Because wavelet transform lack translation invariance, the denoised image exhibits Gibbs phenomena in the neighborhood of discontinuities. We use the Cycle-spinning method proposed by Coifman [11] to suppress such artifacts. Three images by shifting original noisy image in horizontal, vertical and diagonal directions respectively are denoised in the proposed method, then total four denoised images are averaged after registration. The average image is a desired image which suppresses the artifacts.

4. Experiments

We use three standard testing images, Lena, Baboon and Barbara, to demonstrate our method's effectiveness. The variances of the additive noise are 0.01, 0.04 and 0.0025. The results are compared with other denoising algorithms in [2] [3] [4] [5] [6].

The peak signal-to-noise ratio (PSNR), the estimated noise variance $\hat{\sigma_n}$ and time cost are presented in table 1 for each method. From the table, we can find that Crouse's HMT model gives good results, but with much time cost. Romberg's uHMT model gives good performance to Lena, but not very good for the other two images, because the universal parameters are not fit these two images. Donoho's soft thresholding method gives the fastest process but the worst result in these five method. Sendur's bivariate shrinkage model and Xiao's algorithm denoise the noisy images in good performances with low time costs. Our method, after including the Wold decomposition in the estimation of the noise variance, can gain the best performance in a middle time cost.

Figure 2, 3 and 4 show the comparison of the different methods on a local region. Our method outperforms all the other methods in both visual quality and PSNR performance.

5. Conclusions

In this paper, we have proposed a wavelet-domain HMT model with localized parameters and applied it to natural image denoising. The localized parameters are

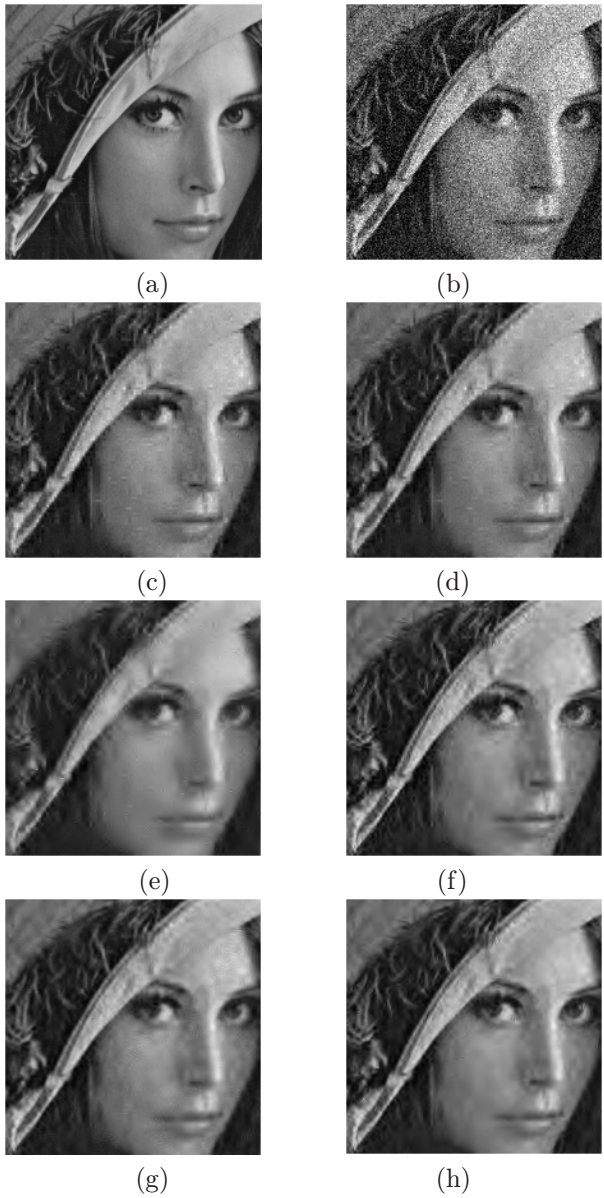

FIGURE 2. Comparing the results of various denoising methods, for Lena corrupted by noise $\sigma_n = 0.1$. (a) original image, (b) noisy image, (c) Crouse's HMT model, (d)Romberg's uHMT model, (e)Donoho's soft thresholding (f) Sendur's bivariate model (g) Xiao's fast estimation (h) our method.

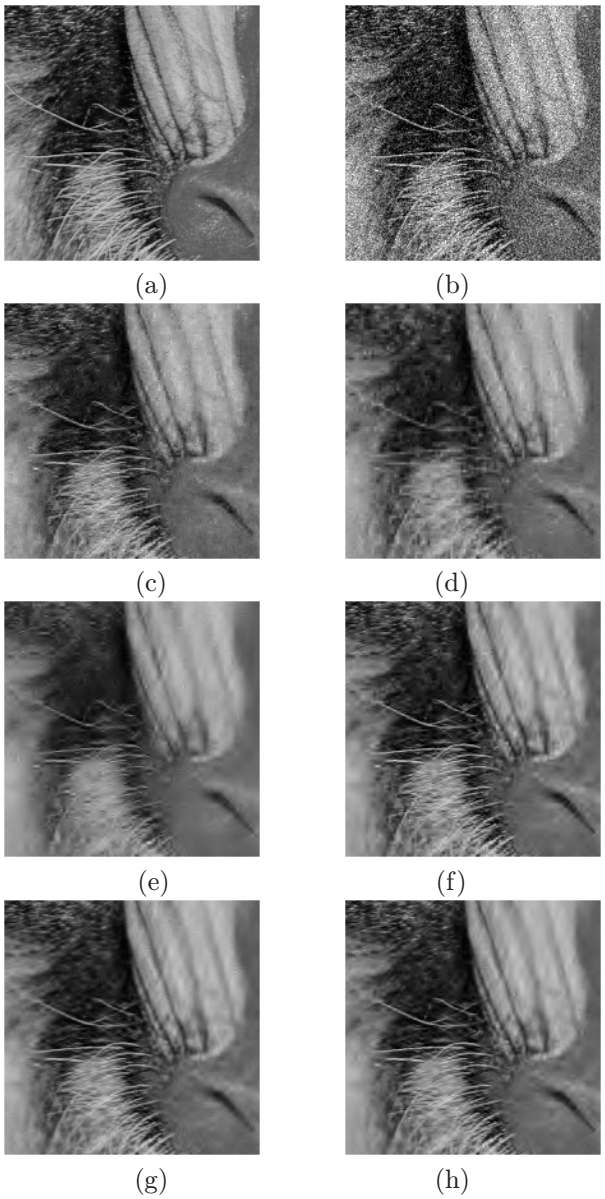

FIGURE 3. Comparing the results of various denoising methods, for Baboon corrupted by noise $\sigma_n = 0.1$. (a) original image, (b) noisy image, (c) Crouse's HMT model, (d)Romberg's uHMT model, (e)Donoho's soft thresholding (f) Sendur's bivariate model (g) Xiao's fast estimation (h) our method.

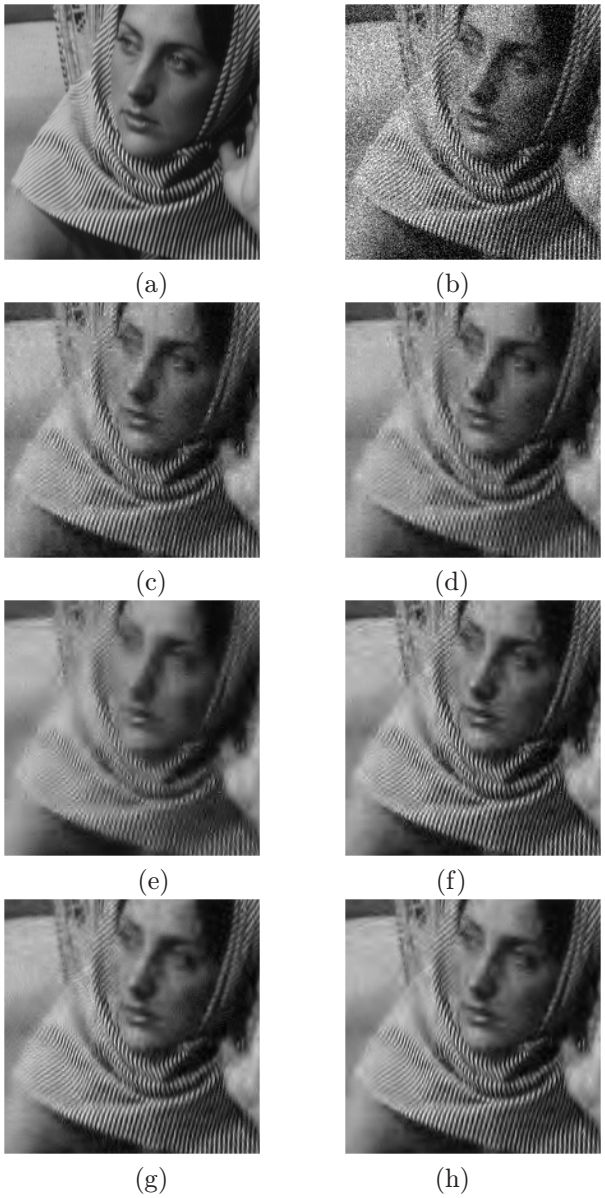

FIGURE 4. Comparing the results of various denoising methods, for barbara corrupted by noise $\sigma_n = 0.1$. (a) original image, (b) noisy image, (c) Crouse's HMT model, (d)Romberg's uHMT model, (e)Donoho's soft thresholding (f) Sendur's bivariate model (g) Xiao's fast estimation (h) our method.

TABLE 1. Comparison of different algorithms

Test images	Qualities	Crouse's HMT model	Romberg's uHMT model	Donoho's soft thresholding	Sendur's bivariate model	Xiao's fast estimation	Our method
Lena $\sigma_n = 0.1$ PSNR = 20.0205db	PSNR (db)	29.1688	29.2112	27.7566	29.6220	29.6101	30.2547
	$\hat{\sigma}_n$	0.1013	0.1013	0.1006	0.1006	0.1006	0.0995
	Time cost (s)	137.8	8.701	1.204	1.468	8.765	25.347
Lena $\sigma_n = 0.2$ PSNR = 13.9636db	PSNR (db)	25.9545	25.5650	25.2048	26.2453	25.9562	27.0709
	$\hat{\sigma}_n$	0.2022	0.2022	0.1993	0.1993	0.1993	0.1879
	Time cost (s)	106.9	9.077	1.377	1.313	8.893	24.578
Lena $\sigma_n = 0.05$ PSNR = 26.0313db	PSNR (db)	32.5526	28.4025	30.4443	32.9460	32.9087	33.2430
	$\hat{\sigma}_n$	0.0521	0.0521	0.0512	0.0512	0.0512	0.0511
	Time cost (s)	126.3	9.717	1.298	1.125	8.925	23.251
Baboon $\sigma_n = 0.1$ PSNR = 19.9942db	PSNR (db)	24.4567	22.2999	21.8771	24.0663	24.2922	24.5978
	$\hat{\sigma}_n$	0.1095	0.1095	0.1084	0.1084	0.1084	0.1035
	Time cost (s)	123.6	8.576	1.283	1.156	8.706	24.638
Baboon $\sigma_n = 0.2$ PSNR = 13.9996db	PSNR (db)	21.5765	20.4227	20.4180	21.2228	21.4799	21.8824
	$\hat{\sigma}_n$	0.2057	0.2057	0.2031	0.2031	0.2031	0.1840
	Time cost (s)	86.78	8.639	1.314	1.469	9.015	24.823
Baboon $\sigma_n = 0.05$ PSNR = 26.0461db	PSNR (db)	27.8668	27.3293	23.7595	27.4995	27.5742	27.8846
	$\hat{\sigma}_n$	0.0645	0.0645	0.0626	0.0626	0.0626	0.0625
	Time cost (s)	97.32	8.857	1.325	1.14	8.702	24.417
Barbara $\sigma_n = 0.1$ PSNR = 19.9875db	PSNR (db)	26.6408	25.2643	24.5679	27.1052	27.6340	27.9056
	$\hat{\sigma}_n$	0.1041	0.1041	0.1023	0.1023	0.1023	0.1012
	Time cost (s)	124.1	8.826	1.247	1.234	8.927	23.729
Barbara $\sigma_n = 0.2$ PSNR = 13.9940db	PSNR (db)	23.2911	22.6676	22.6780	23.7879	24.2670	24.5139
	$\hat{\sigma}_n$	0.2041	0.2041	0.2013	0.2013	0.2013	0.1918
	Time cost (s)	78.23	8.326	1.325	1.406	8.676	24.182
Barbara $\sigma_n = 0.05$ PSNR = 26.0127db	PSNR (db)	30.2944	28.1496	27.2639	30.9790	31.4332	31.8015
	$\hat{\sigma}_n$	0.0557	0.0557	0.0536	0.0536	0.0536	0.0526
	Time cost (s)	142.7	9.248	1.296	1.203	8.910	22.589

estimated by computing the statistics of the classified wavelet coefficients based on spatial adaptive thresholding method. Wold decomposition method is introduced in this method to estimate the noise variance. After separating the deterministic component of texture regions from noise, the estimation is more accurate. Experiments show that the proposed algorithm not only reduces the computational complexity, but also gives superior performance than other methods.

However, as shown in the figures, the result of the denoised image is less than satisfactory if there are too many texture regions in the image. This kind of images need further discussion in order to find some suitable algorithms for these images.

Further work will concentrate on extending this localized HMT model to other applications, such as segmentation, classification and compression.

References

[1] L. Sendur and I. W. Selesnick, "Bivariate shrinkage functions for wavelet-based denoising exploiting interscale dependency," IEEE Transactions on Signal Processing, Volume 50, No. 11, pp. 2744-2756 November 2002.

[2] L. Sendur and I. W. Selesnick, "Bivariate shrinkage with local variance estimation," IEEE Signal Processing Letters, Volume 9, No. 12, pp. 438-441 December 2002.

[3] M. S. Crouse, R. D. Nowak, and R. G. Baraniuk, "Wavelet-based statistical signal processing using hidden markov models," IEEE Transactions on Signal Processing, Volume 46, pp. 886-902, April 1998.

[4] J. K. Romberg, H. Choi, and R. G. Baraniuk, "Bayesian tree -structured image modeling using wavelet domain hidden markov models," IEEE Transactions on Image Processing, Volume 10, No.7, pp. 1056-1068, July 2001.

[5] Zhiyun Xiao, Wei Wen, and Silong Peng. "A fast classification-based parameter estimation technique for wavelet-domain HMT model," Advanced Concepts for Intelligent Vision Systems (ACIVS'04), August 2004, Brussels, Belgium.

[6] D. L. Donoho, I. M. Johnstone, "Ideal spatial adaptation by wavelet shrinkage," Biometrika, Volume 81, pp. 425-455, 1994.

[7] S. Mallat, "A wavelet tour of signal processing," second edition, Academic Press, 1998.

[8] S. G. Chang, B. Yu, and M. Vetterli, "Image denoising via lossy compression and wavelet thresholding," in Proc. IEEE Int. Conf. Image Processing, Volume 1, pp. 604-607, October 1997.

[9] J. M. Francos, A. Z. Meiri, and B. Porat, "A unified texture model based on a 2-D Wold-like decomposition," IEEE Transactions on Signal Processing, Volume 41, No.8, pp. 2665-2678, August 1993.

[10] G. L. Fan, X. G. Xia, "Improved hidden markov models in the wavelet-domain," IEEE Transactions on Signal Processing, Volume 49, Issue 1, pp. 115-120, January 2001.

[11] R. R. Coifman, D. L. Donoho, "Translation-invariant de-noising," in Wavelets and Statistics, A. Antoniadis and G. Oppenheim, Eds. New York. Lecture Notes in Statistics, Springer-Verlag, pp. 125-150, 1995.

Minghui Yang
National ASIC Design Engineering Center
Institute of Automation
Chinese Academy of Sciences
Beijing 100080
China
e-mail: minghui.yang@ia.ac.cn

Zhiyun Xiao
National ASIC Design Engineering Center
Institute of Automation
Chinese Academy of Sciences
Beijing 100080
China
e-mail: zhiyun.xiao@ia.ac.cn

Silong Peng
National ASIC Design Engineering Center
Institute of Automation
Chinese Academy of Sciences
Beijing 100080
China
e-mail: silong.peng@ia.ac.cn